Carbonate alteration associated with lamprophyres and orogenic gold, Southern Alps, New Zealand

Anne Katrin Wellnitz

A thesis submitted for the degree of
Doctor of Philosophy
at the University of Otago, Dunedin,
New Zealand

April 2017

Abstract

In this thesis the chemistry and textures of void-filling hydrothermal carbonate and associated altered metamorphic and lamprophyric rock in western Otago, New Zealand, were studied. With this information a detailed model of the mobility behaviour of various elements is established. Conduits for CO_2-bearing fluids were faults, joints, folds and, in the northernmost part of the study area, volcanic diatremes. The southernmost study area lies in the Shotover Valley, where many of the larger fault zones are auriferous. Throughout the studied area, many larger faults, including the gold-bearing ones, strike W to NW. In addition to these faults, there are also structures (i.e. veins and fold hinges) that trend northwards. The formation of most of the structures happened in the Oligocene -Miocene and was closely connected to the movements along the newly forming Alpine Fault and reverse movements along the Moonlight Fault.

Adjacent to the fluid conduits, the wall rock has been extensively altered. This alteration is especially obvious in greenschist and the altered rock has a pale creamy colour due to the replacement of various metamorphic phases (epidote, chlorite, actinolite) mostly by Fe-bearing carbonate and phyllosilicates. In quartzo-feldspathic greyschists the same metamorphic minerals as in greenschist are unstable in response to the incoming CO_2-bearing fluid. However, as those minerals are less abundant in greyschist, the alteration is less obvious.

Textural and chemical data of the individual metamorphic and hydrothermal minerals forming during replacement were obtained using SEM, microprobe and LA-ICP-MS. The hydrothermal minerals replacing metamorphic minerals describe a diverse array of mineral textures, which give insight into relative solubility of the different mineral phases. The replacement reactions also attest to mobility and immobility of the different major and trace elements. For example, in the breakdown of epidote in rocks which contain metamorphic muscovite, Al is mobilised potentially in F-OH complexes and transported away from the original epidote site, whereafter carbonate forms. In cases where there is no muscovite in the rock, epidote is replaced by muscovite, hence resulting in local loss of Ca. At the same time, the REE of this epidote are also mobilised on microscopic scale (µm to mm) as the growing muscovite cannot accommodate the REE in its crystal structure. These REE are then incorporated in the ankerite replacing the chlorite. On a macroscopic scale (cm to m), Sr, Ba, Rb, K and Cs show the largest mobility during the hydrothermal alteration (sometimes up to 20 times enrichment in the altered rock compared to the unaltered rock) and are often brought into the rock by the hydrothermal fluid. The REE and Al, on the other hand, do not show any signs of mobility at that scale. Overall, of all elements in alteration-sensitive metamorphic minerals, only titanium is shown to be immobile throughout, also on µm scale.

In addition to carbonate forming in the hydrothermal alteration halo around fluid conduits, carbonate is also a common void-filling mineral, such as fractures and vesicles. The chemical composition of these carbonates shows that the different elements are controlled by various factors. Contents of Ca, Sr, Mg, Fe, Mn and according ratios show that these elements can travel metres to tens of metres in the fluid before they are precipitated in carbonate. REE contents and patterns in the carbonate are the product of the interplay between fluid- and rock-dominated processes; in cases were only little rock needs to be leached to form the carbonate, the REE patterns are very similar to the wall rock. In cases where relatively large rock volumes need to be leached to provide the main components of the void-filling carbonate, the REE content of the carbonate is dominated by fluid-controlled processes and the REE patterns reflect the relative solubility of the different REE in the fluid.

Radiogenic isotopic compositions (Nd, Sr) of void filling carbonates and wall rock show that Nd and Sr in the carbonates travel different distances in the fluid conduit; Nd isotopic ratios show that the

bulk of the LREE are transported for short distances in the fluid passing through the void (cm to dm), whereas Sr isotopic ratios confirm that Sr can be for transported many meters by the aqueous fluid. Stable isotope data (C, O) in conjunction with assessing the regional geological and tectonic settings permitted to reconstruct the history and sources of the fluids in the studied areas; after taking temperature effects on isotope fractionation and relative sample locations into account, it is concluded that two main fluid types were present in the studied area. One of these is a mixture of meteoric and magmatic components, while the other fluid interacted extensively with the metamorphic rock in Western Otago, but was most likely originally meteoric-derived water. Only in the volcanic diatremes is there indication that these two fluid types mix. Outside the diatreme, the isotopic composition of the carbonate give evidence that only the second mentioned fluid type was present, including in the auriferous structures and there is no indication that the gold-bearing and magmatic system had any connection to each other

Acknowledgments

A huge Thank You to:

- Morgan Farrant, for being patient and standing my continuous complaining about my PhD. For having critical questions and for being able to look at things differently. - You have been invaluable for the progress of this thesis and for me staying sane-ish.
- James Scott, for helping make this thesis consistent and understandable. For helpful comments, questions and suggestions. For showing me how to do field work New Zealand-style.
- Mike Palin, for great discussions about chemistry and uncountable hours on the LA-ICP-MS analysing minerals. For making the most complex Excel spread sheets in the department.
- Candace Martin, for spending hours and hours with and for me in the clean lab. Thanks for sharing your knowledge with me.
- my examiners -Dave Craw, Travis Horton and Sandra Piazolo- whose critical remarks have helped immensely in improving this thesis, both scientifically and linguistically.
- Daphne Lee, for being a great convenor.
- Scarlett, Sheepy, Goaty, Monty, Carrot and Kumera, for being the happy animals they are.
- my father, for looking after the dogs and holding the fort.
- Lauren Farmer, for telling me about tungsten and REE and being an entertaining and tidy flatmate.
- Nichole Moerhuis, for all the fun times at Uni and the great discussions about geochemistry.
- The Governor's Cafe in Dunedin, for all the coffee. Much of this thesis was written on their premises - thanks for not kicking me out.
- my school, for teaching me how to use Microsoft Excel.
- Brent Pooley, for making countless thin sections for me and for always being extremely helpful.
- Damian Walls, Luke Easterbrook and Dee Roben, for all the support over the years.
- Gemma, Jordan and Madison, for carrying my rocks out of the mountains.
- Robert van Hale and Diane Clark of the Isotrace Lab at Otago University, for analysing all those carbonate samples.
- Greg Holk, for analysing carbonate and quartz for me.
- Dominik Hezel and Frank Wombacher at Bonn University for letting me use their clean lab and instruments.

Table of contents

CHAPTER 1- AN INTRODUCTION 18
1.1) Hydrothermal systems, gold, and alkaline magmatic rocks 19
1.2) Regional Geology 21
1.2.1- The Otago Schist 22
1.2.2- Textural zones 22
1.3) Geological history of western Otago 23
1.3.1- The 1st Episode: Metamorphism of the schist and ductile deformation (Rangitata Orogeny) 23
1.3.2-The 2nd Episode: Exhumation of the Otago Schist and marine transgression 24
1.3.3- The 3rd Episode: Deformation during the early Kaikoura Orogeny 24
1.3.3.1: The Alpine Fault 24
1.3.3.2: The Moonlight Fault 25
1.4) The Alpine Dike Swarm 26
CHAPTER 2-THE STUDY AREAS AND THEIR GEOLOGICAL FEATURES 28
2.1) Location and overall structure of the study areas 28
2.1.1- Study areas 28
2.1.1.1: Study area 1-Bullendale and Copper Creek near Mt Aurum in the Shotover Valley 28
2.1.1.2: Study area 2-Treble Cone and Black Peak area 28
2.1.1.3: Study area 3-Red Rock 28
2.1.1.4: Study area 4-Mt Alta and the eastern flank of Niger Peak 29
2.1.2-Methods 31
2.1.2.1: Naming of samples 31
2.1.2.2: Scanning Electron Microscope 32
2.1.2.3: Microprobe 33
2.1.2.4: Cathodoluminescence 33
2.1.2.5: Chemical analyses of whole rock 34
2.2) Mineralogy and textures of metamorphic rocks in the Otago Schist 35
2.2.1-Greyschist 35
2.2.2-Greenschist 36
2.2.3-Chert, marble and ultramafics. 38
2.3) Structures and features without affiliation to magmatic rocks 39
2.3.1- Cenozoic structures in the footwall of the Moonlight Fault near Mt Aurum 39
2.3.1.1: Folds 39
2.3.1.2: Veins associated with kink folds 40
2.3.1.3: NW-W- trending faults 44
2.3.1.4: Gold mineralised structures 44
2.3.1.4-1: Bullendale Reef 44
2.3.1.4-2: Copper Creek Fault 46

2.3.1.5: Joints and associated veins and faults 49
2.3.2- Cenozoic structures and features around Treble Cone and Black Peak 51
2.3.3- Red Rock-Cenozoic structures west of the Moonlight Fault 52
2.3.4- Discussion of the non-magmatic structures 53
2.3.4.1: Silicified breccias 54
2.3.4.2: Joints 55
2.3.4.3: Tectonic model 56
2.4) Geological features associated with diatremes of the Alpine Dike Swarm 59
2.4.1- Niger Diatreme 60
2.4.1.1: Lamprophyre dikes 60
2.4.1.2: The breccia of Niger Diatreme 61
2.4.1.2-1: The components 61
2.4.1.2-2: Breccia matrix 64
2.4.2- Mount Alta Diatreme 65
2.4.2.1: Lamprophyre dikes in the diatreme 65
2.4.2.2: Diatreme Breccia 66
2.4.2.2-1: The components 66
2.4.2.2-2: Breccia texture (Components + Matrix) 67
2.4.2.3: Quartz Reef 69
2.4.2.4: Veins and other void fillings 70
2.4.2.4-1: Veins and vesicle fillings in lamprophyre 70
2.4.2.4-2: Veins in the clastic diatreme breccias 72
2.4.2.4-3: Veins in greyschist blocks 72
2.4.3-Summary and interpretation of the features associated with the diatremes 72
2.4.3.1: Structure of the diatreme breccias 72
2.4.3.2: Hydrothermal alteration 73
2.4.3.3: Silicified faults and their structural relationship to the diatremes 73
2.4.3.4: Structure and evolution of the diatremes 73
2.6) Summary 75
CHAPTER 3: REACTIONS AND TEXTURES ASSOCIATED WITH HYDROTHERMAL ALTERATION OF OTAGO SCHIST 76
3.1) Methods and samples 77
3.2) Alteration of metamorphic rock -Textures and mineral reactions 78
3.2.1- Hydrothermal alteration in greyschist 79
3.2.1.1: Alteration of greyschist associated with kink-folds - the Murdock Creek Transect. 79
3.2.1.2: Alteration of greyschist associated with silicified fault breccias - the Mt Alta Transect. 81
3.2.2- Alteration of greenschist 84
3.2.2.1: Alteration of greenschist poor in metamorphic muscovite - the Bullendale Transect 84
3.2.2.2: Alteration of greenschist rich in metamorphic muscovite 90
3.2.2.2-1: The Treble Cone Transect 90

3.2.2.2-1: TheBlack Peak Transect 95
3.2.2.3: Examples of alteration in greenschist at Red Rock 97
3.3) Discussion 100
3.3.1- Metamorphic minerals and their replacement mineralogy 101
3.3.1.1: Metamorphic muscovite 102
3.3.1.2: Biotite 103
3.3.1.3: Actinolite 104
3.3.1.4: Chlorite 105
3.3.1.5: Epidote 106
3.3.1.6: Calcite in leucocratic layers 108
3.3.1.7: Titanite 109
3.3.1.8: Sulphides and sulphates 109
3.3.2- Relative tolerance of minerals to CO_2 in the fluids 110
3.3.3- Mineral replacement mechanisms 111
3.4) Conclusions 111
CHAPTER 4: CHEMICAL CHARACTERISTICS OF GOLD-BARREN ALTERATION HALOS AND HOW THEY COMPARE TO GOLD-ASSOCIATED ONES 113
4.1) Methods 114
4.1.1-Whole rock chemistry 114
4.1.2-Mineral trace element composition of minerals 114
4.2) Whole rock chemistry 116
4.2.1- Chemical composition of unaltered metamorphic rock 116
4.2.2- Volume changes during hydrothermal alteration 118
4.2.2.2: Volume and mass changes 118
4.2.2.3: Immobile elements and the mass correction factor 120
4.2.2.4: Values used for comparison 122
4.2.2.5: Outliers 123
4.2.3-Changes of rock chemistry across the alteration halo 124
4.2.3.1: Major elements 124
4.2.3.2: Rare Earth elements 126
4.2.3.3: Large ion lithophile elements 126
4.2.3.4: Chalcophile elements and other metals 128
4.2.3.4: Volatiles 130
4.2.4-Discussion 131
4.3) Composition of metamorphic and hydrothermal minerals 135
4.3.1 - Albite 135
4.3.2 - Metamorphic micas- Muscovite and biotite 136
4.3.3 - Actinolite 138
4.3.4 - Metamorphic chlorite 139

4.3.4.1: Ankerite (partly) replacing chlorite 140
4.3.5 - Epidote 141
4.3.5.1: Hydrothermal muscovite replacing epidote in the Bullendale greenschist 141
4.3.6 - Metamorphic calcite in leucocratic layers 142
4.3.6.1: Ankerite replacing metamorphic calcite in leucocratic layers and other hydrothermal ankerite in TP7A 144
4.3.7- Poikiloblastic calcite spots and anti-axial veins 145
4.3.7.1: Ankerite replacing the calcite in the poikiloblastic spots 145
4.3.8- Titanite and its replacement products 148
4.3.9 -Discussion 148
4.3.9.1: Metamorphic minerals 149
4.3.9.2: Hydrothermal minerals replacing metamorphic minerals 151
4.3.9.2-1: Epidote, chlorite, actinolite and titanite replacement in BUL3C 151
4.3.9.2-2: Epidote and chlorite replacement in the Treble Cone Transect 153
4.3.9.2-3: Calcite replacement by ankerite 154
4.3.9.3: On the Mg:Fe ratio of metamorphic minerals, the replacing ankerite and sulphides 155
4.4) Synthesis of the textural and chemical changes in the studied alteration halos 156
4.4.1- Mineralogical and chemical differences between the different Transects 156
4.4.2-Chemistry of the fluid 157
4.4.3 - Comparison to mesothermal gold deposits in the Shotover and in other parts of the world 158
4.5) Conclusions 160
CHAPTER 5) MAJOR AND TRACE ELEMENT CHEMISTRY OF HYDROTHERMAL AND MAGMATIC CARBONATE .. 162
5.1) Samples and methods 162
5.2) Overview of texture and chemistry of carbonate 162
5.2.1- Veins and faults associated to kink folds 163
5.2.2 - Carbonate in NW dipping fault at Murdoch Creek 165
5.2.3 - Veins in Greenschist at Bullendale 165
5.2.4 - Veins in Greenschist at Red Rock 166
5.2.5-Carbonate at Mt Alta Diatreme 169
5.2.5.1: Veins in several metres big greyschist block in the diatreme breccia 169
5.2.5.2: Veins and vesicle fillings in little-altered lamprophyre 170
5.2.5.3: Sparry veins in highly altered lamprophyre and carbonate in their wall rock 171
5.2.5.4: Clastic fine-grained breccia at Mt Alta 174
5.2.6-Silicified fault breccias 175
5.2.7- Ocelli in lamprophyre 177
5.2.8-Ankeritic marble component in Niger Diatreme 178
5.3) Comparison between the analysed hydrothermal carbonates 178
5.3.1 - Major components-Ca, Mg. Fe, Mn 179
5.3.2-Trace elements-Sr, Ba, Pb, Th, U 180

5.3.3- REE content and patterns 182
5.4) Discussion 185
5.4.2- Abundance of divalent ions (Ca, Mg, Fe, Mn, Sr) 186
5.4.2.1: Whole rock chemistry and element availability 186
5.4.2.2: Lithology- associated controls on carbonate chemistry 188
5.4.2.3: Setting-specific carbonate chemistry 189
5.4.2.3-1: Carbonate in veins at Mt Alta. 190
5.4.2.3-2: Carbonate in and around silicified fault breccias 190
5.4.2.3-3: Carbonate veins at Red Rock 191
5.4.3- Pb, Th and U in the hydrothermal carbonate 192
5.4.4- Rare Earth Elements in carbonate 192
5.4.4.1: REE availability 193
5.4.4.2: Processes controlling the carbonate's REE content 195
5.4.4.3: Summary of the REE chemistry of hydrothermal carbonate 198
5.4.4.4: REE in magmatic ocelli 199
5.4.5- Anomalies in REE patterns in carbonate 200
5.5) Conclusions 201
CHAPTER 6) ISOTOPE GEOCHEMISTRY OF VEINS AND ROCKS 203
6.1) Methods 203
6.1.1-Radiogenic isotopes 204
6.1.2- Stable isotopes 205
6.2) Radiogenic isotopes of rocks and associated carbonate 206
6.2.1- Age correction 206
6.2.2- Isotope ratios of unaltered rock and metamorphic calcite 207
6.2.3- Variation of $^{87}Sr/^{86}Sr$ across alteration halos 208
6.2.4- Discussion 208
6.3) Radiogenic isotope ratios of hydrothermal, metamorphic and magmatic carbonate 210
6.3.1- Strontium 210
6.3.2- Neodymium 212
6.3.3- Discussion 213
6.4) Stable Isotopes - carbon and oxygen 215
6.4.2- Isotope ratio variations across alteration halos 215
6.4.3- Stable and radiogenic isotopic ratios of void-filling carbonate 218
6.4.4- Discussion 218
6.5) Isotopic composition of the fluid 219
6.5.1- Physical conditions of crystallisation - temperature 219
6.5.1.1: Temperature of unaltered wall rock 219
6.5.1.2: Temperature of vein precipitation 220
6.5.2- Isotopic composition of the fluid precipitating the carbonate 220

6.6) Sources of carbon and oxygen in the fluid 223
6.6.1- Source of fluid type 1 225
6.6.2- Sources of components in fluid type 2 225
6.2.2.1: Possibility 1: Fluid from dehydration during metamorphism 225
6.6.2.2: Possibility 2: Fractionated magmatic fluid 226
6.6.2.3: Possibility3: Deeply circulating meteoric fluid 228
6.6.3-Summary of potential sources for volatiles in the fluids 231
6.7) Fe isotopic composition of whole rocks and selected metamorphic and hydrothermal minerals 231
6.7.1- Methods 231
6.7.2- Results 232
6.7.3- Discussion 232
6.7) Conclusions 234
CHAPTER 7) A SYNTHESIS 235
7.1) Mineral reactions 235
7.1.1- Specific mineral reactions 236
7.2) Element mobility in the alteration halo and the fluid conduit 237
7.2.1- Chemistry of void-filling carbonate 238
7.3) Source of the volatile components in the fluids 239
7.4) Remaining questions and future work 240
REFERENCES 242

List of figures

Fig. 1.1) Location of study areas and important Cenozoic features. **18**
Fig. 1.2) Terranes, major faults and extent of Haast Schist in the South Island. **22**
Fig. 1.3) Study areas relative to terranes, textural zones and metamorphic zones. **23**
Fig. 1.4) Map of major Cenozoic features in western Otago. **26**
Fig. 2.1.1) Topographical map with locations of the 4 main study areas. **28**
Fig. 2.1.2) Location of the outcrops and surrounding geology of study area 1. **29**
Fig. 2.1.3) Geology around Treble Cone and Black Peak with outcrop locations. **30**
Fig. 2.1.4) Geology around Red Rock and the Shotover Saddle with outcrop locations. **31**
Fig. 2.1.5) Location and geology around the studied diatremes. **32**
Fig. 2.2.1) Psammitic schist at Treble Cone. **35**
Fig. 2.2.2) Greenschist at Treble Cone and Red Rock. **36**
Fig. 2.2.3) Greenschist analysed in this study. **37**
Fig. 2.2.4) Impure marble collected by A.F. Cooper. **38**
Fig. 2.3.1) Stereoplot of orientations of foliation and folds. **39**
Fig. 2.3.2) Various textures in folded rock at Copper Creek. **40**
Fig. 2.3.3) Kink folds at Murdoch Creek and related micro-textures. **42**
Fig. 2.3.4) Mesh-like carbonate interwoven with quartz in vein. **43**
Fig. 2.3.5) Kink fold hinges are cut by NW striking joints and faults. **44**
Fig. 2.3.6) NW-trending fault zones at Bullendale and Copper Creek. **45**
Fig. 2.3.7) Images of a silicified breccia (probably) of the Bullendale Reef. **46**
Fig. 2.3.8) Structures and textures at the Copper Creek Fault. **47**
Fig. 2.3.9) Quartz-rich rocks of the Copper Creek Fault. **48**
Fig. 2.3.10) Different structural and textural features at outcrop B3. **50**
Fig. 2.3.11) Kink folds in the Treble Cone-Black Peak area. **52**
Fig. 2.3.12) Greenschist with kink folds and co-genetic ankerite veins. **52**
Fig. 2.3.13) Texture and accessory minerals of thick carbonate veins at Red Rock. **53**
Fig. 2.3.14) Schematic model of the change in orientation of several tectonic features. **57**
Fig. 2.4.1) Lamprophyre dikes at Mt Alta Diatreme. **59**
Fig. 2.4.2) Magmatic and alteration-related textures in lamprophyre. **61**
Fig. 2.4.3) Breccia from the central part of Niger Diatreme. **62**
Fig. 2.4.4) Alteration style across component. **62**
Fig. 2.4.5) Albite in marble-like rock components and growth zoning of carbonate. **63**
Fig. 2.4.6) Textures of ankeritic marble component. **63**
Fig. 2.4.7) Texture of the diatreme matrix. **64**
Fig. 2.4.8) Lamprophyre dikes and sills of lamprophyre at Mt Alta. **65**
Fig. 2.4.9) Component of greyschist in the diatreme breccia. **66**
Fig. 2.4.10) Medium-grained and fine-grained breccia in the diatreme. **67**
Fig. 2.4.11) Components and textures of the breccia in the diatreme. **68**
Fig. 2.4.12) Quartz reef at Mt Alta. **69**

Fig. 2.4.13) Secondary vesicle fillings in little-altered lamprophyre at Mt Alta. **70**
Fig. 2.4.14) Ankeritic bodies or veins in highly altered lamprophyre at Mt Alta. **71**
Fig. 2.4.15) Ankeritic veins in a greyschist block in the diatreme at Mt. Alta. **72**
Fig. 2.4.16) Profile across diatremes and reconstruction of Miocene erosion surface. **75**
Fig. 3.2.1) Alteration of greyschist at Bullendale. **79**
Fig. 3.2.2) BSE images of unaltered and altered greyschist. **80**
Fig. 3.2.3) Hydrothermal replacement textures in greyschist at Bullendale. **81**
Fig. 3.2.4) Alteration associated with a quartz reef near Mt Alta Diatreme. **82**
Fig. 3.2.5) Hydrothermal replacement textures in greyschist at Mt Alta. **83**
Fig. 3.2.6) Texture and chemistry of hydrothermal muscovite and carbonate. **83**
Fig. 3.2.7) Greenschist samples of Bullendale Transect. **84**
Fig. 3.2.8) BSE image of unaltered greenschist. **85**
Fig. 3.2.9) Calcite in greenschist. **85**
Fig. 3.2.10) Replacement textures of actinolite and titanite. **87**
Fig. 3.2.11) Replacement textures in the alteration halo. **88**
Fig. 3.2.12) Texture in the completely altered greenschist. **89**
Fig. 3.2.13) Veins in the centre of the alteration halo in BUL3C and BUL4C. **89**
Fig. 3.2.14) Fault and vein producing alteration halos at outcrop TP7. **91**
Fig. 3.2.15) Texture of unaltered greenschist. **91**
Fig. 3.2.16) Replacement textures in moderately altered greenschist. **93**
Fig. 3.2.17) Replacement textures in altered greenschist. **93**
Fig. 3.2.18) Replacement textures in pervasively altered greenschist. **94**
Fig. 3.2.19) Breccia from the fault causing the hydrothermal alteration halo. **95**
Fig. 3.2.20) BSE image of unaltered mica-rich greenschist. **95**
Fig. 3.2.21) Replacement textures in altered greenschist. **97**
Fig. 3.2.22) Carbonate textures in altered greenschist. **98**
Fig. 3.2.23) Metamorphic and replacement textures in greenschist at Red Rock. **99**
Fig. 3.3.1) Model of the change of some parameters during calcite replacement. **108**
Fig. 4.2.1) Composition of unaltered green- and greyschist. **117**
Fig. 4.2.2) Chondrite normalised REE patterns of unaltered green- and greyschist. **118**
Fig. 4.2.3) Immobile vs. immobile elements and immobile vs. mobile elements. **119**
Fig. 4.2.4) Uncorrected and mass-corrected concentrations of immobile elements. **122**
Fig. 4.2.5) Changes of Na, Si and Al concentration across the alteration halos. **123**
Fig. 4.2.6) Changes of CaO, MgO, FeO, and MnO concentrations across alteration halos. **124**
Fig. 4.2.7) REE patterns of samples across the alteration halos. **125**
Fig. 4.2.8) Changes of LILE concentrations across the alteration halos. **127**
Fig. 4.2.9) Concentrations of W, Ta, Sn, Th, U across the alteration halos. **128**
Fig. 4.2.10) Concentrations of chalcophile elements across the halo in the T4 set. **129**
Fig. 4.2.11) Changes of concentrations of C and S in the T4 set. **130**
Fig. 4.2.12) Trend of total Na and not albite bound Si and Al across the alteration halos. **132**
Fig. 4.2.13) K/Cs vs. K/Rb and Ca/ Ba vs. Ca/Sr of unaltered and most altered samples. **134**

Fig. 4.3.1) Selected major and trace element concentrations in albite. **136**
Fig. 4.3.2) Element concentrations in metamorphic micas and their replacements. **137**
Fig. 4.3.3) Selected element concentrations in actinolite and the replacing ankerite. **138**
Fig. 4.3.4) Selected element concentrations in chlorite. **139**
Fig. 4.3.5) Element concentrations of chlorite and ankerite replacing chlorite. **140**
Fig. 4.3.6) Selected major and trace element concentrations in epidote. **141**
Fig. 4.3.7) Selected element concentrations in muscovite replacing epidote. **142**
Fig. 4.3.8) Selected major and trace element concentrations of metamorphic calcite. **143**
Fig. 4.3.9) Selected element content in metamorphic and hydrothermal carbonate. **144**
Fig. 4.3.10) Carbonate composition in greenschist at Red Rock. **146**
Fig. 4.3.11) Element concentrations of titanite and its replacement products. **147**
Fig. 4.3.12) Element concentrations of metamorphic and hydrothermal muscovite. **152**
Fig. 4.3.13) Composition of epidote in TP7D and ankerite in chlorite-rich layers in TP7A. **153**
Fig. 4.3.14) BSE image of ankerite in the poikiloblastic spots in RR 19. **154**
Fig. 4.3.15) Major chemical content of several minerals in TP7A and RR19. **155**
Fig. 4.4.1) Alteration styles dependent on K/H ratio and temperature. **156**
Fig. 5.2.1) Microphotograph and chemical analyses of carbonate in BUL2B. **164**
Fig. 5.2.2) Micro-textures of carbonate in BUL3A. **165**
Fig. 5.2.3) Changes of various elements across the vein in BUL3A. **166**
Fig. 5.2.4) REE and Sr content of ankeritic veins in greenschist at Bullendale. **167**
Fig. 5.2.5) REE, Ca and Sr content of the sparry veins in greenschist at Red Rock. **168**
Fig. 5.2.6) REE, Ca and Sr content of the thin veins in greenschist at Red Rock. **169**
Fig. 5.2.7) Major element, REE and Sr content of veins in greyschist at Mt Alta. **170**
Fig. 5.2.8) REE and Sr content of ankerite in little-altered lamprophyre. **171**
Fig. 5.2.9) Major element content of ankerite in highly-altered lamprophyre. **172**
Fig. 5.2.10) REE content of ankerite in highly altered lamprophyre. **173**
Fig. 5.2.11) Eu content/ anomaly and Sr content of ankerite in lamprophyre. **174**
Fig. 5.2.12) REE and Sr content of ankerite in fine-grained breccia at Mt Alta. **175**
Fig. 5.2.13) Main element and REE content of carbonate in silicified breccias. **176**
Fig. 5.2.14) Sr and Eu contents/ anomaly of carbonate in silicified breccias. **177**
Fig. 5.2.15) REE and Sr content of calcitic ocelli in lamprophyre. **178**
Fig. 5.2.15) REE and Sr content of ankeritic marble from Niger Diatreme breccia. **178**
Fig. 5.3.1) CaO/(CaO+FeO+MgO) and FeO/(FeO+MgO) in all carbonates. **179**
Fig. 5.3.2) Mn and MnO/(MnO+FeO) ratio in the different carbonates analysed. **180**
Fig. 5.3.3) Sr and Ba content in the different carbonates analysed. **180**
Fig. 5.3.4) U, Th and Pb content and Th/U and Pb/U ratios of the carbonates analysed. **181**
Fig. 5.3.5) Comparison of the REE patterns of different carbonate with their host rocks. **183**
Fig. 5.3.6) REE patterns of volcanic rocks of the ADS and carbonate in the diatremes. **184**
Fig. 5.4.1) Precipitating carbonate species in respect to T and Ca/Mg ratio in fluid. **186**
Fig. 5.4.2) Solubility constants of carbonate species and model fluid composition. **190**
Fig. 5.4.3) REE composition of zircon, apatite, monazite and allanite. **193**

Fig. 5.4.4) REE content of carbonate and the calculated available REE. **194**
Fig.5.4.5) Schematic succession of the carbonate in highly altered lamprophyre. **196**
Fig.5.4.6) GWB model of stable phases in a S- and Eu-bearing hydrous fluid. **200**
Fig. 6.1.1) Samples in which Sr isotope ratios were measured in-situ and from solution. **205**
Fig. 6.2.1) Measured Sr and Nd isotope ratios and values corrected for age. **207**
Fig. 6.2.2) Sr and Nd isotopic ratios of unaltered grey- and greenschist. **207**
Fig. 6.2.3) Sr isotope ratios of metamorphic calcite and its host rock. **207**
Fig. 6.2.4) Sr isotope ratios of whole rocks and carbonate across greenschist transects. **208**
Fig. 6.3.1) Overview of all Sr isotopic ratios measured for this study. **210**
Fig. 6.3.2) Isotopic composition of veins in greenschist. **210**
Fig. 6.3.3) Sr isotope ratios of calcite in fault breccias. **211**
Fig. 6.3.4) Sr isotope ratios of carbonate in the diatreme at Mt Alta. **212**
Fig. 6.3.5) $^{143}Nd/^{144}Nd$ vs. $^{87}Sr/^{86}Sr$ ratios of carbonate and different host lithologies. **212**
Fig. 6.4.1) Stable isotope composition of metamorphic calcite. **215**
Fig. 6.4.2) Stable isotope ratios across alteration halos in greyschist and greenschist. **216**
Fig. 6.4.3) O, C, and Sr isotopic composition of hydrothermal and magmatic carbonate. **217**
Fig. 6.4.4) Stable isotopic ratios of hydrothermal carbonate compared to the literature. **218**
Fig. 6.5.1) Fractionation curves of oxygen and carbon isotopes for different substances. **221**
Fig. 6.5.2) Isotopic composition of carbonate and calculated composition of the fluid. **222**
Fig. 6.6.1) Model calculations to explain compositions of carbonates. **223**
Fig. 6.6.2) Model calculations of fluid evolution using Rayleigh Fractionation. **227**
Fig. 6.6.3) Model calculations of Rayleigh fractionation in carbonatite system. **228**
Fig. 6.4.4) Model of the evolution of fluid type 2 if it is meteoric in origin. **229**
Fig. 6.7.1) Fe isotopic ratios in the different samples. **232**
Fig. 6.7.2) $\delta^{56}Fe$ vs Fe content of whole rock and mineral separates. **233**
Fig. 6.8.1) Model of the evolution of fluid type 1 and fluid type 2. **234**
Fig. 7.1) Schematic model of mineralogical changes happening in green- and greyschist. **235**
Fig. 7.2) Model of the differences in gold-barren and gold-associated systems. **237**
Fig. 7.3) Schematic model explaining the REE content in the carbonate in the veins. **238**
Fig. 7.4) Schematic model of the fluids involved in the hydrothermal deposits studied. **240**

List of tables

Table 2.1.1) Common abbreviations used. **34**
Table 3.1) Sample sets studied regarding hydrothermal alteration and methods. **78**
Table 3.2) Terminology to describe the intensity of alteration. **78**
Table 3.2.1) Samples taken of two alteration halos in the Treble Cone/ Black Peak area **90**
Table 3.3.1) List of altering feature types, their orientation and halo width. **100**
Table 3.3.2) Metamorphic minerals and their replacement products. **101**
Table 3.3.3) Mineral reactions and volumetric proportions of reactants and products. **102**
Table 4.1) Samples analysed for whole rock composition. **115**
Table 4.2) Minerals and potential contaminants. **116**
Table 4.2.1) Mass-correction factors calculated for the immobile elements. **121**
Table 4.2.2) FeO content, LOI, divalent Fe, GOI and TLOI in different transects. **131**
Table 4.3.1) Samples and the minerals analysed for TE composition. **135**
Table 4.4.1) Excerpt of the spring analyses and calculated saturation. **157**
Table 5.1.1) Sample names, settings and methods employed on each sample. **163**
Table 5.4.1) Elements and the aspects that control their abundance in the carbonate. **185**
Table 5.4.2) Calculated vein-rock ratios of a selection of veins and their wall rock. **187**
Table 5.2.3) FeO, FeO/CaO and CaO/MgO across the studied alteration halos. **188**
Table 5.4.4) Calculated vein- rock ratios for a selection of veins and the available REE. **195**
Table 5.4.5) Summary of correlation of Sr and Eu content/ anomaly in the samples. **201**
Table 6.3.1) How much GnS and GrS need to contribute to GrS-hosted vein. **213**
Table 6.7.1) Samples analysed for Fe isotopic composition. **231**

List of appendices

Appendix A) Outcrops.
Appendix B) Samples.
Appendix C) Mineral analyses obtained by SEM.
Appendix D) Mineral analyses obtained by Microprobe.
Appendix E) Whole rock analyses: Methods, absolute and mass-corrected concentrations.
Appendix F) LA-ICPMS analyses of metamorphic and hydrothermal minerals in green- and greyschist.
Appendix G) LA-ICPMS analyses of carbonate in voids +/- adjacent rock.
Appendix H) Locations of analysis spots of LA-ICP-MS (trace elements and Sr isotopic ratios).
Appendix I) Calculations of the available amount of various elements from the rock.
Appendix J) Charge balance for substitution of trivalent REE in carbonate.
Appendix K) Radiogenic isotopic compositions of rocks and carbonate and age-corrected values.
Appendix L) Methods of stable isotope analyses and data.
Appendix M) Temperature of crystallisation calculated from calcite composition and isotope ratios.
Appendix N) Rayleigh fractionation re-producing the stable isotope composition of carbonatites.

CHAPTER 1- AN INTRODUCTION

Fluids migrating through the earth's interior play a crucial role in the evolution and history of rocks. Fluids dissolve components in one location and deposit them in another. Fluids are also a mean for convective heat transfer (e.g. Yardley and Bodnar, 2014). Elements transported and deposited by fluids can become relatively enriched at the deposit site and dependent on the element concentrated, may produce deposits of economic importance, i.e. lead, gold or copper (e.g. Hemley et al., 1992; Phillips & Powell, 2010; Landtwing et al., 2005). Fluids play an important role in the pseudomorph replacement of minerals (i.e. Putnis, 2009; Jamtveit & Hammer, 2012; Jonas et al., 2015). During prograde metamorphism, devolatilization is a common process during which fluids with various components (e.g. CO_2, F, H_2S etc) are released from minerals, forming new, less volatile-rich minerals (Winter, 2009). Conversely, the absence of fluids can inhibit reactions to take place, such as during the exhumation of eclogite-facies rocks, allowing eclogite-facies rocks to be exposed at the earth's surface. The process of fluid-rock interaction is also subject in waste management, such as deposition of radioactive waste (Ebert el al., 1991; Lumpkin & Geisler-Wierwille, 2012) or sequestration of industrial CO_2 in the ground, be it in the pore space of the rock (Benson & Cole, 2008, Kaven et al., 2015) or by reaction of the CO_2 with the rock's minerals, producing carbonates (Oelkers et al., 2008; Saldi et al., 2015).

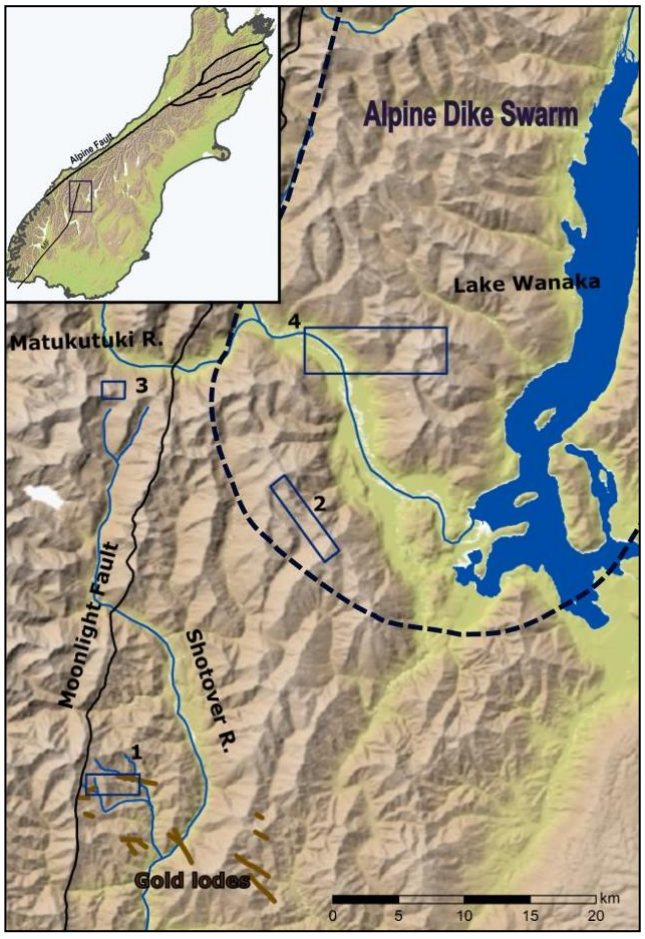

Fig. 1.1) Location of study areas (blue boxes) and important Cenozoic features. The dotted line outlines the extent of the Alpine Dike Swarm. The numbers on the boxes correspond to the numbering of the study areas (See chapter 2 for descriptions).

In this study, various chemical aspects of hydrothermal features in Western Otago were investigated. The hydrothermal are associated with veins, faults, and in some parts volcanic structures. The alteration halos around these structures are visible even from afar due to their bright orange-brown weathering colour, which is the result of the weathering of hydrothermal, Fe-bearing carbonate (ankerite and siderite). This study endeavours to identify the different scales of mobility and source of the various chemical components involved in the hydrothermal system. Although, similar hydrothermal features can be found throughout the world, there are several particularly interesting attributes to the Otago example.

A- Gold and lamprophyres: The studied region comprises mesothermal gold deposits in the Shotover area and part of the Alpine Dike Swarm, an alkaline-predominantly lamprophyric- magmatic suite (Fig. 1.1). Both features formed contemporaneously (Craw et al. 2006).

Gold and lamprophyres are not only in New Zealand found in close spatial and temporal proximity, but also other parts of the world (e.g. Rock & Groves (1988) and references therein). In all of these cases, including the New Zealand one, similar style of hydrothermal alteration is common. Advantageous is that in the Otago case magmatic rocks and gold deposits are spatially isolated. This makes it possible to study each of the hydrothermal systems separately and compare results directly, without having an overlapping of the two different settings, magmatic and non-magmatic/ auriferous (see below for details).

B-Geology) The study areas lie in the "Haast Schist", a body of schists and gneisses which extends over most of Otago and the Southern Alps. Much of this rock complex is made of chemically similar (Pitcairn, 2004) quartzo-feldspathic rocks and only relatively little other metamorphic rocks, such as greenschist or marble (Craw, 1981). This makes a direct comparison of the hydrothermal deposits in the different locations regarding their mineralogical and chemical characteristics feasible.

C-Age) The mountain belt of the Southern Alps is the result of tectonic movements that have been active since the mid-Cenozoic (Batt et al., 2004). The structures studied here formed at the beginning of that orogeny in the mid-Cenozoic (Craw et al., 2006; Cooper et al., 1987). Due to the relatively young age of the hydrothermal features and the extensive study of the Alpine Orogen, later alteration and overprinting events can be identified and considered easier compared to the similar but older deposits of this kind in Australia or Canada.

1.1) Hydrothermal systems, gold, and alkaline magmatic rocks

Hydrothermal systems comprise 4 basic parts:

- the source(s), which provide(s) the components eventually found in the sink,
- path ways for the fluid transporting those components, such as cracks, faults and shear zones
- the sink which is today manifested by void-fillings and alteration-halos in the adjacent rock.
- the fluid which connects these three parts as it travels from source to sink through the pathways.

There are innumerable studies that have investigated on one or more of these 4 parts, focusing of different aspect. Studies on alteration halos, for example, can have several incentives, such as identify the mobility of the different elements (e.g. Bierlein et al., 1999; Hopf, 1993), alteration-related mineralogy (Browne, 1978; Fein et al., 1994; White et al., 2003) or replacement mechanisms and processes (Pearce et al., 2013). Investigation of void-fillings gives information on the chemistry of the precipitating fluid (e.g. Bau & Möller, 1992; Kontak & Jackson, 1999; Smith et al., 2013) and unless the hydrothermal system is still active, several chemical attributes in the alteration halos and void fillings (eg. isotope geochemical composition and element concentrations) need to be used to identify the source of the different chemical components.

It has also been shown that source, path way and sink are generally not spatially isolated. For example, fluid flowing along the pathway will interact with the adjacent rock to attain chemical equilibrium causing a change in fluid chemistry (e.g. Dipple & Ferry, 1992). Another example for such an overlap, are alteration halos similar to those studied here. These halos are treated as "sinks for the components brought in by the fluid. However, this interaction of fluid and rock does not only cause addition of components to the rock but also depletion (e.g. Ague, 1994; Bierlein et al., 2000). Hence

those depleted substances are transported elsewhere, making the sink at the same time also the source.

In many cases the study of hydrothermal systems is related to economically important mineral deposits, such as gold or copper (e.g. Bierlein et al., 2000; Dilles & Einaudi, 1992; Li et al., 1998). Those types of studies investigate, for example, where the previous metal or mineral can be found, what the fluid chemistry was and where the source of the precious components was. This information is gathered with the aim to identify exploration vectors for the different metal deposits.

The hydrothermal system investigated in this study produced gold deposits in the Shotover area. Having formed in an active mountain belt these gold deposits class as orogenic gold deposits. At the same time, they are found in relatively close proximity to an alkaline magmatic suite, the Alpine Dike Swarm. As mentioned above, a similar relationship has also been found in other parts of the world and several studies have investigated the potential genetic link between gold and magmatism and whether the gold could have come from the magmatic rocks (e.g. Ashley et al., 1994; Craw et al., 2006; Taylor et al., 1994; Kerrich & Wyman, 1994; McNeil & Kerrich, 1985). Despite the close spatial relationship, a direct genetic connection between the two systems has not been found and it has been proposed that the tectonic setting is merely favourable for both systems (Kerrich & Wyman, 1994). However, despite gold having no magmatic origin, the source of the fluids involved with the hydrothermal gold deposits could have some connection to the magmatic hydrothermal system.

A well established method to identify the source of fluid components is isotope geochemistry, here namely the ratios of C, O and H isotopes ($^{13}C/^{12}C$; $^{18}O/^{16}O$; $^{2}H/^{1}H$). Above mentioned studies report C and O isotopic ratios. However in many cases the temperature dependent fractionation is not fully discussed, especially for carbon isotope ratios, which is necessary to evaluate the source fully. Specifically, Craw et al. (2006), who investigated the Shotover gold and lamprophyres of the ADS and who also reported carbon and oxygen isotope ratios, did not consider the temperature-dependent isotope fractionation. Craw et al. (2009) also report isotopic compositions in the Shotover gold deposits and do consider temperature-dependent fractionation. However, there are some potential problems with their considerations; primary meteoric water is poor in CO_2. Carbonate in the Otago Schist has a wide range of isotopic compositions (Blattner & Cooper, 1974; Devereux, 1968; White, 1998) as opposed to the confined composition used in Craw et al. (2009). Hence, the isotopic data from Western Otago's hydrothermal deposits need further investigation with respect to their source. This has been done in chapter 6 of this thesis.

Goals and questions

This thesis has two main objectives:

1) Investigate the characteristics of the interaction of hot, CO_2-bearing fluids with metamorphic and igneous rock.

2) Establish the potential sources of the volatile components of the hydrothermal system, especially in the gold-bearing and magmatic system.

Concerning the first objective, the study addresses two main questions regarding the hydrothermal alteration and veins:

A) What are the chemical and textural changes in the rock as the response to the influx of CO_2-bearing fluid? - In order to understand the evolution of a fluid flowing along a pathway and also hydrothermal (economically important) deposits, it is necessary to establish how the fluid interacted with the rock

and what components play a role during this process. As mentioned earlier, the examples examined here are not only the sink for components in the fluid but also the source. Hence, it is of interest to find out what attributes in the wall rock could govern which components are released or bound.

1.B) What processes control the chemistry of hydrothermal carbonate in the different structural setting, i.e. veins and breccias? - Void-filling precipitates are a direct response to the fluid and rocks' chemistry and the degree of their interaction. Which aspects control if the chemistry of the void-filling carbonate is rock- or fluid buffered?

With respect to objective 2, there is one overall question to be answered:

2.A) Throughout the study area, where do the fluids and their dissolved components come from? - This question is not only important for the establishment of the scale of element mobility (e.g. mm vs. m scale) but also addresses potential common or not common sources in the different settings, such as in the magmatic system and the gold bearing system. Hence it allows to establish whether there is a connection between those two systems in Western Otago.

To answer above questions, this thesis is divided into 4 main sections

- Introduction to the field areas, establishing the lithologies present and the structural controls of the hydrothermal deposits (Chapter 2).
- Textural and chemical changes associated with the alteration in the metamorphic rocks (Chapter 3&4).
- Vein carbonate chemistry (Chapter 5).
- Identify potential sources of components in the deposits using different isotope systems Chapter 6).

The final chapter (Chapter 7) gives a synthesis of the information gathered and conclusions drawn in this study. This information is then used to outline a model of the hydrothermal fluid system with respect to the fluid and metal sources and control on element mobility/ transport distances.

1.2) Regional Geology

The islands of New Zealand are the exposed parts of the continent of Zealandia, which is to about 90% submerged. Today, the continent sits on two tectonic plates; the Australian Plate and the Pacific Plate. South of the South Island, the plate boundary is an east dipping subduction zone where the Australian plate is thrust under the Pacific Plate. In the central South Island, the plate boundary is a transpressive dextral fault, the Alpine Fault, which dips at 40-60° to the east (Koons et al., 2003). In Marlborough (northern part of the South Island) the plate boundary splits up into an array of mostly NE striking strike slip faults ("Marlborough Fault System" (i.e. Lamb & Bibby, 1989; Little & Jones, 1998; Fig.1.2). These continue NE-ward into the Cook Strait, where they transition into a W dipping subduction zone with the Pacific plate being subducted under the Australian plate.

New Zealand's basement is made of several tectonostratigraphic terranes and plutonic units (iMortimer, 2004; Landis et al., 1999 and references therein). In the South Island east of the Alpine Fault, units and terranes exposed on land are - from south to north - the Median Batholith (plutonic

unit) and slivers of Takaka Terrane, Brook Street Terrane, Murihiku Terrane, the Dun Mountain-Maitai Terrane, Caples Terrane, the Rakaia Terrane and Pahau Terrane (Fig. 1.2)

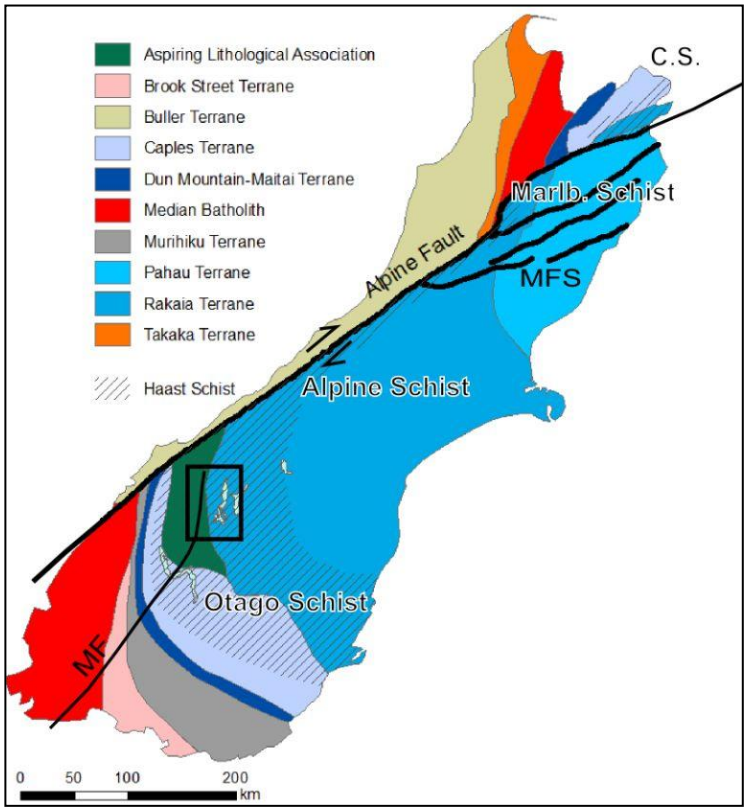

Fig. 1.2) Terranes, major faults and extent of Haast Schist in the South Island (after Mortimer, 2004). MFS=Marlborough Fault System. MF=Moonlight Fault Zone. C.S. Cook Straight. Black box outlines area of Fig.1.3.

In western Otago, the Caples and Rakaia Terranes are separated by the Aspiring Lithological Association. Terranes which lie south of the Median Batholith are exposed in Westland and the West Coast (both are west of the Alpine Fault). These terranes are - from south to north - the Buller Terrane Takaka Terrane (Fig. 1.2).

1.2.1- The Otago Schist

The study areas lie in the Aspiring Lithological Association and Rakaia or "Older Torlesse" Terrane (Fig. 1.2&3). The Rakaia Terrane is mostly made up of quartzo-feldspathic schist and gneiss and some other lithologies, which is mostly greenschist (Kawachi, 1974; Craw, 1984, Mortimer & Roser 1992). The Aspiring Lithological Association is also mostly made of quartzo-feldspathic greyschist, but has a distinctly higher greenschist-greyschist ratio than the Rakaia Terrane (Craw, 1984).

Those two terranes and the Caples Terrane contribute to the "Haast Schist" (i.e. Roser & Cooper, 1990). The Haast Schist is a complex of metamorphic schists and gneisses making up the basement of Otago ("Otago Schist"), a narrow strip (ca. 10-20 km wide) along the Alpine Fault in the hanging wall ("Alpine Schist") and in the basement of the Marlborough Country ("Marlborough Schist") (Fig. 1.2). In the eastern and central part of Otago, which is east of my study area, the schist forms an antiform, which strikes NW-SE and has prehnite-pumpellyite facies rocks on its flanks and greenschist facies rocks in its centre. A similar metamorphic gradient is present in the Alpine Schist, where the grade increases from sub-greenschist in the east to amphibolite facies in west (Mortimer 2000, and references therein). In the studied area, which lies in the boundary zone of Otago and Alpine Schist, there is an increase in metamorphic grade towards the east (Fig. 1.3).

1.2.2- Textural zones

Despite the mostly gradual metamorphic gradient, using mineral paragenesis as indicators to define the metamorphic grade is not practical in the case of the Otago Schist, as the chemical composition of the quartzofeldspathic schist does not cause the growth of a diverse and macroscopically distinct array

of minerals in response to small changes in temperature and pressure. Because of this, other features are often required to classify the metamorphic rocks.

One way is to divide the Haast Schist into zones based on textural features, such as foliation and segregation layers (Hutton & Turner, 1936; Bishop, 1972; Norris & Bishop, 1990). A revised definition of these textural zones (TZ) has been proposed by Turnbull et al. (2001), which is based on the muscovite size, lineation and segregation layers. This subdivision is independent of the terrane affinity of the rock. Overall, 4 main textural zones have been identified (Turnbull et al., 2001): TZ1, 2, 3, 4. Textures and minerals forming in rocks from TZ1 do so at sub-greenschist facies metamorphism. In TZ1 newly grown muscovite is only small and in hand specimen only detrital muscovite is recognised. With increase in textural zone, the amount and size of metamorphic micas and definition of metamorphic textures (foliation, segregation layers, metamorphic veining, lineation) increases. The increase in textural zoning can roughly be correlated with the increase in metamorphic grade (Mortimer, 2000; Turnbull et al., 2001; Fig. 1.3). The study areas lie in Texture Zone 4 (Fig 1.3), which is defined as having mica grains visible with the naked eye, a well-developed, partly crenulated, foliation, deformed quartz veins and segregation layers made either of quartz and feldspar or mafic minerals (mica, chlorite, epidote etc).

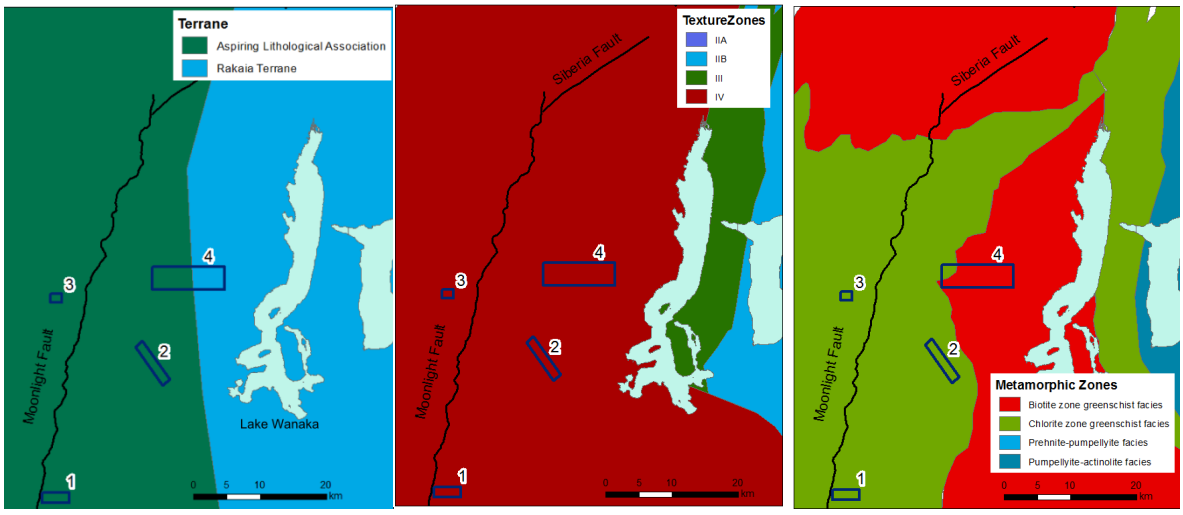

Fig. 1.3) Location of the study areas (boxes) in relation to terranes, textural zones and metamorphic zones as defined by Mortimer (2000) and Turnbull (2001). Numbers in boxes correspond to the numbering of the study areas (see next chapter for details). Propagation of Moonlight Fault and Siberia Fault as proposed by White (2002).

1.3) Geological history of western Otago

In the study areas three main episodes of deformation can be distinguished. The first one involves the formation and shaping of the Otago- and Alpine Schist, the second phase of deformation is linked to extension and exhumation during the Late Cretaceous to Mid-Cenozoic, and the third relates to the here mostly brittle deformation in the Late-Oligocene-Early Miocene during the Kaikoura Orogeny.

1.3.1- The 1st Episode: Metamorphism of the schist and ductile deformation (Rangitata Orogeny)

The terranes today exposed east of the Alpine Fault were accreted to the eastern margin of the Gondwana during the Mesozoic (Howell, 1980; Bradshaw, 1989 and references therein). The Haast Schist itself is interpreted to be mostly meta-sedimentary rocks deposited off the coast of Gondwana,

which after deposition and burial were subsequently deformed and metamorphosed during the Terrane accretion (i.e. MacKinnon, 1983).

In the realm of the study area, multiple events of metamorphism and deformation took place between the Early Jurassic and Early Cretaceous (Mortimer, 2000; Gray & Foster, 2004) resultant to which the fold plane-parallel foliation and major lithological boundaries (e.g. greyschist against greenschist) are now (sub-)parallel to each other, except in fold, (Craw, 1984; Barry, 1966). In today's study areas, deformation and metamorphism took place under greenschist facies conditions (Mortimer, 2000; Craw, 1985), causing the development of segregation layers and veins made mostly of quartz and albite (Craw, 1984; Turnbull et al., 2001; Norris & Henley, 1974; Cox, 1993, Breeding & Ague, 2002). After peak metamorphism structures were deformed further in a mostly ductile manor, forming open folds and crenulation in metapelites or small scaled folds in the more quartz-rich rocks (Craw, 1985).

1.3.2-The 2nd Episode: Exhumation of the Otago Schist and marine transgression

Ar-Ar dating (Gray & Foster, 2004) reveal that the Otago Schist exhumation began in the Early Cretaceous and greenschist-facies rocks in Central Otago were exposed at the surface in the early Eocene (LeMasurier & Landis, 1996). This age is in agreement with the deposition of terrestrial sediments in Southland and East Otago around that time (Kamp et al., 2015).

The exhumation of the Otago Schist was the result of crustal extension caused by the separation of Zealandia from Gondwana beginning in the Cretaceous (Late Albian-Santonian; Laird & Bradshaw, 2004). This extension resulted in the formation of gräben and half-gräben (Laird & Bradshaw, 2004). Additionally, the exhumation was accompanied by the formation of decompression-related joint systems in the metamorphic rock (Weinberger et al., 2010). The active fault formation caused by this rifting seized in upper Cretaceous, after which a time of slow subsidence of Zealandia's passive margins prevailed, overall accompanied by slow marine transgression (Laird & Bradshaw, 2004; Lee et al., 2001). In the late Eocene, formation of graben and half-graben systems in western Zealandia (incl. Western Otago) caused increased subsidence (Kamp, 1986; Carter, 1988), leading to the maximum submergence of Zealandia in the Oligocene (Carter, 1988; Lee et al., 2010). In western Otago this is documented by the deposition of deep water sediments during that time (deposition mostly >200m water depth; Kamp et al., 2015).

1.3.3- The 3rd Episode: Deformation during the early Kaikoura Orogeny

After the ductile metamorphic deformation and extensional tectonics, a change of overall tectonics in the late Oligocene-Early Miocene marked the beginning of the Kaikoura Orogeny. In the South Island, the today still active Alpine Fault initiated in the late Oligocene/ Early Miocene (Cooper et al. 1987, Kamp, 1986). Resultant to this, the tectonic plate accommodating Zealandia was broken up and since then the continent has been on two tectonic plates (Australian and Pacific Plate). Other faults that were active or formed during that time are the Moonlight Fault and Siberia Fault (Fig. 1.3; Turnbull et al., 1975; White et al, 2002). Contemporaneously to the Alpine Fault, the magmatic rocks of the Alpine Dike Swarm intruded the Haast Schist, along a faults and joints (Cooper et al., 1987) and the Southern Alps began to be uplifted (Batt et al, 2004).

1.3.3.1: The Alpine Fault

The most prominent tectonic feature of the Kaikoura Orogeny in the South Island is the Alpine Fault. The Alpine Fault represents the plate boundary of the Australian and Pacific tectonic plates on the South Island. The fault was initiated in the late Oligocene-Early Miocene (Cooper et al., 1987; Kamp,

1986) and has since been active. During its time of activity, the Euler pole of the Australian and Pacific plate has first shifted gradually towards the SE and in the last 5 Ma to the WSW (Sutherland, 1995, Lamarche et al., 1997). Based on this data, it has been suggested that the Alpine Fault was initiated in a transtensional tectonic setting and as the Euler pole moved towards the SE, the Alpine Fault accommodated pure strike slip movements between 20 and 5 Ma ago (Lamarche et al., 1997, White, 1998). At the beginning of Pliocene the pole shifted relatively towards the WSW, which caused the tectonic movement along the Alpine Fault to change to a transpressive regime which lasts till today (Lamarche et al., 1997; Sutherland, 1995; Norris & Cooper, 2000). Today the tectonic character of the fault is transpressional with a dextral strike slip displacement of a 35.5 mm/a and a compressional component of 10 mm/a (Norris & Cooper, 2000). Tectonic movements related to the plate movement have not only been accommodated along the Alpine Fault, but also away from it, as is evident from the dragging and reorientation of terrane boundaries over 100 km away from the fault (i.e. Sutherland, 1999) and formation of faults and joints in the central Southern Alps (Cooper et al., 1987). The overall dextral shear sense of the Alpine Fault is also the reason why the Buller and Takaka Terrane are juxtaposed against the Rakaia and Pahau Terrane (Fig.1.2).

1.3.3.2: The Moonlight Fault

In the extent of the study area, the biggest regional scale Cenozoic fault is the Moonlight Fault (Fig. 1.2 &1.4). The Moonlight Fault is part of a fault system, which extends from the south of the South Island NE-ward to Lake Wakatipu (Norris et al., 1978) from where it propagates in NNE direction to about the same latitude as the northern shore of Lake Wanaka (Turnbull et al., 1975, Craw, 1984). Here it transitions into the Castalia Antiform (White, 2002).

In the region of the study area, the Moonlight fault is a NNE (15°)-trending, steeply (50-65°) to the W dipping fault (Turnbull et al., 1975). Along the fault, slivers of Tertiary sediment have been wedged between the two metamorphic units. The contact of the sediments and the underlying schist is sedimentary (Barry, 1966). In the wider study area these often brecciated sediments are conglomerates, grey sandstone intercalated with sandy bioclastic marine limestone all of which belong to the Bob's Cove Beds (Barry, 1966). These sediments were deposited in a shallow to deep marine environment in the upper Oligocene, when the Moonlight Fault was an extensional feature (Turnbull et al., 1975; Norris et al., 1978). The sediment unit is believed to have been up to several kilometres thick (Turnbull et al, 1975; Turnbull, 2000). In about the Late Oligocene/ early Miocene, the Moonlight Fault (in the study area) was active as an oblique reverse fault (Turnbull et al., 1975; Norris et al., 1978) due to overall change in tectonic movements at that time (Kaikoura Orogeny).

Concurrent with the compressive stage of the Moonlight Fault, folds formed on a regional to outcrop scale (Craw et al., 2006; Barry, 1966). Regional scale folds are the Earnslaw Antiform and Shotover Synform. At about the same time as these folds formed, mostly E-to SE trending Faults formed in the Moonlight Fault's footwall and some of these faults accommodate gold mineralisation (Fig. 1.1&4; e.g. Craw, 1989; Craw et al., 1991 &2006).

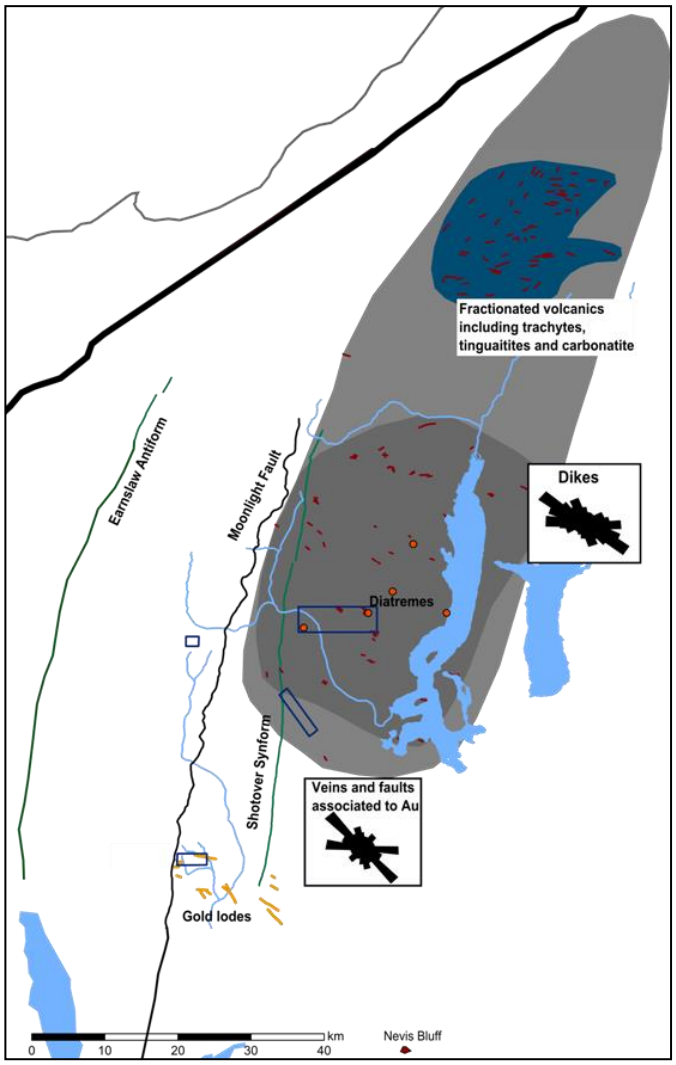

Fig. 1.4) Map of major Cenozoic features. Light grey: Outline of the Alpine dike swarm. Dark grey: High density of dikes (=red lines). Note red patch at Nevis Bluff. Yellow lines: gold lodes. Orange markers: diatremes. Blue boxes: location of study areas. Rose diagrams of orientation of dikes in the Wanaka area and those of veins and faults in the Shotover area associated with gold (own data and data from Craw et al., 2006 & Cooper et al., 1987).

1.4) The Alpine Dike Swarm

The Alpine Dike Swarm (ADS), a mostly alkaline magmatic suite, is made of dikes and diatremes which were emplaced in the Alpine/ Otago Schist. Rocks of this complex are mostly lamprophyric but other lithologies such as trachytes, tinguaities and carbonatites are also found. The dikes and diatremes of this swarm are located in a N-S trending zone, which is mostly west of Lake Wanaka and the Makarora River (Fig. 1.4). The northern border is the Alpine Fault (Cooper, 1986). The southern boundary is drawn roughly along the latitude of Wanaka Township. The age of the intrusives of the Alpine Dike Swarm is 25-20 Ma (Cooper et al., 1987; Adams & Cooper, 1996; Hoernle et al., 2006).

An isolated dike of limburgitic composition is also found at Nevis Bluff between Queenstown and Cromwell (Fig. 1.4; Hutton, 1943). This dike has been dated to be 20.7Ma +/-0.4 (Hoernle et al., 2006). This dike could either be an outlier of the Waipiata Volcanics in Eastern Otago or an outlier of the Alpine Dike Swarm. Due to its geographical isolation and unknown generic affinity, the dike at Nevis Bluff is not included when referring to the geographical extent of the Alpine Dike Swarm.

The magmatic rocks of the Alpine Dike Swarm can be divided into two groups (Cooper, 1986). One is made of mafic to ultramafic, alkaline rocks which contain little or no feldspars; these are ouachitic and camptonitic lamprophyre. The other group comprises volcanics of intermediate chemical composition (specification based on dikes' location in a TAS diagram), such as trachytes and tinguaites. Carbonatites of the ADS belong, based on the chemistry to the first group, but their genesis is closely related to the second one (see below). Lamprophyre is the most common rock type of the ADS and makes up over 60% of the dikes found (Cooper, 1986). Cooper et al. (1979) described spherical structures ("ocelli") in lamprophyric dikes. These are mostly made of calcite, analcime and sodic feldspar. The primary ocelli are believed to have formed from residual fluid-rich phases which form during cooling and crystallisation of the magma and which were drawn into gas vesicles due to the pressure difference (Cooper, 1979). In the study area, ocelli also have been found, which are here primarily filled with calcite.

Dikes of the ADS are found throughout the dike swarm area, but two areas have a high density of dikes; one is in the northern part and the other one is in the Lake Wanaka region (Fig. 1.4). The northern area is lithologically very diverse and contains rocks such as carbonatites, trachytes and camptonite (Cooper, 1986). Outside this area, the only magmatic rock type is lamprophyric in composition. Most of the dikes are less than 1 m, wide but occasionally many metres thick magmatic features are found too, such as at Niger Diatreme (Cox, 1985, own observations) or in the Haast area (Cooper, 1986). The dikes throughout the ADS tend to have specific orientations. In the northern part, dikes predominantly strike E and NE, while they mostly trend S to SE (Cooper, 1986, Fig. 1.4) in the Wanaka area (including the study area). The emplacement of the dikes is controlled by joints and shear zones and at least in the southern portion follow the orientation of the regional joint system (Cooper et al., 1987; Craw, 1984). These structures have been interpreted to have formed at the same time as the melt emplacement and are believed to be related to the initiation of the Alpine Fault (Cooper et al., 1987).

As mentioned above, part of the dike swarm are also diatremes, roots zones of explosive phreatomagmatic eruptions (i.e. White & Ross, 2011 and references therein). Five diatremes occur in the southern part of the Alpine Dike Swarm (Fig. 1.4). These are on the lower, eastern flank of Niger peak, at Mt Alta, at Minaret Peak, at the western shore of Lake Wanaka and the northernmost one is a few km west of Minaret Bay. A potential sixth diatreme is thought to exist in the northernmost part of the ADS (Wallace, 1975). However, no in-situ structures have been found (pers. comm. Scott).

In order to characterise the source of the Alpine Dike Swarm's magma, studies have investigated the different intrusive rocks regarding their trace element and their isotope composition. $^{86}Sr/^{87}Sr$ ratios of the magmatic rocks lie mostly around 0.703 and those of $^{144}Nd/^{143}Nd$ lie between 0.51282 and 0.51291 (Cooper, 1986; Barreiro & Cooper, 1987). These values suggest a mantle source (Cooper, 1986).

Concerning the evolution of the magmatic rocks it has been proposed that the first melts that formed in the mantle are ouachite (ultramafic) and camptonitic lamprophyric composition (Cooper, 1986). These rose towards the surface during which fractionation and also melt separations due to fluid immiscibility took place (i.e. Cooper, 1986; Cooper & Paterson, 2008). The carbonatite in the Alpine Dike Swarm is believed to have formed by immiscibility/ exsolution from a CO_2-rich alkaline silicate parent magma (Cooper & Paterson, 2008). Based on silicate melt-carbonatite partitioning coefficients from different experimental studies and the close spatial association, Cooper& Paterson (2008) concluded that the carbonatites probably exsolved from a tinguatic parent magma.

CHAPTER 2-THE STUDY AREAS AND THEIR GEOLOGICAL FEATURES

2.1) Location and overall structure of the study areas

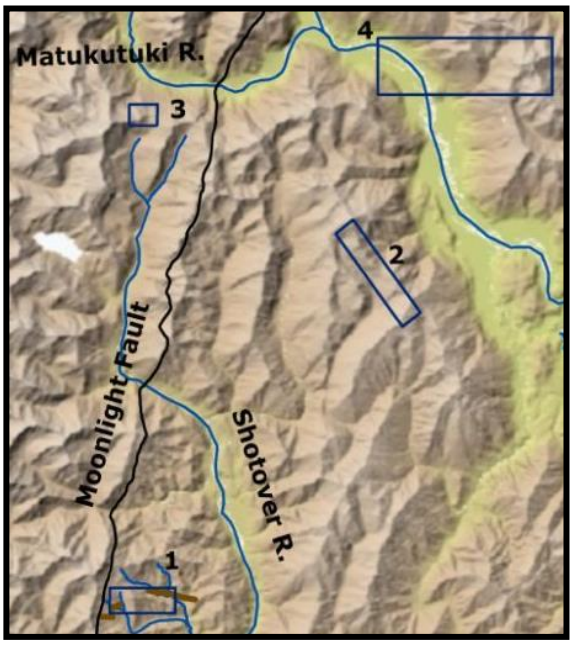

Fig. 2.1.1) Topographical map with locations of the 4 main study areas. 1= Bullendale-Copper Creek; 2= Treble Cone-Black Peak area; 3=Red Rock; 4= Diatremes at Mt Alta and Niger Peak.

For this study, structures in 4 separate areas were investigated. Each of these areas comprises various mid-Cenozoic structures which accommodated fluid flow and the associated precipitation of hydrothermal minerals. These areas are (1) at the old mining sites of Bullendale and Copper Creek in the Mt Aurum Basin in the wider Shotover Valley, (2) the meadows and ridge stretching from Treble Cone to Black Peak, (3) Red Rock at the Shotover Saddle, and (4) the eastern flank of Niger Peak and the northern slope of Mt Alta (Fig. 2.1.1).

2.1.1- Study areas

2.1.1.1: Study area 1-Bullendale and Copper Creek near Mt Aurum in the Shotover Valley

This area was chosen as hydrothermal carbonate is closely associated with gold-bearing structures.

Field work was undertaken around the abandoned mine sites of Bullendale and Copper Creek in the Mt. Aurum Basin in the footwall of the Moonlight Fault (Fig. 2.1.2). In both locations, field work was confined to the river beds and the lower flanks of the creek valleys, as the obstruction of structures by vegetation is least there. Throughout the Shotover area, gold is hosted in predominantly W-E and NW-SE striking silicified faults (Craw et al., 2006; Fig. 2.1.2). Closely associated with these is carbonate in veins, folds and other faults. Focus at both locations were outcrops with kink folded greyschist, veins, faults and alteration halos associated with these structures.

2.1.1.2: Study area 2-Treble Cone and Black Peak area

The area around Treble Cone and Black Peak is neither associated with the Alpine Dike Swarm nor the Shotover Gold System, but nonetheless has carbonate-rich veins, faults and associated alteration halos. Outcrops examined are along the ridge and meadows that stretch from Treble Cone northwards to Black Peak (Fig. 2.1.3). Much of the terrain is covered by tussock grass and rock outcrops are mostly confined to river valleys and ridges. The focus of this field work was put on fault zones and associated alteration halos in greenschist, which is a relatively abundant lithology in this area.

2.1.1.3: Study area 3-Red Rock

An example of carbonate alteration west of the Moonlight Fault can be found at Red Rock. Red Rock is a peak at around 1860 masl on the ridge leading west from the Shotover Saddle (Fig. 2.1.4). Name-giving is the orange colouring of its eastern flanks, which is the result of the weathering of hydrothermally altered greenschist. The zone of ankeritic alteration is about 100 m wide and strikes NNE-SSW and its longitudinal extent is several hundred meters. The northern end is covered by vegetation. Towards the south, it continues into the rock face of Red Rock and diffusely ends after

about 500 m (Fig. 2.1.4). The exact determination of the boundaries of the overall alteration zone and degree of alteration is not possible as, due to the extensive amounts of rock rubble on the ground of the northern slope of the ridge and snow on the southern slope at the time field work was carried out. A couple of hundred metres further east, the main rock type changes to grey pelitic schist. A profile across the alteration zone has been sampled along the ridge (Fig. 2.1.4).

2.1.1.4: Study area 4-Mt Alta and the eastern flank of Niger Peak

This area was chosen as it contains volcanic diatremes and lamprophyric dikes (Fig. 2.1.5), both contain abundant hydrothermal carbonate. At Niger diatreme exposure is poor due to the heavy bracken growth, which often hinders recognition and description of structures. The lower part of this diatreme was examined and sampled along a N-S running profile (Fig. 2.1.5). At Mt Alta, the diatreme is well exposed along a ca. 150 m long, W-facing, vegetation-barren rock wall, along which field work was carried out.

Short descriptions of outcrops and samples are given in Appendix A & B.

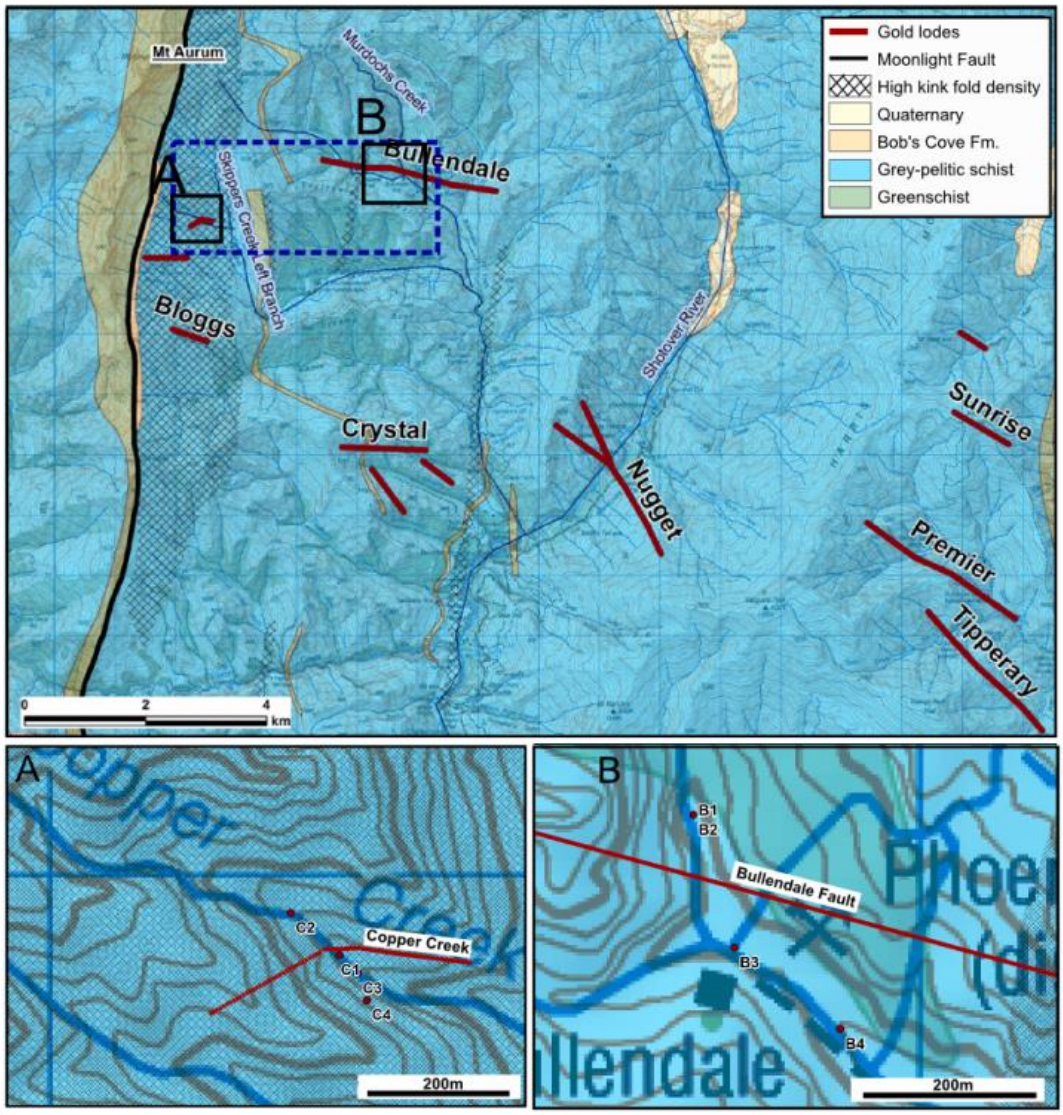

Fig. 2.1.2) Location of the outcrops and surrounding geology of study area 1. Blue box is the outline of study area 1 shown in Fig. 1.1. Maps after Barry (1966), Craw (1981) and MacKenzie et al. (2007).

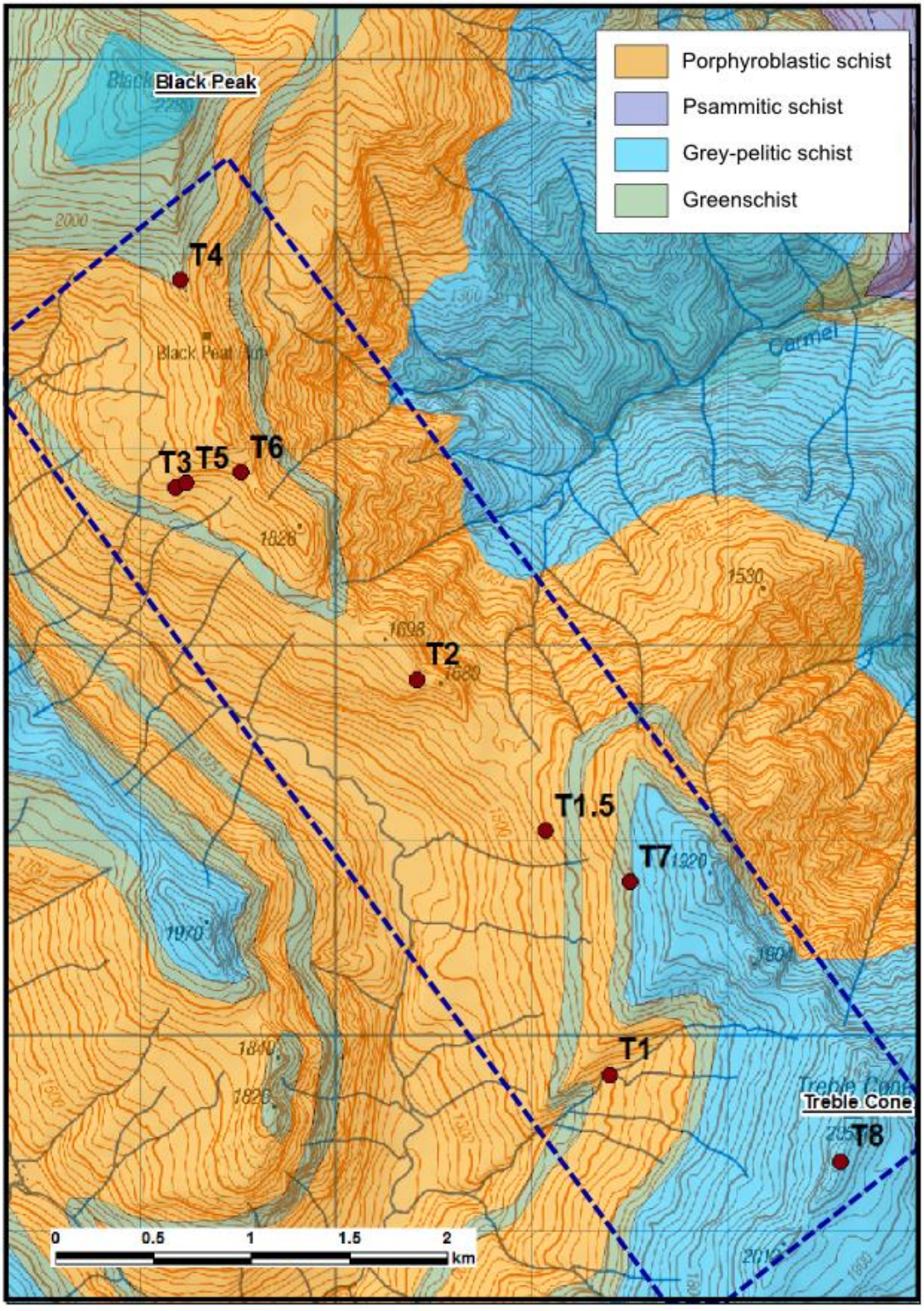

Fig. 2.1.3) Geology around Treble Cone and Black Peak with locations of outcrops. Blue box is the outline of study area 2 shown in Fig. 1.1. Map after Craw (1981).

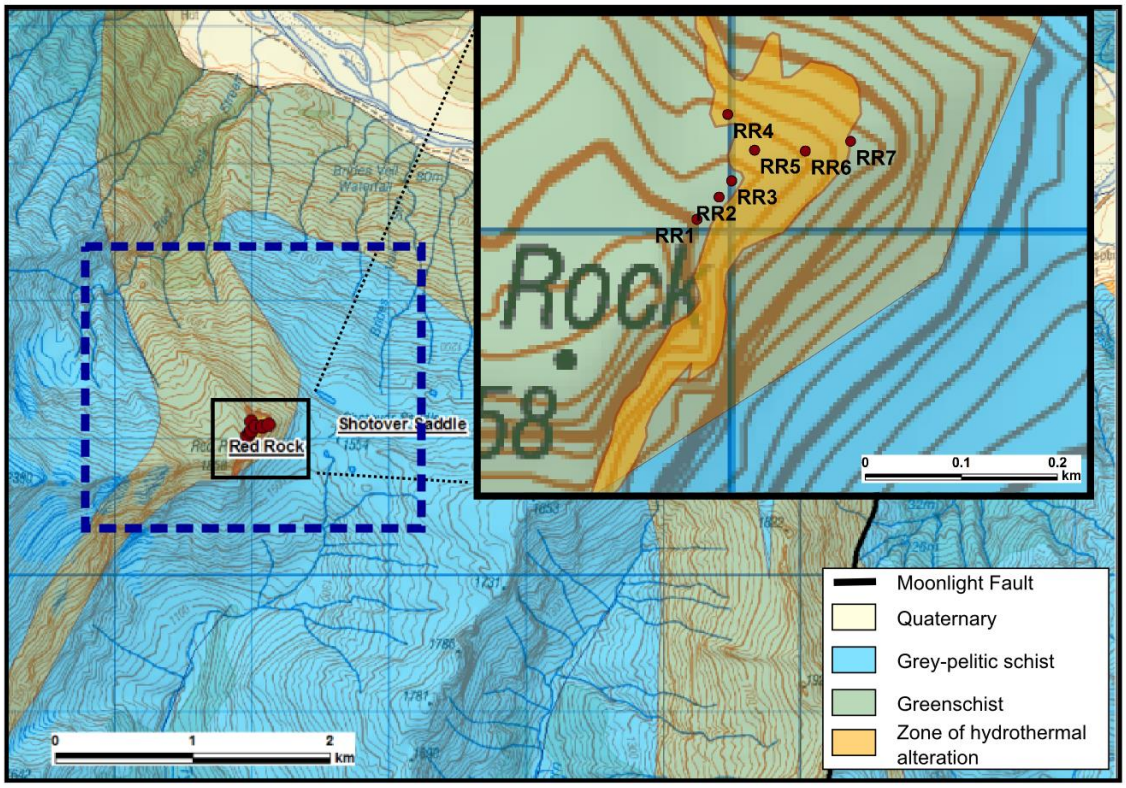

Fig. 2.1.4) Geology around Red Rock and the Shotover Saddle with outcrop locations (After Craw 1981). Blue box is the outline of study area 3 shown in Fig. 1.1. Orange marks orange staining of highly altered greenschist.

2.1.2-Methods

2.1.2.1: Naming of samples

The sample names used in the following descriptions comprise the location of sampling (AD and ALT= Mt Alta; BUL = Bullendale Creek and Murdoch Creek; COP=Copper Creek; ND= Niger Diatreme; RR=Red Rock; TP=Treble Cone/ Black Peak area), a number +/- letters. Common abbreviations are given in Table 2.1.1. Appendix B comprises a list of the sample names and their corresponding OU numbers.

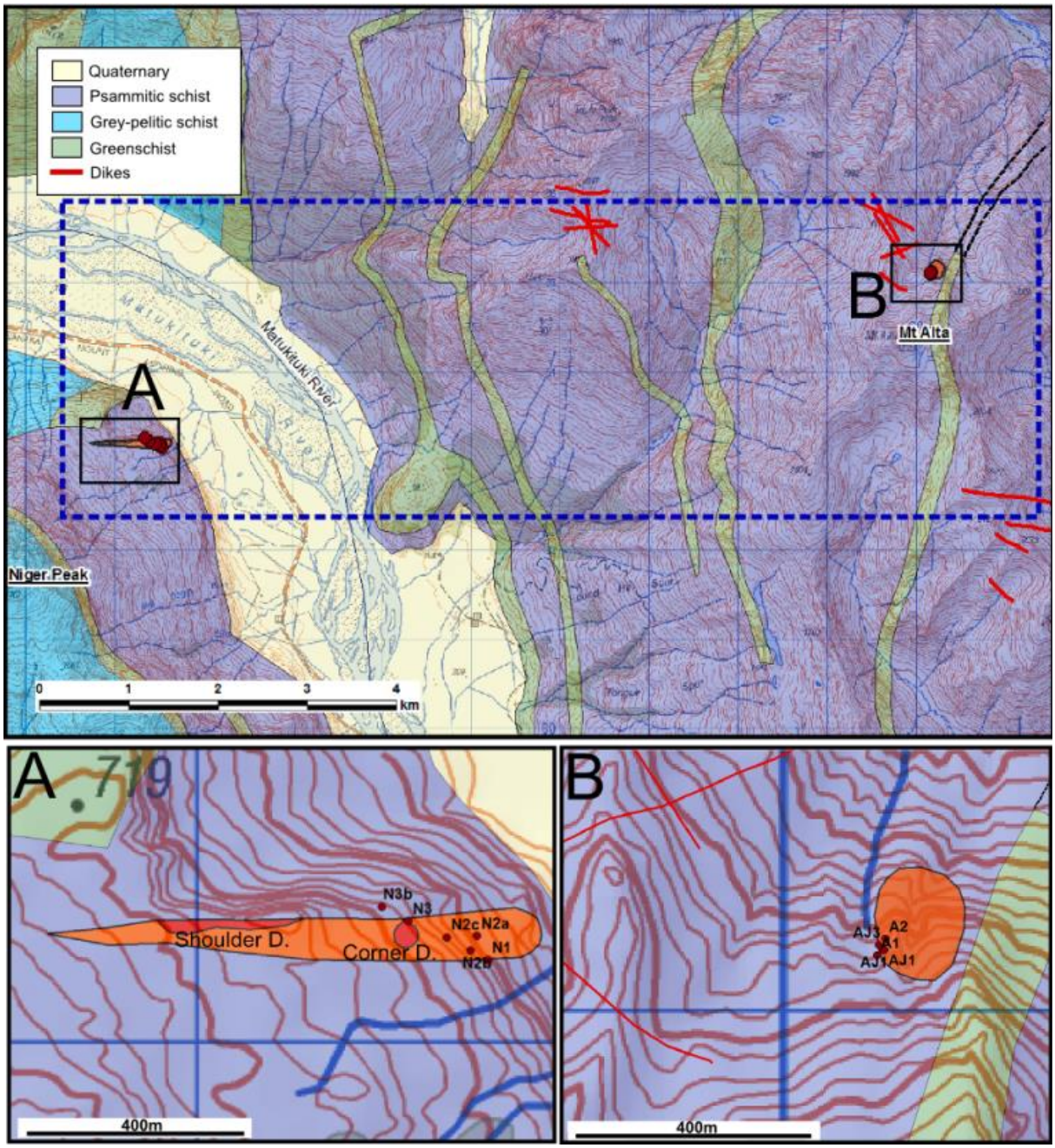

Fig. 2.1.5) Location and geology around the studied diatremes. A shows the geology around Niger Diatreme and B that around Mt Alta Diatreme. Blue box is the outline of study area 4 shown in Fig. 1.1. Maps after Cox (1985), Craw (1981) and Clough (1988).

2.1.2.2: Scanning Electron Microscope

The EDS system of the Zeiss Scanning Electron Microscope at the Otago Centre for Electron Microscopy was mainly used to collect qualitative element maps and backscatter images for textural analyses, and secondarily for point analyses. The rationale for using the EDS-based system was the speed of data collection (point analysis and map acquisition) and accessibility. For most cases of quantitative analysis, the electron beam was calibrated on a polished piece of cobalt. Standards used are the internal factory standards of the instrument. For each analysis, the electron beam (acceleration voltage: 15kV) the induced radiation was collected for over 30 s. The beam diameter is less than 1 µm thick, but due to the long residence time of the beam on the analysis spot, the excitation volume is several micrometers in diameter. For the analyses, polished carbon-coated thin sections were used. The programme used

for processing and the quantification of the elements was AZTEC by Oxford Instruments. Unlike for microprobe analyses, elements quantified are selected after the measurement. The choice of elements is based on mineralogy and the energy dependent intensity spectrum collected. This intensity vs. energy spectrum comprises several peaks which are attributed to the emission of certain elements. The intensity of the peak is directly dependent on the concentration of this element in the mineral analysed. However, in some cases the peak positions of elements overlap, as is the case for Si and Sr and Ti and V. This overlap is particularly pronounced in low intensity emissions. The elements identified by the programme were reviewed regarding this issue. Total weight percent sums of the elements can differ from the ideal sums (always less than 20%, mostly less than 5%), which in those cases is due to missing calibration on the cobalt standard and/or shift of the beam intensity over time. Despite this issue, the molar cation sums in relation to molar oxide ions are generally good. Analyses are give in Appendix C.

Many of the images in this thesis are BSE images which have been overlaid with coloured qualitative element concentration maps, which better illustrate the different mineral phases compared to "normal" greyscale BSE images. For example, chlorite and ankerite have very similar colours in BSE images, but show up well in the layered images (LBSI). However, due to overlapping of different element maps and BSE images, chemical features, such as zoning and relative abundance, can generally not be recognised in these images.

2.1.2.3: Microprobe

Two microprobes were used to measure chemical compositions of minerals. These were the microprobe of the Geology Department at Otago University (now part of the Steampunk Museum in Oamaru) and the microprobe of the Steinmann Institut at the Rheinische Friedrich-Wilhelms Universität in Bonn. The microprobe at Otago was a JEOLX-8600, with two WDS spectrometers. The beam current was set at 20 nA, a diameter of 15-20 µm and acceleration voltage of 15 kV. For analyses using the microprobe in Bonn, a JEOL 8200 Superprobe with 5 spectrometers, the beam diameter was set at less than 5 µm, an acceleration voltage of 15 kV and the current between 14 and 15 nA. In both cases, samples were coated with a thin (<25 nm) layer of carbon.

At Otago, only carbonate in veins was analysed, as here optical microscopy was used for the determination of the analysis position and hence only relatively large features could be analysed. For the measurements of carbonates at Otago synthetic carbonate standards (dolomite, siderite, benitoite) provided by the Smithsonian Institute were used. In Bonn, laboratory internal standards were silicates (omphacite, garnet, feldspar), native metals (iron) and oxides (Cr-oxide). All data collected by microprobe are presented in Appendix D.

2.1.2.4: Cathodoluminescence

For mineral cathodoluminescence imaging, polished rock thin sections were used. The cathodoluminescence imaging was carried out using the set up of the Geology Department of Otago University. In this set up an optical microscope is used. As a "light" source a neutrally charged ion beam (cold cathodoluminescence) is focused on the surface of a polished thin section at low air pressure (vacuum). The instrument is a Technsyn Cold Cathode Luminescence Model 8200 MK II. The ion beam excites the mineral's crystal lattice and radiation is emitted. Only for certain minerals is this radiation in the for humans visible light spectrum. For rocks discussed in this thesis these minerals are calcite, quartz, apatite and zircon. The emitted radiation is "captured" by using a normal photo camera which is set at variously long exposure times depending on the intensity of the emitted radiation. CL imaging was primarily used to show chemical zoning in calcite. For example, the orange coloured radiation

emitted from carbonate is generated by the Mn in the mineral (Townsend et al., 2000). Fe in carbonate causes the wavelength of the emission radiation to shift into the infrared (Townsend et al., 2000) and the carbonate appears dark in photomicrographs. These properties make this technique good to easily distinguish between Fe-rich and Fe-poor carbonates.

2.1.2.5: Chemical analyses of whole rock

For the determination of whole rock composition and isotopic ratios samples were crushed to a fine powder. Prior to crushing, weathered surfaces were cut off to exclude possible contributions of weathering-related chemical changes. The samples were ground in an agate mill (TEMA disk mill) to about sand grain size. A subset was crushed further to a fine powder (grain size < 150 µm). Chemical analyses of whole rock samples were performed by ALS Mineral in Brisbane, Australia. Major, trace, volatile and an array of metals were measured with different instruments using different dissolution techniques. For chemical composition of whole rocks and further detail on which method was used for which element, please refer to Appendix E.

Table 2.1.1) Common abbreviations used in this study.

Term	Abbreviation	Term	Abbreviation
Actinolite	Act	Greenschist	GnS
Albite	Ab	Greyschist	GrS
Amphibole	Amph	Illite	Il
Ankerite	Ank	Kaolinite	Kao
Apatite	Ap	Layered BSE Image	LBSI
Arsenopyrite	Apy	Magnetite	Mag
Backscatter electron	BSE	Muscovite	Mus
Barite	Bar	Plane polarised light	PPL
Biotite	Bt	Pyrite	Py
Calcite	Cc	Pyroxene	Px
Carbonate	Carb	Clinopyroxene-Orthopyroxene	Cpx-Opx
Cathodoluminescence	CL	Quartz	Qtz
Chlorite	Chl	Rutile	Rut
Clinopyroxene	CPx	Siderite	Sid
Crossed polarised light	XPL	Titanite	Tit
Value chondrite normalised	CN	White mica	WM
Epidote	Ep	Zircon	Zc
Hematite	Hem		

2.2) Mineralogy and textures of metamorphic rocks in the Otago Schist

In the study areas, the metamorphic rocks, which host the Cenozoic structures studied, are quartzofeldspathic gneisses and schists, generally referred to as "greyschist", and greenschist. Of these two lithologies, the quartzofeldspathic rock is the most abundant in the Otago Schist. Other metamorphic lithologies in the Otago Schist are metachert, marble and ultramafic bodies, none of which are present in the studied outcrops. The main lithological changes occur perpendicular to the foliation and can happen on a very small scale (centimetre). However, changes of textures and mineral content in a lithology (i.e. epidote-rich vs. porphyroblastic greenschist) can also happen along foliation (Craw, 1984).

2.2.1-Greyschist



Fig. 2.2.1) Psammitic schist at Treble Cone with foliation-parallel layering and metamorphism-related veins oblique to the foliation (image ca. 20 cm wide; outcrop TP8).

The quartzofeldspathic greyschist in the western Otago Schist can be divided into 3 types. These are "grey pelitic schist", "porphyroblastic pelitic schist" and "psammitic schist" (Craw, 1984). All of these contain - in different proportions - quartz, albite, muscovite, chlorite and titanite as main constituents (Craw, 1984). Mt Alta is the only location in this study where biotite is part of the metamorphic assemblage of the sampled greyschist, which is in agreement with the metamorphic mineralogical zone mapped for this area (Fig. 1.3). Niger Diatreme also lies in this zone, but is close to the boundary to the lower grade chlorite zone (Fig. 1.3). All other outcrops lie in the chlorite greenschist zone (Fig. 1.3). The change of the different greyschist lithologies happens on dm to m scale, and areas can only be mapped according to which type is most dominant (Craw, 1984). In the Shotover Valley the dominant rock type is "grey pelitic schist" (="Shotover-type Schist" in Barry (1966)) which is a fissile, muscovite-rich schist. It is made of millimetre thick mica-rich layers, which are separated by quartz- and albite-rich, leucocratic layers. Due to the high mica content this rock deforms easily and post-peak metamorphic, low temperature structures, such as kink folds, can form. Further north, in and around study areas 2, 3, and 4, the dominant greyschist types are "porphyroblastic" and "psammitic" greyschist. Both are petrographically gneisses but are referred to as schist nevertheless, following the regional literature. The psammitic greyschist is massive and overall contains less phyllosilicates than the pelitic schist. Due to this, this rock type does not always have a defined foliation. Psammitic greyschist is present at Mt Alta, Niger Diatreme and Treble Cone. The schist often shows signs of ductile deformation. Folding of the foliation is common on regional and outcrop scale (Craw, 1985) and the schist can be crenulated, as is the case at Mt Alta. Unlike in the Shotover area, the psammitic schist contains abundant quartz-veins (Fig. 2.2.1). These veins are a couple of cm thick and where the veins intersect one another, they form thick nodules. Their metamorphic affinity can also be inferred from microscopic texture of quartz which shows subgrain rotation as it forms under greenschist facies conditions (Stipp et al., 2002).

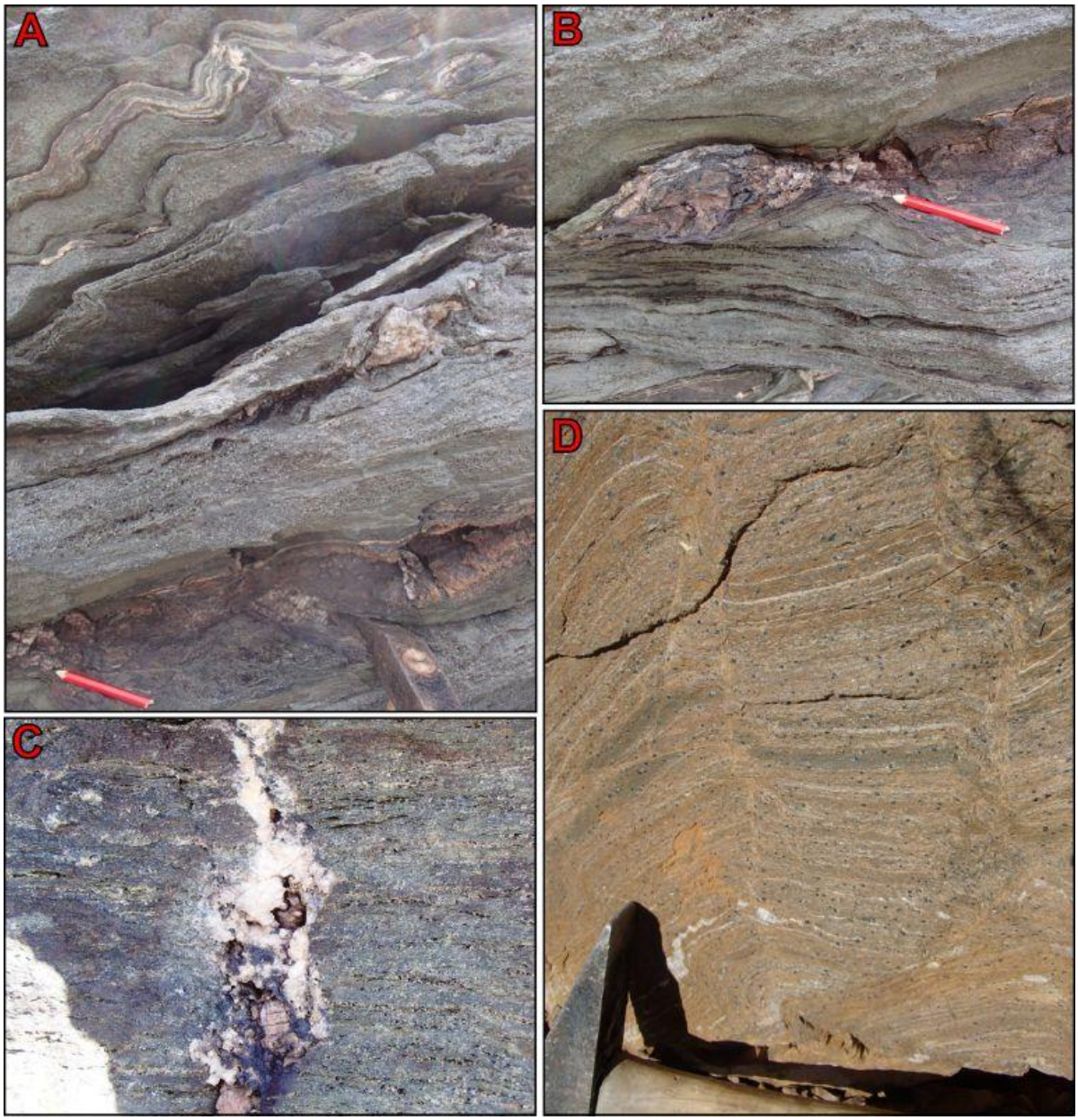

Fig. 2.2.2) A-C: Greenschist at Treble Cone. Outcrop TP5. **A:** Boudinaged calcite-quartz veins and ductilely folded greenschist. **B:** Metamorphic veins made of coarse grained calcite and quartz are boudinaged when parallel to the foliation. **C:** Metamorphic calcite-quartz perpendicular to the foliation. **D:** Greenschist at Red Rock (here hydrothermally altered) contains abundant metamorphic magnetite (black dots).

2.2.2-Greenschist

Throughout West Otago, greyschist is intercalated with greenschist. The greenschist horizons are generally a few centimetres thick (e.g. MacKenzie et al., 2007; Barry, 1966) but can in places reach thicknesses of several hundred meters (see Fig. 2.1.2-2.1.5). Despite being relatively thin, beds of greenschist can be traced along strike for several km, though the type of greenschist may change along strike (Craw, 1984). The metamorphic mineral assemblage for greenschist is albite, chlorite, titanite, amphibole of the tremolite-actinolite solid solution series, epidote, quartz +/- muscovite, +/- magnetite, +/- biotite, +/- stilpnomelane +/- calcite +/- sulphides. Several authors (Barry, 1966; Cooper, 1970) also mention occasional occurrences of crossite, and which formed under high pressure, greenschist facies conditions (Brown, 1977). Similar to greyschist, different types of greenschist have

been recognised (Craw, 1984; Barry, 1966; own observations). The subdivision of these types is based on mineralogy, texture, and relative abundance of the components. For example, the mica content in some of the sampled greenschist from the Treble Cone area can reach up to 15% in the chlorite-rich layers and can contain about 30% calcite. Ductile deformation- and metamorphism-related structures are foliation-parallel segregation layering and folds (Fig. 2.2.2A). Similar to the greyschist, greenschist can contain thick veins which are made of quartz and several cm big crystals of calcite. The veins are either parallel to the foliation where they may are boudinaged, or are about perpendicular to the foliation (Fig. 2.2.2 B&C). Other signs of deformation taking place during metamorphism can be found in greenschist at Treble Cone which can contain millimetre big, inclusion-rich albite porphyroblasts. The inclusions' mineralogy is the same as of the overall rock and within the albite grain are aligned parallel to each other. The clast internal foliation is oblique to today's foliation and occasionally draws a snowball texture. At Red Rock, greenschist contains abundant magnetite (ca. 5 vol-%; Fig. 2.2.2 D) in addition to chlorite, albite, titanite, calcite, +/- muscovite, +/- epidote and quartz. Features that have only been found at Red Rock are poikiloblastic calcite spots in the greenschist.

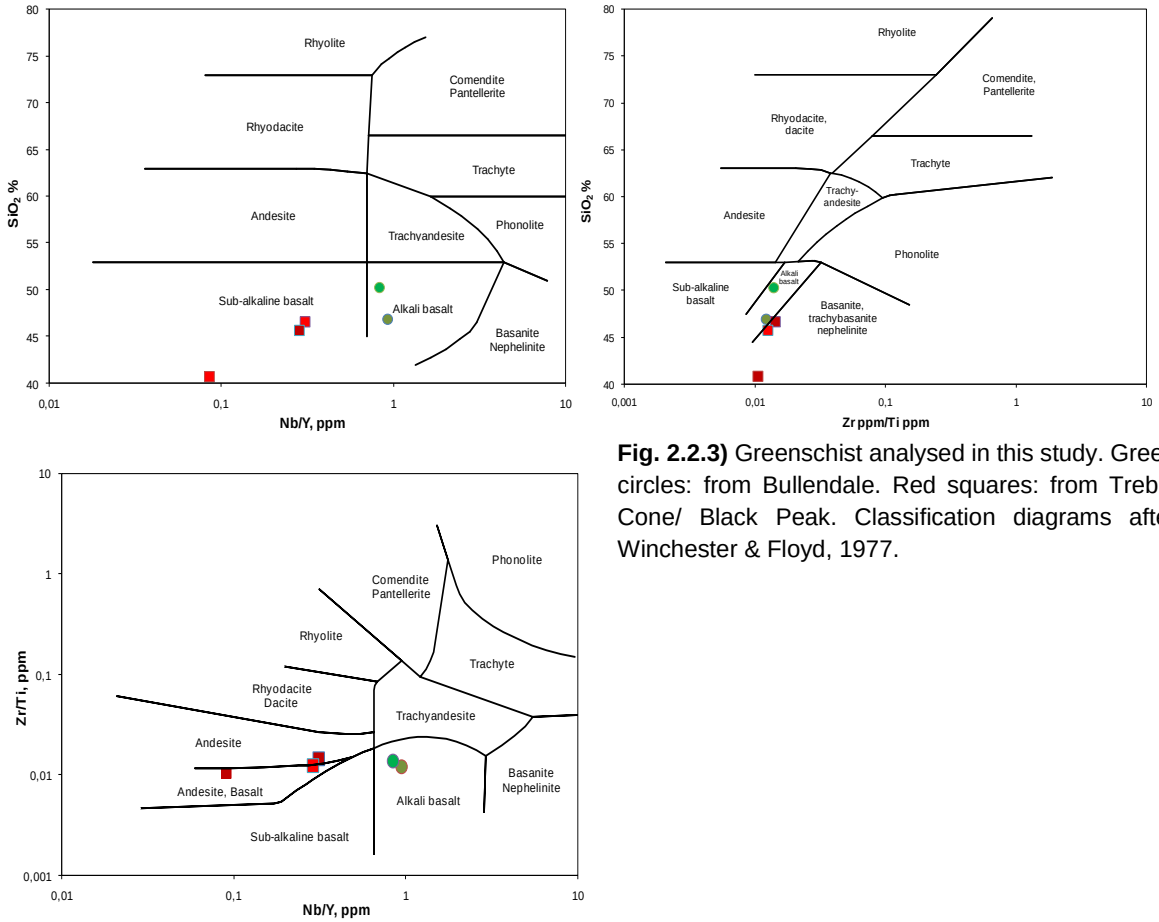

Fig. 2.2.3) Greenschist analysed in this study. Green circles: from Bullendale. Red squares: from Treble Cone/ Black Peak. Classification diagrams after Winchester & Floyd, 1977.

Several protoliths for the greenschist have been suggested (Craw, 1984), and all of which may be valid but for different areas. The thin layers of greenschist amongst the volumetrically dominant greyschist may be originally tuffaceous layers intercalated with the sediment later forming the greyschist, while the thicker greenschist layers are interpreted to be slivers of oceanic crust, as is indicated remnants of pillow basalts in some outcrops (Craw, 1984). Most of the greenschist is basaltic to sub-alkaline basaltic in composition (Bierlein & Craw, 2009). The greenschist from Bullendale Creek also falls into the alkali-basalt field. Greenschist from the Treble Cone/ Black Peak area plot into different groups on the different chemical classification diagrams by Winchester & Floyd (1977) (Fig. 2.2.3). This reflects the high calcite content of these rocks. As carbonate is essentially free of Si, Nb, Zr

and Ti (see chapter "Vein chemistry"), it causes the rock to have a lower Si content Nb/Y ratio, but similar Zr/Ti ratios compared to the other basalt. The cause of the high calcite and muscovite content in these rocks could be contamination with sedimentary material or hydrothermal alteration which took place prior to the end of metamorphism.

2.2.3-Chert, marble and ultramafics.

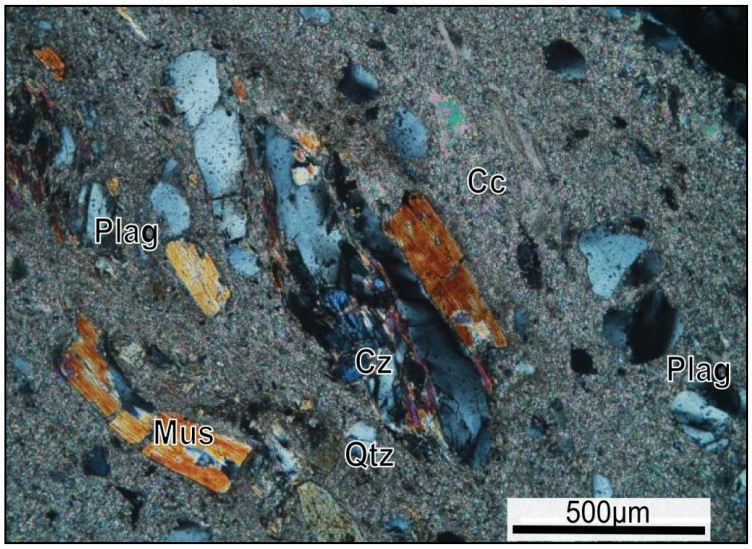

Fig. 2.2.4) Impure marble contains muscovite, quartz, plagioclase (plag) and clinozoisite (Cz) (OU27828, collected by A.F. Cooper).

Generally in association to greenschist, other metamorphic lithologies have been reported. These volumetrically minor phases in the Otago Schist have not found in-situ at the studied outcrops. However, they will partly be discussed later in the thesis and hence I will briefly introduce them here. The most common of these rock types is a quartz-rich rock referred to as metachert. Apart from quartz, it contains piemontite, stilpnolmelane, +/- spessartine (Craw, 1984). Bands of the metachert can be up to 100 m thick, but are only traceable for a couple of hundred metres along strike (Craw, 1984).

Throughout greenschist, thin, non-continuous bands (a few centimetres to 6 dm) of marble have also been described (Barry, 1966; Craw, 1981, Cooper, 1970, Gamble, 1984). Most of the marble is to over 95% made of calcite, but occasionally impure marbles have been recognised (Cooper, 1970). These impure marbles contain albite, mica, clinozoisite and quartz as "contaminating" phases (Fig. 2.2.4).

Additionally, pods of ultramafic composition are found embedded in greenschist throughout the Otago and Alpine Schist (Cooper, 1970; Craw, 1984; Cooper & Reay, 1983). Ultramafic pods are made of magnesian minerals such as tremolite, Mg-rich chlorite and talc (Craw, 1984; Cooper, 1970).

2.3) Structures and features without affiliation to magmatic rocks

2.3.1- Cenozoic structures in the footwall of the Moonlight Fault near Mt Aurum

In the Shotover area, the Moonlight Fault juxtaposes massive porphyroblastic greyschist and greenschist against the fissile, finely laminated schist ("Grey pelitic Schist") and overlying sediments of the Bob's Cove Beds (Barry, 1966; Craw, 1984; Fig. 2.1.2). In the hanging wall of the fault, the foliation dips steeply towards the W and is sub-parallel to the fault surface, while in the foot wall foliation is folded and has on average a more gentle towards the W dipping orientation (Barry, 1966).

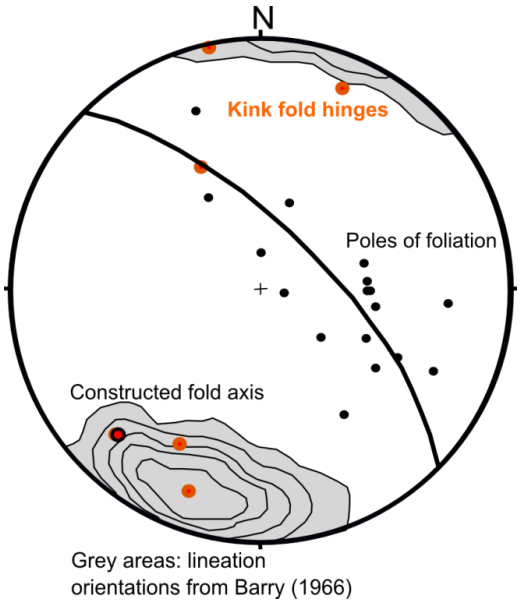

Fig. 2.3.1) Stereoplot of poles of foliation from Bullendale and Copper Creek with from foliation orientations constructed fold axes and measured kink fold hinges measured at the two sites. As a comparison, kink fold hinges, reported in Barry, 1966, are also shown.

2.3.1.1: Folds

In the foot wall of the Moonlight Fault occur roughly N-S trending folds, which are of the same age and genetically related to the Moonlight Fault, (Barry, 1966, Craw et al., 2006). Folds of this generation form structures of meso- to macroscopic scale. Macroscopic folds are the Shotover Antiform east and the Earnslaw Synform west of the Moonlight Fault (Fig. 1.4). Mesoscale folding is recognised due to systematic variations of the foliation orientation (Fig. 2.3.1). At outcrop scale, chevron-type folds are present which either have round or angular hinges, making the latter kink folds. Fold hinges strike N-NE. Fold axis orientations and the fold axis constructed from the foliation orientations collected in this study are in agreement with data of Barry (1966; Fig 2.3.1).

In the Mt. Aurum Basin and surrounding area, kink folds occur in distinct N-S trending zones which are mostly about 100 m wide but right next to the Moonlight Fault, kink folds are common in a nearly 2 km wide zone (Barry, 1966) (Fig. 2.1.2). The frequency of these zones decreases away from the Moonlight Fault. The amplitude of the kink folds ranges from a few cm up to a couple of dm (Barry, 1966; own observations). Genetically connected to these folds are foliation-parallel, thin (less than a few mm) shears in the limbs of the folds (MacKenzie et al., 2007). In the hinges, phyllosilicate minerals have been reoriented and moved, often filling the "gap" in the fold hinge (Fig. 2.3.2).

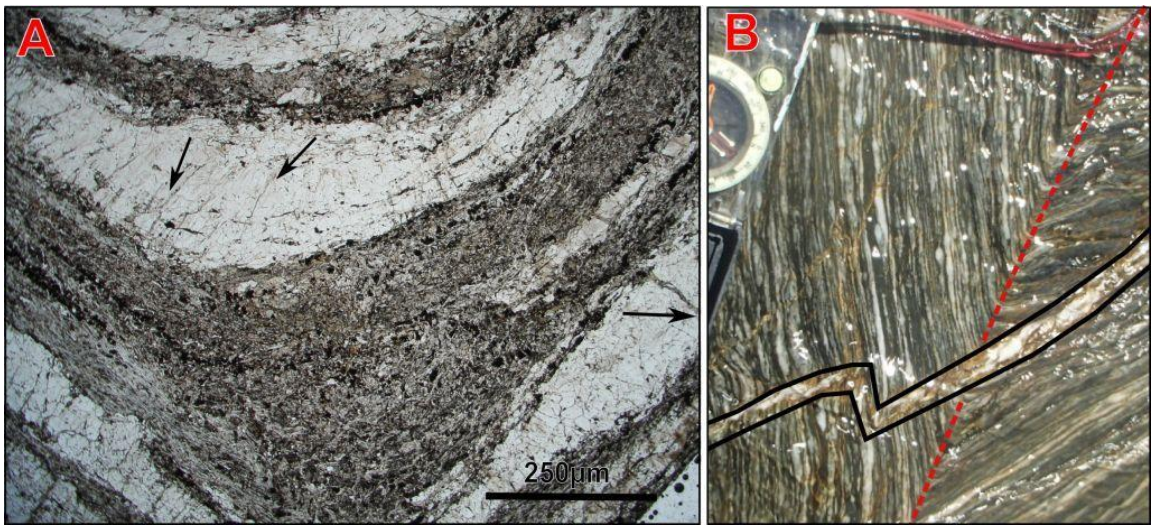

Fig. 2.3.2) A: The leucocratic layers of the folded rock is streaked with carbonate veinlets (for example arrows) which widen towards the outer part of the fold and which have a fan-like arrangement. The layers on the hinges are thicker than in the limbs, especially the phyllosilicate-rich layers (lower part of the image). COP2A. **B:** A carbonate-quartz vein (black solid line) cutting across the fold axial plane of a kink fold (red dashed line) is deflected at a relatively thick leucocratic layer. (outcrop C2).

2.3.1.2: Veins associated with kink folds

Carbonate veins and veinlets are ubiquitous in and around kink folds. Kink folds hinge zones can be host to carbonate veinlets which describe a "schistosity fan" across the hinge and which become wider towards the outer part of the fold (Fig. 2.3.2A). Craw et al. (2006) also describe carbonate veins which follow the fold axial planes. In some places ankerite-rimed quartz veins can also cut across the foliation and fold axial plane (Fig 2.3.2B). This particular vein has been deflected at internal material boundaries.

Associated with kink folds, swarms of veins and occasionally thin fault breccias can be found, such as at outcrop B2 in Murdoch Creek. At this outcrop, the hinges of the kink folds trend NNW-SSE (340-350°) and veins roughly follow the strike of the kink fold hinges (Fig. 2.3.3 A). The zone of veins and kink folds is surrounded by an about 1 m wide alteration halo in the greyschist (further details of this alteration are given in chapter 3). On microscopic scale, the thicker of the vein-breccia structures at this location (sample BUL2B; Fig. 2.3.3 B) reveal a complex succession of multiple carbonate and quartz growth generations and deformation events. In the sample studied (BUL2B), 4 carbonate vein generations have been identified based on CL images and vein orientations (Fig. 2.3.3 C).

1) Carbonate (calcite and ankerite) and quartz parallel to the vein's outer boundaries build the main vein.
2) Iron-bearing, partly oscillatory zoned calcite (darker orange CL colours). The course of these veins varies (0-60° to stage1 vein) and often follows grain boundaries in the older vein quartz. The transition of the orientation of these veins (0-60° to main vein) is graudual.
3) Veinlets made of Fe-bearing calcite cutting above described features perpendicular to the main vein orientation (Red box in Fig. 2.3.3 C&D).
4) The fourth stage is marked by intrusion of calcitic veinlets. The late stage veinlets often follow grain boundaries.

The sample also shows that carbonate precipitation preceded but also followed that of quartz (Fig. 2.3.3, Arrows). Evidence for deformation after and during precipitation is preserved in microstructures in the hydrothermal vein quartz. These evidence are undulous extinction and linear zones of subgrain formation. Another indicator of deformation is the rims of some carbonate veins which are fine grained and brecciated (Fig. 2.3.6 E**)**. With further deformation, these textures can develop into faults accompanied by coherent, millimetre to centimetre thick fault breccias.

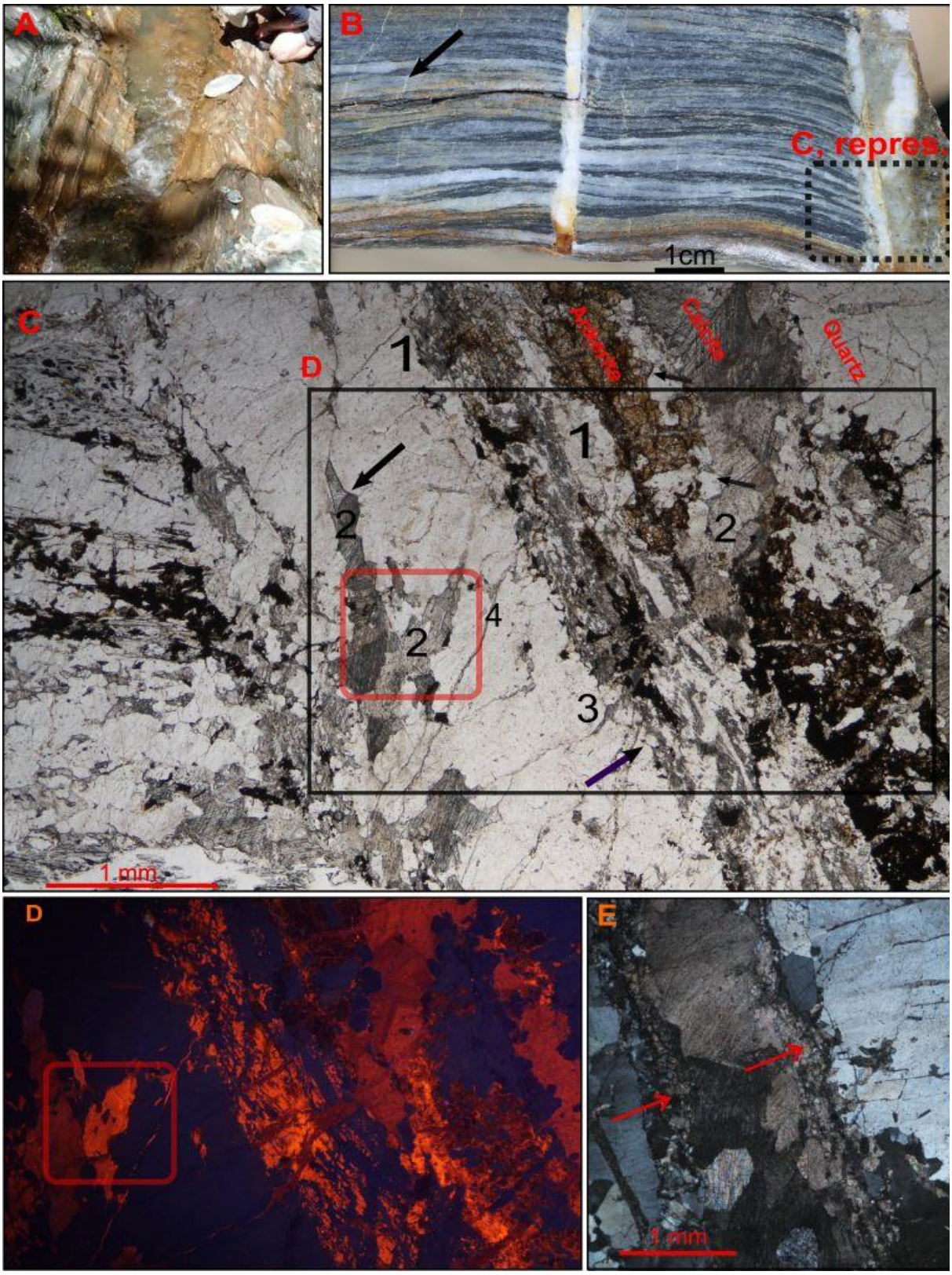

Fig. 2.3.3) A: Kink folds at Murdoch Creek. The strike of the veins is similar to the strike of the kink folds' fold axial plane. (Outcrop B2). **B:** Cross sectional view of a hand specimen from this location with variously wide calcitic veins (small ones indicated by arrows). In right part of image are veins and fault breccias. The box is a representative location where C would have been from. BUL2B. **C:** PPL. The picture shows various vein orientations and material. The numbers refer to the succession of the mineral precipitation. 1 refers to the oldest and 4 the youngest veining event. The arrows point towards euhedral grain boundaries. The red box highlights stage 2 veins which have differing orientations. **D:** CL image. It shows the different carbonate vein generations,

compositions and oscillatory zoning. Composition does not necessarily coincide with grain boundaries (compare red box in C&D). BUL2B. **E:** Parts of carbonate vein can be bounded by very small grained, presumably brecciated carbonate (Red arrows). BUL2B.

A feature in this particular sample (BUL2B) is a net-like carbonate and quartz structure (Fig. 2.3.4 A&B). Of both minerals, quartz and carbonate, the crystallographic lattice is continuous over an area of several mm² even if "interrupted" by one another. Individual grains of calcite in this mesh sometimes contain blocky ankerite and some small grains of muscovite (Fig. 2.3.4 C).

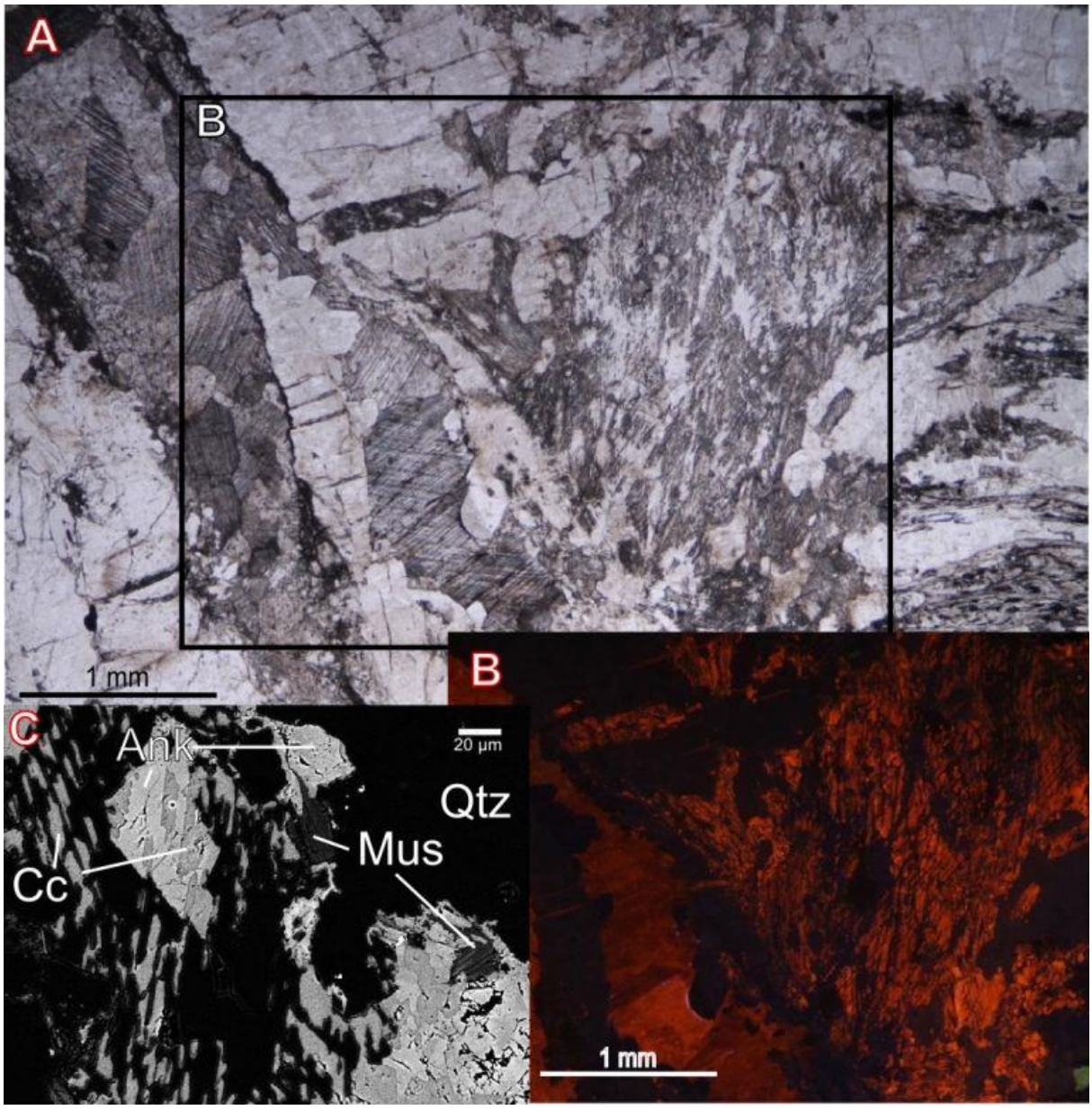

Fig. 2.3.4) A: PPL. Mesh-like carbonate interwoven with quartz in the thicker vein shown in Fig2.3.3 B-E. **B:** CL image shows that most of the carbonate is calcitic. **C:** BSE image. In some parts calcite (grey) occurs together with ankerite (lighter grey). Muscovite is small and rare (dark grey). (All BUL2B).

2.3.1.3: NW-W- trending faults

Throughout study area, NW- to W-trending faults occur. In the Bullendale area, these faults cut across N trending veins, faults and kink folds, partly bending the hinge lines (Fig. 2.3.5). The faults often have distinct polished fault surface (Fig.2.3.6 A.1 & B.1) and on some surfaces, slickenlines could be identified and which are sub-horizontal.



Fig. 2.3.5) Kink fold hinges are cut by NW striking joints and faults. Outcrop B4.

The fault rocks comprise mostly schist fragments which have extensively sheared and/ or been broken (Fig.2.3.6 A.2 & B.2). Additionally, they contain veins of calcite +/- quartz that form networks and partly following grain boundaries. Several generations of veining are recognised (Fig.2.3.6 B.3). In the more brittlely brecciated fault rocks, such as COP3A, the rock immediately in contact to this fault surface is finely brecciated; the fragments are cemented by calcite and the grains become finer towards the surface and calcite cement decreases (Fig.2.3.6 B.4).

2.3.1.4: Gold mineralised structures

Throughout the Shotover Valley area, large W- and NW-trending fault zones with thick, competent fault breccias are found. These are important features as they can be host to gold mineralisation (Craw, 1989). The gold is associated with arsenopyrite and pyrite, either as inclusions or as free gold in their proximity (Craw et al., 2006). The NW- trending faults dip moderately (mostly around 60°) to the south, while the more E-trending ones dip at a similar angle to the NE (Fig. 2.1.2). Where examined, this drag indicates a normal sense of shear (Craw et al., 1991). In the study area, two of these fault structures are present, both of which have been mined in the past for gold. These are the Bullendale Reef and Copper Creek Reef.

2.3.1.4-1: Bullendale Reef

From the underground mining and research done in relation to the mining, it was established that the "Bullendale Reef" comprises several roughly parallel sheets of lensoidal silicified fault breccias (Barry 1966, and references therein). The slickensides on their outer surface indicate that at least the last movement of the fault was that of a normal fault (Barry 1966, and references therein). Smaller shear zones, with a normal sense of shear, occur every 30-50 cm within a few tens of metres of the Bullendale fault zone (MacKenzie et al., 2007).

The Bullendale Reef is not exposed at the surface today but within the bed of Murdoch Creek big boulders of silicified breccias are found. These boulders are most likely from the Bullendale Reef or a secondary structure of it. In this breccia, components are predominantly made of fragments of silicified breccia, fragments of hydrothermal quartz and less commonly of schist. The schist components can contain ankerite, which has the habit of phyllosilicates, potentially as a replacement of chlorite. Ankerite also occurs as grains in the quartz components, but not within the matrix (Fig.

2.3.7). The breccia components are cemented in a matrix of hydrothermal mica and kaolinite. Amongst the matrix minerals, pyrite, arsenopyrite, and small grains of rutile are embedded (Fig. 2.3.7). The coarser pyrite can also contain inclusions of galena and sphalerite. Where exposed, arsenopyrite grows over pyrite.

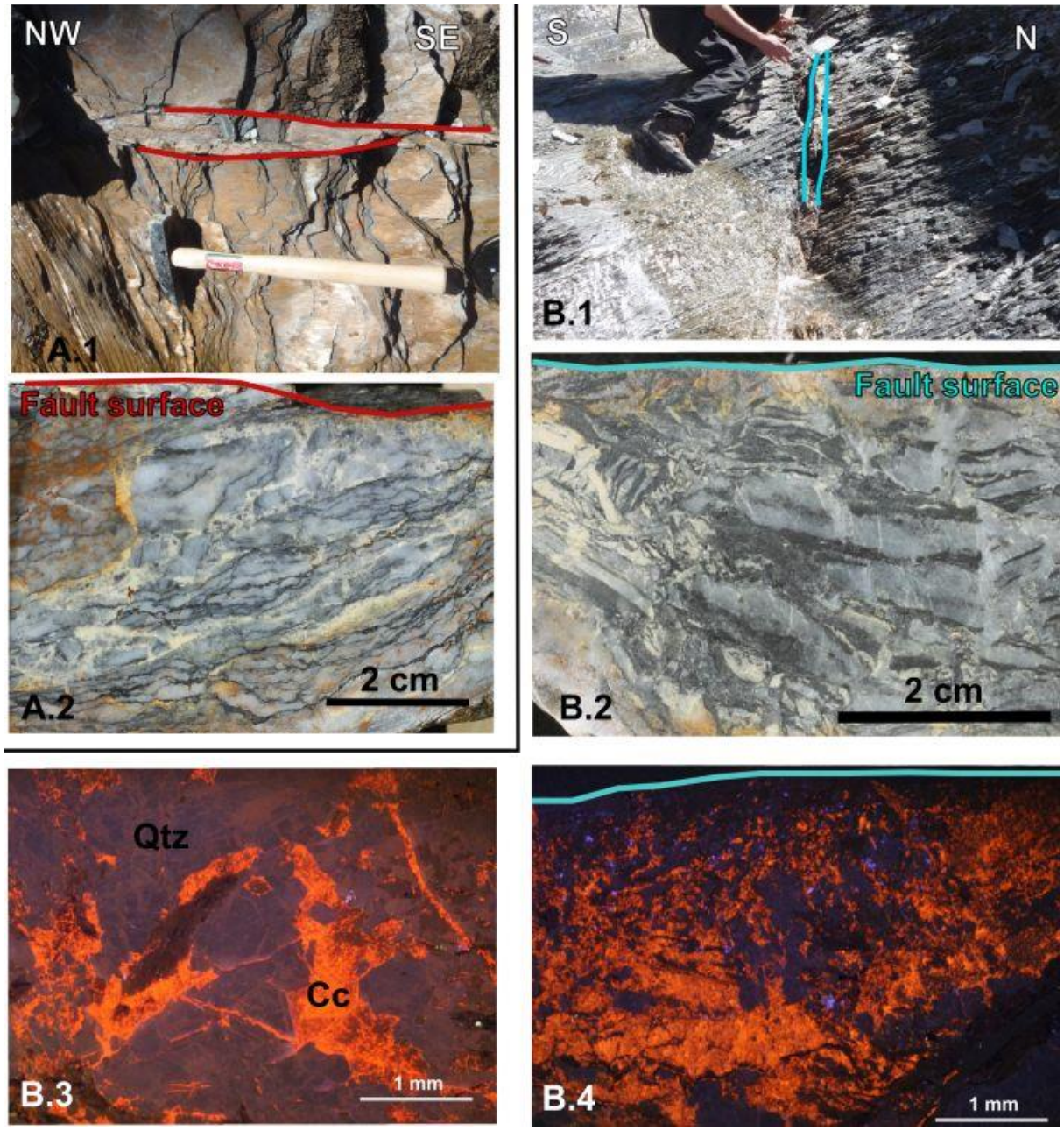

Fig. 2.3.6) NW-trending fault zones at Bullendale (sample BUL4A, outcrop B4) **(A.1)** and Copper Creek (sample COP3A, Outcrop C4) **(B1).** Both fault zones are less than 1 dm wide and have distinct polished fault surfaces on either side. **A.2:** The fault rock at Bullendale is veined and contains phyllosilicate-rich shears. BUL4A. **B.2:** The fault rock in the Copper Creek fault is veined and brecciated. COP3A. **B.3**: CLI. Several generations of veins (orange) cutting hydrothermal quartz (dark) (COP3A). **B.4:** The fault surface (top) is bordered by a zone of brecciated schist, cemented by calcite. The brecciated fragments get finer towards the fault surface and calcite cement decreases. COP3A.

2.3.1.4-2: Copper Creek Fault

Unlike Bullendale Reef, the silicified-fault breccia at Copper Creek is well exposed, i.e. at outcrop C1 (Fig. 2.3.8 A-E). The fault dips at around 55° towards N and can be traced over several hundreds of meters on the south facing slope in Copper Creek (= true left of Copper Creek). When it transits onto the true right of Copper Creek (at outcropC1), the strike of the silicified breccia is ENE (Fig. 2.1.2). Where found, slickensides on the fault surface are parallel to the fault dip. The fault is marked by a distinct layer of silicified breccia (Fig. 2.3.8 B & C). The rock in the hanging wall of the fault is a fissile greyschist intercalated with decimetre thick layers of more competent schist. This schist is structurally largely intact but highly altered (Fig. 2.3.8 A & B).

The alteration halo is about 10 m wide. Within the halo in what was originally most likely a greenschist, chlorite has been replaced by kaolinite, quartz, ankerite and magnesian siderite; along grain boundaries barite precipitated. The quartz has the texture of a phyllosilicate (Fig. 2.3.8 D). Titanite has been broken down and the titanium is incorporated by newly grown rutile. Close to the fault, abundant sulphides are found in the altered rock. These sulphides are pyrite, which is often slightly corroded at the rim, and arsenopyrite, which surrounds the pyrite (Fig. 2.3.8 C). Arsenopyrite forms euhedral grains. Fissure veins in the altered rock are filled with kaolinite, embedding "freely suspended" clusters of ankerite.

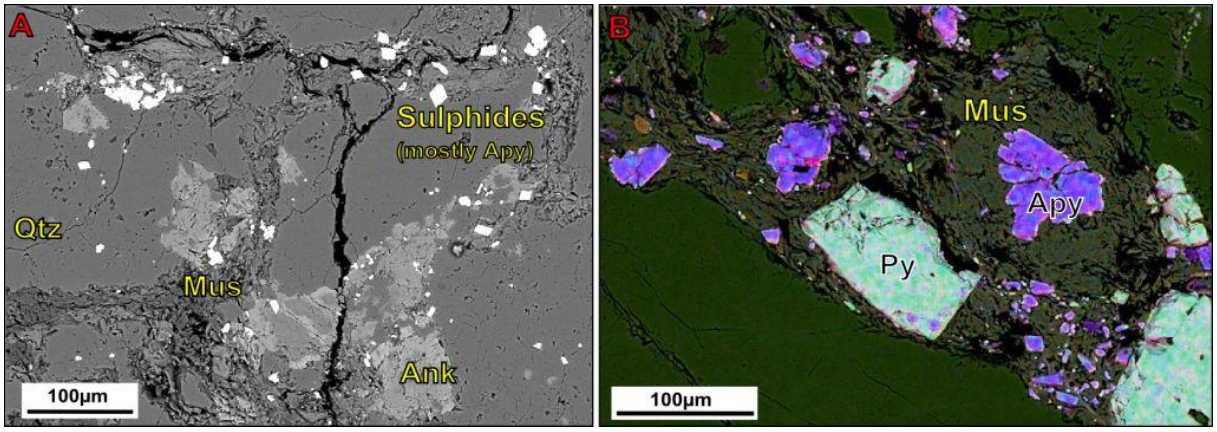

Fig. 2.3.7) A: BSE image of a silicified breccia (probably of the Bullendale Reef). Components are largely made of quartz with some ankerite. Sulphide occurrences are confined to grain boundaries and cracks. **B:** Layered element map. The breccia matrix is made of hydrothermal muscovite and sulphides. All BUL1.

Following the breccia along strike, different fault-related structures are found. The rock directly above the fault surface (on the northern side) can be thoroughly veined by ankerite-rimmed quartz veins (Fig. 2.3.9 A.1). These veins are at an about 10° angle to the fault surface. At the contact to the fault, the veins intersect each other multiple times and the veins generally do not have the rims of ankerite, except when in contact to fragments of wall rock (Fig. 2.3.9 A.1). In thin section, the quartz veins show zones and bands of smaller, rotated grains (Fig. 2.3.9 A.2 & A.3). This gives this part a similar texture and appearance as the silicified breccia. The silicified breccia itself can vary in thickness and reach several dm and be made of several centimetre thick breccias. These are separated by 1-2 millimetre thick dark, sulphide-rich, micaceous stylolites (Fig. 2.3.9 B.1 & 2). Sulphides in the fault breccia's stylolites are arsenopyrite and pyrite. The arsenopyrite forms small euhedral grains which are either on their own or surrounding bigger, partially corroded pyrite grains. The pyrite grains can contain inclusions of galena and sphalerite. No stibnite has been found associated to the E-trending

fault. The silicified fault breccia(s) contain only very little ankerite; ankerite occurs in the quartz-rich layers, where it forms irregularly shaped, ragged-bounded grains, which are sometimes in contact to hydrothermally slightly overprinted muscovite (Fig. 2.3.9 B.2 & 3) and/ or the ankerite forms veinlets crosscutting the fault breccia structure. Some of the carbonate shows signs of resorption (black arrows in B.2 in Fig 2.3.9). As also noted by Craw et al. (2006), the E-W trending fault is offset along a roughly N-S trending vertical structure, which they interpret to be Moonlight Fault-related.

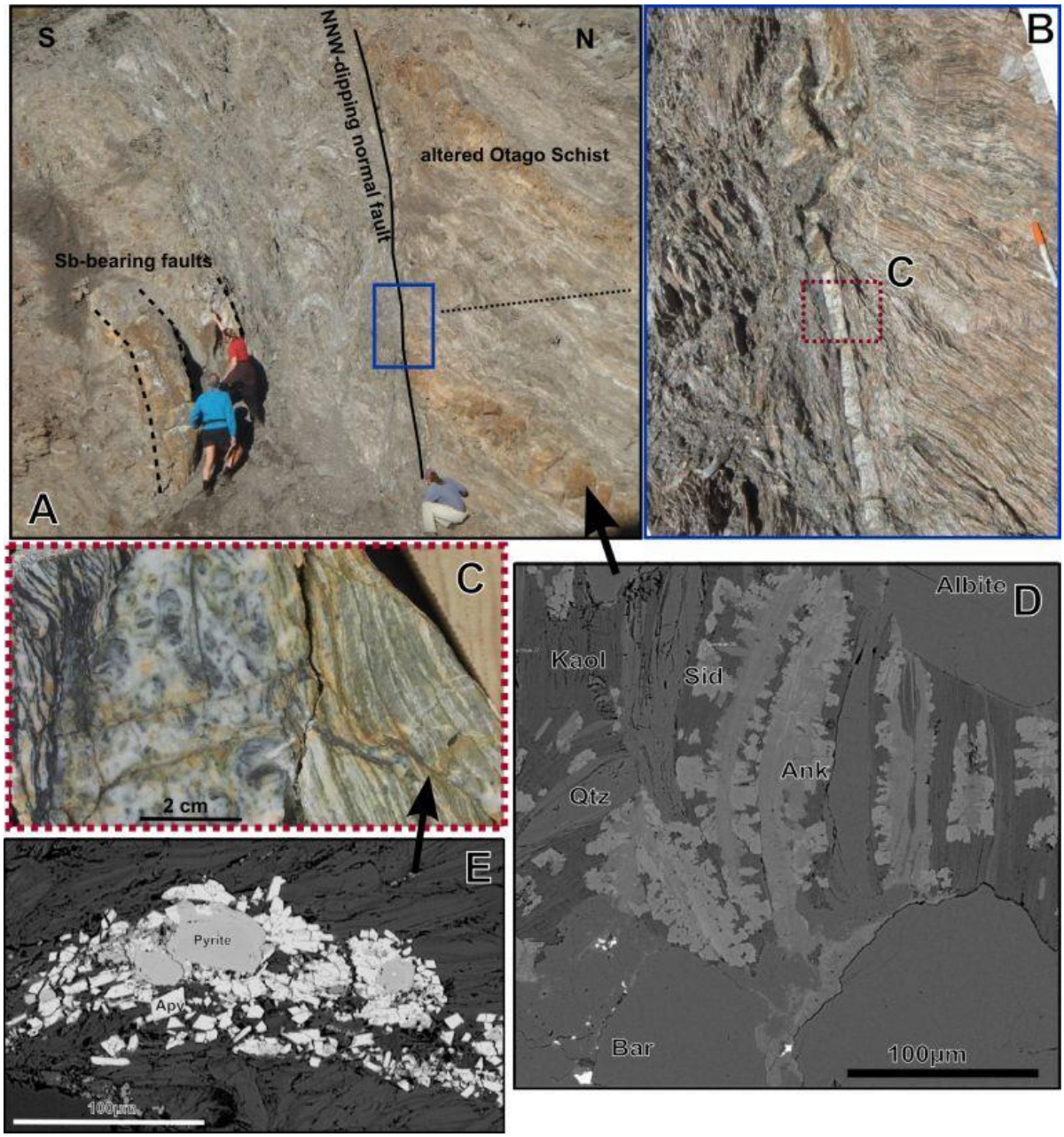

Fig. 2.3.8) A: Cross sectional view of the E-W trending, gold-bearing fault zone at Copper Creek (Outcrop C1). In the structurally lower part of the shear zone, stibnite -bearing fault zones are present (COP1D). **B&C:** The fault is here bound by a ca. 5 cm thick layer of silicified breccia, separating the altered wall rock in the hanging wall and strongly sheared and brecciated rock within the fault zone in the footwall (COP1A). **D:** In the wall rock, hydrothermal phases (carbonate, quartz and kaolinite) occur and along grain boundaries barite (bright white) is present. COP2D. **E:** Slightly corroded pyrite is surrounded by arsenopyrite. The embedding mineral is muscovite which along cleavage planes has partly been replaced by hydrothermal muscovite.

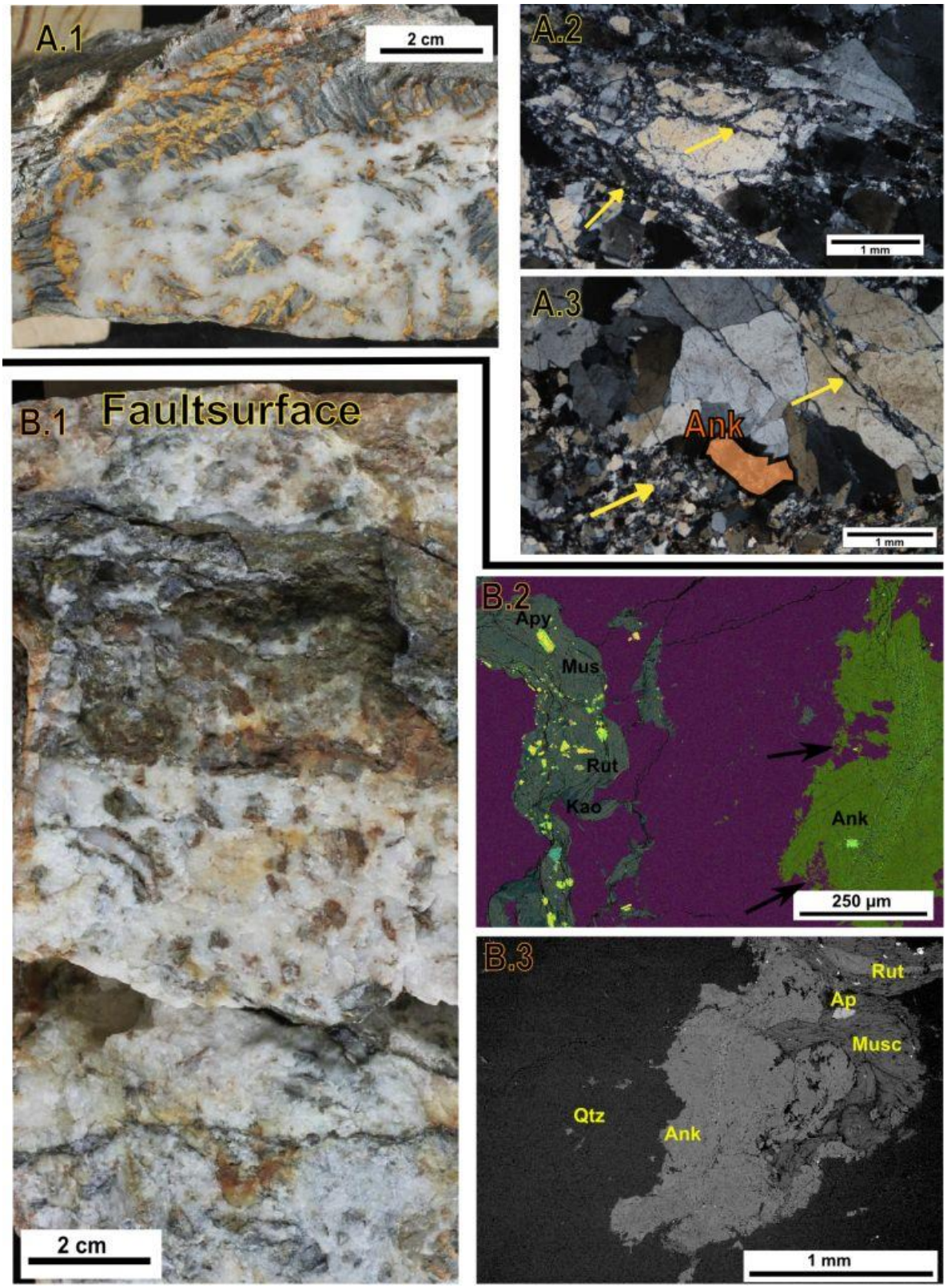

Fig. 2.3.9) Rocks of the E-W trending Copper Creek Fault. A.1 and B.1 are displayed relative to their bounding fault, which is marked by a distinct polished fault surface. **A.1:** Many qtz-ank veins penetrate the rock and are especially common close to the fault surface. Close to the fault surface, there is only little ankerite in the veins and which is mostly in contact to schist or within it. **A.2 & 3:** Within the quartz veins, small deformation zones are present (arrows). **B.1:** The silicified breccia is mostly made of quartz with some other components embedded. Three distinct breccia layers are distinguished and separated by grey stylolites. **B.2:** Stylolites comprise muscovite which embeds arsenopyrite and rutile. **B.3:** Components in the quartz-rich part of the breccia are made mostly of muscovite and ankerite. The muscovite is finely intercalated with kaolinite/ illite. The ankerite has ragged grain boundaries and

there are signs of resorption (Black arrows in B2). (COP2B; COP2C) Despite coming from the same outcrop, the samples were not originally connected.

Structurally below the silicified breccia is a several metre thick zone of brecciated and sheared schist. The foliation has been rotated towards the fault surface and dips steeply towards the north (Fig. 2.3.8). At the outcrop examined (C2), at the southern end of fault zone, zone (ca. 2 m away from the top shear, perpendicular to the fault's strike) are 2 solidified, ca. 1 dm thick, NE-SW striking, steeply to the NW dipping fault breccias (Fig. 2.3.8). These are rich in quartz and are in places impregnated by structurally younger stibnite. These Sb-bearing fault breccias are cut perpendicular to their strike by faults and slickenlines on both of these dip steeply towards the W.

2.3.1.5: Joints and associated veins and faults

A set of joints or small faults is present at the confluent of Murdoch Creek and Bullendale Creek (outcrop B3; Fig. 2.3.10 A & B). These joints have a similar trend as the kink folds (Fig. 2.3.10 C). The joints can be filled with hydrothermal precipitates, which are, in the case examined, carbonate and kaolinite. The rim next to the rock is made of ankerite with interstitial calcite. The contact to the kaolinite-rich centre of the vein is defined by a fine-grained, needle-like, more Mg-rich ankerite (BUL3B; Fig. 2.3.10 B). The central part of the vein is made of kaolinite and some muscovite, embedding single grains or small cumulates of ankerite with Mg-rich ankerite at the rim (Fig. 2.3.10B). At this outcrop, the joints are in the footwall of a moderately (38°) NW- (298°) dipping fault which juxtaposes the jointed and veined rock against a block of kinked greyschist in the hanging wall (Fig. 2.3.10 A). The movement along the fault resulted in the formation of a thin (less than 2cm) fault breccia and, in dilatational sites of the fault, an about 2-3 cm thick carbonate vein formed (BUL3A; Fig. 2.3.10 A).

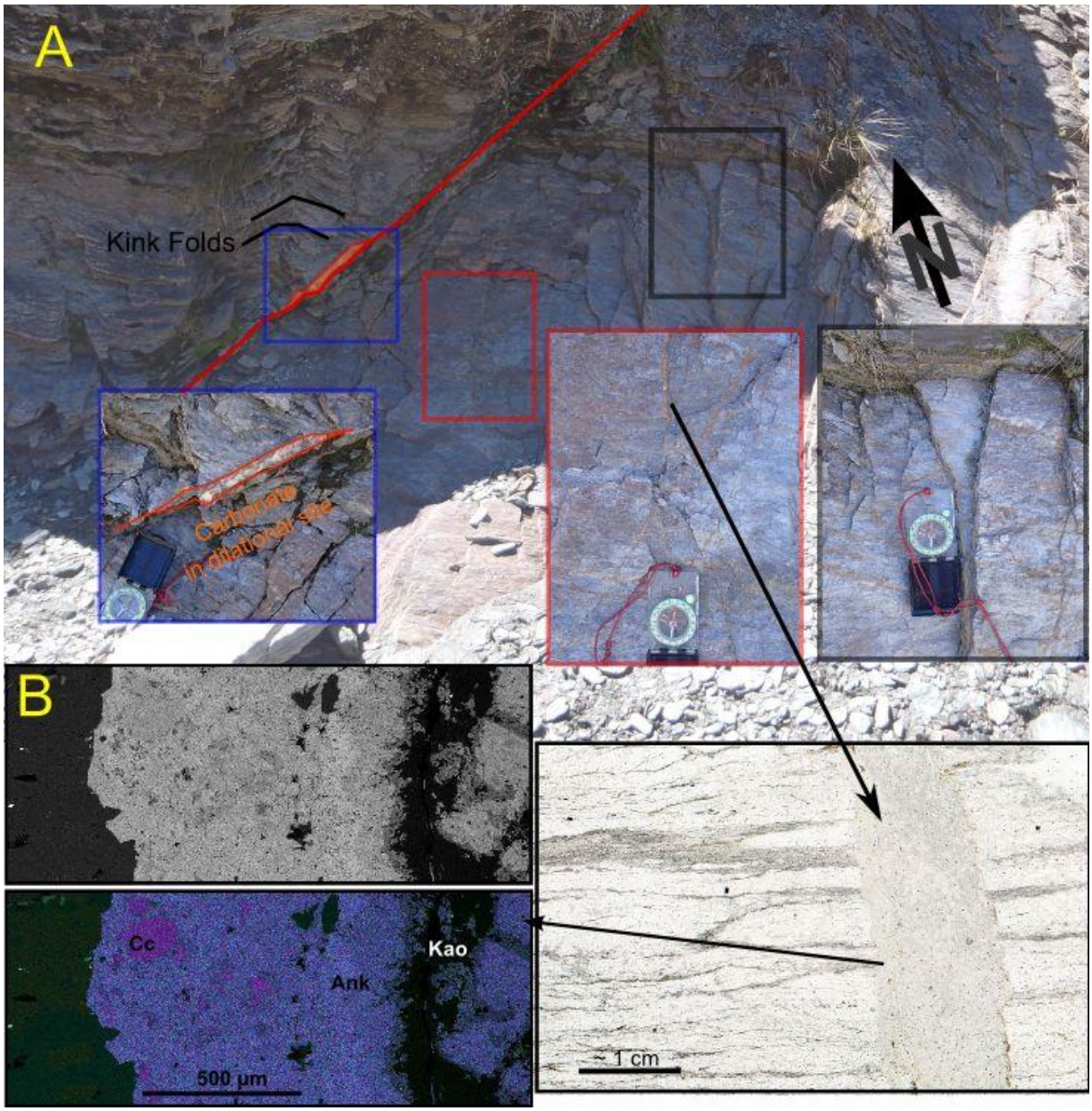

C)

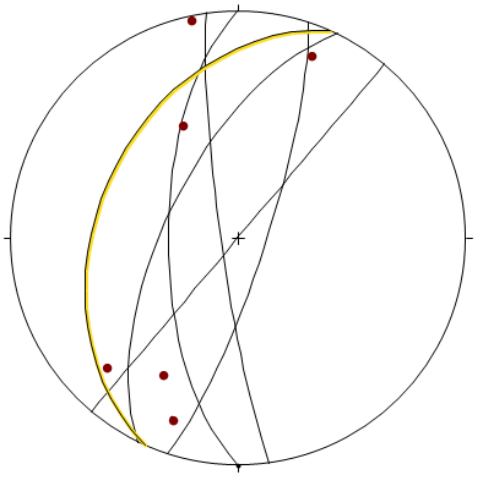

Fig. 2.3.10) A: Different structural features at outcrop B3. Blue box: Fault with carbonate (calcite) in dilational site (sample BUL3A, not shown here). In the hanging wall are kink folds. Red and black box:: Joints controlling vein emplacement in the foot wall of the fault.
B: The vein material in the joints (Top: BSI; Bottom: Layered image). The vein rim is made of ankerite (blue) with interstitial calcite (pink). The carbonate at the interface to the vein centre is rich in Mg and poorer in Fe. The centre is made of cumulates of the same carbonate as the rim, an d is embedded in kaolinite. BUL3B.
C: Joint surfaces and veins at this outcrop= black great circles. Kink fold hinges =Red dots at other outcrops. Fault at this outcrop = yellow.

2.3.2- Cenozoic structures and features around Treble Cone and Black Peak

The foliation in this area dips shallowly (ca. 10-20°) west to south. Cm to dm wide, wavy, open and some tight folds with fold hinges plunging roughly 5° towards NNE (014°) deformed the foliation ductilely. Structures that formed below greenschist facies conditions are faults, joints and kink folds. Kink folds occur in small isolated areas and have amplitudes of a few centimetres (Fig. 2.3.15). Their hinges strike NE-SW (240/10), which is in agreement with values measured by Craw (1981) in this area. Often spatially associated with these folds are ankeritic veinlets that often spread out parallel to the foliation (Fig. 2.3.11).

Fault zones can be found at several locations (outcrops TP. 1,4 & 7) These fault zones strike E to ESE, are often several meters wide and are accompanied by quartz and ankerite veins, as well as alteration halos in the adjacent rock. The fault breccias are made of brecciated and veined metamorphic rock and silicified breccias. They are generally covered with scree. The silicified breccias are mostly made of hydrothermal quartz and ankerite. Ankerite can contribute about 20 vol-% to the breccia (TP1.3). Apart from quartz and ankerite, the breccias contain fragments of the wall rock, rutile and zircon (both presumably from the wall rock) and hydrothermal ZnS. Some of the grain boundaries of ankerite to quartz trace euhedral crystal shapes and the ankerite has grain boundary-parallel zoning. Additionally, the breccia textures show chaotic grain arrangement and development of micro-breccias. Due to the lack of marker horizons and not exposed fault surface, the shear sense of the fault zones could not be established. A more detailed description of the fault zones and their associated rocks and alteration halos is given in chapter 3.

Veins in the wall rock of the big faults measured at TP1 & 4 strike between 100° and 120° and dip moderately to steeply (45- 80°) northward. Throughout the area, joints are present. These strike either NNE (10) or SE (120-130) and are dipping steeply (80-85°). At TP7, north-trending joints cut ankeritic veins, but crosscutting relationships could not be established in other places. Overall, field work here was undertaken with focus of chemical aspects of fluid flow, such as alteration of the metamorphic rock and fluid source and a more thorough structural study of this area could be undertaken in the future.

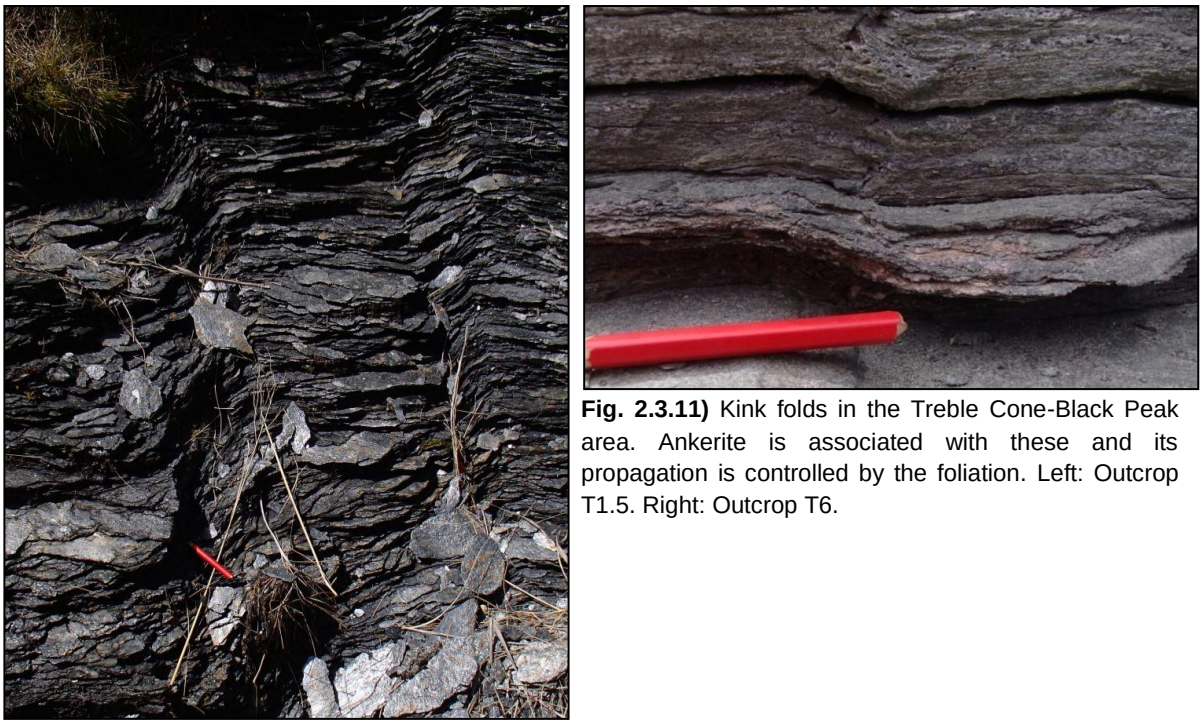

Fig. 2.3.11) Kink folds in the Treble Cone-Black Peak area. Ankerite is associated with these and its propagation is controlled by the foliation. Left: Outcrop T1.5. Right: Outcrop T6.

2.3.3- Red Rock-Cenozoic structures west of the Moonlight Fault

The outcrops at Red Rock are located in or next to a N-S-trending zone of orange rock which is hydrothermally altered greenschist (Fig. 2.1.4). The transition of unaltered to highly altered rock can be sharp or gradual. In the eastern portion of the studied area, greenschist is intercalated with grey pelitic schist. The greyschist and parts of the greenschist show isoclinal folding with steep fold axial plains and the fold axis is oriented 220/17.



Fig. 2.3.12) Greenschist with kink folds and co-genetic ankerite veins. In one limb the veins are predominantly parallel to the foliation. In the other they often cut across it (arrows). In the hinges the carbonate layers are thicker than in the limbs. RR1.

Kink folds in greenschist are open to tight with an amplitude on the cm scale and the wavelength of a few dm. Associated with kink folds is ankerite (Fig. 2.3.12), which, depending on the limb it is in, is either mostly parallel to the foliation or cuts across the foliation. The foliation-parallel carbonate is thicker in the hinges than in the limbs (Fig. 2.3.12). The fault hinges are partly sheared and foliation-parallel veins terminate on either side of the shear. Similar to the other study areas, veins are ubiquitous within the alteration halo. These veins are made of carbonate +/- quartz. Thinner veins (<1cm) can form networks, whose propagation is often controlled by the greenschist's foliation. Throughout the outcrop, thick (2-3 cm) carbonate veins occur and which have irregular boundaries to the embedding greenschist. Where measured, the sparry veins have similar orientations (340/40) to

the foliation (320-337/45-80). However, these thick carbonate veins can form dense networks, forming a matrix-supported breccia clearly cutting the foliation (Fig. 2.3.13 A & B). These veins are made of sparry carbonate, predominantly ankerite, but also contain chalcopyrite, which occurs generally close to the vein's wall rock (Fig. 2.3.13 B). The ankerite embeds structurally euhedral, hydrothermal, zoned quartz, which is occasionally double-ended prismatic (Fig 2.3.13 C). Late stage calcite fills interstitial spaces in the centre of the veins (Fig 2.3.13D).

In addition to the veins, faults are ubiquitous throughout the outcrop at Red Rock. These faults are manifested by cm to dm-thick breccias made of fragments of altered greenschist and hydrothermal quartz and carbonate. Entering the zone of altered greenschist from the W, after about 15m one crosses a 1 m wide zone which contains blocks of silicified breccia. This breccia is made of hydrothermal quartz and is streaked with mm to nearly cm wide ankeritic veins containing chalcopyrite.

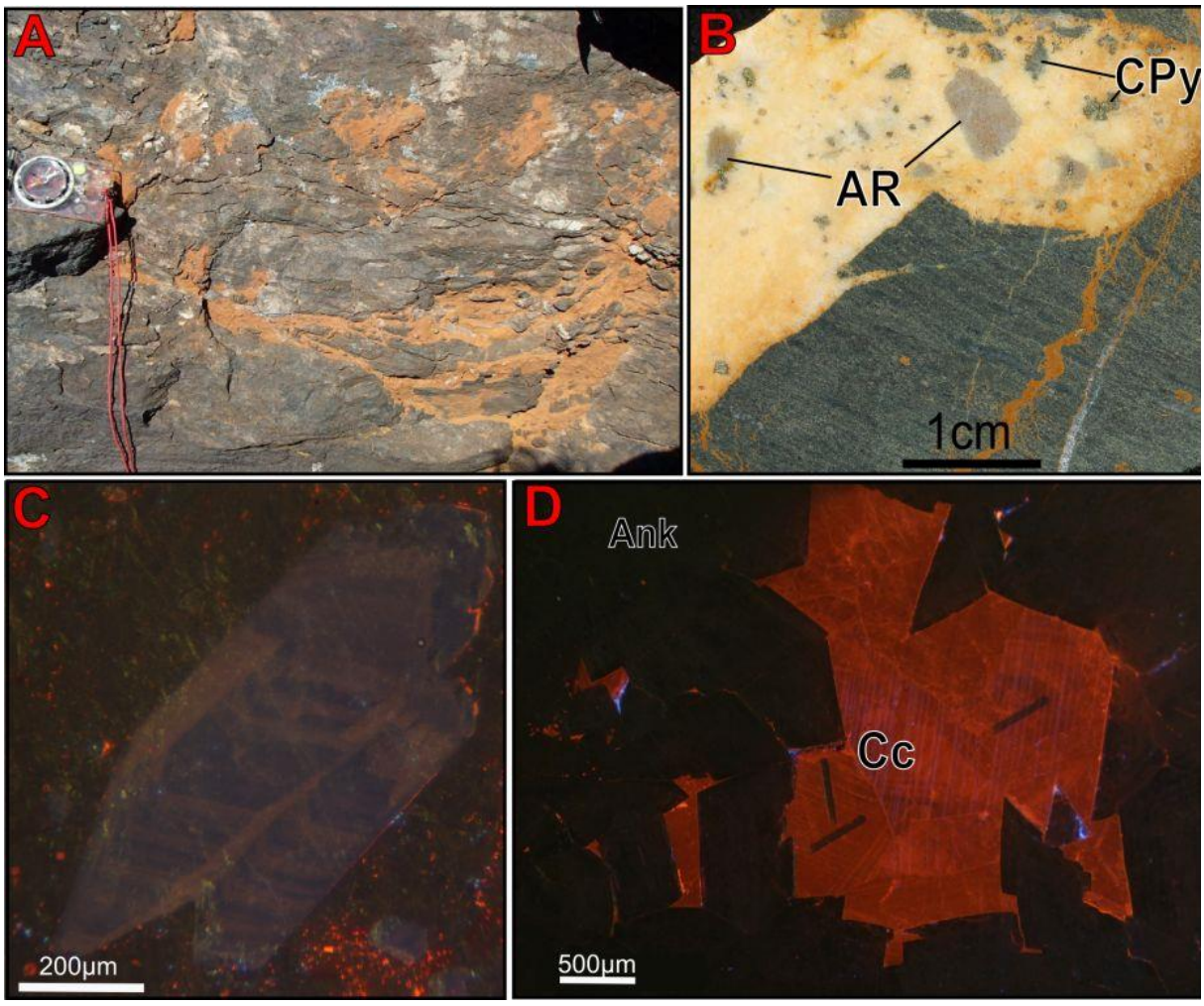

Fig. 2.3.13) A: Several cm thick carbonate veins at Red Rock form networks in the greenschist. **B:** The veins in A contain several mm big chalcopyrite grains and highly altered greenschist. The greenschist in the wall rock shows no macroscopically visible hydrothermal alteration. AR=hydrothermally altered greenschist. CPy=chalcopyrite. RR20. **C:** CLI. Hydrothermal, chemically zoned, "doubled-ended", quartz in the ankeritic vein "matrix". RR20. **D:** CLI: Late stage calcite fills late stage cavities in the otherwise mostly ankeritic vein. Note black lines are laser tracks. RR20.

2.3.4- Discussion of the non-magmatic structures

Comparing the structures in the study areas described above shows that there are some similarities and some differences. All areas have structures that form at low temperature in the upper crust

(<300°C), such as veins, kink folds and faults. A major difference between the structures in the footwall and the hanging wall of the Moonlight Fault is the prominent copper mineralisation at Red Rock.

Regardless of outcrop location, it is evident by the abundance of hydrothermal deposits that the low-temperature structures (faults, kink folds, joints) accommodated fluid flow. The euhedral shape of the mineral grains (carbonate and quartz; Fig. 2.3.3C; 6B.3; 13C&D) in these deposits shows that mineral crystallisation took place in fluid-filled cavities. The varying carbonate compositions, oscillatory zoning (Fig. 2.3.18C), resorption (Fig. 2.3.8E; 12) and the alternating precipitation of different minerals, i.e. carbonate and quartz (Fig. 2.3.3.C; 18D) give evidence that the chemistry of the fluid changed over time. The cause for precipitation may have also changed during the history of some of the structures as is indicated by the net-like calcite-quartz grains displayed in Fig. 2.3.7 and which are entirely different to anything else seen in the different samples. The net-like mineral cluster may have formed by co-precipitation of the carbonate and quartz. If this is true, then the easiest mechanism how this could take place is by reducing pressure. In all other main precipitation mechanisms (pH, T), quartz and carbonate have opposing behaviours (see below for references). Additionally, it can be deduced that because the net-like structure is controlled by the crystal structure of the carbonate and not fractures, the mineral precipitation probably took place under locally very low differential stress, such as in a fluid filled cavity.

Additionally, textures provide evidence that fluid flow happened throughout the history of the activity of the studied tectonic structures. Carbonate veins, that are parallel to fold axial planes, as described by Craw et al. (2006), and those describing a "schistosity fan" (Fig 2.3.2A), show that fluid flow took place during folding. Veins cutting across the fold axial plane show that fluid flow took place also afterwards (Fig 2.3.2B). At Red Rock, the texture of kink folds and spatially associated ankeritic carbonate (Fig. 2.3.16) also show that both formed contemporaneously. The big and small W-NW trending faults are also accompanied by genetically related veins (Fig. 2.3.6) or are made of hydrothermal quartz forming the silicified fault breccias (Fig. 2.3.8 & 9). On microscopic scale there is also evidence for a genetic connection of tectonic movements and fluid flow. The veins of the first 2 stages in Fig 2.3.5 enclose angles of less than 45° in the examined thin section and the transitions from one to the next is gradual, indicating that the orientation of the principal stress axes changed on a local scale continuously. (The term "stages" hence only refers to what is seen in the sample and a continuous process probably took place.) Other evidence for the connection of deformation and fluid flow can be found in the abundant fault breccias in the areas and which also show multiple precipitation and brecciation events (see below).

2.3.4.1: Silicified breccias

Microtextures show that the silicified breccias formed by multiple precipitation and brecciation events, as can be deduced from the existence of zones of subgrain rotation and the embedding of cumulates of (mostly) hydrothermal quartz in a fine grained matrix (Fig. 2.2.7 & 9).

A (presumed) precursor of a silicified breccia is the vein-rich hand specimen displayed in Fig. 2.2.9. These veins show a decrease of ankerite, an increase in quartz and intersection of separate veining events and shearing towards the fault surface. This can be attributed to re-dissolving of previously precipitated ankerite and (near) simultaneous precipitation of quartz. As remnant ankerite only occurs when in contact to the schist or within it, it indicates a different "micro-environment" in the vicinity of the rock (see below).

The dissolution of carbonate and precipitation of quartz could be attributed to several factors, namely pressure, temperature, pH and CO_2 content. A decrease in pressure would cause precipitation

of quartz (Willey, 1974, Walther & Orville 1983); however, the same is true for carbonate, or at least calcite (Millero, 1982; Hawley & Pytkovicz 1969, Segnit et al., 1962). Hence, changes in pressure are probably not the controlling factor. Within the range of temperature and pressures of this study many carbonates are less soluble with increasing temperature (i.e. Segnit, 1962, Fein & Walther, 1987; Helz &Holland, 1965; Benezeth et al., 2009, Sun et al. 2009; Wigley 1973). For quartz, solubility increases with increasing temperatures (Siever, 1962, Morey et al., 1962, Walther & Orville 1983; Fournier & Potter, 1982). Hence, a decrease in temperature promotes growth of quartz over carbonate. However, an increase in temperature does not explain why carbonate remains stable in contact to schist, as in a system such as this fluid also penetrated the rock, hence also exchanging heat. and elevating the rocks temperature. Regarding pH, it has been shown that quartz solubility increases above a pH of 6 (at least at 70°C) (Knauss & Wolery, 1988). This concurs with Walther & Orville (1983) who found that SiO_2 forms complexes with OH^- ions and they take this to be the reason for the reduced solubility of silica in CO_2 -bearing fluids as opposed to pure H_2O fluids, provided everything else being equal. Admittedly, Walther & Orville conducted their experiments at temperatures above 400°C; however, the results by Knauss & Wolery (1983) suggest that the solution species of quartz is the same at low temperatures and hence one would also expect a decreased solubility of quartz with decreasing pH. At the same time carbonate solubility increases with decreasing pH and increasing CO_2 content (i.e. Manning, 2013 and references therein; Segnit et al., 1962).

An indication that the succession of carbonate and quartz is indeed due to changes in fluid chemistry is supported by the fact that ankerite is present in contact to the greyschist. In rock, the fluid is often interpreted to precipitate carbonate as the reaction with the hydrous metamorphic minerals releases OH^- molecules, hence increasing the pH (i.e. Craw, 1989; also see chapter 3 for details). This would mean that in close vicinity of the rock the pH would be locally higher than in the fluid, provided the site is rock-buffered.

Hence overall, the formation of the silicified breccias probably involved not only several brecciation and precipitation event, but also a decrease of pH over time which would promote solubility of carbonate and precipitation of quartz. The reason for this pH decrease may be related to a higher CO_2 content (or perhaps other components) in the fluid. Another indicator for a change in fluid chemistry is that pyrite often became corroded at the rims before arsenopyrite precipitated.

2.3.4.2: Joints

Throughout the region, joints are common. The structural age of these veins is often hard to asses. At Treble Cone, E-W trending joints are similar in their orientation to the faults and may be connected to those. The N-trending joints seem to be at least partly younger than the ankeritic veins, as they cut across veins.

Joints are very common in the Otago Schist and Weinberger et al. (2010) showed that joints, at least in eastern and central Otago, form during decompression during exhumation due to release of strain energy. This effect formed a set of joints which are perpendicular to the metamorphic lineations. This could also be the case in the Shotover area, as the metamorphic lineations dips shallowly WNW, and which is about perpendicular to the strike of the joints at B3 (Fig. 2.3.10). In a second option the joints would have formed due to the Cenozoic deformation associated to the Alpine Fault (Cooper et al., 1987). Indications that this may the case is that lamprophyre dikes of that age are controlled by joints (Craw, 1981; Cooper et al., 1987).

Regardless of the uncertainty of the age, the material filling joints and cracks is quite interesting. In the cases examined (at outcrop B3 and in the altered rock of Copper Creek Fault), joints and fissure veins are filled with kaolinite and ankerite. In all cases, small cumulates or single grains of

ankerite swim in a matrix of kaolinite (Fig. 2.3.10B), indicating that the carbonate particles were suspended in the fluid before being accreted at the vein rim. The association carbonate and kaolinite/ muscovite is typical for the mineralogy in the alteration halo (see chapter 3). It is interesting though that the kaolinite forms a precipitate from a fluid as this shows that Al was mobile in the fluid which is in contrast to many studies (i.e. Carmichael, 1969; Ragnarsdottir & Walther, 1985). It has been shown that mobility of Al increases considerably when forming complexes with various ligands (i.e. Korzhinsky, 1986; Kuyunko et al., 1983). For the conditions in this case (carbonate stability pH range, T between 150 and 300°C), complexes with mostly OH^- and F^- would be dominant (Tagirov & Schott, 2001). The F could come from metamorphic muscovite which generally contains some F (Deer et al., 2003) and which would have been released into the fluid during metamorphic for hydrothermal muscovite replacement. The particles of carbonate crystals are freely swimming in the vein kaolinite, suggesting that carbonate crystallised before the kaolinite (Fig. 2.3.10B). This would concur with the solubility of Al being larger at higher pH (Tagirov & Schott, 2001), while carbonate is not. Texturally and mineralogically similar to the joint fillings are fissure veins found at Copper Creek.

2.3.4.3: Tectonic model

Regarding tectonic structures, the most detailed data in this study has been recorded for the sites at Bullendale and Copper Creek. These show that the relationships of the different features in the Shotover area are complex and their absolute and relative age is often not unambiguously identifiable. In most outcrops, northward-trending structures (fold, faults, veins, joints) are cut by NW-trending faults, joints and the silicified, partly Au-mineralised, W-NW-trending faults. This suggests that the more W trending features are younger than the north-trending ones. This is also supported by the existence of components with kink folds in fault breccias of the E-W trending, auriferous Copper Creek Fault (Craw et al., 2006). However, at Copper Creek, the same silicified fault breccia of the Copper Creek Fault is offset by a N-S trending structure (fault or fold plane) (Fig. 2.3.5). Based on this, it was concluded that the silicified faults at Copper Creek and the kink folds both formed as a response to the movement along the Moonlight Fault (Craw et al., 2006).

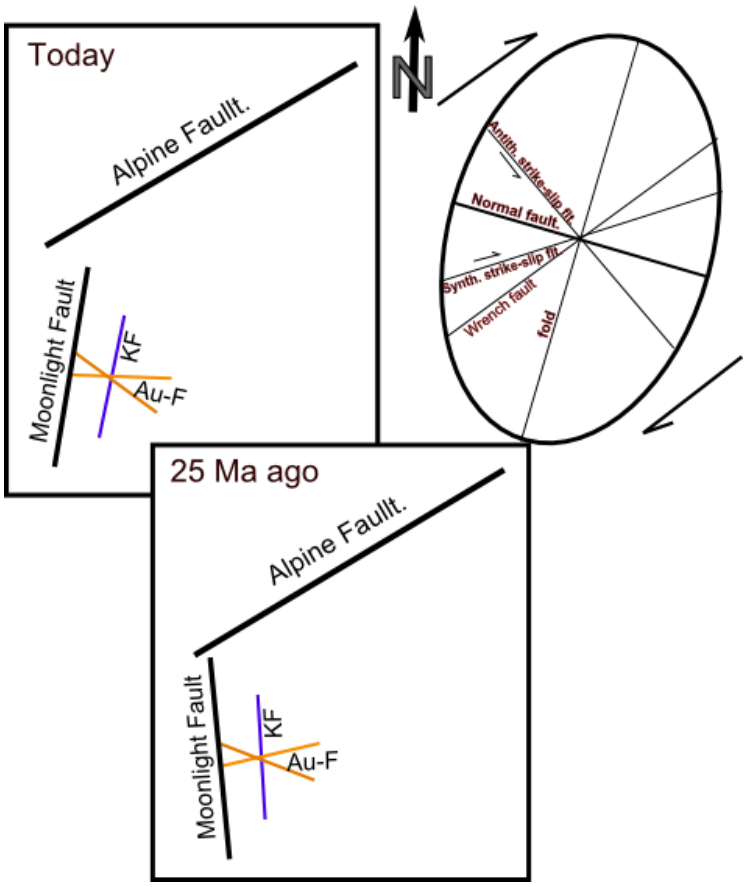

Fig. 2.3.14) Schematic model of the orientation of several tectonic features as today and 25Ma ago, based on White 2002. The ellipse shows different features as they form in a strike slip fault setting (modified from Cooper et al., 1987).

Overall, the formation of the E-SE trending normal faults in the Shotover have been suggested to be related to a monocline in the area, which is defined by the systematic change of the orientation of the foliation and the coinciding termination of the Shotover Antiform (Craw et al., 2006). However, Craw et al. did not explain the kinematics of the faults and were also not sure how old the monocline actually is. An answer to the problem of the normal faults forming may be explained by looking at the regional tectonic regime in the area. Cooper et al. (1987) proposed that the movement of the Alpine Fault caused the formation of several different structural features in the Southern Alps, following a wrench model associated to strike slip faults. The structures forming would be strike slip faults, normal faults and folds. Coincidentally, the orientation of the gold mineralised faults are similar to those of normal faults and strike slip faults as predicted by Cooper et al. (1987) (Fig. 2.3.14, strain ellipse). However, the Alpine Fault caused dragging of large scale structures and hence today's orientation needs to be corrected to the time they formed. This has been done by White (2002); for the time of initiation, the Moonlight Fault (in the study area) this correction results in a change of an angle of about 20° (White, 2002; Fig. 2.3.14; boxes). Despite this, the orientations of the faults in the Shotover still fit relatively well to the orientation of the structures predicted by Cooper et al. (1987). However, according to Cooper et al.'s model only one of the faults observed should be a normal fault while the other one would be a strike slip fault. This is not always the case here as the gold-bearing faults are normal faults (Craw et al., 2006). This discrepancy may be explained by considering the different lithologies involved with the movements along the Moonlight Fault. In the immediate hanging wall of the Moonlight Fault occurs massive greenschist, while soft, fissile greyschist makes up the footwall in the Shotover area (Fig. 2.1.2). As the Moonlight Fault is steeply dipping, compressional movements should be accommodated in the easier to deform footwall. These three aspects are similar to indenter-type models as applied in the eastern European Alps and the Himalayans (Ratschbacher et al., 1991; Tapponnier et al., 1982). In these scenarios, the compression causes extrusion parallel to the indenter (here the greenschist) via strike slip faults and overall extension parallel to the main fault (i.e. Frisch et al., 2000). In the case here, this extension would be accommodated by originally strike slip fault and the low to negative stress would be associated with the strike slip component of the Alpine

Fault. To prove or disprove this very tentative model a more comprehensive structural data set needs to be collected throughout the wider Shotover area and numerical or experimental models carried out.

Regarding the offsetting of the Cooper Creek fault along an N trending feature, it needs to be remembered that the Moonlight Fault continued to be an active reverse fault (Turnbull et al., 1975) and hence related deformation in the foot wall should also continue, especially close to the fault which would cause overprinting of older structures, such as the Copper Creek Fault.

Concerning the structures at Red Rock, the N-S trending orange alteration halo suggests that the predominant fluid conduits may also be N-S trending. However, this is in contrast to the orientation of the thicker veins in this area, which are ENE trending. Though the latter coincides with the orientation of the foliation, it seems unlikely that such big structures are purely controlled by foliation in an overall quite massive greenschist. Overall, as focus in this study was put on the mineralogical and chemical aspects, a thorough structural study of the Red Rock area is needed to establish the exact structural features and their paragenesis, and to find the kinematics of the faults. It would also help to answer whether the faults here are genetically related to the Moonlight Fault.

2.4) Geological features associated with diatremes of the Alpine Dike Swarm

The two diatremes studied here vary strongly in size and shape. Alta Diatreme, which is on the northern flank of Mt Alta, just below the summit, has a circular to slightly oval shape with a diameter of ca. 160m (Gamble, 1984) (Fig. 2.1.5). Niger Diatreme, on the other hand, can be followed for ca. 850 m along its E-W strike but is less than 100 m wide (Cox, 1985) (Fig. 2.1.5). Niger- and Alta Diatreme are embedded in psammitic greyschist. At both locations, joints dip steeply northwards to vertically. The joints in the area control the emplacement of the dikes (Craw, 1984, Cooper et al., 1987, Fig. 2.4.1 A). At Alta Diatreme some of the dikes are cut by joints, which like the dikes, trend E-W. The joints are partly filled with ankerite (Fig. 2.4.1B). Niger Diatreme trends roughly parallel to this joint system. At Mt Alta, shallowly north dipping faults displace the lamprophyre dikes (Fig. 2.4.1A) and the diatreme breccia. In both settings, weathering often thoroughly obscures primary (metamorphic and diatreme-related) mineralogy of matrix and components. This is, for example, the replacement of ankerite by limonite and the oxidation of sulphides.

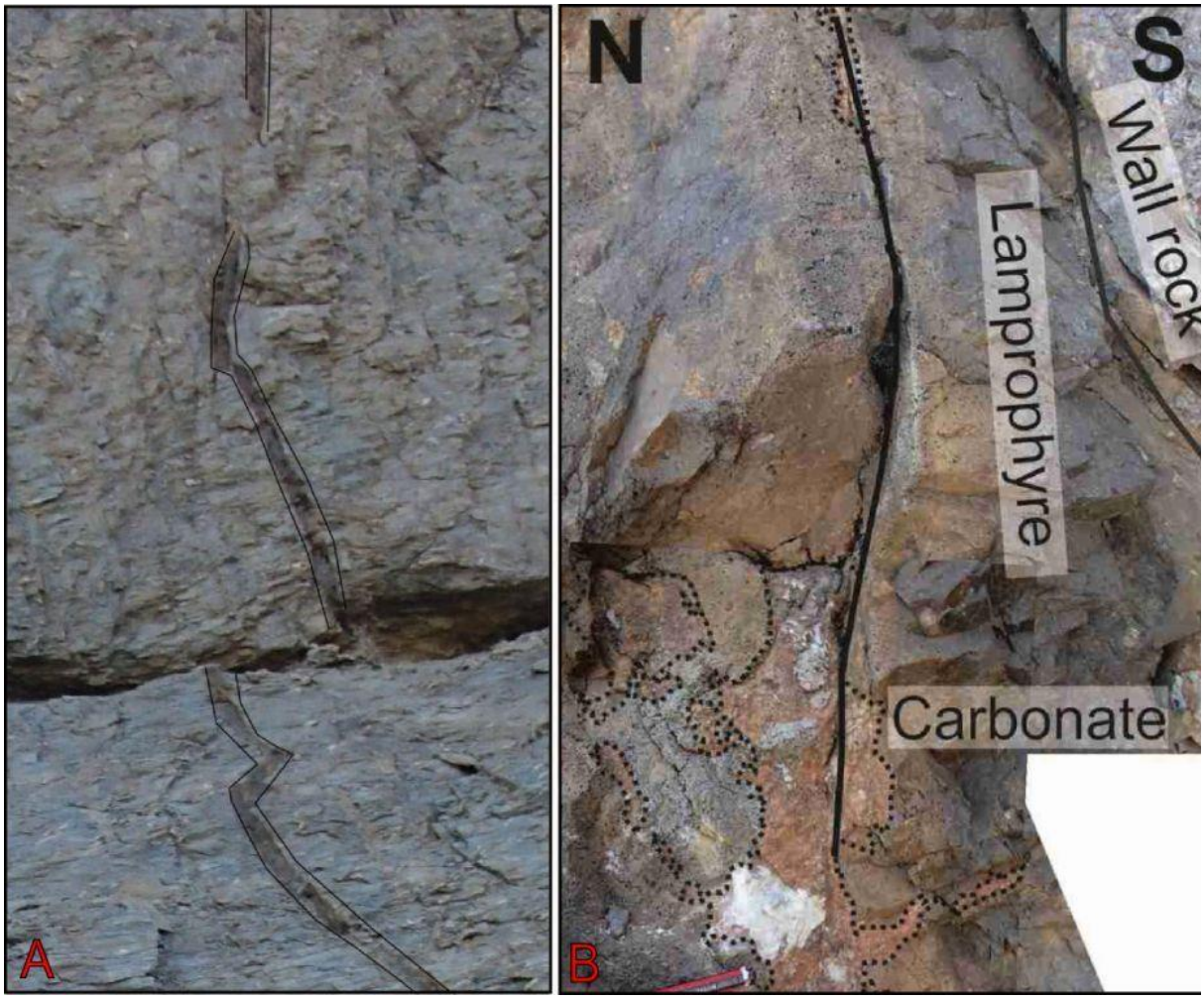

Fig. 2.4.1) A: A lamprophyre dike (ca. 30 cm wide) intruded parallel to joints at Mt Alta Diatreme. The dike is offset by a shallowly to the N dipping Fault. **B:** In a lamprophyre dike at Mt Alta carbonate veins (dashed line) partly follow the orientation of a joint (solid line) in the dike. Width of image about 40 cm. (Both images at outcrop A1).

2.4.1- Niger Diatreme

As mentioned in section 2.1, the lower part of the Niger Diatreme was studied. The southern border is against quartzo-feldspathic schist. This boundary is not well constrained and is marked by an about 30 m wide zone with several metres big blocks of greyschist. Due to the plant growth and the size of the blocks, the determination of an exact boundary was not possible in this study. The schist - psammitic greyschist- at the southern periphery of the diatreme is well foliated with distinct leucocratic and melanocratic layers. The rock is streaked with the thick quartz veins. In the cross section studied, the northern border of the diatreme is marked by the about circular Corner Dike (nomenclature Cox 1985) (Fig. 2.1.5). Further to the west, the large Shoulder Diatreme marks the northern border of Niger diatreme (Fig. 2.1.5). The Shoulder Diatreme is an about 200 m long, E-W trending body of lamprophyre with breccias on its boundaries (Cox, 1985).

2.4.1.1: Lamprophyre dikes

Apart from the large Corner Dike and in the Shoulder Diatreme, thinner (a few dm) lamprophyre dikes are present throughout the diatreme. These can be massive or contain abundant vesicles, such as at outcrop N2a (Fig. 2.1.5). Samples of in-situ lamprophyre dikes were taken from the "Corner Dike" and a dike which is about 50 m north of Niger Diatreme (outcrop N3 & N3b; Samples: ND3B & C). Both samples are vesicle-free, massive rocks and both samples are composed of 3 main parts: 1) macroscopically dark grey fine grained lamprophyric rock, (2) embedding xenoliths or parts of those and (3) ocelli. The lamprophyre rock itself is made of phenocrysts which are embedded in a more fine grained feldspathic matrix, which in this area has been determined to be oligoclase to calcic anorthoclase (Cooper, 1979). Primary phenocrysts are Ti-augite, biotite, amphibole (kaersutite), smaller grains of apatite and Ti-magnetite. Apatite and Ti-magnetite are common throughout the rock, but are particularly concentrated around ocelli. Ti-augite locally forms clusters with the magnetite. Pyrite occurs in the lamprophyre matrix itself and occasionally the calcitic ocelli. The lamprophyre shows some signs of hydrothermal alteration. Minerals in the lamprophyre which form due to alteration are biotite, albite, muscovite, calcite, ankerite and magnesian-siderite (Fig. 2.4.2). The rock's magmatic matrix is replaced by albite (Cooper, 1979). In the cases studied here, this albite contains either ca. 5 Vol-% of a few micrometer big inclusions of white mica and ankerite, or the matrix is entirely made of carbonate. Ti-augite has broken down to ankerite (in contact to the remaining pyroxene) and mica (mostly at the outer rim). The mica is mostly biotite and sporadically muscovite. The amphibole is largely stable at these early stages of alteration. In some places, the amphibole was replaced by a finely inter-grown mix of rutile and Si, K, Fe, Mg, Ca-bearing phases, probably ankerite and white mica +/- quartz.

In the samples of unaltered lamprophyre dikes, only xenoliths of peridotite or parts of it (i.e. fragments of olivine and orthopyroxene) were found. However, lamprophyre dikes in other locations (i.e. Mt Alta) also contain greyschist and marble-like fragments. Components are less than 1 cm in diameter, but up to 4 cm big peridotite (harzburgite) nodules have been described by Cox (1985) and Scott et al. (2014). In the samples examined, most of the peridotite has been replaced by talc, serpentine and or carbonate, with the first replacement taking place along cracks and grain boundaries.

The ocelli in the lamprophyre are spherical to ellipsoidal (0.5 -1.5 mm in diameter) bodies within the lamprophyric matrix and are primary magmatic textures. Magmatic ocelli-filling minerals are calcite, which embed euhedral crystals of amphibole, titanium-augite, and needles of apatite. These needles are either entirely in the ocelli or may grow from the lamprophyre into the ocelli (Fig.

2.4.2 B). The primary phases in the ocelli may be partly or entirely replaced by ankerite, analcime, muscovite, a K-Al-silicate and/ or a combination of the K-Al-silicate with feathery muscovite inclusions (Fig. 2.4.2). The ankerite is often intercalated with little inclusions of calcite. The analcime in the ocelli is a mixture of mostly analcime and many tiny (<10 µm) inclusions of ankerite, and white mica. Regarding analcime in ocelli, it has been suggested that the analcime may be magmatic (Cooper, 1979; Demeny et al., 1997) and potentially (at least partly) alteration-related. As analcime here is not a pure phase and contains many inclusions similar to replacement-related features it is suggested that in the case here analcime is a secondary phase.

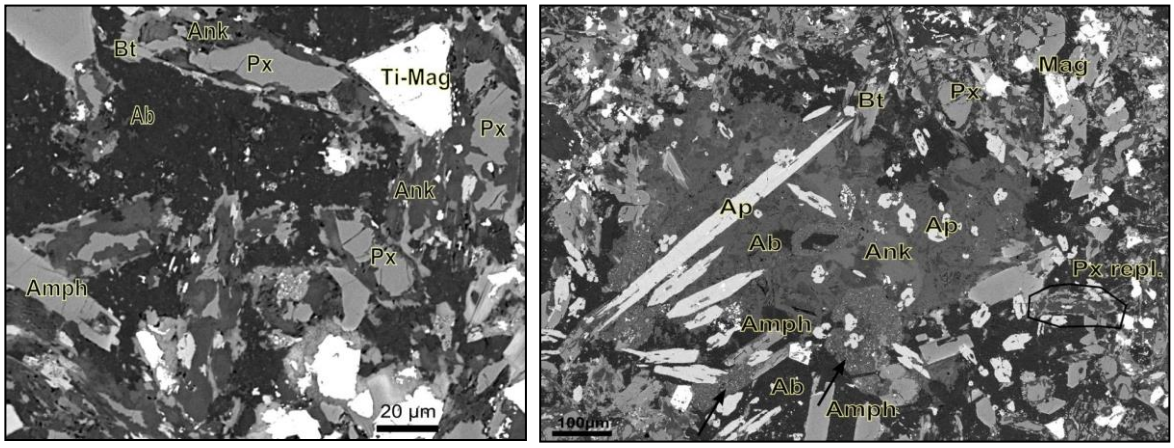

Fig. 2.4.2) **Left:** Magmatic kaersutite (amph), titano-magnetite, augite (Px) in a secondary matrix of albite, muscovite and ankerite. The pyroxene is mostly replaced by carbonate and mica. **Right:** Ocelli filled with primary magmatic phases (i.e. apatite, amphibole) and secondary minerals (ankerite, mix of K-Al-silicate and muscovite mix). Amphibole has been replaced by a finely inter-grown mix of rutile and Si, K, Fe, Mg, Ca-bearing phases, probably a mix of ankerite, white mica +/- quartz.

2.4.1.2: The breccia of Niger Diatreme

The diatreme breccia can be divided into its 2 main constituent: components and matrix.

Components are mainly fragments of psammitic greyschist, but lamprophyre, and greenschist are also common. Except for greyschist, components are generally less than 20 cm in diameter (Fig. 2.4.3). Greyschist clasts on the other hand range from less than a centimetre to several metres across, depending on their position in the diatreme. At the southern border, components are meters in diameter and the breccia is component-supported. In the central and northern part of the diatreme the components become smaller (about 1.5 dm and smaller) and with decreasing grain size of the components, the breccia is increasingly matrix-supported. Most clasts are hydrothermally altered. The alteration halos follow clast boundaries and occasionally cracks in the components (e.g. 2.4.3).

2.4.1.2-1: The components

Psammitic **greyschist** is the most common type of fragment found in the diatreme breccia. The foliation is crenulated or planar, and the rock is generally well layered, with albite-quartz and muscovite-rich layers. Unaltered greyschist components are made of quartz, albite, muscovite, chlorite, titanite +/- epidote and the rock is mineralogically and texturally similar to the rocks outside the diatreme. Despite metamorphic textures still being easily recognisable, post- metamorphic alteration is ubiquitous. Phyllosilicates are partly to fully replaced by hydrothermal muscovite and/ or kaolinite. Albite is sericitised and metamorphic pyrite oxidised. This kind of alteration is similar throughout the diatreme. There is no evidence for growth of carbonates during the alteration of the greyschist components in the diatreme or adjacent to it.

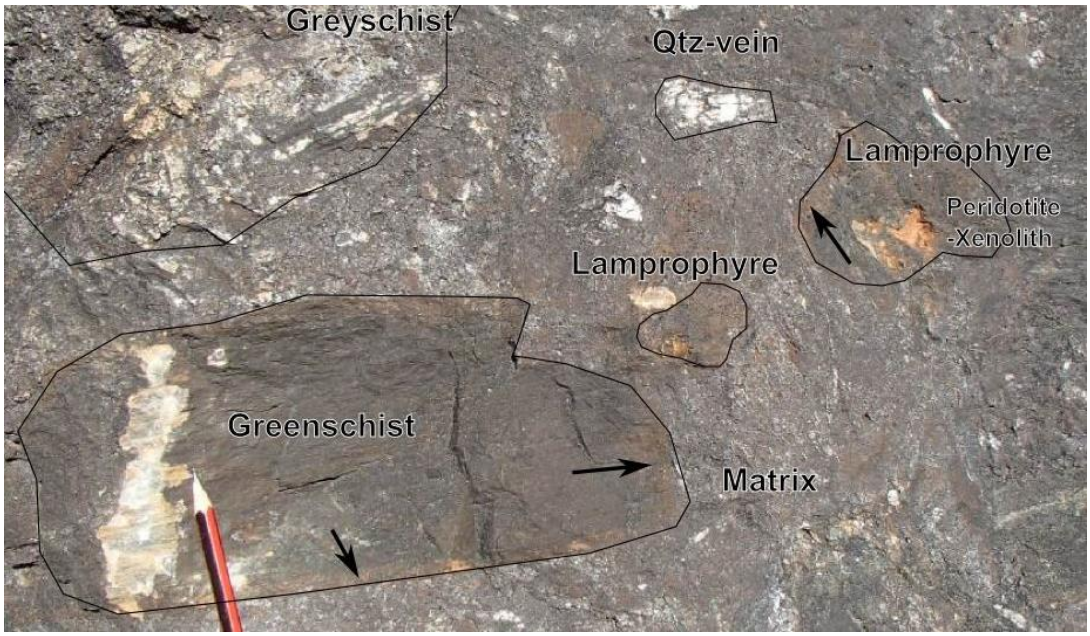

Fig. 2.4.3) Breccia from the central part of Niger Diatreme. Weathering makes it difficult to identify borders of components. Many components have an orange alteration rim (arrows). Lamprophyres can contains xenoliths (here peridotite). The fragment of quartz vein is part of greyschist. Outcrop N1.

Just like greyschist, **greenschist** fragments are often altered, especially when they are less than a couple of centimetres in diameter. Titanite is pseudomorphically replaced, amongst others, by rutile. Chlorite, which is in the initial stages of break down reaction, looks "dusty" in transmitted light due to sericitic/ kaolinitic inclusions. In more advanced stages of alteration, chlorite is replaced by kaolinite and/ or muscovite and the albite sericitised. In some clasts, a zoning of the chlorite replacement minerals is distinguishable; at the clast rim metamorphic chlorite is replaced by kaolinite and sericite more towards the centre (Fig. 2.4.4). Due to the similar style of alteration it is often hard to determine if the altered rock is an altered greyschist or greenschist. However, original greenschist has a larger concentration of kaolinite/ hydrothermal muscovite, as the original metabasites have higher concentration of chlorite than greyschist.

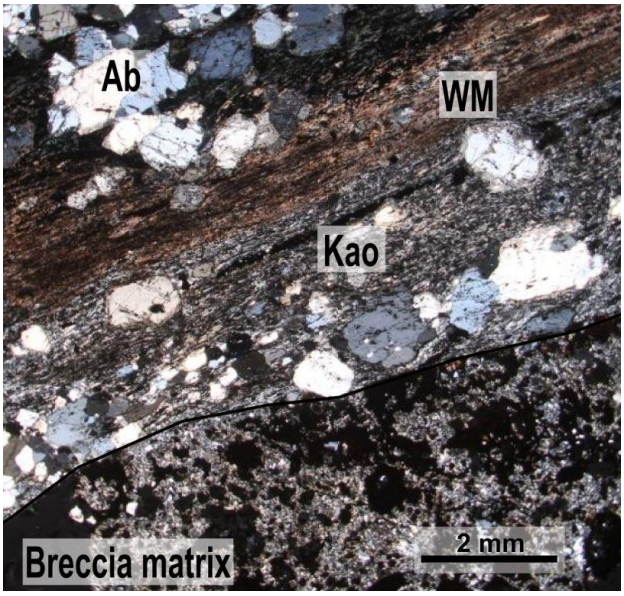

Fig. 2.4.4) At the rim of a greenschist fragment the dominant phyllosilicate is kaolinite, while it is white mica in more central parts. ND1D.

Components of a calcite-rich (ca. 85 vol-%), **marble-like rock** is found throughout the central part of the diatreme breccia. Apart from calcite, it contains muscovite, fine grained albite and calcite, some chlorite, rutile and apatite. A foliation is defined by layers made of muscovite, fine -grained albite and calcite, rutile, and rare chlorite. Additionally, albite forms grains of ca. 0.5-1.5mm in diameter. These grains often have single twinning, are rich in carbonate inclusions (Fig. 2.4.5) and some have bands or cores of tiny inclusions which however are not necessarily parallel to today's grain boundaries (Fig. 2.4.5). EDS element maps indicate that the inclusions may be mostly muscovite. The boundaries of the big albite

grains are lobate and sometimes there is only "skeletal" feldspar left (Fig. 2.4.5). Muscovite may be corroded on grain boundaries too.

Apart from the calcitic rocks, there are some clasts in the diatreme breccia that are texturally similar but contain ankerite instead of calcite. Much of this ankerite has small, randomly arranged inclusions which could be fluid or gas bubbles. The ankerite has a blocky compositional zoning (Fig. 2.4.**6**). Embedded in the ankerite are euhedral albite grains similar to the calcitic marble described above, but there is no skeletal albite. In places of the same samples these albite grains form cumulate like structures. Similar to the calcitic marble a foliation is defined by the arrangement of fine-grained muscovite, albite, apatite and rutile (Fig. 2.4.6). These rocks sometimes have miarolitic cavities, often lined by euhedral carbonate crystals.

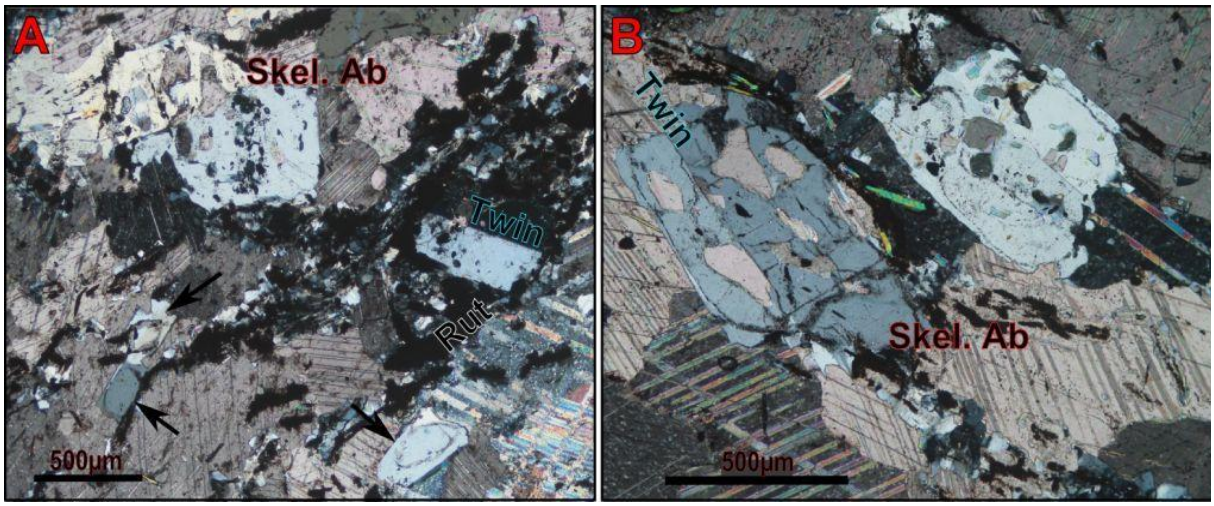

Fig. 2.4.5) A: Skeletal albite (Skel. Ab) and smaller euhedral albite grains with band of inclusions (arrows) embedded in calcite. **A&B:** Single twins in albite are common. Both ND2A and taken in XPL.

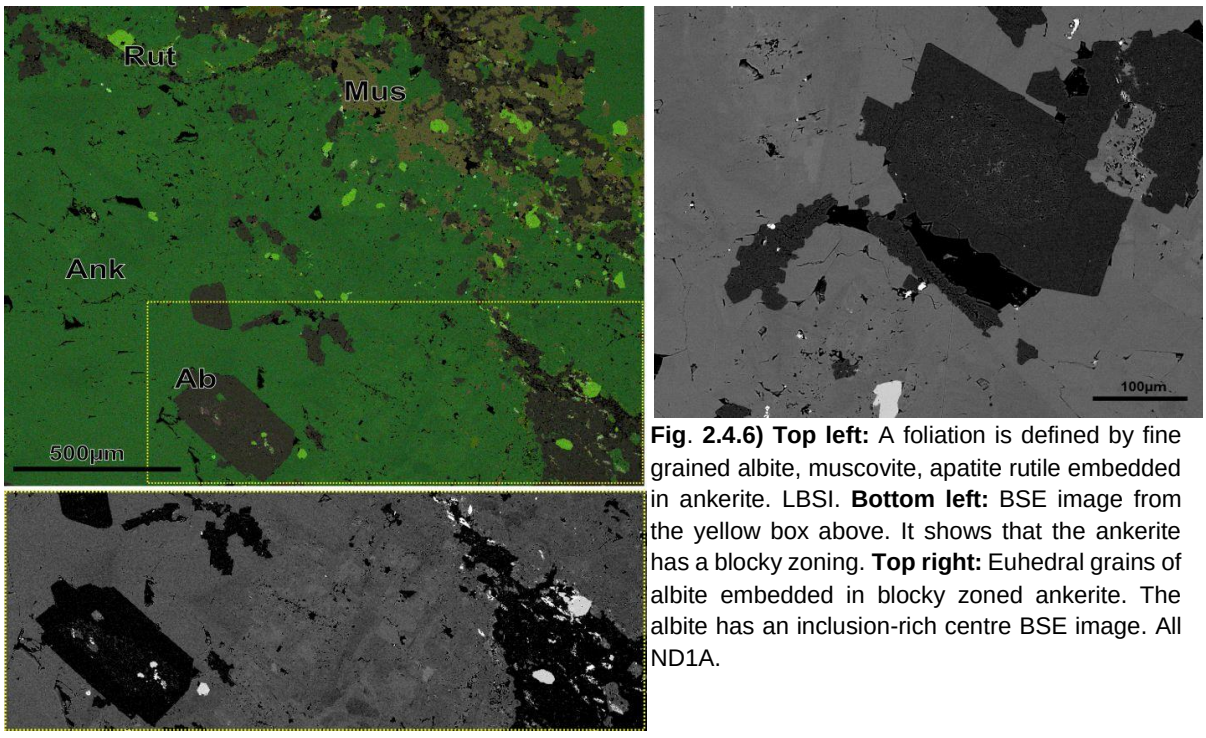

Fig. 2.4.6) Top left: A foliation is defined by fine grained albite, muscovite, apatite rutile embedded in ankerite. LBSI. **Bottom left:** BSE image from the yellow box above. It shows that the ankerite has a blocky zoning. **Top right:** Euhedral grains of albite embedded in blocky zoned ankerite. The albite has an inclusion-rich centre BSE image. All ND1A.

Components made of **lamprophyre** in the diatreme breccia are completely hydrothermally altered. Most of the magmatic minerals have been replaced and only the shape of bigger structures such as phenocrysts and ocelli are recognisable, but the mineralogy of these features has also changed. The matrix of the altered rock is composed of fine grained Na-Al-silicate (probably albite), muscovite, apatite and carbonate. The calcite in the ocelli is replaced by ankerite. Lamprophyre components themselves may contain fragments of rock. These are altered greyschist, marble (see above) and highly altered peridotite. The original peridotite has been entirely replaced by chlorite and talc. Wormy spinel structures that form by the reaction of breakdown reaction of garnet to spinel (e.g. Smith, 1977), are the most conclusive evidence that the components used to be peridotite.

2.4.1.2-2: Breccia matrix

Components throughout the diatreme are embedded in a matrix, which is made mostly of fine-grained, pearly, ribbon-like albite, bigger sub-to euhedral albite grains, grains of ankerite, millimetre big grains of Fe-hydroxide (probably weathered ankerite) and small needle-shaped apatite and rutile (Fig. 2.4.7). Rutile also forms isolated grains or small clusters (e.g. in ND1C) and can contribute up to 1 vol-% to the matrix.

Many of the bigger albite grains are twinned. The structure of inclusion trails in some of the bigger albite grains indicate that they are derived from metamorphic rock (e.g. in ND1B). The ankerite forms variously sized grains and cumulates. The smaller isolated grains (diameter <100µm) sometimes have a euhedral grain shape. However, many, especially bigger ankerite grains/ cumulates, have ragged grain boundaries. BSE images reveal a complex zoning that this raggedness at the carbonate rim coincides with chemically slightly different carbonate (Fig. 2.4.7). The ankerite surrounded by the ragged rims is also complexly zoned. The bigger ankerite grains have roughly circular rims/ bands or cores which are rich in inclusions. The ribbons are variably thick. The grain boundaries of the ankerite are often parallel to crystal surfaces. The ragged grain boundaries may have formed by partial dissolution after precipitation or competition of growth co-crystallising albite. Other phases in the matrix can be fragments of chlorite and muscovite.

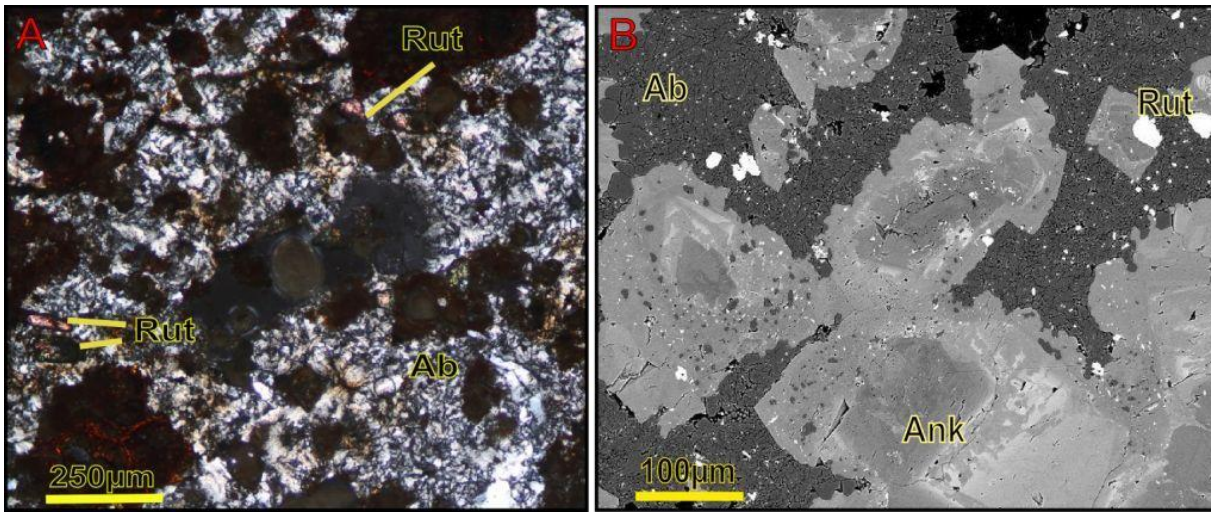

Fig. 2.4.7) Examples of the breccia at Niger Diatreme. **A:** XPL microphotograph. The diatreme matrix is mainly made of an optically pearly albite-dominated mineral mix, iron-hydroxide, ankerite and isolated grains of rutile. **B:** BSE image. In the albitic matrix (grey) are also small grains of rut and Ap (both white). The ankerite grains in the matrix are complexly zoned. Both ND1D.

2.4.2- Mount Alta Diatreme

The diatreme at Mt Alta, just like Niger diatreme, is dominantly made of variously sized psammitic greyschist fragments embedded in a finer grained matrix. The breccia is cut in many places by lamprophyre dikes, which are variably intensely altered.

2.4.2.1: Lamprophyre dikes in the diatreme

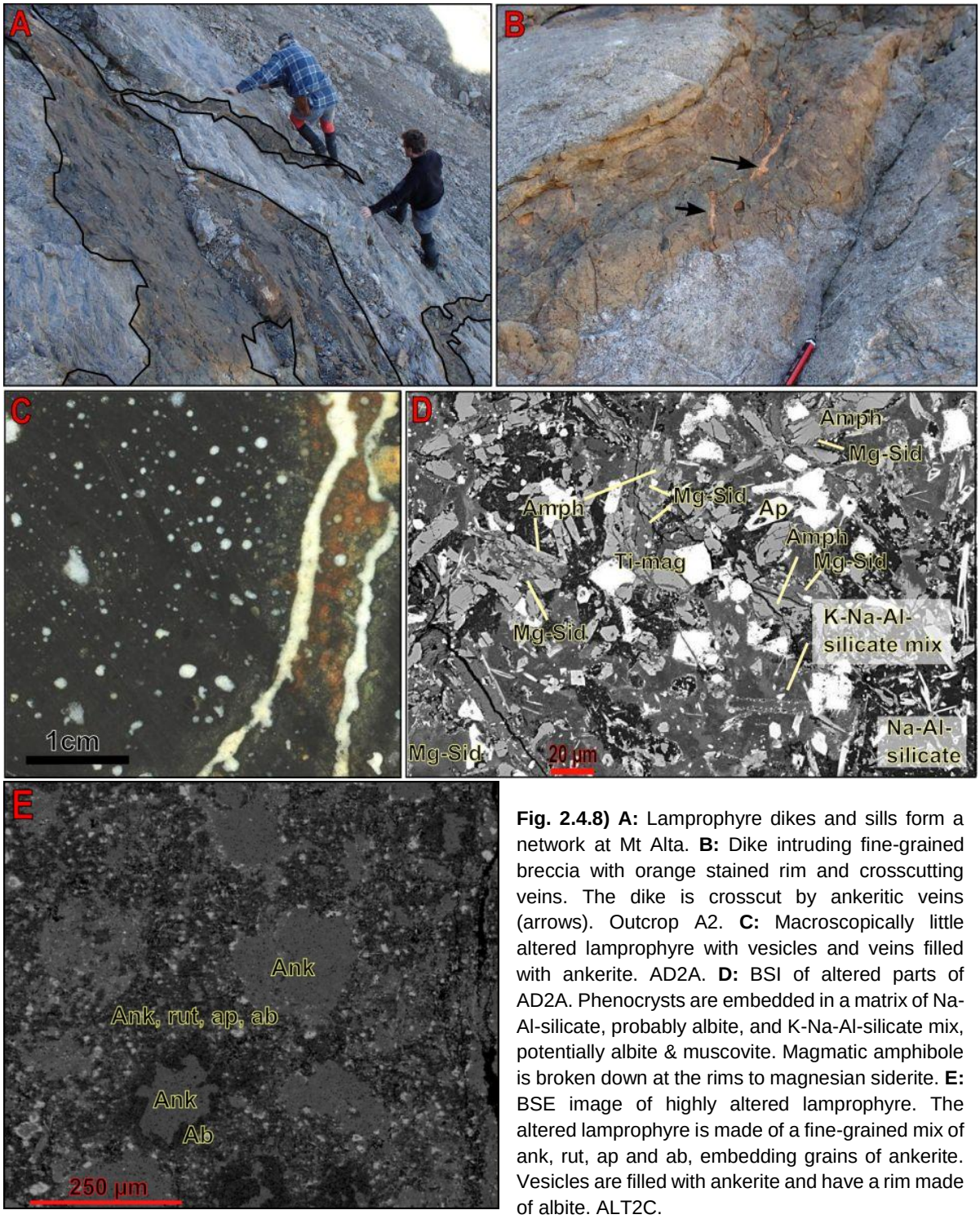

Fig. 2.4.8) A: Lamprophyre dikes and sills form a network at Mt Alta. **B:** Dike intruding fine-grained breccia with orange stained rim and crosscutting veins. The dike is crosscut by ankeritic veins (arrows). Outcrop A2. **C:** Macroscopically little altered lamprophyre with vesicles and veins filled with ankerite. AD2A. **D:** BSI of altered parts of AD2A. Phenocrysts are embedded in a matrix of Na-Al-silicate, probably albite, and K-Na-Al-silicate mix, potentially albite & muscovite. Magmatic amphibole is broken down at the rims to magnesian siderite. **E:** BSE image of highly altered lamprophyre. The altered lamprophyre is made of a fine-grained mix of ank, rut, ap and ab, embedding grains of ankerite. Vesicles are filled with ankerite and have a rim made of albite. ALT2C.

Lamprophyres form a complex network of dikes and sills in the diatreme (Fig 2.4.8 A). Little altered dikes have an orange rim at the contact to the wall rock (Fig 2.4.8 B). In the dikes, vesicles are predominantly filled with ankerite. The texture of the void fillings is further discussed below. The

alteration of these magmatic rocks ranges from little to strongly, which expresses itself in the amount of replacement of the original mineralogy. The least altered lamprophyre sample (e.g.AD2A) contains ankerite veins and vesicles are filled by ankerite (Fig 2.4.8 C). However, the lamprophyre itself contains much of its original magmatic assemblage, such as Ti-magnetite, needles of apatite, amphibole, Ti-augite and biotite. These magmatic minerals are embedded in a secondary matrix of albite or a very fine grained mixture of Na-K-Al-Si bearing phases, potentially albite and muscovite. Despite being mostly unaltered, some replacement reactions can be seen in some locations. Here amphibole phenocrysts are replaced at their rims by magnesian siderite (Fig. 2.4.8 D). The matrix also hosts anhedral grains of ankerite and smaller needles of magnesian siderite. Magnesian siderite occasionally forms rims around the ankerite grains. In dikes of highly altered lamprophyre (e.g. ALT 2C, AD2G), the magmatic mineralogy has close to entirely been replaced by secondary minerals, but the overall magmatic texture and phenocryst habits are preserved. The matrix is now made of fine grained albite (or potentially another Na-Al-silicate?), ankerite and rutile (originally probably Ti-magnetite) and original apatite (Fig. 2.4.8 E). Ankerite fills vesicles and replaces magmatic phenocrysts which according to the shape could have been amphibole, olivine and/ or pyroxene.

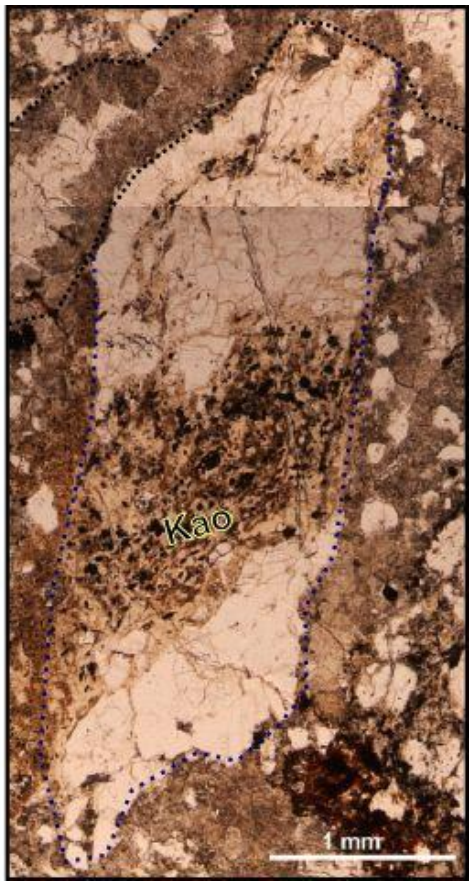

Fig. 2.4.9) Medium-grained breccia of Diatreme at Mt Alta. Component of greyschist (inside blue dotted line) in a finer grained matrix and veins. The component has a segregation layering and crenulation related to metamorphism. One layer is made mostly of kaolinite and rutile, which have both formed by hydrothermal alteration.

2.4.2.2: Diatreme Breccia

2.4.2.2-1: The components

Components found in this diatreme are mostly greyschist and less common lamprophyre. Some smaller components can also be fragments of silicified breccia. The **greyschist** clast sizes range from less than a centimetre up to several metres in diameter. The smaller components have been thoroughly altered. There are two main kinds of alteration found in the clasts, ankeritic and argillic alteration. Signs for ankeritic alteration are ankerite, which occurs disseminated in the leucocratic layers and which replaced some of the minerals in the phyllosilicate-rich layers, probably chlorite and epidote. Muscovite is found in textural equilibrium with the ankerite in this style of alteration. Argillic alteration expresses itself by phyllosilicates, muscovite and probably also chlorite, having been replaced by clay minerals such as kaolinite (Fig. 2.4.9). Despite the alteration, metamorphic textures of the schist, i.e. foliation and crenulation, are still recognisable. Fragments of **lamprophyre** are partly to entirely altered and their original magmatic structure is often hard to recognise. The lamprophyre matrix is made mostly of fine grained albite, with ankerite, rutile and needles of apatite. Of these, the apatite needles are in the same structural setting and have the same habit as apatite in unaltered lamprophyre. Angular grains made of ankeritic carbonate (Fig. 2.4.11A) are found throughout the

lamprophyre. These are most likely replacements of phenocrysts, such as pyroxene or peridotite xenoliths. Vesicles are filled with ankerite.

2.4.2.2-2: Breccia texture (Components + Matrix)

The geometry of the diatreme is complex. Across the diatreme, the size of clasts varies from a few mm up to several meters. The grain size of matrix also ranges from less than 1 to several mm. The greatest part of the diatreme is made of component-supported breccias with only a little matrix. However, breccias with components that are small (less than 2dm) generally have a matrix-supported texture. The components in the breccia are variable in size, ranging from 1mm up to several cm (Fig 2.4.10 A). These components are altered greyschist, altered lamprophyre, silicified breccias, fragments of hydrothermal quartz, and ankerite (Fig 2.4.11 A-C). Some greyschist fragments are extensively veined, which causes them to be broken up into smaller fragments (Fig 2.4.11 B). Occasionally lamprophyre components contain ankeritic veins, which terminate at the interface to the breccia matrix (Fig 2.4.11 C). The matrix is made of angular fragments of albite, quartz, and ankerite (Fig 2.4.11 B & C). Interstitial spaces are filled by ankerite, muscovite and fine-grained albite and quartz. In some cases components are supported by lamprophyre, rather than a clastic matrix. The lamprophyre is highly altered and is mostly made of fine grained albite (<50 µm), some rutile, ankerite and needles of apatite. The matrix-forming lamprophyre does not have vesicles.

Apart from this medium-grained breccia, a fine-grained, matrix-supported breccia can also be found Mt Alta Diatreme (Fig 2.4.10 B). This breccia forms distinct bodies with steeply dipping boundaries (Gamble, 1984). This type of breccia is made to ca. 90% of sand-sized grains. The few components bigger than this are fragments of greyschist and lamprophyre. The lamprophyre can also contain the smaller components of greyschist.

The matrix in both breccia types is made of granular albite, ankerite, and muscovite and/ or highly altered lamprophyre made of fine-grained albite, muscovite, ankerite, rutile and apatite (Fig 2.4.11 D & E).



Fig. 2.4.10) A: Medium-grained breccia with chaotically arranged schist and lamprophyre components. **B:** Fine-grained breccia in the diatreme.

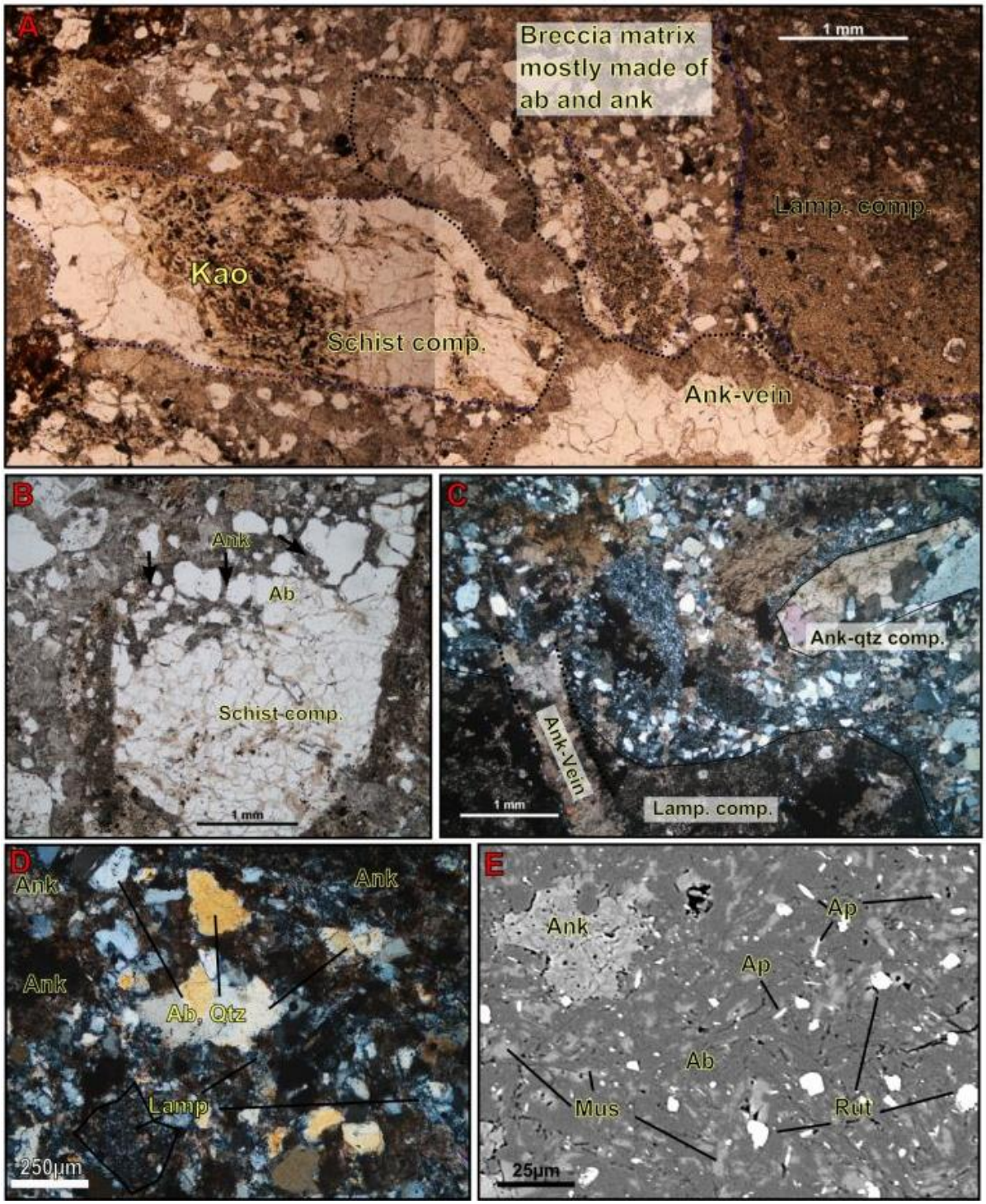

Fig. 2.4.11) A: PPL. The "medium-grained" breccia is made of variously sized components of different lithologies (predominantly greyschist, lamprophyre). Components are hydrothermally altered. The big schist component is the same as in Fig. 2.4.9. The matrix is mostly made of ab and ank. Irregularly shaped veins fill voids The contact of the veins to the breccia is diffuse/ gradual. **B:** PPL. A greyschist component is riddled with ankerite, breaking the component up (arrows). **C:** XPL. The ankerite vein in the lamprophyre component terminates at the contact to breccia's matrix. Note the refraction of the interface surface. The breccia also contains fragments made of hydrothermal ankerite and quartz (right part of image) A, B, C from ALT3A. **D:** XPL. Photomicrograph of a medium-grained breccia. AD1G. The breccia matrix is made of albite, quartz, altered lamprophyre and ankerite. **E:** BSI. Close up of a lamprophyric part of the breccia depicted in D. The lamprophyre is made of a fine grained ap, mus, rut embedded in ab.

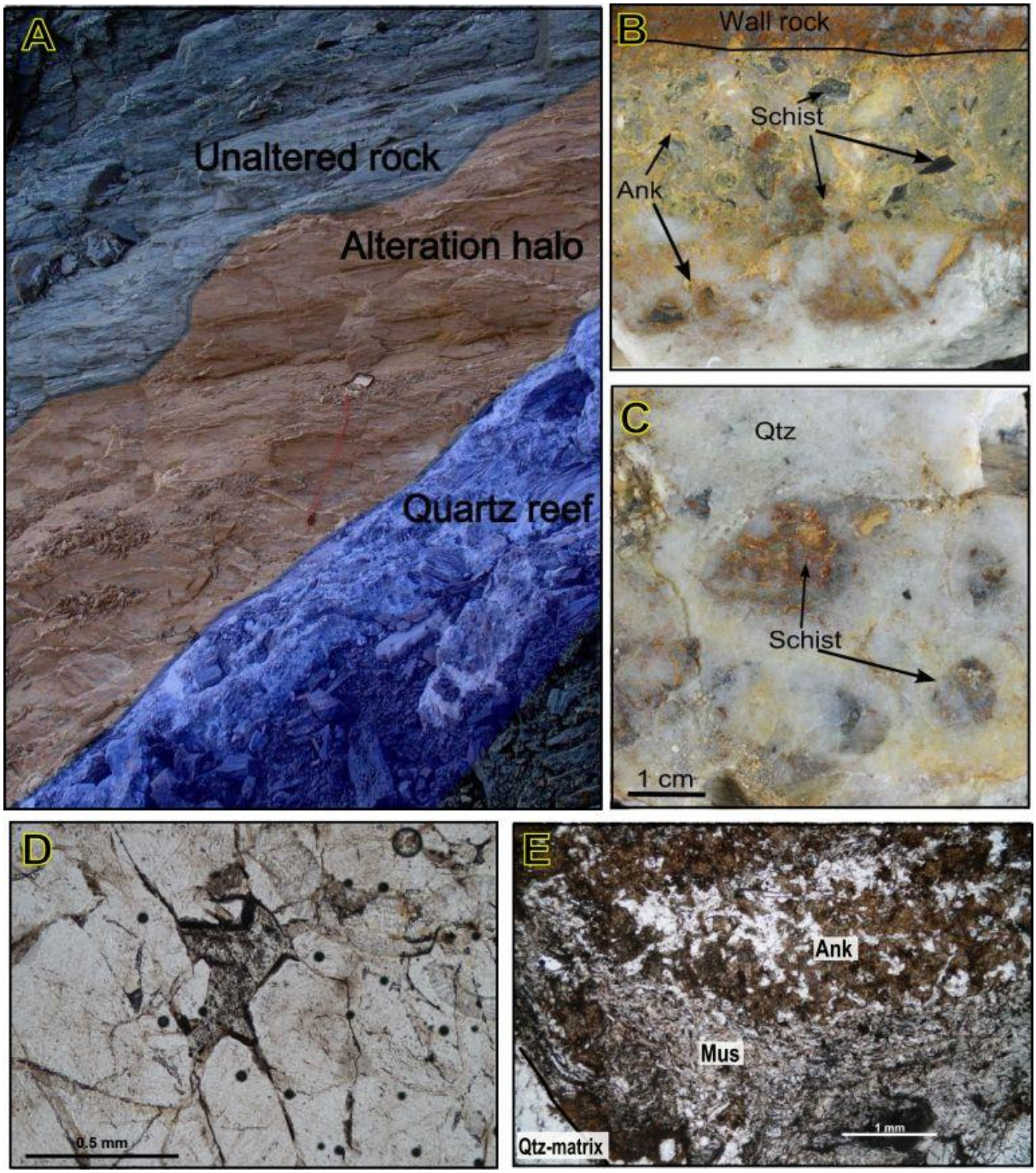

Fig. 2.4.12) A: The quartz reef is surrounded by an orange alteration halo. **B:** Close up of the contact of the reef. The breccia adjacent to the greyschist is especially rich in ankerite (AD1B). **C:** Sample from the central part of the reef. AD1A. Compared to the rim, the centre is dominated by hydrothermal quartz. B & C same scale. **D + E:** Microphotographs of the central part of the reef. PPL. **D:** Contact of euhedral quartz grains pointing into an ankerite filled space. ALT3A. **E**: Folded schist component in the breccia. It is made up of metamorphic muscovite and secondary ankerite. ALT3A.

2.4.2.3: Quartz Reef

Features found at Mt Alta but not Niger Diatreme are several dm thick silicified breccias. These post-metamorphic structures are referred to as "quartz reefs" by Clough (1988). Up to 5 m thick reefs have been reported (Clough, 1988) and some quartz reefs near Mt. Alta have been found to be slightly enriched in gold (ca. 1 ppm) (Clough, 1989). Additionally, some of these structures contain high levels

of Cu (>1000ppm). This high Cu content does not coincide with the elevated Au content in the other reefs. Two of these quartz reefs occur ca. 30 west of the diatreme and are less than 1 m apart. Both strike N-S (orientation: 270/62), and are 30- 40cm wide. The schist is stained orange on both sides of the quartz breccia for 1 metres due to ankeritic alteration (Fig. 2.4.12 A). The more diatreme-proximal breccia was sampled from the centre, across into the adjacent altered and unaltered schist (ALT3B, AD1A, B, C, C2). (The alteration is described in the chapter 3). In the centre of the reef, the breccia (AD-1A+ ALT3B) contains fragments of greyschist and clusters of hydrothermal quartz and ankerite. The components in the breccia are variable in size, ranging from milli- up to several decimetre (Fig. 2.4.12 C). In some of the components made of coarse grained quartz, the pre-brecciation contact of ankerite and hydrothermal quartz are preserved. This and the crystal habits show that both minerals grew in a vein setting into a fluid-filled cavity (Fig. 2.4.12D). The schist clasts show signs of ankeritic alteration and contain carbonate throughout the rock. Muscovite on the other hand is preserved and does not have optical signs of replacement i.e. by kaolinite (Fig. 2.4.12 E). The breccia matrix is made mostly of quartz, and some carbonate and white mica.

The contact of the reef with the wall rock (psammitic greyschist) is marked by an about 5 cm wide breccia (AD1B), which is richer in ankerite and has smaller components (smaller than 1 cm) than the centre of the quartz reef (Fig. 2.4.12 B). Despite differing proportions of constituents, i.e. more ankerite in the matrix, the mineralogy of the breccia at the rim (AD1B) is the same as further in the centre, but the microtextures differ. Grains of ankerite are often not made of big single grains, but are cumulates of small crystals, giving the carbonate a fine grained, "sugary" texture and compositional zoning. Locally, late stage carbonate veins cut the silicified breccia. There is no evidence of argillic alteration in the schist fragments as is also the case in other breccias of the diatreme.

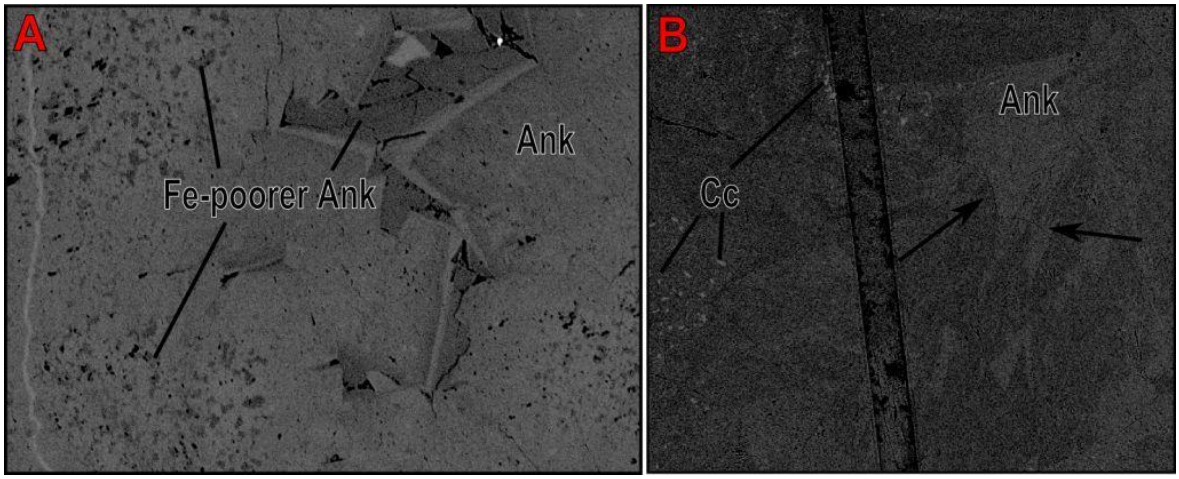

Fig. **2.4.13)** Vesicles are filled with ankerite which form euhedral grains (A centre view, arrows in B) in the ankerite are inclusions of relatively Fe-poorer ankerite (A) or calcite in relatively Fe-poor dolomite (B). Note LASER track in B, crosscutting the calcite inclusions. Both AD2A and BSE images.

2.4.2.4: Veins and other void fillings

Veins in the diatreme are abundant and occur in all lithologies and settings. They are mostly ankeritic but central parts of the veins can be made of silica.

2.4.2.4-1: Veins and vesicle fillings in lamprophyre

Ankeritic veins and vesicle fillings also occur in little altered lamprophyre. Veins are nearly straight and are less than 1 cm thick. Optically these veins and the surrounding vesicles fillings are predominantly murky. Central parts of the veins may be filled with quartz. The boundary of ankerite and quartz trace a euhedral crystal shape. Chemical zoning of carbonate filling the vesicles is blocky, outlining semi-

euhedral carbonate crystals (Fig. 2.4.13). Additionally, they also contain round domains full of inclusions of relatively Fe-poorer ankerite, calcite, quartz and/ or voids which are all embedded in the vesicle's ankerite (Fig. 2.4.13). Associated with the calcite are small grains of barite. Where examined the calcite is found in domains of more Fe-rich ankerite, but less commonly in more Mg-rich ankeritic parts of the ankerite-filled vesicles.

In addition to the relatively straight and thin veins, irregular shaped, several cm thick veins and bodies of sparry ankerite are found in hydrothermally thoroughly altered lamprophyre (i.e. AD2B, ALT2C, ALT2G) (Fig. 2.4.13 A &Fig 2.4.1 B). These bodies often occur in zones, where the vesicles are relatively big (several mm) and abundant. In thin section, two optically distinct types of carbonate are recognisable; a clear white ankerite in the centre of the vein and a murky grey ankerite at the rim. The murky carbonate forms euhedral grains, which have a clear outer layer that is again bound by a thin layer of murky ankerite (Fig. 2.4.14 C). The contact to the highly altered lamprophyre is marked by a thin layer of a Na-Al-silicate, probably albite, which forms tapered crystals and which are encased in Fe-rich carbonate (Fig. 2.4.13 D).

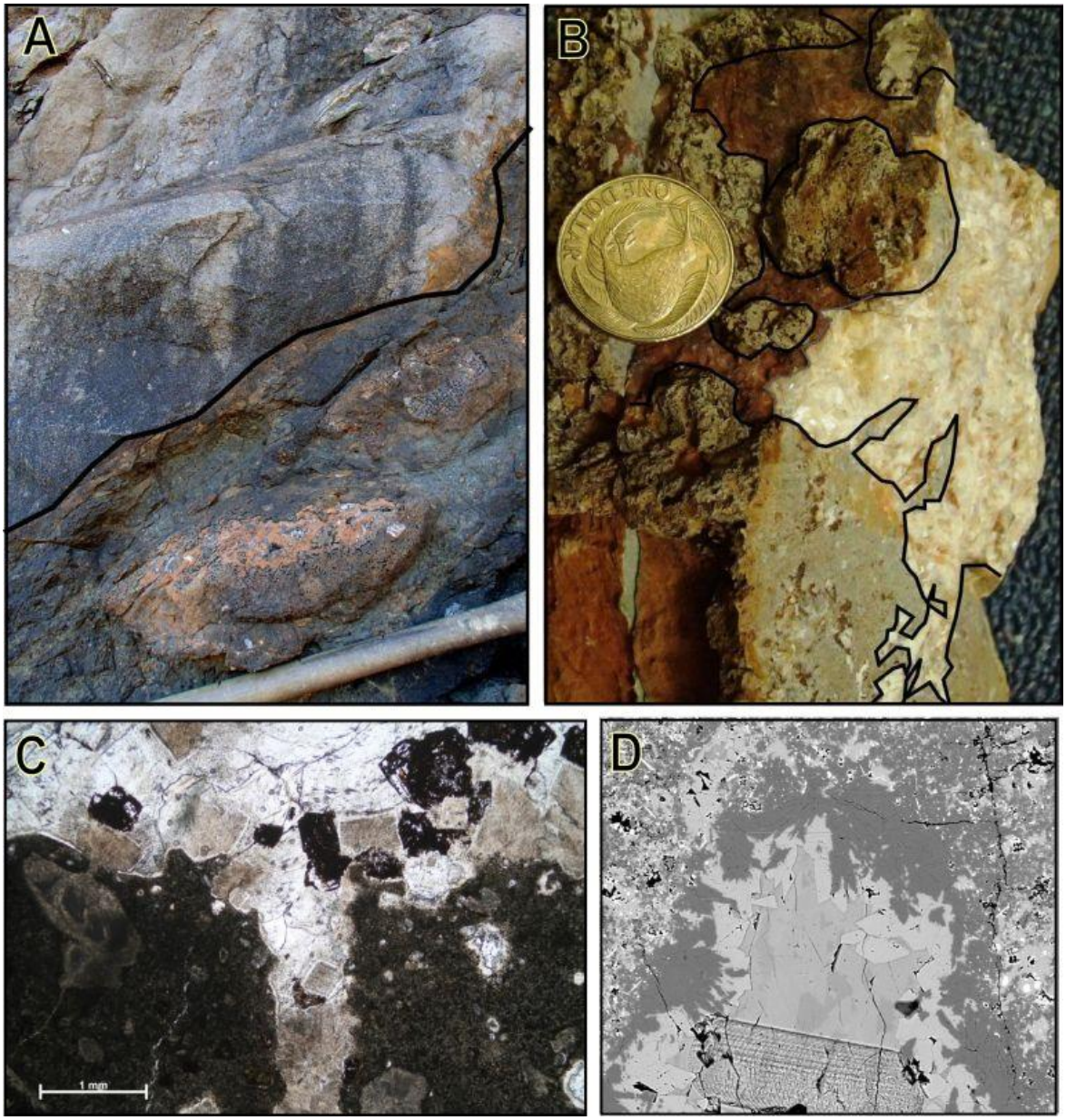

Fig. 2.4.14) A: Ankeritic bodies or irregularly bounded veins in lamprophyre. **B:** The carbonate is sparry and adjacent wall rock is thoroughly altered. **C:** Microphotograph of sparry carb-vein. In the wall rock ankeritic grains

(murky brown) are replacements of phenocrysts.PPL. ALT2C. **D:** Vesicle filling. Na-Al-silicate at rim (dark grey) encased by Fe-rich carbonate (light grey). Width of image: ca. 0.6 mm. Note: Laser track in lower part of image.

2.4.2.4-2: Veins in the clastic diatreme breccias

Texturally and optically similar to the sparry veins in lamprophyre are veins found in medium-grained, clastic breccia (Fig **2.4.9**). These veins fill gaps in the breccia matrix. These veins can also embed rock fragments, such as schist. The rims of the veins are made up of murky ankerite and the central part is clear. There is, however, no lining with albite or another Na-Al silicate (Fig **2.4.9 Top**). Pyrite can be found associated to the veins. Its distribution is controlled by grain boundaries indicating a younger age than the carbonate.

2.4.2.4-3: Veins in greyschist blocks

Veins are generally around 0.5 and 1 cm thick, but can be thicker where two or more veins intersect, entraining fragments of the surrounding schist (Fig. 2.4.15). The veins of the swarm form a conjugate set. The carbonate in the veins forms a murky rim and largely clear centre. However, throughout the veins replacement of the carbonate by Fe- hydroxide along cracks and grain boundaries is common. Further textures and characteristics of these veins will be discussed in chapter 5.

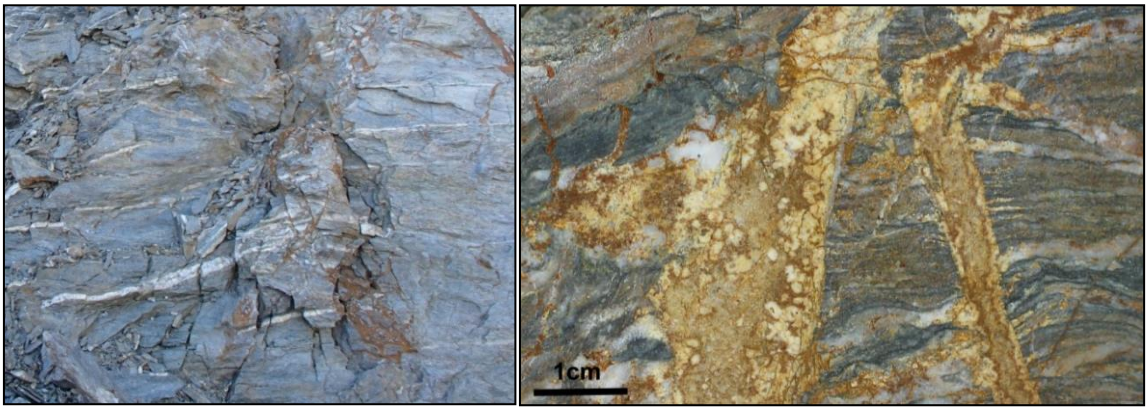

Fig. 2.4.15) Right: Ankeritic veins form a conjugate network in a greyschist block in the diatreme at Mt. Alta. width of image c. 1 m. **Left:** The veins are made of differently textured ankerite. ALT1.2.

2.4.3-Summary and interpretation of the features associated with the diatremes

2.4.3.1: Structure of the diatreme breccias

For most component types in the diatreme breccias, their affinity/ origin is clear. The only components, which are unclear are the components mostly made of calcite or ankerite in Niger Diatreme. Considering the foliation and mineralogy (albite, muscovite, rutile) suggests that the calcitic rocks are impure metamorphic marble, similar to the marbles described by Cooper (1979) (compare Fig. 2.4.5&6 and Fig 2.2.5). Concerning ankeritic rock, the similar texture and, apart from the carbonate species, similar mineralogy supports the interpretation that it formed by hydrothermal alteration of the calcitic marble.

Despite having similar components, the makeup of the matrix in the two diatremes differs. Most of the matrix at Niger Diatreme is made of fine-grained, pearly albite embedding larger albite grains, complexly zoned ankerite, apatite and rutile. The angular albite grains are interpreted to be derived from schist, while the small needles of apatite and rutile are probably derived from magmatic

rocks. Regarding the ankerite in the matrix (Fig. 2.4.7), the complex and irregular zoning suggests precipitation-dissolution-and precipitation taking place, but overall enlarging the grain. This most likely happened in a fluid-dominated environment with changing conditions over time. At Mt Alta, the breccia matrix is made of angular albite and quartz, most likely schist-derived, as well as ankerite and lamprophyre (Fig 2.4.11). The pearly albite in the matrix of Niger Diatreme is found in many altered volcanic rocks (aphanitic texture; Gifkins et al., 2005) and shows high degree of fluid flow and hydrothermal alteration after the diatreme's breccia emplacement. Judging by the apatite and rutile amongst the pearly albite, this is probably altered lamprophyric material. Overall, many components in the diatreme breccia show evidence of carbonate alteration previous to the brecciation but are also cross cut by veins and it is suggested that fluid flow persisted throughout the formation history of the diatreme.

2.4.3.2: Hydrothermal alteration

In both diatremes two types of alteration have been recognised, argillic and ankeritic. Both kinds of alteration can occur together. Argillic alteration occurs at low temperature (<300°C) and when the fluid is deficient in K relative to H^+ (Tosdal et al., 2009), while carbonate alteration depends on CO_2 fugacity in the fluid (i.e. White et al., 2003). Within the diatreme, I predominantly found pyrite as sulphur-bearing, alteration-related phase, but other sulphides have also been reported, such as PbS, ZnS, $CuFeS_2$, FeS_2 at Mt Alta, where they are concentrated in some brecciated and silicified dike margins (Gamble, 1984). However, their exact structural position in the dike margins is not given.

2.4.3.3: Silicified faults and their structural relationship to the diatremes

Similar to the silicified fault breccias examined at Bullendale, Copper Creek and Treble Cone, the quartz reef at Mt Alta shows signs of repeated mineral precipitation and brecciation associated with movement along a fault. Analogous, fragments of the surrounding rock, here greyschist, were incorporated in the breccia during this process. The abundance of ankeritic carbonate in the rock fragments and in veins, be it breccia components (Fig. 2.4.12D) or late-stage, crosscutting veins, indicate that flux of CO_2-bearing fluid took place at least before and after the formation of the breccia. The age of the quartz reefs relative to the diatreme could not be established based on the field relations. Gamble noted that the quartz reefs cut lamprophyre dikes which would date them to be younger. However, it appears that the regional joints crosscut the quartz breccia and no lamprophyre components have been found in the breccia, suggesting diatreme and quartz reef could be of a similar age. Supporting this is that some lamprophyre dikes strike N-S, which coincides with the quartz reefs.

2.4.3.4: Structure and evolution of the diatremes

The cross cutting relationship of the dikes and joints and the strike of Niger Diatreme shows that dikes and E-W trending joints are about the same age, which is in agreement with Craw (1985) and Cooper et al. (1987). The structure of both diatremes is complex due to a multiphase evolution of several events of brecciation, intrusion of lamprophyric magma, alteration of wall rock and formation of veins taking place (Gamble, 1984; Cox, 1985; own results). A multistage formation of the diatreme is consistent with reviews by Valentine & White (2012) and Lorenz (1986) concerned with diatreme evolution. The clastic fine-grained breccias in the Mt Alta Diatreme are structures as they form when gas-rich particle "debris jets", which are triggered by a gas-rich explosion (generally phreatomagmatic), break through the already existing coarser diatreme breccia (i.e. Ross & White 2006, Ross et al., 2008). Before but also throughout the volcanic activity and brecciation history of the diatremes, intrusion of lamprophyric bodies took place. The irregular propagation of lamprophyre dikes in the diatreme (Fig.

2.4.8A) is accordance with the model by Valentine & White (2011) where dikes in the lower part of diatremes are generally non-planar due to the brecciated and mechanically inhomogeneous rock. The commonly occurring vesicles in lamprophyre attest for a gas-rich melt. It is also evident that after the dike's emplacement fluids percolated through the rock, precipitating, amongst other minerals, ankerite. The euhedral grain shapes of the hydrothermal carbonate and silicate rim in the highly altered rock (Fig. 2.4.14D) suggest that the carbonate precipitated into cavities. Miarolitic cavities attest that carbonate precipitation happened in at fluid/ gas pressures equal or higher than the confining pressure. The bodies and veins of sparry carbonate in the highly altered lamprophyre occur in zones where the vesicles are relatively big (Fig. 2.4.14A), suggesting that the carbonate precipitated in millimetre to several centimetre big vesicles/ cavities, which appear to be mostly magmatic vesicles in the lamprophyre, rather than dissolution cavities. Presumably during the void-filling event, the alteration of the lamprophyric wall rock took place. 2.5) Depth of formation of structures in study areas In all areas studied structures are brittle, suggesting deformation temperatures below 300°C and at a low depth. In all of the study areas, the alteration mineral assemblage lacks pressure sensitive minerals. Due to this, the depth and pressure of formation was evaluated based on geography and regional geological features (similar to Craw, 1995). Additionally, in some locations fluid inclusions data given in the literature were used to aid this endeavour.

For the diatremes, the depth of formation is hard to determine precisely. Diatremes are structures that extend less than about 3 km into the ground (White & Ross, 2011), but a depth estimate based on the outcrop structure is not possible as the structure depends on the overall size of the diatreme. Nevertheless some constraints on depth can be given; in both locations the existence of miarolitic cavities and the strong brecciation indicate a formation at shallow depth. An aspect to consider is that the diatremes occur at different elevations. The lowest one is at ca 400 m a.s.l. (Wanaka shore) and the highest at ca. 1800m a.s.l, hence an altitude difference of ca. 1400 m. Niger Diatreme today can be traced over an elevational difference of ca. 200 m starting at ca. 450m a.s.l up to 650 m a.s.l. No major fault is reported between the different diatreme occurrences (QMAP) and no major relative vertical shift between the diatremes should have taken place since their formation. Based on this I suggest that the outcrop at Mt Alta formed at 0.5 to 1 km, while that exposed at Niger formed between 1.5 and 2.5 km depth. Including overall tilt of metamorphic foliation since the Cenozoic, Craw (1995) reconstructed the Miocene erosion surface and largely concurs with these depth estimates, though placing the Niger Diatreme at a slightly deeper depth of about 3km (Fig. 2.4.16).

Considering the relative positioning of the outcrops to the Tertiary erosion surface at the base of the Bobs Cove Formation (refer to the map in Fig. 2.1.2) and the overall moderately to the W dipping foliation, the structures at Copper Creek and Bullendale in the Shotover are interpreted to have formed between 1 and 3 km depth relative to the Tertiary erosion surface. This approach is similar to that taken in Craw (1989). There may have been several km of sediment of Bobs Cove Beds at Lake Wakatipu (Turnbull et al., 1975). These sediments may have been thinner in the Shotover area (Craw, pers. com.). Nonetheless there are sediments also in that area (Fig. 2.1.2) and hence need to be considered for estimating the depth of vein formation increases to about 2-4 km. This is broadly consistent with estimates obtained by Craw (1989), who estimated pressures of 400-800 bars based on fluid inclusions in hydrothermal quartz in this area. These pressures correspond to 1.5-4 km in case of lithostatic pressure or 4-8 km at hydrostatic pressure. Outcrops at Treble Cone are today at an elevation of between 1600-1800m. Hence, they are today higher than the structures at Copper Creek, Bullendale and Niger Diatreme. Taking the overall relatively flat lying foliation and the relative location in respect to Bullendale, Mt Alta and Niger Diatreme, it is estimated that the outcrops at Treble Cone/Black Peak formed at a depth of 1-4 km. At Red Rock, relative to the other outcrops, vertical

displacement due to movement along the Moonlight Fault needs to be taken into account, too. Fission track data in Tippet & Kamp (1993) cannot resolve any movement less than 4 km. Reconstructions by Craw (1995), which are again based on geology and topography, suggests that about 2-4 km of rock have been eroded away at Red Rock since the Miocene.

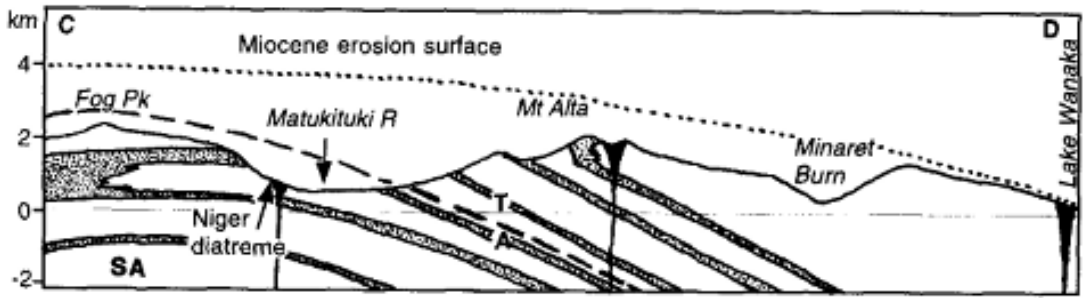

Fig. 2.4.16) Profile across diatremes at Niger, Alta, and Lake Wanaka. Dotted line: Reconstruction of Miocene erosion surface. SA: Shotover Antiform (From Craw, 1995).

2.6) Summary

In this chapter, the different areas focused on in this study have been introduced in respect to their locations, their host lithologies and tectonic features. The different aspects in each study areas are put into context relative to each other and are also tied into relation with regional scale structures, such as the Moonlight Fault. The 4 study areas can be subdivided into those with magmatic features (study area 4) and those without (study areas 1-3). The magmatic features studied here are dikes and diatremes which are part of the Alpine Dike Swarm. . For most of the structures, it could be shown that they are of a similar age (Oligocene-Miocene) and whose activity and formation can be linked to the movement along the Alpine Fault and Moonlight Fault. In the footwall of the Moonlight Fault, many larger faults trend W to NW and which in the Shotover are partly auriferous. However, here are also smaller structures that trend northward such as kink folds and associated veins. Common in all of the 4 study areas are brittle structures which accommodated abundant fluid flow, precipitation of hydrothermal carbonate and alteration of the rock adjacent to these structures. Based on the relative positioning of the outcrops today, it is suggested that none of the brittle structures formed at more than 6 km depth. In all cases, textures of minerals in veins and faults give evidence that vein minerals crystallized in fluid- filled cavities. Nonetheless, it could also been shown that there are many different types of microscopic textures and minerals, despite often similar wall rock composition. At Copper Creek and Bullendale, for example, there are signs of occasional Al mobility (Example) and hydrothermally grown, vein-associated chalcopyrite is abundant at Red Rock but not in the other study areas. A first look into the alteration of hydrothermal alteration of the fluid conduit's wall rock revealed that alteration styles are ankeritic, argillic and/ or sericitic and hydrothermal alteration is most obvious and advanced in greenschist and lamprophyres, due to the high content of alteration-sensitive minerals.

CHAPTER 3: REACTIONS AND TEXTURES ASSOCIATED WITH HYDROTHERMAL ALTERATION OF OTAGO SCHIST

Associated with fluid-conducting structures, such as faults and joints, mineralogical and chemical changes in the adjacent wall rock are common, resulting in the formation of alteration halos. Such alteration halos can be of interest for several reasons. Many mineral and metal deposits of economical importance are situated in hydrothermally altered country rock. In Carlin-type gold deposits, for example, the gold is located in hydrothermally altered rock rather than veins or ore shoots. Skarn deposits are also a classical example of ore deposits which form due fluid entering and reacting with the country rock (Meinert, 1992). However, even when alteration halos in otherwise unaltered rock are not bearers of precious metals themselves, they are often used as exploration vectors to find potentially mineralised bodies (e.g. Gemmel, 2007; Large et al., 2001; Large & McGoldrick, 1998).

Hydrothermal alteration halos not only act as sinks for elements dissolved in the incoming fluid but also as sources for other hydrothermal deposits further along the fluid conduit. Studying the mineral reactions taking place in the alteration halo aids the understanding of what processes control the redistribution of elements. Which external components are locked into the rock and how is this achieved. Which minerals break down due to the fluid influx and what can this tell us about the fluid chemistry? What aspects control such element mobility? Are the elements likely transported as hydrated ions in the fluid or could they form soluble complexes with ligands, such as CO_3^{2-} or F^-? For example, in the cases studied here, CO_2 from the fluid cause break down of several minerals, often producing carbonates in the process. The information on the minerals particularly susceptible to CO_2 influx and what hydrothermal minerals form, particularly how much carbonate forms, can be utilised when assessing potential lithologies for the sequestration of anthropogenic CO_2.

Other aspects that can be investigated are how the fluid penetrated the rock. For hydrothermal alteration to take place, rock permeability plays a crucial role. Primary permeability (i.e. pores) in the rocks studied here is very low and hence it raises the question how fluid penetrated the metamorphic rock up to several metres away from the primary fluid conduit. Did the fluid penetrate the rock uniformly or did it utilise structural controls, such as grain boundaries or cleavage plains? The study of microtextures also gives insight into the type of replacement (dissolution-precipitation vs. diffusion) and relative solubility of mineral phases (e.g. Putnis, 2009).

In this study, several examples of hydrothermally altered rocks from the different study areas have been investigated, focusing especially on the different scales of element mobility. There are several reasons why I chose to conduct this work in western Otago. Signs of hydrothermal alteration are ubiquitous in western Otago showing that at that time hydrothermal alteration is not an exception but the rule in this area. As has been discussed in the previous chapter, all outcrops formed in similar crustal levels, i.e. within a few km of the surface and at a similar time; except Red Rock, where the age is not entirely clear. Both lithologies investigated (greenschist and greyschist) have mostly a similar mineral assemblage. These aspects support the validity of the comparison of the halos in the different locations.

Notable differences are that the studied alteration halos are situated in various different geological settings, such close to magmatic rocks (Mt Alta Transect), close to gold deposits (Murdoch Creek and Bullendale Transect) or without any of these structures (Treble Cone, Black Peak and Red Rock Transect). This allows to investigate, if there is any major or minor differences between these different geological settings. Related to this is also that none of the here described halos and their

related altering features have significant gold concentrations. However, we know that there are contemporaneous halos surrounding gold-bearing structures in the Shotover Valley, such as at Bullendale and Copper Creek (Fig. 2.1.2, See Craw et al. (2006), MacKenzie et al. (2007) and chapter 2.3 this study for descriptions of the gold-bearing structures at). Hence, this study will also allow to compare between the gold-bearing and gold-barren alteration halos at Bullendale and Copper Creek.

In order to describe the hydrothermal alteration halos and unravel the processes which took place to form them, 5 main questions were addressed:

1. Which metamorphic minerals break down in response to the incoming fluid and which hydrothermal minerals replace them?
2. Where does replacement initiate and how do replacement reactions progress?
3. What is the composition of the metamorphic and hydrothermal minerals and what controls the chemical composition of these minerals?
4. What was the scale of mobility of major and trace elements?
5. What was the source of the components in the altered rock?

As suggested by the title in this chapter I will focus on the mineralogical changes that are associated with the hydrothermal alteration. Additionally, some aspects of element mobility will be discussed. However, mineral chemistry and changes in whole rock chemistry are focus in chapter 4 and will also be discussed in depth in chapter 4. Question 5 will be addressed in chapter 4 but most extensively in chapter 6.

3.1) Methods and samples

Overall, transects across 6 different alteration halos have been studied extensively; 4 of these halos are hosted by greenschist and 2 by greyschist (Table 3.1). Additionally, some aspects of the alteration in greenschist from Red Rock have been characterised and addressed (Table 3.1). Of the two lithologies studied, alteration is more apparent in greenschist compared to greyschist for which reason focus has been put on alteration of greenschist. Samples of each transect were taken in a profile across an alteration halo, perpendicular to the altering feature. During sampling, it was attempted to take samples from the same foliation-parallel horizon or as close to the same horizon as possible to avoid lithological and chemical changes. BUL3C and BUL4C, both from Bullendale, are the only transects which are based on single hand specimens. The transects, their lithology and aspects studied are listed in Table 3.1.

To characterise the alteration, samples of each transect were examined in hand specimen and thin section. The thin sections were analysed for microtextural and chemical attributes using the Zeiss SEM. Minerals in sample BUL3C was additionally analysed chemically by Electron microprobe. For more detailed methods see the previous chapter. To describe the intensity and nature of alteration a set of terms were used (Table 3.2).

Table. 3.1) Sample sets studied regarding hydrothermal alteration and methods that were applied. BUL from Bullendale; AD from Mt Alta; RR from Red Rock; TP from Treble Cone/ Black Peak area. For outcrop locations (in brackets) refer to the maps in chapter 2. ME= Major elements; TE: Trace elements. WR= Whole Rock.

Name of transect	Lithology	Sample names	Mineral replacement reactions	Texture and chemistry of altering feature	ME and TE of minerals	WR chem.
Discussed in chapter			3	3&5	4	4
Murdoch Creek	Greyschist	BUL2A, B, C	√	√	√	√
Mt Alta	Greyschist	AD1A-C2	√	√	√	√
Bullendale	Greenschist	BUL3C	√	√	√	√
Bullendale	Greenschist	BUL4C	√	Partly	-	√
Treble Cone	Greenschist	TP7A-D	√	-	√	√
Black Peak	Greenschist	TP4A-F	√	-	√	√
Red Rock	Greenschist	RR18-19	√	-	√	-

Table 3.2) Terminology to describe the intensity of alteration used in this and the following chapters.

Unaltered	No re-crystallisation or new mineral growth as a result of influx of fluid associated with Miocene-Oligocene events.
Altered	A rock that has been changed (mineralogically and/ or chemically) due to the influx of fluid associated with Miocene-Oligocene events.
Altering feature	The manifestation of the fluid conduit along which the fluid causing the alteration entered the rock. Such features are fault breccias and veins.
Post-metamorphic mineral growth	Growth of minerals after metamorphism of the rock. This growth event can have happened during the hydrothermal alteration event but may have also been earlier.
Weak alteration	First calcitic veinlets and beginning breakdown of epidote and titanite
Moderate alteration	Near complete to entirely complete breakdown of epidote, beginning breakdown actinolite and titanite, beginning breakdown of chlorite
Advanced alteration	Complete replacement of epidote, near complete to complete replacement of actinolite, titanite. Partial replacement of chlorite. Beginning replacement of metamorphic muscovite and calcite
Pervasive alteration	Complete breakdown of epidote, actinolite, titanite. Near complete replacement of calcite by ankerite.
Complete alteration	Chlorite, calcite, epidote and actinolite have been fully replaced by hydrothermal minerals.

3.2) Alteration of metamorphic rock -Textures and mineral reactions

The following chapter will discuss the alteration associated with greyschist and then greenschist protoliths. First the two transects in greyschist will be described (Murdoch Creek and Mt Alta Transect), then the alteration in greenschist, starting with muscovite-poor greenschist from Bullendale which is followed by the mica- and calcite rich greenschist from Treble Cone/ Black Peak. Finally, aspects of alteration at Red Rock will be described.

For the description of hydrothermal rock alteration, the studied rock package, or transects, can be divided into three main parts: **hydrothermally unaltered rock**, **hydrothermally altered rock,** i.e. the alteration halo, and the **altering feature**, which is the manifestation of the conduit along which the fluid entered the rock; today the altering features are manifested by veins and/ or fault breccias. Although it is referred to as the altering feature, in the transects studied here there is often not a single feature but actually several, such as a swarm of veins and smaller faults (i.e. Murdoch Creek). In the hydrothermally altered part of a transect, the intensity of alteration increases gradually towards the altering feature. The thickness of the alteration halos varies between a few cm up to several meters.

Generally, the wider the feature, the wider the alteration halo, with a ratio of about 1:3 between altering feature and visible alteration halo. A more exact ratio is not possible to determine for the transects here due to the often diffuse nature of the altering feature (i.e. vein swarm, rather than one thick vein at Murdoch Creek) or the outcrop situation where the "altering feature" is obscured by scree (e.g. Treble Cone Transect).

3.2.1- Hydrothermal alteration in greyschist

3.2.1.1: Alteration of greyschist associated with kink-folds - the Murdock Creek Transect.

In the bed of Murdoch Creek near the historic Bullendale Mine site (Outcrop B2 in Fig. 2.1.2), a N-S trending, about 0.7 m wide zone of orange stained greyschist is very well exposed (Fig. 3.2.1). This alteration is associated with a set of carbonate-quartz veins and small faults (Fig. 3.2.1). The **unaltered** greyschist from outside the halo (BUL2C) consists of albite, quartz, muscovite, epidote/clinozoisite, chlorite, titanite, apatite, rutile, and zircon (Fig. 3.2.2). The rock is segregated into layers of leucocratic (albite, quartz, calcite) and melanocratic minerals (muscovite, chlorite, epidote, titanite etc). In the melanocratic/ micaceous layers, chlorite and muscovite are found in close proximity, inter-finger or share grain boundaries parallel to the cleavage. Metamorphic muscovite in the samples is a solid solution of celadonite and pure muscovite. Epidote is located within the micaceous layers, where it forms small (less than 0.5mm) round to ellipsoidal grains. Titanite often forms clusters made of ca. 50µm long titanite grains (Fig. 3.2.2 A). Calcite occurs disseminated within the leucocratic layers. While not visible macroscopically, the schist outside the visible alteration halo shows some evidence for post-metamorphic alteration. Calcite also occurs in post-peak metamorphic veins.



Fig. 3.2.1) Alteration of greyschist in Murdoch Creek at Bullendale. **Left:** The labels indicate the sampled locations of this 0.7 m-wide greyschist alteration transect. **Right:** The alteration is related to carbonate veins and faults (the latter not shown in image).

Within the **moderate-advanced altered** greyschist (sample BUL2A) many original metamorphic minerals, like quartz, albite, muscovite, rutile, and apatite are still present (Fig. 3.2.2 B). However, the metamorphic epidote, titanite and chlorite are absent. Instead, the micaceous layers contain small (<500 mm) round to ellipsoidal grains of ankerite with some siderite at the grains' edges (Fig. 3.2.2B). Carbonate forms a network of veinlets and isolated "pearls" throughout the schist and which follow grain boundaries, cleavage planes of phyllosilicates and cracks (Fig. 3.2.2 B).

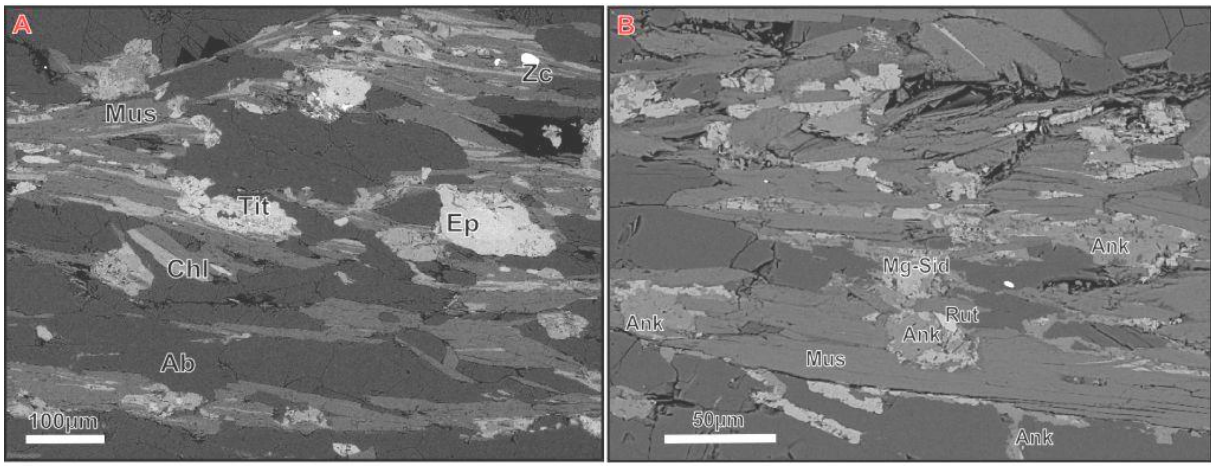

Fig. 3.2.2) BSE images of **(A)** unaltered and **(B)** moderate-advanced altered greyschist. In **A,** metamorphic chlorite and muscovite inter-finger or are inter-layered. Epidote occurs in ellipsoidal grains and titanite often forms clusters. BUL2C. In **B,** rounded to elliptical grains of hydrothermal ankerite and magnesian siderite are embedded within metamorphic muscovite. Ankeritic veinlets follow grain boundaries. BUL2A.

Advanced altered greyschist occurs within the central part of the alteration halo, adjacent to the veins. Along grain boundaries and cleavage planes metamorphic muscovite is partially replaced by hydrothermal muscovite (Fig 3.2.3A, white box). Hydrothermal muscovite contains predominantly Si, Al, K, O, and H and only very little Fe and Mg. In the altered rock, metamorphic chlorite is absent but hydrothermal chlorite is present in association with hydrothermal muscovite and carbonate veins (Fig. 3.2.3 A). Within a few cm of the veins in the centre of the alteration halo, the disseminated metamorphic calcite and the calcite veins have been partly replaced by ankerite (Fig. 3.2.3 A). Titanite has been pseudomorphically replaced by aggregates composed of euhedral prisms and very fine-grained rutile crystals (<10µm), inter-grown with fine-grained calcite, quartz +/- muscovite, +/- Fe-bearing calcite (Fig. 3.2.3 B). Galena, chalcopyrite, stibnite, and sphalerite are part of the alteration assemblage but present in only very small quantities in the altered greyschist and the veins.

Throughout the central part of the alteration halo at Murdoch Creek, **veins** made of calcite, ankerite +/- quartz are present (Fig. 3.2.1). The veins are may reach 5-10 mm in width and are predominantly composed of carbonate and quartz. Veins less than 1 mm wide are best developed within greyschist leucocratic layers, while they are often diffuse or discontinuous in the micaceous layers. Small faults that are associated with the thicker veins have produced clastic fault breccias, which were described in chapter 2.3 (Fig. 2.3.3 & 4).

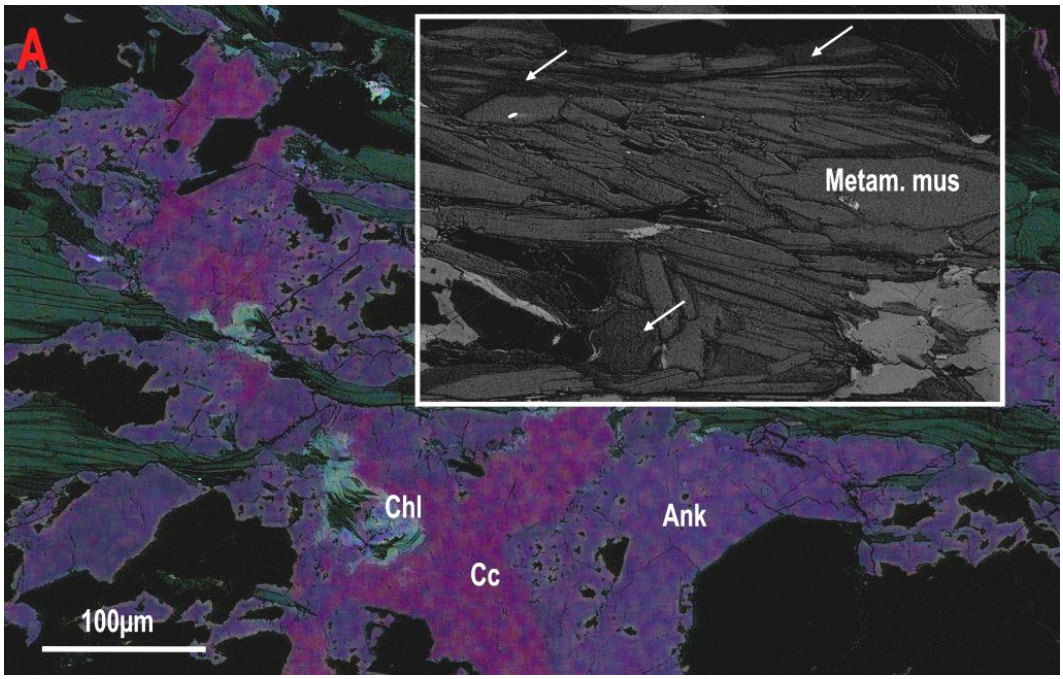

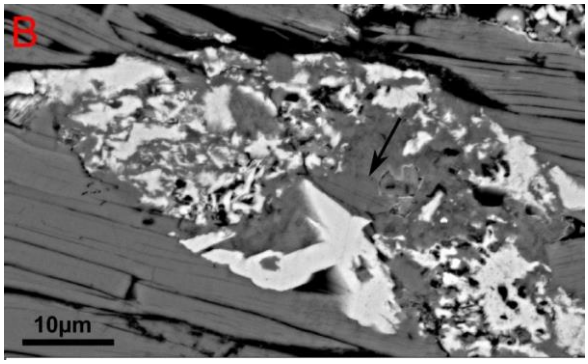

Fig. 3.2.3) Advanced alteration in greyschist. **A** Cc in a vein trending from upper left to lower right has been partly replaced by porous ankerite. Hydrothermal chlorite has precipitated close to hydrothermal muscovite. The white box outlines the BSE image of the under lying area and shows the replacement of metamorphic muscovite by hydrothermal muscovite (arrows) at grain boundaries and cleavage planes. BUL2B. LBSI. **B:** BSE image. Rutile, muscovite, and little calcite, ankerite and quartz describe the shape of a euhedral titanite grain. The muscovite can display a cleavage (black arrow). BUL2B.

3.2.1.2: Alteration of greyschist associated with silicified fault breccias - the Mt Alta Transect.

A transect of altered and unaltered greyschist samples were taken across a 1 m wide zone adjacent to a N-S trending silicified breccia at Mt Alta (Fig. 3.2.4) The silicified breccia have been described in chapter 2.4, where they are referred to as "Quartz reef".

The **unaltered** metamorphic wall rock contains quartz, albite, metamorphic muscovite (celadonite-muscovite solid solution), biotite, epidote, some chlorite (Fe:Mg>1), apatite, rutile and zircon. Similar to the greyschist from Bullendale, these minerals have segregated into layers predominantly made of albite and quartz or of optically darker mineral (Fig. 3.2.5 A). In the phyllosilicate-rich layers, biotite is commonly inter-grown with chlorite. Titanite is absent in the unaltered sample (AD1C2), but there are some areas are composed of rutile and calcite +/- quartz (Fig. 3.2.5 B), which resemble euhedral titanite grains. It is unclear whether this replacement of titanite is related to the ankeritic alteration because epidote and chlorite are both still present in the specimen. Rare calcite veins have propagated irregularly through the rock, following grain boundaries and locally forming small bodies in the adjacent phyllosilicates.

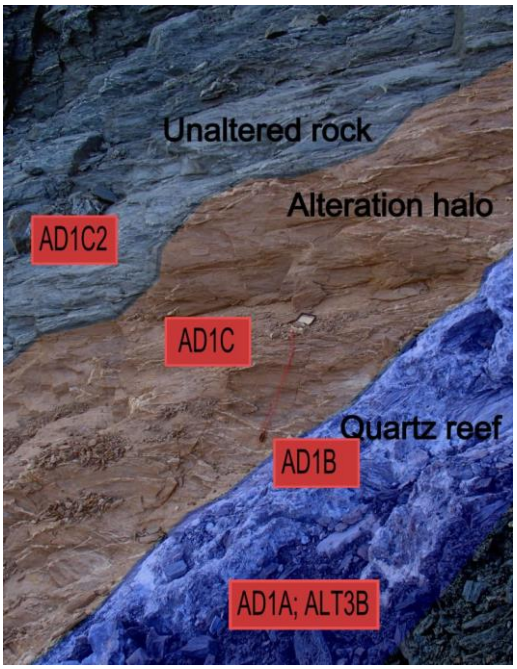

Fig. 3.2.4) Outcrop of greyschist and alteration associated with a quartz reef near Mt Alta Diatreme. Red boxes represent the locations each sample was taken from. Outcrop A1. Compass in centre view for scale.

The hydrothermally altered greyschist of the Mt Alta transect (AD1C) has an orange-brown colour instead of the darker grey of the unaltered rock. The degree of alteration can be classed as **moderate to advanced**. The altered rock contains pre-hydrothermal albite, quartz and muscovite, but no biotite or epidote. Carbonate veins are abundant and in the phyllosilicate-rich layers irregular vein-like bodies composed of ankerite and calcite occur (Fig. 3.2.5 C). There are also composite lenses of siderite and calcite with minor ankerite that are within and parallel to the cleavage of white mica (Fig. 3.2.5 D). The siderite and calcite are in sharp contact with each other, with siderite often on the outside and calcite commonly on the inside of these composite grains (Fig. 3.2.5 D). The white mica adjacent to the composite carbonate is muscovite and either illite or kaolinite (too fine to be distinguished with EDS) that form finely alternating lamellae (Fig. 3.2.6). In close proximity to the composite carbonate patches, the white mica contains more Al but less Fe, K and Mg compared to distal portions of the same grain (Fig. 3.2.6). This trend corresponds to a higher proportion of illite (K-poor hydrothermal muscovite)/ kaolinite relative to hydrothermal muscovite. Small (<10µm) elongate rutile grains are concentrated along the phyllosilicate's cleavage planes (Fig. 3.2.6).

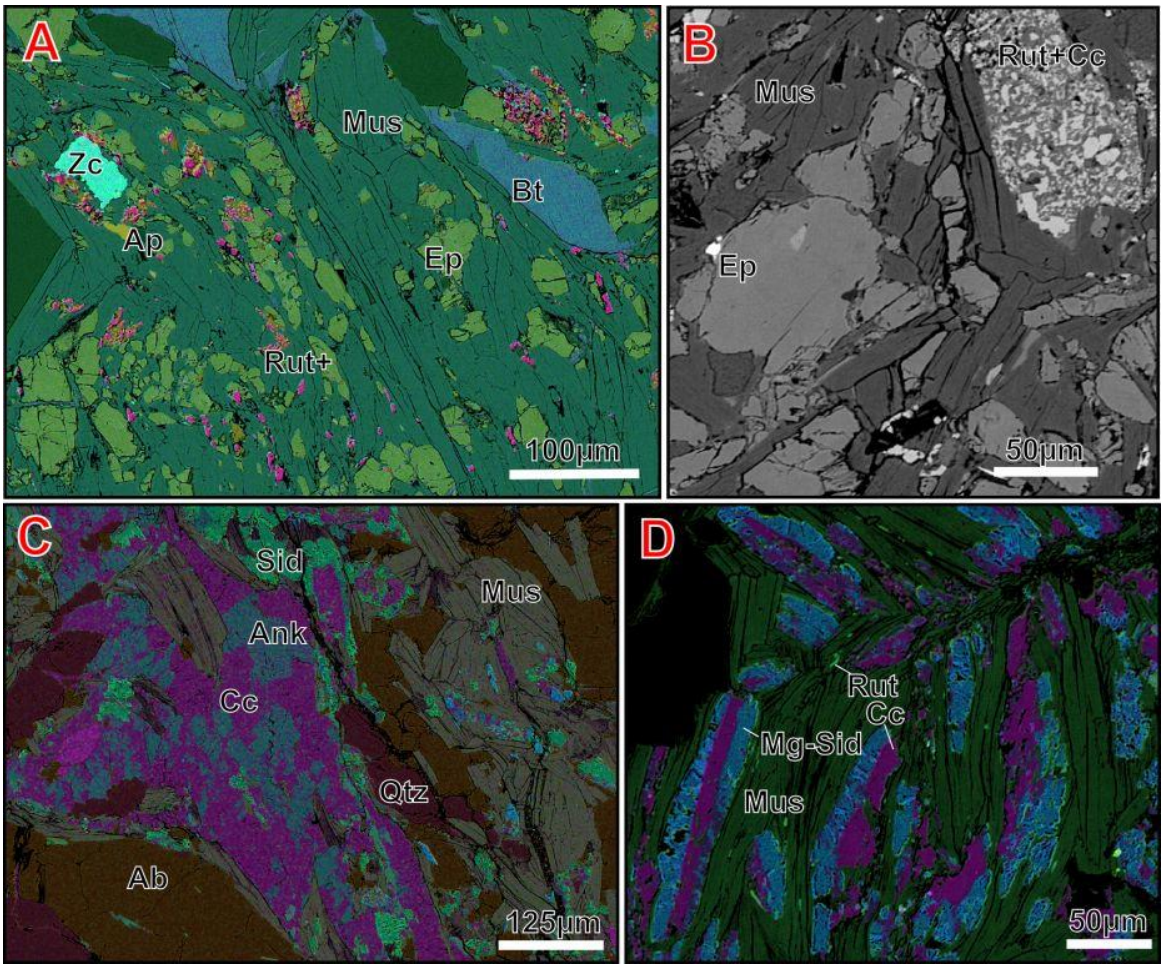

Fig. 3.2.5) A & B: LBSI of unaltered greyschist. AD1C2. **A:** Melanocratic layers in unaltered greyschist are made of epidote, muscovite and biotite, rutile, calcite, some zircon and apatite. **B:** BSE image. Rutile and calcite occur in aggregates in the melanocratic layers (upr. right corner). **C & D:** LBSI of intermediate altered greyschist. AD1C. **C:** Carbonate (cc and ank) form sparitic, vein-like bodies. Here ankerite forms blocky grain within the calcite. **D:** Intercalated with hydrothermal muscovite are calcite and magnesian siderite, the latter of which has been partly replaced by secondary Fe-hydroxide.

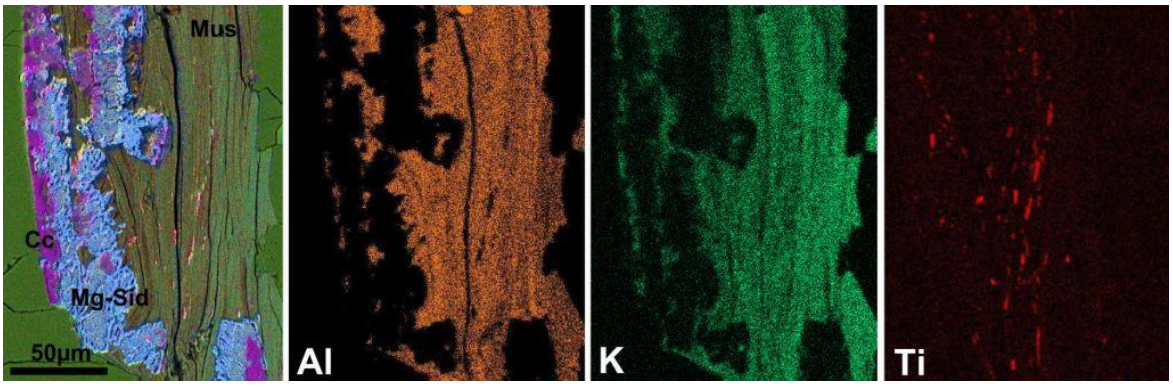

Fig. 3.2.6) Close up of a carbonate-mica composite. Far left image: LBSI. The 3 right ones: element distribution maps. The pyllosilicate adjacent to the alteration-related carbonate is chemically zoned and is made of slivers of muscovite and illite or kaolinte. They embed small grains of rutile (see Ti concentration map).

3.2.2- Alteration of greenschist

Although greenschist is less common than greyschist in the Otago Schist, more examples of hydrothermally altered greenschist are presented here. As mentioned above, this is due to the more pronounced alteration in this rock type, which is the result of the higher content of the "unstable" phases (e.g. epidote, chlorite, titanite). In the following description, 2 transects through greenschist are discussed in detail. These are divided into two groups: Greenschist originally poor in metamorphic muscovite, i.e. not visible with the naked eye **(Bullendale Transect)** and greenschist originally rich in metamorphic muscovite, i.e. visible with the naked eye **(Black Peak and Treble Cone Transect)**. Lastly, I will describe and discuss some aspects associated to the alteration of greenschist at Red Rock.

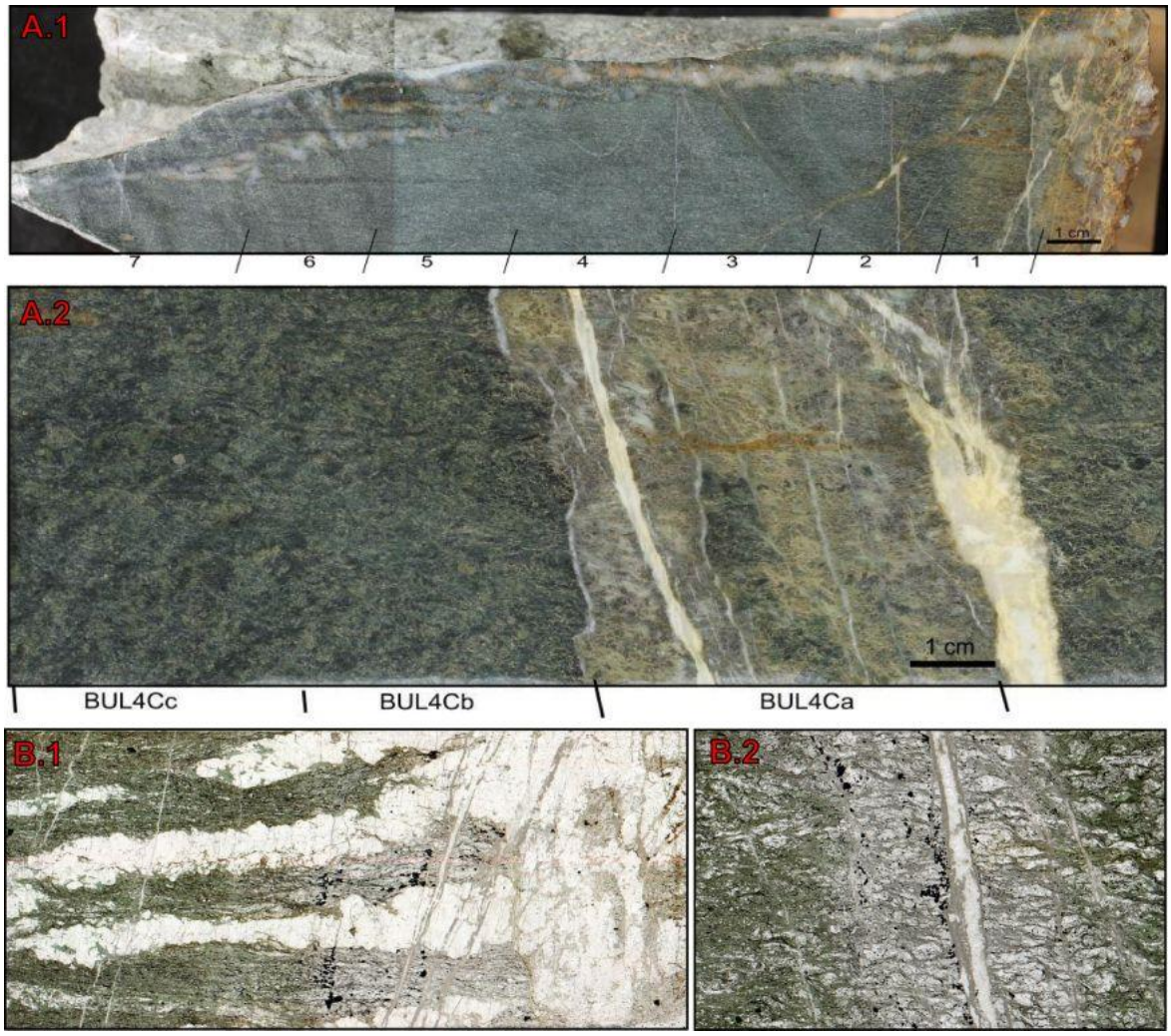

Fig. 3.2.7) A.1. & A.1: Samples discussed in section 3.2.2. **A.1:** BUL3C. **A.2:** BUL4C. The numbering and naming below each image refers to the sub-samples which have been analysed for their whole rock composition (See chapter 4). **B.1 & B.2:** Microphotographs (PPL) of BUL3C **(B.1)** and BUL4C **(B.2)**. Each image is about 35-40 mm wide. In BUL3C, the halo transitions gradually into unaltered rock, while in BUL4C, it is bound by calcite veins. Opaque phases are sulphides, mostly pyrite.

3.2.2.1: Alteration of greenschist poor in metamorphic muscovite - the Bullendale Transect

Alteration in greenschist is examined in two hand specimens collected from the river at the old Bullendale mining site (BUL3C and BUL4C; Fig. 3.2.7)**.** Both samples contain carbonate-quartz veins surrounded by a several cm wide alteration halo that gradually grades (BUL3C) or abruptly transitions (BUL4C) into macroscopically unaltered greenschist (Fig 3.2.7 A; Fig. 3.2.7B). As the alteration and

mineral reactions are very similar in the two samples, they are described together and are referred to as the **Bullendale Transect.**

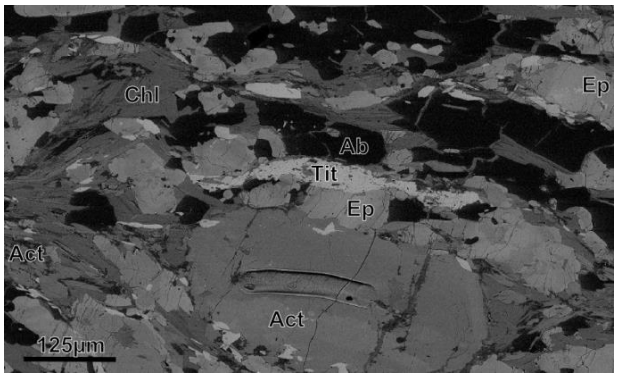

Fig. 3.2.8) Unaltered greenschist at Bullendale comprises chlorite, epidote, titanite, apatite, albite (BUL3C). Note: LASER track in actinolite. BSE image.

The macroscopically **unaltered rock** contains chlorite, epidote, actinolite, titanite, muscovite, apatite, albite, quartz and calcite and has a distinct foliation. BUL3C, additionally, has distinct layers either rich in dark coloured minerals (chlorite, epidote, actinolite, titanite, muscovite, apatite) or light coloured minerals (albite, quartz, calcite) (Fig.3.2.7A). BUL4C contains slightly more muscovite (c. 5% in the dark layers) than BUL3C (c. 1% in the dark layers). Of the dark minerals, chlorite is the most abundant and makes up most of the green layers. Amongst the chlorite grains are epidote, titanite, Mg-bearing actinolite and some apatite and quartz (Fig 3.2.8). Epidote has a patchy zoning. Muscovite is inter-grown with chlorite. Calcite either forms big grains in the leucocratic layers (Fig. 3.2.9 A) or occurs in the chloritic layers as small elongate grains parallel to the chlorite cleavages (Fig. 3.2.9 B). This calcite can be found as small networks that have propagated parallel to grain boundaries, cracks and cleavage planes, and which may be part of the hydrothermal alteration event (Fig. 3.2.9 A & B).

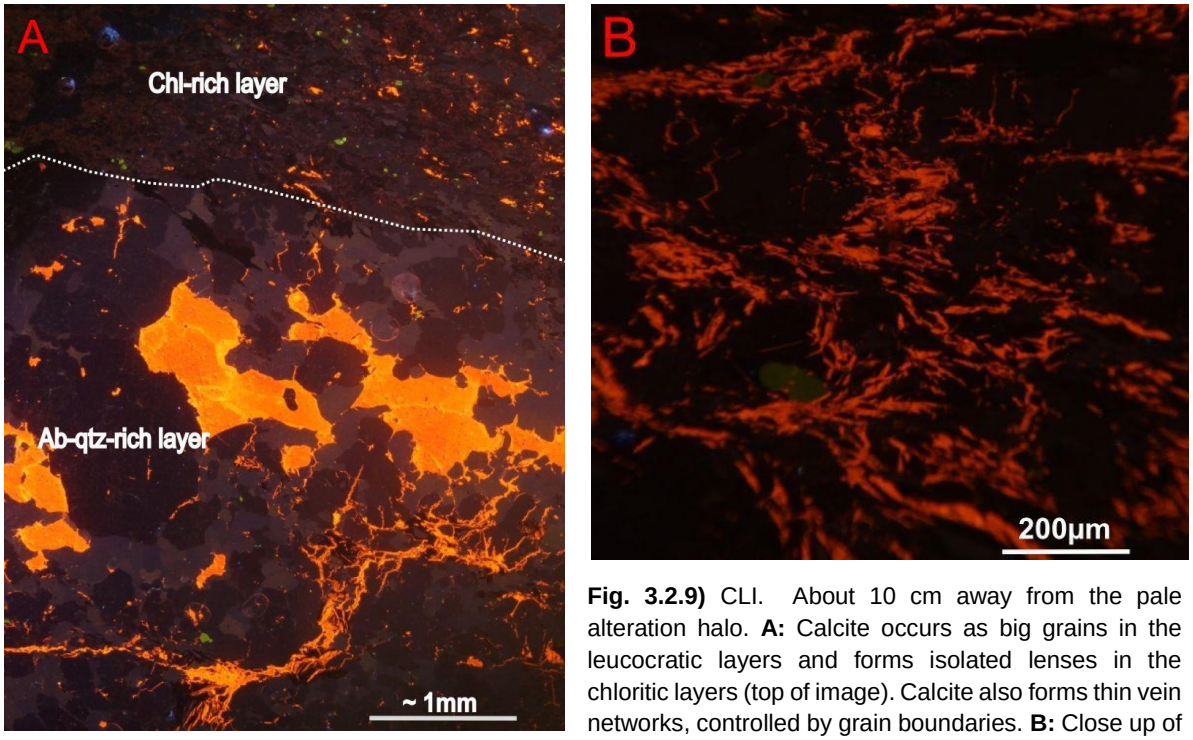

Fig. 3.2.9) CLI. About 10 cm away from the pale alteration halo. **A:** Calcite occurs as big grains in the leucocratic layers and forms isolated lenses in the chloritic layers (top of image). Calcite also forms thin vein networks, controlled by grain boundaries. **B:** Close up of calcite veinlet networks in chloritic layers. Both BUL4C.

The first clear signs of a hydrothermal **alteration** are found ca. 7 cm centimetres outside of the visible alteration halo. Here some of the metamorphic minerals are partially replaced by hydrothermal minerals. For example, epidote occasionally contains chlorite-ankerite or sometimes muscovite veinlets, which are roughly perpendicular to the foliation. Chlorite is partially replaced by a mix of ankerite and calcite. Titanite is partly replaced by rutile and quartz (Fig. 3.2.10 A &B, arrows).

About 5 cm away from the centre of the alteration halo replacement has progressed further, and the degree of alteration can be classed as **weak to moderate.** Actinolite has partially been replaced by quartz and carbonate (calcite and ankerite) at grain boundaries and cleavage planes. The two replacing minerals generally form two distinct rings tracing the original actinolite grain shape with porous quartz right next to the actinolite and the ankerite on the outer edge (Fig. 3.2.10 A&B). The ankeritic rim can be zoned with an increase of Ca and decrease in Mg towards the outside of the rim. The quartz rim contains small pieces of another mineral, which appears to be ankerite (too small to analyse with the SEM). The actinolite replacement texture is independent of the mineral adjacent to the amphibole. Towards the central veins the degree of replacement of actinolite increases but the style remains similar (Fig. 3.2.10 B). In a few parts of the moderately altered greenschist, the actinolite between the ankerite-quartz veinlets has been replaced by calcite, but still has distinct rims of quartz and carbonate, but here ankerite and calcite (Fig. 3.2.10C). In the weak to moderately altered rock, pseudomorph replacement of epidote initiates and epidote has partially been replaced by muscovite +/- small amounts of calcite (Fig. 3.2.11 A). The muscovite is porous and remaining epidote forms isolated small ellipsoidal grains and/ or little bodies with ragged boundaries embedded in the muscovite. The ellipsoids are aligned parallel to each other, apparently parallel to the cleavage plains of the muscovite (Fig. 3.2.11 A). Just outside of the visible alteration halo, chlorite is partially replaced by ankerite and muscovite (Fig. 3.2.11D).

In the part of the greenschist where the alteration is **moderate to advanced**, the colour of the rock changes from green to cream-colour which also defines the visible alteration halo (Fig. 3.2.7). This change is due to a drastically increased content of carbonate and muscovite and mostly absent "green" minerals (i.e. chlorite, epidote), giving rise to the distinct colour change. Calcite grains in the albite-quartz layers are partly replaced by ankeritic carbonate with various Mg and Fe content, as evident by different colours in CL images (Fig. 3.2.11B). The zoning of this ankeritic carbonate is blocky (Fig. 3.2.11 B). The most advanced calcite replacement coincides with veinlets which terminate at the calcite grain. Within the alteration halo, most of the titanite is fully replaced by rutile, quartz and calcite. Chlorite is increasingly replaced by ankerite and muscovite. In some places the ankerite is inter-grown with dolomite (Fig. 3.2.11 C). Carbonate and muscovite are distinctly separated. Within the outer edge of the light coloured halo, remnants of actinolite are present and are still surrounded by the distinct quartz-ankerite rim succession as is also found outside the visible halo.

In the central part of the alteration halo, i.e. **pervasively altered rock**, all titanite, epidote, and most of the metamorphic chlorite and actinolite are gone. Additionally, carbonate forming from breakdown of chlorite is ankerite associated with magnesian siderite. In places, the two chlorite - replacing mineral species - carbonate and muscovite - form a cauliflower-like structure (Fig. 3.2.11 D). The muscovite's cleavage appears to follow the shape and cleavage of the original chlorite, and so does the zoning/phase transition of the carbonate - Mg-Siderite and ankerite (Fig. 3.2.11 D). Replacement textures of actinolite breakdown as found in less intensely altered rock are more and more lost and actinolite breakdown products "mix" with those of chlorite replacement.

In the **completely altered rock,** i.e. within a few mm of veins, intertwined ankerite and well-developed hydrothermal muscovite with occasional lenses of quartz make up the rock's originally melanocratic layers (Fig. 3.2.12). There are no textural evidences for the previous existence of actinolite or chlorite; Millimetre big, roundish grains of hydrothermal muscovite +/- calcite mark locations where epidote used to be. Rutile-quartz-carbonate aggregates inhabit original sites of titanite. Unlike in less intensely altered parts of the samples, the carbonate is ankerite rather than calcite in these titanite-replacing cumulates. Despite the loss of the shapes of chlorite and actinolite grains, foliation and layering can still be recognised throughout the rock (Fig. 3.2.12).

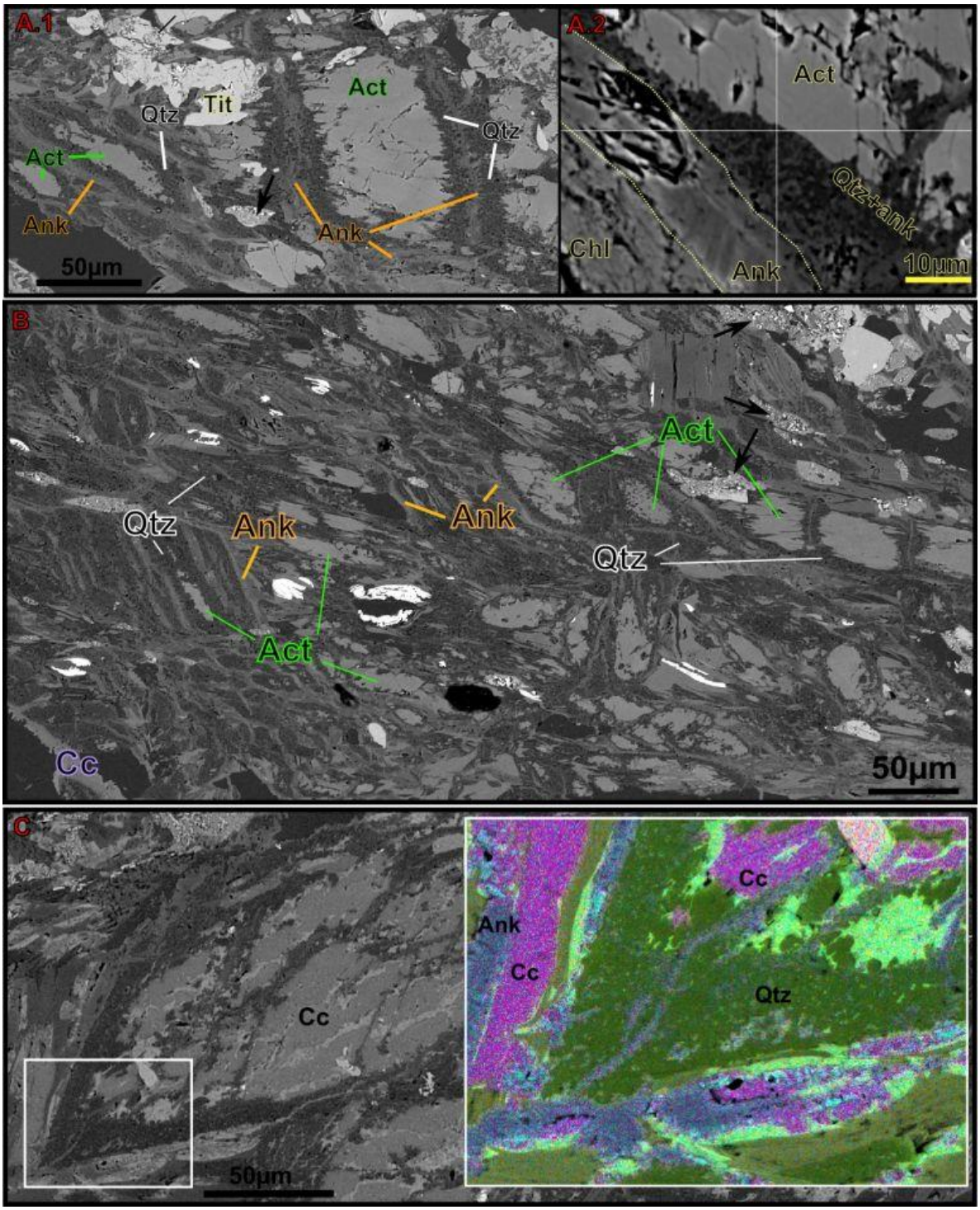

Fig. 3.2.10) A: Replacement of actinolite and titanite. **A.1:** Replacement of actinolite follows grain boundaries and cleavage planes and the replacement is pseudomorph. Titanite is partially replaced by rut and qtz (black line at the top). **A2:** Remnant actinolite is surrounded by a rim of porous qtz which contains tiny inclusions of ank. Adjacent is a layer of ankerite. **B:** Different degrees of actinolite replacement. Right: actinolite is still present in the centre the qtz-ank rims. With progressing degree of alteration, actinolite is increasingly replaced and eventually only the characteristic bodies of qtz with ankeritic rims are present (left side of image). Titanite shows partial to complete replaced by rut, qtz and cc. **C:** Similar replacement texture to A & B, except that the interior is made of calcite rather than ankerite. The LBSI in white box shows that the quartz-rich rim contains ankerite.

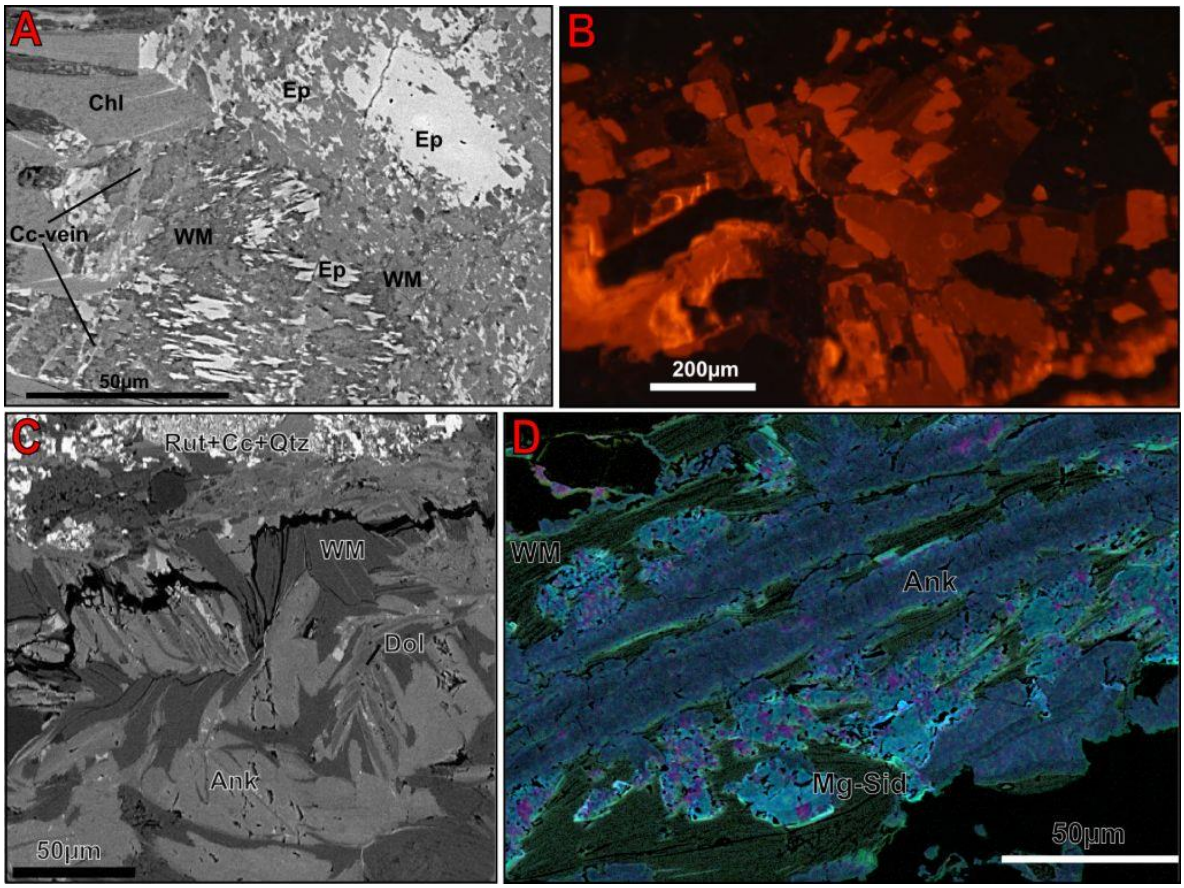

Fig. 3.2.11) A: Epidote is partly replaced by porous muscovite. Remnant epidote is aligned parallel to the muscovite's cleavage. Calcite veinlets cut across the original epidote but not chlorite. BSE image. **B:** CL image. Ankeritic carbonate replacing calcite in the leucocratic layers is blocky and the replacement is gradual with each block being relatively homogenous as can be told by the homogenous orange colours. Note the LASER tracks with bright orange halo. **C:** Chlorite is entirely replaced by spatially well separated muscovite and carbonate (ankerite and dolomite). **D:** Total replacement of chlorite by hydrothermal muscovite and ankerite. The ankerite is zoned parallel to the cleavage of the old chlorite and makes a cauliflower-like texture. All BUL3C.

Within the macroscopically visible alteration halo sulphides formed, predominantly in thin zones parallel to the carbonate veins in the chloritic layers (Fig. 3.2.7). Sulphides are predominantly pyrite, but there are also some grains of chalcopyrite and tetrahedrite. The tetrahedrite forms inclusions in chalcopyrite. Chalcopyrite can be found as inclusions in pyrite.

The **altering feature** in the centre of the alteration halo comprises veins and fault breccias. The veins are up to 5 mm wide, although most are ca. 1 mm wide. The thicker veins are made of several minerals with the rims being ankeritic and in the central part they can be filled with calcite and quartz (Fig. 3.2.13A). Veins of roughly 1 mm thickness are composed of zoned ankerite with optical murky carbonate at the rim and clearer one in the centre. The murkiness is caused by many tiny pores, presumably fluid inclusions. The ankerite at the vein rim forms euhedral grains, with the ends pointing into the vein, and internally a fine oscillatory zoning. Some veins also contain barite and double-ended quartz is found at the rim (Fig. 3.2.13B). Late stage calcitic veins can also contain hydrothermal chlorite (Fig. 3.2.13C). Apart from veins the central part of the halo also contains small-scale fault breccias. The fault breccia shows several brecciation events as manifested by differently oriented zones of subgrain rotation (Fig3.2.13C). Similarly, cross cutting relationships of veins also give evidence of multiple vein intrusion and hence deformation events (Fig 3.2.13C and Fig. 3.2.7 A.2 right hand side of image, by scale bar).

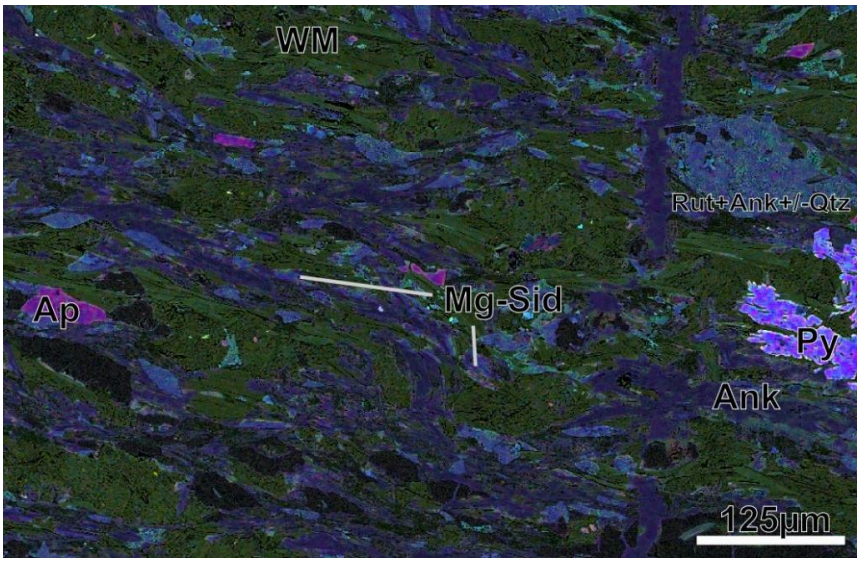

Fig. 3.2.12) LBSI. Completely altered greenschist. In the central part of the alteration, foliation is still preserved. Except for titanite, apatite (which metamorphic) and epidote, old mineral outlines are not preserved.

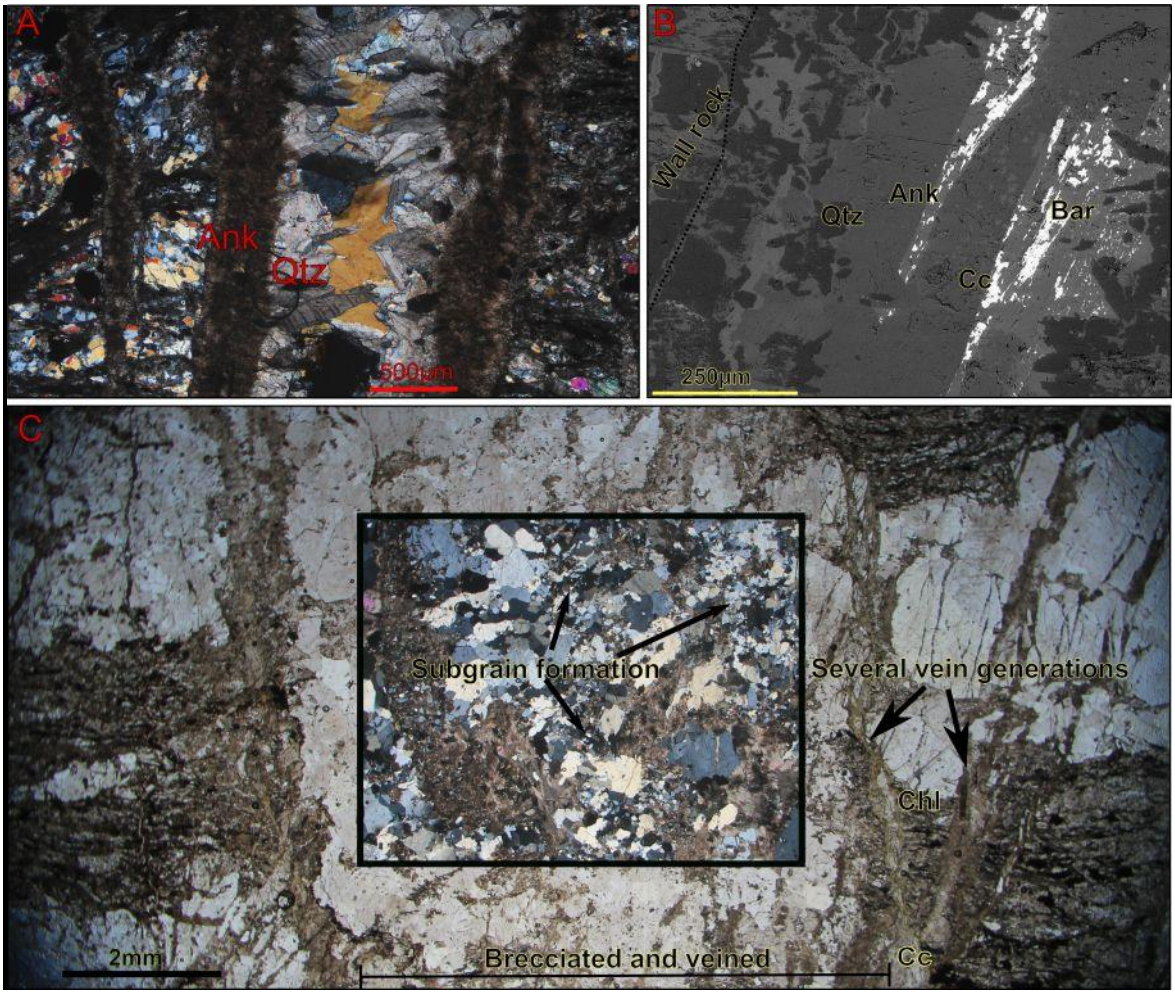

Fig. 3.2.13) Veins in the centre of the alteration halo in BUL3C and BUL4C. **A:** Multi-component vein with murky ankerite at the rim, clear ankerite crystal pointing into the centre which is made of quartz (yellow). BUL4C. XPL. **B:** Veins containing slivers of barite, calcite and double-ended quartz crystals embedded in ankerite.BUL3C. BSE image. **C:** PPL & XPL in black box. Fault breccia and veins in the centre of the alteration halo. In the breccia, several zones of subgrain formation developed (arrows in XPL section). Late stage calcitic veins also contain hydrothermal chlorite.

3.2.2.2: Alteration of greenschist rich in metamorphic muscovite

Alteration of originally muscovite-rich greenschist is described on the basis of samples from two transects in the Treble Cone-Black Peak area (Fig. 2.1.3). These are the Treble Cone Transect (TP7A-D) and the Black Peak Transect (TP4A-F). In both cases, the centre of the altering feature is a fault producing a silicic-ankeritic breccia, which produced a 1-3 m wide visible alteration halo. Unfortunately, in both cases the fault zone are eroded down but are marked by plenty of fragments of fault breccias in the rubble.

Table 3.2.1) Samples taken of two alteration halos in the Treble Cone/ Black Peak area and their estimated distance to the halo-central fault zone.

Sample	Width of alteration halo (macroscopically visible)	Distance from altering feature	Alteration-related colour visible in hand specimen	Signs of post-metamorphic alteration in thin section
TP7A	1-2 m	0.7 m, was about 20cm above TP7B.	Yes	Yes
TP7B	1-2 m	0.8 m	Yes	Yes
TP7C	1-2 m	4m	No	Yes
TP7D	1-2 m	6m	No	No-uncertain
TP4A	3 m	2.5 m	Yes	Yes
TP4B	3 m	3.5 m	Yes	Yes
TP4C	3 m	4.5 m	No	Yes
TP4D	3 m	5.5 m	No	Very little
TP4E	3 m	7 m	No	No
TP4F	3 m	9 m	No	No

3.2.2.2-1: The Treble Cone Transect

The greenschist examined here originates from N of the fault zone. The lithology south of the fault zone is greyschist.

The **unaltered greenschist** contains chlorite, quartz, albite, muscovite, calcite, epidote, apatite, titanite and some hematite as main constituents. The rock is layered with leucocratic layers, (albite, calcite, quartz) and melanocratic layers (chlorite, epidote, titanite, muscovite, apatite, quartz, hematite). Quartz in the melanocratic layers is found amongst the chlorite, forming grains with the habit of a phyllosilicate (Fig. 3.2.15A). Grains of epidote are usually less than 1 mm in diameter. Titanite forms small grains (<100µm) throughout the green layers (Fig. 3.2.15A). Albite often makes bigger inclusion-rich porphyroblasts throughout the rock, in addition to forming smaller, anhedral grains in the leucocratic layers. The mineralogy of the inclusions is the same as that outside of the albite augen, including calcite. In the leucocratic layers, calcite forms several millimetre big grains between the smaller albite and quartz grains, and can make up to ca.75% of the leucocratic layers (Fig. 3.2.15 C&D). The examined rock sample of unaltered greenschist contains some signs of post-metamorphic mineral growth. Some smaller epidote grains began to be replaced by chlorite (Fig. 3.2.15B). Calcite forms little veinlets along grain boundaries and little cleavage-parallel lenses in chlorite. Calcite also makes up thicker veins crosscutting the foliation (Fig. 3.2.15 C&D). The contact of the calcite in the wall rock and vein calcite is marked by a bright orange in the CL image in the calcite in the wall rock adjacent to the vein. This calcite is also more murky compared to the other metamorphic calcite away from the vein (Fig. 3.2.15 C&D).

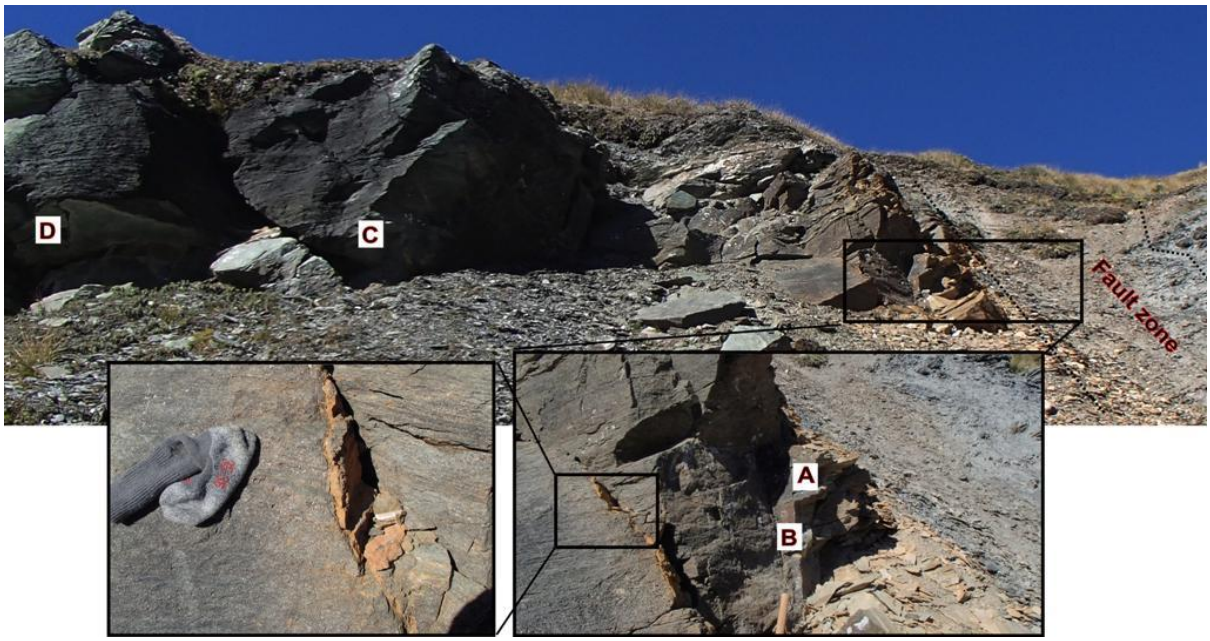

Fig. 3.2.14) Fault with alteration halo at outcrop T7. Letters correspond to samples taken at this location. Thick carbonate veins are also accompanied by alteration halos. North is on the left.

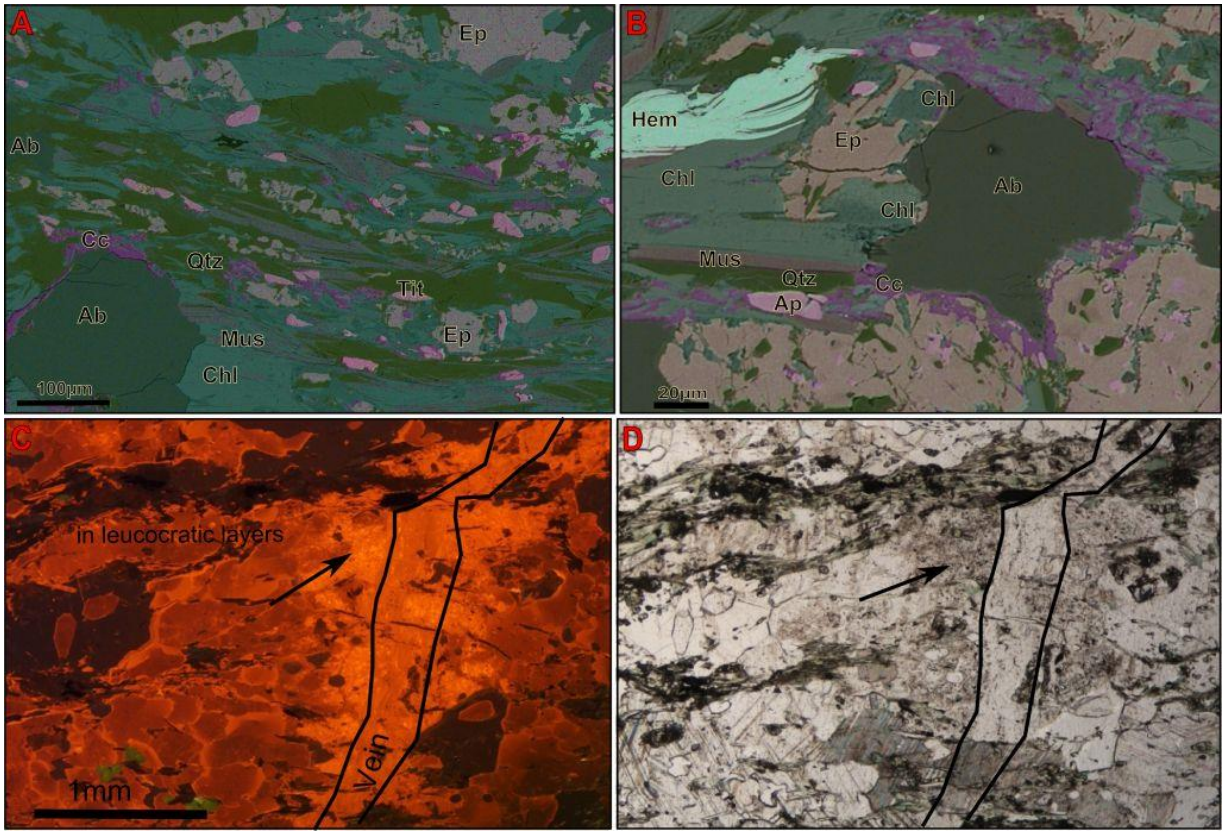

Fig. 3.2.15) A: Texture of unaltered greenschist. Chlorite and muscovite are most abundant in the leucocratic layers. Intercalated with the chlorite is quartz. **B:** Epidote is partly replaced by chlorite. Calcite forms veinlets following the chlorite's cleavage and grain boundaries. **C:** CLI. Much of the light layer here is made of calcite. A calcite vein cut across the foliation (brighter orange). Note the relatively bright orange of the adjacent calcite (arrow). **D:** PPL of figure C. The calcite adjacent to the vein is murky (arrow). All TP7D.

About 4 m from the fault zone (sample TP7C), evidence of a **moderate alteration** can be recognised. Titanite is replaced by rutile, quartz +/- calcite when it occurs close to grain boundaries, cracks and occasionally cleavage plains (Fig. 3.2.16). No epidote is found in the chloritic layers and only occurs in albite as inclusions. Within the chloritic layers, small (<100µm), round nodules made of fine grained quartz, hydrothermal muscovite, and occasionally calcite occur (Fig. 3.2.16). Calcite is also found in the chloritic layers forming cauliflower-like cumulates, whose propagation is controlled by the cleavage planes of the chlorite (Fig. 3.2.16).

About 0.8 m away from the fault the degree of alteration is **advanced**. Muscovite and chlorite contents are lower than further away from the altering feature while those of carbonate, hydrothermal quartz and kaolinite increase. Most titanite has been replaced by rutile, quartz and calcite and sometimes some hydrothermal mica. The rock also contains similar quartz-carbonate nodules as found further away from the fault. However, here they contain more carbonate, which is ankerite rather than calcite, and there is also no muscovite (Fig. 3.2.16 vs 17A). Cauliflower-like carbonate in the chloritic layers like in the less altered sample also occurs but it is here more common and is ankerite rather than calcite (Fig. 3.2.16 vs 17B). The ankerite grains are also bigger and often better defined compared to the calcite in the less altered rock (Fig. 3.2.16 vs 17 A&B). The ankerite's chemical zoning is about parallel to the foliation (Fig. 3.2.17 B), where the outer part is generally slightly more Fe-rich at the grain rim compared to the central part of the grain. Interstitial spaces in the carbonate cumulates are filled by kaolinite (Fig. 3.2.17). In the leucocratic layers, the metamorphic calcite shows signs of re-crystallisation, such as smaller grains at individual grain rims, though the composition remains calcitic (Fig. 3.2.17 C & D).

About 0.7m away from the fault zone, the degree of alteration is **advanced**. The cauliflower-like textured ankerite is recognisable in many places (Fig. 3.2.18 A). Additionally, well-defined ankerite grains form lenses in the chlorite and in many places there is clear indication that the growing ankerite pushed the chlorite apart along the cleavage planes (Fig. 3.2.18 B). Closely associated with the ankerite is kaolinite. Kaolinite is also found isolated amongst the chlorite, where it forms well defined grains parallel to the cleavage (Fig. 3.2.18 A). No metamorphic muscovite is found in the rock. Calcite in the leucocratic layers is mostly replaced by ankeritic carbonate. This ankerite either forms small sugary grains or crystallographically continuous carbonate which has a blocky zoning. The sugary carbonate generally occurs at the rim of the original calcite grain (Fig. 3.2.18C&D). Occasionally, small patches of calcite can be found in these grains and they are likely remnants of the original calcite. Areas made of either carbonate type are porous. In the "sugary" carbonate pores are in between grains, while in the other one, pores are within the carbonate grain. In the centre of this carbonate barite can be been found (Fig. 3.2.18C).

The **fault zone** in the centre of the alteration halo strikes about ESE-WNW and is several metres (c. 3m) wide (Fig. 4.2.14). Similar to the other fault zones in this area, no solid outcrop of the fault zone is exposed. It is covered by scree, predominantly made of altered greenschist (Fig. 3.2.14). In proximity of the fault, variously thick veins penetrate the rock, often also with individual ankeritic alteration halos surrounding them (Fig. 4.2.14). For this reason, the overall alteration halo has an irregular shape and varying thickness, as haloes overlap.

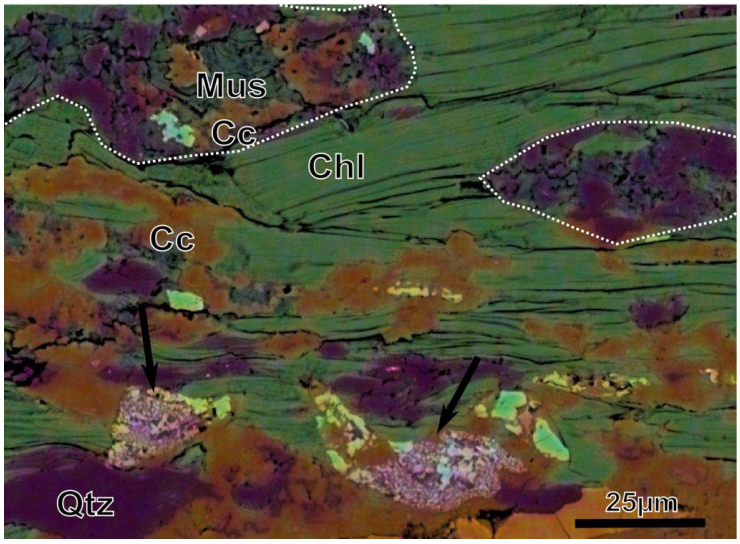

Fig. 3.2.16) LBSI. Replacement textures of moderate alteration. White outline: Knots of finely inter-grown quartz, hydrothermal muscovite and some calcite embedded in metamorphic chlorite. Arrows: Rutile, calcite and some quartz forming clusters in the shape of titanite. Centre view: Cauliflower-like calcite grows in chloritic parts. TP7C.

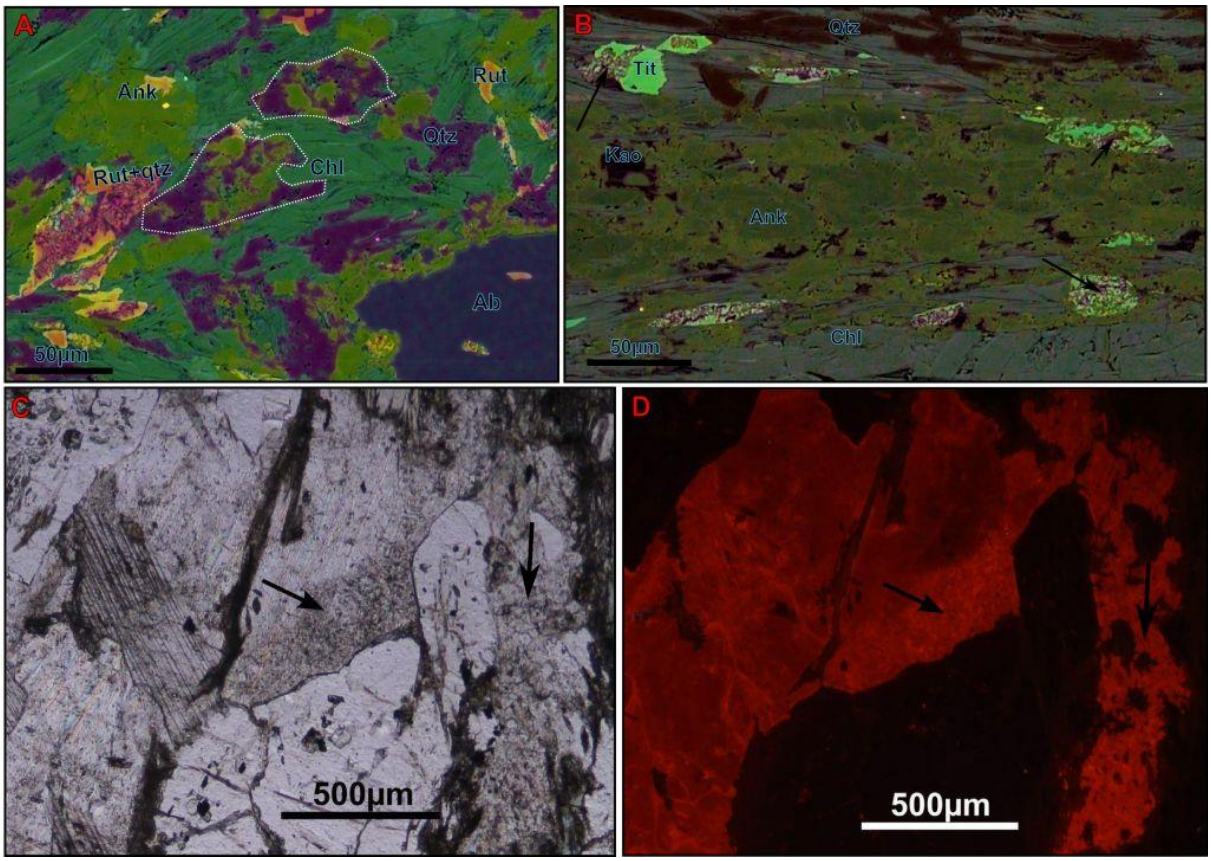

Fig. 3.2.17) Advanced alteration **A:** Cauliflower-like ankerite grains are found throughout the chloritic layers. White outlines mark areas made of calcite (yellow) and quartz (purple). LBSI. **B:** Ankerite in the chlorite can form bigger cumulates with interstitial places filled by kaolinite. Arrow: partial replacement of titanite by rutile, quartz and carbonate. LBSI. **C & D:** PPL & CL image. The calcite in the leucocratic layers is recrystallised at the grain's rim (grainy texture= murky in PPL) but is calcitic in composition. All TP7B.

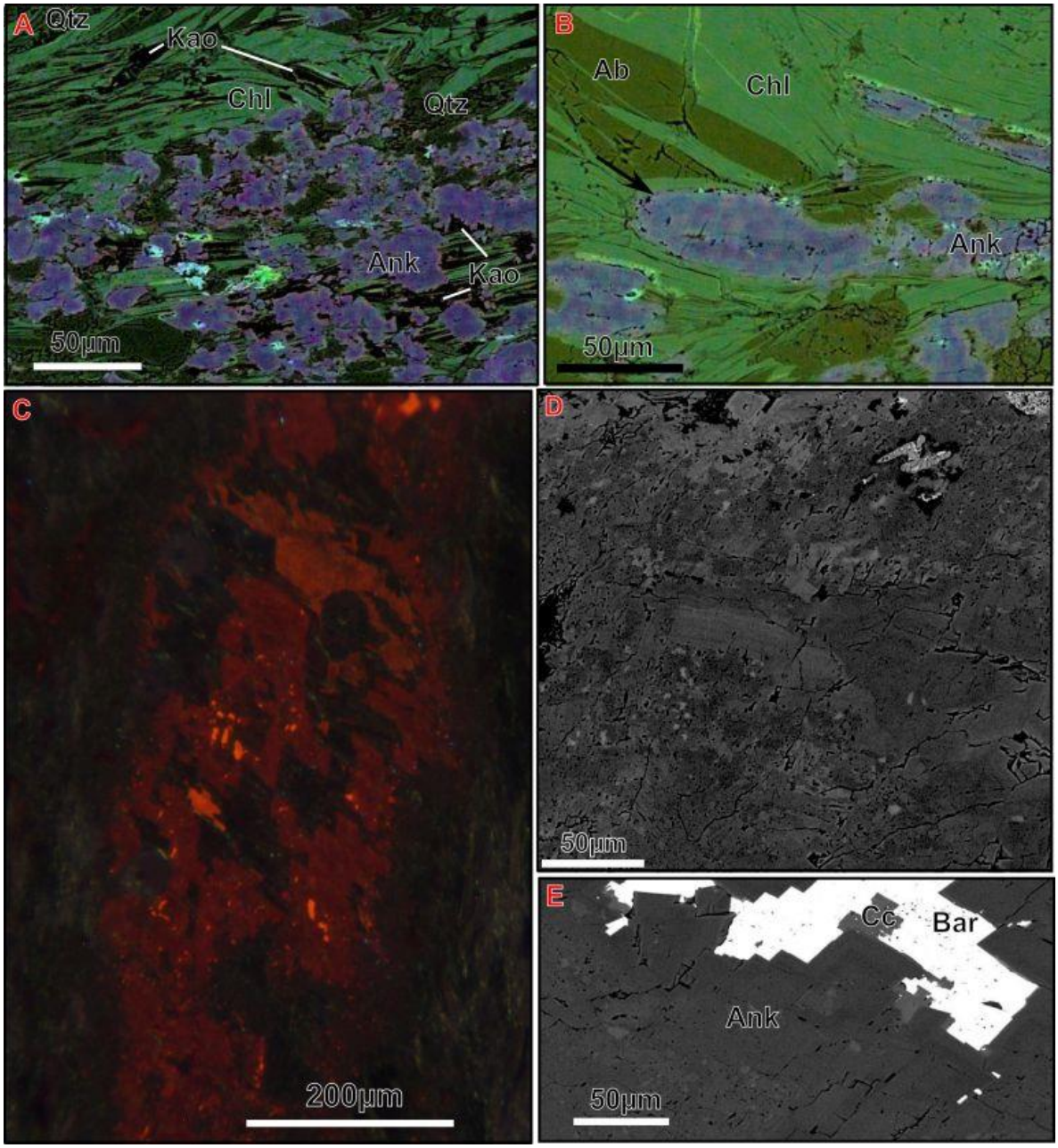

Fig. 3.2.18) Pervasively altered rock**. A:** Ankeritic forms cauliflower-like aggregates in the chloritic layers, cutting across chlorite grains. Quartz and kaolinite fill the interstitial spaces. Parallel to the chlorite's cleavage grows kaolinite. LBSI. **B:** Ankerite forms lenses, pushing the chlorite apart along the cleavage planes (black arrow). LBSI. **C:** Calcite in the leucocratic layers is replaced by chemically inhomogeneous, blockily zoned ankeritic carbonate. CL image. **D:** BSE image of a carbonate grain similar to that in image D. Grainy, chemically inhomogeneous ankerite occurs at the rim of the carbonate in (top & bottom of image), while carbonate with blocky zoning occurs predominantly in the centre of the grain as also shown in image D. **E:** Barite associated with the carbonate in the leucocratic layers. BSE image. All TP7A.



Fig. 3.2.19) Breccia from the fault causing the alteration halo at outcrop T4. The breccia is made of quartz and ankerite.

3.2.2.2-1: TheBlack Peak Transect

This series of rocks are altered and unaltered greenschist from a ca. 9m wide zone adjacent to a fault zone on the southern flank of Black Peak. The fault zone is covered by scree and boulders (Fig. 3.2.19). Over 6 metres away from the altering feature, the rock (samples TP4E and F) shows neither macro- nor microscopic conclusive evidence for mineral replacement associated with the fault zone. The **unaltered greenschist** of this transect has a mica content of about 15% in chloritic layers. Other major constituents of the greenschist are albite, chlorite, epidote, titanite, calcite, apatite and quartz. The rock is well foliated and often has millimetre-thick layers, which are rich either in phyllosilicates or albite, quartz and calcite. In phyllosilicate layers, chlorite is inter-grown with muscovite and both are generally aligned parallel to the foliation (Fig. 3.2.20). Occasionally, quartz occurs within chlorite where it forms lensoidal, phyllosilicate-shaped grains. Epidote grains are around 100µm in diameter and are only slightly bigger than the titanite grains (Fig. 3.2.20). Calcite forms big grains (1-2mm) within the leucocratic layers. In some unaltered samples, calcite also occurs amongst the chlorite, where it forms small lensoidal grains parallel to the foliation and cleavage. Due to the small grain size, it is not clear if it is "alteration-related" calcite. Albite occurs either together with quartz in the leucocratic layers embedding the bigger calcite grains, or as inclusion-rich porphyroblasts throughout the rock (Top of Fig. 3.2.4). The inclusions are mineralogically the same as outside the porphyroblast and the chlorite is chemically the same as that in the "outside" the albite porphyroblast. A few small grains of metamorphic pyrite and chalcopyrite can be found throughout the unaltered rock. The first signs of post-metamorphic rock mineral growth are found ca. 5.5 m away from the fault, in TP4D. Here carbonate forms little veinlets along the grain boundaries of epidote. No mineral breakdown has been observed.

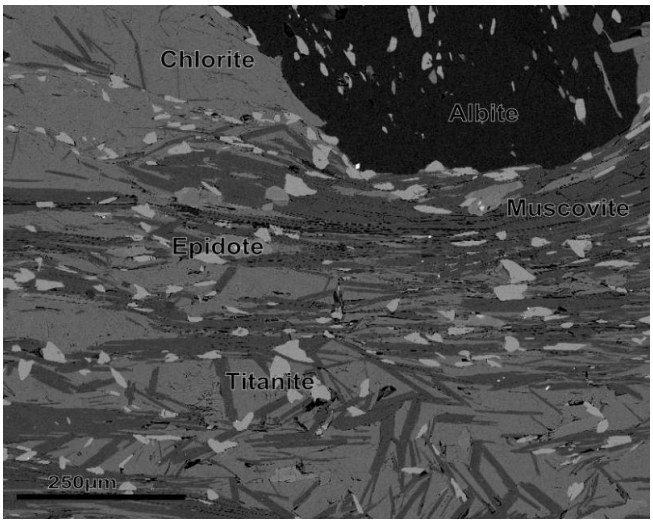

Fig. 3.2.20) Unaltered mica-rich greenschist. Inclusion-rich albite porphyroblasts (top) embedded in a matrix of chlorite, muscovite, epidote and titanite. Epidote is a similar size as titanite.

About 4.5 metre away from the fault (TP4C), clear indicators for fault-related alteration are found. This alteration can be classed as **moderate**. Epidote is only present as inclusions in the albite porphyroblasts, but nowhere else in the rock. The great majority of titanite grains are partly to completely replaced by rutile, calcite (Fig. 3.2.21), and sometimes quartz which fills the spaces between the rutile and calcite. In the moderately altered rock, the textural relationship between muscovite, chlorite, quartz and carbonate is complicated. Muscovite forms well defined elongate grains and is generally

in contact to well defined, non-porous quartz or chlorite (black box in Fig. 3.2.21). In contrast to this, there are also lenses and cumulates of lenses which are made of small slivers of chlorite +/- ankerite embedded in porous quartz (Fig. 3.2.21). These lenses are aligned parallel to the metamorphic chlorite's cleavage planes (Fig. 3.2.21). However, in places the quartz-chlorite lenses cut across metamorphic chlorite, muscovite and quartz (Black box in Fig. 3.2.21). Also within the chlorite, alteration-related carbonate forms lenses, where it pushes the chlorite's cleavage planes apart (Fig. 3.2.21). The carbonate is mostly ankerite, but calcite and dolomite also occur. The boundaries between these carbonate species are patchy and diffuse (Fig. 3.2.21). Towards the altering feature the degree of alteration increases and progressively more of the original, alteration-sensitive mineralogy has been replaced. In addition to the above mentioned alteration minerals, kaolinite occurs within 3.5 m of the fault zone (in TP4B), where it forms platy grains parallel to the cleavage planes of chlorite and muscovite.

About 2.5 m (sample TP4A) away from the altering feature, the degree of alteration in the greenschist can be described as **advanced**. The only place titanite and also epidote are found is as inclusions in the albite porphyroblasts. However, along cracks in albite, inclusion minerals have also been replaced by hydrothermal minerals. In the chloritic layers, titanite has been entirely replaced by rutile, quartz and calcite. Here quartz is more common than calcite, which differs from the moderately altered rock (TP4C), where calcite is more common in the titanite replacement assemblage (see above).

In the chloritic layers, the grain boundaries of the hydrothermal carbonate in the chloritic layers are well defined and the carbonate species are ankerite and magnesian-siderite (Fig. 3.2.22). This carbonate either forms lenses, where the cleavage planes of the surrounding muscovite or chlorite are pushed apart, or it forms cauliflower-like grains growing across the grain boundaries of pre-existing chlorite (Fig. 3.2.22 B). In bot cases, distinct chemical zoning and carbonate species change (from siderite to ankerite and vice versa) is present. For one, there is a flame-like one which is about perpendicular to the long axis of the carbonate grain (Fig. 3.2.22A & B). This zoning/ carbonate species boundary is over-or underlain by a chemical zoning/ carbonate species transition, which is about parallel to the cleavage of the surrounding chlorite/ muscovite (Fig. 3.2.22 A). There is no definite textural indicator as to which of the two zonings/ species transition boundaries came first. In the chloritic layers, especially where the replacement of chlorite is advanced or complete, muscovite grains are thinned out or cut and hydrothermal carbonate occurs (Blue arrows in Fig. 3.2.22 A, also black box in Fig. 3.2.21). Quartz-rich, lensoidal cumulates similar to those chlorite- and ankerite- containing quartz lenses embedded in chlorite in the moderately altered sample (Fig. 3.2.21), are also recognised in the advanced altered rock. However, here the inclusion in the quartz is mostly ankeritic (Fig. 3.2.22 A). Apart from replacement reactions, carbonate can form partly oscillatory zoned veins following grain boundaries and cracks (Fig. 3.2.22 C). The calcite in leucocratic layers has a thin, very fine grained rim of ankerite at the contact of the calcite to the other minerals in the rock.

The sulphide content of the rocks in this transect increases gradually towards the centre of the alteration halo. The newly growing sulphide, pyrite, partly replaces pre-existing chalcopyrite. This replacement is not necessarily complete, even in the advanced altered samples. Additionally, new pyrite grows in elongate clusters of smaller hypidiomorph grains parallel to the foliation. In the centre of these clusters small grains of chalcopyrite may be found.

As stated already above, rocks of the fault zone in the centre of the alteration, i.e. **the altering feature**, do not crop out anywhere in-situ. Instead the fault zone marked by a ca. 3 m wide zone of scree, which is made of altered, partly kinked greenschist and cm-thick breccias, made of hydrothermal quartz and ankerite (Fig. 3.2.19). Based on the rocks in the scree, it appears that the centre of the

alteration halo is made of several smaller faults and veins, rather than one wide fault zone, such as at the Mt Alta Transect. Based on the orientation of the scree distribution and vein orientations at this location, the fault zone appears to strike about ESE-WNW.

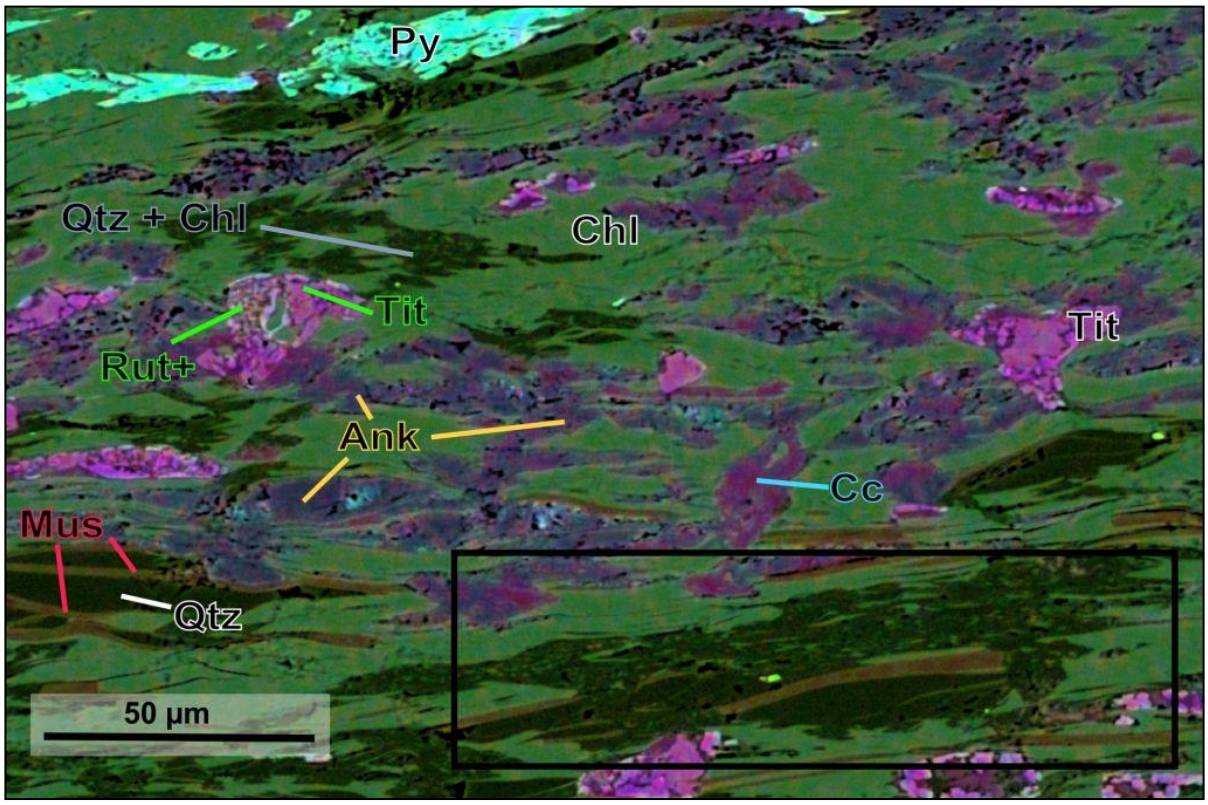

Fig. 3.2.21) Chlorite (light green) embeds lenses of chlorite and quartz (dark green) (maroon = muscovite). The carbonate in the chloritic layers is predominantly ankeritic (purple), but calcite also occurs (pink) and little dolomite (not distinguishable in this image). Titanite (bright pink) is replaced by rutile and calcite. Black box: Chlorite is intertwined with muscovite and inclusion-rich quartz. The inclusions are chlorite. Note the difference of the texture of the quartz in contact to the muscovite and the more porous one in the chl-qtz mix. TP4C. LBSI.

3.2.2.3: Examples of alteration in greenschist at Red Rock

In the eastern part of the alteration halo at Red Rock, samples RR18 and RR19 were taken. RR 18 is greenschist with poikiloblastic "spots" of calcite and calcitic veins (Fig. 3.2.23 A&B). RR19 is the altered counterpart of this rock. The unaltered greenschist is dominated by chlorite, albite, quartz, titanite, apatite and calcite (Fig. 3.2.23 C). The calcite occurs predominantly in poikiloblastic spots and is homogenous in composition, as is evident by the constant shade of orange in the CL image(Fig. 3.2.23 A&B). In proximity to the spots, titanite has been replaced by rutile calcite +/- quartz. Calcitic veins in this rock have a fibrous, syntaxial growth texture and a vein wall-parallel zoning (Fig. 3.2.23 B).

In RR19, the calcite in the poikiloblastic spots has been replaced by ankerite. Other alteration-related features are ankerite growing along grain boundaries and (more) breakdown and replacement of titanite (Fig. 3.2.23 D). Nonetheless, many metamorphic minerals, like chlorite or muscovite are present in the rock (Fig. 3.2.23 D). Neither RR18 nor RR19 contain epidote or signs that it used to be present. In the hydrothermally altered rock, magnetite, which is also present in the pristine metamorphic greenschist, is partly (Fig. 3.2.23 E) to fully replaced by hematite.

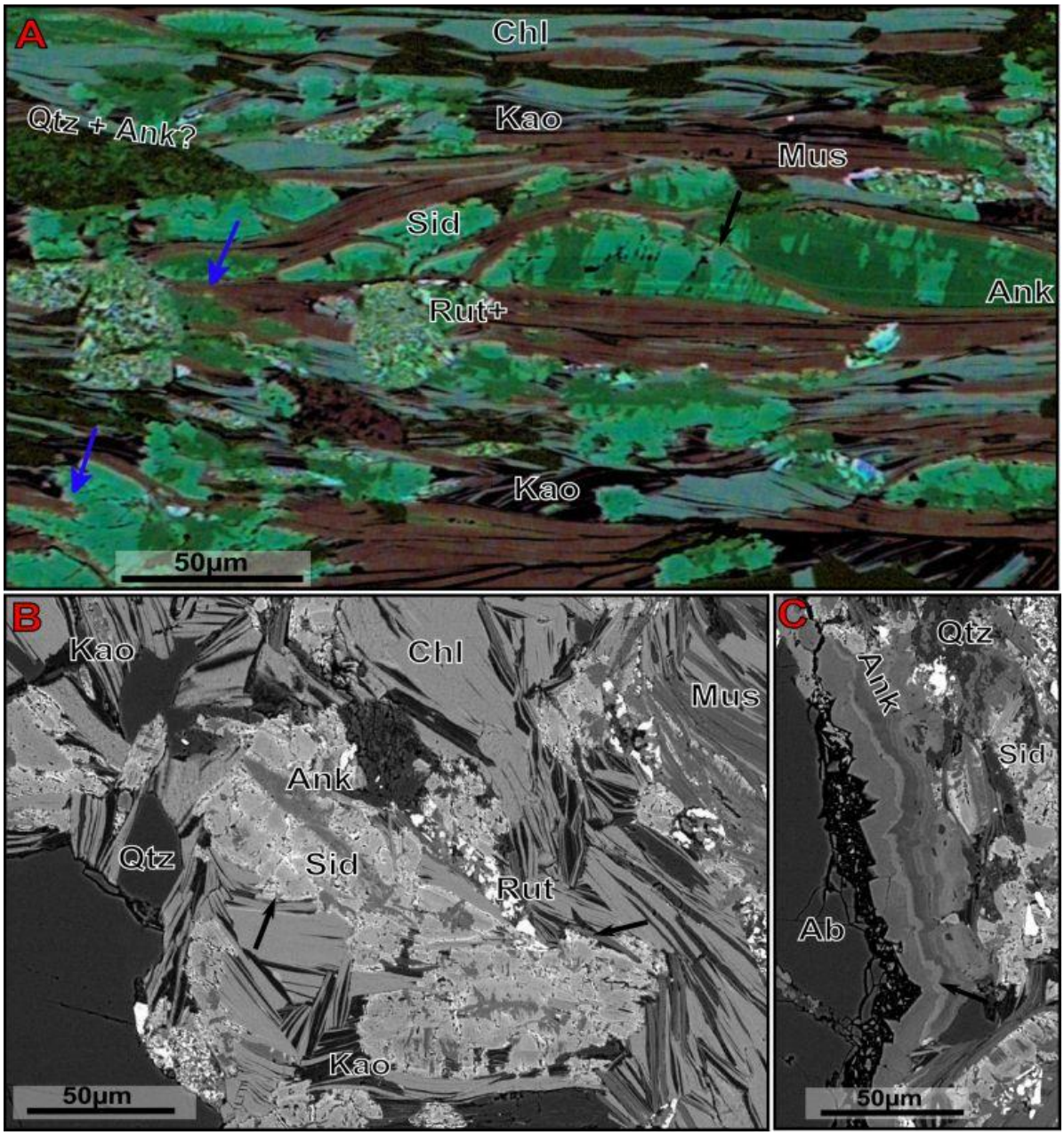

Fig. 3.2.22) A: Metamorphic chlorite and muscovite are intertwined. Ankerite and magnesian siderite replace chlorite and muscovite and have a cauliflower-like texture or form lenses in the chlorite. In both cases, the carbonate has a complicated zoning, parallel and perpendicular to the chlorite's cleavage. Muscovite (maroon) amongst the ankerite has begun to be broken down (blue arrow). LBSI. **B:** Complexly zoned, cauliflower-like grains of carbonate (Ank and Sid) cutting across kaolinite and chlorite (arrow). BSE image. **C:** Oscillatory zoned ankerite tracing the outlines of albite porphyroblasts. BSE image. All PT4A.

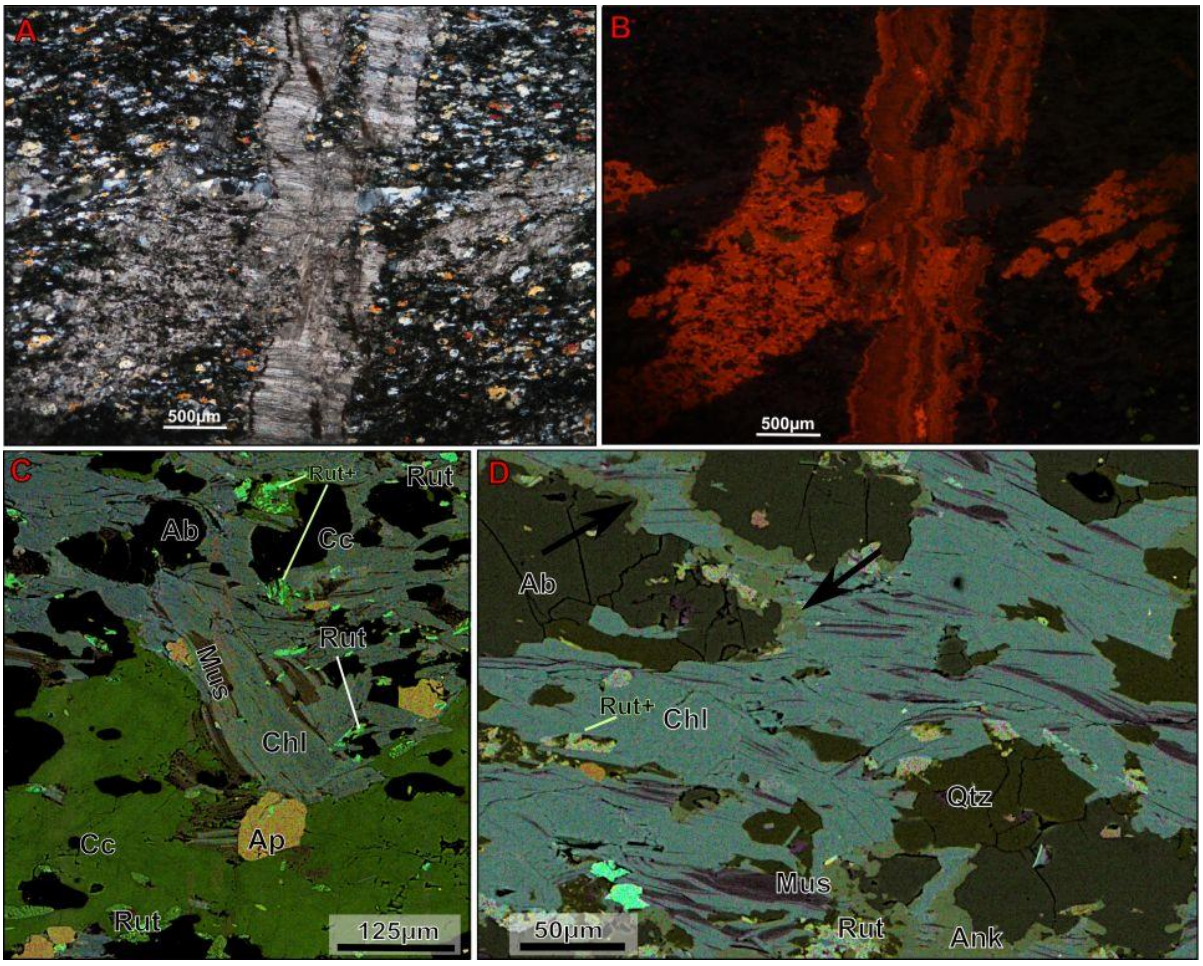

Fig. 3.2.23) A & B: XPL & CLI. Poikiloblastic calcite spots and vein in greenschist at Red Rock. RR18. **B:** The vein has a syntaxial growth texture. The calcite in the spots is chemically homogenous as evident by the same shade of orange throughout. (Note: lighter spots are by titanite replacement sites.) **C:** Unaltered greenschist. RR18. Calcite occurs predominantly in the calcitic spots (bottom) and occasionally along grain boundaries (green lenses very top, centre left). Titanite is broken down to rut, cc +/- qtz. LBSI. **D:** Ankerite follows grain boundaries of chlorite and replaced the chlorite partially at the edges (arrows). RR19. **E:** Metamorphic magnetite has been replaced at the rims by hematite. RR19. BSE image.

3.3) Discussion

The descriptions in the previous sections show that all transects have some similarities but also differences.

Similarities

- In all cases, fault breccias and veins in the centre of the alteration halos cut the foliation at high angles
- The euhedral crystal shapes of vein fillings (i.e. Fig. 2.3.3; 2.4.12D; 3.2.13 A&B) show that minerals precipitated into fluid-filled cavities. Veins and breccias show evidence for multiple brecciation, veining and infiltration events (Fig. 2.3.3; 3.2.7&13 C).
- The alteration-sensitive minerals are titanite, actinolite, epidote, chlorite, muscovite, biotite and calcite. These minerals are replaced by carbonates, quartz, rutile, hydrothermal muscovite and/or kaolinite. Stable minerals are quartz (at least in leucocratic layers), albite, apatite and zircon.
- Mineral replacement initiates in zones of relatively high fluid permeability (cleavage, grain boundaries, cracks. Fig. 3.2.2B; 3; 10; 22; 23 D&E) Hence, fluid flow in the rock will have been highest and furthest, parallel to foliation, which has also been found in previous studies of similar features compared to here (e.g. Fein et al., 1994; Yardley & Lloyd, 1995).
- Initial replacement is pseudomorph but with more intense degrees of alteration especially shapes of smaller mineral grains are obliterated due to the mixing of products from several break down reactions.
- Increase of sulphide content towards the altering feature.

Differences

- Due to the relative higher abundances of the especially alteration-sensitive phases, alteration is most pronounced in greenschist; greenschist contains c. 3 times more chlorite, epidote and titanite than greyschist. Admittedly, metamorphic muscovite, which is common in greyschist, is also sensitive to the hydrothermal alteration. However, this mineral only breaks down at more intense degrees of alteration compared to epidote, titanite and actinolite. Additionally, metamorphic muscovite is replaced by other phyllosilicates, commonly hydrothermal muscovite (Fig. 3.2.3A), and hence mineralogical changes can often only be recognised in BSE images.
- The width of the alteration halos varies; some halos are only a few cm wide (e.g. Bullendale Transect). The alteration halo at Murdoch Creek is several dm wide, while others (e.g. Treble Cone Transect) are several meters wide (Table 3.3.1).
- The nature and orientation of the altering feature differ (Table 3.3.1).
- The break down mineralogy differs from transect to transect (see next section).

Table 3.3.1) List of altering feature types, their orientation and the width of the visible halos in the different transects. Red Rock is excluded as this information was not recorded for that site.

Transect	Type of altering feature	Width of visible halo	Orientation
Murdoch Creek	Qtz and Carb veins and small faults sub-parallel to N-trending kink folds	0.7 m	NNW
Mt Alta	C. 40 cm wide silicified, N-trending Fault breccia	1 m	N
Bullendale (BUL3C)	Qtz and Carb veins and small faults	2 cm	-
Bullendale (BUL4C)	Qtz and Carb veins	3 cm	-
Treble Cone	Fault zone, several meters wide	1-2 m	ESE
Black Peak	Fault zone, several meters wide	3 m	ESE

- Sulphide content of altered rock differ from case to case, e.g. high (several Vol-%) in the Bullendale transect but less than 1 Vol-% in the Murdoch Transect.

3.3.1- Metamorphic minerals and their replacement mineralogy

It has been shown in the descriptions that some metamorphic minerals (e.g. epidote, chlorite, titanite) are not present in the altered rock but are in the unaltered counterpart, hence that they are not stable during the alteration process. Despite knowing this, in only some transects or some mineral reactions could the specific reaction paths been traced directly. A transect, where this was always possible is the Bullendale Transect (BUL3C/4C), as in here a continuous cross section of the alteration halo was sampled. In all other transects/ alteration halos studied here, the replacement products of many minerals were determined based on textural evidence (.e. grain shape and relative position). A summary of mineral replacement reactions is listed in Table 3.3.2. For the different replacement reactions (Table 3.3.1), balanced equations facilitating the involved phases could be formulated (See next section for details).

Using the molar proportions of those mineral reactions, the volumetric proportions of each component were calculated (Table 3.3.3). Volume of the fluid dissolved phases, such as CO_2 and cations, and H_2O are not considered in the calculations as they are not "locked" in the system. The volumetric calculations are necessary as each mineral has a different density and, for example, 8 mole of Quartz have a much smaller volume than 2 mole of chlorite. Only after this step has been completed it is possible to assess whether replacement was isochemical or not.

Table 3.3.2) Break down products of epidote, chlorite, biotite, titanite, actinolite, muscovite and calcite identified for the different transects.

Transect	Metamorphic mineral	Breakdown mineralogy	Figure
Murdoch Creek	Epidote	Ankerite +/- siderite	Fig. 3.2.2
	Chlorite	Ankerite +/- siderite?	Fig. 3.2.2
	Titanite	Rutile, calcite, quartz +/- ankerite, +/- muscovite	Fig. 3.2.3
	Muscovite	Hydrothermal muscovite	Fig. 3.2.2
Mt Alta	Epidote	? Carbonate	-
	Chlorite	? Carbonate	-
	Biotite	Siderite, calcite, hydro. mus, kaolinite/ illite, rutile	Fig. 3.2.5D &6
	Muscovite	Hydrothermal muscovite	
Bullendale	Epidote	Muscovite & little calcite	Fig. 3.2.11A
	Chlorite	Muscovite & carbonate (mostly ank)	Fig. 3.2.11C&D
	Titanite	Rutile, quartz, carbonate (cc and ank)	Fig. 3.2.11C & 12
	Actinolite	Quartz & ankerite +/- calcite	Fig. 3.2.10
	Calcite	Ankerite	Fig. 3.2.11B
Treble Cone	Epidote	?Inclusion-rich quartz-muscovite-ankerite nodules, turning into cauliflower-like ankerite with intensifying alteration. Contributing to ankeritic lenses in chlorite?	Fig. 3.2.17A & 18A (&B?)
	Chlorite	Cauliflower-like ankerite & some kaolinite. Contributing to ankeritic lenses in chlorite?	Fig. 3.2.17B & 18A&B
	Titanite	Rutile, quartz +/- carbonate	Fig. 3.2.16
	Muscovite	Kaolinite	-
	Calcite	Ankerite	Fig. 3.2.18C
Black Peak	Epidote	Ankerite & Kaolinite?	Fig 3.2.21 & 22
	Chlorite	Quartz, Ankerite/Mg-Siderite & kaolinite	Fig 3.2.22
	Titanite	Rutile, quartz, carbonate (ankerite)	Fig. 3.2.21&22A
	Muscovite	Kaolinite	-
	Calcite	Ankerite (only at grain rims)	-

In many of the replacement reactions carbonate is part of the replacement assemblage, and the carbonate species (calcite-dolomite-ankerite-siderite) change across each transect and in section 3.3.2 discussing each mineral breakdown reaction, different formulas have been provided accounting for the different carbonate species forming. However, everything that is related to this systematic change in carbonate species, including element mobility, will be discussed in section 3.3.3.

Overall, the mineralogical changes in the alteration halos studied here are very similar to those found in orogenic gold deposits (e.g. Craw et al., 2009; McCuaig & Kerrich, 1998; MacKenzie et al., 2007; Phillips & Powell, 2010; White et al., 2003). These are the minerals that are unstable during alteration and the minerals forming, including the abundance of pyrite mineralisation. I will discuss the similarity and dissimilarity between gold-bearing and gold-barren alteration halos in the chapter 4, after it has been established how large chemical changes in the different alteration halos are.

Table 3.3.3) A: List of mineral reactions and the volumetric differences between reactants and products. **B:** Total volume of the components involved in the reactions listed in A.

A:	Reaction (ideal)	Reactants (A^3)	Products (A^3)	Volume in- or decrease	How much? (A^3)
V1	Metam.mus -> kao	467.9	490.9	Increase	23.0
V2	3Bt +CO2 -> 9Sid +1Mus+ 6 Qtz + H2O	747.3	897.1	Increase	149.8
V3	1 Act + 7CO2 +3Cc(aq)= 8Qtz + 5Ank +H2O	639.5	863.0	Increase	223.5
V4.b	3 Chl + 15CO2+7.5 Ca2+= 7.5 Ank + 2 Mus+3Qtz+9H2O	1047.8	1423.6	Increase	375.8
V4.c	3 Chl + 15CO2= 15 Sid + 2 Mus+3Qtz+9H2O	1047.8	1309.6	Increase	261.8
V4.e	1 Chl + 5CO2= 5Sid +1 Kao + 1Qtz	349.3	444.2	Increase	94.9
V4.d	1 Chl + 5CO2 + 5 Ca(aq)= 2.5 Ank +1 Kao + Qtz	349.3	482.2	Increase	132.9
V5.a	3Ep + CO2 +K= 2.5 Mus + 6 Cc +1.5Qtz	701.1	1009.3	Increase	308.2
V5.c	2 Ep + 8CO2+Mg/Fe -> 2.5Kao + 4 Ank	467.4	858.5	Increase	391.1
V6	2Cc +CO2 = Ank	122.7	112.4	Decrease	10.3
V7	1Tit + CO2=1Cc + 1Rut + 1Qtz	92.5	130.2	Increase	37.7

B:	Cc	Ank	Sid	Chl	Act	Qtz	Ep	Bt	Mus	Kao	Tit	Rut
V1									467.9	490.9		
V2			437.3			225.9		747.3	233.9			
V3	184.0	561.8			455.5	301.2						
V4.b		842.8		1047.8		112.9			467.9			
V4.c			728.8	1047.8		112.9			467.9			
V4.e			242.9	349.3		37.6				163.6		
V4.d		280.9		349.3		37.6				163.6		
V5.a	368.0					56.5	701.1		584.9			
V5.c		449.5					467.4			409.1		
V6	122.7	112.4										
V7	61.3					37.6					92.5	31.2

3.3.1.1: Metamorphic muscovite

The metamorphic muscovite found in the rocks sampled here is a solid solution of celadonite and pure muscovite. In the greyschist samples from **Murdoch Creek Transect** (BUL2A-C) this muscovite is replaced by hydrothermal muscovite (Fig. 3.2.3, Rea 1.a) which has also been found by MacKenzie et al. (2007). In the **Mt Alta Transect** metamorphic muscovite has also been partly replaced by hydrothermal muscovite. In the transects from study area 3 (Treble Cone/ Black Peak Transect) there

are indications that metamorphic muscovite is unstable (i.e. resorption and cutting of muscovite grain) and that it has been replaced by kaolinite (i.e. increase of kaolinite content in rock). This reaction can be formulates as in Rea 1.b.

Metamorphic muscovite -> hydrothermal muscovite [Rea. 1.a]

$KFe_{0.2}Mg_{0.2}Al_2Si_{3.3}O_{10}(OH)_2 + 0.2\ Al^{3+} + 0.3HCO_3^- \rightarrow KFe_{0.05}Mg_{0.05}Al_{2.2}Si_{3.3}O(OH)_2 + 0.15\ FeMg(CO_3)_2 + 0.3H^+$

Pure muscovite component in metamorphic muscovite-> Kaolinite

$2KAl_3Si_3O_{10}(OH)_2 + 3H_2O + 2H^+ \rightarrow 3Al_2Si_2O_5(OH)_4 + 2K^+$ [Rea. 1.b]

3.3.1.2: Biotite

As biotite is not present in the altered rock but is abundant in the unaltered rock in the **Mt Alta Transect,** it has been concluded that biotite is also an unstable phase during the hydrothermal alteration. The biotite is most likely broken down to the muscovite-carbonate-rutile aggregates depicted in Fig. 3.2.5 D & 6. There are several aspects supporting this hypothesis; the heterogeneous composition of the white mica (Fig. 3.2.6) supports that it is an alteration-related phase. This is further supported by its different habit and inhomogeneous composition compared to metamorphic muscovite (compare Fig. 3.2.6 with muscovite in 3.2.5 A-C). The probably most conclusive indicators that the carbonate-muscovite-rutile mineral aggregates are indeed the result of biotite breakdown are the small rutile grains in the white mica grains. These follow the mica's cleavage planes, indicating they are exsolution phases. Biotite in the unaltered rock has ca. 0.6wgt% Ti, which is more than 5 higher than in metamorphic and hydrothermal muscovite and carbonate (Refer to Appendix D & F; also Dahl, 1969; Douche, 1993, Guidotti et al., 1977). Hence, the Ti needs to be accommodated in another mineral after biotite's breakdown. In this case it is rutile as neither muscovite nor carbonate is capable of accommodating (all) the Ti. A similar biotite breakdown reaction and in a similar setting has been described by Schwartz (1958) and the reaction can be written as

Biotite -> magnesian siderite + hydrothermal muscovite. [Rea. 2.a]

$3\ K(Mg,Fe)_3AlSi_3O_{10}(OH)_2 + 9CO_2 + 2H^+ \rightarrow 9\ (Mg,Fe)(CO_3) + KAl_3Si_3O_{10}(OH)_2 + 2K^+ + 6SiO_2 + 2H_2O$

TiO_2 in biotite -> TiO_2 (Rutile) [Rea. 2.b]

The zoning of the hydrothermal mica depicted in Fig. 3.2.6 shows that the chemical components from biotite were differently mobile. The zoning is likely the result of active leaching of K, and Mg, Fe, Si and an associated passive enrichment of Al. The increase of Al towards the carbonate corresponds with the decrease in K, hence decrease of muscovite but increase of kaolinite/ illite content in the hydrothermal muscovite. The Mg and Fe from the biotite are transported until they concentrated enough to form magnesian siderite. Ti from the biotite was entirely immobile, forming the rutile needles.

As can be seen in above equations 2.a & 2.b, the occurrence of magnesian siderite in association with biotite breakdown is expected for an isochemical break down reaction, but calcite is not. This shows that Ca was added to the biotite replacement site. Based on the fact that the siderite occurs next to the hydrothermal mica and that ankerite is very rare here, it is suggested that the initial CO_2-bearing fluid was poor in Ca and the carbonate received its divalent cations from the biotite. During a later stage, the fluid's Ca/CO_2 ratio would have had to increase enough to form the calcite

(based on Rosenberg & Holland, 1964; White et al., 2003; Davies et al., 1990). This possibly happened after biotite breakdown was complete, as otherwise the Mg and Fe present should allow for ankerite to be stable rather than calcite. The availability of Ca may be achieved due to the breakdown of a Ca-bearing phase, such as epidote, or it could be derived from an external source.

3.3.1.3: Actinolite

Actinolite breakdown has only been observed in the greenschist from Bullendale, i.e. **Bullendale Transect**, where initiating actinolite breakdown involves the formation of ankerite and quartz (Fig. 3.2.10). Discounting minor components of the amphibole (e.g. Al or Na) the actinolite breakdown reaction can be written as:

Actinolite -> quartz + ankerite **[Rea. 3]**

$Ca_2(Mg,Fe)_5Si_8O_{22}(OH)_2 + 7CO_2 + 3CaCO_{3\,(aq)} \rightarrow 8SiO_2 + 5Ca(Mg,Fe)(CO_3)_2 + H_2O$

During the initial and intermediate stages of alteration, replacement of actinolite always follows the same basic pattern; remnant actinolite is surrounded by a grainy rim mostly made of quartz, which itself surrounded by ankerite. In accordance with the values in Table. 3.3.3 in many actinolite replacements there is volumetrically slightly more quartz than carbonate. The independence of the mineral in contact to the original actinolite suggests that the texture of the actinolite-replacing quartz and carbonate rims (Fig. 3.2.10) forms due to the breakdown of the amphibole alone and has no major metal input from the immediately adjacent minerals. At more intense degrees of alteration the outlines of old actinolite cannot be recognised anymore and it is proposed that breakdown products of actinolite and chlorite intermingle.

The rim texture around the remnant actinolite suggests strongly that the silica of the actinolite was not transported as far as the Mg, Fe, and Ca. The comparatively little mobility of the quartz may be explained by considering the speciation of SiO_2 in a hydrous fluids. Dissolved silica forms $H_4SiO_4*2H_2O$ molecules (Walther & Orville, 1983). By adding CO_2 to this fluid, the activity of H_2O is reduced and, everything else being equal, should reduce the amount of silica soluble in the fluid. Hence, quartz precipitates predominantly in the old actinolite site. The Ca, Fe, Mg as possible carbonate formers, on the other, are mobilised slightly further and are then precipitated. Reasons for the carbonate precipitation could be pressure drop, pH increase or temperature increase. Pressure drop would be associated with the formation of a cavity due to the dissolution of the actinolite. A local pH increase seems unlikely seeing that the fluid contains abundant CO_2. Temperature differences can occur especially at lower degrees of alteration, as the fluid is hotter than the surrounding rock (see chapter 6 for details). Hence, the areas with much fluid (grain boundaries) would be (slightly) hotter than areas within original metamorphic minerals.

In the cases where actinolite has been pseudomorphically replaced by calcite, but still has the alteration rim of quartz and ankerite (Fig. 3.2.10C), Si, Mg and Fe from the actinolite need to leave the system locally. At first this seems to be "at odds" with above explanation. However, it could be attributed to a different CO_2 and Ca content in the fluid at different stages during alteration. It is suggested that the ankerite-quartz rim formed during a high CO_2 content in the fluid and a high CO_2/Ca ratio, while the calcite formed from a fluid pulse, which had a lower CO_2/CaO ratio and a lower CO_2 content. The lower CO_2/Ca ratio should stabilise calcite rather than ankerite (based on Davies et al., 1990; White et al., 2003; Rosenberg & Holland, 1964), while at the same time quartz would be more soluble in the less CO_2-rich fluid (Walther & Orville, 1983).

3.3.1.4: Chlorite

Positions occupied by chlorite in the unaltered sample of the greyschist in the **Murdoch Creek Transect** are occupied by Mg-siderite in the altered rock (Fig. 3.2.2 A&B), suggesting that the carbonate may be the breakdown product of chlorite. The breakdown reaction can be formulated as:

Chlorite -> Mg- Siderite [Rea 4.a]

$(Mg,Fe)_5Al_2Si_3O_{10}(OH)_8 + 5\ CO_2 \rightarrow 5\ (Mg,Fe)CO_3 + Al_2Si_2O_5(OH)_{4\ (aq)} + SiO_{2\ (aq)} + 2H_2O$

In the **Mt. Alta Transect** there are no clear textural indicators what chlorite was replaced by, although it is likely that some of the carbonate formed due to the breakdown of chlorite.

In the **Bullendale transect** (BUL3C/4C), chlorite is replaced by ankerite (and some dolomite or magnesian siderite; Fig. 3.2.11) and muscovite. The reaction follows as:

Chlorite -> Ankerite + muscovite [Rea. 4.b]

$3\ (Mg,Fe)_5Al_2Si_3O_{10}(OH)_8 + 15CO_2 + 2K^+ + 7.5Ca^{2+} \rightarrow 7.5\ Ca(Mg,Fe)(CO_3)_2 + 2KAl_3Si_3O_{10}(OH)_2 + 3SiO_2 + 9\ H_2O + 2H^+ + 7.5\ (Mg,Fe)^{2+}$

Chlorite -> Mg-siderite + muscovite [Rea. 4.c]

$3\ (Mg,Fe)_5Al_2Si_3O_{10}(OH)_8 + 15CO_2 + 2K^+ \rightarrow 15(Mg,Fe)CO_3 + 2KAl_3Si_3O_{10}(OH)_2 + 3SiO_2 + 9\ H_2O + 2H^+$

Regarding volumetric proportions of the replacement minerals of chlorite in the Bullendale greenschist, the volumetric ratio of mica to carbonate should be roughly 1:1.5-1.8. Locally, this seems to be the case. However, especially in intensely altered part of the Bullendale transect, breakdown products of chlorite and actinolite mix and it is not possible to determine which hydrothermal mineral resulted from which breakdown reaction. That this reaction was not isochemical can be deduced from the replacement mineralogy -ankerite and muscovite- and requires at least addition of Ca and K and extraction of Fe and Mg (Rea. 4.b).

In the **Treble Cone and Black Peak Transects**, in the moderately altered samples, chlorite entrains hydrothermally formed lenses/ cauliflower-like shaped carbonate +/- kalonite in Treble Cone and Black Peak Transect (Fig. 3.2. 16, 17 & 21,22) and lenses of quartz +/- chlorite in Black Peak Transect & Fig. 3.2.21, black box). Based on the textural setting it is proposed that at least part of this carbonate is the result of chlorite breakdown. Overall, the chlorite replacement reaction for these samples can be written according to reaction 4.d and 4.e, which are essentially the same as reaction 4.a.

Chlorite -> Calcite+ kaolinite +quartz [Rea. 4.d]

$(Mg,Fe)_5Al_2Si_3O_{10}(OH)_8 + 5\ CO_2 + 5Ca^{2+} \rightarrow Al_2Si_2O_5(OH)_4 + 5\ CaCO_3 + SiO_2 + 2H_2O + 5\ (Fe,Mg)^{2+}$

Chlorite -> Ankerite + kaolinite +quartz [Rea. 4.e]

$(Mg,Fe)_5Al_2Si_3O_{10}(OH)_8 + 5\ CO_2 + 2.5Ca^{2+} \rightarrow Al_2Si_2O_5(OH)_4 + 2.5\ Ca(Mg,Fe)(CO_3)_2 + SiO_2 + 2H_2O + 2.5\ (Fe,Mg)^{2+}$

(**Chlorite -> Mg- Siderite + kaolinite +quartz** [Rea. 4.f]

$Mg,Fe)_5Al_2Si_3O_{10}(OH)_8 + 5\ CO_2 \rightarrow Al_2Si_2O_5(OH)_4 + 5\ (Mg,Fe)CO_3 + SiO_2 + 2H_2O$

Concerning the cauliflower-shaped ankerite, the volume of ankerite is more than 4 times of that of kaolinite (Fig. 3.2.18 A), which shows that some at least the Al, Si and OH are transported out

of and Ca brought into the chlorite replacement site (see epidote-section for more detail on this). With respect to volumetric changes, the ankerite forming lenses in the chlorite pushes the adjacent phyllosilicates' cleavage planes apart (Fig. 3.2.18 B; 22 A). The values in Table 3.3.3 shows that the volume of ankerite is smaller than that of chlorite in cases where the ankerite is produced solely by chlorite breakdown. Hence, in order to form a lens as seen in Fig. 3.2.18B, part of the carbonate's components need to be transported into the site where the mineral growth initiates, making it essentially a vein-like structure. Nonetheless, in addition to the transport into the site of "lensoidal" ankerite, there is also breakdown of chlorite as is suggested by the thinning of the chlorite grain in contact to the carbonate (black arrow in Fig. 3.2.18 B).

3.3.1.5: Epidote

In the greyschist from the **Murdoch Creek Transect**, the ankeritic grains depicted in Fig. 3.2.2 B are interpreted to be pseudomorph replacements of epidote. This conclusion is based on the fact that epidote with similar grain shape and size occurs in the unaltered rock of this transect and that this epidote also occupies the same structural position as the ankerite (Fig. 3.2.2 A). In the greyschist from **Mt Alta Transect** there are no clear indicators what epidote has been replaced by.

In Murdoch Creek

Epidote -> Ankerite+/-siderite

Potentially similar to Black Peak Transect (see below)

In the least to unaltered samples of the Bullendale and Treble Cone greenschist, epidote replacement by chlorite and calcitic veins has been observed (Fig. 3.2.15 B). A similar texture is not found in any of the altered samples. Replacement of epidote by chlorite has been described in similar settings by McCuaig & Kerrich (1998). However, they postulate the involvement of actinolite for this reaction to take place but actinolite is not present in substantial quantities in the rock from Treble Cone and it may be that the epidote for chlorite replacement reaction was part of a different alteration event. Despite this uncertainty, it can still be determined how the epidote breakdown reaction evolves in the more altered parts of the two transects.

In the greenschist of the **Bullendale Transect**, epidote is ultimately replaced by muscovite and minor amounts of calcite (Fig. 3.2.11A; Rea. 5.a). The volumetric ratio of muscovite to calcite should be about 3:2 ([V5] in Table 3.3.3). The values [V5] show furthermore that the hydrothermal muscovite would occupy about 80% of the original epidote site. With a lower Fe content in epidote this number would even increase to nearly 100% for pure clinozoisite. Hence, in the case here the epidote site is occupied by the compared to calcite less soluble muscovite. Calcite on the other hand is "forced" to stay in solution and precipitate elsewhere.

Epidote -> Muscovite + Calcite $_{(aq)}$ + Quartz$_{(aq)}$ [Rea.5.a]

$3Ca_2Fe_{0.5}Al_{2.5}Si_3O_{12}(OH) + H_2O + 6CO_2 + 2.5K^+ \rightarrow 6CaCO_{3\,(aq)} + 2.5KAl_3Si_3O_{10}(OH)_2 + 1.5\ SiO_{2\,(aq)} + 1.5\ Fe^{3+}_{(aq)} + O^{2-}_{(aq)}$

In the **Treble Cone Transect**, quartz-mica-calcite aggregates appear where epidote used to be (Fig. 3.2.16). Towards the fault, these aggregates become more carbonate-rich (Fig. 3.2.17) and instead of calcite, they contain ankerite as carbonate (Fig. 3.2.18). The break down product of epidote in the

Black Peak Transect is not entirely certain. Comparing the structural position of epidote it may be that epidote is replaced by (some of) of the ankerite in the chloritic layers (compare Fig 3.2.20 and 21&22). It has been mentioned above that some of the ankerite in the chloritic layers in the altered samples of the two transects also comes from chlorite breakdown. Nonetheless, three potential reactions that consume epidote can be formulated for the Treble Cone, Black Peak (and Murdoch Creek) Transect :

<u>In Treble Cone Transect</u>

Epidote -> Quartz + muscovite + calcite-> Ankerite [Rea. 5.b]

$3Ca_2Fe_{0.5}Al_{2.5}Si_3O_{12}(OH) + H_2O + 6CO_2 + 2.5K^+ \rightarrow 6CaCO_3 + 2.5KAl_3Si_3O_{10}(OH)_2 + 1.5\ SiO_2 + 1.5\ Fe^{3+}{}_{(aq)} + O^{2-}{}_{(aq)}$

$CaCO_3 + CO_2 + H_2O + (Fe, Mg)^{2+}{}_{(aq)} + \rightarrow Ca(Mg,Fe)(CO_3)_2 + 2H^+$

$KAl_3Si_3O_{10}(OH)_2 + SiO_2 \rightarrow 3Al^{3+}{}_{(\text{into kaolinite})} + 4SiO_{2\,(aq)} + K^+{}_{(aq)} + 2OH^- + 4O^{2-}$

Epidote -> Quartz + kaolinite + calcite-> Ankerite [Rea.5.c]

$2Ca_2Fe_{0.5}Al_{2.5}Si_3O_{12}(OH) + 4\ H_2O + 4CO_2 \rightarrow 4CaCO_3 + 2.5Al_2Si_2O_5(OH)_4 + SiO_2 + 0.5\ Fe_2O_3$

$CaCO_3 + CO_2 + H_2O + (Fe, Mg)^{2+}{}_{(aq)} + \rightarrow Ca(Mg,Fe)(CO_3)_2 + 2H^+$

<u>In Murdoch Creek and Black Peak Transect</u>

Epidote -> Ankerite+/-siderite

Potentially similar to Treble Cone transects (see below)

Epidote -> Quartz + kaolinite + calcite-> Ankerite [Rea.5.c]

$2Ca_2Fe_{0.5}Al_{2.5}Si_3O_{12}(OH) + 4\ H_2O + 4CO_2 \rightarrow 4CaCO_3 + 2.5Al_2Si_2O_5(OH)_4 + SiO_2 + 0.5\ Fe_2O_3$

$CaCO_3 + CO_2 + H_2O + (Fe, Mg)^{2+}{}_{(aq)} + \rightarrow Ca(Mg,Fe)(CO_3)_2 + 2H^+$

Comparing the breakdown reactions, it is striking that different to Bullendale greenschist, epidote in greyschist and greenschist of Treble Cone and Black Peak is ultimately replaced predominantly by ankerite rather than muscovite or kaolinite. This is interesting as there are no apparent reasons why there should be a different replacement mineralogy, as even in the absence of K in the altering fluid, kaolinite could form instead of muscovite [Rea. 5.c]. Hence, Al and Si of the epidote (+/- chlorite at Treble Cone and Black Peak) are mobilised in these transects. This is remarkable insofar as Al is often considered immobile (i.e. Floyd & Winchester 1979).

The mobility of aluminium and breakdown mineralogy may be related to the different metamorphic mineralogy of the rocks prior to alteration. Unlike the greenschist from the Bullendale Transect, all other samples contain abundant metamorphic muscovite, which in those samples is partially replaced by hydrothermal mica and/ or kaolinite. Muscovite contains some F (Deer et al. (2003) and references therein) and during the breakdown of muscovite, this F is released into the fluid. The reason why this F is not bonded with Ca to form fluorite may be because the F content is below fluorite saturation or more likely F^- is itself bonded with OH^-, in accordance with the models of Tagirov & Shott (2001). Together with OH^-, F^- can form complexes with the Al which increases the solubility of Al (Tagirov & Shott, 2001). As this Al-F-OH complex formation should happen at an around neutral pH, it would allow that carbonate can precipitate, while the Al-complexes are mobile. Local mobility of Al during replacement of anorthite during weathering has also been found by Wang et al. (1995), though they did not explain why. Similar to the conclusions drawn here, Wang et al. also point out that element considered immobile on macroscopic scale can be mobile on a small scale.

3.3.1.6: Calcite in leucocratic layers

Despite advanced alteration, calcite in leucocratic layers only shows signs of replacement in close proximity of the altering feature, such as in BUL3C and TP7A (Fig. 3.2.11B; compare 17D and 18C&D). The replacement of calcite by ankerite can be formulated as:

Calcite-> Ankerite **[Rea. 6]**

$2CaCO_3 + (Fe,Mg)^{2+}_{aq} \rightarrow Ca(Mg,Fe)(CO_3)_2 + Ca^{2+}_{(aq)}$

In contrast to the carbonate in the leucocratic layers, for carbonate in the chloritic layers the transition from calcite to ankerite happens at a greater distance to the altering feature, hence lower intensities of alteration (i.e. Fig. 3.2.17). Resultant to this is that calcite and ankerite can occur in the same rock. The relative stability of calcite can be attributed to several factors. As mentioned earlier, fluid flow takes place along cleavage planes, grain boundaries and cracks. As calcite grains in the leucocratic layers are bigger than mineral grains in the phyllosilicate-rich layers, element transport will be higher in the latter. Following, replacement will be faster in the phyllosilicate-rich layers and the carbonate there will attain chemical equilibrium quicker with the fluid. Additionally, there is a locally different Ca/(Mg+Fe) ratio within the rock; in the phyllosilicate-rich layers this would be lower than in the leucocratic layers due to Fe and Mg coming from chlorite, epidote +/- muscovite. Assuming the CO_2 content is similar throughout (or slightly higher in the leucocratic layers due to the presence of metamorphic calcite), calcite would be the stable carbonate to form in the leucocratic layers while it would be ankerite in the other layer type (Davies et al., 1990; White et al., 2003; Rosenberg & Holland, 1964). Hence, even when re-crystallisation of the metamorphic carbonate takes place the re-precipitating carbonate can be calcite, as is indeed the case in TP7B (Fig. 3.2.17 C& D).

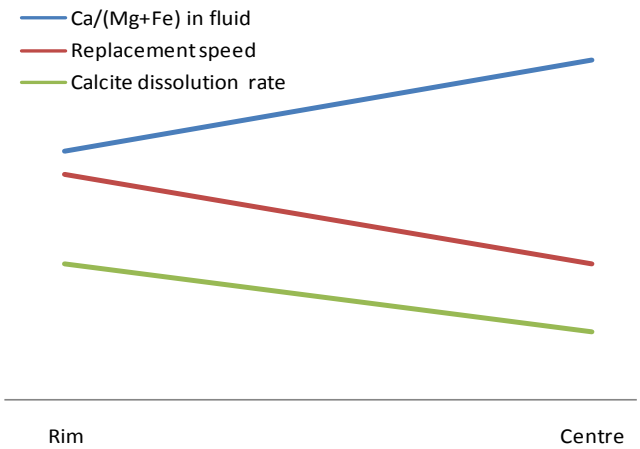

Fig 3.3.1) Conceptual model of the course of some important parameters with ongoing calcite replacement by ankerite. The replacement starts at the rim and work into the centre of the old calcite grain.

Where metamorphic calcite had begun to be replaced by ankerite, two distinct textures are recognised. At the original grain's rim, the carbonate is a fine grained, porous ankeritic carbonate (Fig. 3.2.17D). In the centre of the original grain, the carbonate is also ankeritic but with a blocky, sometimes oscillatory zoning (Fig. 3.2.11 & 17C&D).

Similar grainy textures as at the grain's rim have been described in replacement of calcite by dolomite (Jonas et al., 2015), aragonite by calcite (Perdikouri et al., 2013) feldspar for feldspar (Walker et al., 1995) or andalusite for muscovite (Ferry, 2000). In contrast to this stand many other mineral replacements where the crystallographic lattice is continuous across the mineral interface (i.e. Fein et al., 1994; Raufaste et al., 2011) and also the replacement of the calcite in the centre of the carbonate grain here (based on thin section microscopy).

The different replacement textures (grainy vs. blocky zoning) may form as a result of differing fluid vs. dissolved metals ratio, chemical gradient and diffusion rate/ flow velocity through the already replaced mineral (similar to Jonas et al., 2015): the grainy ankerite forms at an early stage of alteration

and along grain boundaries. Hence, the fluid driving the alteration is abundant and contains a relatively high concentration of Mg and Fe. With ongoing replacement and movement of the reaction front into the replaced grain, the limited diffusion rate of the fluid and dissolved Mg and Fe through the reaction rim and the progressive incorporation of Fe and Mg in the newly growing carbonate will cause the fluid at the reaction front to attain progressively a higher Ca/(Fe+Mg) ratio compared to the fluid outside the grain (Fig 3.3.1; Jonas et., 2015). With ongoing replacement, the fluid will additionally have a reduced supply of Fe and Mg as there is only a limited amount of these elements in the rock. As the chemical gradient of solid and fluid becomes smaller in the centre of the calcite, replacement in the centre is slower than for the grainy carbonate at the rim (Jonas et al 2015; Putnis and Mezger 2004) and resultant less calcite is dissolved by the fluid (Fig 3.3.1). The correspondingly slower precipitation rate allows the carbonate to form one crystal rather than many small ones, which is energetically preferable.

A process which may aid the replacement of the calcite by ankerite cannot only be found in the chemical aspects of the system but also physical ones. The replacement of calcite by ankerite results in a decrease of volume (Table 3.3.3; V9). As the interface between calcite and ankerite in the centre of the grain can be continuous (Fig. 3.2. 11B; 18A) this should result in a distortion in the lattice along the mineral boundary and put stress on the interface of the two minerals. This would be in agreement with other studies, where (a) the variation in the crystal lattice orientation (twin planes in Pearce et al., 2013), (b) stress related to crystal lattice distortion, (c) crack formation during mineral replacement reactions (Perdikouri et al., 2013) and (d) stress between minerals induced by mineral growth (Wang et al., 1995) are cited as driving factors for replacement and/ or localisation of the re-crystallisation sites.

3.3.1.7: Titanite

In all samples, titanite breakdown produces rutile whose occurrence is confined to the old outline of the titanite grains (i.e. Fig. 3.2.3 B). This shows that Ti is an immobile element during the alteration, even on micrometer scale. Ideally, the titanite breakdown reaction would further form calcite and quartz [Rea. 2].

Titanite -> Quartz + rutile + calcite [Rea. 7]

$CaTiSiO_5 + CO_2 \rightarrow CaCO_3 + TiO_2 + SiO_2$

In many cases, these two phases have been identified, however in many others only one of the two and/or other minerals, such as muscovite or ankerite, have been identified (i.e. Fig. 3.2.3B arrow). It follows that small scale mobility of Ca and Si can be encountered. The mobility of Si and Ca is in agreement with the mobility of these elements in other mineral breakdown reactions, e.g. that of actinolite. Mobility of titanite-derived components is also in agreement with discrepancy between the volume increase calculated for this reaction (Table 3.3.3) and the lack of textural evidence of such a volume increase.

3.3.1.8: Sulphides and sulphates

In all samples, the sulphide content increases with intensifying alteration. This relationship is generally considered to be the result of bonding of S from H_2S in the fluid with the Fe from chlorite, metamorphic muscovite and/or epidote (see chapter 4; e.g. Craw et al., 2009 and references therin; MacKenzie et al., 2007). The H_2S in the fluid does not only provide the sulphur for the pyrite but can also act as a

reducing agent; the replacement of epidote by carbonate requires that trivalent iron from epidote is reduced to divalent iron. This can be achieved by oxidation of S^- in H_2S according to below formulas.

$$2H_2S_{(aq)} + Fe_2O_{3(in\ ep)} \rightarrow FeS_2 + FeO_{(in\ carb)} + H_2O \quad \textbf{(Evans et al., 2006)}$$

$$H_2S_{(aq)} + 4\ Fe_2O_{3\ (in\ ep)} \rightarrow H_2SO_{4\ (aq)} + 8\ FeO_{(in\ carb)} \quad \textbf{(Evans et al., 2006)}$$

The second equation may explain why the altered rocks not only contain sulphides but at the same time also barite (Fig. 3.218E). The sulphuric acid produced according to the equation can then react with Ba from the rock or in the fluid to form barite.

$$Ba^{2+} + H_2SO_{4\ (aq)} \rightarrow BaSO_4 + 2H^+$$

3.3.2- Relative tolerance of minerals to CO_2 in the fluids

. Above descriptions show that some of the metamorphic minerals are less tolerant to the hydrothermal alteration than others, i.e. titanite vs. chlorite. These relative mineral stabilities are a direct feedback of the tolerance of the mineral for the CO_2 content in the fluid.

The CO_2 content is not the same across the alteration halo and is highest in the centre and smallest at the halo edges. This variation is attributed to a successive reaction of the fluid with the wall rock; at the fluid inlet, the fluid has its highest CO_2 content. With ongoing fluid flow along the fluid conduit, the fluid enters further and further into the rock. As a result to the fluid flowing through the rock, minerals break down generally forming carbonate, which extracts some of the CO_2 from the fluid. As the fluid penetrates further into the rock, further reactions of fluid and rock take place, due to which the frontal part of the flow will become gradually depleted in CO_2 relative to the "fresh" unreacted fluid at the inlet.

From the textures and relationships described in section 3.2, it is concluded that titanite, epidote and actinolite have a lower tolerance for CO_2 in fluid than chlorite. The succession of breakdown of first epidote and actinolite and then chlorite is in agreement with thermodynamic models calculated by White et al. (2003), who investigated the alteration assemblage of a greenschist from the Kalgoorlie gold deposit and which is similar to that from Bullendale. Concerning the stability of titanite, Craw (2002) showed that, everything else being equal, titanite should be able to "tolerate" a higher CO_2 content in the fluid compared to epidote. Such a relationship is found in the Treble Cone and Black Peak samples, where epidote is absent from altered rock while some titanite may remain.

Despite uncertainties regarding the age in some cases (chlorite-parallel calcite in Fig. 3.2.9B and 15) and some other exceptional cases (see below), it has been shown that there is overall a systematic succession of hydrothermal carbonate from calcitic at the halo rim to dolomitic to ankeritic to sideritic carbonate in the halo centre (Fig. 3.2.3; 9A; 10 - 12; 16-18; 21-23). These carbonate zones overlap spatially. The succession of calcite - dolomite/ankerite - magnesite/siderite from halo rim towards the centre is a common feature in hydrothermal alteration halos of this kind (i.e. Davies, 1990, Fein et al., 1994, Phillips, 1986; White et al., 2003). Hence, with increasing CO_2 content in the fluid, first calcite then dolomite and then siderite is stabilised. The succession can also be expressed as Ca/CO_2 and Ca/(Mg+Fe+Ca) ratios; at high values of these ratios, calcite is stable and with an decreasing value it is ankerite/ dolomite and then siderite/magnesite (Davies et al., 1990; White, 2003; Rosenberg & Holland 1964).

Concerning single cases outliers, such as the occurrence of calcite in the breakdown of actinolite (Fig. 3.2.10) and which has been explained in section 3.3.1, it is noted that during the history

of fluid-induced alteration the chemistry or temperature of the fluid probably changed episodically. A change in fluid chemistry is also supported by the veins and faults (Fig. 3.2.13), which give evidence for multiple veining events during which the precipitate mineral changed, such as quartz vs. ankerite. With respect to the intersecting zoning/ mineral boundaries displayed in Fig. 3.2.22 it is concluded that, the ankeritic carbonate and the chlorite-cleavage-parallel zoning predates the sideritic carbonate, which grows perpendicular to the cleavage; the sideritic carbonate requires a relatively higher CO2 content (= more progressed and intense degree of alteration) than the ankerite to be stable.

3.3.3- Mineral replacement mechanisms

Pseudomorph mineral replacement can either take place by diffusion or dissolution-precipitation. Of these two processes, replacement by dissolution-precipitation is generally the faster one (Putnis, 2009 and references therein). To distinguish which of these two took place in the current study, the textures of the replacement minerals give information. The boundaries between original and replacing minerals are sharp. The replacement minerals are more porous than the metamorphic minerals they form from (epidote->muscovite (Fig. 3.2.11A), calcite ->ankerite (Fig. 3.2.18D), actinolite -> quartz (Fig. 3.2.10)) or they form a polycrystalline, randomly oriented replacement product (Fig. 3.2.18D). All these replacement textures are found to be typical for fluid-driven dissolution-precipitation processes (Putnis, 2009). Additionally, none of minerals that have been replaced give evidence of chemical depletion or enrichment at the contact to replacement minerals (based on BSI), which would be indicative for diffusion-driven processes (Putnis, 2002).

Crucial for replacement processes via dissolution-precipitation is the presence of a "carrier fluid". This poses no problem here, as in all cases discussed evidence for abundant fluid flow has been identified, such as oscillatory vein zoning or spatial connection of precipitates to zones of high fluid permeability (i.e. grain boundaries). The porosity in the replacement minerals ensures transport to and from the replacement site (i.e. Jonas et al., 2015; Putnis, 2002). With the fluid-controlled replacement, material was transported to (i.e. CO_2 or K) and from the mineral replacement sites, such as Fe or Ca (see reactions 1-10 below).

Values in Table 3.3.3 show that in most cases the volume of the replacement minerals is larger than that of the mineral they replace. Theoretically, this should stop the replacement early in its tracks, as the replacement mineral should "block" the way for new fluid to the replacement site (i.e. review by Putnis 2002). Concerning this "problem", Ferry (2000) has proposed that in the whole replacement system (solids AND volatiles) the volume of the precursor system is always larger than the replaced one, as the volatiles in their free form have a much larger volume than when they are mineral-bound. However, in the cases here, replacement often involves release of water and hence Ferry's explanation loses its validity. An aspect to consider is that the replacement processes are strongly fluid-controlled, and it is proposed that the relative solubilities of the different replacement minerals play a more important role than total volume changes.

3.4) Conclusions

The study of the hydrothermal alteration in greyschist and greenschist has shown that metamorphic epidote, chlorite and titanite break down in response to the incoming CO_2-bearing fluids, while quartz, zircon, apatite are albite do not. The replacement of the metamorphic minerals took place by dissolution-precipitation and initial mineral replacement is pseudomorph. Hydrothermal minerals commonly forming are carbonate, hydrothermal muscovite, rutile, kaolinite, quartz and pyrite. In all cases the amount of hydrothermal minerals increases with intensifying alteration.

The relative CO_2 tolerance sequence, from least to most tolerant, is epidote < titanite < metamorphic muscovite/ chlorite. Across the alteration halos a systematic change of hydrothermal carbonate species in the phyllosilicate-rich layers is recognised, with calcite at the rim of the halo through to dolomite, ankerite and finally Mg-siderite in the halo's centre, next to the altering feature. This succession is the result of decreasing CO^2/Ca ratios towards the outer edge of the halo. This decrease is the result of the CO_2-bearing fluid percolating through and reacting with the rock, producing carbonate minerals and hence progressively losing CO_2.

Replacement textures and mineralogy are controlled by the relative solubility of hydrothermal minerals, chemical gradients, diffusion- and replacement rates. For example, in the replacement of actinolite, relative solubility differences of quartz and ankerite cause the formation of the distinct quartz-carbonate rims around the remaining actinolite; quartz is less soluble in CO_2-bearing fluid compared to carbonate and hence does not get transported as far by the fluid. An example of replacement textures likely controlled by different replacement rates can be found in the replacement of calcite in leucocratic layers. The grainy ankeritic carbonate at the rim of the old calcite grain would resemble relatively fast replacement rates, while in the centre of the original grains the carbonate would have precipitated at a slower rate due to limited diffusion through the grainy ankerite rim, giving it time to form a single grain with a continuous crystal lattice. An example of replacement textures controlled by differing metal-mobility has been identified in relation to epidote replacement. There appears to be a relationship between the metamorphic muscovite content of the rock prior to the alteration and mobility of the Al from epidote. This Al mobility is interpreted to be the manifestation of the Al having been mobilised in F-OH complexes, with F (and OH) coming from the metamorphic muscovite; muscovite is also an unstable mineral phase during the hydrothermal alteration.

Overall, the relative mineralogical changes in the alteration halos presented in this chapter are similar to halos associated with orogenic gold deposits and I will go further into detail on this in the next chapter.

CHAPTER 4: CHEMICAL CHARACTERISTICS OF GOLD-BARREN ALTERATION HALOS AND HOW THEY COMPARE TO GOLD-ASSOCIATED ONES

It has been shown in the previous chapter that within the metamorphic wall rock various minerals are broken down and replaced in response to the influx of hydrothermal fluids. These mineral reactions are inevitably connected with mobilisation of elements, as has partly already been discussed. In this chapter, focus is put on this element mobility. It will be discussed which major and trace elements are mobile, how far they can travel, if they become enriched or depleted in the rock and which aspects can control their mobility. The magnitude and consistency of chemical change in the altered rock give information on how much out of disequilibrium the fluid was with the rock also giving information where different components may have come from. Another aspect of hydrothermal alteration halos is that the "sink" studied here is at the same time also the source for sinks further along the fluid conduit. Hence the study on the chemistry of alteration halos can not only give information on potentially deposits at the site (e.g. Large et al., 2001; Gemmel, 2007; Christie et al., 2003) but may also give potential information on element enrichments elsewhere.

Throughout this thesis, I focused particularly on the Rare Earth Elements (REE), which comprise the lanthanides (La-Lu) +/-Y. The REE are often used to gain information about different geological processes, such as mineral crystallisation succession and component sources. The reason why elements of this element group can be used for this are their very similar chemical but differing physical properties (Henderson, 2013). The lanthanides have the same electron configuration in their outer orbitals ($5p^6 6s^2$) and only differ in the electron distribution of their d- and f-orbital. Correspondingly, ions of the REE have generally a trivalent charge and the different element behaviour during chemical processes is largely controlled by their physical properties, predominantly ionic size which decreases with increasing atomic number. This causes them to partition differently into minerals/ molecules. Such differences in REE concentrations are best displayed in plots where the concentrations of the REE are plotted against their atomic number. In these plots, due to their varying abundance in nature the REE concentrations are usually normalised against a standard material, such as the primitive mantle or chondrite (Henderson, 2013). The REE plots can have spikes, especially high or low concentrations for certain elements, generally Eu and/ or Ce. The reason for this is that these REE occur not only as trivalent ions but can form either divalent (Eu^{2+}) or quatro-valent (Ce^{4+}) ions. The different ionic charges and radii of those ions compared to their trivalent counterparts causes them to behave differently during chemical reactions (e.g. Bau, 1991), resulting in REE patterns to have above mentioned spikes, or "anomalies".

The REE have been focus of several studies on fluid-induced alteration of rocks (e.g. Hopf, 1993; Wood, 2006; Ordóñez-Calderón et al., 2008). In association with orogenic gold deposits it has been shown that the REE are immobile on a macroscopic scale (Bierlein et al., 1999). This poses the question if this is also the case for the alteration halos here and whether this is also the case on a microscopic (µm-cm) scale. The REE mobility in response to mineralogical changes within rock has been part of various studies (e.g. Bea et al., 1994; Gaspar et al. 2008; Rolland et al., 2003; Spandler et al., 2003). However, to my knowledge there is no comprehensive study of the REE in various minerals in hydrothermal systems similar to those here (alteration caused by CO_2-bearing, ca. 200°C hot, low salinity aqueous fluids). This lack of information will partly be due to the difficulty of obtaining REE concentrations in minerals (see section 4.1 and 4.3) as in most minerals the REE are trace elements (conc. >0.1%) and mineral grains are small (see chapter 4.3 for details).

In order to characterise the chemical changes and address the questions about element mobility, this chapter is divided into two main parts. In the first part, I will discuss chemical changes of the whole rock across the different alteration halos described in chapter 3. In the second part, I will go into detail of chemical composition of metamorphic and hydrothermal minerals in the wall rock. Together with the data already discussed in chapter 3, it is then possible to establish which of the major and trace elements are mobile and if they are mobile on a micro-, milli-, centi- or meter scale.

In the final part of this chapter, the different aspects of the studied alteration halos will be compared and aspects of the fluid chemistry discussed. Furthermore, it will be shown what major differences between the gold-barren and gold-associated alteration halos are.

4.1) Methods

4.1.1-Whole rock chemistry

Of the transects described in the previous chapter (Table. 4.1) the concentrations of 81 elements were measured. Elements determined include major elements, LILE and the REE. In addition to these 81 elements, metals like Cu, Hg, Ag and volatile components such as C and S were quantified for the TP 4 set. The measuring method and full list of analysed elements and rocks have been given in chapter 2 and are given in appendix E.1& E.2. Unless otherwise stated contents of the REE are chondrite normalised.

The closer to the altering feature (veins and/ or faults), the more pronounced and visible the alteration becomes, which is due to an increase of mineral replacement, but also increased veining. During the sample preparation it was attempted to exclude as many veins as possible from the altered rock sample, as the main objective of this part of the study was to investigate the chemical changes of the metamorphic rock. This was largely successful, except for parts of BUL3C (see below).

4.1.2-Mineral trace element composition of minerals

Due to the low concentration of the trace elements (TE), SEM and microprobe are not practical to use for their quantification due too long measuring times or because the element concentrations are below detection limits. Instead, LASER Inductively Coupled Plasma Mass Spectroscopy (LA-ICP-MS) was used to determine the concentration of the trace element in the minerals. The instrument used was the "Nu Instruments -Nu Plasma-HR MC-ICPMS" at the Centre of Trace Element Analysis of Otago University. Drawbacks of this technique are that it is destructive and, due to the several tens of µm wide LASER beam, has also a lot smaller spatial resolution than microprobe and SEM. For these LAICPMS analyses, polished, ca. 50µm thick thin sections were prepared. The locations for analysis were determined by optical means (transmitted and reflected microscopy). The trace element data are obtained by ablating tracks into the mineral of interest using a Resonetics RESOlution M-50-LR excimer 193 nm laser ablation system with a laser repetition rate of 5-10 Hz, and a propagation speed of 5-10µm/s. I chose tracks over holes as tracks don't ablate the mineral as deeply and because the mineralogy can change on a very small scale. Hence, using tracks ensured that (mostly) only the mineral of interest was ablated. The spectrometer measures signals every 0.6 sec. Tracks or the processed sections of tracks had an ideal length, equivalent to 40s ablation time, to have a large point count and correspondingly optimize precision. However, here the tracks or track sections are often shorter due to small grain sizes or contamination of parts of the track by other mineral phases. The shortest track sections are an equivalent of 10 s, which is still 4 seconds longer than required for a reliable analysis. The beam was between 23 and 70µm in diameter. The choice of minimum beam diameter was limited

by the sensitivity of the instrument, the concentration of each element in the analysed mineral and size of the mineral grains. The raw data are standardised against a synthetic glass standard ("NIST610"), which was provided by the National Institute of Standards and Technology. To monitor instrument-related drift, this standard was analysed about every half hour with the same LASER and track parameters as the samples. Raw mass peak count rates were background subtracted, corrected for mass biased drift and converted to concentrations using an offline spreadsheet. The monitor isotope for was Ca-43 (carbonates) and Si-29 (silicates or mineral mixes). Assessing precision of the different mineral analyses cannot be done here as each grain was only analyzed once and because they are chemically generally inhomogeneous. However, in the past the same LA-ICP-MS system has produced data with good precision (1σ deviations $\leqslant$5% for conc. $\geqslant$10ppm, $\leqslant$20% for con: 1–10 ppm and $\leqslant$50% for conc: 0.1–1 ppm; Martin et al., 2013).

Table 4.1) Samples analysed for whole rock composition. Transects are the same as described in chapter 3.

Sample	Subsample of a handspecimen?	Degree of alteration	Major mineralogy	Displayed in
Bullendale Transect				
BUL4Ca	Yes	pervasive	Ab , Qtz, Fe-carb, mus, rut, chl, ap	Fig. 3.2.7 A.2
BUL4Cb	Yes	moderate-advanced	Ab, qtz, ank, mus, tit, rut, chl, ap, act, ep, cc	Fig. 3.2.7 A.2
BUL4Cc	Yes	unaltered-weak	Ab, qtz, tit, rut, chl, ap, act, ep, cc	Fig. 3.2.7 A.2
Bul3c-1	Yes	Pervasive & veined	Ab, qtz, Fe-carb, mus, rut, chl, ap, cc, qtz and ank veinlets	Fig. 3.2.7 A.1
Bul3c-2	Yes	advanced	Ab, qtz, rut, chl, ap, act, ep, Fe-carb, cc	Fig. 3.2.7 A.1
Bul3c-4	Yes	moderate	Ab, qtz, tit, rut, chl, ap, act, ep, Fe-carb, cc	Fig. 3.2.7 A.1
Bul3c-6	Yes	Weak-unaltered	Ab, qtz, tit, rut, chl, ap, act, ep, cc	Fig. 3.2.7 A.1
Bul3c-7	Yes	unaltered	Ab, qtz, tit, rut, chl, ap, act, ep, cc	Fig. 3.2.7 A.1
Black Peak Transect				
TP4A	No	Advanced	Ab, qtz, tit, rut, chl, ap, Fe-carb, mus, kao, cc	Table 3.2.1
TP4B	No	Moderate-advanced	Ab, qtz, tit, rut, chl, ap, Fe-carb, mus, kao, cc	Table 3.2.1
TP4C	No	Moderate	Ab, qtz, rut, tit, rut, chl, ap, cc ep (very little),	Table 3.2.1
TP4D	No	Unaltered	Ab, qtz, tit, chl, ap, ep, mus, cc	Table 3.2.1
TP4E	No	Unaltered	Ab, qtz, tit, chl, ap, ep, mus, cc	Table 3.2.1
TP4F	No	Unaltered	Ab, qtz, tit, chl, ap, ep, mus, cc	Table 3.2.1
Treble Cone Transect				
TP7A	No	Advanced	Ab, qtz, tit, rut, chl, ap, Fe-carb, kao	Fig. 3.2.14
TP7B	No	Moderate-advanced	Ab, qtz, tit, rut, chl, ap, mus, Fe-carb, kao	Fig. 3.2.14
TP7C	No	Moderate	Ab, qtz, tit, rut, chl, ap, mus, carb	Fig. 3.2.14
TP7D	No	Unaltered	Ab, qtz, tit, chl, ap, ep, mus, cc	Fig. 3.2.14
Mt Alta Transect				
AD1C	No	Moderate-advanced	Ab, qtz, rut, ap, mus, Fe-carb, cc	Fig. 3.2.4
AD1C2	No	Unaltered	Ab, qtz, rut, chl, ap, ep, mus, bt, cc	Fig. 3.2.4
Murdoch Creek Transect				
BUL2A	No	Moderate	Ab, qtz, rut, ap, mus, Fe-carb, cc	Fig. 3.2.1
BUL2C	No	Unaltered	Ab, qtz, tit, chl, ap, ep, mus, cc	Fig. 3.2.1

The limited spatial resolution of the LA-ICP-MS often poses a problem when trying to analyse single minerals, as especially alteration-related minerals are often finely inter-grown with each other. In cases the analyses are contaminated by other phases, it is often not possible to give the exact concentrations of elements in the mineral analysed. Nonetheless, the contaminated mineral analyses still give semi-quantitative and good qualitative information about the magnitude of element content and changes during reaction. During processing of the data and selection of analyses, for each mineral group certain contaminants were examined for. Especially Ti (except for micas, rutile and titanite measurements), Zr and P were monitored, in order to keep influence by rutile, titanite, zircon, apatite and monazite (all potentially REE-rich phases) small. Table 4.2 gives an overview of each analysed minerals and potentially contaminating elements examined for.

Contents of the REE are chondrite normalised. I chose chondrite over shale (e.g. PAAS) for normalisation as in the literature most mineral REE contents are given relative to chondrite, hence making comparisons easier.

Table 4.2) Minerals and potential contaminants examined for during processing and choice of LA-ICP-MS analyses.

Mineral	Potential contaminants examined for
Ankerite	Ti, P, Zr, K, Rb, Si
Calcite	Ti, P, Zr, K, Rb, Si, (Fe, Mg from silicates)
Biotite	P, Zr, Ca
Muscovite	P, Zr, Ca
Epidote	Ti, P, Zr, Mg, K
Actinolite	Ti, P, Zr
Titanite	P, Zr
Rutile+ breakdown minerals	P, Zr

Some of the measurements have concentrations below the detection limit (bdl) of the instrument. Values that are recorded as "BDL" are not displayed as 0 but are left blank in the plots. As less ablated material equals an overall smaller intensity signal at the mass spectrometer, "BDL" values are especially common for the last batch of BUL3C measurements as the beam diameter was only 23µm wide Data is listed in appendix F.

4.2) Whole rock chemistry

In this section the major and trace element composition of the samples listed in Table 4.1 will be described and discussed.

4.2.1- Chemical composition of unaltered metamorphic rock

Apart from the mineralogy, green- and greyschist can easily be distinguished by their chemical composition (Fig. 4.2.1). Greenschist has higher contents of Fe_2O_3, CaO, MgO and Ti compared to greyschist, which corresponds to the bigger proportion of chlorite, titanite and epidote +/- actinolite in the greenschist. In unaltered greenschist from the Bullendale Transect, K_2O does not exceed 0.5 wt-%, while unaltered greenschist from the Treble Cone Transect (TP7) contains 0.7 wt-% of K_2O. This reflects its higher content of muscovite compared to the greenschist from Bullendale. The greenschist of the Black Peak Transect (TP4), where muscovite is macroscopically easily recognisable, has K_2O concentrations of around 1 to 1.2 wt-%. The greenschist from the Bullendale and Treble Cone Transect (TP7) are referred to as "mica-poor", while the greenschist of Black Peak Transect (TP4) is referred to as mica-rich. In contrast to the greenschist, greyschist samples have K_2O concentrations between 2 and 3 wt-%. Apart from K, greyschist also contains more silica and sodium than greenschist, due to the greater proportion of quartz-albite-rich vs. phyllosilicate-rich layers. The higher concentration of Rb, Ba and Cs, but lower Sr concentrations in greyschist can be attributed to the higher content of muscovite but smaller abundance of carbonate and epidote. Th and U concentrations in greyschist are about an order of magnitude higher than in the mica-poor greenschist from Bullendale. The

concentrations in mica-rich greenschist (TP4) have intermediate concentrations for Th and U (Fig. 4.2.1). The Th/U ratio is biggest for greyschist and the mica-rich greenschist (Th/U= 3.5-4.2) whereas the greenschist from Bullendale has ratios around 2.7. Th/U ratio in TP7 samples is ca. 0.6. Greenschist have a higher content of Cr and V than greyschist (Fig. 4.2.1). The concentrations of Zr, Ga, Nb, Hf, Dy, Yb, W, Sn and Ta are similar in both rock types and do not show lithology-specific variations (Fig. 4.2.1).

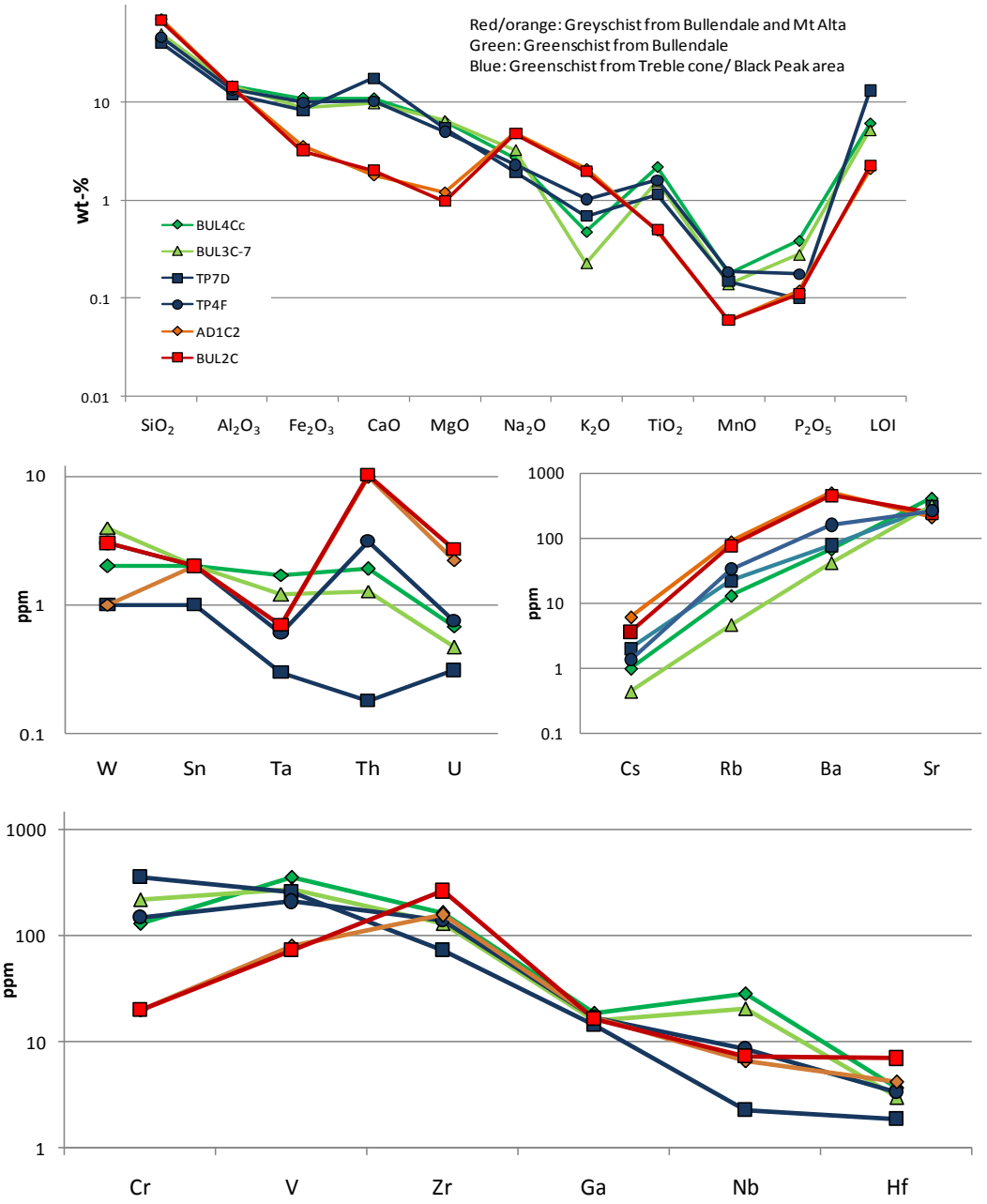

Fig. 4.2.1) Concentrations of the major and trace elements of unaltered green- and greyschist.

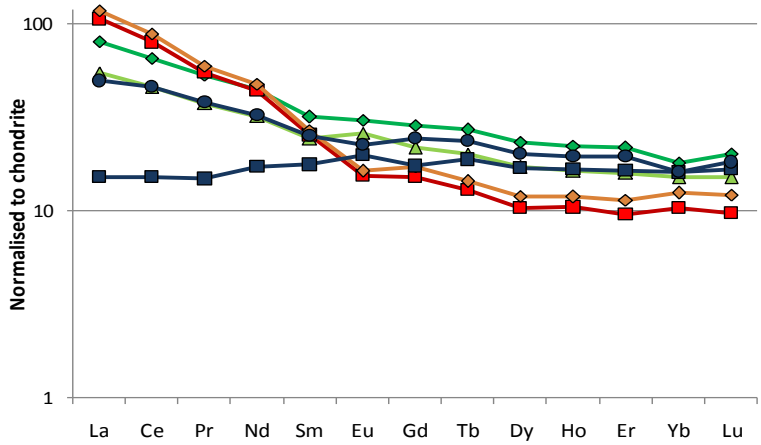

Fig. 4.2.2) Chondrite normalised REE patterns of the unaltered green-and greyschist. Symbology same as in Fig. 4.2.1.

In all cases, the concentrations of the REE have been normalised to chondrite (values from McDonough & Sun, 1995, CN=chondrite noramlised value) and the normalied values will be discussed here. La values in greyschist range between 106 and 138, and of Lu between 9 and 15. In most greenschist samples La chondrite-normalised values are between 43 and 82 and Lu values are around 14 to 21 (Fig. 4.2.2). The Lu values of the TP7 samples are similar to those of the other greenschist samples (16 to 17.5$_{CN}$) but La values are smaller (11 to 15.2$_{CN}$) (Fig. 4.2.2). The REE patterns in all samples can be divided into two sections. The first section includes the elements from La to Eu and the second section those from Gd to Lu. The elements from La to Eu decrease gradually with a relativelly steep gradient La/Eu = 1.7 - 2.8 $_{CN}$ for greenschist (except TP7 samples) and 6.7-8 $_{CN}$ for greyschist. Values of elements beyond Eu are similar for both lithologies (Gd/Lu = 1.2-1.5 $_{CN}$ for green- and greyschist). For the TP 7 (samples Treble Cone Trasnect) there is a similar division but the values for elements between La and Eu increase slightly (La/Eu =0.66 -0.86$_{CN}$). The overall pattern of each subdivision is smooth and a clear anomaly for Ce and Eu has not been found in any of the samples.

4.2.2- Volume changes during hydrothermal alteration

Before comparing the whole rock chemical data of (sub-)samples, it is necessary to consider several aspects that could falsify the conclusions drawn later.

4.2.2.2: Volume and mass changes

Issues to consider regarding the chemical changes are potential mass and volume changes during alteration due to the growth of new minerals. For example, if a rock is silicified and only SiO_2 is added to the rock, the precipitation of the silica in a mineral (e.g. quartz) causes an increase of the rock volume/ mass. The total number of particles of the other elements is unchanged, but their concentration per mass unit decreases. In other words, when comparing 1 kg of original rock to the same mass of altered rock, it would appear that i.e. Fe or Mg have been removed from the rock, although the low concentration is only due to the "dilution" by SiO_2.

In most cases, it is not known what the magnitude of these volume/mass changes was. Methods such as those by Grant (1986) and Gresens (1967) can account for these changes and allow comparisons of the altered and unaltered rock using the concentrations of elements immobile during fluid-induced alteration. Naturally, these kinds of methods are only applicable if the compositions of rocks across a transect prior to alteration were the same.

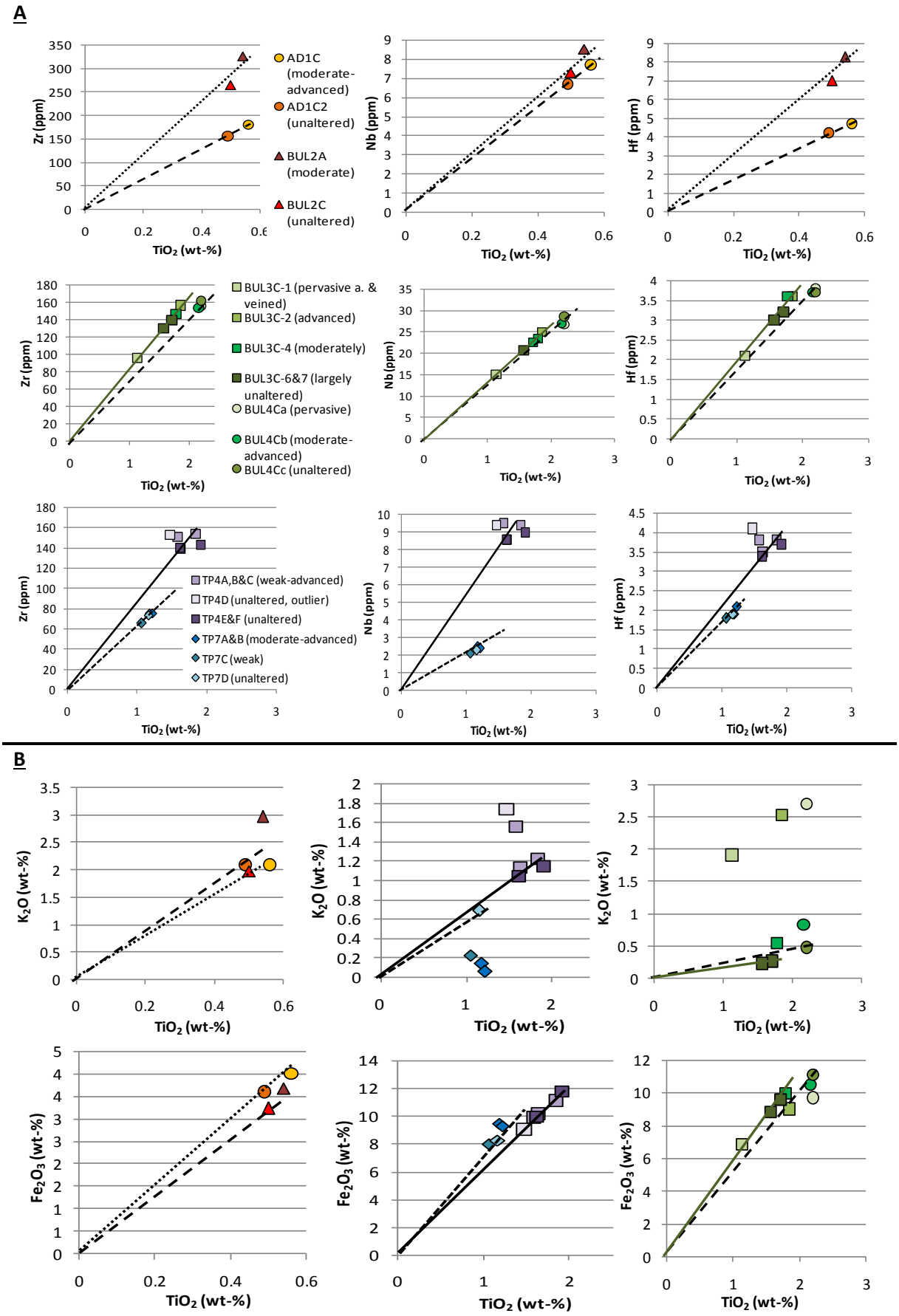

Fig. 4.2.3) A: Plots of various generally immobile elements plotted against TiO_2, which is also generally immobile. The lines show linear trends for each transect. **B:** K_2O vs. Ti_2O and Fe_2O_3 vs. Ti_2O. Note: Each transect needs to be treated individually as we are interested in the chemical changes across each transect.

4.2.2.3: Immobile elements and the mass correction factor

Ti, V, Cr, Nb, REE, Hf, Al are elements often immobile during hydrothermal alteration processes (Floyd & Winchester, 1978; Carmichael, 1969; Ragnarsdottir & Walther, 1985). However, it has been shown that these elements can be mobile under certain conditions (i.e. Jiang et al., 2005; Tagirov & Shott, 2001, Pan & Fleet, 1996; Kerrick, 1988) and this could potentially be the case here, too. Other aspects to consider are sample-specific mineralogical abundances. The Al concentration, for example, strongly depends on the albite content in the rock, which is variable due to the variably thick and frequent leucocratic albite-rich layers. Hence, Al concentrations vary and Al is unsuitable for the calculation of the correction factor, even if it is immobile during the alteration. For these reasons, it is necessary to evaluate which elements are immobile during alteration and were similarly abundant prior to alteration. This can be done using the technique used by Ague et al. (1994) which not only allows for identifying immobile elements but is also an excellent way to show if the rock across a transect was indeed chemically similar before alteration. The excellent linear covariance of Ti, Hf, Zr and Nb in the Treble Cone, Bullendale and Mt Alta Transect and good covariance in the Murdoch Creek and Black Peak transect (Fig. 4.2.3A) supports that these elements were immobile during alteration. It also suggests that the composition of the composition of the rock across the Treble Cone, Bullendale and Mt Alta Transects was very similar prior to alteration and that today's differences in element concentrations in the rocks are the result of mass change due to alteration. In the case of the Murdoch Creek and especially Black Peak Transect, the relatively large scatter shows that the rocks from the transects were slightly dissimilar prior to alteration. This dissimilarity is particularly large for sample TP4D, which has been labelled as an outlier due to this. For a comparison I also plotted examples of potentially mobile elements, here K_2O vs. $TiO_2$and Fe_3O_4 vs. TiO_2 (Fig. 4.2.3B). There is no linear covariance of K and Ti content, supporting that K is highly mobile. Although small, in many transects there is also a deviation from a linear covariance for Fe_3O_4 vs. TiO_2 plots, suggesting some mobility of Fe (Fig. 4.3.B).

Although Ague's method works well for displaying overall changes due to alteration, it is not easy to display gradual changes across transect and see if certain elements have a similar mobility trend. This is especially the case where several samples were taken across an alteration halo. Due to this issue, I used the same principles as Ague et al (1994) but chose a slightly different approach to assessing element mobility; after having established that the concentrations of immobile elements (Ti, Hf, Zr, Nb) were very similar prior to alteration in most samples of a transect (see above), it is possible to calculate the loss and gain of these elements during the alteration process. As an example: If the concentration of Nb is 6 ppm in the unaltered rock, but 3 ppm in the altered rock, the alteration must have caused an increase in rock mass by a factor of 2. This "correction" or "mass correction" factor (in the example here it is 2) can then applied to the values of all measured elements and the calculated concentrations of elements of altered and unaltered samples can directly be compared. It needs to be noted that the concentrations that these calculations do not add up to 100. Instead, the total sum represents the total mass gain (sum>100%) or mass loss (sum<100%) associated with the alteration and hence the calculated % are technically g/(100g of original rock mass). For this reason they are referred to as wt-%* or ppm*.

As already pointed out earlier, in most samples of a transect the intensity of alteration increases gradually towards the altering feature. An exception is the Black Peak transect, where TP4E and F do not show signs of alteration, i.e. mineral break down (see chapter 3). For the calculations, the

sample originally located furthest away from the central alteration halo is taken as the least altered or unaltered one and that closest the most altered one. The calculation of the mass-corrected concentrations follows the following equations:

$$K=(K(TiO_2)+K(Hf)+K(Zr)+K(Nb)):4=\left(\frac{C^*(TiO2)}{C(TiO2)}+\frac{C^*(Hf)}{C(Hf)}+\frac{C^*(Zr)}{C(Zr)}+\frac{C^*(Nb)}{C(Nb)}\right):4$$

$K \bullet C(element) = C_K$ for mass changes "corrected" concentration

K=Correction factor to account for mass changes during alteration

C = concentration of element in altered rock

C* = concentration of element in unaltered rock

C_K = for mass changes "corrected" concentration

The quality of the concentration "correction" is displayed in Fig. 4.2.4 and shows that the corrected values of the immobile elements plot closer to each other than the original uncorrected values. Mass-correction factors lie between 0.8 and 1.03 (Table 4.2.1), hence showing that only minor mass changes took place associated with the alteration. A point to keep in mind is that all of the elements used for the mass correction factor are in minerals predominantly found in the melanocratic layers, which are zircon, titanite and rutile. Hence, strictly speaking this calculation accounts only for mass changes in the melanocratic layers, not the leucocratic ones, which are mostly made of quartz and albite.

Table.4.2.1) Mass-correction factors calculated for the immobile elements (Ti, Hf, Zr, Nb). The average of these values in each sample is applied to all element concentrations measured in that sample.

Sample	Hf*	Zr*	TiO2*	Nb*	K
AD1C	0.89	0.87	0.88	0.87	0.88
AD1C2	1.00	1.00	1.00	1.00	1.00
BUL2A	0.84	0.81	0.93	0.86	0.86
BUL2C	1.00	1.00	1.00	1.00	1.00
BUL3C-1	1.43	1.36	1.39	1.36	1.39
BUL3C-2	0.83	0.83	0.85	0.83	0.84
BUL3C-4	0.83	0.89	0.88	0.88	0.87
BUL3C-6	0.94	0.94	0.92	0.91	0.93
BUL3C-7	1.00	1.00	1.00	1.00	1.00
BUL4Ca	0.97	1.04	1.00	1.07	1.02
BUL4Cb	1.00	1.05	1.02	1.06	1.03
BUL4Cc	1.00	1.00	1.00	1.00	1.00
TP7A	1.00	0.97	0.98	0.92	0.97
TP7B	0.90	0.97	0.95	0.96	0.95
TP7C	1.06	1.11	1.09	1.10	1.09
TP7D	1.00	1.00	1.00	1.00	1.00
TP4A	0.89	0.93	1.03	0.91	0.94
TP4B	0.89	0.91	0.88	0.91	0.90
TP4C	0.97	1.01	0.99	1.00	0.99
TP4D	0.83	0.92	1.10	0.91	0.93
TP4E	0.92	0.98	0.85	0.96	0.92
TP4F	1.00	1.00	1.00	1.00	1.00

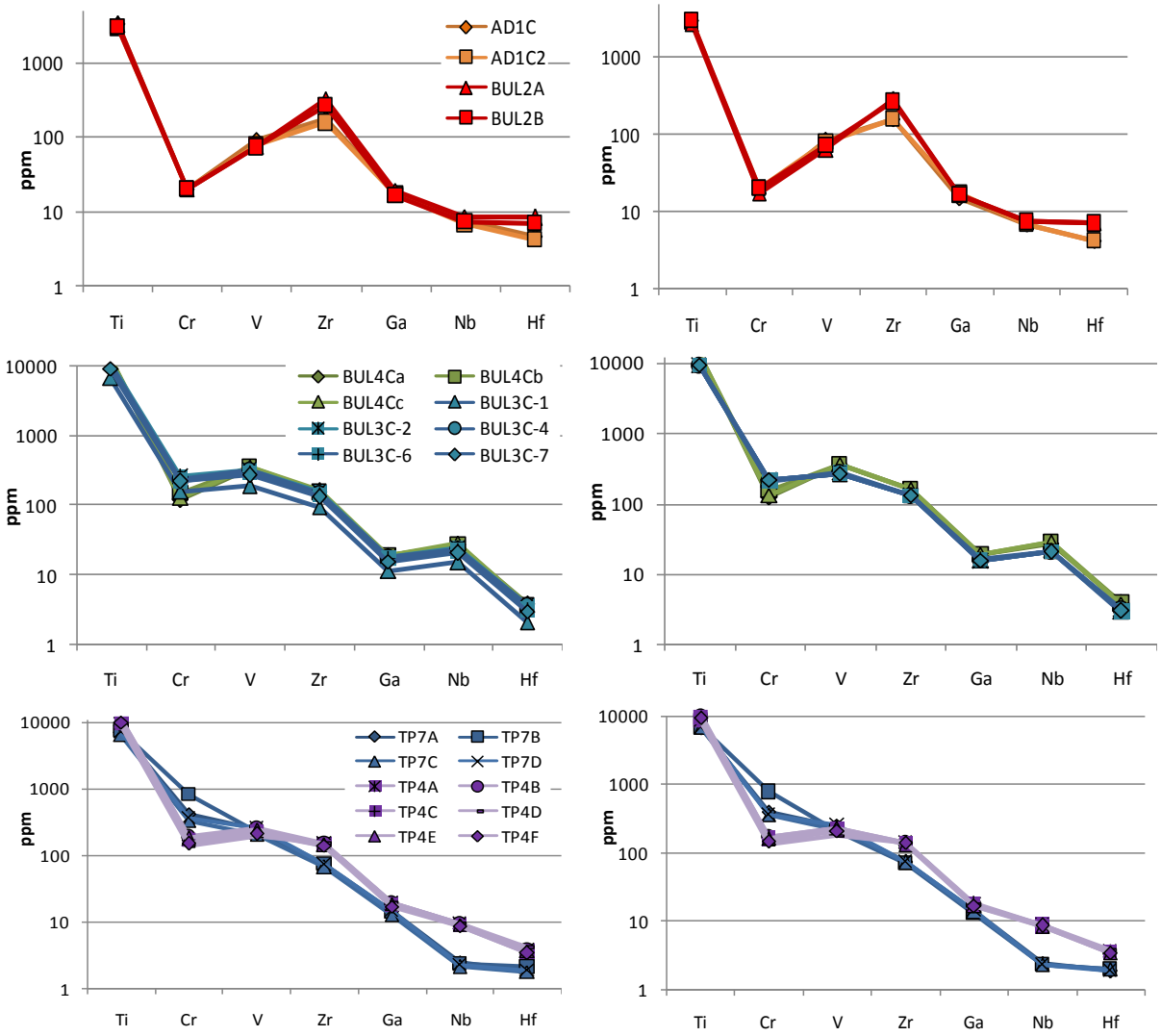

Fig. 4.2.4) Left: original concentration values of some generally immobile elements. **Right:** Mass corrected values of the same elements.

4.2.2.4: Values used for comparison

Except for elements abundant in leucocratic layers (Al, Na, Si), the values of the other elements given are those corrected for mass changes, using mass correction values from Table 4.2.1 and comparisons have been done based on these values, unless otherwise stated. When referring to the absolute change of element contents it generally refers to the difference of the least-/ unaltered and the most altered sample. As the correction values are dependent on which element is chosen as immobile and as they do not account for pre-alteration related differences, values of concentration differences are not absolute but are still a good quantitative guide.

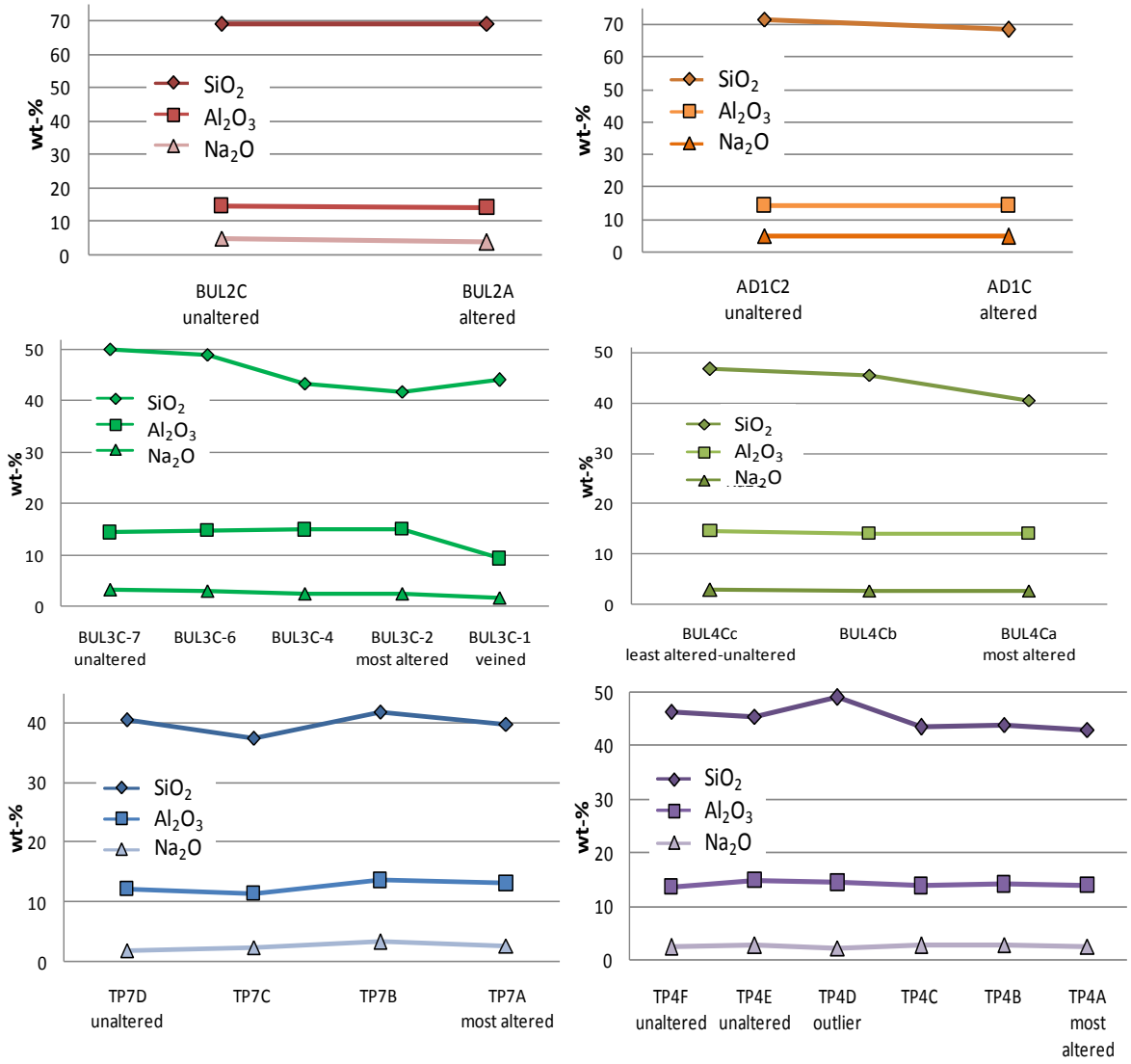

Fig. 4.2.5) Changes of Na, Si and Al concentration across the alteration halos. Using non-mass corrected values.

4.2.2.5: Outliers

When comparing the samples against each other, a few samples "stick out". Outliers are TP4D and the most altered sample of the BUL3C set, BUL3C-1. The differences are either caused by to significantly different mineral assemblages prior to alteration (relatively high content of muscovite in TP4D) or large number of veins in the sample, as in BUL3C-1 (Fig. 3.2.5 A.1). These samples are displayed in the plots, but are not considered when describing the general chemical changes across the alteration halos. Nevertheless, these samples do give insight into other aspects of element behaviour and will be discussed later.

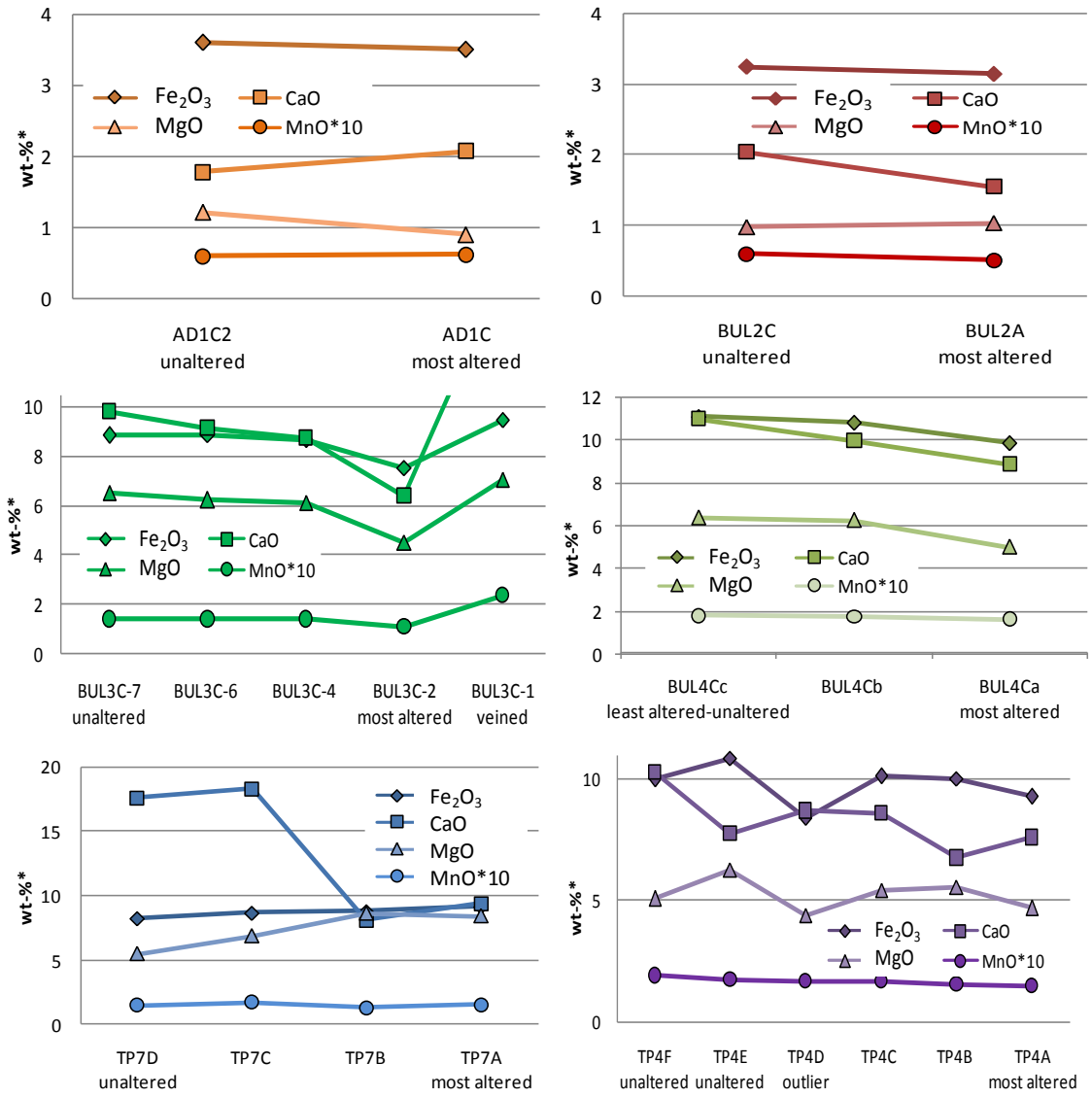

Fig. 4.2.6) Trend of concentrations of CaO, MgO, FeO, and MnO across alteration halos. Concentrations of MnO are multiplied by 10 for easier display. Using mass-corrected values for graphs.

4.2.3-Changes of rock chemistry across the alteration halo

4.2.3.1: Major elements

In all samples, SiO_2 is either relatively depleted or unchanged in the altered rock (Fig. 4.2.5). In greenschist samples from the Treble Cone/ Black Peak area (TP4 and 7), the SiO_2 concentrations drop by 0-3 wt-%*. In the other greenschist sets, the change is about 6 wt-%* for BUL4C and 9 wt-%*for BUL3C. In the greyschist samples, the SiO_2 content remains roughly the same for the set collected at Murdoch Creek (BUL2A,C) or drops by c. 3 wt-%* at Mt Alta (AD1C/1C2). Changes of Al concentrations are less consistent and are also not lithology- or setting-dependent. Values may overall decrease (BUL4C, BUL2A/C), increase (BUL3C, TP7) or remain the same (AD1C/2; TP4). Changes of sodium concentrations overall follow the trend of aluminium, although there may be differences of the trend in some samples of a transect (Fig. 4.2.5).

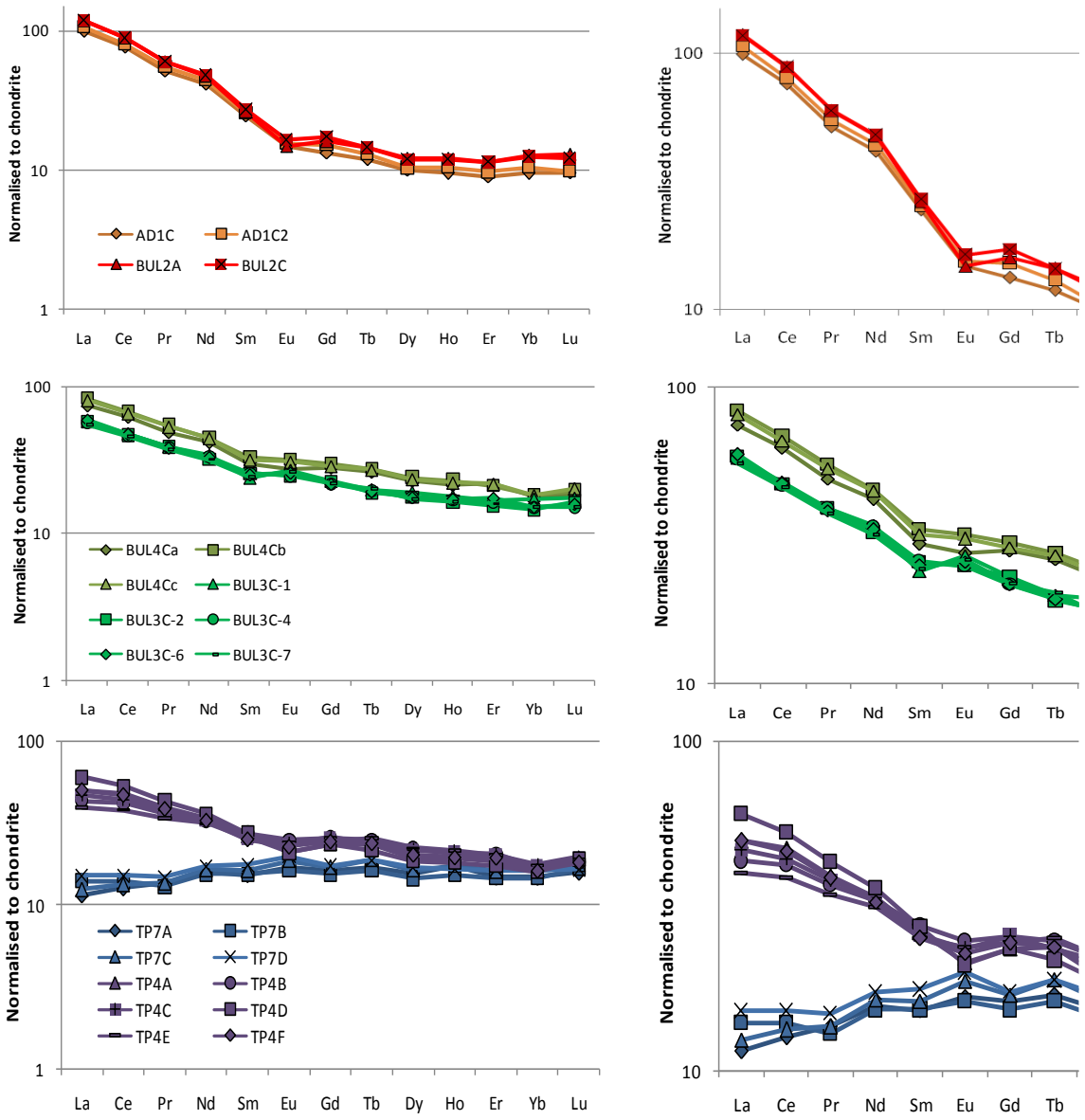

Fig. 4.2.7) REE patterns of samples across the alteration halos. Right close up of La-Tb. Naming the same as in previous figures. All plots use log-scale and values are mass-corrected.

In greenschist samples from Bullendale, the change of MgO, Fe_2O_3, CaO and MnO is consistently negative from unaltered to most altered sample (Fig. 4.2.6). Mass-corrected values of CaO and MnO drop by 2-3.5 wt-%* and 0.02-0.03 wt-%* respectively. Concentrations of MgO decrease by 1.3-2 wt-%*, while those of Fe_2O_3 decrease by about 1.2 wt-*%. A similar trend as in the Bullendale greenschist is observed in TP4 samples, albeit not as consistent. MnO concentrations decrease slightly (ca. 0.03 wt-%*), and Ca concentrations are on average also slightly lower in altered samples (TP4A-C) compared to the unaltered ones (TP4D-F) (Fig. 4.2.6). However, concentrations of MgO and FeO are similar across the alteration halo. In the TP7 set, concentrations of CaO drop by ca. 8%, while concentrations of MnO are similar across the alteration halo. In contrast to the other greenschist samples, in the TP7 set Fe_2O_3 and MgO contents increase gradually towards the centre of the alteration halo (ca. 1 wt-%* and 3 wt-%* respectively) (Fig. 4.2.6). In the greyschist set from Mt Alta, CaO concentrations are slightly higher in the altered sample compared to the unaltered one (c. 0.2 wt-%*; Fig. 4.2.6). MnO contents are the same across the halo, while the altered sample contains less FeO and

MgO than the unaltered sample (Fig. 4.2.6). In the greyschist set from Bullendale, concentrations of CaO, MnO and FeO are lower in the altered sample, while the content of MgO higher. The total concentration changes in both greyschist samples is a lot smaller than of the same elements in the greenschist samples and never exceeds 0.6 wt-%*. This corresponds with greyschist having overall smaller concentrations of these elements. In none of the sample sets do P concentrations change systematically which is in agreement with the stability of apatite, the main P-bearing phase in these rocks (see chapter 3).

4.2.3.2: Rare Earth elements

Rare earth element (REE) concentrations do not change systematically or considerably across the sampled alteration halos (Fig. 4.2.7). In some cases, such as TP4 and BUL4C, the slope of the normalised REE pattern may change slightly but these changes are not systematic.

4.2.3.3: Large ion lithophile elements

The Large Ion Lithophile Elements (LILE), which comprise the heavier alkali (K, Rb and Cs) and earth alkali elements Sr and Ba, show the biggest changes across all studied alteration haloes, in relative percentage (Fig. 4.2.8). In the greenschist from Bullendale (BUL3C&4C), Sr and Ba concentrations increase by ca 2 -3 times (Sr: 500 to 1000 ppm, Ba: c. 60 to 160ppm). The concentration of K_2O is ca 6 to 10 times higher in the most altered samples (K_2O: 2.1-2.8 wt-%*) compared to the unaltered sample parts (K_2O: 0.5-0.6 wt-%*). Rubidium is enriched by a factor of 9-20 (from 4-13 to 102-115ppm) and caesium concentration are 5 to 10 times higher in the most central part of the alteration halos (4.4-4.8 ppm compared to 0.4-0.9 ppm). In the greenschist of Black Peak Transect (TP4), a similar trend is present, though changes are not as prominent and consistent as in the Bullendale greenschist. Sr and Ba concentrations increase by less than 30 wt-%* (Fig. 4.2.8) and those of K and Rb by less than 60% (K_2O: 1 to 1.4 wt-%; Rb: 33 to 50 ppm). Cs concentrations are ca. 2.3 times higher in the most altered sample compared to the least altered one. In the sample set from Treble Cone Transect (TP7A-D), changes of the LILE concentrations are different to the other greenschist samples. Towards the fault causing the alteration, concentrations of Sr and Ba increase by an overall factor of about 4 (Fig. 4.2.8), which is similar to the greenschist samples from Bullendale. However, K and Rb concentrations drop by up to over 90% for K and 85% for Rb (Fig. 4.2.8). Changes of Cs concentration are not as consistent as for Rb and K and show relative enrichment in the least altered sample. Overall, Cs concentrations follow a similar trend as Rb and K (Fig. 4.2.8), indicating overall depletion. In the greyschist transects, changes of the LILE contents do not show nearly as prominently as the greenschist. In the set from Murdoch Creek, there is an increase of K, Rb, and Cs by about 30%, whereas Sr and Ba are depleted. In the greyschist samples collected at Mt Alta, the LILE become depleted or remain roughly the same (Fig. 4.2.8).

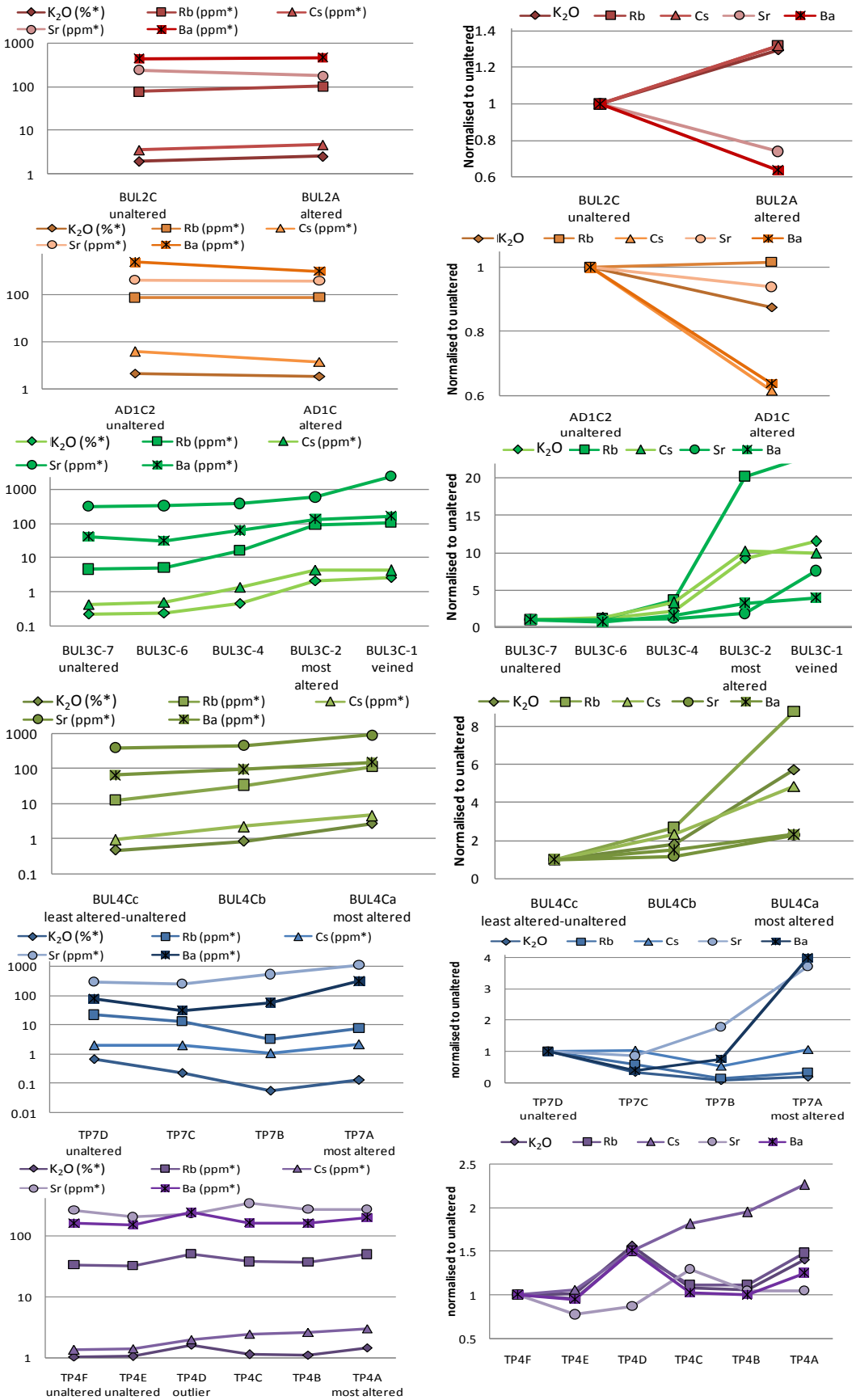

Fig. 4.2.8) Left: Absolute concentrations of LILE across the different transects. Right: Values are normalised against sample taken furthest away from altering feature. Both graph types use mass-corrected concentrations.

4.2.3.4: Chalcophile elements and other metals

Elements discussed in this paragraph are W, Sn, Ta, Th, and U. Across most alteration haloes (Murdoch Creek (BUL2A&C); Mt Alta (AD1C-1C2); Treble Cone (TP7); Black Peak (TP4)), tungsten concentration values change only little or inconsistently (Fig. 4.2.9). In the Bullendale Transect (BUL3C & BUL4C), tungsten concentrations are also in the range of a few ppm in the unaltered and moderately altered rock. However, unlike in the other transects, there is a strong increase of tungsten concentrations in those parts that are within a few centimetre vicinity of the veins in the centre of the alteration halo (Fig. 4.2.9). In sample BUL4C, tungsten concentrations increase from ca. 2 ppm abruptly to 51 ppm. In the most altered part of the BUL3C sample, an increase of W content is also present but which is less abrupt compared to the BUL4C sample. In the strip about 3-1.5 cm away from the thicker central veins (BUL3C-2), the W concentrations increase to 23 ppm from less than the 4 ppm in the parts further away from the central veins (Fig. 4.2.9). Concentrations of Sn, Ta, Th and U do not change systematically across the alteration haloes.

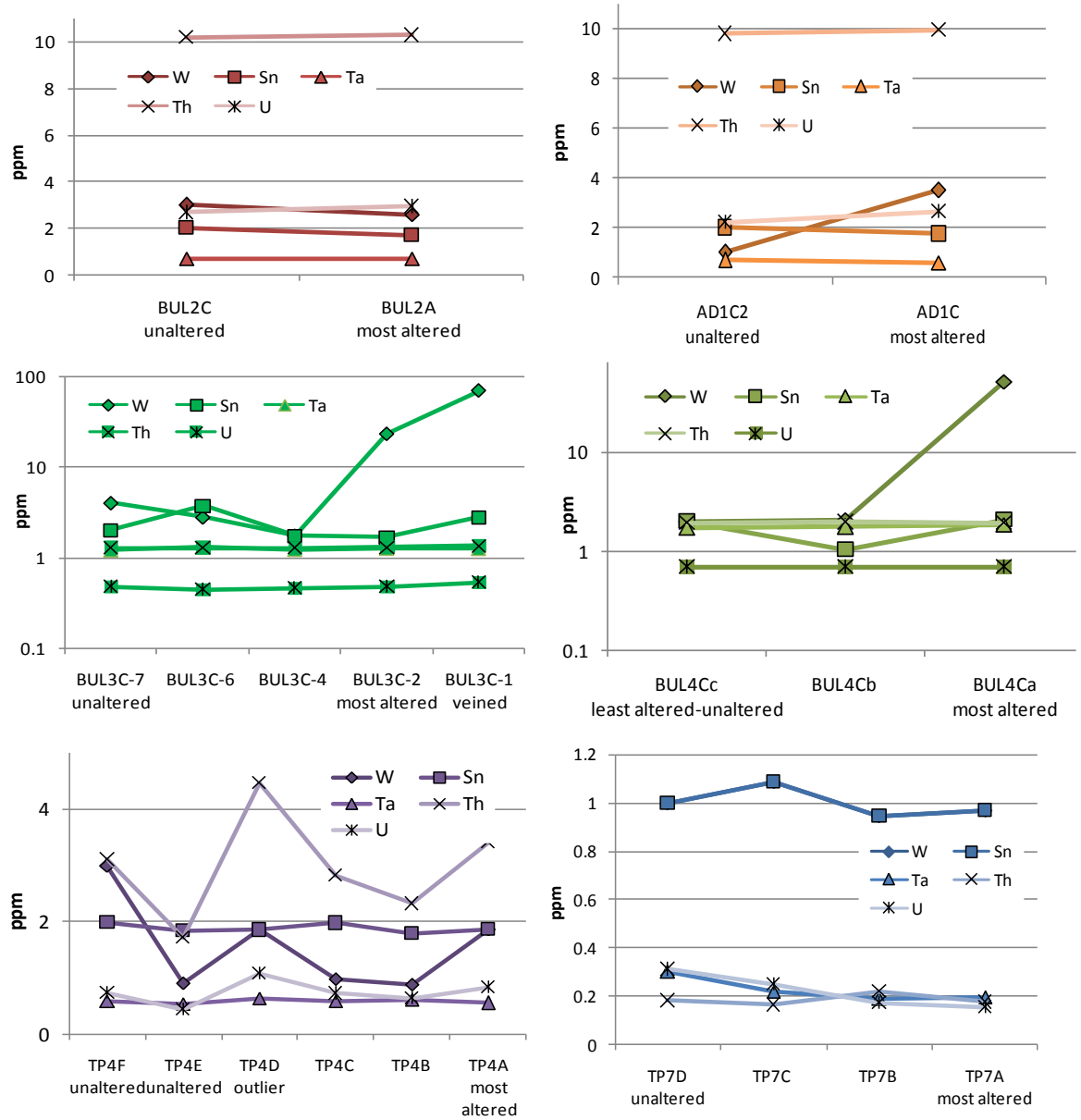

Fig. 4.2.9) Concentrations of W, Ta, Sn, Th, U across the different alteration halos. Using mass-corrected values.

For the Black Peak Transect (TP4A-F), concentrations of chalcophile elements were determined (Fig. 4.2.10). Contents of these elements never exceed 110 ppm. The concentrations of Mo and Ag are below detection limit throughout this set. This is also the case for Cd and Sb in some samples. Across the alteration halo, the concentrations of Bi, Tl, Cd, Co, Cu, Li, Ni, and Pb don't change systematically. Concentrations of Sb and Hg overall increase towards the centre of the alteration halo. Arsenic concentrations also seem to increase slightly towards the centre of the alteration halo. There is an overall slight decrease in Se, Te, Cd, and Zn; however the concentration differences are not very distinct.

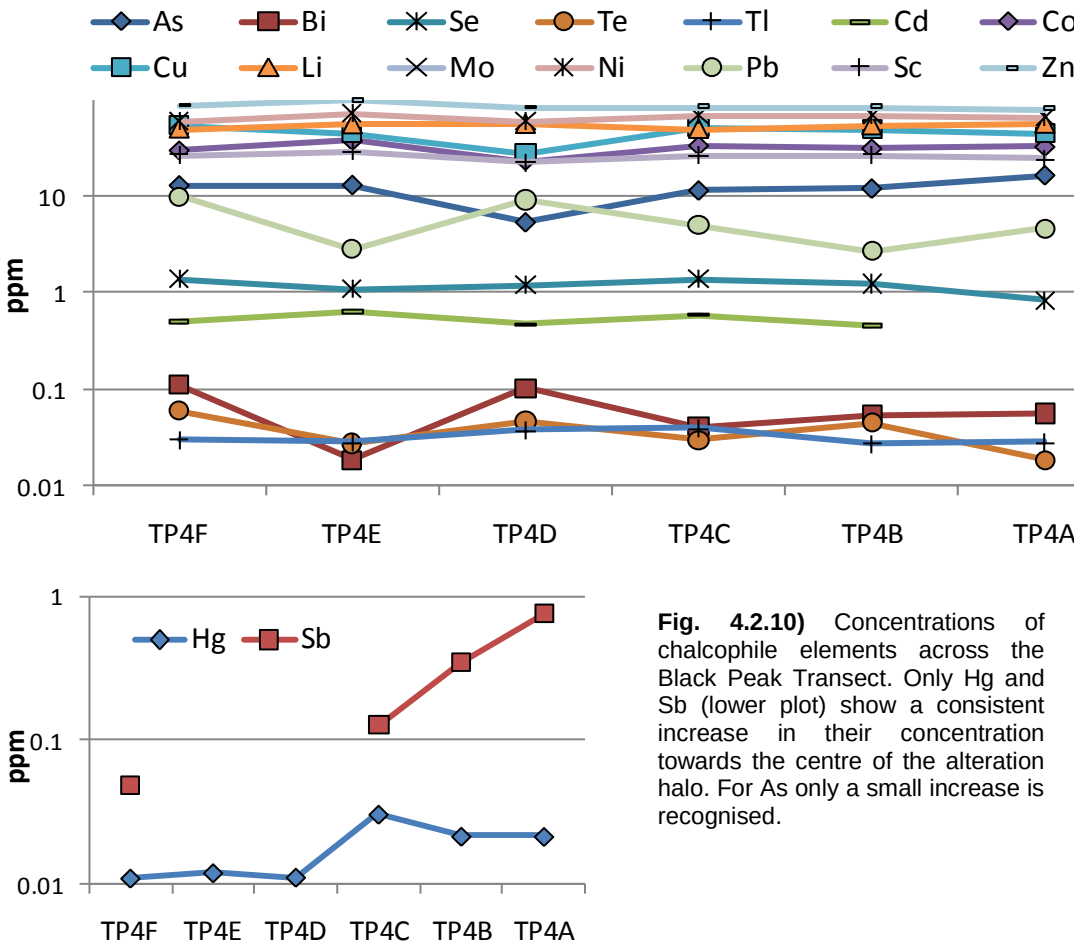

Fig. 4.2.10) Concentrations of chalcophile elements across the Black Peak Transect. Only Hg and Sb (lower plot) show a consistent increase in their concentration towards the centre of the alteration halo. For As only a small increase is recognised.

4.2.3.4: Volatiles

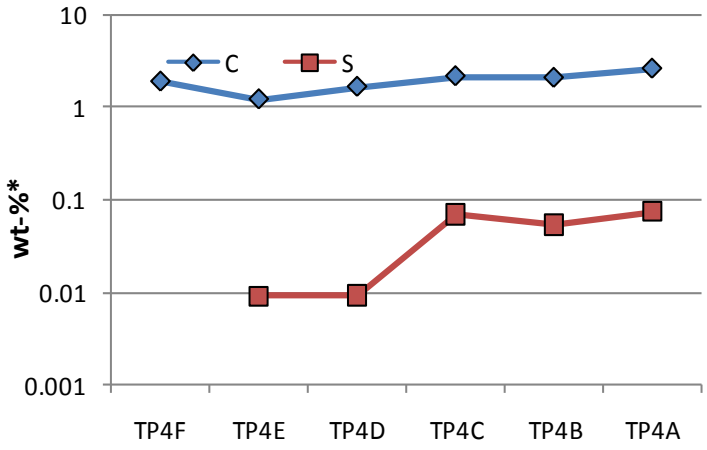

Fig. 4.2.11) Concentrations of C and S across the Black Peak Transect. Mass-corrected values.

All samples contain volatiles, such as water or CO_2, which are to the greatest part bound in the crystal structures of minerals, i.e. in chlorite or calcite. Small volumes of volatiles are in fluid inclusions and other pore spaces. Apart from the Black Peak Transect, in no other sets were the concentrations of C and S or other volatiles measured. However, as a semi-quantitative measure for volatile content the "loss of ignition" (LOI) can be used. To obtain the LOI, a portion of the sample is burned in a furnace at 1000°C. During this process, hydrous, carbon- and sulphur-bearing minerals break down, releasing the bound volatiles, reducing the sample's mass. However, at the same time, iron which occurs as divalent ions in minerals will become oxidised to its trivalent state, which causes a gain in mass of the burned, solid sample (Gain of Ignition=GOI). This gain is 11% per wt-% FeO. Hence, the "LOI" measured this way is actually a combination of mass loss because of evaporation of volatiles and a mass gain due to oxidation of iron. To obtain just the volatile component of the LOI and hence the True Loss of Ignition (=TLOI), the gain of ignition needs to be accounted for. For this, the relative proportion of divalent and trivalent iron in each sample needs to be estimated. In the altered samples, all Fe is divalent, as the only Fe-bearing minerals here are ankerite, Pyrite and remnant chlorite. In the unaltered and little altered rocks some iron is trivalent, as these rocks contain epidote. Correspondingly, the epidote needed to be estimated, which was done by microscopic means (Table 4.2.2). In all transects, the calculated TLOI increases from least to most altered sample (Table. 4.2.2). In the greenschist from Bullendale, the TLOI increases by 6-8%. In the Treble Cone samples, the difference is about 2.5-3%. In both greyschist sets, the TLOI increases by ca. 2% (Table 4.2.2). As mentioned above, for the Black Peak transect (TP4), the contents of C and S have been quantified. The concentrations of C in unaltered samples are about 1.9% which is the reflection of the relatively high amount of metamorphic calcite in these rocks. S contents in unaltered greenschist of this transect are about 0.1 ppm (Fig. 4.2.11). Across the Black Peak Transect, the concentrations of S and C increase towards the altering feature (Fig. 4.2.11). Combining the TLOI of volatiles as calculated in Table 4.2.2 with the C and S content in the samples of the TP4 set, it is possible to calculate the amount of H_2O across the alteration halo (assuming there are no other major volatiles in the samples). The results of these calculations are shown in Table 4.2.2 and shows that overall the H_2O content decreases towards the fault.

Table 4.2.2) Measured Fe content and LOI of all samples, estimated divalent Fe and from these values calculated GOI and resultant TLOI from volatiles. Using mass-corrected values.

Sample	Meas.Fe_2O_3 (wt-%)	Meas. LOI (wt-%)	Fe^{2+} of total Fe	Calc. GOI (wt-%)	Calc. TLOI (wt-%)	LOI-CO2-S=H2O (wt-%)
BUL4Ca	9.88	14.57	1.00	0.99	15.55	
BUL4Cb	10.83	8.88	0.70	0.76	9.64	
BUL4Cc	11.10	6.10	0.60	0.67	6.77	
Bul3c-1	9.48	23.43	1.00	0.95	24.27	
Bul3c-2	7.54	11.39	1.00	0.75	12.15	
Bul3c-4	8.68	7.51	1.00	0.87	8.38	
Bul3c-6	8.88	4.93	0.70	0.62	5.55	
Bul3c-7	8.85	5.22	0.60	0.53	5.75	
TP4A	9.28	11.82	1.00	0.93	12.75	2.05
TP4B	10.03	10.08	1.00	1.00	11.09	2.33
TP4C	10.13	10.69	1.00	1.01	11.71	2.61
TP4D	8.42	8.69	0.70	0.84	9.53	2.55
TP4E	10.89	7.48	0.70	1.09	8.57	3
TP4F	10.00	9.75	0.70	1.00	10.75	2.75
TP7A	9.18	15.40	1.00	0.92	16.32	
TP7B	8.79	12.89	1.00	0.88	13.76	
TP7C	8.67	17.38	1.00	0.87	18.24	
TP7D	8.24	13.34	0.60	0.49	13.83	
AD1C	3.51	3.90	1.00	0.35	4.25	
AD1C2	3.61	2.08	0.50	0.18	2.26	
BUL2A	3.15	3.63	1.00	0.31	3.94	
BUL2C	3.25	2.28	0.50	0.16	2.44	

4.2.4-Discussion

The above comparisons show that chemical changes across the alteration halos can show an overall trend although these trends are often not consistently gradual, especially where the different samples of a transect were originally several decimeters to meters apart (TP4, TP7). These deviations from the overall trend can be attributed to chemical differences of the rocks prior to alteration. Overall, chemical changes across the alteration halos are a combination of various compositions prior to alteration and mobility during fluid flow and alteration and if the magnitude of pre-alteration compositional differences is bigger or in the order of that induced by fluid flow, it is not possible to assess mobility of the components in question.

To assess the potential mobility of Si, Al, and Na, observations made in the previous chapter (chapter 3) need to be used. From these observations, it is known that in the studied samples albite and quartz in leucocratic layers are stable during the alteration and hence do not contribute to the fluid's element load. Using the rock's Na content, it is possible to estimate how much of the rock's Al and Si is bound in albite and following how much is not in the albite (Fig. 4.2.12). The Al not bound in albite will be mostly in the melanocratic layers, while Si will be in both layer types. Concentrations of the "unbound" Al show no systematic trend or big change across the alteration haloes, also after applying the mass correction factors (Fig. 4.2.12). These unsystematic and small differences are most likely the result of mineralogical differences prior to alteration rather than alteration-related element

mobility. Immobility of Al on a large scale (>cm scale) is also in accordance with studies of Carmichael (1969) and Ragnarsdottir & Walther (1985). The concentrations (corrected and uncorrected values) of Si, which is not bound in albite, decreases towards the centre of the alteration halo in all but one case (BUL2A/C) (Fig. 4.2.11). If this decrease was due to thinner leucocratic layers, hence less albite and correspondingly less quartz, albite-unbound Si and total Na concentrations should have a similar trend. This is however not the case (Fig.4.2.12), indicating that some of the Si is actually leached from the rock and partly incorporated in the veins. The overall slight decrease of Si content is also in agreement with data collected by MacKenzie et al (2007). The release of Si from the rock also corresponds with the production of SiO_2 during the breakdown of actinolite and chlorite (See chapter 3.2), which would also (partly) explain why changes in silica content are relatively large and consistent in greenschist-hosted halos, especially in the Bullendale Transect; these rocks contain relative to greyschist much chlorite and the Bullendale greenschist also actinolite.

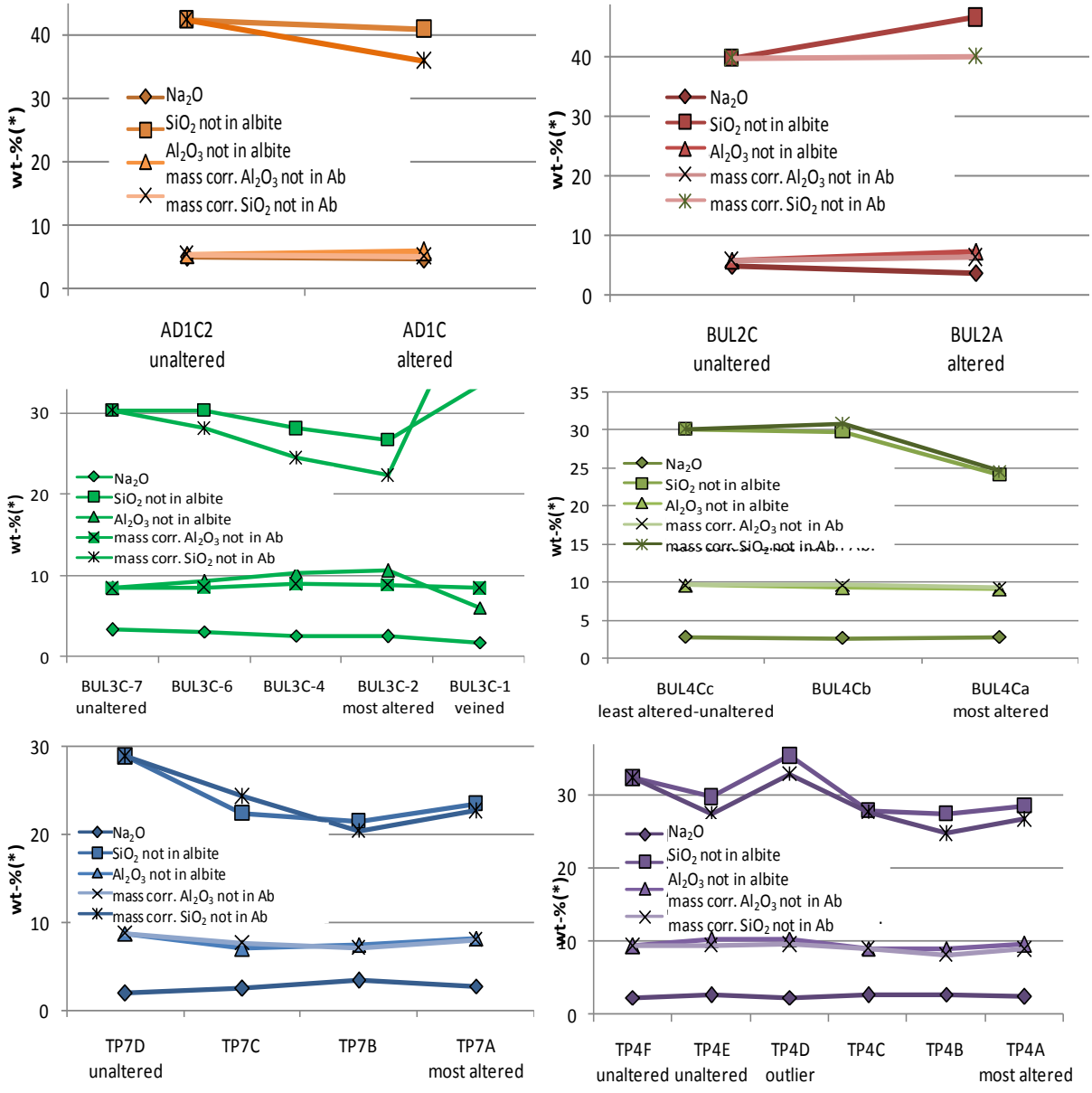

Fig. 4.2.12) Trend of Na and not-by-albite-bound Si and Al across the alteration halo. 3 of the 4 graphs in each plot use concentration values that are not mass-corrected. As a comparison and because Al also occurs in the melanocratic layers mass-corrected values are plotted.

Across all samples sets, the similar trends of Mg and Fe changes (Fig. 4.2.6) reflect that these two elements occur in the same mineral solid solutions, such as in chlorite, biotite and ankerite, and during the break down of these minerals, Mg and Fe are released at the same time. The depletion of Mg, Fe, Ca, and Mn towards the centre of the alteration halo in the greenschist samples from Bullendale (Fig. 4.2.6) is steady and consistent and can be attributed to element mobility during alteration. The high concentrations of Ca, Mg, Fe and Mn in the vein-rich altered part of BUL3C (BUL3C-1) (Fig. 3.2.7A.1 & Fig. 4.2.6) indicate that these elements become incorporated in the vein ankerite, which is the most common carbonate in the veins. In the TP7 set, Fe and Mg increase and Ca decreases towards the alteration halo can be correlated with the replacement of the metamorphic calcite by ankerite in the leucocratic layers (Fig. 3.2.18C-E).

Differences in the REE contents and patterns across all studied alteration halos are unsystematic and small (Fig. 4.2.7) and can be related to pre-alteration variations in the rock composition, showing that within the rock, REE are immobile on a cm to meter scale. This has also been found for studies of alteration halos similar those studied here (e.g. Bierlein et al., 1999). These findings would further support the hypothesis made by Michard & Alberede (1986) which states that REE mobilising below 350°C requires unrealistically high fluid/ rock ratios (>100000).

Of the examined elements, the LILE showed the most pronounced changes across the alteration halo. Due to their chemical similarity (ionic radii, charge, group in the Periodic Table of Elements), the changes in concentrations of Ba and Sr and those of K, Rb, Cs often have the same enrichment or depletion trend (Fig.4.2.8). The small changes of the LILE in the Treble Cone / Black Peak transects, compared to the greenschist from Bullendale Transect, can partly be attributed to their pre-alteration mineralogy. The unaltered rocks in both Treble Cone/ Black Peak Transect contain relative to the greenschist from Bullendale high amounts of metamorphic calcite and muscovite. These two minerals are rich in the LILE (see section 4.3 of this chapter for details). The relatively pronounced decrease of Ca and increase of Fe, Mg, Ba and Sr from TP7B to TP7A in the Treble Cone Transect correlates with the replacement of metamorphic calcite by ankerite and growth of barite in the TP7A sample (Fig. 2.3.18C-E). In the Treble Cone Transect, the decrease of K and Rb concentrations towards the alteration halo can be attributed the replacement of metamorphic muscovite by kaolinite (Fig. 3.2.22).

Overall, the reason why changes in greyschist-hosted alteration are not as distinct as in the greenschist sets is probably not only a reflection of pre-alteration differences of the samples, but also that the fluid which mostly flows through greyschist will closer to equilibrium with greyschist than greenschist. A strong support for this hypothesis are the different ratios of the LILE. Ca/Ba and Ca/Sr ratios of unaltered greyschist are higher than of altered greenschist which is due to the influx of Sr and Ba in the rock. In comparison, the altered greenschist is similar to greyschist and the spring waters emanating from the Haast Schist today (Barnes et al., 1978; Fig. 4.2.13). Concerning K/Rb and K/Cs ratios, the altered greenschist (except TP7) has similar element ratios as greyschist. Altered rocks of the TP7 set are similar to most of the warm springs analysed by Barnes et al., 1978 (Fig. 4.2.13). The reason why waters of hot springs are displayed is that their chemistry may be an indication of the chemistry of hot fluids that passed through the Otago Schist in the Cenozoic, as in both cases hot fluids pass through similar lithologies (Otago & Alpine Schist). The similarity of the different ratios of the LILE of altered greenschist and the unaltered greyschist and the relatively small difference of the altered greyschist vs. the unaltered greyschist, strongly suggest that the bulk of the the LILE in the altered greenschist (and greyschist) were derived from greyschist. This conclusion goes hand in hand with the

hypothesis stated above concerning a larger disequilibrium of greenschist with the incoming fluid compared to the greyschist. Overall, this is hardly surprising, considering that greyschist is much more abundant in the Otago Schist than greenschist. The extraordinarily low K/Cs values in the altered samples of greenschist of TP7 can be attributed to breakdown of muscovite due to low K/H^+ ratio in the fluid.

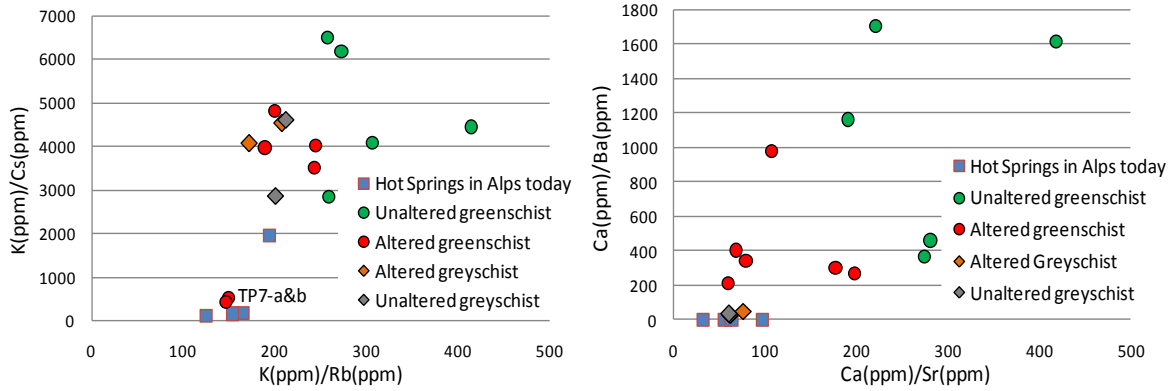

Fig. 4.2.13) K/Cs vs. K/Rb and Ca/ Ba vs. Ca/Sr of unaltered and most altered samples of each transect. Hot Springs emanating from the Otago Schist today (analyses in Barnes et al., 1978) are plotted for comparison.

The increase of W only right next to the altering feature and which has only been found in the Bullendale sets (Fig. 4.2.8) suggests that W enters the system with the fluid but that tungsten cannot be transported within the rock. This most likely due to different chemical conditions in the wall rock compared to the fluid (e.g a different pH, oxygen fugacity, temperature), although it is not clear how W is transported in hydrous fluid (Lauren Farmer, pers. communication, 2016).

In all sample sets, the S content increases within the altered zone as is evident by the increase in sulphide mineral content in all studied transects, especially the Bullendale Transect, (Chapter 3.2) and additionally the whole rock analysis of TP4 samples (Fig. 4.2.9) The increase of the LOI in the alteration halo (Table 4.2.2) also reflects the increase in S but especially CO_2 in the rock. The latter is evident by the growth of carbonate in the altered rock and analysis of the TP4 set (Fig. 4.2.9). The loss of water calculated for the TP4 set (Table. 4.2.2) correlates with the breakdown of epidote and chlorite and replacement by the anhydrous ankerite and quartz and relatively little water-rich kaolinite. Though analyses are missing, the Bullendale greenschists are also expected to be dehydrated even more profoundly as chlorite gets entirely replaced by ankerite and less-water rich muscovite.

4.3) Composition of metamorphic and hydrothermal minerals

Mineral chemistry, in combination with whole rock chemical data, allows full assessment of the probable cause of mobility, such as whether an element is mobile because of the chemistry of the fluid or whether its mobility is controlled by the minerals that grow in the replacement site (as already partly discussed in chapter 3). It is the goal in this section to quantify this major and trace element mobility for each replacement reaction further. Especially mobility of trace elements are of interest here as studies which give trace element compositions of common minerals are relatively rare and are limited to rocks with well developed and large mineral grains (e.g. Bea et al., 1996).

For the analysis of the different minerals, major element concentrations were determined by SEM and/ or MP, while for trace elements LA-ICP-Ms was used. Due to the spatial resolution limit of the LA-ICP-MS only certain minerals in certain samples could be analysed (see Table 4.3.1). In the following section, the data is presented on mineral to mineral basis and not from transect to transect, like in chapter 3.2. Some mineral analyses are not from transects described in chapter 3, i.e. albite in ND1A (marble). These analyses are given to provide comparison to the other analysis.

Table 4.3.1) Samples and the minerals analysed for TE composition by LA-ICP-MS and whole rock composition. WRC=Analysed for whole rock chemistry across the alteration halo.

Sample set	Metam. Cc	Metam. musc	Hydr. mus	Bt	Chl	Ab	Act	Ep	Ank	Tit	Rut+	WRC
BUL2B	X											X
AD1C						X						X
AD1C2		X		X								X
BUL3C	X		X				X	X	X	X	X	X
BUL4C	-											X
TP7A	X								X			X
TP7D	X							X				
RR18	X				X							X
RR19					X				X			-
ND1A						X						

4.3.1 - Albite

Albite trace element analyses have been obtained from the euhedral grains in the ankeritic marble from Niger diatreme (ND1A) and from altered greyschist of Mt Alta Transect (AD1C). In both cases, measurements are contaminated by other mineral phases. In the marble, the contamination is indicated by relatively high K, Rb and Zr concentrations, most likely due to contamination by muscovite and zircon (Fig. 4.3.1). In the schist albite, the high Ca content suggests contamination by calcite (Fig. 4.3.1).

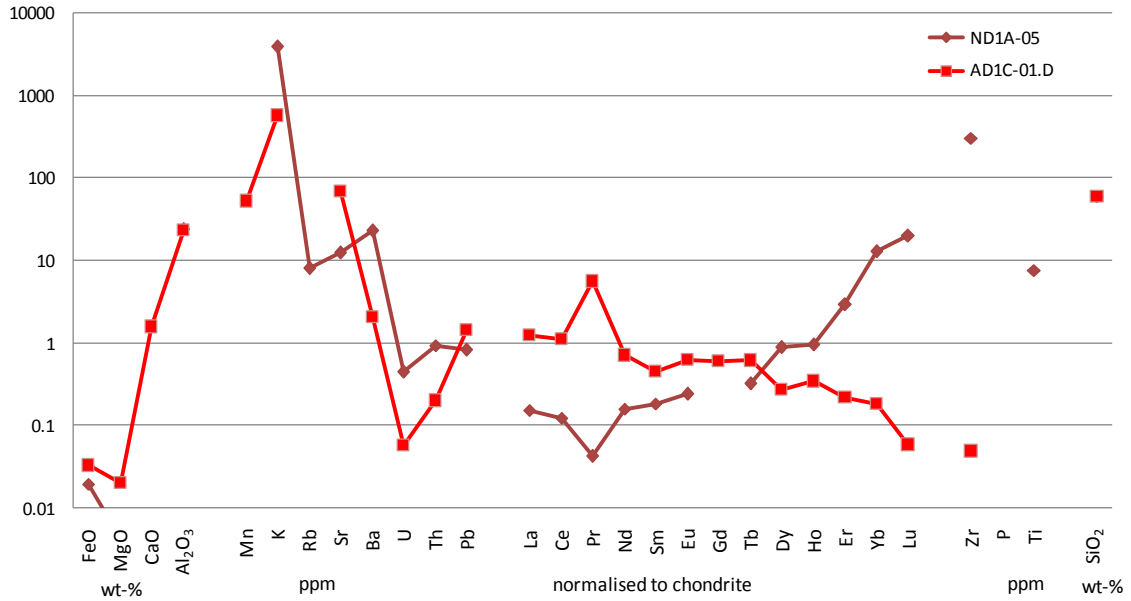

Fig. 4.3.1) Selected major and trace element concentrations in albite from a schist and ankeritic marble. Both measurements are contaminated; ND1A by muscovite and zircon (high K &Zr). AD1C by calcite (high Ca).

4.3.2 - Metamorphic micas- Muscovite and biotite

Trace element content of metamorphic biotite and muscovite has been determined in the unaltered greyschist sample from Mt Alta Transect (AD1C2). Biotite contains several thousand ppm of Ti and several hundred ppm of Rb and Ba (Fig. 4.3.2A). Contents of Ba are about a magnitude higher in muscovite than biotite. In both mineral types, Sr concentrations are over a magnitude lower than those of Ba. The chondrite normalised REE pattern of both micas has a slight negative slope and REE concentrations are generally smaller than 10_{CN} (Fig. 4.3.2A&B). There is no distinct Eu anomaly, but some measurements have a well developed negative Ce anomaly. Lead concentrations are more than a magnitude bigger than those of U and Th in biotite. This relationship can also be found in muscovite, but it less pronounced (Fig. 4.3.2).

The chemical composition of biotite and the breakdown related carbonate (Fig. 3.2.6) are shown in Fig. 4.3.4 and which illustrates that the magnesian siderite is slightly enriched in Fe relative to the biotite. Sets of metamorphic and hydrothermal muscovite have been analysed for major element content in samples from the two greyschist transects (BUL2B and AD1C/C2). Hydrothermal muscovite has a lower Si, Mg and Fe but bigger Al contents than metamorphic muscovite (Fig. 4.3.2D). This corresponds to an increase of the muscovite relative to the alumo-celadonite component. The absolute difference for is an increase by 5-6 wt-% for Al and a drop of Si content by about 2 wt-%, and for Mg and Fe, 1.5 and ca. 3 wt-% respectively, which also coincides with findings of MacKenzie et al. (2007).

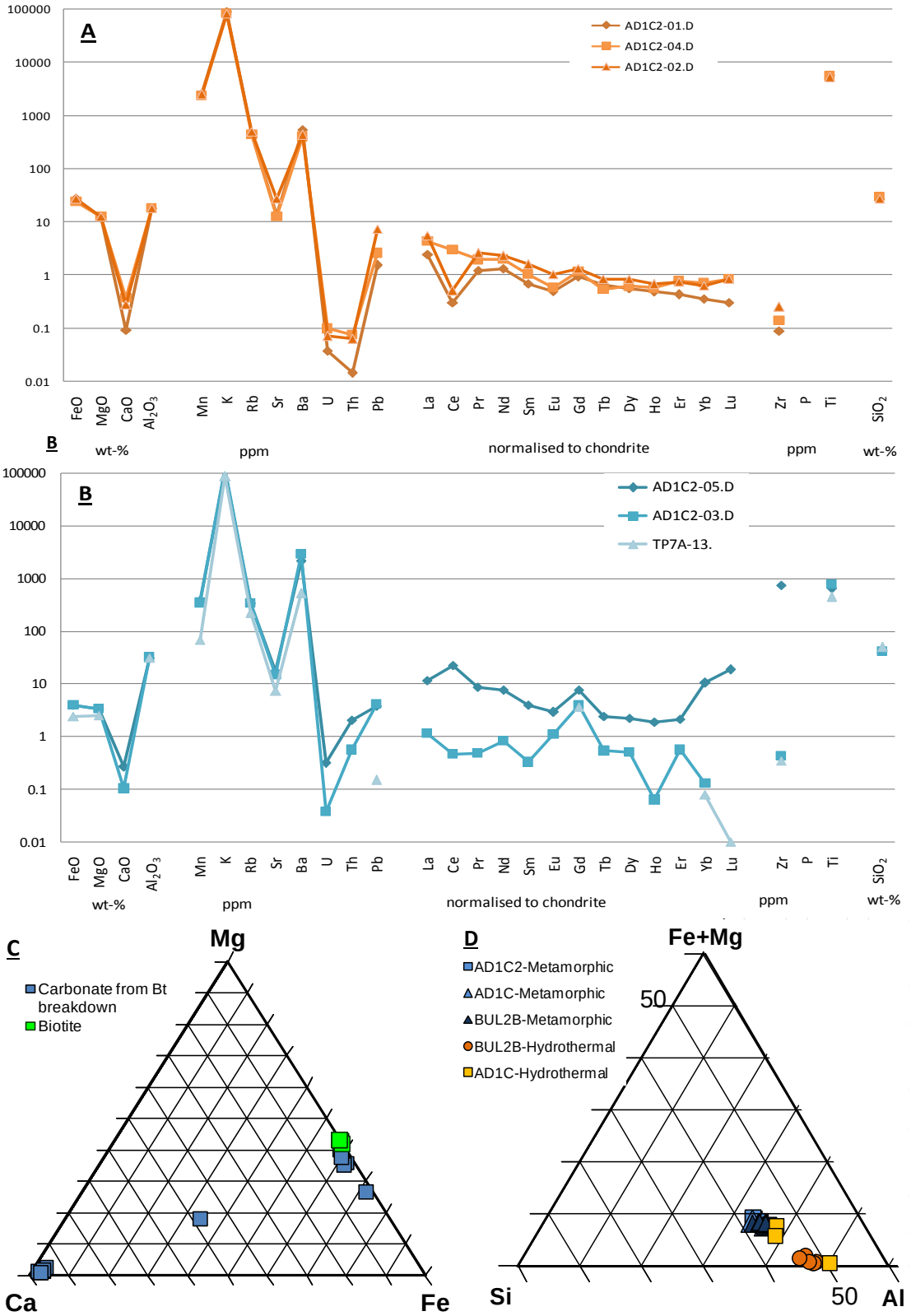

Fig. 4.3.2) Selected major and trace element concentrations in biotite in greyschist **(A)** and muscovite in greyschist and greenschist **(B)**. **C:** Molar proportion of carbonate compositions in the lamellae intercalated with white mica compared to metamorphic biotite. Blue: carbonate (in AD1C); green: biotite (in AD1C2). See Fig. 3.2.6 for the texture. **D:** Metamorphic muscovite in greyschist (blues) and hydrothermal muscovite (oranges). Molar proportions.

4.3.3 - Actinolite

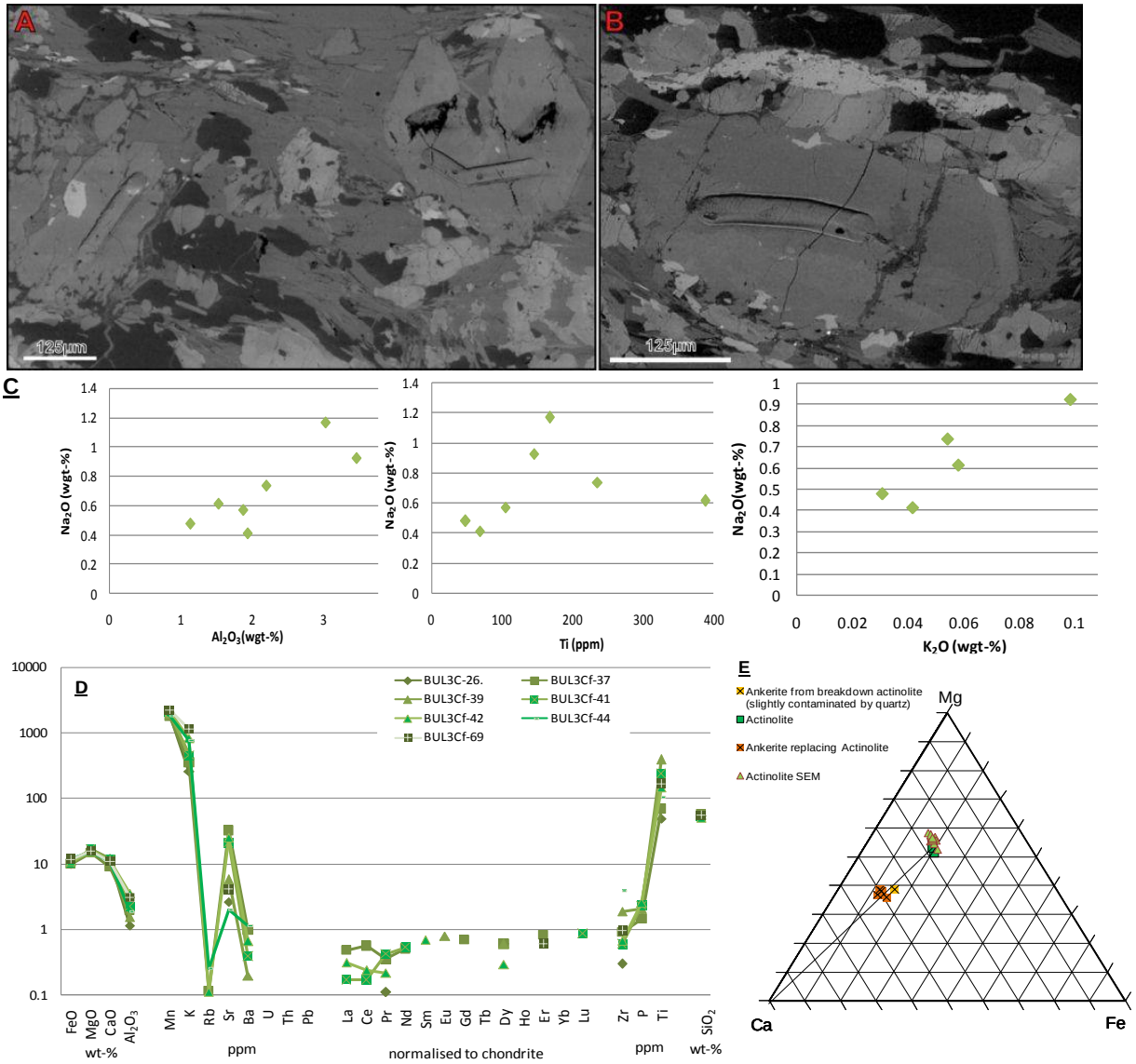

Fig. 4.3.3) A&B: BSE images of actinolite analysed by LA-ICP-MS. Note that the LASER track sometimes cuts veinlets. Possible contributions of these veinlets were filtered out during processing of the raw data. **C:** Na_2O vs Al_2O_3. Na_2O vs Al_2O_3. Na_2O vs Ti. LA-ICP-MS data. **D:** Selected major and trace element concentrations in actinolite. **E:** Composition of actinolite and ankerite replacing it. Note: the ankerite may not be clean and the measurement may be "contaminated" by the quartz that also forms during the reaction. This quartz contamination however, does not change the Mg:Fe:Ca ratio of the carbonate it is in contact with, as quartz doesn't contain these Mg, Fe, and Ca. Except where indicated, all data from MP analyses. All BUL3C.

In actinolite K, Na and Al content can be correlated in a linear fashion and limited also Na vs. Ti (Fig. 4.3.3C, examples of analysed actinolite in Fig. 4.3.3 A&B), which corresponds to an increase in hornblende component in the actinolitic amphibole. Mn concentrations in actinolite are several thousand ppm, those of K up to 1150ppm and those of titanium 60-400 ppm (Fig. 4.3.3D). The amphibole has low concentrations of REE, with chondrite normalised values smaller than 1 (Fig. 4.3.3D). In the replacement of actinolite the ankerite forming has a higher Ca/(Mg+Fe) ratio than the actinolite but the same Fe:Mg ratio (Fig. 4.3.3E).

4.3.4 - Metamorphic chlorite

Metamorphic chlorite in all samples (example in Fig. 4.3.4 A) has very low concentrations of most measured trace elements (Fig. 4.3.4B). Sr and Ba values are low (less than 50ppm), with Ba generally being slightly more abundant than Sr. The Ti content can be several hundred ppm. Consulting BSE images and optical microscopy, there are no indications of any Ti-bearing phases, such as rutile or ilmenite, in the analysed chlorite, suggesting that some Ti is accommodated in the chlorite's crystal lattice .

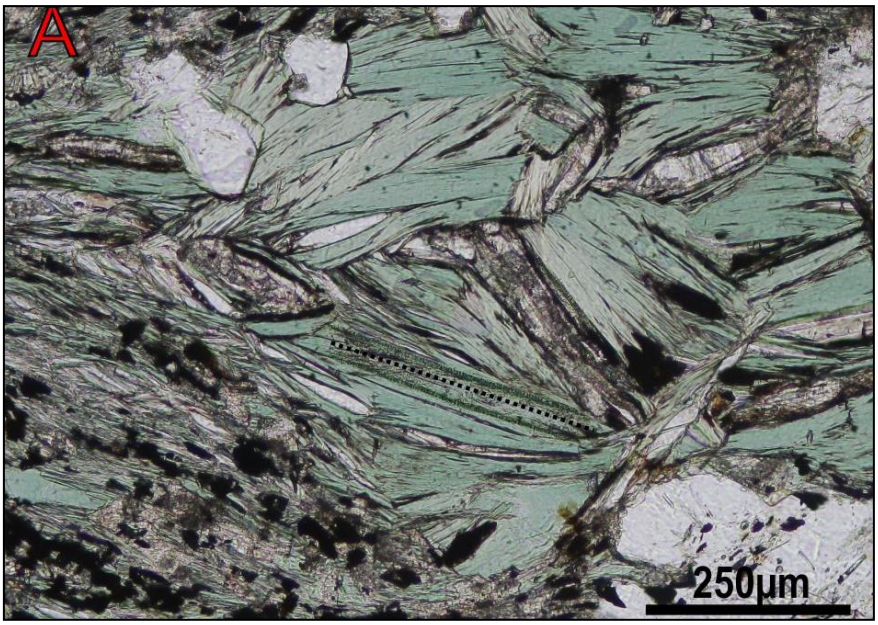

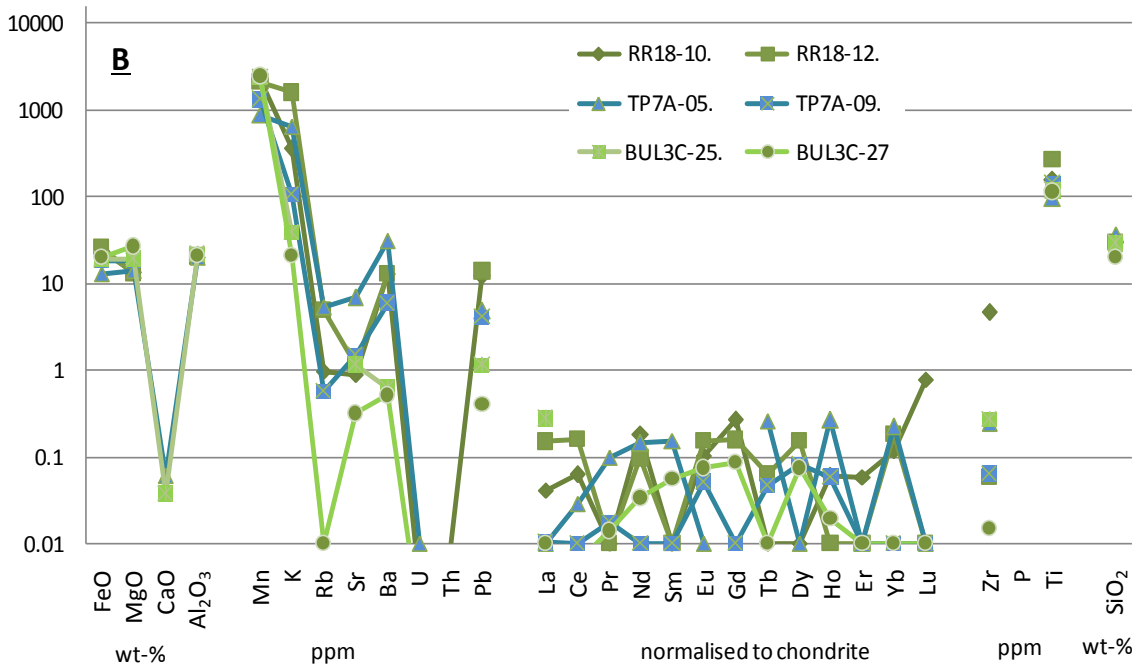

Fig. 4.3.4) A: Micro-photograph of chlorite: dotted line shows location of LASER track. PPL. **B:** Selected major and trace element concentrations in chlorite.

4.3.4.1: Ankerite (partly) replacing chlorite

Ankerite which is found in chloritic layers has been analysed in the Treble Cone and Bullendale Transect. Concerning the major element content of the ankerite and chlorite, in the Bullendale Transect the ankerite has naturally higher Ca content than the chlorite and a slightly higher Mg: Fe ratio (Fig. 4.3.5A). In the Treble Cone Transect in the cauliflower-like ankerite described in chapter 3 (e.g. Fig. 3.2.17B) the Mg:Fe ratio is slightly higher in the central part of the ankerite grain but similar at the grain rims compared to the metamorphic chlorite in those rocks. The trace element content of this carbonate shall be described further on in this chapter, as not all of this cauliflower-like carbonate is the replacement of chlorite in the rock. In the greenschist from Bullendale (BUL3C), ankerite that could be traced to have formed by the breakdown of chlorite (see chapter 3) was also analysed by LA-ICP-MS (Fig. 4.3.5B). Due the small grain size compared to the LASER beam and intricate intergrowth of this ankerite with other breakdown product of chlorite, i.e. muscovite, "ankerite" analyses contain some K, Rb, and Si (Fig. 4.3.5C). Compared to the metamorphic chlorite in the sample, this ankerite-dominated mineral mix has ca. 10 times higher concentrations of REE. Additionally, there is an even bigger enrichment in Eu, giving the REE pattern a positive Eu anomaly (Fig. 4.3.5C). The analysed ankerite-mineral-mix also has higher concentrations of Ba and Sr than the chlorite. Ti concentrations are similar to small in comparison to chlorite.

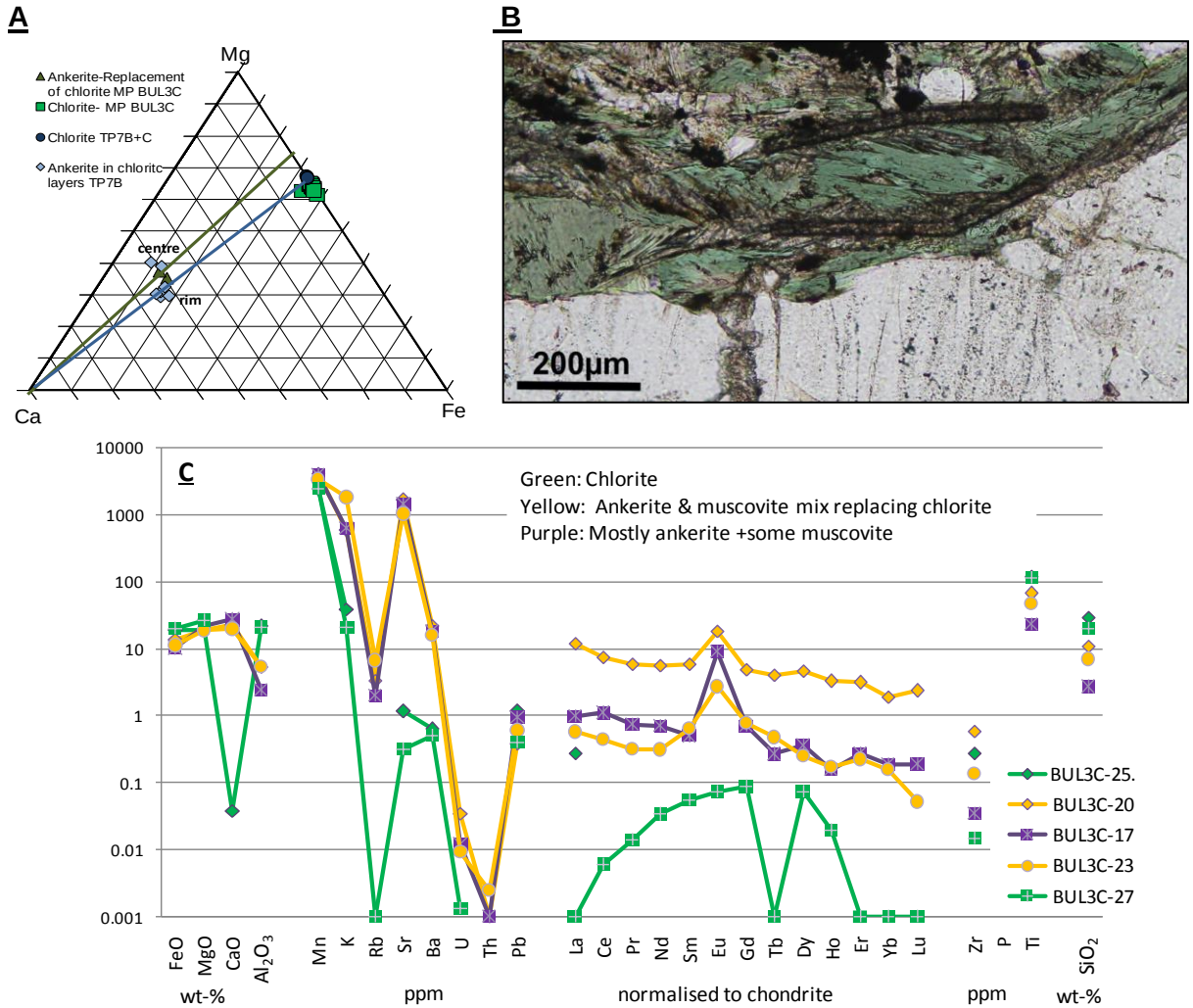

Fig. 4.3.5) A: Example of LASER tracks in ankerite that forms from the breakdown of chlorite in BUL3C. **B:** Ca, Fe, and Mg content of chlorite and the replacing ankerite for different greenschist samples. Lines indicate ideal mixing line of Ca with ankerite and the theoretical chlorite as proto-mineral. Centre and rim refers to the position of analysis in the grain (see Fig. 3.2.17B). **C:** Chemical composition of metamorphic chlorite and its replacing ankerite in BUL3C.

4.3.5 - Epidote

Trace element concentrations of epidote have been obtained from BUL3C and TP7D. Although the same mineral, the trace element content, especially of the REE, differs from sample to sample. Epidote in BUL3C has chondrite-normalised REE patterns with steady negative slopes (Fig. 4.3.6). The epidote in TP7D has a convex REE pattern with the maximum at Dy. The difference of the pattern between the two samples is predominantly defined by the different concentration in the LREE (La-Sm). La-Sm ratios of epidote in BUL3C are larger than 1, with chondrite-normalised La values ranging between 400 and 540 and those of Sm between 190-230 (Fig. 4.3.6). In TP7D, La-Sm ratios are smaller than 1 and La chondrite-normalised values range from 13 to30 and 30 to 130 for Sm. In both samples, the concentrations of the HREE (Er-Lu) are similar and chondrite-normalised values range from ca. 120 for Er to 40 for Lu (Fig. 4.3.6). The concentrations of the MREE (Gd-Ho) are often also similar across samples.

4.3.5.1: Hydrothermal muscovite replacing epidote in the Bullendale greenschist

As has been deduced from textural evidence in chapter 3, epidote in the greenschist from Bullendale breaks down predominantly to muscovite and which could be analysed by LA-ICP-MS (Fig. 4.3.7 A). Compared to the precursor epidote, the muscovite has much lower concentrations of REE, U, Mn, Sr, Ca and Fe, but has higher concentrations in Mg, K, Rb, and Ba (Fig. 4.3.7B).

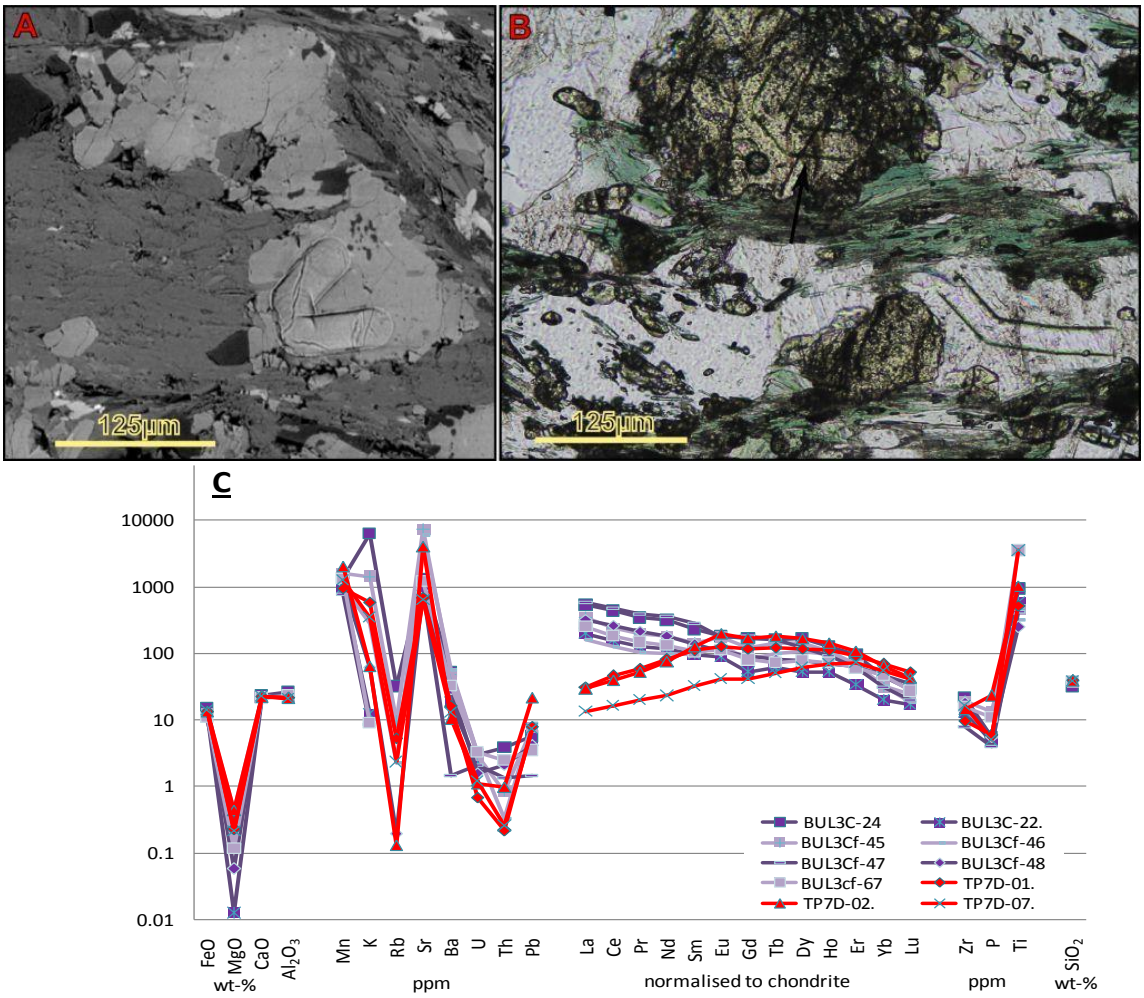

Fig. 4.3.6) A: BSE image of LASER tracks in epidote in BUL3C. **B:** PPL. Example of epidote analysed in TP7A (yellow grain). The other track is in calcite (white grain). **C:** Concentration of a selection of major and trace elements in epidote in greenschist. Red: TP7D. Violet: BUL3C.

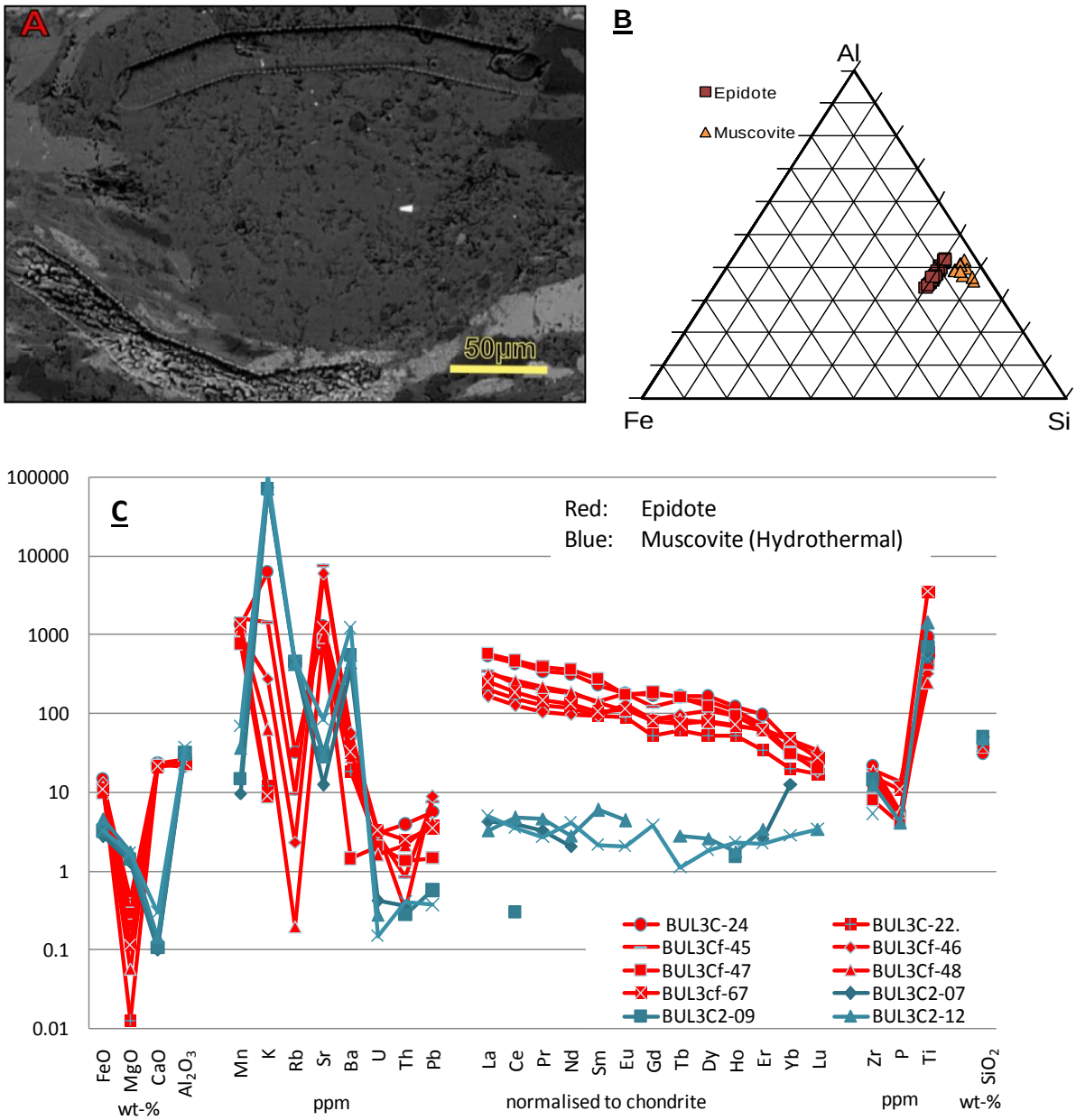

Fig. 4.3.7) A: BSE image of hydrothermal muscovite that formed pseudomorphically after epidote. **B:** Composition of epidote and epidote-replacing muscovite. MP data. **C:** Major and Trace element content of hydrothermal mica (blue). For comparison the composition of epidote from this sample is also shown. All BUL3C.

4.3.6 - Metamorphic calcite in leucocratic layers

Metamorphic calcite in leucocratic layers has been analysed in two greenschist samples (TP7D and BUL3C) and in one greyschist (BUL2B). Additionally, it was possible to analyse a calcitic inclusion in an albite porphyroblast in the leucocratic layers in TP7A (Fig. 4.3.8A). This calcite is a remnant of metamorphic calcite in the otherwise hydrothermally overprinted rock. In addition to the calcite within the rock of TP7D, the chemical composition of a calcitic vein in TP7D (Fig. 3.2.15C&D) was determined. This vein formed after metamorphism but most likely prior to the ankeritic alteration, which was concluded as the greenschist of TP7D is otherwise unaltered.

The calcite in the leucocratic layers across samples has a remarkably similar REE composition. In all cases, the REE patterns show a depletion in the LREE and MREE relative to the HREE (Fig. 4.3.8B). This

depletion is larger for greenschist-hosted calcite than greyschist-hosted calcite (Fig. 4.3.8B). In the calcitic vein analysed in TP7D (Fig. 3.2.15 C&D), the range of REE concentrations are similar to those of the leucocratic layers. However, the REE patterns from the vein flatten off towards the MREE and HREE, unlike the calcite in the leucocratic layers, which have a non-constant gradient (Fig. 4.3.8B). The composition of the calcite inclusion in the albite porphyroblast in TP7A has some similarities to the calcite in the leucocratic layers, but also to the vein in TP7D. The Ce and Sr concentrations are similar to veins, but the REE pattern is "intermediate" between those two calcite types (Fig. 4.3.8C). The calcite in the inclusion also contains more Fe than the vein and is in that respect more similar to the calcite in the leucocratic layers in TP7D (Fig. 4.3.8 C).

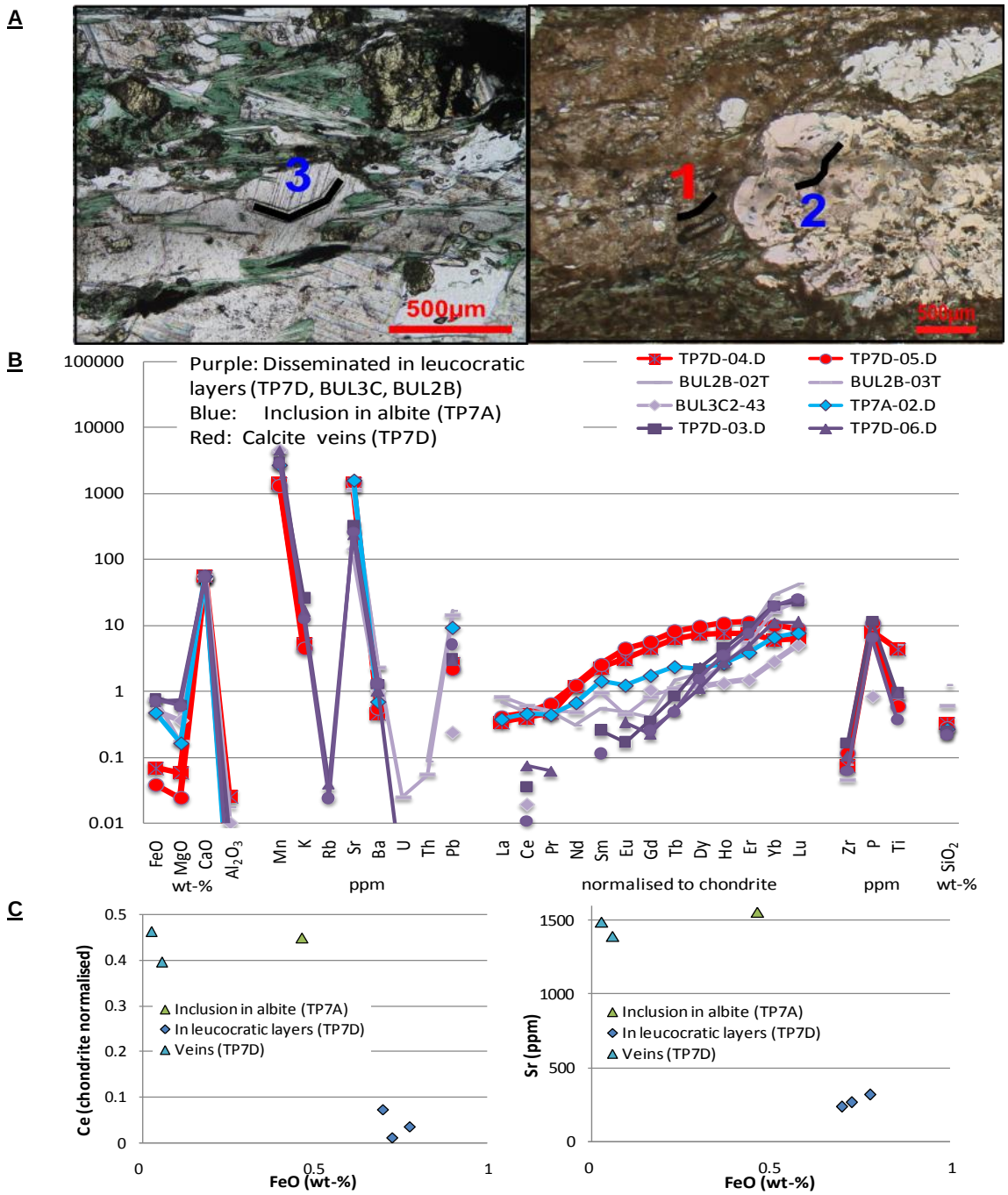

Fig. 4.3.8) A: PPL of TP7D (left) and TP7A (right). Numbering refers to numbers of the analyses. Blue numbers mark calcite and red marks ankerite (see next figure for the ankerite's composition). **B:** Trace element content of metamorphic carbonate in various settings and lithologies. **C:** Ce vs. FeO and Sr vs. FeO diagrams of calcite in TP7D and A.

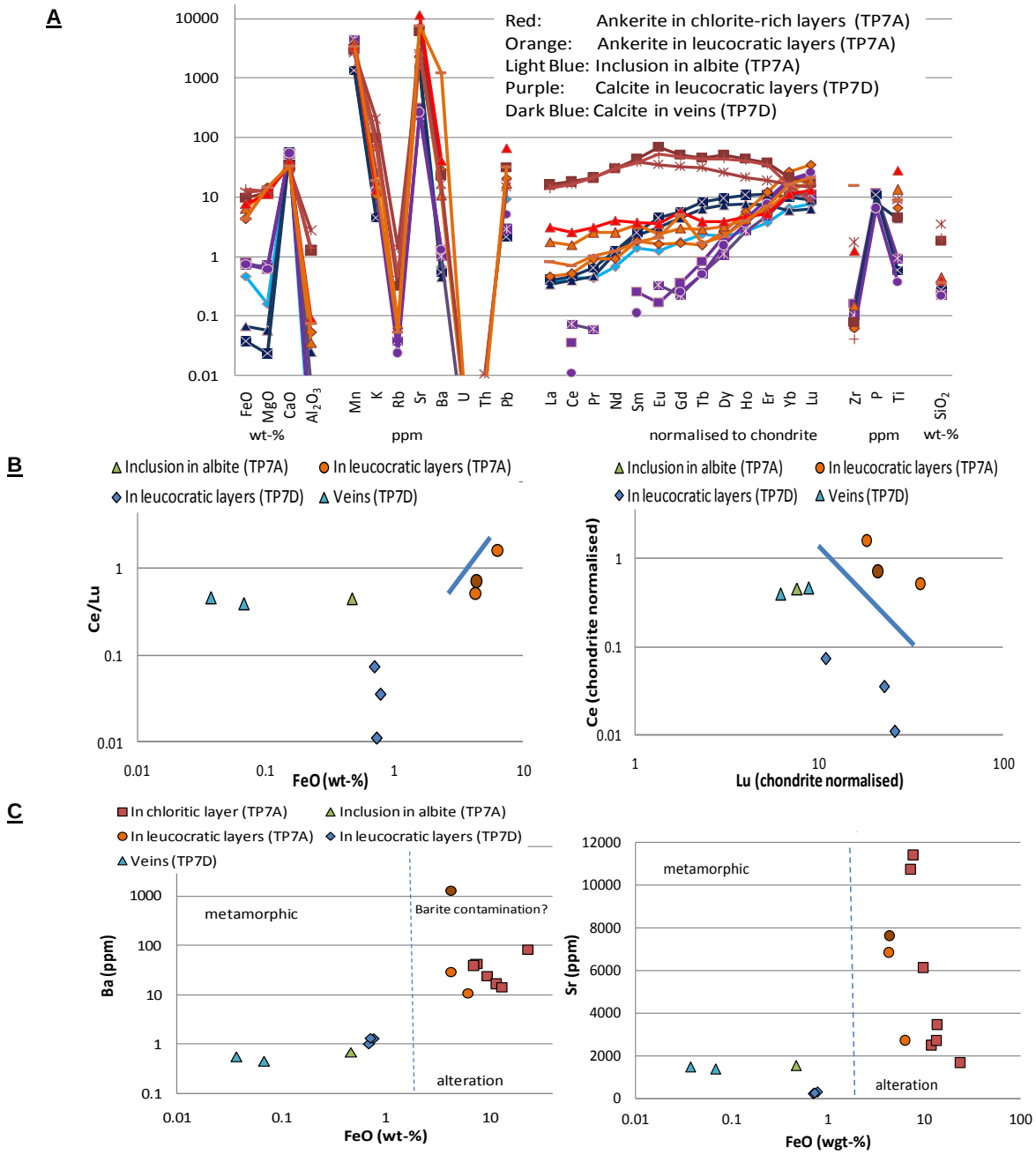

Fig. 4.3.9) A: Composition of carbonate in various textural positions in altered and unaltered samples of the Treble Cone Transect. **B:** Ce/Lu vs. FeO and Ce vs. Lu of carbonate in leucocratic layers in unaltered (blue and green) and altered rock (oranges). Note: The barite contaminated analyses (see C) does not show any abnormal Ce content or Ce/Lu. **C:** Alteration-related carbonate in Ba vs. FeO and Sr vs. FeO plots clearly plot in different fields compared to metamorphic calcite.

4.3.6.1: Ankerite replacing metamorphic calcite in leucocratic layers and other hydrothermal ankerite in TP7A

In TP7A, ankerite in the leucocratic layers and in the chlorite-rich layers (= cauliflower-like carbonate as depicted in Fig. 3.2.17B) was analysed (Fig. 4.3.9). As has been shown in the previous chapter

(section 3.2), the ankeritic carbonate in the leucocratic layers is the replacement product of the metamorphic calcite in these sites and chemically inhomogeneous and in a few places the original calcite can even be recognised (Fig. 3.2.18 C-E). The LASER tracks cut across these inhomogeneous grains and the trace element concentrations obtained are therefore an average of the grains' compositions. The REE pattern of the ankerite in the leucocratic layers has a steady positive slope. This slope and absolute values are similar to the calcitic vein in TP7D and the inclusion in TP7A (Fig. 4.3.9A). Compared to the calcite in the leucocratic layers in TP7D, the hydrothermal ankerite is slightly enriched in LREE and MREE. Ce/Lu ratios of the alteration-related ankerite is on average slightly higher than that of the pre-alteration calcite and the two carbonate groups also plot in different fields on a Ce vs. Lu plot (Fig. 4.3.9B). (This is also true when calculating the molar proportions from the weight% and normalising it to one mole of carbonate, which accounts for volumetric differences of, for example, 1 g of calcite compared to 1 g of ankerite.) The hydrothermal ankeritic carbonate in leucocratic layers is richer in Fe, Sr and Ba compared to the pre-alteration carbonate in leucocratic layers, veins and albite inclusion (Fig. 4.3.9C).

The ankerite in the chloritic layers has a slightly concave REE pattern with the maximum at Tb (except for one measurement: TP7A-8; Fig. 4.3.9A). Compared to the ankeritic carbonate in the leucocratic layers, this carbonate is also more Fe-rich, but has a lower Mg content. Ba contents are similar and Sr is similar to slightly higher in the carbonate in the chloritic layers (Fig. 4.3.9C).

4.3.7- Poikiloblastic calcite spots and anti-axial veins

As described in chapter 3, metamorphic calcite has also been found in poikiloblastic calcite spots (RR18) which were also analysed with the LA-ICP-MS. Due to the poikiloblastic nature of the spots, analyses can be slightly contaminated by adjacent phases. Especially one analysis is contaminated and has a quite high Ti content (from rutile; see yellow line with red triangles in plot, Fig. 4.3.10A). However, this does not have a significant effect on the REE pattern, which has a steady positive slope for all of these analyses. Apart from the calcite spots, RR18 also contains well zoned, anti-taxial calcitic veins. The veins have higher REE concentrations than the calcite in the poikiloblastic spots, and patterns have an overall negative slope with a convex shape due to a slight enrichment of Pr to Gd. Sr concentrations in spots and vein are about the same (between 1100 -1700 ppm; Fig. 4.3.10C).

4.3.7.1: Ankerite replacing the calcite in the poikiloblastic spots

In RR19, the calcite in the poikiloblastic spots has been replaced by ankerite. This ankerite has REE concentrations between 1 and 50 times chondritic values with slightly convex shaped, overall negative sloping REE patterns (Fig. 4.3.10B). This pattern is similar to ankeritic veins in this sample and also similar to the calcitic veins in the unaltered sample RR18. Within RR19, there is a systematic trend regarding the Eu content in veins and ankeritic spots. In this sample, the structurally youngest vein has no Eu anomaly, the structurally older one a slight positive one. The ankerite in the spots has, on average, the biggest Eu anomaly in this sample (Fig. 4.310D). Sr concentrations of all ankerite (veins and spots) in RR19 are smaller relative to the calcite in RR18 (veins and spots)(Fig. 4.310C).

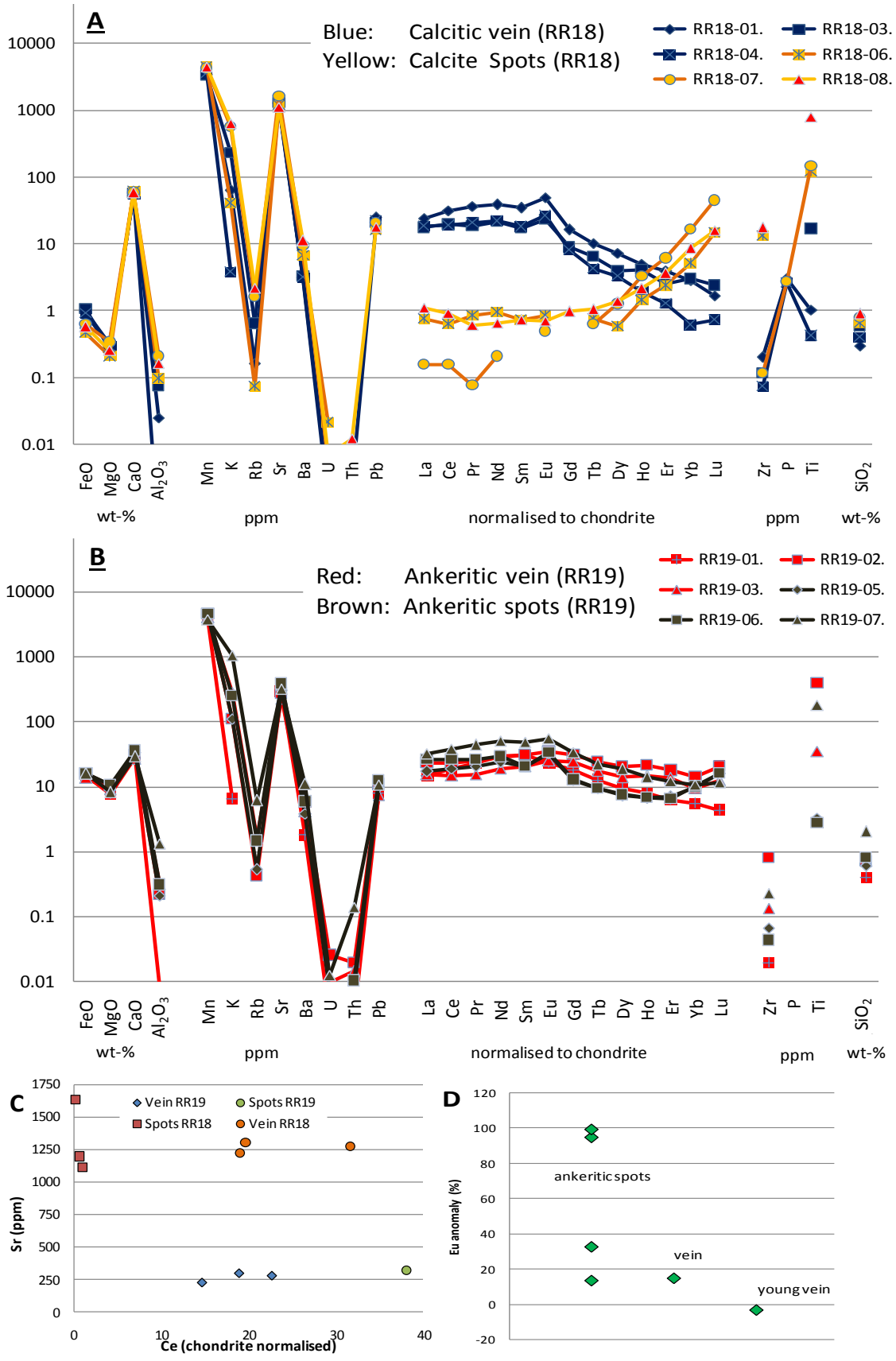

Fig. 4.3.10) A: Chemical composition of calcite spots and calcite veins in unaltered rock. RR18. **B:** Chemical composition of ankeritic spots and ankeritic veins in altered rock. RR19. **C:** Sr vs. Ce of the different carbonate in RR18 and RR19. Note the different colour-coding to A & B. **D:** Size of Eu anomaly in RR19 in relation to the structural position.

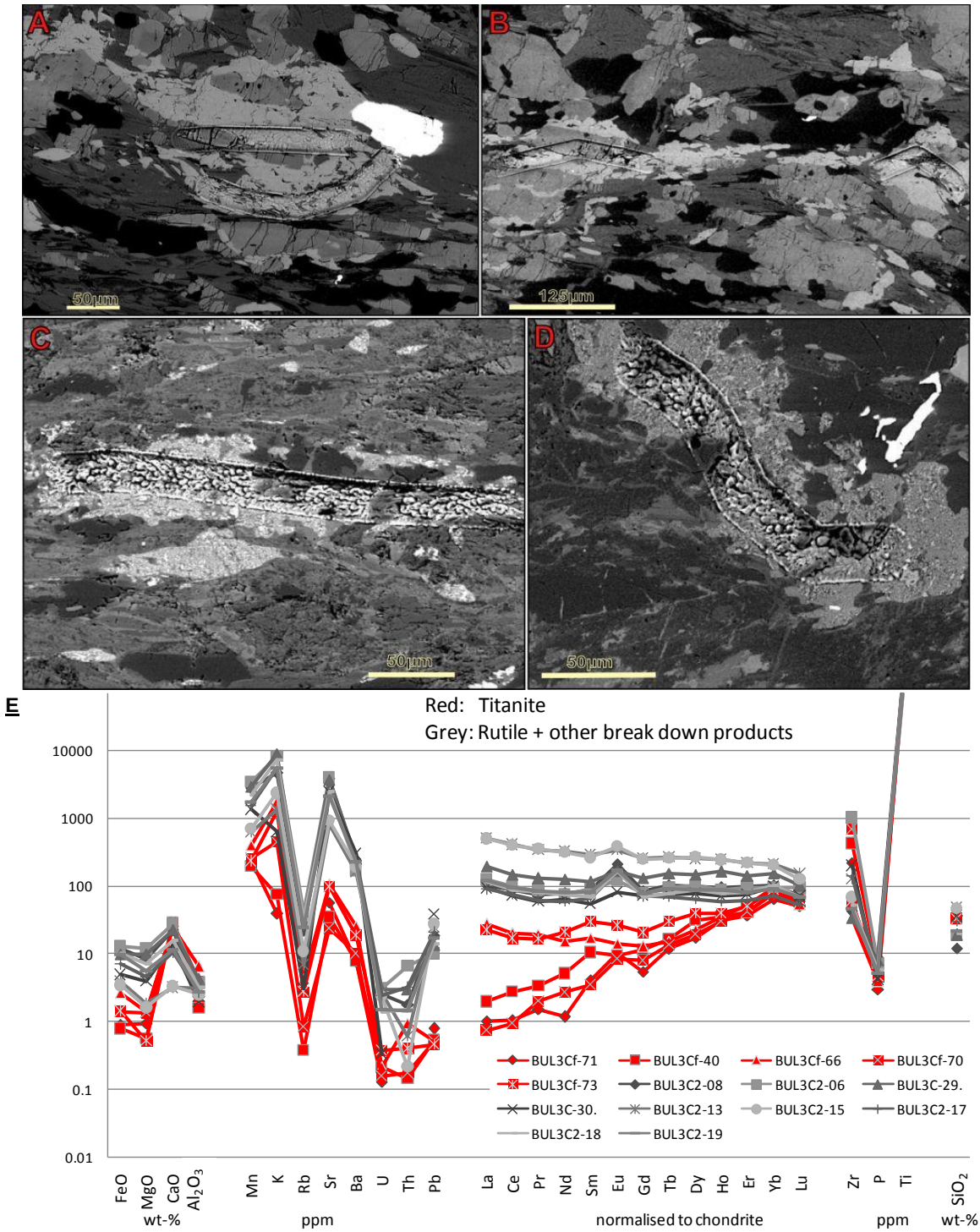

Fig. 4.3.11) A&B: Examples of titanite clusters analysed for TE composition. **C&D:** Examples of rutile + calcite + quartz forming from titanite. Note: In all of the examples, cut the tracks across adjacent minerals. Their contribution was largely filtered out during processing. Images display what the average grains looked like and some of the data of the shown LASER tracks were not used as they were too contaminated. **E:** Chemical composition of titanite and rutile-calcite-quartz mix that formed from titanite break down.

4.3.8- Titanite and its replacement products

Titanite and its breakdown products have been analysed in BUL3C. Due to the limited spatial resolution of the LA-ICPMS, analysis of single grains of metamorphic titanite and its replacement products is not possible. However, titanite and its replacement minerals occur in clusters and it is possible to set laser tracks that are (mostly) within the constraint of these clusters (Fig. 4.3.11 A&B). As the LASER tracks are set using optical microscopy, in most cases the tracks cut across adjacent minerals, mostly chlorite and muscovite (Fig. 4.3.11 A&B). During processing of the raw data only section of the measurement were taken where contamination by these phases was minimal. These sections were at least 10 s long, which is about 4 s longer than needed for a reliable analysis. Despite this "filtering" of the data, analysis are often contaminated to some extent and it is necessary which of the chemical features can be attributed to titanite and its replacement products and which to its the contaminants. By microprobe it was established that metamorphic titanite contains about 1wt-% of Al_2O_3 (appendix D) and Al_2O_3concentrations above 2% in the LA-ICP-MS analyses are certainly due to contamination by muscovite and/ or chlorite. Chlorite contamination would also be evident by the relatively large FeO and MgO content (>1%) in the analysis. Similarly, the presence of muscovite can be inferred from the slightly elevated K content (Fig. 4.3.11). The titanite analyses have a linear REE pattern with a variously steeply climbing positive slope and is enriched in the HREE. Concentrations of Ba are 1-20 ppm and those of Sr mostly around 20-100 ppm. (Fig. 4.3.11C).

As described earlier (Chapter 3.2), titanite in BUL3C breaks down to rutile, quartz, calcite/ ankerite. Despite the contamination issues commented on above, two major chemical changes can be inferred to be related to the breakdown of titanite and growth of the rutile and other secondary phases. The total content of Sr and Ba increase by about an order of magnitude and the REE pattern changes. The concentrations of the HREE are similar to those of the original titanite but the concentrations of the LREE and MREE increase resulting in a REE curve with a near horizontal to slightly negative slope and a positive Eu anomaly.

4.3.9 -Discussion

Concentrations of the trace element in minerals discussed in this study are very variable. Their content in the different minerals is a representation of the different physical/ chemical properties of the elements, such as whether the ions that can fit into the crystal lattice of a mineral, but also of supply and relative partitioning behaviour. The extent to which an element can be incorporated by a mineral depends on its ionic size, charge, ionic potential and electronegativity (modified Goldschmidt Rule). According to Goldschmidt's Rule, only ions which differ by less than about 15% in size from the main element can be substituted in the crystal site. Ionic size matters as with the substitution of one of the major elements by another element, stress is induced on the crystal lattice. The more different in size this substituting ion is compared to the main element in this crystal site, the bigger the strain in the lattice which limits the substitutability (i.e. Blundy & Wood, 1994; Wang & Xu, 2001). All ionic radii reported in this study are taken from Shannon (1976) and are, unless otherwise stated, those of the ion in six-fold coordination. Another factor to account for is the ionic charge of the substituting trace element. In the ideal case the trace element ion has the same charge as the element they are replacing. Goldschmidt's rule states that elements differing by one electron's charge can also enter the lattice, as long as this is balanced out by another substitution which cancels this out.

4.3.9.1: Metamorphic minerals

Metamorphic minerals analysed for their trace element composition are albite, muscovite, biotite, actinolite, chlorite, epidote, calcite and titanite. As mentioned in chapter 4.3.1, albite measurements are contaminated by zircon and muscovite or calcite. As the REE concentrations are low and patterns are correspondingly divers, it is suggested that the REE patterns in the albite analyses (Fig. 4.3.1) are controlled by the contaminants and that albite does not contain significant amounts of REE; zircons have REE patterns with a distinct positive slope and enrichment of the HREE (i.e. Hoskin & Black 2000) and this the origin of the positive REE slope in the albite of the ankeritic marble ND1A (Fig. 4.3.1). In the greyschist, the contaminant is calcite, as evident by the high Ca-content in the analysis (Fig. 4.3.1), causes the slight negatively sloping REE pattern of the albite-analysis. The overall low concentrations of divalent and higher charged ions in the albite analyses reflect on the crystal structure of albite, which is made of large Na^+ ions and Si-and Al- centred octahedra (Prewitt et al., 1976).

The low concentrations of REE, Th, U and Y, but high concentrations of Ba, Rb, Cs, Nb and Ta in the metamorphic muscovite and biotite fit well with findings by Bea et. (1994), who studied trace element compositions of biotite in magmatic systems and who also report similar REE patterns and concentrations, including the "occasional" negative Ce anomaly. Muscovite and biotite are the only minerals of those reported here, where Ba concentrations are significantly higher than those of Sr. The high concentrations of Ba relative to Sr can be attributed to the difference in ionic radii of these two element. The radius of Ba^{2+} is 0.135 nm, whereas that of Sr^{2+} is 0.118 nm. Unless the atom is located in a lattice imperfection, the only space where these big ions can "fit" is in the space of the K^+, which has an ionic radius of 0.132 nm. Hence, though not the same charge, Ba^{2+} being a similar size as K^+ will partition more into mica than the smaller Sr. Mg and Fe in both minerals occupy the octahedron site, which in pure muscovite is filled with 2/3 of the mineral's Al (Richardson & Richardson, 1982). Rb and Cs being mono-valent ions of a size of 0.152 nm 0.167nm respectively (at CN=6) fit into the spot of K (Deer et al., 2003) and concentrations of these elements are correspondingly relative to other minerals enriched in micas (Fig. 4.3.2, refer to appendix E for Cs value). The low concentrations of REE in the micas resemble the lack of suitable spaces in the silicates crystal lattice, which are either too big, like the site occupied by K, or too small, like the Mg- and Fe centred octahedra. The latter is also in agreement the low REE contents in chlorite (Fig. 4.3.4) which only has Mg- and Fe-centred octahedra (Deer et al., 2009).

Epidote is the most REE-rich metamorphic minerals analysed here. REE contents are in the range of epidote analysed in mafic blueschist by Spandler et al. (2003), and are on average slightly higher than epidote in granodiorite (Bea, 1996). Zoisite, an epidote-group mineral, can have differing REE patterns and concentrations for different samples (Spandler et al., 2003), which is in agreement with the finding here. Sr concentrations of the epidote are about 2 orders of magnitude higher than those of Ba. This can be explained by the smaller radius of Sr^{2+} compared to that of Ba^{2+}. In the epidote's crystal structure big trace element ions, such as Sr and Th and the REE, occupy the A-crystal site, which also accommodates the Ca (Deer et al., 1986). However, as Ba^{2+} differs by far more than 15% from the radius of Ca^{2+} (0.135 nm vs 0.1nm) it does not fit into the crystal site well, as is reflected by the low concentrations of Ba compared to those of Ca and Sr. Overall, all Ca-bearing minerals presented in this study have higher concentrations of Sr than Ba, which is a reflection of this principle and showing that the Ca-filled crystal sites are sufficiently big to also accommodate the relatively big Sr^{2+} but not so much the even bigger Ba^{2+} ion. This is in good agreement with the general practice of using Sr as a proxy for Ca.

Concerning the composition of actinolite, the higher concentration of Sr compared to Ba, strongly suggests that these elements are again accommodated by the Ca-crystal site. With respect to

the REE content of metamorphic amphiboles, Skublov & Drugova (2003) conducted a study on REE composition of granulite and amphibolite facies amphiboles and showed that with decreasing metamorphic temperature, the REE content also decreases. Projecting this to greenschist facies conditions it is consistent with the very low REE concentrations in actinolite in the rocks here. It however does not appear that the low concentrations found in the actinolite here is limited by its capability to accommodate the REE, as tremolite should be able to accommodate REE in the Ca-crystal site. Instead, it is proposed that the REE pattern in the amphibole is a result of the competition with other coexisting minerals, which have higher relative REE partitioning coefficients, such as apatite or epidote.

Concerning the REE patterns of titanite, again contamination from adjacent phases need to be accounted for first. With respect to the REE patterns of the titanite measurements, as neither chlorite nor muscovite (potential contaminants) contain significant amounts of REE (see Fig. 4.3.2 & 4), it can be concluded, that titanite in the Bullendale greenschist has a (slight) enrichment of the HREE relative to the LREE. Titanite trace element chemistry has been part of several studies, showing that titanite can have LREE enriched (Bea, 1996; Pan et al., 1993), MREE enriched (Bea et al., 1994; Horie et al., 2008) or HREE enriched (Pan et al., 1993; Spandler et al., 2003) chondrite normalised patterns. Based on the variability of REE patterns, Pan et al. (1993) concluded that titanite does not have a strong selectivity for certain REE relative to other coexisting minerals.

Regarding metamorphic calcite, the strong depletion of LREE and partly MREE is interesting as the calcitic veins in Fig. 3.3.10 clearly show that calcite can have much higher contents of these elements. A high variability of REE content in calcite has also been found in other studies (i.e. Bau & Möller, 1992; Kontak& Jackson, 1998). Nevertheless, low levels of REE in metamorphic calcite have also been mentioned by Spandler et al. (2003).

Based on above discussion it is concluded that the trace element, specifically the REE content of a mineral is not only controlled by its crystal structure, but also on the other mineral it coexists with. To my knowledge there are no studies that specifically investigate the size of these partition coefficients in metamorphic rocks. However, some qualitative statements can be made based on the relative REE content of the analysed minerals. Of the minerals analysed, epidote, titanite, calcite and actinolite should be able to accommodate REE in their crystal lattice (in the Ca -site). Of these minerals, epidote has by far the highest concentrations of LREE and MREE. It is suggested that epidote has of these minerals the highest partition coefficients for the LREE and MREE, followed by titanite and then calcite. Actinolite would have the lowest partition coefficients for the LREE and MREE. The compositional data suggest that the calcite, titanite and epidote have about a similar partition coefficient for the HREE, as they have similar concentrations in the HREE, while actinolite again only has a small partition coefficient for these elements. That epidote is the dominant major REE-bearing component in the rock is also supported similarity of the REE pattern epidote and the rock the epidote is hosted by; the REE pattern of the epidote is similar to that of their host rock (both greenschist)(Fig. 4.3.6 and Fig. 4.2.2) with only some relatively small, though significant differences. The concentrations of REE in epidote are about 1 order of magnitude bigger than those of the whole rocks and the REE gradients are more "extreme". In BUL3C, La/ Lu ratios of epidote are between 8-20 while that of the wall rock it is around 3.6. In the TP sample epidote has La/Lu ratios between 0.3-0.7, but the wall rock (TP7D) has a ratio of 0.9. The discrepancies can be attributed to other major REE-bearing phases in the rocks, such as apatite, zircon and monazite. Nevertheless, as the epidote composition is directly controlled by the whole rock composition, it is again emphasised that epidote is the dominant, REE-incorporating major mineral phase in the metamorphic greenschist facies rocks.

4.3.9.2: Hydrothermal minerals replacing metamorphic minerals

4.3.9.2-1: Epidote, chlorite, actinolite and titanite replacement in BUL3C

The higher Ca/(Mg+Fe) ratio but similar Fe:Mg ratio of the ankerite compared to the precursor actinolite (Fig. 4.3.3) can be achieved in two ways: either Fe and Mg were transported out of the replacement site, or Ca added to it. Both scenarios are possible, however, considering that calcite veins in this section of altered rock prove the existence of "free" calcium, suggests that the latter is most likely. Ca could partly be derived from epidote (McCuaig & Kerrich, 1998). The Al and Na of the actinolite (see appendix D & F), cannot be accommodated by quartz and carbonate. The released Na is probably incorporated in the crystallisation of hydrothermal white mica in the rock. Indications for this are that the hydrothermal muscovite contains on average more Na (0.6 wt-% NaO) than its parents, epidote (0.01 wt-% NaO) and chlorite (0.01wt-% NaO) (see below). The Al of the actinolite can either be transported away by the fluid and contribute to the formation of hydrothermal muscovite or kaolinite, or form very fine grained kaolinite in the quartz rim around the original actinolite grain. Regarding the latter, the rim is very fine grained and a definite answer cannot be given due to the limits of the instruments used.

Hydrothermal mica which replaces epidote in BUL3C is chemically very different to the epidote (Fig. 4.3.7). Relative to epidote, the high Ba, K, Rb, Cs and Mg content in mica reflects the ability to accommodate these elements in its crystal structure (see above) and also that these elements are mobile during the alteration of the greenschist (Fig. 4.2.6 & 8). Of these elements, Ba, K, Cs and Rb were brought into the rock with the fluid (Fig. 4.2.8), while Mg comes from chlorite and/or actinolite. Th and Pb in the hydrothermal muscovite is strongly suggested to be derived from the epidote as it is rich in these elements (Fig. 4.3.6), compared to the other potential sources (actinolite, chlorite, titanite, calcite). Another indicator for this is that epidote and the replacing mica have similar ratios of Pb to Th and Th to U. The hydrothermal mica's much lower concentrations in REE than the epidote suggest that it cannot accommodate these elements. This is in agreement with the metamorphic muscovite analysed which also contains only small concentrations of REE. The similar REE content suggests that in both cases, the micas contain the maximum content of REE possible. Overall, the metamorphic muscovite is chemically very similar to hydrothermal mica (Fig. 4.3.12). Both have smaller concentrations of Sr than Ba, have low concentrations of the REE and flat REE patterns. However, the hydrothermal muscovite contains more Cs, Rb, but less K, Mn and Mg than the metamorphic muscovite (Fig. 4.3.12). In both cases, the trace element content is a clear reflection of the mica's ability to accommodate only certain elements.

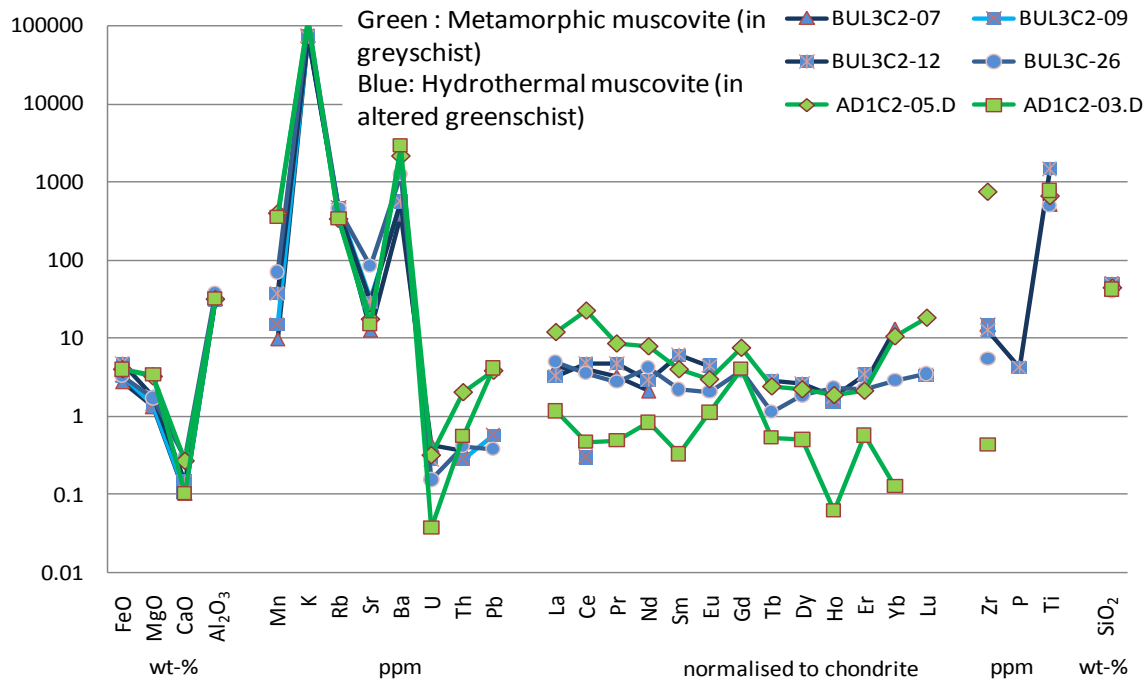

Fig. 4.3.12) Selected major and trace element concentrations of metamorphic (green) and hydrothermal muscovite (blue).

Concerning the ankerite that forms from the breakdown of chlorite in BUL3C (Fig. 4.3.5A), the Ca, Sr and the REE in the chlorite-replacing carbonate (Fig. 4.3.5) cannot be supplied by the chlorite as chlorite is poor in Ca, Sr and REE (Fig. 4.3.4). This is also true, if all of the chlorite's Ca, Sr, and REE is concentrated in the ankerite, which only occupies about half of the original chlorite site, while the rest is accommodated in hydrothermal muscovite (Fig. 3.2.11 C&D). It has been shown in section 4.2.4, that Sr is brought into the rock with the fluid and hence at least some of the ankerite's Sr probably comes from the fluid. Ca and REE need to come from within the rock as these elements show either depletion (Ca; Fig. 4.2.6) or no change (REE (Fig. 4.2.7) in response to the alteration. Based on the previous discussions, the source for the REE and Ca is most likely epidote and potentially titanite. The positive Eu anomaly in the chlorite-replacing ankerite (Fig. 4.3.5) suggests that either the source had a positive Eu anomaly or that Eu had different chemical properties compared to the other REE. Concerning the source, neither epidote nor titanite have a positive Eu anomaly (Fig. 4.3.7 & 11), hence not supporting the first hypothesis. In the second case the Eu anomaly would be attributed to the differing behaviour of Eu when it is in divalent rather than trivalent state (Bau, 1991). Eu^{2+} has not only a similar ionic radius to Sr^{2+} but also the same charge, which should give it similar properties regarding its solubility and partitioning into the carbonate's crystal lattice. The interpretation that the fluid had a low oxygen fugacity, which is necessary for divalent Eu to be stable (Bau, 1991), is supported by abundance of pyrite and other sulphides in the sample (BUL3C) and which are spatially and temporarily associated to the veining and alteration event (Fig. 3.2.7).

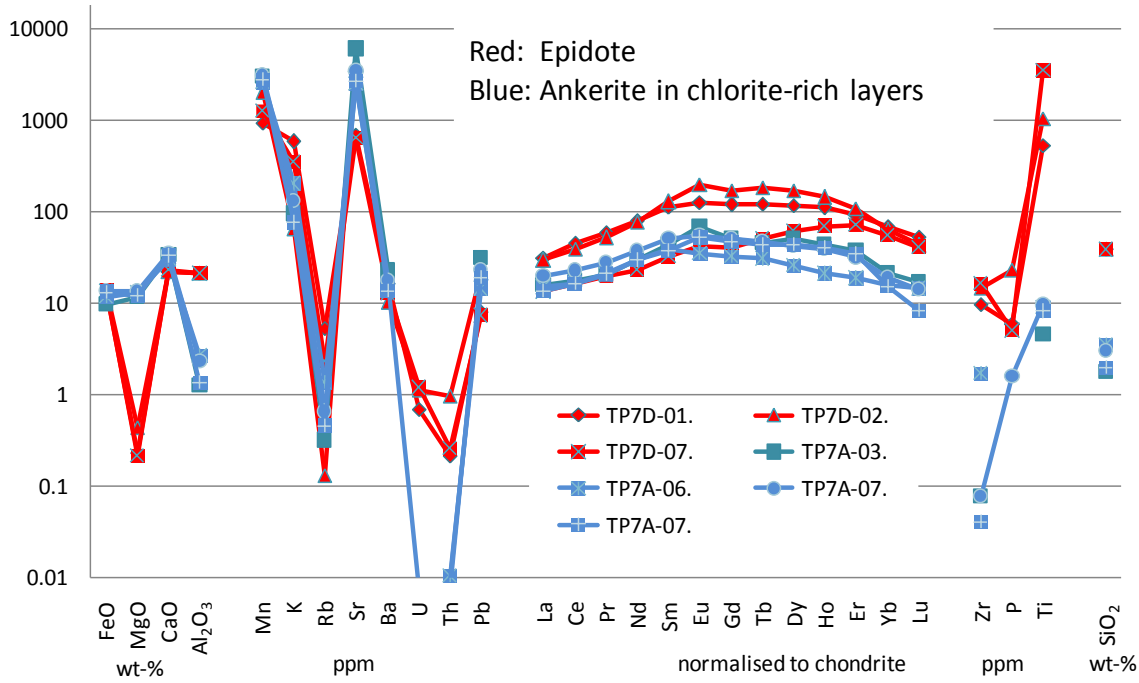

Fig. 4.3.13) Major and trace element composition of metamorphic epidote in TP7D and ankerite in chlorite-rich layers in TP7A.

As mentioned earlier, due to the LASER beam size analyses of titanite and its replacement products (rutile, quartz and carbonate) are often contaminated by phases adjacent to the grains. In the cases here, the increase of K, Ba and Rb is related to contamination by the REE-poor hydrothermal muscovite, which is ubiquitous in the altered rock (Fig. 3.2.11C&12). Nevertheless, as muscovite is poor in most other trace elements, the differences observed for Sr and REE between titanite and its replacement aggregates can be attributed to element mobility. In the replacement of titanite, the increase of Sr (Fig. 4.3.11) can be attributed to the accommodation of fluid-derived Sr in the carbonate which is part of the titanite replacement assemblage (Fig. 3.2.11C). The REE identified in the analyses of titanite replacement products are most likely accommodated in the calcite, as the main cations in rutile (Ti^{4+}) and quartz (Si^{4+}) are much smaller (<0.042nm) than the trivalent REE cations (>0.86nm), disabling these two minerals to accommodate large amounts of REE. The change of REE patterns between titanite and replacement products clearly shows again (as in the case of chlorite and epidote replacement in this sample) that the REE are mobilised on a microscopic scale. Mobility of REE derived from the replacement of metamorphic titanite at T<200°C corresponds with results of Horie et al. (2008). The flat REE pattern of the titanite replacement product assemblage is similar to the ankeritic veins (see chapter 5) and ankerite replacing chlorite in this rock, though concentrations are about an order of magnitude higher. The similarity of REE patterns may indicate that in the central parts of the alteration halo, the fluid homogenised regarding REE prior to precipitation of the alteration minerals. However, although there is ample of evidence for REE mobilisation on a µm to mm scale, there is no indication that the REE in this sample are mobile on cm- scale as has been shown above (see Fig. 4.2.7).

4.3.9.2-2: Epidote and chlorite replacement in the Treble Cone Transect

Of the carbonate types described in Fig. 4.3.9, only the origin of the ankerite in the chloritic layers is the replacement of chlorite and that of epidote (chapter 3.2.2). A clear sign that chlorite contributes to ankerite is that the carbonate contains Mg which is not a component of epidote and the only possible Mg source in the rock is chlorite. Fe in the ankerite can be derived from the epidote but also from chlorite (Fig. 4.3.15). On the other hand the REE give clear indication that the carbonate also

obtained elements from epidote; the REE patterns of this hydrothermal ankerite are similar to epidote in the unaltered sample (Fig. 4.3.13) suggesting that the REE are mostly derived from epidote, especially seeing that chlorite does not contain significant amounts of REE. Concentrations of U and Th on the other hand are lower than in epidote (Fig. 4.3.13), which is consistent with the carbonate's inability to take these elements (too high charge (tetra-rather than divalent, too small ionic radius; Shannon, 1976).

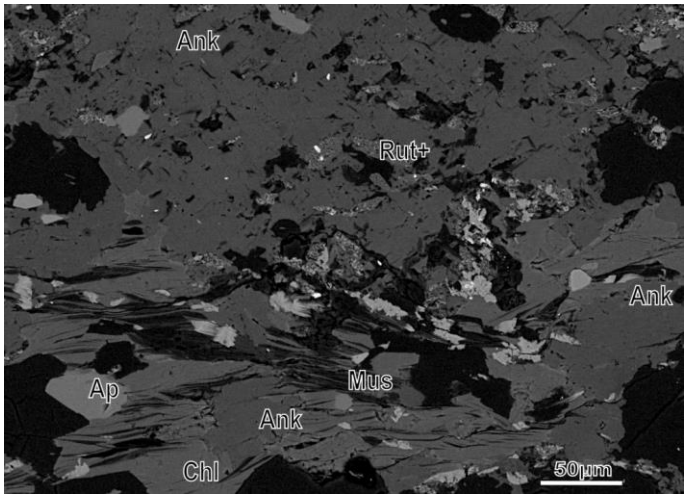

Fig. 4.3.14) The ankerite in the poikiloblastic spots in RR19 are chemically homogeneous and are have the same content in major components as the carbonate in chloritic layers, as can be inferred from the same and monotonous grey scale.

4.3.9.2-3: Calcite replacement by ankerite

Based on the groupings and linear trend identified in Fig. 4.3.9 B&C, it is suggested that with the replacement of calcite by ankerite in TP7A, LREE and MREE are transported into the calcite site. Admittedly, the difference in concentrations is small and it could be argued to be related to pre-alteration differences. However, a mobility of LREE and MREE would be supported by findings related to the replacement of the calcite spots in RR18 and RR19, where the ankerite replacing the calcite has a considerably different REE composition to the calcite in the unaltered sample (Fig. 4.3.10). Assuming the metamorphic calcite was similar to the calcite in RR18, this would mean that with the Fe and Mg, LREE and MREE were brought into the replacement site. The reason why the change of REE in TP7A is not as distinct as in RR19 may be the "intermediate" replacement status of the carbonate in TP7A; in RR19, ankerite has the same composition throughout as can be inferred from the same grey shade in BSE images in Fig. 4.3.14. The ankeritic carbonate in TP7A is chemically zoned and original calcitic parts are still present in the grains (Fig. 3.2.18 C-E) unlike the chemically homogeneous ankerite in RR19 (Fig. 4.3.14). Additionally, the Mg, Fe and Ca content of the ankerite in the leucocratic layers differs from that in the chloritic layers, which is more Fe-rich (Fig. 4.3.15). These are signs that the carbonate in the altered rock of TP7A did not reach equilibrium throughout the rock, unlike in RR19. As with the replacement of calcite by ankerite, the content of Mg and Fe will increase, the content of these two elements are a measure of progress of replacement and in this case also the degree of disequilibrium. Fig. 4.3.15 B&C shows that there is an about linear trend of Mg and Fe content and Ce/Lu supporting above statements. The independence of Sr and Fe content shown in Fig. 4.3.9 C shows that Sr must -compared to the REE, Fe and Mg- circulate through the rock freely and is also quite abundant.

Concerning the Eu anomaly depicted in Fig. 4.3.10D, the trend of a high anomaly in older structure to lower anomalies in younger ones, can either be attributed to different sources or a change in the dominant Eu ion. If the latter is the case, this succession would mean the oxygen fugacity increased during the alteration and veining event in this sample and hence that first divalent and then trivalent Eu was available to the crystallising carbonate.

4.3.9.3: On the Mg:Fe ratio of metamorphic minerals, the replacing ankerite and sulphides

Ankerite forming from chlorite breakdown often also has a higher Mg/Fe ratio than the precursor chlorite (Fig. 4.B) and hence requires that either Mg is added to the site or Fe extracted from the replacement site. In the Bullendale Transect, addition of Mg from actinolite, the only other major Mg bearing mineral, in those rocks can be disregarded as there is no indication that Mg and Fe from actinolite are mobilised as the ankerite has the same Mg: Fe ratio as the actinolite it replaces (Fig. 4.A). Consulting, the whole rock composition, addition of Mg from an external source also did not take place. This points towards chlorite-derived Fe having been incorporated by another alteration-related mineral. The hydrothermal muscovite contains only very little Fe (<1%). The other possibility are the alteration related sulphides, i.e. pyrite and chalcopyrite (MacKenzie et al., 2007 and references therein) and the ankerite replacing calcite in the leucocratic layers. As calcite in the leucocratic layers is only unstable at very intense degrees of alteration compared to chlorite, sulphides as Fe-sink are plausible. This coincides with hydrothermal sulphides predominantly occurring in the chloritic layers (Fig. 2.C.1). In the Treble Cone Transect the ankerite also has partly a higher Mg:Fe ratio than the chlorite which can be explained in the same manner as the rock also contains hydrothermal sulfides in the chloritic layers. Some of the Mg and Fe are also in the ankerite in the leucocratic layers. However, the Mg content of this carbonate is proportionally bigger than the Fe content (compared to the chlorite (Fig. 4.3.15A) which again supports that some of the chlorite's Fe is incorporated in the hydrothermal pyrite.

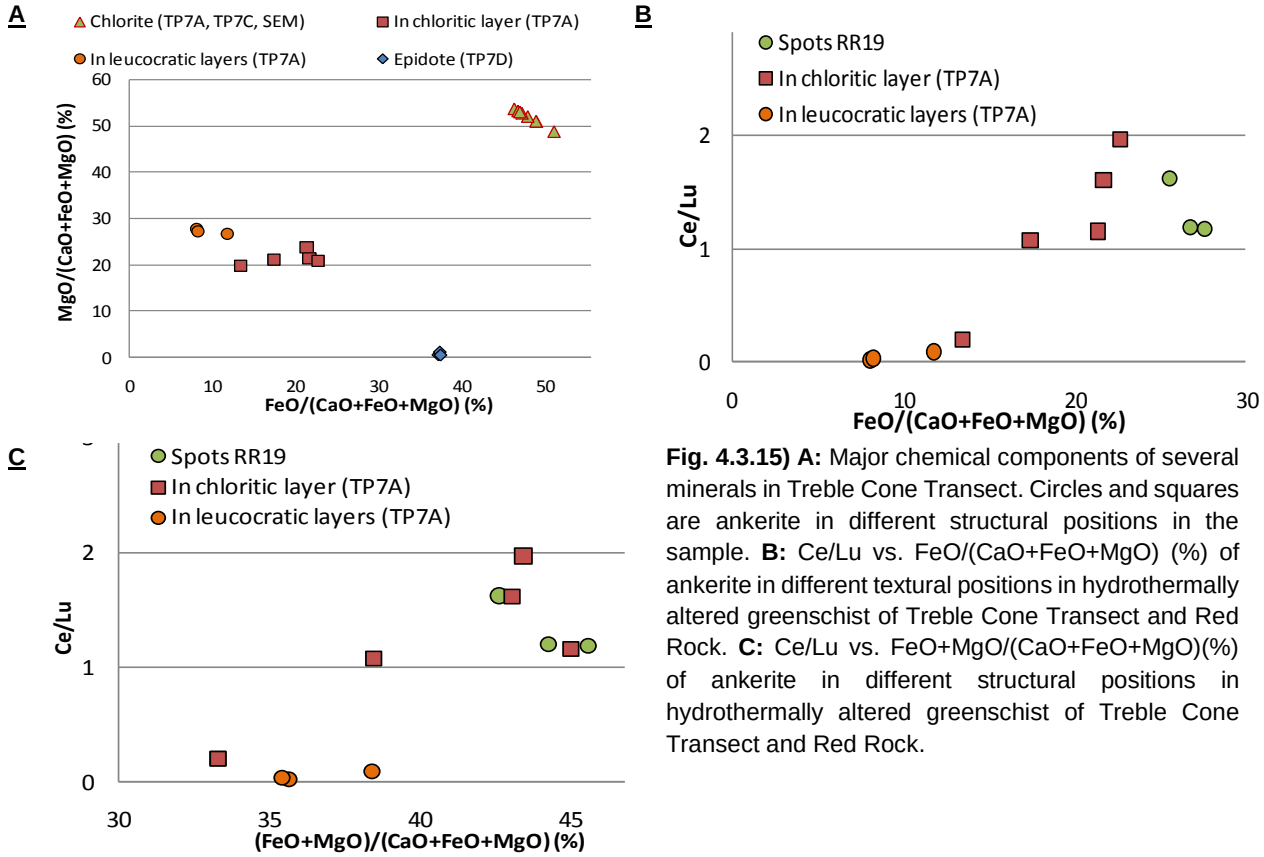

Fig. 4.3.15) A: Major chemical components of several minerals in Treble Cone Transect. Circles and squares are ankerite in different structural positions in the sample. **B:** Ce/Lu vs. FeO/(CaO+FeO+MgO) (%) of ankerite in different textural positions in hydrothermally altered greenschist of Treble Cone Transect and Red Rock. **C:** Ce/Lu vs. FeO+MgO/(CaO+FeO+MgO)(%) of ankerite in different structural positions in hydrothermally altered greenschist of Treble Cone Transect and Red Rock.

4.4) Synthesis of the textural and chemical changes in the studied alteration halos

4.4.1- Mineralogical and chemical differences between the different Transects

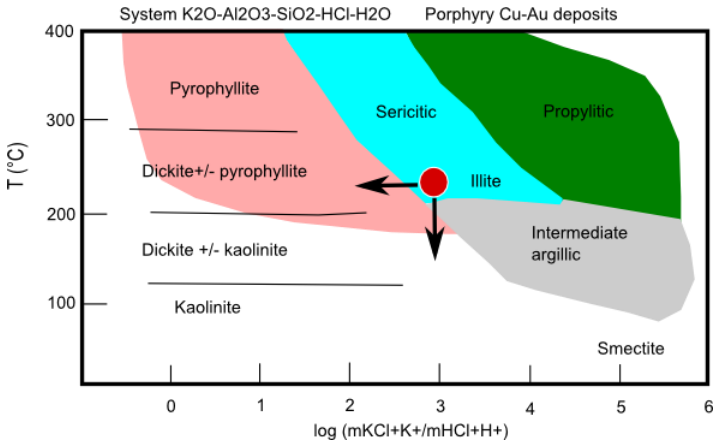

Fig. 4.4.1) Alteration styles and phyllosilicate assemblage in dependence of K^+/H^+ ratio and temperature. Pressure@1kbar. Modified after Tosdal et al. (2009). Red dot is a representative composition of the fluid at Bullendale. The growth of kaolinite in the greenschist of Treble Cone can be due to a fluid with a relative lower K/H+ ratio or a lower temperature.

In chapter 3.2 it has been shown that there are some major differences between the greenschist sets from Bullendale and Treble Cone/ Black Peak Transect. In the samples from Treble Cone/ Black Peak, muscovite breaks down, the absolute K content decreases or only slightly increases, kaolinite forms -especially in TP7- and epidote-derived Al is mobilised locally. In the Bullendale samples, on the other hand, muscovite grows, the rock overall gains K, and Al derived from epidote breakdown is immobile. Whether muscovite or kaolinite is stable during the alteration, depends essentially on the K^+/H^+ ratio (Tosdal et al., 2009). If this ratio is high enough muscovite is stable, otherwise it is hydrous Al-silicates, like kaolinite or pyrophyllite (Fig. 4.4.1). There are three ways this variation in mineralogy can be achieved:

1) low pH in the fluid
2) low K concentration in the fluid
3) low temperature in the system (rock and fluid)

1) The increase of the rock's total Fe and Mg in theTreble Cone Transect (TP7) support a lower pH than in the other systems, as the solubility of Fe-and Mg carbonate increases in a fluid with a lower pH. At the same time it also increases the solubility of Ca, but calcite may already be closer to saturation than siderite and magnesite, or dolomite for that matter. A possible insight gives chemical analyses of warm springs analysed by Barnes et al. (1978). Calculations of saturation regarding the main carbonate mineral species in these fluids (using the program "The Geochemist Workbench" (=GWB); Table. 4.4.1) show that the waters are generally more saturated in calcite than magnesite. The same is true regarding Fe in water from Copland River.

2) At Bullendale, the fluid contained abundant K as is evident by the overall increase of K in the rock. At Treble Cone the K content decreases in the TP7 set, suggesting the fluid was potentially "undersaturated" in K and could hence dissolve some of the rock's K and transport it out of the system. An indication that this may have been the case is that the similar rock type at TP4, which have a similar breakdown paragenesis as the TP7samples, but no obvious depletion in K. It is however not supported by Barnes data as K concentrations increase with decreasing pH.

3) As has been shown earlier (Fig. 2.4) alteration of rocks at Treble Cone could have been at a slightly shallower depth than those at Bullendale (chapter 2.3) and hence the ambient temperature would have also been lower than in the Shotover. Referring to Fig. 4.4.1, it shows that fluids with the same

H/K ratio can form different alteration related minerals by lowering the temperature (Tosdal et al., 2009 and references therein). Coupled with that is also that the fluid may have been different chemically due to a closer connection to solute-poor meteoric waters.

Considering the difference in settings and the reconstructed lower crustal levels of formation (see chapter 2), option 3 is probably most likely the controlling factor in the sets studied.

Table 4.4.1) Excerpt of the spring analyses by Barnes et al. (1978) and calculated saturation (the more negative the number, the more undersaturated the fluid is regarding the mineral. The more positive the more saturated). Note: low Fe is in Wanganui sample due to oxidising conditions (trivalent=close to insoluble compared to Fe2+).

Sample ID	Unit	Copland River	Waiho River	Lower Wanganui River	Upper Wanganui River
Temperature	C	56	43	40	40
pH	pH	6.1	6.18	6.45	6.9
Ca++	mg/l	87	26	15	13.2
Mg++	mg/l	4.5	1.9	1.8	0.55
Fe++	mg/l	0.65	0.75	0	0
Aragonite	log Q/K	-0.4508	-1.087	-1.457	-0.9676
Calcite	log Q/K	-0.2892	-0.9239	-1.294	-0.8046
Magnesite	log Q/K	-1.717	-2.337	-2.536	-2.51
Siderite	log Q/K	-0.4911	-0.5947		

4.4.2-Chemistry of the fluid

Concerning the CO_2 content of the fluid within the alteration halos, no direct measurements, i.e. fluid inclusions, were carried in this study out. However, some information may be gained from the previous studies researching this area. In hydrothermal quartz related to the gold mineralised systems in the Shotover, fluid inclusions are made of CO_2 and salt-poor hydrous fluids (Craw, 1989, 1991; Koons & Craw 1991, Craw et al., 2009 and references therein). At Mt Alta, fluid inclusions in hydrothermal quartz reported by Clough (1988) suggest pure water to CO_2-bearing hydrous fluids. These mostly CO_2-poor fluid inclusions stand in stark contrast to the abundance of carbonate minerals and the carbonate species (i.e. siderite) as these show clearly that abundant CO_2 passed through the system. Regarding this there may be the answer in Craw (1989), who describes a fluid inclusion predominantly made of CO_2. This shows that CO_2 may have been in the fluid, but was exsolved due to immiscibility with decrease in pressure and/ or temperature. Also, the fluid captured in the quartz most likely does not resemble the fluid forming the carbonate in the veins and alteration halo. This would coincide with the statements made earlier that fluid chemistry probably changed during the time of fluid flow and precipitation along a structure. Overall, based on the textural evidence, such as carbonate at vein rims and quartz in the centre and structure of silicified breccias (Fig. 2.3. 9), I suggest that in each pulse of fluid low, fluid was initially relatively CO_2-rich but became overall successively CO_2 poorer which would also enhance a higher solubility of quartz over carbonate (Walther & Orville, 1983). The multiple veining events, observed in several examples (i.e. Fig. 2.3.3; 3.2.13) show that this cycle could repeat several times. However, nonetheless the absolute CO_2 cannot be determined with these methods.

The lack of fluid inclusion data in minerals directly related to the alteration events in the wall rocks requires exploration of other means potentially giving insight into the CO_2 content of the fluid and thermodynamic models can be used to gain information about the fluid composition (Will et al., 1990; White et al., 2003; Craw, 2002). As mentioned in the previous chapter, the thermodynamic

model presented in White et al. (2003) calculates the alteration assemblage of a greenschist similar to the greenschist set from Bullendale. White et al.'s model also shows that the fluid requires only relatively little CO_2 to first break down amphibole (at 300°C about 0.05% of fluid), then clinozoisite (at 300°C about 15% of fluid) and only at very high CO_2 contents (at 300°C about 80% of fluid) does chlorite break down. A relatively CO_2-rich fluid necessary to break down chlorite correlates well with findings here, where chlorite is only entirely replaced in close proximity to the altering feature (BUL3C/4C). Nevertheless 80% for the chlorite-out reaction is unrealistically high. Concerning this "problem", it needs to also be noted that the temperature in the wall rock here was well below 300°C (the lowest temperature modelled by White et al. (2003)). This statement is based on the shallow depth (< 6km) of formation of the structures here. With a geothermal gradient of 30°C this is a maximum temperature of 180°C. Even when considering that the fluid would have raised the temperature it does justify a temperature in the wall rock of 300°C. Experiments by De Caritat et al. (1993) show that stability of chlorite with CO_2 increases about exponentially with increasing temperature which is dependent on the chlorite composition and salinity of the fluid. However it is noted that their chlorite is sub-greenfacies chlorite with a different chemical composition than the chlorite in the greenschist facies rocks here. Additionally, the minerals studied in the rocks here are in a metastable state as they are greenschist facies rocks at sub-greenschist facies conditions. Hence pure influx of fluid would drive reaction in the wall rock as it would provide means of element transport and activation energy. Hence, none of the available information described above can give us a solid estimate for the CO_2 content in the fluid. Instead, only a maximum estimate can be given by considering immiscibility curves of fluids. Referring to Fig. 15 in McCuaig&Kerrich (1998) a fluid with low salinity at around 200°C and about 1.5-2 kbar would be exsolve gas at about 9 mole-% dissolved CO_2, which would be a maximum CO_2 content.

Concerning other aspects of the fluid chemistry causing the alteration, the stability of apatite suggests that the fluid inside the rock had a pH around neutral to basic, as it has been shown that apatite solubility increase strongly with a increasing acidity (Guidry & Mackenzie, 2003; Harouiya et al., 2007, Somasundaran et al., 1985; Valsami-Jones et al., 1998). This is also supported by the precipitation of carbonate in the wall rock and in the vein, which becomes less soluble at higher pH (Manning et al., 2013 and references therein).

In all cases studied, there is an increase of the sulphide - generally pyrite - content towards the altering feature, hence showing that the fluids also contained sulphur. The succession of tetrahedrite-chalcopyrite-pyrite in the greenschist from Bullendale show in addition to S, Cu and Sb were transported by the fluids and the content of these components probably changed over time. The variation of these components could be related to a difference in other components in the fluid. For example, an increase in Cl content causes a higher solubility of Cu in hydrothermal fluids (Seyfried & Ding, 1993; Hemley et al., 1992; Liu & Phail, 2005). Another factor causing this Cu mineralisation may be that Cu is enriched in greenschist relative to greyschist (Pitcairn, 2004).

4.4.3 - Comparison to mesothermal gold deposits in the Shotover and in other parts of the world

Although partly spatially closely associated (in the Shotover-hosted cases), none of the alteration halos discussed in chapter 3 and chemically characterised in this chapter are directly connected to gold deposits. Nonetheless, the mineral reactions and chemical changes described in chapter 3 and 4 are very similar to those found in many mesothermal gold deposits (Davies et al., 1990; Bierlein et al., 1999 & 2000; McCuaig & Kerrich, 1998 and references therein, White et al., 2003). Similar to orogenic gold deposits (Bierlein et al., 1999), there is no large scale mobilisation of the REE in any of the halos studied.

In the study area, fault zones that have been identified in the past to contain gold are the faults at Copper Creek and Bullendale Creek (Craw et al. 2006; MacKenzie et al., 2007). The alteration in the

rock adjacent to these fault zones are partly described in chapter 2.3.1.4 and are shortly summarised here: In the highly altered greenschist taken in the hanging wall of the fault of Copper Creek, chlorite has been entirely replaced by kaolinite, magnesian siderite and ankerite and quartz (COP 1E; Fig. 2.3.8) in accordance to Rea. 4.e &f (in chapter 3). In the greyschist sampled from this fault zone (COP1A, COP2B, Fig. 2.3.9), the carbonate forming in the wall rock is ankeritic and muscovite is replaced by hydrothermal mica, which is similar to alteration associated with the Bullendale Reef (MacKenzie et al., 2007). The reason why there is different phyllosilicate mineralogy is likely not the result of different fluid compositions coming into the rock, but actually show the influence of the wall rock's composition. Greyschist contains abundant muscovite while greenschist does not; in the alteration halos components from the fluid and wall rock mix and hence in greyschist the K/H ratio would have been higher than in greenschist, causing the hydrothermal muscovite to be stable in the greyschist but not greenschist. As both greyschist samples were taken within a few cm of the fault, this shows that in the wall rock even close to the fault the mineral crystallisation was not fully fluid-buffered or that chemical equilibrium was not attained. Considering that in the greyschist samples metamorphic muscovite has only been replaced at the grain rims, supports non-equilibrium between greyschist and fluid.

The growth of kaolinite in the greenschist at Copper Creek is different to the growth of muscovite in the greenschist from Bullendale. At the same amount of K in the fluid this would require a lower pH or lower temperature (Fig. 4.3.1). Considering that both deposits formed at a similar depth, the temperature in the Copper Creek fault-related halo was most likely not colder than the rock at Bullendale, and hence a difference in temperature is unlikely the reason for the different phyllosilicates forming. The fluid in the case of the Copper Creek fault hence probably had a lower K^+/H^+ ratio than in the Bullendale examples, which would equate to a lower pH (taking the K content is similar). A lower pH in the fluid would also correspond with conclusions drawn in chapter 2.3.4 that the texture of the in the silicified fault breccias formed by lowering of the pH in the fluid. A neutral to slightly acidic pH has been proposed for the fluids in mesothermal gold deposits, supporting this hypothesis (Bierlein et al., 1999; Craw, 1989; Davies et al., 1990; McCuaig & Kerrich 1998 and references therein; Yardley et al., 1993).

For gold to precipitate in these environments, it has been shown that S is necessary to be present in the fluid, as gold is generally considered to be transported in complexes with HS^- (Seward et al., 2014) and precipitation of gold can be formulated as:

$Au(HS)_2^- + 0.5\ H_2 \rightarrow Au(s) + H_2S + HS^-$ (Phillips & Powell, 2010)

Gold solubility is highest around the pH where the concentration of HS^- and H_2S are equal and concerning oxygen fugacity at only slightly reducing conditions (near the hematite-magnetite transition, within the pyrite stability field; e.g. Craw, 1989; Phillips & Powell, 2010). The transition of $[HS^-] = [H_2S]$ is close to the carbonate buffer $[H_2CO_3] = [HCO_3^-]$. The abundant carbonate in the veins and altered rock clear gives evidence for carbonate species in the fluid. Above relationship between sulphur and carbonate is likely the reason why a pH favourable for a high gold solubility can be maintained in the fluid whilst it passes through the rock (Phillips & Evan, 2004).

The main sulphide found in the alteration halos studied in chapter 3 is pyrite. As discussed and formulated earlier, the S comes into the rock as H_2S or HS^- with the fluid and this S then reacts with Fe from chlorite, epidote and muscovite to form the pyrite.

$2H_2S_{(aq)} + Fe_2O_{3(in\ ep)} \rightarrow FeS_2 + FeO_{(in\ carb)} + H_2O$ (Evans et al., 2006)

$2HS^-_{(aq)} + FeO_{(from\ silicate)} \rightarrow FeS_2 + H_2O$

A major difference between the gold-bearing and gold-barren alteration halos in this area in the presence of arsenopyrite. Arsenopyrite together with pyrite can be found abundantly in the altered wall rock but also in the fault breccias, where they are generally found in the matrix embedding the quartz grains (Fig. 2.3.7). At Bullendale and Copper Creek the arsenopyrite formed after pyrite did. Additionally, in many cases the pyrite has been corroded at the grain edges, hence shows that it was destabilised again after its formation. The arsenopyrite, which often grows around the pyrite, on the other hand, shows no such features and instead forms well developed crystals (Fig. 2.3.8).The arsenopyrite producing equation is:

$2\ FeO_{(from\ silicates/\ pyrite)} + H_3AsO_{3\ (aq)} + 0.5H_2O + 3H_2S \rightarrow FeS_2 + FeAsS + 5H_2O$ (Craw et al., 2009

Overall, in all orogenic gold deposits in the Southern Alps, Au mineralisation is closely associated with arsenopyrite (Craw et al., 2009) and is also in other mesothermal gold deposits around the world (i.e. Genkin et al., 1998; Morey et al., 2008; Mumin et al., 1994) though neither elevated As nor Hg or Sb contents in the hydrothermally altered rock are necessarily an indicator for Au mineralisation (MacKenzie et al., 2007, McCuaig & Kerrich 1998 and references therein). The dependency of arsenopyrite and gold may have several reasons, such as a common source (Pitcairn et al., 2006, Large, 2012) or could be due to common properties during transport in the fluid (Bessinger & Apps 2003; Pokrovski et al., 2002). At TP4 it has been shown that As concentrations increase minorly towards the centre of the fault (Fig. 4.2.9). However, the As content in the fluid may not have been high enough to promote elevated gold concentrations in the fluid. Alternatively the temperature may have been (also) lower than at the gold deposits in the Shotover.

4.5) Conclusions

In his chapter, chemical changes in the rock caused by hydrothermal alteration and during mineral replacements were examined. Whole rock analyses have shown that in all cases the most mobile element group during the hydrothermal alteration event are the LILE (up to 20 times increase). In the cases examined, the ratios of different LILE suggest that the LILE in the altered rocks (green- and greyschist) are mostly derived from greyschist, which is in agreement that greyschist is more common in the area than greenschist. Another element that can have a strong enrichment is W (up to 35 times). However, W shows enrichment only in the immediate surroundings of the altering feature which suggests that W is only mobile in the fluid, but not the wall rock.

The REE content in the metamorphic minerals is controlled by crystallography and relative partition coefficients. Here, metamorphic minerals with no Ca, e.g. muscovite and chlorite, have low concentrations of the REE (typically <10 chondritic values), while minerals with Ca can contain significantly more REE, such as epidote (>100 chondritic values). Of the Ca-bearing minerals, epidote has the highest partitioning coefficient for the LREE and MREE. This is followed by titanite, calcite and lastly actinolite.

It could further been shown that during mineral replacements not only are various major components of minerals mobile, but also trace elements. It has further been demonstrated that some elements are mobile on microscopic scale, though the whole rock analyses demonstrated that these

are not mobile on a macroscopic scale (>cm). Of all measured elements contained in the alteration-sensitive mineral only titanium is immobile on a micrometers and meter scale.

Above comparisons have shown that during the replacement of minerals the REE can be mobile in some cases (i.e. replacement of epidote, titanite and chlorite in BUL3C) while they are not in others (replacement of epidote by ankerite in TP7). This mobility can directly be linked to which mineral precipitates in the replacement site. Hence, the mobility of REE is not only dependent on the fluid chemistry, but also if the replacing mineral can accommodate the REE. Hydrothermal mica cannot accommodate the REE, hence "forcing" them to remain in solution. However, when carbonate forms as a result of mineral breakdown, the REE are taken up by the carbonate from the fluid immediately after dissolution as they can fit into the carbonate's crystal structure. This hypothesis is in agreement with conclusions made by Köhler et al. (2005) who found that REE during the dissolution of apatite are released into the fluid if this is undersaturated in rhadophane (a phosphate), but are not found in the fluid if the fluid is saturated in radophane. However, although the REE are mobile on a µm to mm scale, whole rock chemical analyses have shown that the REE are not systematically moved further than this within the rock.

The alteration halos studied here are similar to those found around gold-bearing faults, be it in the Shotover area or elsewhere in the world, e.g. Australia. Different between the gold-bearing and gold-barren deposits is that the gold-bearing ones contain arsenopyrite in addition to pyrite and the phyllosilicate mineralogy in the altered rock (kaolinite rather than muscovite in the altered greenschist), suggesting a different, potentially more acidic, fluid chemistry in the gold-bearing deposits.

CHAPTER 5) MAJOR AND TRACE ELEMENT CHEMISTRY OF HYDROTHERMAL AND MAGMATIC CARBONATE

In the study areas, there are 6 main settings where carbonate occurs: 1) in veins, 2) in breccias, 3) in ocelli, 4) in vesicle fillings, 5) as replacement products due to the breakdown of minerals in the wall rock, and 6) as primary phases in the metamorphic wall rock. In this chapter carbonate of the first 4 and some of the fifth type is described and discussed. Most of types 5 and 6 were discussed in the previous chapter.

Hydrothermal carbonate as vein filling, like it is described here, is a precipitate from a fluid. As such, it gives insight into several aspects of fluid chemistry, metal transport and component sources. In this chapter, I will discuss the chemical composition of the carbonate from the different settings in order to establish what controls the chemical composition of the carbonate. A special focus was again put on the REE chemistry of the carbonate. Studying the chemical behaviour of the REE has been part of many studies, be it in hydrothermal fluids (i.e. Migdisov & Williams-Jones, 2007; Haas et al., 1994; Michard, 1989; Bau, 1991) or in carbonates (Ramos et al., 2012; Kontak& Jackson, 1999; Rimstidt et al., 1998; Bau & Möller, 1992; Möller et al., 1991; Bau & Alexander, 2006). Those studies show that the REE composition of carbonates can be very diverse and it is still not well established which aspects control the REE transport in hydrothermal fluids (i.e. Migdisov et al., 2016 and references therein). Analysing carbonate hosted in various settings and lithologies but which formed at similar physical conditions as is the case here can aid in identifying such controls.

In addition to the REE patterns and contents in the different carbonates, I have also investigated the relationships between Sr and Eu contents. This was done as Eu in geological environments can occur as divalent and trivalent ions (e.g. Bau, 1991). Eu^{2+} is similar to Sr^{2+} in size and charge (Shannon, 1976), suggesting these two elements may behave similarly during fluid-driven processes. In its divalent ionic state Eu would hence class as a LILE, which are highly mobile in aqueous fluids, rather than a HFSE, a group of elements (including trivalent REE ions) largely immobile in aqueous fluids (Carmichael, 1969; Floyd & Winchester, 1978; Ragnarsdottir & Walther, 1985). It has already been shown in the previous chapter that there seems to be some relationship between occurrence of pyrite, i.e. reducing conditions, and a relative to the other REE enrichment of Eu in newly growing carbonate (e.g. Fig. 4.3.5). This raises the question, if a consistent correlation between pyrite occurrence, Sr and Eu content can be found in the different void-filling carbonates.

5.1) Samples and methods

Characterisation of the major and trace element composition of the carbonate was done by using the EDS system of the ZEISS SEM, WDS of the microprobes, and by LASER ablation with the ICPMS. The procedure and instruments of these methods are the same as described in the previous chapters. ICPMS data are given in appendix G. Overview of the samples and employed methods are given in Table 5.1.1.

5.2) Overview of texture and chemistry of carbonate

The setting and (micro-) structural features of different carbonate occurrences were described in the previous chapters. A short synthesis of the textures of the carbonate and additional information are given in the following chapter together with their chemical composition. Those sections deal with the mineralogy of the carbonates, their REE patterns, the relationship between Sr and Eu content, and

potential other aspects of chemistry. Unless otherwise stated all values given for the REE are normalised to chondrite.

Note: In some sections the carbonate analysed is very brown and oxidised. However, when comparing their chemical analyses with clear carbonate there is no difference in quality of the carbonates' compositional data. The murky carbonate analysed has its murkiness from many tiny fluid or gas inclusions. For the analyses, the potential contamination by the fluid or gas is negligible for the elements considered.

Table 5.1.1) Sample names, settings and methods employed in each sample.

Sample	Setting	Shown in figure	Chemistry of carbonate (vein/ breccia)	Isotopic composition (Chapter 6)	Alteration of wall rock (Chapter 3&4)
BUL2B	Vein in greyschist, sub-parallel to kink folds	2.3.3 & 4; 13 B&C	YES	YES	YES (BUL2A, 2C)
BUL3A	Vein in greyschist, dilational site in fault, late stage	2.3.10A, blue box	YES	YES	-
BUL3C	Vein in greenschist	3.2.7 A1 & B1	YES	YES	YES
RR20	Sparry vein in greenschist	Fig. 2.3.13	YES	YES	-
RR18	Cc-Vein in greenschist	3.2.23 A&B	YES	YES	YES
RR19	Ank-Vein in greenschist	Appendix H	YES	YES	YES
ALT 1.2	Vein in greyschist block in diatreme breccia	2.4.15	YES	YES	-
ALT2C	Vein in highly altered lamprophyre	2.4.8E & 14	YES	YES	-
AD2B	Vein in highly altered lamprophyre	-	YES	YES	-
AD2A	Vein in little altered lamprophyre	2.4.8 C & D	YES	YES	-
ALT2B	Clastic diatreme breccia	Similar to 2.4.11 A-C	YES	YES	-
COP2C/2B	Silicified Breccia	2.3.9	YES	YES	-
TP1.3	Silicified Breccia	Appendix H	YES	YES	-
AD1B	Silicified Breccia	2.4.12 B	YES	YES	-
ND3B	Ocelli	2.4.2	YES	YES	-
ND1A	Ankeritic marble	2.4.6	YES	YES	-

5.2.1- Veins and faults associated to kink folds

Carbonate from the veins at Murdoch Creek Transect were analysed (Fig. 2.3.3, Fig. 5.2.1). The carbonates in different micro-structural settings are different chemically, which is most obvious in the chondrite-normalised REE patterns. 4 REE patterns are recognised in one sample, the pervasively altered greyschist (BUL2B):

1) Calcite which builds up most of the main vein (stage 1 and 2 in Fig. 2.3.3) has a flat REE pattern with a slight negative Eu anomaly (13-18% less Eu than for a flat pattern) (analysis 5&6). A similar pattern is found in calcite, which is a vein perpendicular to the main vein and within the fault breccia (analysis 7) (Fig. 5.2.1 A&B).

2) Ankerite with a similar orientation as the main vein has also a similar REE pattern as the calcite of 1 but with a slightly positive Eu anomaly (analysis 10).

3) A calcitic veinlet that cuts across the main vein (stage 3) and which is embedded in vein quartz, is highly depleted in LREE and MREE compared to the HREE and has a distinct positive Eu anomaly (analysis 9). This pattern is similar to calcite found disseminated within the wall rock (analysis 2&3).

4) Veinlets in the wall rock have similar LREE concentrations as the ankeritic and first stage calcite in the bigger veins but have considerably and increasingly higher concentrations of HREE+Y (analysis 1&4). The slope of the REE pattern is similar to that of the metamorphic calcite and the late stage calcite in the vein quartz (analysis 2, 3 & 9) (Fig. 5.2.1 A&B).

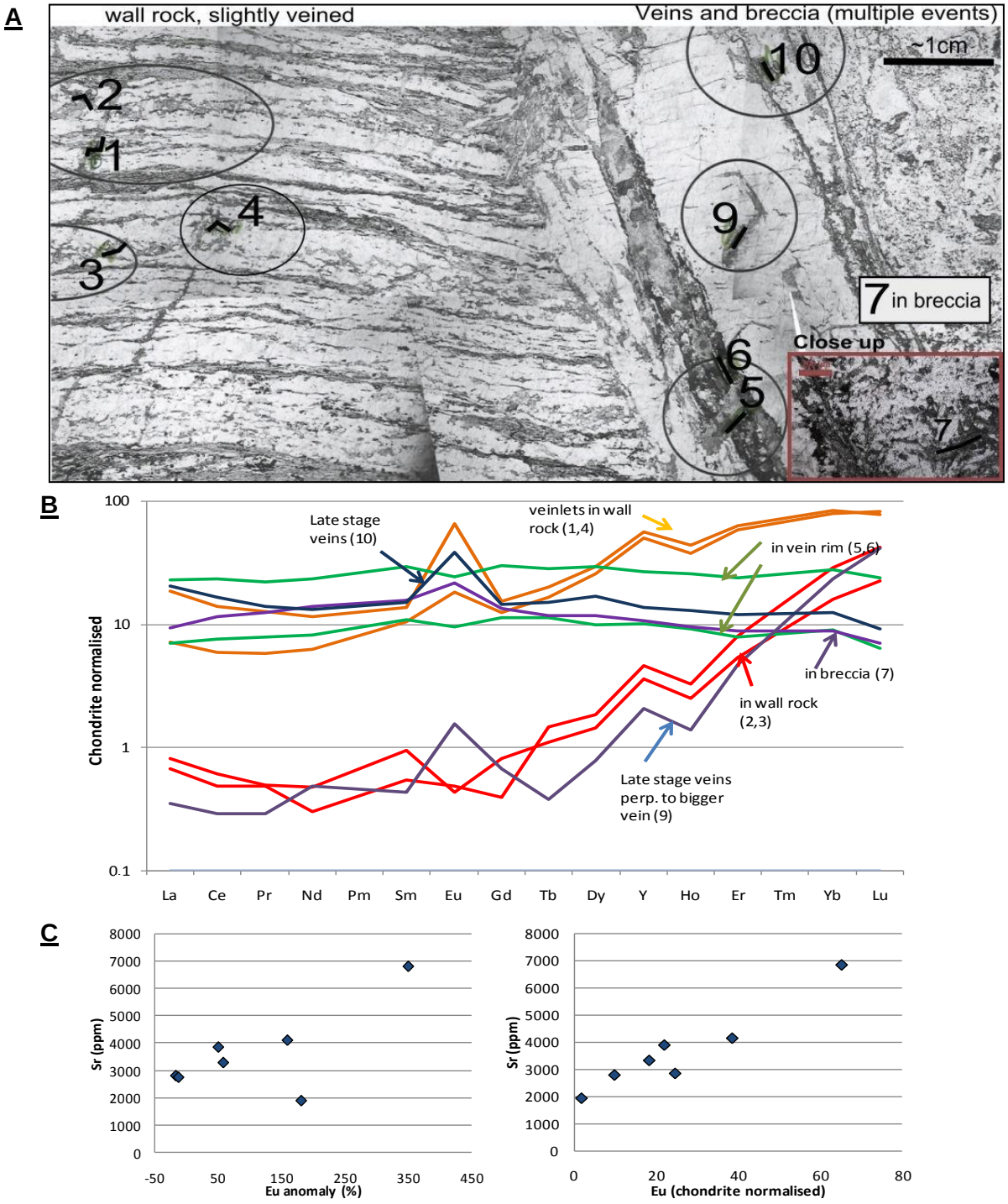

Fig. 5.2.1) A: PPL. Microphotograph with locations of analyses. BUL2B. **B:** REE composition of the carbonate. Numbers correspond to those of the analyses shown in A.**C:** Correlation of Sr and Eu content and Eu anomalies in carbonate in the main vein (no small veinlets in wall rock or metamorphic carbonate are shown).

The veinlets in the wall rock have the largest Eu content and anomalies compared to the other carbonate analyses in this sample. For all vein analyses, the Eu content and size of the Eu anomaly correlates with the Sr concentrations (Fig. 5.2.1C). (Eu* (Eu anomaly)=Eu/((Sm-Gd)/2) all values normalised to chondrite)

5.2.2 - Carbonate in NW dipping fault at Murdoch Creek

Dilatational sites of faults can be sites of calcite precipitation as is, for example, the case in a NW-dipping fault at Murdoch Creek (Sample BUL3A), and which has been described earlier (See Fig. 2.3.10; blue box). The carbonate in these veins is mostly calcitic with only the rims having an ankeritic component (Fig. 5.2.2A). At the rim calcite and ankerite are finely interwoven with each other (Fig. 5.2.2B). Quartz and carbonate at the rim of the veins have euhedral grain shapes and the quartz is partly corroded at its rims and has interconnected inclusions of ankerite (Fig. 5.2.2B).

Trace element analyses have been gathered across the vein (Fig. 5.2.2A). Note that as the trace element compositions are obtained by LASER ablation, the composition of the carbonate at the rim represents the average composition of the intertwined ankerite and calcite. Across the veins, systematic trends of chemical changes are apparent. With an increase of Fe and Mg content, hence bigger ankerite- calcite ratio in the analysis, concentrations of Mn, REE, U, Th and Pb also increase, but there is no change in Sr content (Fig. 5.2.3A). The REE patterns throughout the vein are smooth and without any pronounced Eu anomaly (Fig. 5.2.3B). Nevertheless, the patterns do show mineralogy dependent differences. In calcite in the vein centre, the Pr/ Lu ratios lie between 0.8 and 1.4, whereas the ankerite-influenced ratios at the vein's rim are slightly higher (1.7-2) (Fig. 5.2.3C). A similar increase from calcite to ankerite-dominated parts can also be seen for the La/Ce ratio. (Fig. 5.2.3D). Across the vein there is no correlation between Sr and Eu contents (Fig. 5.2.3E).

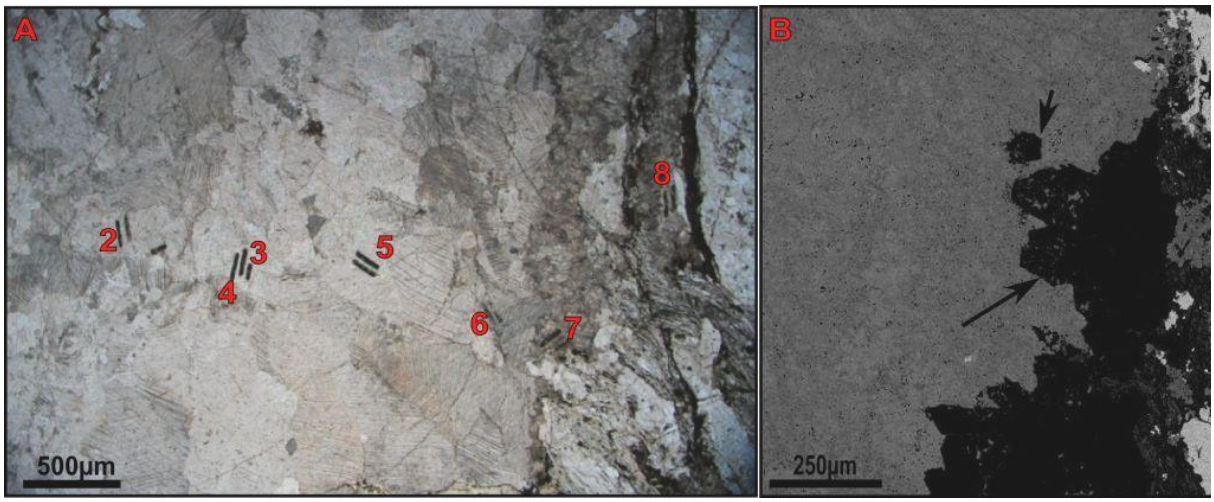

Fig. 5.2.2) A: PPL. Microphotograph with locations of analyses in several cm thick calcitic vein from outcrop B3. Note that analysis 8 is located in a separate branch of the vein. BUL3A. **B:** The rim of the vein is made of a finely interwoven mix of calcite and ankerite (different greyscales). Euhedral quartz grains are partly corroded at the rims (arrows). BUL3A.

5.2.3 - Veins in Greenschist at Bullendale

Of the two samples of greenschist (BUL3C & BUL4C), only carbonate veins from BUL3C were analysed for their trace element composition (Fig. 5.2.3). These are mostly ankeritic, with only some late stage

veins being calcitic. The REE patterns of the vein carbonate have a moderately negative slope with La/Lu ratios ranging from just under 2 up to 11, but lie mostly between 2 and 3 (Fig. 5.2.4B). All veins have positive Eu anomalies (30-123%). Strontium concentrations correlate roughly with the size of the Eu anomalies, but not with the Eu concentration (Fig. 5.2.4C.

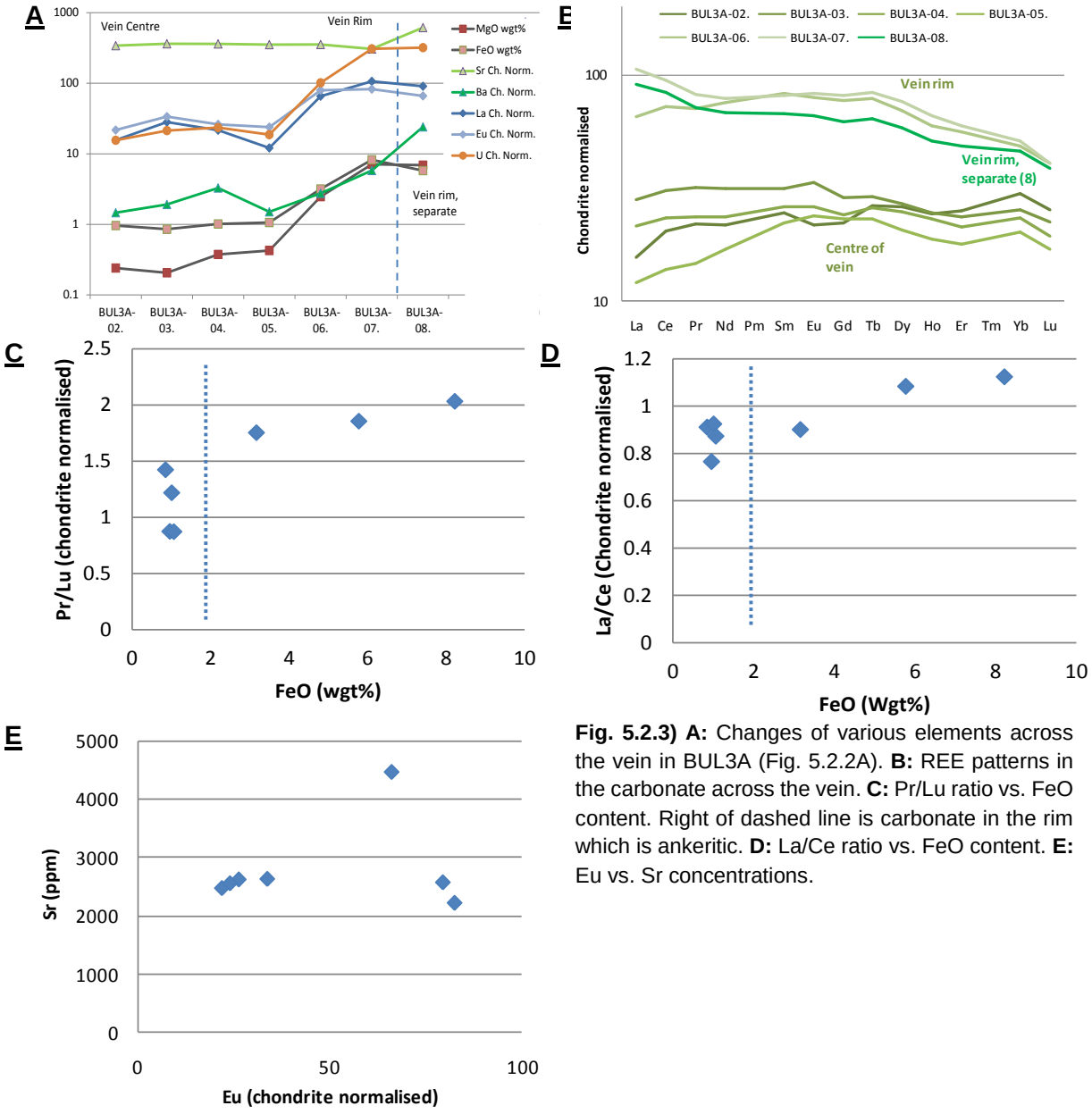

Fig. 5.2.3) A: Changes of various elements across the vein in BUL3A (Fig. 5.2.2A). **B:** REE patterns in the carbonate across the vein. **C:** Pr/Lu ratio vs. FeO content. Right of dashed line is carbonate in the rim which is ankeritic. **D:** La/Ce ratio vs. FeO content. **E:** Eu vs. Sr concentrations.

5.2.4 - Veins in Greenschist at Red Rock

At Red Rock, several cm thick, sparry veins were analysed (Fig. 5.2.5) These veins are mostly made of ankerite and calcite (in the vein centre), embedding chalcopyrite and quartz (Fig. 2.3.13). The calcite is distinctly richer in Sr compared to the ankerite (Fig. 5.2.5B). Both carbonate minerals, however, have very similar REE contents and REE patterns which show enrichment in MREE relative to the LREE and HREE and no distinct Eu anomaly (Fig. 5.2.5B). The Sr content in the different carbonate species is largely independent of Eu (and La) content (Fig. 5.2.5C).

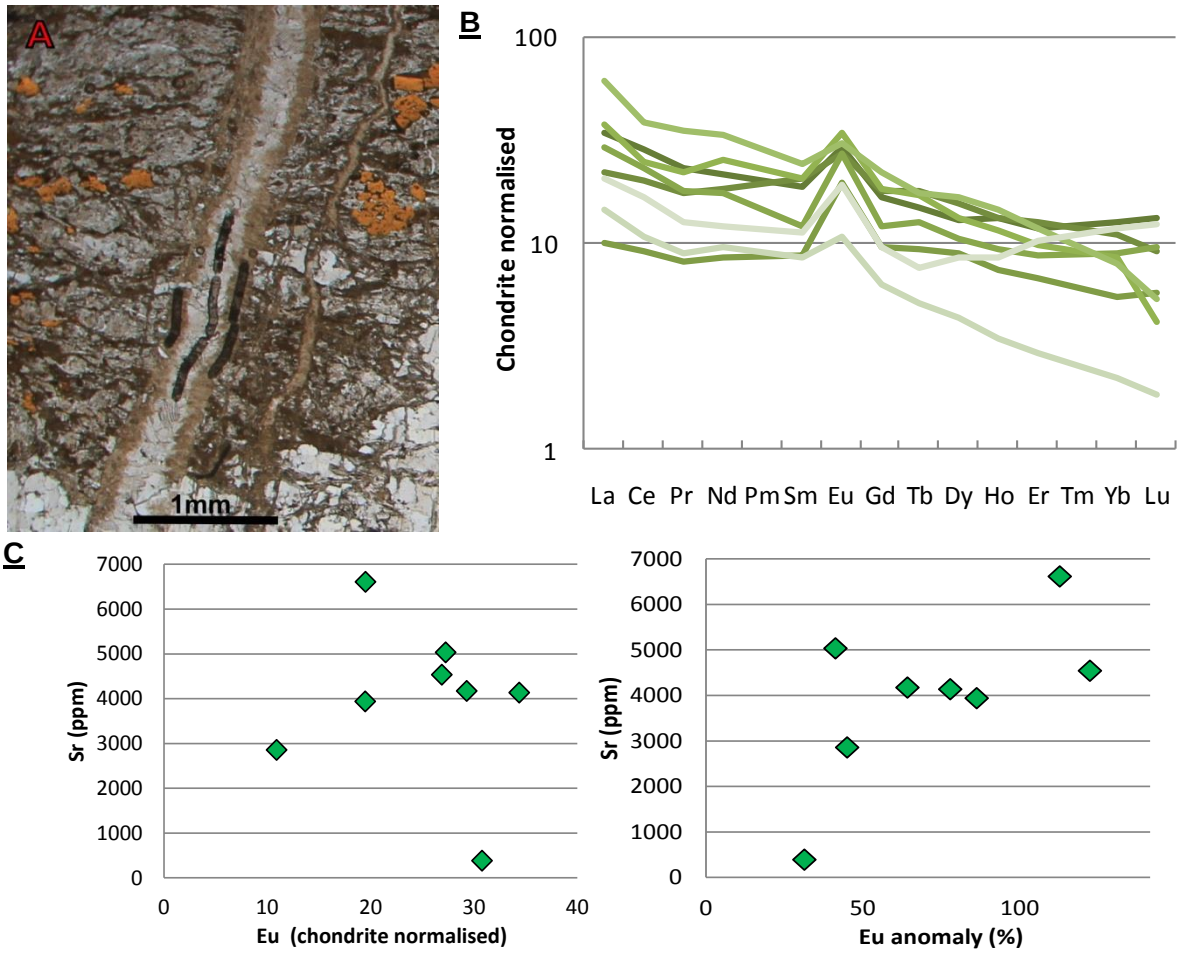

Fig. 5.2.4) A: Example of ankeritic veins in greenschist analysed by LA-ICP-MS. **B:** REE content of the ankeritic veins in greenschist. **C:** Sr vs Eu content and Sr vs Eu anomaly.

In addition to the thick, chalcopyrite-bearing, sparry veins described above, carbonate veins in greenschist that contains poikiloblastic carbonate spots were analysed (RR18 & RR19). One vein type analysed is made of calcite and formed prior to alteration (RR18; Fig. 3.2.23 A&B), while the other is ankeritic and is related to the ankeritic alteration in the Cenozoic. The compositions of these two vein types have already been mentioned in the previous chapter, but will be presented here again for comparison. Regardless of mineralogy, the REE patterns of these veins are similar to those of the thicker sparry veins of RR20 (Fig. 5.3.5 B & 6A). Considering both samples, there is a rough positive correlation of Ca and Sr content (Fig. 5.3.6A). There is no distinct correlation between Eu content and Sr content or between Sr content and the size of Eu anomaly (Fig. 5.3.6B).

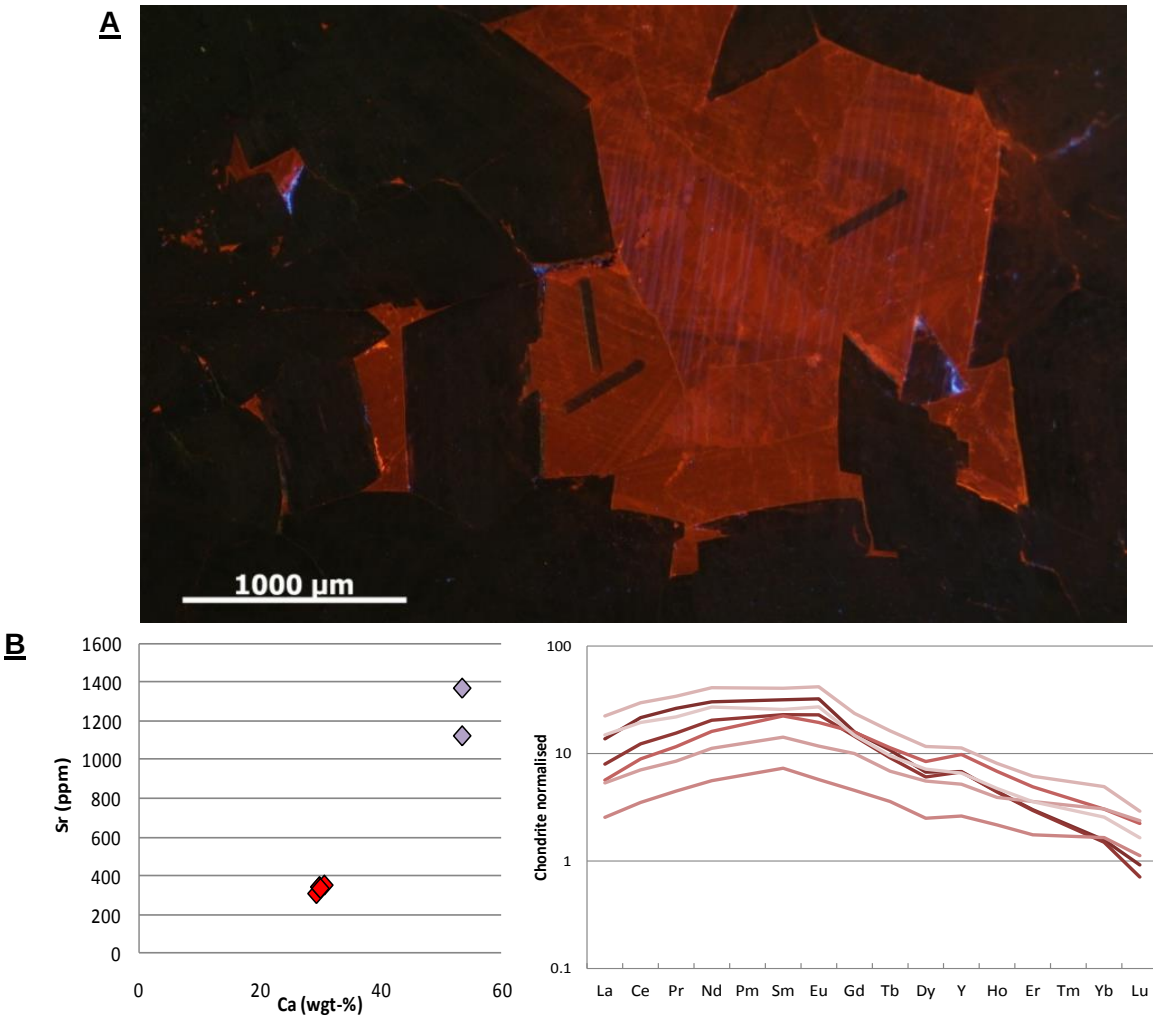

Fig. 5.2.5) A: Texture of the sparry veins at Red Rock. **B:** Relation of Sr and Ca content and REE patterns of calcite and ankerite. **C:** Sr vs Eu. In both X-Y pots: Purple = calcite. Red = ankerite. All RR20.

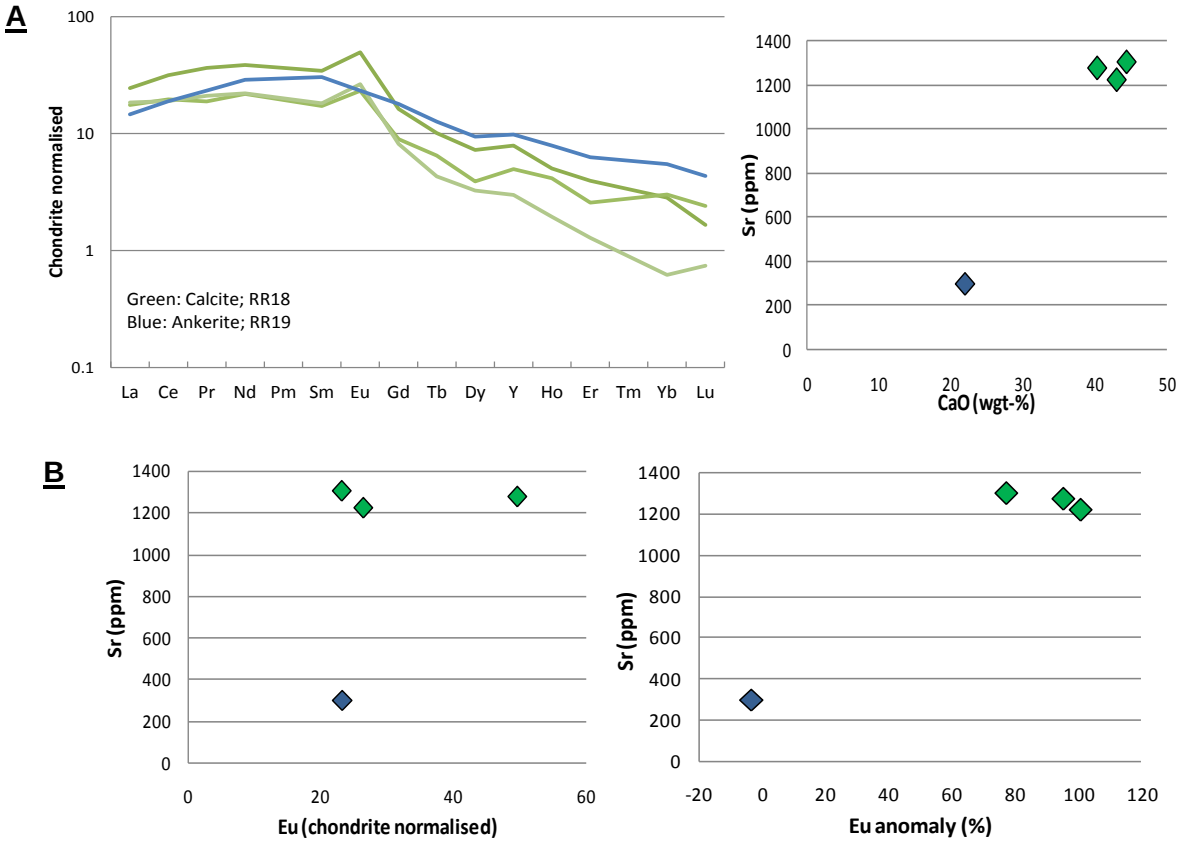

Fig. 5.2.6) A: REE patterns of the thinner carbonate veins at Red Rock and plot of CaO vs. Sr content. **B:** Sr vs Eu content and Sr content vs Eu anomaly. The latter shows some positive linear correlation across samples, but a slight negative linear one just in the RR18 sample. Colour coding the same throughout this figure.

5.2.5-Carbonate at Mt Alta Diatreme

5.2.5.1: Veins in several metres big greyschist block in the diatreme breccia

The carbonate compositions shown in this section are from veins which have been described in chapter 2.4 (Fig. 2.4.15). As can be seen in Fig. 2.4.15, these veins have cloudy-looking rims, which are also recognisable in thin section (Fig. 5.2.7 A&B). In thin section, three main carbonate textures are recognised. The rim is made of a murky, brown, partly oxidised, irregularly big carbonate grains (1) while the centre is filled with optically clear carbonate (2) (Fig. 5.2.7A). Suspended in parts of the vein are "flowery" murky brown ankerite cumulates (3) (Fig. 5.2.7B).

Regardless of location (rim, centre, flowers) in the vein, the carbonate is mostly ankeritic in composition with only some parts being calcitic to dolomitic (up to 10mol-% magnesite component) (Fig. 5.2.7 C). REE concentrations in the ankerite lie between 1 and 100 times chondritic values and patterns may have a negative to positive slope, which is mostly due to varying LREE and MREE concentrations (Fig. 5.2.7 D). Calcitic parts of the veins contain less REE than the ankerite in the vein, but the REE pattern is similar (Fig. 5.2.7 D). Sr and Eu contents show a slight linear correlation (Fig. 5.2.7 E).

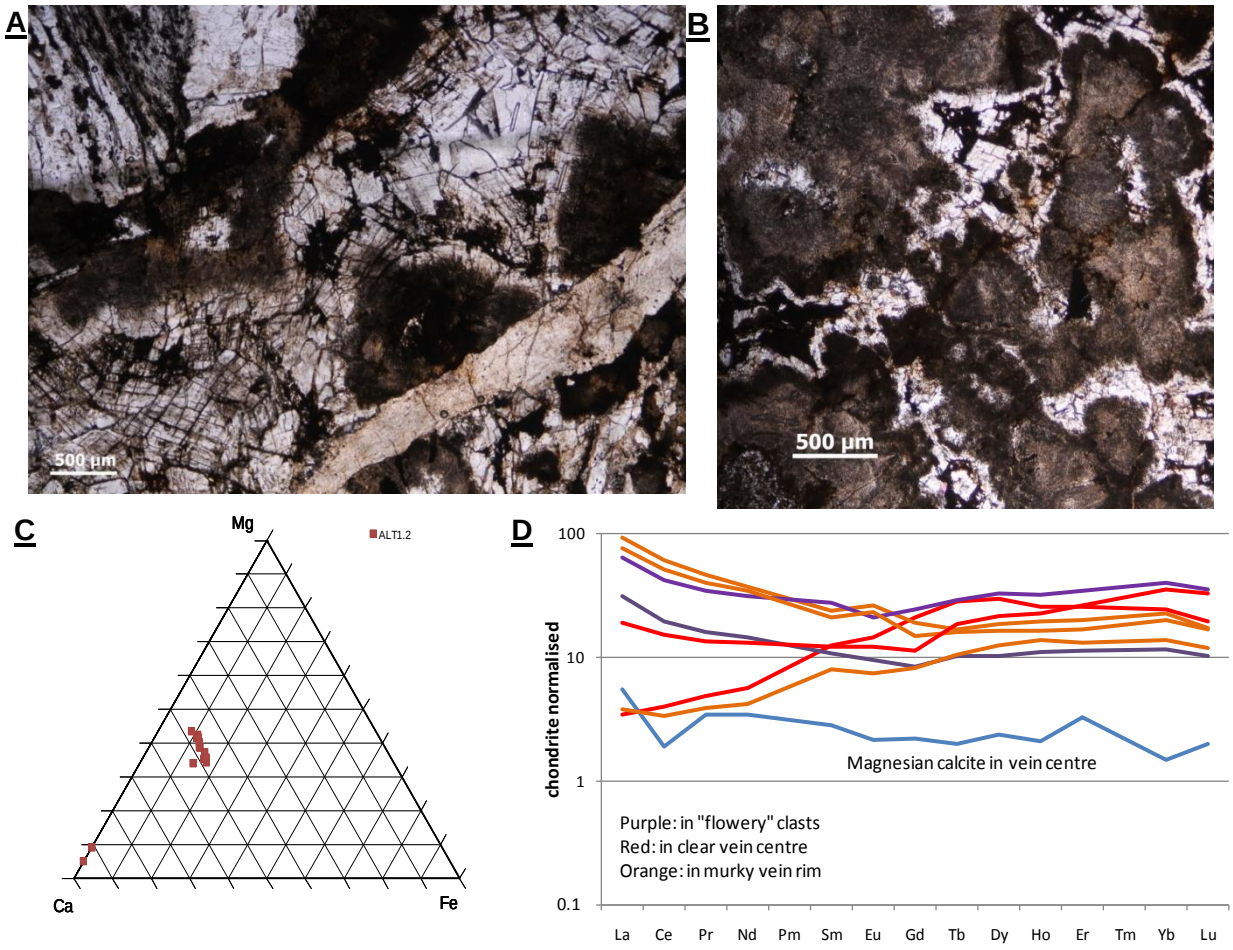

Fig. 5.2.7) A: PPL. Ankeritic vein with murky carbonate at the rim (type 1) and clear in the centre (type 2). **B:** Flowery carbonate clasts are embedded in ankerite parts of the vein (type 3). **C:** Major composition of the carbonate. D: REE content of the carbonate in the different micro-structural settings as shown in A and B. E: Sr vs Eu content which shows a slight linear correlation. All ALT1.2.

5.2.5.2: Veins and vesicle fillings in little-altered lamprophyre

A sample of veins and vesicles in little-altered lamprophyre is AD2A, of which the textures and petrography have already been described in chapter 2.4 (Fig. 2.4.8C&D; 2.4.13). As mentioned earlier, the carbonate in the vesicle fillings has tiny calcitic inclusions (Fig. 2.4.13B), which are too small to resolve with the LASER system used and analyses incorporating these inclusions are dominated by the far more abundant embedding ankerite. Independent of optical appearance and setting, the carbonate is chemically similar throughout the samples. The REE patterns have La/ Lu >1 and all have a large positive Eu anomaly (ca. 100 to 1000%; Fig 5.2.8A). There is no correlation between Eu content or anomaly and Sr content (Fig. 5.2.8B).

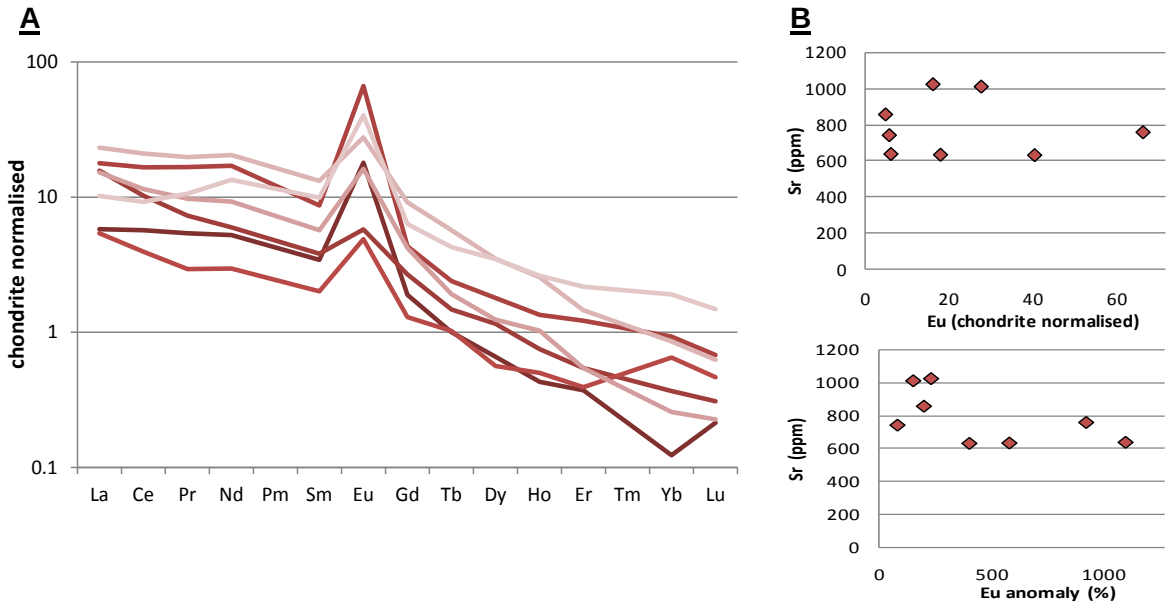

Fig. 5.2.8) A: REE content of ankerite filling veins and vesicles in little-altered lamprophyre. **B:** Sr vs. Eu content and Sr vs. Eu anomaly. All AD2A.

5.2.5.3: Sparry veins in highly altered lamprophyre and carbonate in their wall rock

In chapter 2.4, irregularly shaped carbonate veins and bodies have been described (Fig. 2.4.14). Of these, carbonate in two samples (ALT2C &AD2B) was analysed for its chemical composition. In addition to the vein material, vesicle fillings, xenoliths and carbonate clasts in the adjacent rock were analysed (Fig. 5.2.9&10). The carbonate clasts in the wall rock are replacements of magmatic minerals or phenocryst. For the ALT2C samples, the microprobe of Otago University was used for determination of major element composition of carbonate in different micro-textural positions, such as at the vein rim, in clasts in the rock or the vein centre (Fig. 5.2.9 A). The major elements composition of murky and clear carbonate in ALT2C is very similar, although on average the murky carbonate (at vein rim and replacements) is slightly more Mg-rich than the clear carbonate in the optically clear vein centre (Fig. 5.2.9 B). This can also be deduced from the different greyscales in BSE images (Fig. 5.2.9 A, red box). The carbonate is ankeritic in composition with about 50% calcite and between 8 and 20% siderite component (Fig. 5.2.9 B). In both sample, ALT2C and AD2B, major element concentrations were determined by LA-ICP-MS, which yielded a similar carbonate composition for both samples. Comparisons between Fig. 5.2.9 A and B show a difference between the MP and ICPMS data for the ALT2C sample, which can be attributed to the difference in the two methods. (Major composition is more accurate using the MP).

Despite the similarity of the carbonate's major element contents (Fig. 5.2.9 B&C), trace element concentrations differ considerably in and between sample. REE contents range from 0.1 to 120 times chondritic values (Fig. 5.2.10). In the two samples analysed, overall 7 patterns are identified.

Type A (Fig. 5.2.9 A): The clear carbonate in the vein centre in ALT2C has a bell-shaped REE pattern with an enrichment of Ce, Pr, Nd, Sm and Eu; Pr and Nd values are up to 30 times chondritic values while the other REE concentrations have chondrite normalised values of less than 5. There is no Eu anomaly **(Fig. 5.2.10 B).**

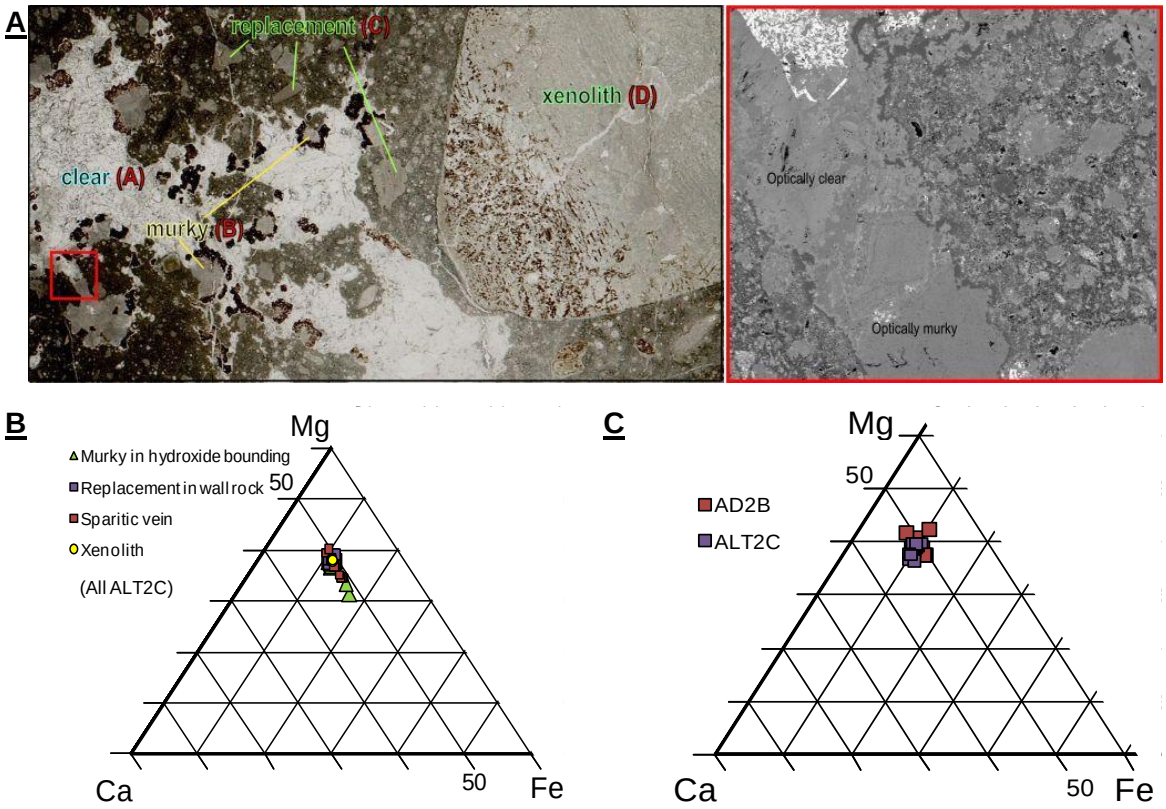

Fig. 5.2.9) A: Left PPL of ALT2C highlighting the carbonate in different settings. Width of image c. 2cm right: BSE image of Red box. The optically murky carbonate has a darker greyscale (= more Mg) than the clear one. Width of image c. 1mm **B:** Composition of the carbonate in the different settings as determined by microprobe. **C:** Major elemental composition of ALT2C and AD2B as determined by ICPMS. The carbonates are very similar across samples. However, note the difference between the two techniques.

Type B (Fig. 5.2.9 A): In ALT2C, the murky carbonate which is rimed by secondary Fe-hydroxide and is located at the vein rim has a REE pattern with a definite and steady negative slope (La/ Lu ratio> 20) with only a slight, if at all, negative Eu anomaly **(Fig. 5.2.10 B).**

Type C (Fig. 5.2.9A): Ankerite is common in the highly altered lamprophyric wall rock, where it replaces magmatic minerals and phyenocrysts, whose original mineralogy is unknown. This type of ankerite has been analysed in ALT2C. This carbonate has slight negative slope (La/Lu ratio between 1.6 and 3.3, normalised to chondrite) with a slight enrichment of Ce, Pr, and Nd **(Fig. 5.2.10 C).**

Type D (Fig. 5.2.9A): The sample of ALT2C contains a rounded green component, which is also made of ankerite (Fig. 5.2.8). It has a REE pattern with a positive gradient which towards the HREE flattens off (Fig. 5.2.10B). The xenolith component contains rounded spheroids (a few 100µm across) that are unlike the rest of the component made of clear carbonate. These clear parts have trace element concentrations identical to those of the clear veins **(Type A.2=Type A) (Fig. 5.2.10B)**.

Type X (Fig. 5.2.10 A): The clear carbonate in the other sample (AD2B) has a La/Lu ratio <1 and a slight negative Eu anomaly. La values range between 0.3 and 5.The REE patterns flatten off from Tb onwards and sometimes have a very subtle negative slope **(Fig. 5.2.10 B).**

Type Y (Fig. 5.2.10 A): The REE pattern of the murky carbonate at the vein rims in AD2B has a slight bell shape, with an enrichment of the LREE and MREE with Ce, Pr and Nd being enriched relative to La. These murky veins also have a distinct positive Eu anomaly **(Fig. 5.2.10 B).**

Type Z (Fig. 5.2.10 A): The lamprophyre in AD2B contains a clast made of clear, sparry ankerite and whose REE content and pattern is similar to the that of the clear carbonate in the ALT2C. (Type Z ~

Type A; **Fig. 5.2.10 C**). Additionally, the Sr content is more similar to the carbonate in ALT2C compared to the other carbonate in AD2B.

In both samples, vesicles in the lamprophyre are filled with murky and clear carbonate and these are chemically identical to their optically similar counterparts in the veins (**Fig. 5.2.10 C)**.

In AD2B, there is a proportionality of Sr content and the size of the Eu anomaly of the vein- and vesicle-filling carbonate (Fig. 5.2.11). The same is also true for Sr and Eu content (Fig. 5.2.11). The component in AD2B (type Z) shows no correlation between Sr and Eu content or Eu anomaly in relation to the vein and vesicle fillings in that sample. For ALT 2C, which has no distinct Eu anomalies no proportional relationship between Sr and Eu content can be drawn (Fig. 5.2.11).

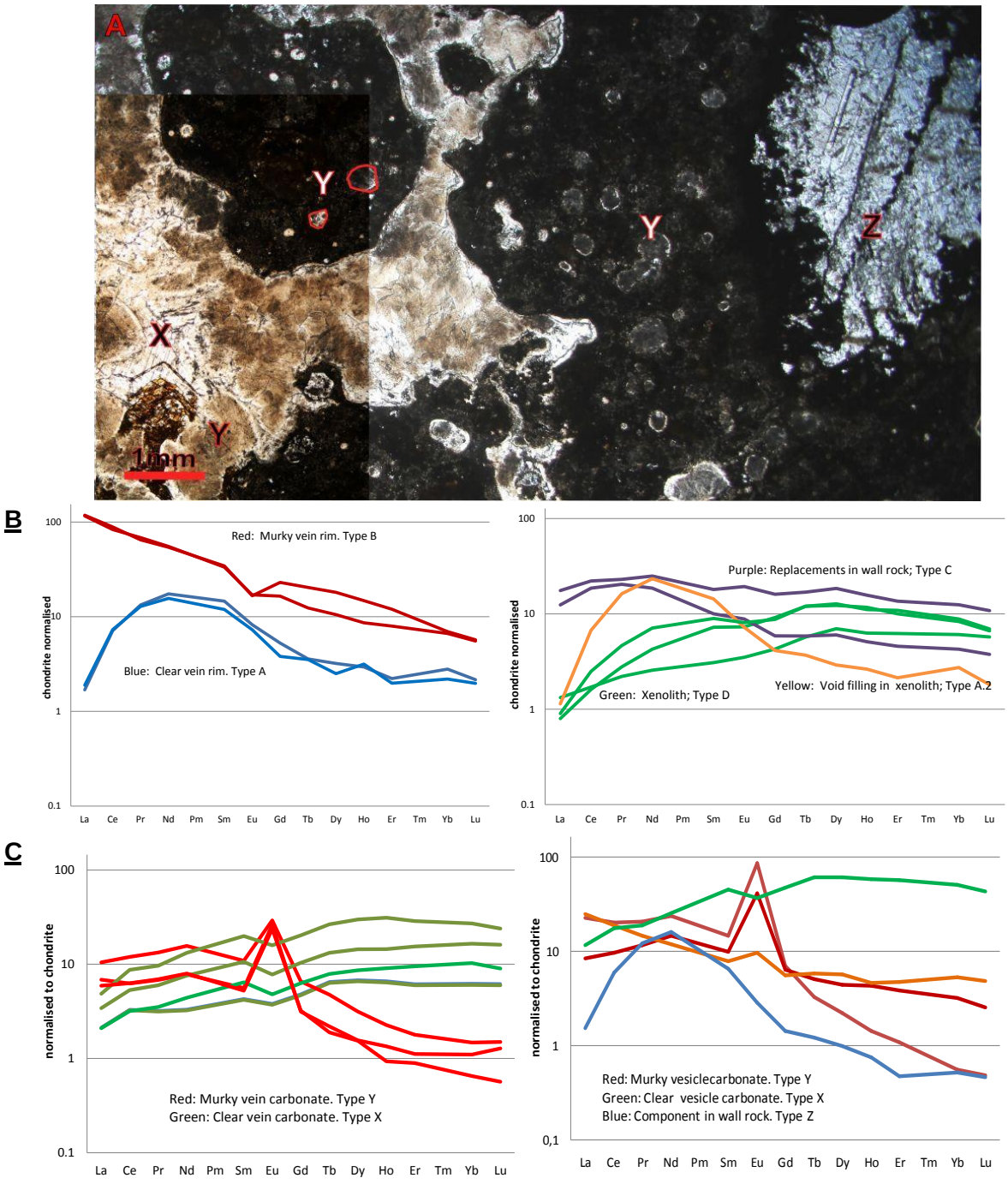

Fig. 5.2.10) A: PPL. Example of different carbonate types in AD2B. **B:** REE patterns of the different types of carbonate in ALT2C. Naming the same to that in Fig. 5.2.9A. **C:** REE patterns of the different types of carbonate in AD2B.

The green colour of the xenolith in ALT2C (type D) is due to a high concentration of chromium. It also contains high concentrations of Ni (around 500 ppm), Sc (around 40 ppm vs less than 20 in the other carbonate) and Co (around 40 ppm vs. less than 20ppm). Ni, Co, and Cr are enriched in peridotite compared to continental crust (Jagoutz et al., 1979; Wedepohl, 1995) suggesting that this component used to be peridotite. Vesicles in this xenolith, filled with type A carbonate (A.1 (Fig. 5.2.10B) indicate that not only was the peridotite replaced by ankerite but also that some of this was dissolved/ or corroded during this process.

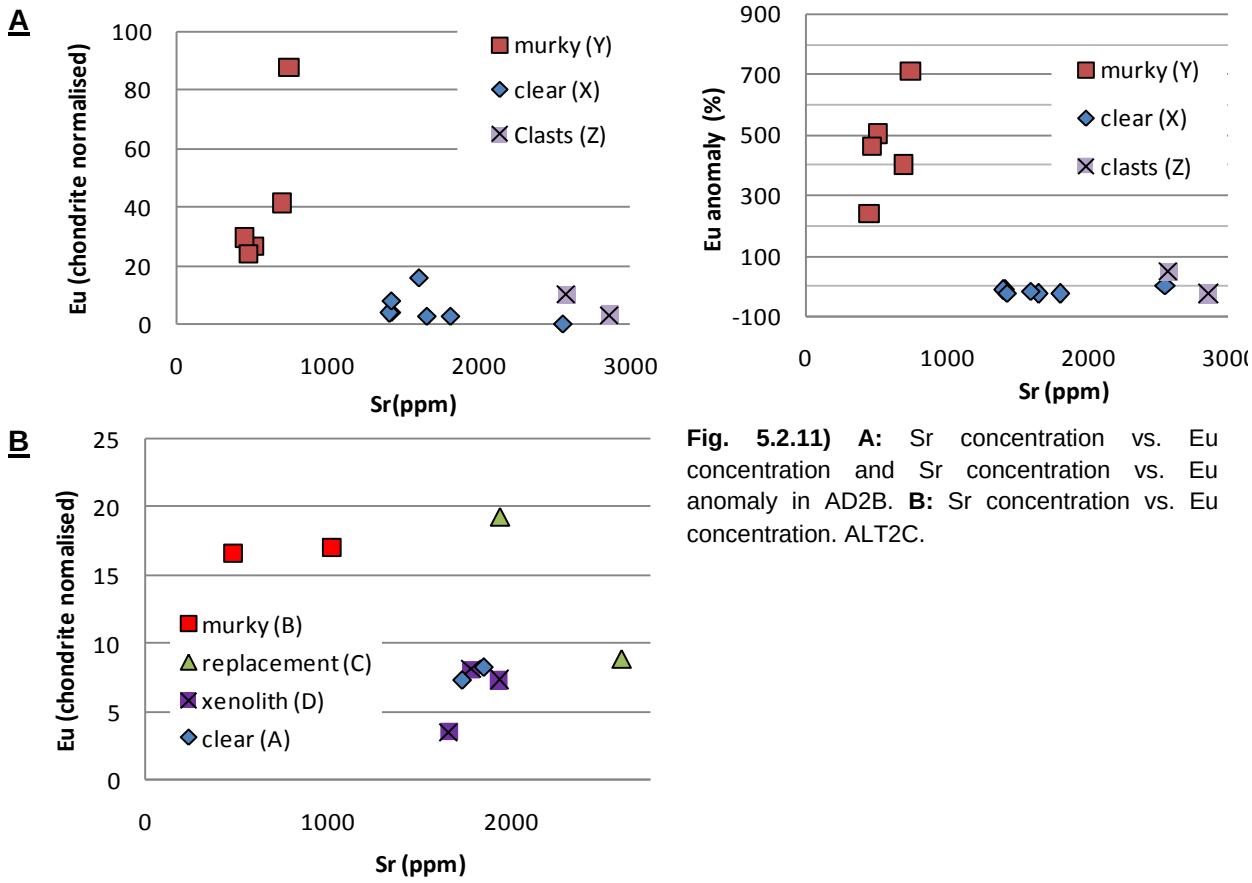

Fig. 5.2.11) A: Sr concentration vs. Eu concentration and Sr concentration vs. Eu anomaly in AD2B. **B:** Sr concentration vs. Eu concentration. ALT2C.

5.2.5.4: Clastic fine-grained breccia at Mt Alta

Carbonate in a fine-grained breccia sample from Mt Alta was analysed for its chemical composition (Fig. 2.4.10 B; 2.4.11 D&E; 5.2.12 A). The carbonate analysed is always part of a few millimetres big components in the breccia (Fig. 5.2.12 B). Carbonate in the matrix was generally too small to be analysed or not identifiable amongst the other minerals with the optical system used. The carbonate is ankeritic in composition and has a concave REE pattern, with an enrichment of Pr and Sm (Fig. 5.2.12 C). The REE pattern shows no Eu anomaly and there is no correlation between Sr and Eu content (Fig. 5.2.12D).

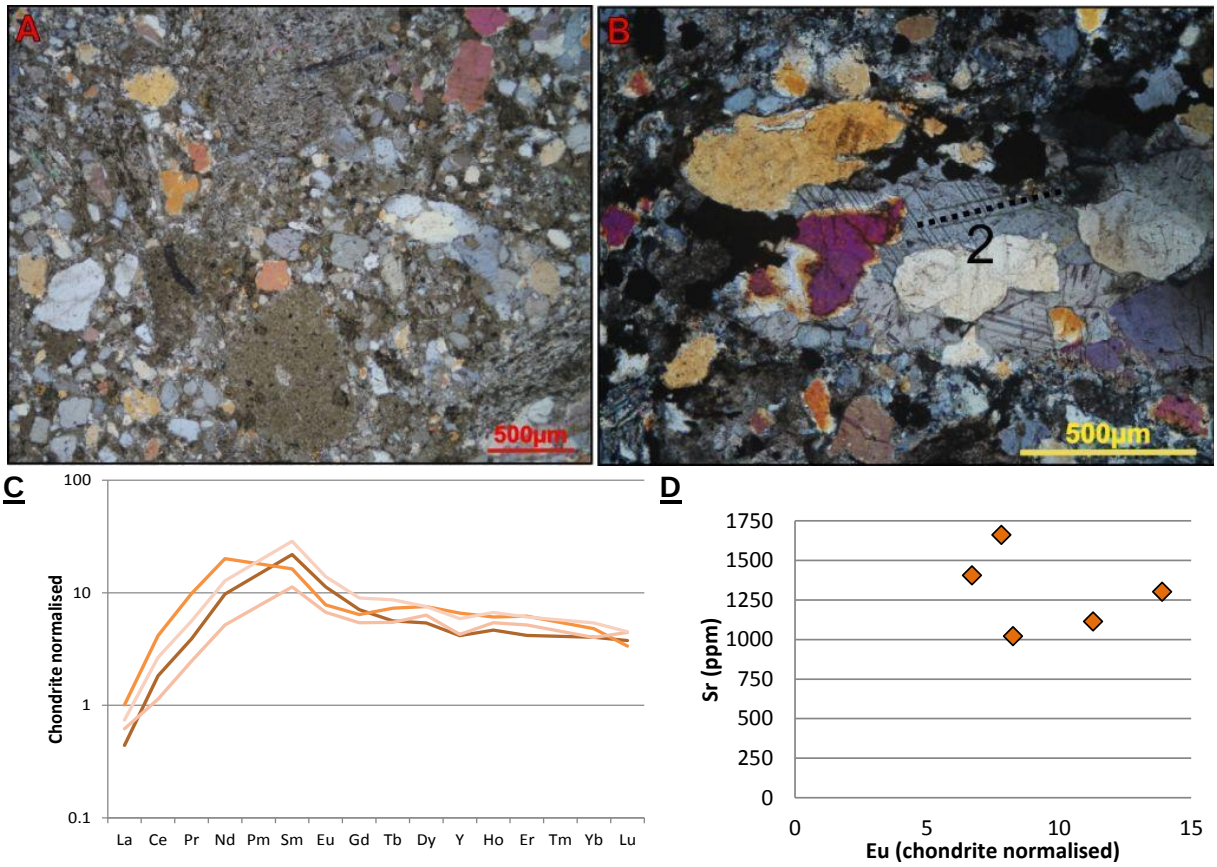

Fig. 5.2.12) A: XPL and reflected light combined. Texture of fine-grained clastic diatreme breccia. Note dark LASER tracks in two components. **B:** Example of analysis spot (dashed line). The carbonate is within a component of the breccia. Number corresponds to analysis number. XPL. **C:** REE patterns of carbonate in the components of the fine-grained clastic diatreme breccia at Mt Alta. **D:** Sr vs. Eu content. All ALT2B.

5.2.6-Silicified fault breccias

Faults with silicified breccias are found in most of the study areas. These breccias strongly have varying carbonate contents, from nearly none (Bullendale) up to c. 20% (Treble Cone). Carbonate analyses have been gathered from breccias near Treble Cone (TP1.3), Mt Alta (AD1A and B) and Copper Creek (COP2C). In the Copper Creek example, ankeritic veins right next to the fault have been analysed and are reported here due to their spatial and genetic relationship to the fault and breccia (COP2B) (Fig. 2.3.9). At Mt Alta, carbonate from the outer few centimetres of the N-S-trending reef have been analysed (AD1B, Fig. 2.4.12 B). The sample from Treble Cone/ Black Peak area is from the fault zone at outcrop T1 (Fig. 2.1.3).

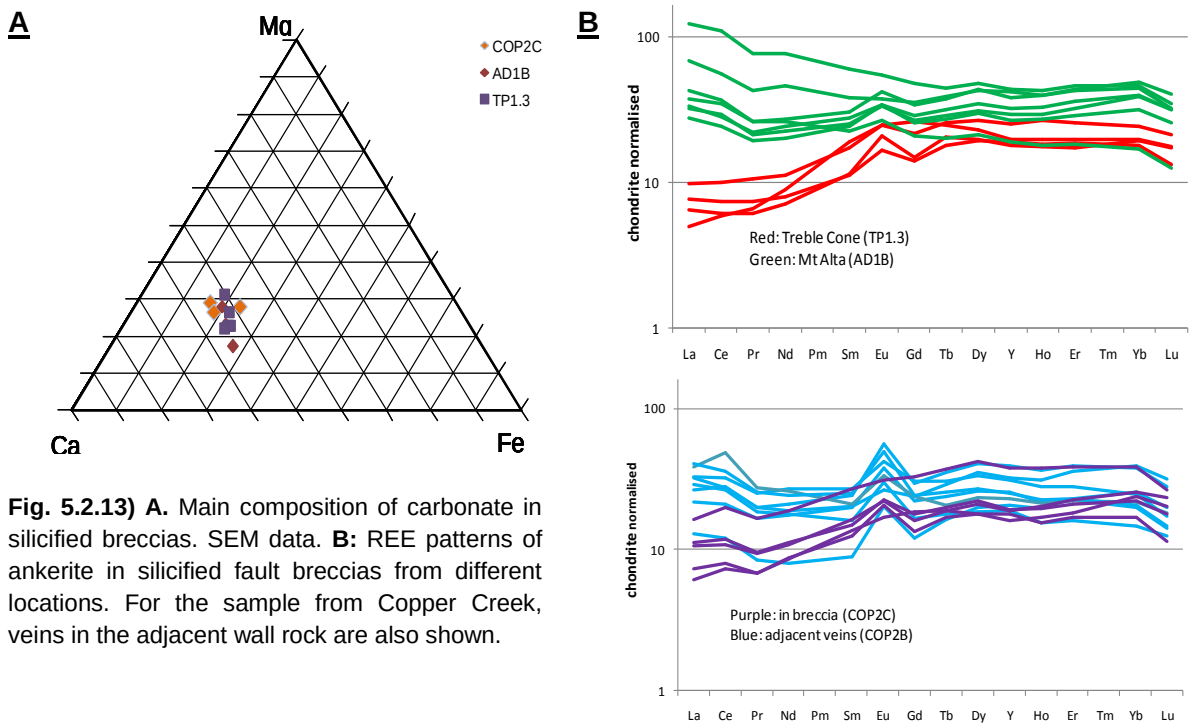

Fig. 5.2.13) A. Main composition of carbonate in silicified breccias. SEM data. **B:** REE patterns of ankerite in silicified fault breccias from different locations. For the sample from Copper Creek, veins in the adjacent wall rock are also shown.

In all of these breccias, the carbonate is ankeritic in composition. Ca makes up between 50 and 55% of the carbonate, while Mg contributes between 26 and 32% (Fig. 5.2.13 A). Fig. 5.2.13 A shows that in carbonate from TP1.3 and AD1B decreasing Mg concentrations cause a simultaneous increase of Ca and Fe (Fig. 5.2.13 A). Apart from major element contents, the carbonate from the different breccias are also similar regarding their MREE and HREE content (Fig. 5.2.13 B). Due to the difference in LREE concentration, REE patterns can have a mostly neutral up to a positive slope. Exceptions are found in some carbonate analyses of the Mt Alta example where REE slopes are negative. In many analyses, the REE patterns show a slight positive Eu anomaly (Fig. 5.2.13B). The ankeritic veins which are next to the fault surface at Copper Creek are chemically quite similar to the carbonate within the fault breccia, but on average concentrations of the LREE and MREE are higher and the veins have a more pronounced positive Eu anomaly (Fig. 5.2.13 B) compared to the carbonate inside the silicified breccia. Regarding Sr and Eu contents only in COP2C is a proportionality recognised, and only carbonate of TP1.3 shows a proportional behaviour of Eu anomaly and Sr content (Fig. 5.2.14).

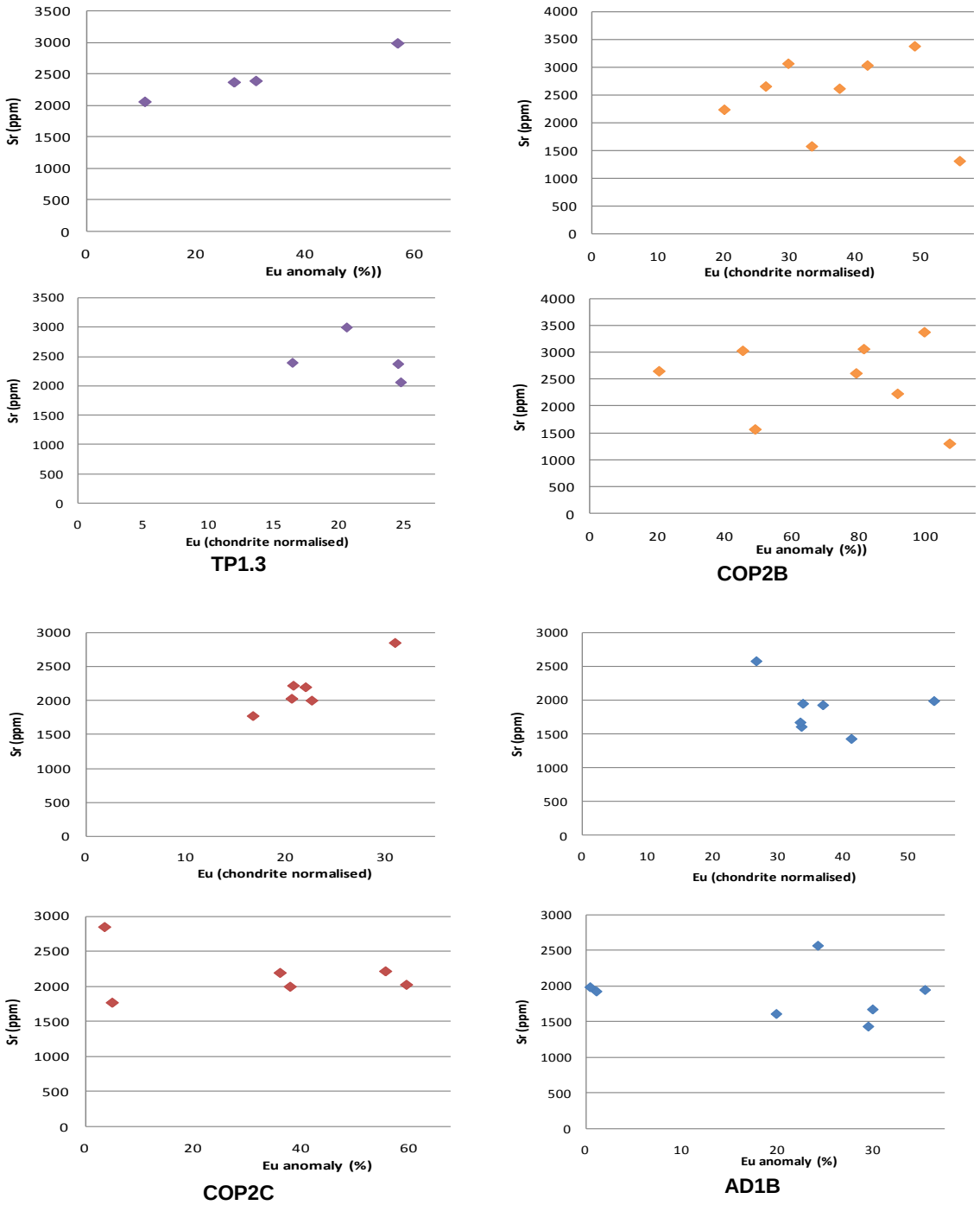

Fig. 5.2.14) Sr vs. Eu content and Sr content vs. Eu anomaly for the carbonate in and next to the different silicified fault breccias.

5.2.7- Ocelli in lamprophyre

Magmatic calcitic ocelli have been analysed in a sample of lamprophyre from the northern boundary of the Corner Dike at Niger Diatreme (ND3C, Fig. 2.4.2 and associated chapter). The calcite is chemically uniform and has the highest LREE content of all carbonate analysed (La>200 chondritic values; Fig. 5.2.15). The La/Lu ratio is 110+/-50 and REE patterns have a distinct positive Eu anomaly (around 225% on average; Fig. 5.2.15). There is also a rough correlation of Sr content and Eu anomaly (Fig. 5.2.15).

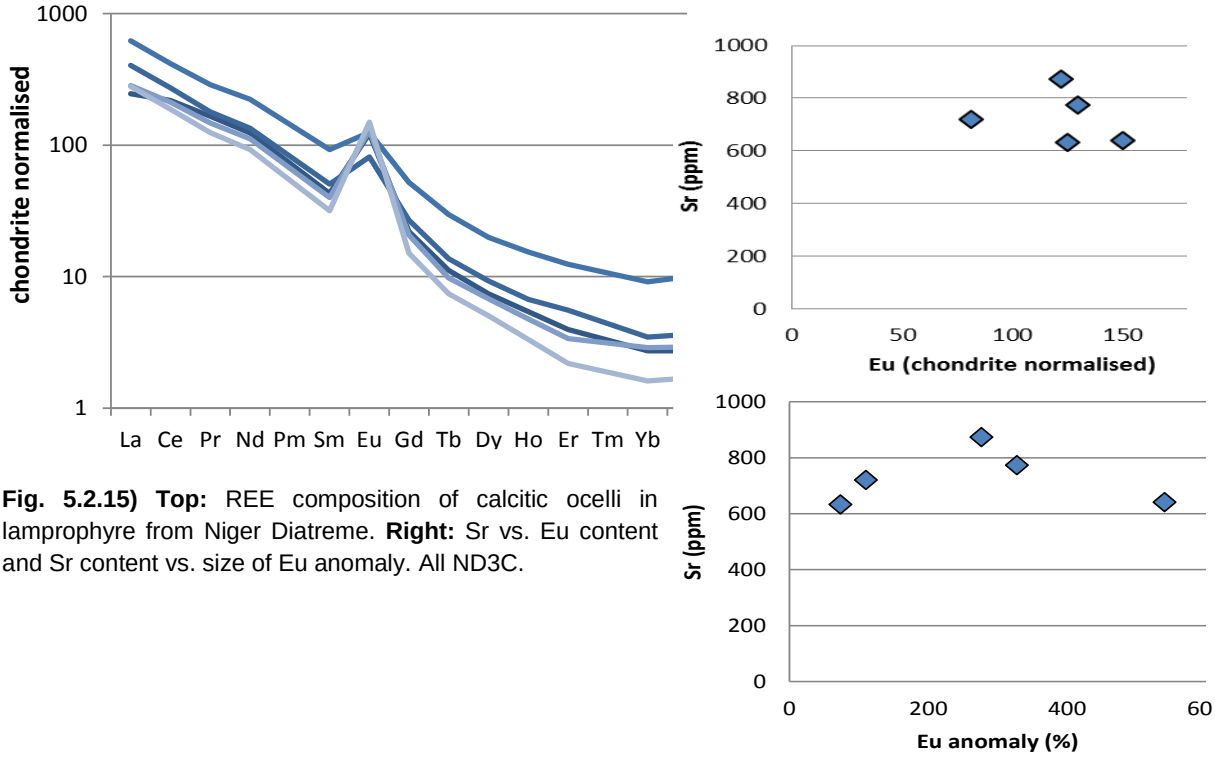

Fig. 5.2.15) Top: REE composition of calcitic ocelli in lamprophyre from Niger Diatreme. **Right:** Sr vs. Eu content and Sr content vs. size of Eu anomaly. All ND3C.

5.2.8-Ankeritic marble component in Niger Diatreme

The ankeritic marble at Niger Diatreme (Fig. 2.4.6) has REE concentrations of less than 20 chondritic values. The chondrite normalised REE pattern is slightly convex with an enrichment of the MREE. Concentrations are slightly lower of the LREE than the HREE (Fig. 5.2.16). No distinct Eu anomaly is present in the sample but Sr and Eu concentrations correlate linearly (Fig. 5.2.16).

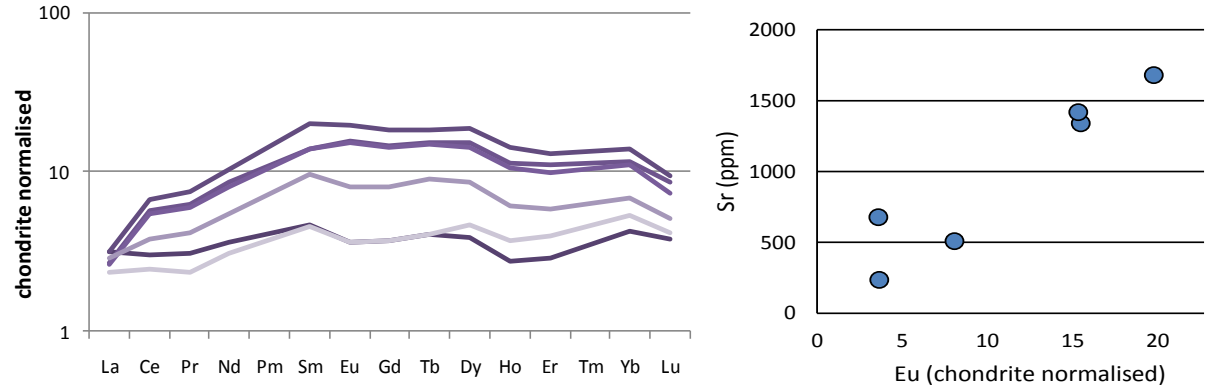

Fig. 5.2.16) REE patterns of ankerite in the ankeritic marble. ND1A. Eu and Sr content show a linear trend.

5.3) Comparison between the analysed hydrothermal carbonates

In the following sections, different chemical aspects of the carbonate from the different settings are presented and compared. Data used are only those obtained by LA-ICP-MS. For comparison, the compositions of the wall rock lithologies are also plotted. Except for U, Th and Pb, I used whole rock data collected by me. For Pb, Th and U contents, concentrations given in Pitcairn (2004) were used.

This was done due to the general lack of Pb analyses for "my" rocks and although U and Th were determined in this study, I used Th and U concentrations from Pitcairn for consistency. The chemical composition of lamprophyre (and carbonatite) are taken from Copper (1986), Cooper & Paterson (2008) and Clough (1989). The ankeritic marble is not included in the comparison, as the composition of the wall rock is not known.

5.3.1 - Major components-Ca, Mg. Fe, Mn

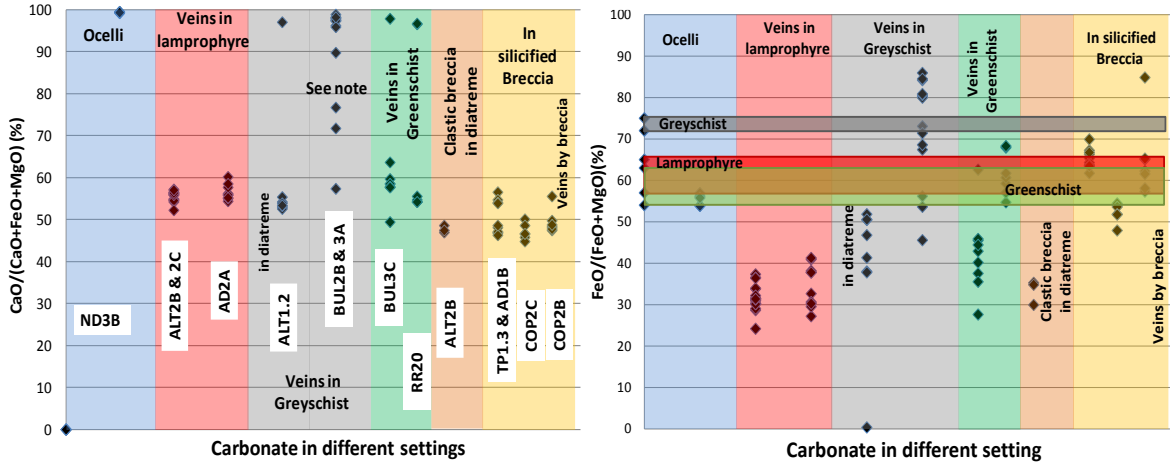

Fig. 5.3.1) Content of CaO/(CaO+FeO+MgO; %) and FeO/(FeO+MgO; %) (all ratios from wt-%) in the analysed carbonate. For comparison, the ranges of values of these quantities of the different host-rocks are also displayed. Note: The intermediate CaO concentrations in the greyschist-hosted veins are those analyses where the LASER cuts across calcite and ankerite. X-axis just for display.

Calcite is especially common in greyschist. The veins in the large greyschist block in Mt Alta diatreme are an exception, as here the veins are ankeritic (ALT1.2) (Fig. 5.3.1). Ankerite is the dominant carbonate in greenschist, lamprophyre, and silicified fault breccias (general observations of the last chapters and Fig. 5.3.1). Fault breccias, which are dominated by schist fragments and which only have little to no hydrothermal quartz, predominantly contain calcitic carbonate, too (i.e. COP3A, BUL4B).

The average FeO/(FeO+MgO) [wt-%/wt-%] ratio of the carbonate in veins hosted by greyschist is generally higher than in greenschist- and lamprophyre-hosted veins (Fig. 5.3.1). This correlates well with greenschist and lamprophyre having lower FeO/(FeO+MgO) values than greyschist (whole rock). An exception to this is carbonate in the clastic fine-grained breccia (ALT2B) and greyschist-hosted veins (ALT1.2) in Mt Alta Diatreme and the carbonate in the silicified breccia at Copper Creek (COP2C), where FeO/(FeO+MgO) ratios are relatively low (Fig. 5.3.1). The veins in the wall rock of the silicified breccia at Copper Creek (COP2B) have notably higher Fe-Mg ratios than the carbonate in the breccia and are more like the carbonate in the other silicified breccia at Treble Cone and Mt Alta (Fig. 5.3.1). Compared to the Fe-ratios of the hosting wall rock, FeO/(FeO+MgO) ratios of veins are between 10 and 30% smaller. The calcitic ocelli have Fe-Mg ratios similar to the hosting lamprophyre (Fig. 5.3.1).

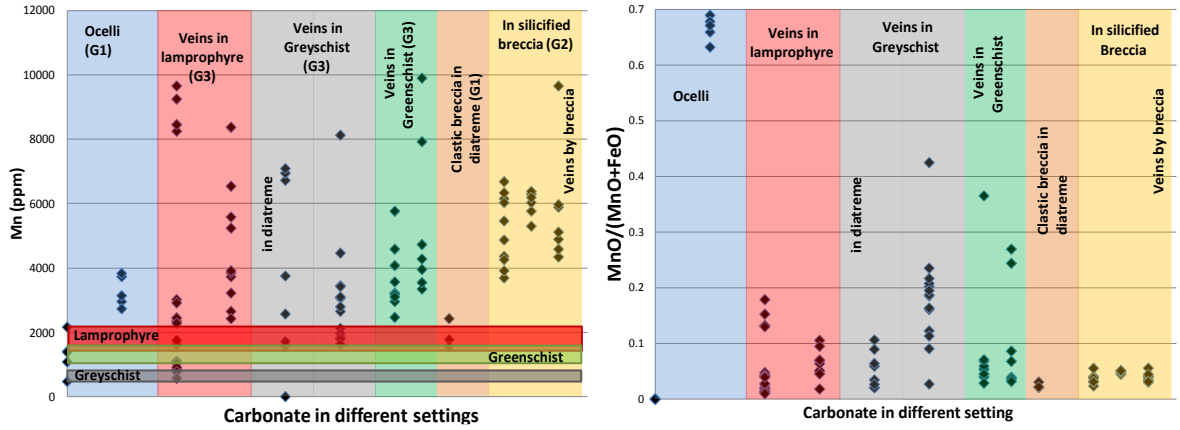

Fig. 5.3.2) Mn content and Mn/ Fe ratio in the different carbonates analysed. G stands for group, see text.

With respect to Mn content, the analysed carbonates can be divided into 3 main groups (Fig. 5.3.2). Group 1 comprises carbonate in ocelli, and clastic fine-grained breccia in the diatreme, where Mn concentrations are on average lowest and values lie between 1500 and 4000 ppm. The second group is made of carbonate found in and around silicified breccias and range (except for one analysis) between 3500 and 5000 ppm. The third group comprises veins in lamprophyre, greyschist and greenschist where values scatter over very wide range (between 500 and 10000 ppm Mn) even in single samples (Fig. 5.3.2).

The largest range of MnO/(FeO+MnO)[wt-%/wt-%] is found in carbonate in veins in greyschist. Ocelli have the highest MnO/(FeO+MnO) value. In the other carbonate types, the MnO/(FeO+MnO) ratios are similar throughout (Fig. 5.3.2). The high ratios in greyschist-hosted veins and ocelli correlate with this carbonate being calcitic (compare Fig. 5.3.1&2).

5.3.2-Trace elements-Sr, Ba, Pb, Th, U

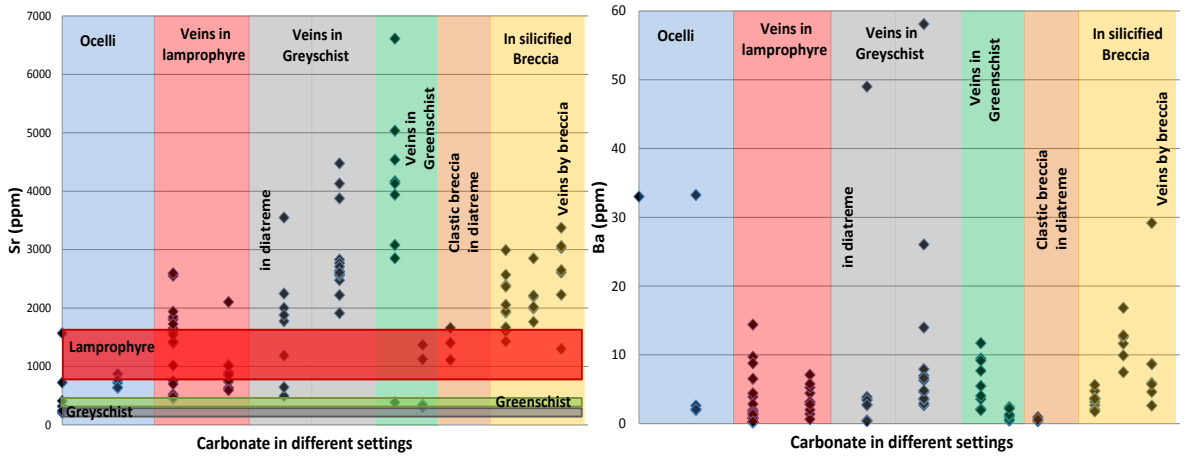

Fig. 5.3.3) Sr and Ba concentrations in carbonates analysed. Note: Ba concentrations of the host rocks are much higher than those of the carbonate and outside the displayed values.

Strontium concentrations lie between 230 and 6600 ppm and most carbonate populations overlap (Fig. 5.3.3). The lowest values are in carbonate of the ocelli, while the largest are in veins in greyschist and greenschist from the Bullendale/ Murdoch Creek sampling sites. Veins from the Bullendale/ Murdoch Creek sites also have the widest range of values (900-5000 ppm for greyschist-hosted veins and between 300-6500 ppm in greenschist). On average, the lowest concentrations are in carbonate associated with the Alpine Dike Swarm; Sr concentrations in veins in lamprophyre, ocelli, veins in the

large greyschist block in the diatreme and clastic breccia never exceed 3700 ppm and are mostly smaller than 2000 ppm. Sr concentrations of carbonate in silicified breccias are very similar in all study areas; these concentrations are in the range of the diatreme-hosted structures but are slightly higher on average (around 2200 ppm as opposed to 500 – 1500 ppm) (Fig. 5.3.3). The veins associated with the silicified fault at Copper Creek (COP2B) are, on average, slightly richer in Sr than the carbonate within the breccias (COP2C).

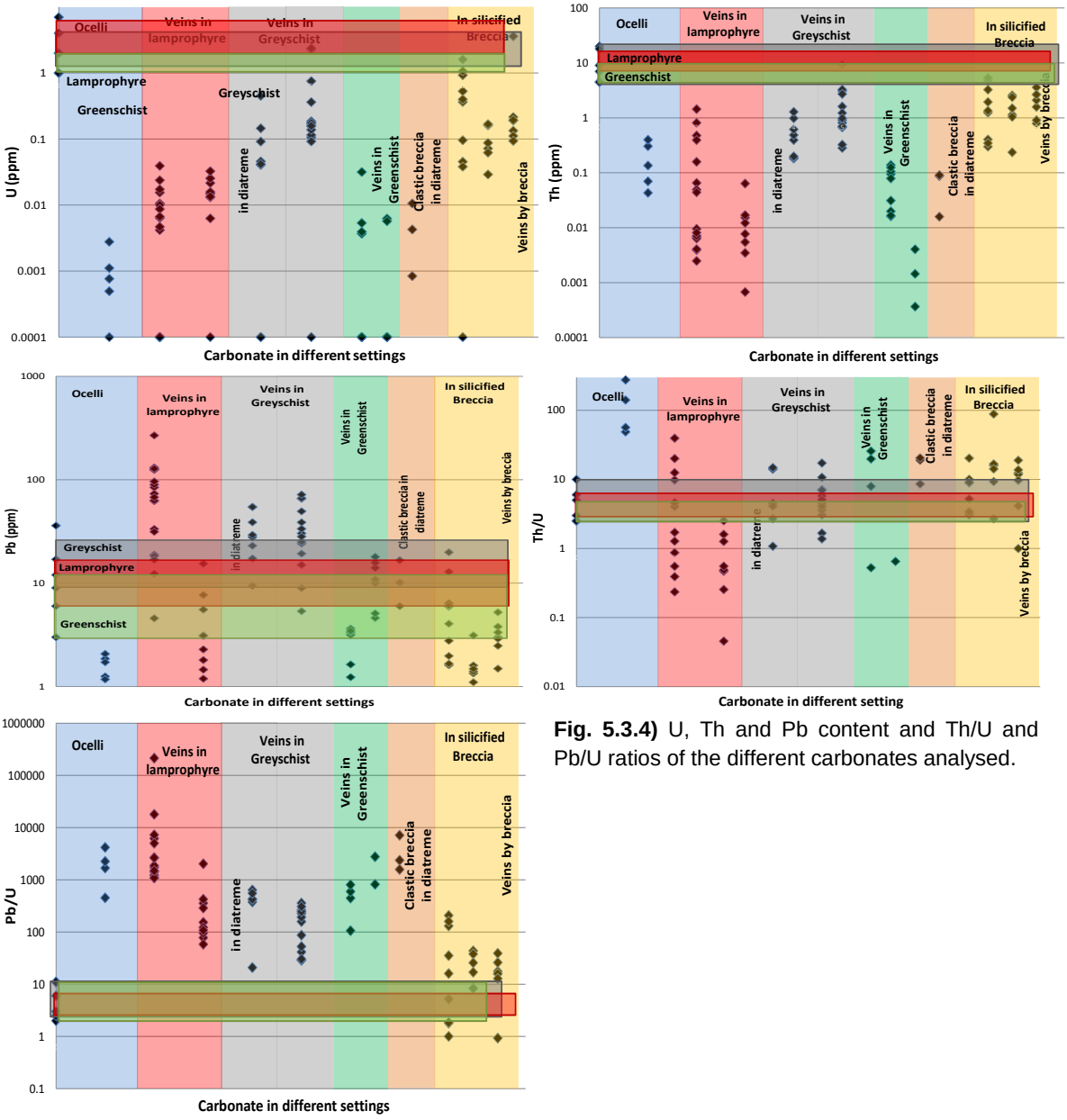

Fig. 5.3.4) U, Th and Pb content and Th/U and Pb/U ratios of the different carbonates analysed.

Throughout, Ba contents are mostly less than 15 ppm, but can occasionally be up to 60 ppm, such as in carbonate from greyschist from Bullendale (Fig. 5.3.3). These high values are rare and isolated. In all cases, the carbonate is highly depleted in Ba compared to their host rock (Ba concentrations (ppm): greenschist:33-68; greyschist:440-500; lamprophyre: 90-1090) and there is no systematic correlation of the carbonate composition and host rock, setting or carbonate mineralogy.

Relative to Th and U, Pb is most abundant in all carbonates analysed and can contribute several hundred ppm to the mineral (Fig. 5.3.4).Th and U concentrations, on the other hand, lie between 0 and 10 ppm, with U on average less abundant than Th. Compared to the hosting lithology, Pb

concentrations in the carbonate are similar to the host rocks, while Th and U are much lower. The lower U and Th contents in the lamprophyre- and greenschist-hosted veins reflect the lower U concentrations in lamprophyre and greyschist relative to greyschist. Pb/U ratios of the carbonate are on average many times higher than of the host rocks, while Th/U ratios are on average similar to the host rocks (Fig. 5.3.4). For the carbonate in the silicified breccias, Pb/U ratios are most similar to the wall rock, while the other carbonates have Pb/U 1-3 orders of magnitude larger than their host rock. These ratios are quite large especially for carbonate hosted in lamprophyre and greenschist (Fig. 5.3.4).

5.3.3- REE content and patterns

In Fig. 5.3.5 & 6 the REE contents and patterns of the different hydrothermal carbonates are compared with their hosting lithology. For this, I used the whole rock data presented in chapter 4.2 (Fig. 4.2.7). As the mineralogy of the greenschist at Red Rock is quite different from any of the analysed greenschist in this study, the plot of the veins from Red Rock comprise all composition of the greenschist analysed in this study to give a rough idea on the potential source. (Greenschist analyses by Cooper et al. (2016) (see below for details) are in the range of those analysed here.) For the carbonate in the fine-grained breccia from Mt Alta Diatreme (ALT2B), the composition of lamprophyre and greyschist are plotted for the comparison. Again, I omitted the ankeritic marble from the comparison as I cannot be sure of the composition of its closest wall rock. For the comparison of carbonate hosted in lamprophyre, I used data from the literature (Clough, 1989; Cooper, 1986), as lamprophyres weren't analysed in this study. These data often do not comprise concentrations of the MREE and HREE. Due to this, I included Y which in the REE plots sits, according to its ionic radius, between Dy and Ho. Carbonatite compositions are taken from Cooper & Patterson (2008).

Fig. 5.3.5 & 6 show that there is often a big difference between the composition of the whole rock and the carbonate it is hosted by especially for the LREE. The difference is especially large for carbonate in highly altered lamprophyre and for veins and breccias in greyschist.

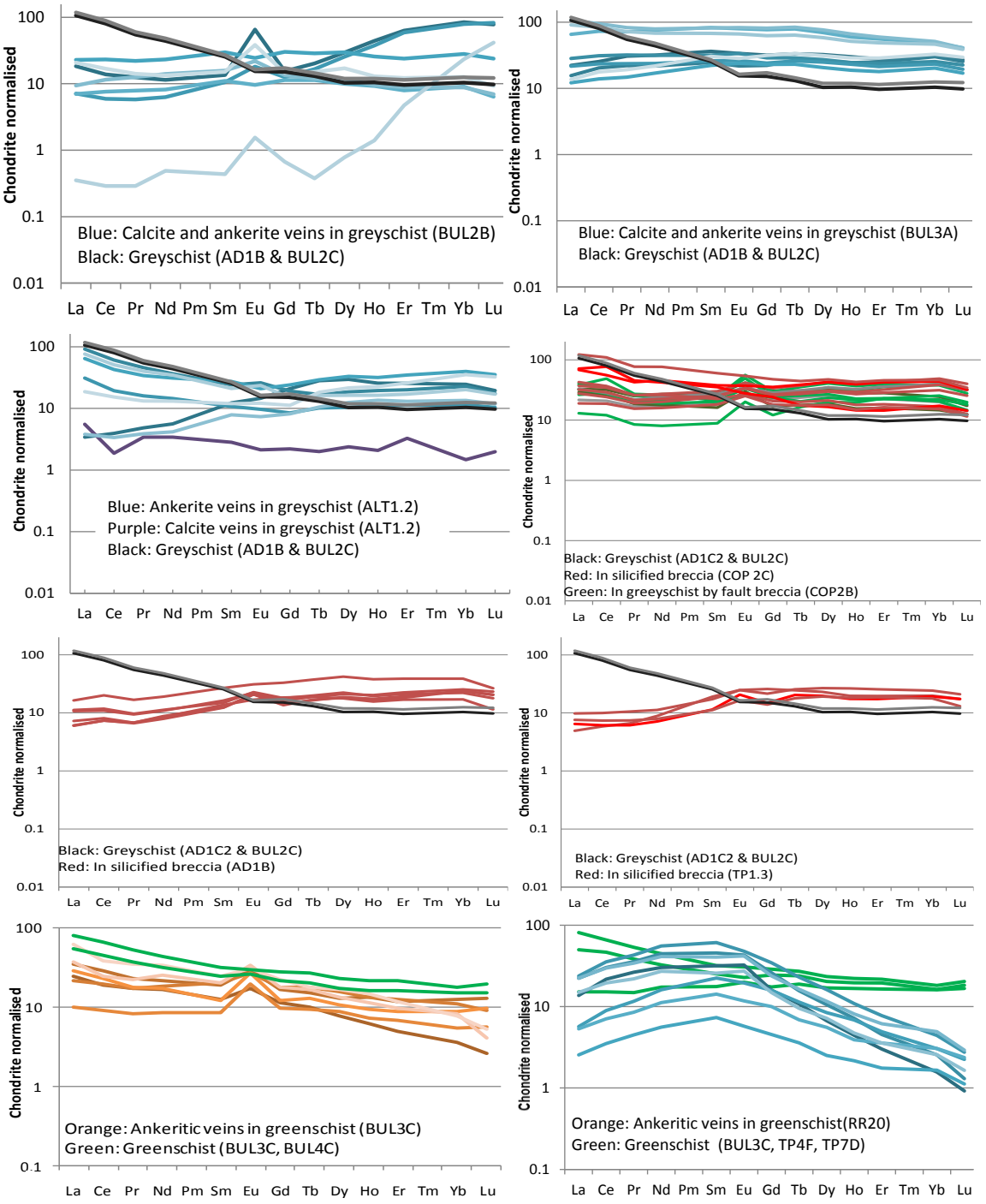

Fig. 5.3.5) Comparison of the REE patterns of different carbonate with their corresponding host rock. The top six plates show veins (Blue) and carbonate in silicified breccias (Red/Green) compared to their host rock, greyschist (Black). The lower two plates show veins in greenschist at Bullendale and Red Rock. Note that the composition of the wall rock around veins from Red Rock is not known and instead composition of all greenschist analysed in this study are plotted as a rough guide.

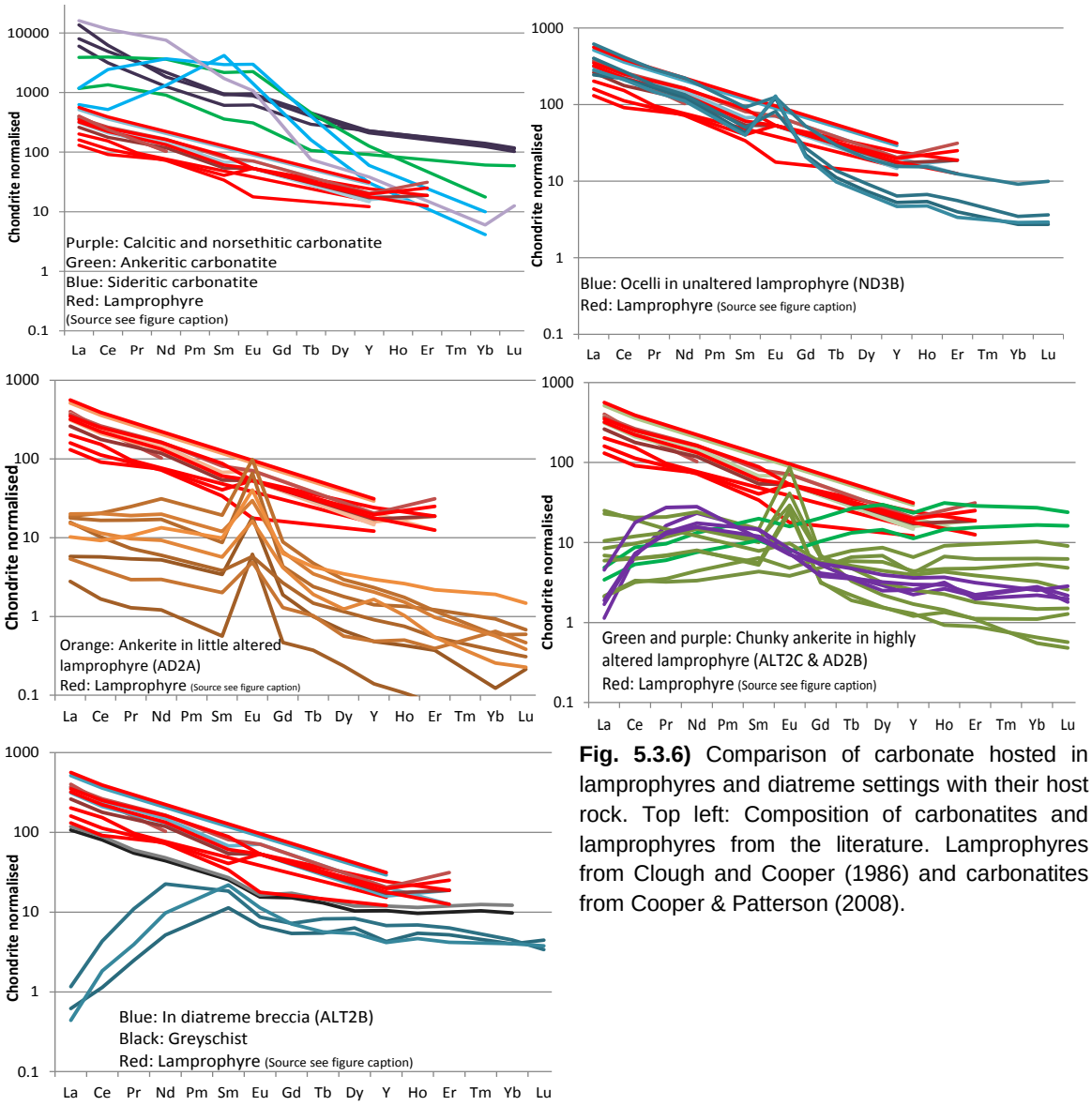

Fig. 5.3.6) Comparison of carbonate hosted in lamprophyres and diatreme settings with their host rock. Top left: Composition of carbonatites and lamprophyres from the literature. Lamprophyres from Clough and Cooper (1986) and carbonatites from Cooper & Patterson (2008).

5.4) Discussion

Table 5.4.1) Elements and the physical aspects that control their abundance in the analysed carbonate.

Element/ chemical feature	Dependent on:
Mineralogy	Setting, less so wall rock
Sr, Mn	Wall rock and setting
FeO/(FeO+MgO)	Setting and wall rock
Ba	Independent
U, Th	Rock
Pb/U ; Pb	Setting, less so wall rock
REE	Setting

All of the vesicle-, vein-, breccia- and ocelli-hosted carbonate presented above grew into fluid filled cavities as has been shown in the previous chapters (i.e. by euhedral grain shapes, oscillatory zoning). Hence, all components in the carbonate must have been in the solution prior to precipitation. The residence time and mobility of the different carbonate components may vary, depending on chemical and physical changes in the fluid throughout time and/ or space. The comparisons in the previous section show that different elements can have different factors controlling their abundance, such as setting, mineralogy and host lithology. However, in most cases there are several aspects that play a role (Table 5.4.1). A simplistic model for the fluid's history and the vein precipitate comprises four main stages:

1) The initial fluid source(s): providing H_2O, CO_2, and metals.
2) The path way: Interaction of the fluid with the wall rock. Pick up and deposition of fluid-dissolved components, which is dependent on lithology, mineralogy and physical and chemical conditions in the fluid. Given conditions do not change, the fluid should reach equilibrium with the wall rock. This provides a base load of elements in the fluids.
3) The sink: Physical and chemical conditions (e.g. pressure, temperature, pH, wall rock) control the chemistry of the fluid just before carbonate precipitation.
4) The precipitate: The precipitate's chemistry is influenced by the fluid and its crystallographic structure.

Having identified the major factors controlling the carbonate's chemistry, it is also necessary to evaluate which of these stages is controlling the precipitate's chemistry. An example of crystallography-controlled element content in the analysed carbonate is Ba. Ba concentrations in all analysed carbonate are low (a few ppm), which reflects the "inability" of the calcite's and ankerite's crystal structure to accommodate the large Ba ion. Ba^{2+} has an ionic radius of 0.135 as opposed to 0.1 (Ca^{2+}) or 0.063 (Fe^{2+}) (Shannon, 1976). In the few cases Ba concentrations in analyses are high (>20 ppm) this can probably be attributed to contamination by barite, which is often found in association with the hydrothermal carbonate (see chapter 3). Low Ba concentrations in vein carbonate have also been reported by Kontak & Jackson (1999).

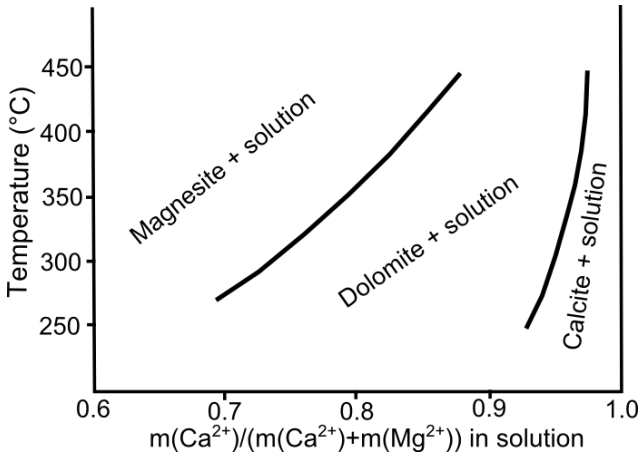

Fig. 5.4.1) Precipitating carbonate species in respect to temperature and Ca and Mg content (molar fractions) in the fluid. Modified from Rosenberg & Holland (1964).

In addition to aspects related to element supply and crystallography, the relative proportion of elements in the fluid also need to be considered. Concerning the carbonate system, Rosenberg & Holland (1964) determined experimentally (in a temperature range of 275-425°C) that, whether calcite, dolomite or magnesite precipitate in a Mg-Ca-bearing fluid-precipitate system depends upon the Mg/ Ca ratio in the fluid and temperature. It follows that the fluid differs chemically from the precipitate (Fig 5.4.1). With respect to the Mg-Ca ratio, the stability fields of calcite and dolomite increase towards lower temperatures, while the stability field of magnesite decreases. This is similar to the findings of Wigley (1973), who investigated the stability of dolomite and calcite at ambient temperatures. To my knowledge no experimental studies have been conducted in a Ca-Mg-Fe system investigating the stability of ankerite. However, as Mg and Fe are similar in ionic charge and radius, as a first approximation both elements are treated as "Mg". In summary, the fluid needs to be quite rich in Ca compared to Mg and Fe in order to precipitate calcite. Rosenberg & Holland's and Wigley's studies show that the lower the temperature the more "likely" the fluid is calcite saturated compared to dolomite (larger calcite stability range) and the fluids can hence contain less and less Ca but can still precipitated calcite. This relationship may explain why late stage veinlets in greenschist, which presumably formed at lower temperatures, are calcitic rather than ankeritic.

5.4.2- Abundance of divalent ions (Ca, Mg, Fe, Mn, Sr)

5.4.2.1: Whole rock chemistry and element availability

The sources for the metals in the veins are most likely the rock in the vicinity of the carbonate deposits; these rocks are greyschist, greenschist and/ or lamprophyre. However, the whole rock composition of these lithologies may not necessarily represent the element budget available to the fluid. As has been discussed in chapter 2.3, 2.4 and 3, only some minerals break down during the hydrothermal alteration. In the metamorphic rocks, albite, quartz (at least in the leucocratic layers), apatite, zircon do not react with the incoming fluid and hence cannot provide their element content to the fluid. Epidote, calcite, chlorite, actinolite, chlorite and muscovite on the other hand do break down and hence their element content is available to the hydrothermal fluid. Concerning the available budget from lamprophyre, it has been shown in chapter 2.4 that the only alteration-unaffected mineral in lamprophyre is apatite.

As none of the alteration-insensitive minerals contain significant amounts of Fe, Mg or Mn, the whole rock composition of these elements is representative of the budget available the hydrothermal fluid. This is different for Sr and Ca, as these elements are major components in apatite. To obtain the available Sr and Ca budget from each lithology, it was calculated how much Ca and Sr are bound in the apatite. This amount was then subtracted of the whole rock composition. The apatite content is estimated based on the whole rock's P concentration after subtracting what may be in monazite (max. 5%, see below). By using the ideal apatite formula the amount of Ca bound in apatite can be calculated.

These calculations show that between 0.5 (greyschist) and about 1.5wt-% CaO (lamprophyres) are bound in apatite, which corresponds to 5 - 12% of the total CaO (wt-%) of the rock. The Sr content in apatite was estimated based on the data presented in Belousova et al. (2002; 3000 ppm Sr for the lamprophyre and 500 ppm for metamorphic rock). The results of the calculations show that Sr bound in apatite is only a small proportion (mostly less than 5 %) of the total Sr available in the rock (see appendix I for constant and values). Overall, it shows that the whole rock compositions of the metamorphic and magmatic lithologies are a good proxy for the Mg, Ca, Fe, Mn, and Sr available to the fluid.

Table 5.4.2) Calculated vein-rock ratios of a selection of veins relative to their wall rock. Colour code: Red: >16. Pink: 8-16. Yellow: 2-8. Light green: 1-2. Dark green: <1.

In Greyschist					
spot	**FeO**	**CaO**	**MgO**	**MnO**	**Sr**
BUL2B-05T	0.350	28.354	0.161	4.555	12.519
BUL2B-06T	0.415	28.162	0.219	6.552	12.256
BUL3A-02.	0.312	28.398	0.220	4.192	10.960
ALT1.2-55	3.126	15.666	14.348	3.382	2.188
ALT1.2-58	4.429	15.666	12.231	8.075	9.945
Silicified Breccia and veins nearby					
spot	**FeO**	**CaO**	**MgO**	**MnO**	**Sr**
AD1B-01.D	6.127	13.995	9.133	10.472	7.108
AD1B-02.D	6.111	13.385	9.538	13.247	7.390
AD1B-03.D	6.437	13.835	9.206	7.949	11.372
COP2C-04.	5.125	13.166	12.062	13.556	9.702
COP2C-05.	5.204	12.647	12.669	13.704	8.945
COP2B-04	5.780	13.792	9.854	9.323	13.541
COP2B-06	5.757	13.572	10.103	12.655	11.721
Greenschist					
spot	**FeO**	**CaO**	**MgO**	**MnO**	**Sr**
BUL3C-04	1.233	3.187	1.819	5.139	15.073
BUL3C-05	0.732	3.132	2.398	2.625	19.795
BUL3C-06	1.026	3.137	2.132	2.756	13.588
Lamprophyre					
spot	**FeO**	**CaO**	**MgO**	**MnO**	**Sr**
AD2A-01T.	0.790	3.133	2.089	5.071	0.527
AD2A-03T.	0.663	3.247	2.200	1.951	0.619
AD2A-06T.	0.830	3.275	1.926	3.377	0.633
AD2A-07T.	0.692	3.502	1.835	3.955	0.751
AD2A-09T.	0.539	3.297	2.318	0.540	1.761
AD2A-10T.	0.856	3.222	1.959	3.166	0.496
AD2A-12T.	0.576	3.390	2.138	2.366	0.846

To assess how much rock (mass) is at least needed to make the same mass of vein, vein/rock ratios for the different elements have been calculated for a selection of vein compositions relative to their host lithology (Table 5.4.2). For these calculations, I used the actually measured rock concentration values rather than the calculated "available" ones described above, as the difference

between measured and calculated available budget is small. For the calculation of vein/rock ratio it is assumed that all elements are leached from the rock. This is not the case, as has been shown in chapters 3 and 4; however, this vein/ rock ratio is a good illustration of the different degrees of enrichment for the varying element. Vein/rock ratios are given in Table 5.4.2. Vein/rock ratios of Ca, Mg, Fe, Mn are larger for greyschist-vein pairs than greenschist- vein- and lamprophyre-carbonate pairs. Sr vein/rock ratios are on average slightly bigger in the greenschist pairs than greyschist pairs (Table 5.4.2). The smallest vein-rock ratios for Sr are those in lamprophyre and veins hosted in greenschist at Red Rock (Table. 5.4.2) Assuming that in all cases the fluid will be saturated in the major components at a similar concentration, to precipitate the vein carbonate fluid needs to interact with more rock in the greyschist-hosted settings than in the greenschist- or lamprophyre-hosted ones.

5.4.2.2: Lithology- associated controls on carbonate chemistry

In many cases the Fe/(Fe+Mg) ratio is host rock dependent and the on average higher Fe/(Fe+Mg) ratios of greyschist-hosted veins (BUL2B, 3A) compared to those in greenschist or lamprophyre corresponds to the unaltered host lithologies having a higher Fe/(Fe+Mg) ratio (Fig. 5.3.1). This suggests that the carbonate received much of its Fe and Mg from its host lithology. Nonetheless, the Fe/(Fe+Mg) ratios across the veins (rim and centre) are generally smaller than that of the whole rock (Fig. 5.3.1). (Fe/(Fe+Mg) ratios greater than the wall rock are only found in calcite which has less than 2wgt % FeO or MgO.) This suggests that a differentiation process took place prior to carbonate crystallisation. This could be related to three processes:

1. by precipitating an Fe-bearing phase "along the way",
2. due to contemporaneous precipitation of another Fe-bearing phase in the sink area, or
3. due to different solubilities of Fe and Mg.

Table 5.2.3) FeO, FeO/CaO and CaO/MgO of samples across the studied alteration halos.

Sample	FeO(wt-%)	FeO/MgO	CaO/MgO	Sample	FeO(wt-%)	FeO/MgO	CaO/MgO
BUL4Ca	8.97	1.97	1.77	**Bul3c-1, vein rich**	8.17	1.34	2.19
BUL4Cb	9.68	1.73	1.60	**Bul3c-2**	6.79	1.67	1.42
BUL4Cc	9.99	1.74	1.73	**Bul3c-4**	7.77	1.42	1.43
AD1C	3.23	3.93	2.32	**Bul3c-6**	7.96	1.42	1.47
AD1C2	3.25	2.98	1.48	**Bul3c-7**	7.97	1.36	1.51
BUL2A	2.82	3.03	1.50	**TP4A**	8.41	1.98	1.62
BUL2C	2.93	3.32	2.08	**TP4B**	8.86	1.81	1.22
TP7A	8.51	1.08	1.11	**TP4C**	8.91	1.86	1.58
TP7B	8.24	1.01	0.93	**TP4D**	7.70	1.92	1.99
TP7C	7.81	1.26	2.66	**TP4E**	9.57	1.73	1.24
TP7D	7.42	1.50	3.20	**TP4F**	9.00	1.97	2.03

Regarding the first possibility, it is hard to prove or disprove this hypothesis, as there is no information of what has happened at depth. Supporting the second case are hydrothermal sulphides, such as pyrite, that precipitated at a similar time as the carbonate and which would take some of the Fe available (MacKenzie et al., 2007). Indications that this may be a controlling factor is that in samples with little sulphide (i.e. BUL2B, 3A), the FeO/(FeO+MgO) ratios of carbonate are more similar to the wall rock than in pyrite-rich samples , such as the greenschist from Bullendale (Fig. 5.3.1). The third possibility can be checked by looking at the chemical composition of altered and unaltered rock adjacent to the veins (see chapter 3). If the vein received its Mg and Fe indeed from the wall rock and the Fe-Mg ratio discrepancy between vein and unaltered wall rock is caused by different solubilities,

the altered rock should be more depleted in Mg than Fe, which would show in an increase of the Fe/Mg ratio... And behold, this is the case in BUL3C and BUL4C, which are also the most reliable sample sets regarding the chemical changes associated with the hydrothermal alteration (Table. 5.4.3). This is in agreement with the solubility of the end member carbonate magnesite and siderite, as magnesite is more soluble than siderite (Fig. 5.4.2 A; Benezeth et al., 2009 & 2011). Correspondingly, the FeO/MgO ratio drops in the vein-rich part of the BUL3C set (BUL3C-1, Table. 5.4.3) which reflects that the Mg from the adjacent rock is concentrated in the veins.

To explain why the two main carbonate species (ankerite and calcite) form in certain lithologies and settings, the following model is proposed; due to the higher solubility of calcite compared to siderite and magnesite at higher temperature (Fig. 5.4.2 A; Benezeth et al., 2009 & 2011; Segnit et al., 1962; Rimstidt, 1997), fluid contains a base load of Ca and only relatively little Fe and Mg (Fig. 5.4.2B). This is supported by the hot spring water analyses in Barnes et al. (1978), where the water is more undersaturated in magnesite than calcite (Table. 4.4.1). When the fluid passes through Fe-and Mg-rich rock, such as greenschist, Ca, Mg and Fe are leached out by the fluid. This addition of metals will shift the fluid closer to saturation and precipitation of carbonate. As in that case, much of the element load originates from the greenschist wall rock, the fluid has at that stage a low Ca/(Fe+Mg) ratio, which "shifts" the fluid towards the dolomite (and ankerite) stability field (Fig. 5.4.1). In the cases where calcite precipitates, the fluid with the base load Ca, Mg, Fe reaches saturation probably not predominantly because of input from the surrounding rock, but because of other changes in the system, such as reducing pressure, degassing of CO_2 and/ or increasing pH.

A lithological control can in many cases also be recognised for Mn and Sr content of the carbonate (Fig. 5.3.2). Concerning Sr contents in carbonate in green- and greyschist, Sr contents are relatively similar, though on average slightly smaller for greyschist-hosted veins. The similarity of concentrations may indicate that in both cases the fluid carried similar background levels of Sr. However, at the site of the carbonate precipitation Sr from the adjacent wall rock is also incorporated by the vein carbonate. As there is more Sr in greenschist compared to greyschist (Fig. 5.3.3), the average Sr content in greenschist-hosted veins is also higher. Vein/rock ratios of Ca and Sr in the different rock types are different (Table 5.4.2), which is remarkable as Ca and Sr often occur in the same minerals (see chapter 4). Hence, between source and sink a differentiation between these two elements needs to take place. This differentiation may be attributed to the different solubilities of Sr and Ca carbonate in water. Helz & Holland (1965) have shown that at temperatures above 180°C strontianite is more soluble than calcite. Additionally, Ca is more abundant in the wall rock compared to Sr. Hence, fluid passing through the rock (mostly greyschist) dissolves Sr and Ca but will get relative to calcite become enriched in strontianite over time.

5.4.2.3: Setting-specific carbonate chemistry

As mentioned above, in some cases the carbonate chemistry is not host rock- but mostly location/setting-dependent. As will be discussed below, the carbonate chemistry can be attributed to mixing of components from different sources, chemistry of the fluid or varying temperature of precipitation.

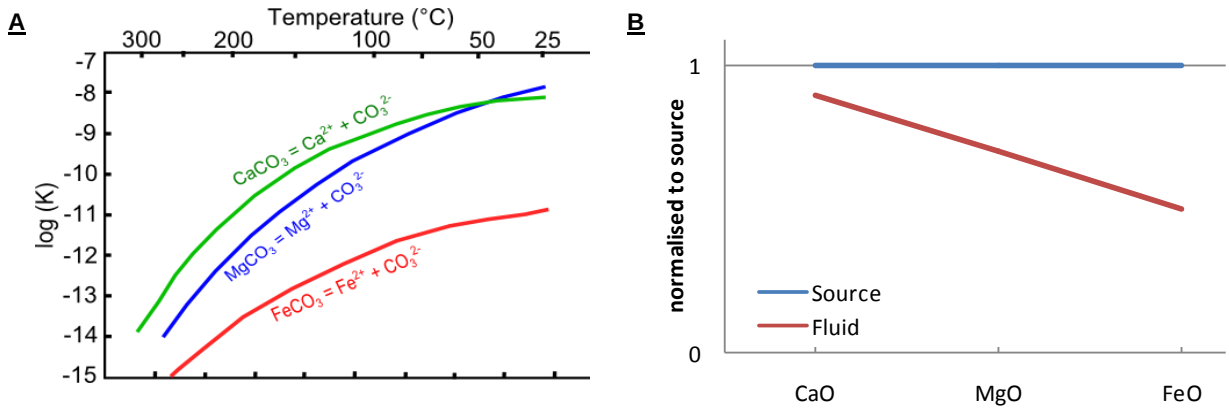

Fig. 5.4.2) A: Solubility constants of various carbonate species in aqueous fluid. Data from Benezeth et al. (2009) & (2011) and Segnit et al. (1962). **B:** Model of the fluid's composition in contact to the source assuming equilibrium and saturation and no previous element load.

5.4.2.3-1: Carbonate in veins at Mt Alta.

An example of mixing from different sources can be found for carbonate hosted in the diatreme at Mt. Alta. Veins taken from a greyschist block in the diatreme breccia (ALT1.2) have chemical properties different to greyschist-hosted ankeritic veins at Bullendale (BUL2B; Fig. 5.3.2). The average Mn concentrations in these diatreme-hosted veins are higher compared to those found in greyschist-hosted veins outside the diatreme and MnO/(MnO+FeO) ratios are in the range of lamprophyre-hosted veins or greenschist hosted veins (Fig. 5.3.2). These properties are a reflection of mixing of Mn derived from greyschist and lamprophyre; of all possible source rocks, lamprophyre has the highest Mn and greyschist has the lowest Mn content. Additionally, the differing Ca, Mg, Fe, values and their ratios in the veins of ALT1.2 compared other greyschist-hosted veins (Fig. 5.3.2) suggest that these elements are also derived from both, greyschist and lamprophyre. Such mixing is also suggested to take place for carbonate in the clastic breccia at Mt Alta (ALT2B; Fig. 5.3.2).

5.4.2.3-2: Carbonate in and around silicified fault breccias

An example of chemically distinct carbonate is the hydrothermal carbonate in and around silicified breccias (section 5.2.6; Yellow shading in Fig 5.3.1-4). Despite being hosted in greyschist, this carbonate differs in many aspects from the other carbonate hosted in greyschist. The carbonate in the breccias is poor in large ions (Ca^{2+}, Sr^{2+} and Pb^{2+}) (Fig. 5.3.1, 3&4) but relatively rich in the smaller ions, namely Mn^{2+} (Fig. 5.3.2) and Fe^{2+}. Fe-Mg ratios are similar to other greyschist-hosted veins (Fig. 5.3.2), indicating that the Fe and Mg are largely derived from greyschist. The high Fe-Mn ratio and high Mn, but low Sr concentrations can be explained by (1) mixing with lamprophyre-derived elements (2) precipitation of a Sr-Pb-Ca-rich phase, or (3) a different chemistry of the fluid influencing the solubilities of metals. The first case is unlikely as there is no indication of lamprophyre involvement in the carbonate chemistry based on the FeO/(FeO+MgO) (Fig. 5.3.1) ratio and there are no lamprophyre dikes found in the Shotover or around Treble Cone. If there was a connection to unexposed lamprophyre at depth, one would expect a gradual change of Mn values in the breccia-hosted carbonate from most influenced at Mt Alta to least in the Shotover; this is not the case.

Concerning option 2, there are no minerals precipitated in the structures that would preferentially take Pb, Ca, and Sr.

Regarding possibility 3 (different chemistry of the fluid), indications that this may be the case is the entirely different structure of the feature (silicified fault breccia vs. veins), high proportion of quartz and resorption of earlier precipitated carbonate (see Fig. 2.3.9 in chapter 2.3). Differences in the fluid could be pH, different ligands and different physical aspects, such as temperature and

pressure. It has been discussed earlier (chapter 2.3.4.1) that of these options a different pH and fluid chemistry are most likely the causes for the different structure of the silicified faults, as also proposed in section 4.4.2 (with respect to the crystallisation of kaolinite rather than muscovite). Concerning the carbonate in and near the fault breccia, a lower pH during formation of carbonate in the silicified breccia would increase solubility of all carbonate. This could concentrate siderite and magnesite over strontianite and calcite in the fluid, given that calcite and strontianite closer to saturation even at a higher pH. The relatively low concentration of the large cations suggests that the complexing agents in the fluid may have also been different compared to in other settings.

5.4.2.3-3: Carbonate veins at Red Rock

At Red Rock, Sr concentrations in alteration-related carbonate are low compared to the greenschist-hosted veins from Bullendale (Fig. 5. 2.6). Reasons for that may be a relative to the Bullendale setting lower CO_2 partial pressure, hence lower carbonate solubility (1), different ligands (2), differing solubility due to the higher temperature and no transport-related concentration of Sr over Ca (3) or different source rock chemistry (4).

Option 1 (lower CO_2 partial pressure) seems unlikely as at Red Rock the same reactions of metamorphic minerals are found as in the Bullendale greenschist, such as the breakdown of chlorite and titanite.

Concerning possibility 2 (different ligands in fluid), the abundant chalcopyrite suggest that the fluid was indeed different from that at Bullendale. Cu transport is often attributed to presence of Cl in the fluid (i.e. Seyfried & King, 1993) and it may be that this would have an effect on the solubility of Sr in the fluid..

With respect to the third option (higher temperature), calcite and strontianite are less soluble at higher temperatures (Manning et al., 2013 and references therein; Helz & Holland, 1965). Hence, the background load in the fluid that enters the greenschist at Red Rock would have had a lower content in Sr (and Ca, Mg and Fe) than at Bullendale. When it enters the Ca, Fe, Mg, Sr rich rock, the fluid would quickly saturate in and precipitate carbonate which would be similar to the Bullendale case. However, compared to the Bullendale example the background level of Sr would be lower. Saturation in the major carbonate (calcite and presumably dolomite) would also be at lower calcite concentrations, disabling transport-related concentration of Sr over Ca, as described above). It was tried to obtain the temperature for the Red Rock site, which was however unsuccessful (see next chapter).

Concerning, option 4 (low Sr content of the wall rock), the mineralogy in greenschist at Red Rock support this option. Except for calcite, all of the minerals abundant in the greenschist at Red Rock are low in Sr (chlorite, albite, quartz). Hence, fluid in or close to equilibrium with this type of rock would have a lower Sr content than fluid in equilibrium with more Sr-rich lithologies, such as at Bullendale. The composition of the wall rock may also explain why there is abundant copper mineralisation at Red Rock. Greenschist in the Otago Schist has on average slightly higher Cu contents than quartzo-feldspathic schist (Pitcairn, 2004) and the copper mineralisation at Red Rock could the representation of the fluid largely receiving its element load, including Sr and Cu, from greenschist which forms a relatively big body at and around Red Rock (Fig. 2.1.4). (This may also explain why tetrahedrite, a Cu-mineral is found in the greenschist of Bullendale but nowhere else (see chapter 3.)

Of the four mechanisms described above, the last one seems to be the most reasonable one.

Concerning the carbonate in the lamprophyre-hosted veins, Sr concentrations are also relatively low and the same explanations as at Red Rock may be applied. Considering that the

lamprophyres and diatremes are magmatic features, the associated hydrothermal system is likely also hotter, supporting possibility 3 to be the reason for the relatively small concentrations of Sr in the veins. Relatively hot fluid flows through lamprophyre which is rich in all components common in the carbonates. Hence the fluid does not leach much rock prior to precipitation, inhibiting enrichment of Sr over Ca (Table 5.4.2)

5.4.3- Pb, Th and U in the hydrothermal carbonate

Contents and ratios of Pb, Th and U in the different carbonates (Fig. 5.3.4) reflect the elements' different ionic properties and solubilities. Th and U are expected to be low in the carbonate as they, for one, belong to the generally weakly soluble HFSE (i.e. Floyd & Winchester, 1978; supported by the results of chapter 4.2, this study) and for another have unfavourable ionic charge for the carbonate's crystal structure (both generally four times positively charged ions). The occurrence of galena in various rocks examined here (see chapter 2.3) strongly suggests that the Pb present in the hydrothermal system is divalent. Divalent Pb classes a LILE (Winter, 2001), enabling it to be mobile in water. Additionally, Pb^{2+} fits relatively well into the carbonate crystal as it has divalent charge and has a similar radius as Sr^{2+} (Pb^{2+}= 0.119nm; Shannon, 1976). Another aspect to consider is that apatite and zircon, which are alteration-insensitive phases, are, relative to Pb, rich in Th and U (Förster, 1998; Ionov et al., 1987; Watson et al., 1997). As Pb concentrations are host lithology-dependent (Fig. 5.3.5), it is suggested that the Pb is locally derived. This would also coincide with results in Mortensen et al. (2010) who showed based on Pb isotopes in sulphides associated with the Shotover gold deposits that Pb (and Au) are derived probably from the Otago Schist.

5.4.4- Rare Earth Elements in carbonate

It has been shown in section 5.2 and 5.3.3 that REE patterns in hydrothermal carbonate can be very divers and can be different even within single samples (i.e. Fig. 5.2.10). (Concerning aspects related to charge balance which needs to take place with the substitution of the trivalent REE in a crystal site usually occupied by a divalent ion please refer to appendix J.) It has also been shown that there is no correlation of mineralogy (ankerite or calcite) and REE content. This suggests that crystallography has only a minor influence on the REE content here, which is in agreement with Kontak & Jackson (1999), Terrakado & Masuda (1988); Zhong & Mucci (1995). The textures of the carbonate, such as euhedral crystal shape or chemical zoning following grain shapes, shows that all of the carbonate's components, including the REE, must have been in solution prior to precipitation. This is further supported by the partly large vein-rock ratios for the major elements, such as Ca (Table 5.4.2).

REE are generally considered to have a low solubility just as hydrated ions (i.e. Migdisov et al., 2016; Poitrasson et al., 2004), which is due to their small ionic radius and high ionic charge, classing them as in hydrous fluid near insoluble HFSE (Winter, 2001). However, it has been shown that in some cases REE mobility increases (i.e. Rolland at el., 2003; Jiang eta al., 2005 and references therein) which is caused by the REE bonding with "ligands" (i.e. OH^-, CO_3^{2-}, SO_4^{2-}), forming complexes (i.e. Pan & Fleet, 1996; Wood, 1990; Haas et al., 1995; Poitrasson et al., 2004; Brookins, 1989 and references therein). Which of these ligands is the most abundant is not only dependent on availability but also temperature and pH (Brookins, 1989 and references therein; Haas et al., 1995; Migdisov et al., 2009; Migdisov & Williams-Jones, 2007; Poitrasson et al., 2004; Wood, 1990). At a precipitation temperature between 200 and 300°C and at intermediate pH conditions, the most likely ligands are fluorine, hydroxide, chlorine, carbonate and sulphate (Haas et al., 1995, Poitrasson et al., 2004, Migdisov et al., 2009 & 2016).

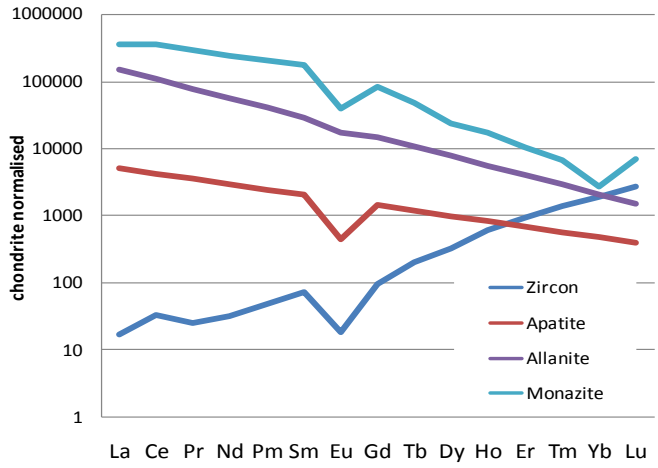

Fig. 5.4.3) REE composition of zircon, apatite, monazite and allanite. Data are average values from Förster, 1998 (Monazite), Belousova et al 2002/ own analysis (Apatite) and Hoskin & Black 2000 (Zircon); Allanite after Janots et al 2008, 2006).

5.4.4.1: REE availability

Similar to the main divalent constituents of the carbonate, it is necessary to evaluate the difference between the source rock composition and the actual available amount of REE. Source rocks are greyschist, greenschist and lamprophyre. In the rocks studied here, especially zircon, monazite, allanite and less so apatite are especially rich in REE and only few grains of these minerals can dominate the REE chemistry of the whole rock (Stosch, 2002). Of these minerals, apatite and zircon are certainly not affected by the alteration, as is described in chapter 3.2. Monazite grains (all Ce-Monazite) found in greyschist are very small and it could not be established if monazite is affected by the alteration. However, monazite has been shown to be only soluble at low pH (i.e. Poitrasson et al, 2004; Oelkers & Poitrasson, 2002; Cettinger et al., 2005) similar to apatite (Valsami-Jones et al., 1998; Guidry & Mackenzie, 2003; Harouiya et al., 2007). As apatite is stable during alteration, stability of monazite is also inferred. Regarding allanite, only one grain of Ce-allanite has been found (in AD1C2). This grain shows some secondary alteration but no mobilisation of REE. However, AD1C2 is, except for a few calcite veins, hydrothermally unaltered and mobility may different at higher degrees of hydrothermal alteration. This statement is supported by the observations made in chpater 4.3, where the REE are for example mobilised during the replacement of epidote by muscovite. No monazite and allanite have been found in greenschist or lamprophyre. Summarizing, apatite, monazite and zircon cannot contribute their incorporated REE to the fluid. In respect to allanite, an epidote-group mineral, the REE may be mobilised during alteration. However, even if the REE from allanite are mobilised during alteration, allanite is quite rare and the likelihood that the fluid flowing along a crack or fault interacts with an allanite grain is far smaller than for the more common minerals, such as chlorite or epidote.

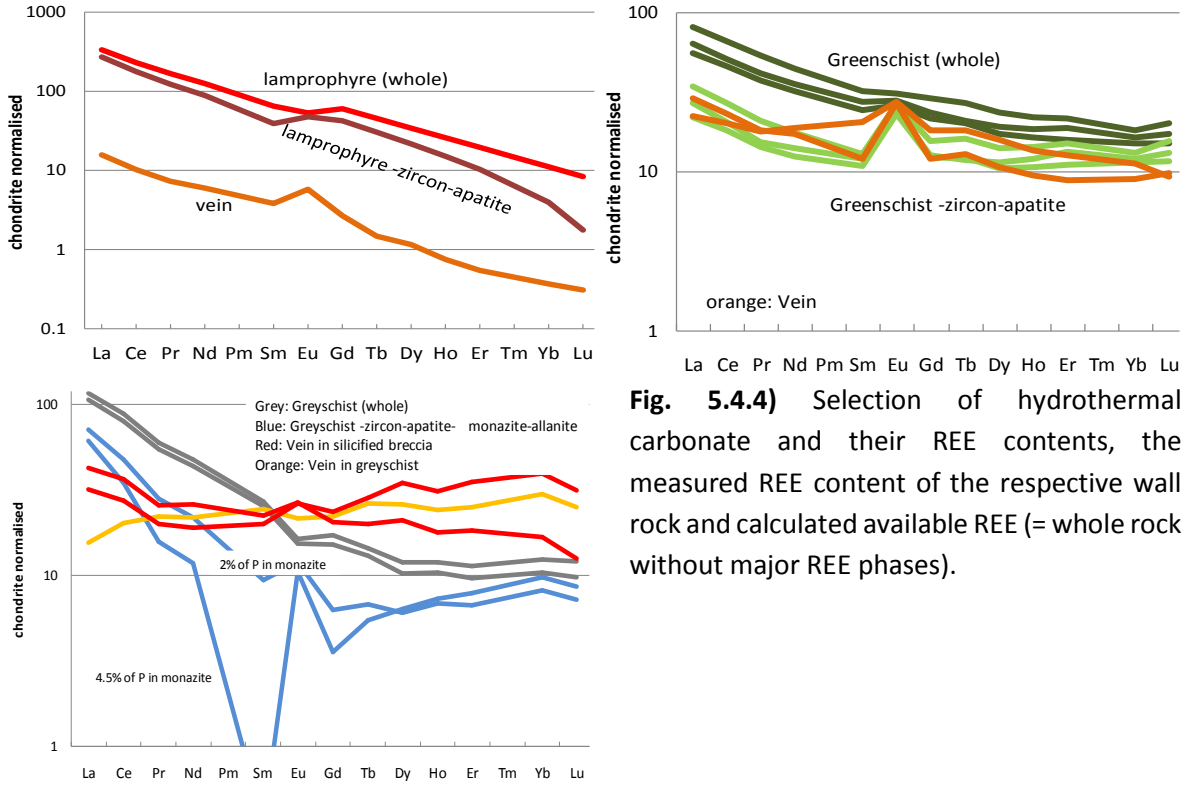

Fig. 5.4.4) Selection of hydrothermal carbonate and their REE contents, the measured REE content of the respective wall rock and calculated available REE (= whole rock without major REE phases).

Due to the stability of above mentioned REE-rich mineral phases, the difference between the whole rock composition and the actually available amount of REE is potentially significant. This difference can be determined by calculating the amount of REE bound by zircon, apatite, monazite +/- allanite. None of the afore mentioned stable minerals have been analysed in this study, but estimates of their REE composition can be made based on literature data (Fig. 5.4.3) (Förster, 1998 (monazite); Hoskin& Black 2000 (zircon) Belousova et al. (2002), Allanite (Janots et al 2008, 2006). For the calculations it is assumed that all Zr identified in the whole rock analyses is contained in zircon. P is in apatite as well as monazite and hence the relative proportions of these minerals in the wall rock need to be established. This was done using SEM BSE images. In most greyschist, monazite is estimated to contain roughly 2-5 % of the total P. Concerning the potential occurrence of allanite, estimation of allanite abundance in the rocks cannot be made based on the whole rock chemistry, as there are no "marker" elements that are exclusive to allanite. However, as monazite has a similar REE content as allanite (Fig. 5.4.3) and because both minerals are about similarly (un-)common in the rock, calculating the available REE budget for various amounts of monazite should also account for potential allanite in the rock. Additionally, the lower estimates regarding monazite content in the rock would take into account that some of the REE in the potentially unstable or present allanite are leached out of the rock by the fluid.

The results of these calculations are shown in Fig. 5.4.4 (Values and constants used are in appendix I). For lamprophyre the calculations give a REE pattern that is very similar to the original rock, with only a slight depletion in the HREE. For REE derived from greenschist in Bullendale, the REE of the available source are relative to the whole greenschist depleted in LREE and MREE and the REE pattern has a positive Eu anomaly. In greyschist the available REE budget is depleted in the LREE and MREE relative to the whole rock, which is due to the occurrence of monazite +/- allanite in the rock (Fig. 5.4.4). Naturally, the magnitude of this depletion depends on the concentration of monazite/allanite; in the case here, if the monazite content exceeds 4.5 %, the available concentrations of some REE become negative (Fig.5.4.4). However, if the concentrations of the different REE in monazite are

smaller than assumed, the maximal possible amount of monazite in the rock increases. Using the calculated REE values, the calculated vein/ rock ratios (Table 5.4.4) show that especially in lamprophyre and greenschist-hosted carbonate only little rock needs to be leached to provide the "required" REE in the vein carbonate.

Table 5.4.4) Calculated vein- rock ratios for a selection of veins and the available REE from the host rock. Colour code: dark green<1; light green=1-2; yellow>2.

In Greyschist	La	Ce	Pr	Nd	Sm	Eu	Gd	Tb	Dy	Ho	Er	Yb	Lu
BUL2B-05T	0.13	0.53	0.94	1.28	5.06	2.14	5.57	4.44	4.66	3.56	3.25	3.11	2.99
BUL2B-06T	0.04	0.18	0.34	0.45	1.88	0.84	2.10	1.76	1.56	1.29	1.08	1.00	0.80
BUL3A-02.	0.09	0.47	0.94	1.20	4.20	1.90	4.10	4.12	4.10	3.38	3.41	3.34	3.17
ALT1.2-55	0.02	0.09	0.21	0.31	2.10	1.28	3.89	4.39	4.67	3.58	3.46	2.74	2.45
ALT1.2-58	0.37	0.99	1.45	1.71	4.68	1.83	4.48	4.53	5.22	4.43	4.73	4.44	4.41

Silicified Breccia	La	Ce	Pr	Nd	Sm	Eu	Gd	Tb	Dy	Ho	Er	Yb	Lu
AD1B-01.D	0.19	0.65	0.93	1.34	4.71	2.95	5.29	4.85	5.48	4.55	4.91	4.40	3.93
AD1B-02.D	0.18	0.67	0.91	1.24	4.29	2.94	4.90	4.46	4.86	4.07	4.38	4.31	3.97
AD1B-03.D	0.25	0.85	1.10	1.44	3.82	2.34	3.83	3.13	3.34	2.49	2.48	1.87	1.57
COP2C-04.	0.06	0.25	0.40	0.60	2.78	1.93	2.99	2.94	3.30	2.81	3.05	2.82	2.91
COP2C-05.	0.04	0.19	0.29	0.49	2.12	1.81	2.50	2.64	2.84	2.34	2.47	2.65	2.55
COP2B-04	0.17	0.61	0.79	0.98	2.75	2.62	3.11	2.76	2.93	2.16	2.17	1.62	1.57
COP2B-06	0.18	0.64	0.85	1.04	3.44	2.32	4.39	4.46	5.52	4.34	4.84	4.40	3.97

Greenschist	La	Ce	Pr	Nd	Sm	Eu	Gd	Tb	Dy	Ho	Er	Yb	Lu
BUL3C-04	1.01	1.20	1.39	1.60	2.02	1.16	1.51	1.55	1.45	1.19	1.04	0.96	0.75
BUL3C-05	0.46	0.54	0.64	0.74	0.85	0.83	0.81	0.80	0.83	0.66	0.57	0.47	0.47
BUL3C-06	0.46	0.54	0.64	0.74	0.85	0.83	0.81	0.80	0.83	0.66	0.57	0.47	0.47

Lamprophyre	La	Ce	Pr	Nd	Sm	Eu	Gd	Tb	Dy	Ho	Er	Yb	Lu
AD2A-01T.	0.02	0.03	0.04	0.06	0.09	0.38	0.04	0.03	0.03	0.03	0.04	0.03	0.12
AD2A-03T.	0.06	0.06	0.06	0.07	0.10	0.12	0.06	0.05	0.05	0.05	0.05	0.09	0.17
AD2A-06T.	0.07	0.09	0.14	0.19	0.22	1.39	0.10	0.08	0.08	0.09	0.12	0.24	0.38
AD2A-07T.	0.07	0.12	0.20	0.35	0.49	2.07	0.21	0.16	0.14	0.12	0.11	0.15	0.34
AD2A-09T.	0.02	0.02	0.02	0.03	0.05	0.10	0.03	0.03	0.03	0.03	0.04	0.16	0.26
AD2A-10T.	0.07	0.11	0.16	0.23	0.31	0.62	0.16	0.11	0.12	0.10	0.09	0.14	0.22

5.4.4.2: Processes controlling the carbonate's REE content

Rock-controlled processes

Comparing the available REE budget against the carbonate and the carbonate's host rocks (Fig.5.4.4) shows that the REE patterns of veins hosted in the greenschist at Bullendale (BUL3C; Fig. 5.2.4 & Fig.5.4.4) and little altered lamprophyre (AD2A; Fig. 5.2.8 & Fig.5.4.4) are very similar to the available REE budget from greenschist and lamprophyre (Fig.5.4.4). This strongly suggests that the REE were directly derived from the wall rock of the vein carbonate. This is also in agreement with the low vein/rock ratios of these samples (mostly <1; Table 5.4.4) which shows that only little rock needs to be leached to provide the REE found in the vein.

Fluid-controlled processes

Concerning calcite and ankerite hosted in greyschist (Fig. 5.4.4), the REE patterns of the carbonate and those of the available budget from greyschist are different especially concerning the LREE. Some of the discrepancy can be attributed to the assumptions made regarding the abundance and concentrations in the REE-rich minerals (apatite, zircon, monazite, allanite) used for the calculations above. Nevertheless, despite these uncertainties, in many cases this cannot satisfactorily explain the REE patterns, specifically where REE patterns differ in a single sample (i.e. ALT2C, AD2B, BUL2B, BUL3A) (Fig. 5.3.5). In those cases a differentiation process needs to take place while the REE are suspended/ dissolved in the fluid.

In some cases, the different patterns can be explained by *"successive precipitation"*. Veinlets in BUL2B, for example, have a strong enrichment in HREE and depletion of LREE (Fig. 5.3.1B). These veinlets are, at least partly, late stage, and the lower concentration of the LREE may be caused by depletion of the fluid due to earlier precipitated carbonate, preferentially taking the LREE (e.g. Rimstidt, 1998). This conclusion is supported by the slightly negative REE slope in earlier veins in this sample, Fig. 5.3.1B. Accordingly, after initial carbonate precipitation, the remaining fluid would have been depleted in LREE and relatively enriched in HREE. Together with the REE the first carbonate also incorporated Ca, therefore also causing depletion in Ca and other major components. This leaves the issue of fluid saturation to precipitate the second stage of carbonate. To achieve saturation physical conditions the pH needed to increasing or the pressure decrease. In addition to these two processes, the fluid may also was replenished, in which case the carbonate chemistry in the veinlets would suggest that the Ca was brought into the site by the fluid but that the source of the less mobile REE was exhausted due to the earlier fluid passing through this source leaching the available REE out.

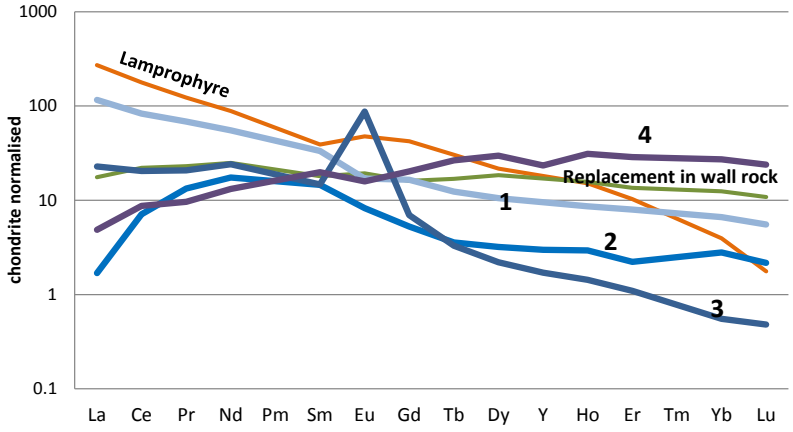

Fig. 5.4.5) Schematic representation of REE composition and succession of vein- and vesicle-filling carbonate in highly altered lamprophyre of AD2B and ALT2C. The orange line is the calculated available REE budget from lamprophyre. The numbering refers to the relative age of the carbonate. 1 oldest, 4 is youngest.

An example where the different REE patterns can be attributed to the differing fluid chemistry are the sparry veins and vesicle fillings in highly altered lamprophyre at Mt Alta Diatreme (ALT2C and AD2B; Fig. 5.3.9&10). As shown earlier the carbonate from these samples display a systematic change of REE patterns (Fig. 5.4.5): the structurally oldest carbonate at the vein rim in ALT2C (Fig. 5.2.9A; type B) has a negative REE slope (1 in Fig. 5.4.5), which is similar to the available REE from the wall rock (orange line in Fig. 5.4.5). This pattern can be achieved by the REE being derived from the surrounding lamprophyre without much differentiation taking place whilst the REE are in solution; the REE are "brought" into solution but as soon as a REE accommodating mineral (here carbonate) precipitates, the REE fall out of solution, too. This is essentially indistinguishable from sorption-dominated fluid chemistry as described by Bau (1991).

The depletion in LREE in the structurally younger, clear carbonate causes the carbonate to have a concave REE pattern (2 in Fig.5.4.5; Fig. 5.2.9A & 10B, Type A). The LREE depletion may be caused by the presence of a phase in the source or sink preferentially incorporating La and Ce over all

other REE and not making these elements available to the carbonate. However, I don't know of any minerals that would preferentially only take La and Ce and I have not found any evidence for such minerals in my analyses. This suggests that the "convex" REE pattern is the result of fractionation of the REE taking place whilst dissolved in the fluid. Comparing the shape of the carbonate compositions with the complex stabilities reported by Migdisov et al. (2009) indicates that the dominant ligand would have been chloride or potentially fluoride. It has been stated by Migdisov et al. (2016) that mobilisation of large amounts of REE by fluoride complexes is unlikely as fluoride has a low solubility at intermediate pH conditions, suggesting that chloride would be more likely here.

Stage 3 carbonate at the rim of AD2B has only slightly convex REE pattern (Fig.5.4.5; type Y in Fig. 5.2.10A&C). This pattern may reflect that the REE in the fluid are partly controlled by halogenide complexes (Migdisov et al., 2016) and partly by direct input from the wall rock. This intermediate composition indicates that the fluid did not attain chemical equilibrium regarding complex stability prior to precipitation. Alternatively the negative slope of the carbonate's REE pattern could be could be caused by complexing with a different ligand. Apart from halogenides, only nitrate has been predicted to produce a fluid with a negative slope in the REE pattern (Haas et al., 1995). However, presence of nitrate seems less likely than a host rock-dominated carbonate composition.

The fourth stage carbonate (Fig. 5.2.10A&C type X; stage 4, Fig.5.4.5) has a HREE enriched and LREE depleted pattern relative to the lamprophyre. Either this represents derivation from a different source (i.e. specific mineral in the lamprophyre such as type D carbonate in Fig. 5.2.10B) or it represents a fluid that was dominated REE complexes. Referring to stability data from Haas et al. (1995), this pattern would coincide with a fluid whose REE load is controlled by hydroxide or carbonate complexes. Considering that carbonate is ubiquitous in the system, this would be the favourable choice. However, though the stability graphs in Haas et al. (1995) are similar to low temperature waters analysed by Luo & Byrne (2004) and Otha & Kawabe (2000) experimental data for higher temperatures are missing and therefore my hypothesis cannot be confirmed. A difference in ligands complexing with the REE during the evolution of the vein, may also account for the relatively diverse REE pattern in the veins hosted in a greyschist block in the diatreme breccia at Mt Alta (ALT1.2; Fig. 5.2.7).

The different ligands interpreted to be responsible for the different REE patterns in the carbonate hosted in altered lamprophyre at Mt Alta (Fig. 5.4.5) could be related to different sources for the components in the fluids. These sources are most likely the Otago Schist and the ADS. Several studies have shown that fluid inclusion in hydrothermal veins hosted by Otago Schist contain fluid with a low salinity (i.e. Craw, 1989; Koons & Craw, 1991 and references therein). No data exists on the composition of the fluid primarily associated with the Alpine Dike Swarm (Cooper, pers. comm). However, chlorine- and fluorine-bearing minerals have been found in carbonatites of the ADS (taeniolite and baotite; Cooper, 1996; Cooper et al., 1995), indicating that the Cl +/- F interpreted to be involved in the formation of the carbonate of stage 2 and 3 (Fig. 5.4.5) could have been derived from the magmatic fluid source. Complexing of REE with halogenides has also been proposed to be the cause of a convex REE pattern of Ferro-carbonatites further north in the ADS (Cooper et al., 2015).

The concave REE patterns of calcite and ankerite veins at Red Rock (Fig. 5.2.6) are similar to fenitised greenschist adjacent to carbonatite dikes north of this study area (Cooper et al., 2016). Similar to the greenschist at Red Rock, Cooper et al.'s greenschist also contains magnetite. Different is that "their" rock contains about 25% biotite. Cooper et al. (2016) interpret the concave REE pattern in their altered rock (compared to the flat REE pattern in the unaltered greenschist) to be the result of the REE being transported into the rock in complexes with carbonatite-originated chloride. The occurrence of chalcopyrite at Red Rock may point towards a saline fluid composition, as the solubility of Cu increases

with Cl content (Seyfried & King, 1993; Liu & McPhail, 2005). However, at Red Rock the pre-alteration calcitic veins in RR18 have essentially the same REE content as the ankeritic veins (Fig. 5.2.6) which would require a similar fluid chemistry for many million years. This is unlikely and it is suggested that the fluid's and carbonate's REE composition is controlled by the host rocks mineralogy rather than the "external" fluid chemistry. However, to confirm or disprove this hypothesis more data needs to be collected in the Red Rock hydrothermal system, such as whole rock composition of altered and unaltered greenschist at that site.

Regarding the carbonate hosted in greyschist and in silicified breccias (Fig. 5.4.4), the discrepancies regarding the available REE from the wall rock and the REE pattern of the carbonate can partly be attributed to the assumption made during the "availability-from-the-source calculation". However, the compared to greenschist larger vein/rock ratios for the major components (Ca, Fe, Mg) (Table. 5.4.2) shows that fluid needed to pass through more rock relative to greenschist-hosted veins before the same degree of saturation with respect to calcite or ankerite was achieved. Similarly, the vein/rock ratios for REE are relatively large, especially MREE and HREE (generally > 2, Table 5.4.4). This suggests that also REE were in solution for a longer time than in greenschist-hosted veins before carbonate precipitation took place. Hence, the carbonate's composition will be a representation of fluid-controlled processes, which take place while the elements are dissolved in the fluid. It follows, that as the REE are more soluble when forming complexes, the fluid should carry the REE predominantly as complexes. Hence, with the fluid trending towards chemical equilibrium, its chemical composition will begin to represent the stability of these REE complexes relative to each other, as opposed to the source's composition. It is then this fluid-controlled process that can be recognised in the chemical composition of the vein-filling carbonate in greyschist.

Another indication that complexing plays an important role in the formation of greyschist-hosted veins can be found in the thick carbonate vein of BUL3A (Fig. 5.2.2&3). Here the vein rim have REE pattern with a slight negative slope, hence more similar to the wall rock compared to the carbonate in the centre, where the REE slope is slightly concave to slightly positive and REE concentrations are overall lower (Fig. 5.2.3), hence supporting a REE solubility controlled by hydroxide- and/or carbonate-REE- complexes. Alternatively it could reflect the progressive crystallisation of carbonate from the fluid, like in BUL2B. However, it appears unlikely that the 2-3 cm thick carbonate vein of BUL3A formed from a single, large reservoir of carbonate-REE-bearing fluid.

5.4.4.3: Summary of the REE chemistry of hydrothermal carbonate

The cases discussed above show that the REE patterns of carbonate are controlled by a complex interplay of dominant-ligand species, saturation of the fluid with respect to the main carbonate species, disequilibrium and available REE from the wall rock.

Rock-controlled carbonate chemistry

In cases were only little rock volumes need to be leached to provide the major elements (Ca, Fe, Mg), such as in greenschist and lamprophyre, the fluid is quickly closer to saturation in these major components. Correspondingly, the REE, which are mobilised at the same time as the major elements of carbonate, will not be in solution for long either and precipitate shortly after dissolution. Due to the short time in solution, the fluid does not have time to attain chemical equilibrium regarding REE complexes. Additionally it may be that in these cases the fluid is the REE are not bonded in complexes, as initially they are "forced" into solution due to the breakdown of their original carrier minerals, e.g.

epidote, and lack of appropriate carrier minerals forming immediately after break down (similar to Köhler et al.,2005).

Fluid-controlled chemistry

In cases where relatively large volumes of rock need to be leached to provide for the vein material, such as in greyschist-hosted veins and fault breccias (i.e. BUL2B & 3A, COP2C) components, including REE, are in solution for longer. During this time REE-complexes should become dominant, as complexes are more soluble than simply hydrated REE. In case that carbonate or hydroxide are the dominant ligands, the carbonate's REE pattern should have a simple positive slope (Haas et al., 1995), in case of halogenides it should be a convex one (Migdisov et al., 2009). Another case of fluid-controlled carbonate compositions are found in the thick sparry veins in highly altered lamprophyre (ALT2C, AD2B). Although the vein/rock ratios for the major elements (Mg, Fe, Ca) are small, the REE patterns of the carbonates points towards involvement of ligands which in turn may indicate that in this fluid ligand concentrations may have been relatively high, relative to outcrops elsewhere. This is in agreement with the veins being hosted by a volcanic diatreme and potentially relatively saline fluids at some stages of the carbonate precipitation. These fluids may have also had other properties, be it of chemical (e.g. pH, source) or physical nature (e.g. higher temperature).

The reason why mobility of REE is not recognised in the whole rock chemistry of the altered host rock of the veins (i.e. BUL3C and BUL4C, Fig. 4.2.7) may be explained by consulting the vein/ rock ratios for the REE. The greenschist from Bullendale (BUL3C&4C) is the only set were the zone right next to the halo-central veins was analysed and hence are most likely to show potential REE mobility. For the carbonate veins in these rocks, the vein/ rock ratios for REE are mostly smaller than 1 (Table 5.4.4) and to make a vein of 5 mm thickness, the zone from which the REE are leached is less than 1 cm wide. The thickness of these zones is thinner than the rock samples analysed for the whole rock composition (>1.5 cm), and hence this is below resolution. Additionally, not all the REE (and other elements in carbonate) are washed out of the rock and the leach zone would be more diffuse and subtle.

5.4.4.4: REE in magmatic ocelli

The ocelli in lamprophyres formed by separation of the calcitic and silicic phase during crystallisation of the lamprophyric melt (Cooper, 1979). To evaluate the relative abundance of the trace element in the ocelli and the silicic part of the lamprophyre, partition coefficients for carbonatites -silicic melt (i.e. Martin et al., 2013, Veksler et al., 2012) were used. These models can be used here despite the reported lamprophyre compositions being bulk lamprophyre and ocelli, as the ocelli only make up 1-2% of the entire rock volume. In both of these experimental studies, carbonatite in equilibrium with the silicic part of the consolidated melt is slightly depleted in the HREE. This is similar to what is observed for the ocelli and lamprophyre here (Fig. 5.2.15& 3.6), despite most likely differing T, P and chemical conditions. However, not concurring with the experimental data is the lower concentration of Sr in the ocelli compared the lamprophyres. This may simply be due to the ocelli being measured in a different lamprophyre compared to the lamprophyres that provided the whole rock analyses. However, the higher content of Sr in the lamprophyre seems to be consistent for samples from different locations (Cooper et al., 1986; Clough, 1988). The discrepancies between the ocelli and the carbonatite in the experiments is probably caused by the ocelli forming separating from the silicic magmatic material only after a certain amount of crystallisation has taken place, instead of the sudden cooling as in the experiments by Veklser et al. and Martin et al.. Hence, it may be that the Sr was incorporated into an earlier crystallising phase. These may be apatite or amphibole, both of which form

needles at the rims of and pointing into the ocelli (Fig. 2.4.2), showing that they grew into a fluid-filled cavity and in which later the calcite precipitated.

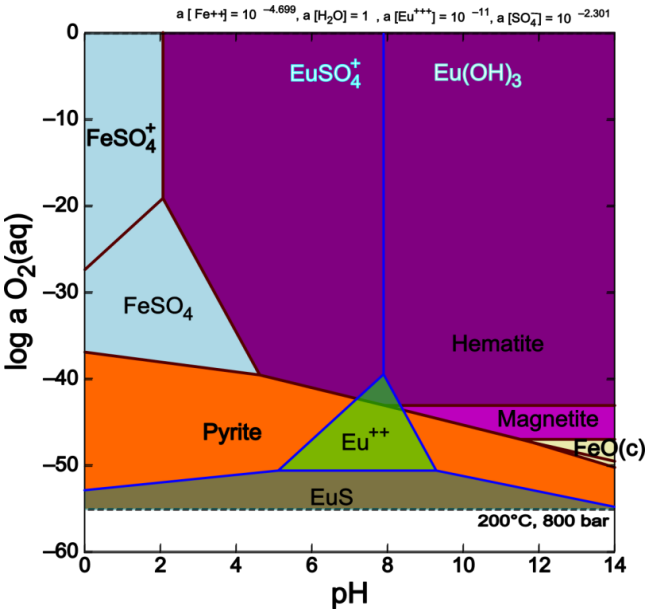

Fig.5.4.6) GWB model of stable phases in a S- and Eu-bearing hydrous fluid. The stability field of divalent Eu and pyrite overlap. Conditions and concentrations are based on Craw (1989) and Poitrasson et al. (2004).

5.4.5- Anomalies in REE patterns in carbonate

In the REE patterns of the carbonate presented in chapter 5.2 Eu anomalies can be recognised in many analyses. Eu anomalies are generally attributed to the different oxidation states of Eu, which can be tri- or divalent (e.g. Bau, 1991; Wood, 1990). The change of tri-to divalent oxidation state is a function of oxygen fugacity, temperature, pH and pressure (Bau, 1991). The higher T and pH are, the higher is the "critical" oxygen fugacity where the transition of di- to trivalent Eu takes place (Bau, 1991). In many samples hydrothermal pyrite or other sulphides occur, attesting for a low oxygen fugacity. The stability field of pyrite and divalent Eu overlap (Fig. 5.4.6). Coincidentally, the occurrence of pyrite and other sulphides coincides with positive anomalies in many hydrothermal carbonate samples, but not all (Table 5.4.5). Accordingly, many samples without Eu anomaly quite often also do not contain sulphides (Table 5.4.5).

The reason why divalent Eu should be enriched in carbonate can be attributed to the properties of divalent Eu. In its divalent state, Eu has a similar ionic radius as divalent Sr (Sr^{2+}=1.18A; Eu^{2+}=1.17A; Shannon, 1976). And teh reason why Eu should be enriched in carbonate can have 3 main reasons: carbonate crystal structure, source and differentiation process taking place while the REE are in solution.

Concerning case 1, carbonate should favour Eu substitution over the other REE, as divalent Eu has the ideal ionic charge and also fits in the carbonate crystal lattice, in analogy to Sr (Rimstidt et al., 1998). This would give the REE patterns a positive Eu anomaly. Concerning the source as the cause for a Eu anomaly, calculations of the available REE budget (Fig. 5.4.4) show that most of the patterns of the available REE have positive Eu anomalies which is caused by the negative anomalies of the alteration-insensitive minerals (monazite, zircon and apatite). If this is the controlling factor, the carbonate should not display any relationship between the Eu and Sr content. A fluid induced differentiation would be based on a different mobility of Eu^{2+} in fluid, compared to the other REE. To my knowledge there are no experimental or numerical studies that quantify the solubility of divalent Eu. Bau (1991) evaluated theoretically the behaviour divalent Eu in aqueous fluid but only accounts for Eu complexing with the same ligands as the other REE. However, divalent Eu classes as a LILE (Winter, 2001) and should therefore also have similar properties in aqueous fluid. If fluid transport is the controlling factor for the REE content in the carbonate, the carbonate should have a positive correlation of Sr vs. Eu content and Sr vs. Eu anomaly.

Above described Eu-content- controlling mechanism (crystallography, fluid transport, source) are only end members fluid and several can take place from case to case. The inconsistency regarding

the correlation of Sr vs. Eu content or Eu anomaly (Table 5.4.5) supports this. Concerning the fluid-controlled chemistry, it also needs to be questioned if divalent Eu in the fluid had the time to reach equilibrium in respect to its similarity to Sr^{2+}. Immediately after leaving the source, trivalent REE (incl. Eu^{3+} and Eu^{2+}) the Eu content in the carbonate will reflect the source. This is probably the case for many analyses (BUL3C, AD2A). Over time and potentially some mineral precipitation, Sr and divalent Eu are more likely to stay in the fluid due to the higher solubility compared to trivalent REE. When this is the case, the precipitates from this fluid should have a positive Eu anomaly and Eu and Sr content should correlate positively. This hypothesis is supported by the late stage veinlets in sample BUL2B (Fig. 5.3.1). These have a strong positive Eu anomaly and which largely corresponds to a high Sr content. However, there is no rule for the relationship between Sr and Eu, as too many processes play a role in the Eu, REE and Sr chemistry of the carbonate (oxidation state of the Eu, source, solubility, degree of chemical equilibrium).

Table 5.4.5) Summary of correlation of Sr and Eu content/ Eu anomaly in the different samples. Colour coding corresponds to earlier correlations in section 5.3.

Linear c orrelation	Sr content vs. Eu content correlate	Sr content vs. Eu anomaly correlate
Total	BUL2B AD2B ND1A	BUL2BALT2C AD2B TP1.3 COP2C
Some	BUL3C (anti-proportional) ALT1.2ND3B	BUL3CALT1.2ND3BALT2B (anti-proportional)
None	BUL3ARR20ALT2C AD2A TP1.3 COP2B COP2C AD1B ALT2B	BUL3A RR20 AD2A COP2B AD1B
Distinct Eu anomaly	**COP2B, BUL3C, ND3B, BUL2B**	
No distinct Eu anomaly	**RR20, BUL3A, ALT1.2, ND1A, ALT2C, AD2B (some), ALT2B, COP2C**	
Pyrite or other sulphide	**COP2C, BUL3C, ND3B, ALT1.2, (TP1.3; ZnS), (RR20; chalcopyrite), (BUL2B; ZnS, PbS)**	

5.5) Conclusions

The carbonate analyses presented in this chapter have shown that the chemistry of carbonate minerals in veins, vesicles and breccias depends on wall rock lithology, setting, the carbonates' crystal structure and if rock- or fluid-controlled processes dominated.

The carbonate species (calcite and dolomite) is largely setting dependent and also gives evidence that Ca, Mg, Fe and Mn can be transported several meters at least, allowing for mixing from several source rocks to take place. For example, the veins of ALT1.2, which are hosted by greyschist in the diatreme, have Fe, Mg, Mn, and Ca contents and ratios intermediate between those of lamprophyre in the diatreme and greyschist-hosted veins at Bullendale.

The generally lower Fe/Mg ratio in the veins compared to the wall rock probably reflects that siderite is less soluble than magnesite and also that some of the rock's Fe is incorporated by pyrite in the wall rock.

The carbonate in the silicified fault breccias is relative to greyschist-hosted veins at Bullendale poor in Ca, Sr and Pb, rich in Mn and Fe, but has similar Fe-Mg ratios. In relation to this, it was suggested that this may be an indicator for a different fluid composition, such as a lower pH, which formed the partly gold- bearing breccias. This conclusion concurs with those made in chapter 4.

In many cases, veins are more enriched in Sr than Ca compared to their wall rock, which reflects that Sr becomes enriched in the fluid. This attribute is most likely due to a higher solubility of strontianite compared to calcite at higher temperatures.

Crystallographic controls for the carbonate chemistry play a role for the Ba content in the carbonates; the low concentrations of Ba in the analysed carbonate are a sign of the carbonates' inability to accommodate the large divalent Ba ion (radius = 0.135nm) their crystal structure.

Concentrations of the REE in most carbonate analyses lie between 1-100 chondritic values independent of carbonate species (ankerite or calcite) and REE patterns are different from setting to setting. These different patterns in the carbonates are the reflection of two main processes competing, rock- and fluid-controlled processes. To assess which one is dominant, the wall rock compositions need to be considered. However, unlike for the major components of the carbonate, the whole rock composition does not necessarily resemble the amount of REE available to the fluid. This is due to alteration-insensitive, REE-rich minerals (apatite, zircon monazite +/- allanite). It shows that the REE patterns of the REE available from lamprophyre are similar to the whole lamprophyre. For greenschist and greyschist on the other hand the available source is relatively depleted in LREE and MREE, especially in greyschist.

Fluid-controlled processes, i.e. relative REE-complex stability in solution, governing the REE carbonate chemistry are prevalent in sites where relatively large amounts of rock need to be leached to provide the major components of the carbonate (Ca, Mg, Fe). On the other hand, where this is only little rock volumes need to be leached to provide Ca, Mg and Fe, the REE patterns in the carbonate resemble those of the wall rock.

Sr and Eu contents do not have a systematic correlation which is due to too many factors potentially controlling the minerals chemistry (oxidation state of Eu, source, relative solubility, whether chemical equilibrium has been attained).

CHAPTER 6) ISOTOPE GEOCHEMISTRY OF VEINS AND ROCKS

In this chapter isotope geochemical tools are used to identify the sources of various components that played a role in the hydrothermal vein- and breccia fillings and alteration halos studied here. To determine the source of the components in the carbonate veins, the isotope ratios of carbon ($^{13}C/^{12}C$), oxygen ($^{18}O/^{16}O$), strontium ($^{87}Sr/^{86}Sr$) and neodymium ($^{143}Nd/^{144}Nd$) have been determined for a selection of samples. These samples are unaltered metamorphic rock, altered metamorphic rock and different types of void-filling and hydrothermal carbonate. These 4 isotopic systems were chosen because they belong to key element groups in the veins and in the wall rock. The Nd system can be regarded as a proxy for the source of the LREE, while Sr isotope ratios give insight into the provenance of the LILEs and Ca. The origins of the volatile components in the fluid are represented by isotopic ratios of oxygen and carbon. There are two main reasons why I am interested in the source of these components. For one it complements the goals of chapter 3, 4, and 5 where it was evaluated how far the different components have travelled. For another, using especially the stable isotope systems, the question posed at the start of this thesis and which is incorporated in the title of this thesis can be addressed: Is there a connection between the magmatic and gold-bearing hydrothermal system?

Before going into detail on the data, I would like to briefly recapitulate on the basic aspects important in isotope geochemistry. In isotope geochemistry the ratio of two isotopes of one element are measured and this information is then used to evaluate potential sources. The isotope systems utilised here can be divided into two main groups: stable (oxygen, carbon and iron) and radiogenic (neodymium and strontium). In stable isotope systems both of the elements contributing to the ratio formed in stars prior to the consolidation of Earth and their isotopic ratio in a material does not change over time. In radiogenic systems, one or two of the isotopes that contribute to the ratio forms by radioactive decay of another isotope (mother isotope) in addition to nucleo-synthesis. In the Sr system, part of the ^{87}Sr is produced by radioactive decay of ^{87}Rb, while the breakdown of ^{147}Sm creates ^{143}Nd.

The reason, ratios of the different isotopes of an element can give information about their source is that they vary in different geological settings. This variation is due to the different behaviour of the different isotopes during chemical reactions (e.g. during dissolution, crystallisation, fluid transport and fluid -rock interaction) caused by the differing masses of the isotopes or due to changing oxidation states of the element during redox-reaction (Hoefs, 2008). Mass-dependent fractionation is a function of the relative difference between the masses of the isotopes analysed for and hence with increasing atomic number of the element the mass-dependent isotope fractionation decreases. Correspondingly, in the case here, mass-dependent fractionation only affects the isotopes of the stable isotope systems but not the "heavy" radiogenic isotope systems. Fractionation due to different oxidation states of the elements can theoretically play a role in all of the three stable isotope systems used here, but is expected to be especially important in the Fe isotope system; it has been shown earlier that Fe occurs in its trivalent state (e.g. in epidote) and divalent state (e.g. in carbonate). For the radiogenic isotope systems mass-dependent and oxidation-state dependent fractionation do not have to be considered as in both cases the atomic mass of each isotope is relatively large and because ions only occur in one valency; Sr ions are divalent and Nd ions are trivalent. However, as these are "radiogenic systems", the isotope ratio of the analysed material is governed by the rate of radioactive decay and the partitioning of the daughter and mother isotopes into the analysed substance.

6.1) Methods

In all cases, isotope data are reported as ratios of two isotopes, as the mass spectrometer cannot measure absolute concentrations. Values obtained for the oxygen and carbon systems are given

relative to international standards. For oxygen this is the, Vienna-Standard Mean Ocean Water (V-SMOW). Carbon values are given relative to a cretaceous belemnite from South Carolina (PDB). Ratios of Sr and Nd isotopes are not normalised, as is common practice.

6.1.1-Radiogenic isotopes

Strontium and neodymium isotopic ratios of rocks and minerals were measured either from solution or in-situ. In-situ analyses could only be done on carbonate, as carbonate contains effectively no rubidium, which would otherwise influence the analysis (see below). Nd isotopic ratios were also analysed from solution as the substances analysed also contain the other REE which would falsify the analysis. For Sr analysis, the Quadrupole-ICP-MS system (Agilent 7500 cs/ce Quadrupole ICP MS) at the Centre of Trace Element Analysis of Otago University was used. Neodymium analyses were run either at Rheinische Friedrich-Wilhelm Universität zu Bonn, Germany using a NEPTUNE MS-ICP-MS or at Melbourne using an Agilent 7700 Quadrupole ICP MS.

To monitor drift of the instrument and ensure good precision of analyses, standards were measured about every half hour. For the solution measurements of Sr and Nd isotope ratios several different standards were used (BHVO2 & BCR: international rock standards which were run through the same column procedure as the samples. SRM987: International standard which is acquired by the analysing laboratory already as a solution ready to be analysed). For the in-situ measurements of Sr isotopic ratios, the standard is a piece of a tridacna clam was used ($^{87/86}$Sr= 0.7092). This standard is a lab internal-standard, whose value was obtained using an international standard tridacna (EN-1).

For in-situ measurements polished thin sections of about 50µm thickness were used. The position of measurement was determined by optical means (transmitted and reflected light microscopy). Depending on carbonate grain size, the width of the LASER tracks differed from case to case. The same LASER system and instrument were used as for the trace element analyses but the ablated particle stream was lead into a q-ICP-MS rather than the MC-ICP-MS. During processing of the raw data the signal of ^{85}Rb and in some cases ^{89}Y were monitored. ^{85}Rb was taken as a proxy of Rb content. Rb forms an isotope with the mass 87u which is the same mass as ^{87}Sr. To monitor instrument-dependent drift of values, lab internal standards were analysed about every 30 min for in-situ analyses or every ten analyses for analyses from solution. Generally the measured raw ^{87}Sr/^{86}Sr values of standards and samples did not correspond with the real values but are slightly larger or smaller than the actual value (due to instrument specific variations on the day of analysis). To account for this the difference between measured and real value, the difference between real and measured values of the SRM 987 standard was calculated (Real value of standard-measured value of standard= difference) and this difference was added to the measured value of the other standards (to check if the value is accurate) and the samples (measured value + difference = real value of sample). In Fig. 6.1.1 shows that the average of the in-situ measurements are very similar to the solution measurements showing there is no method induced differences. Although the error is usually bigger than for solution-based isotopic measurements (see figures in this chapter and appendix K for values), analyses of Sr isotopic ratios of carbonate were mostly gathered by LA-ICP-MS as, similarly to the trace element analyses, this method gives a very good spatial resolution and carbonate in different micro-structural settings can be analysed.

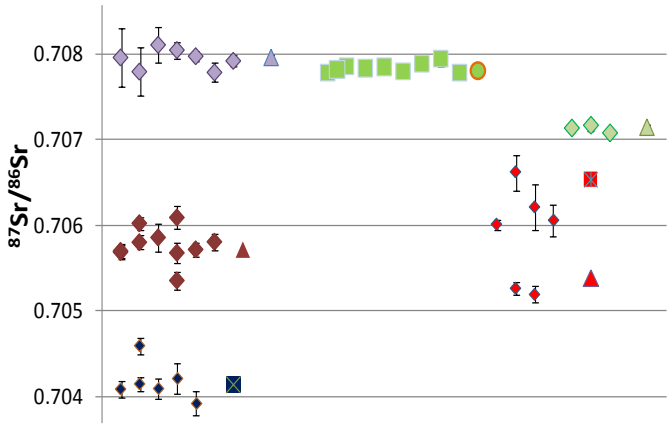

Fig. 6.1.1) Analyses of samples for which Sr isotope compositions were measured in-situ and by solution. Diamond shapes: in-situ. Other shapes (all from solution; circles: whole rock; squares: carbonate separates from wall rock; triangles: mineral separates from veins. X-axis just for display.

For the determination of whole rock isotopic composition, it was necessary to separate the strontium from rubidium, because of the issue outlined above. However, I determined the Sr isotopic ratio from solution not only of whole rock samples, but also of some carbonates (See in chapter 6.2 and appendix K for samples). The separation of Sr from Rb was done by ion exchange chromatography which was based on the method described in Pin et al. (2003). Samples were dissolved in acid in a Teflon™ vial under elevated temperatures. In the case of whole rock samples, the acid used was a mix of 40% HF and concentrated HNO_3. For carbonate dissolution, concentrated HCl was used. After the dissolution, samples were dried down. Following this, two setups were used. In the cases only Sr was analysed for, the dried down sample was taken up in 2ml 3N HNO_3 which was added to a chromatographic column (heat shrink Teflon™) which was filled with 250µl of Eichrom Sr.Spec resin (50-100µm). The sample-laden resin is treated with variously concentrated HNO_3 (3N for removal of matrix, 0.05N for sample collection). To ensure all elements that could influence the ICPMS measurement are removed from the solution (other than Sr), the collected Sr-rich solution is run again through the same column.

In the second setup, Nd and Sr needed to be separated from the sample. This method follows that of Weis et al. (2006). The sample is dissolved in HCl and loaded onto a primary column (glass) which is filled with AG50W-X8 resin. The sample-bearing resin was then washed with variously concentrated HCl (see Weis et al., 2006). After this, a Sr split is collected. More HCl was filtered through the columns. The eluted solution contains the REE of the sample. The Sr split was dried down and loaded onto the same columns used for Sr separation as described above. This sample split was run through the same process, but only once. The REE split is dried down, taken up in 0.25 N HCl and loaded onto a column filled with 670µl of Eichrom Ln. Spec. (50-100µm). Using various volumes of 0.25N HCl, the unwanted REE are removed and the Nd collected.

6.1.2- Stable isotopes

In this study, stable isotopes (C and O, expressed as $\delta^{13}C$ and $\delta^{18}O$) ratios of 50 carbonate samples are reported. Some samples have been analysed several times leading to a total analyses number of 89. 78 of these analyses were carried out at the University of Otago. The other 11 were obtained using the facilities of the University of California. In both cases, the same basic measuring setup was used. Samples (separates and whole rock) were ground to a powder finer than 100 µm in diameter. This powder was then reacted with 105% anhydrous phosphoric acid and the evolved gas was analysed in by a Thermo Scientific GasBench mass spectrometer. Samples analysed in California were reacted with phosphoric acid for 3 hours, at 70°C. Samples analysed in California have been measured generally only once.

Calcite analysis run at the Otago lab were run for at least 15 hours. Ankeritic samples for several days at 50°C. For the ankerite analyses, $\delta^{18}O$ were corrected for the O fractionation between

phosphoric acid and the evolved CO_2 gas using partition coefficients of Rosenbaum & Sheppard (1986). Each sample has been measured twice in succession to establish precision. Errors reported are 2*standard deviation of the difference between these two values. A full description of the method and data quality is given in the appendix L. The list of analyses used for display is given in appendix L.3.

For the analyses of $\delta^{18}O$ in quartz, grains of pure quartz were separated from coarsely crushed vein or breccia material of 5 different samples. These separates were sent to the University of California, where they were crushed further to a fine powder (grain size<100µm). The samples were then analysed following the procedure of Taylor & Epstein (1962). The data are given relative to V-SMOW.

The methods for Fe isotope analyses are given in the corresponding subchapter 6.7.

6.2) Radiogenic isotopes of rocks and associated carbonate

$^{143}Nd/^{144}Nd$ and $^{87}Sr/^{86}Sr$ values have been determined of a selection of pristine metamorphic rocks and metamorphic and hydrothermal carbonate. Additionally, Sr isotopic ratios of some altered greenschist samples have been measured.

6.2.1- Age correction

Before presenting and discussing the different data, it is necessary to consider the potential difference of the radiogenic isotope ratios measured and the value at the time of formation of the deposits studied. Concerning Sr isotopic ratios of whole rock samples, an age-correction of the measured $^{87}Sr/^{86}Sr$ ratio is necessary as the rock samples contain Rb, hence radioactive ^{87}Rb. Using a veining age of 25 Ma, assuming the Rb-87 content to be 27.8% (=global average) of the Rb in the sample today, and taking Sr and Rb concentrations obtained in chapter 4, an age-corrected $^{87}Sr/^{86}Sr$ ratio can be calculated. For samples, where Sr concentrations are not known, concentrations were estimated based on Sr concentrations of similar lithologies. The age-correction shifts the measured ratios to lower $^{87}Sr/^{86}Sr$ values (Fig. 6.2.1). The magnitude of correction strongly depends on the type of rock. For unaltered greenschist the shift is smaller than the symbols used for the graphs and for greyschist the graph symbols still overlap (Fig. 6.2.1). All carbonate analysed have very low Rb concentrations (<1ppm) and their Sr/Rb ratios are far greater than 1000. Hence, the measured isotopic ratios have not changed since their precipitation and an age-correction is not necessary.

With respect to Nd isotopic ratios, an age-correction needs to be performed for whole rock samples and carbonate, as both contain ^{147}Sm, the mother isotope of ^{143}Nd. This correction is done analogous to that of strontium isotopic ratios. Similar to the strontium system, Nd isotopic ratios decrease with age. The magnitude of correction is similar for all carbonate and whole rock samples, due to the relatively small fractionation between Sm and Nd, and the young age compared to the half life of ^{147}Sm. The initial values plot at slightly lower values than the measured ones (mostly by less than 0.0001 difference) and are close to independent of mineralogy and lithology (Fig. 6.2.1). The same calculations have been carried out for Nd isotopic ratios of lamprophyre, tinguaites and carbonatite reported in Barreiro & Cooper (1987). These calculations show that the difference is in the range of the samples analysed in this study (Fig. 6.2.1). Hence, I will use the measured not age-corrected values, because this eliminates the uncertainties regarding starting parameters. (For the constants used and values see appendix K).

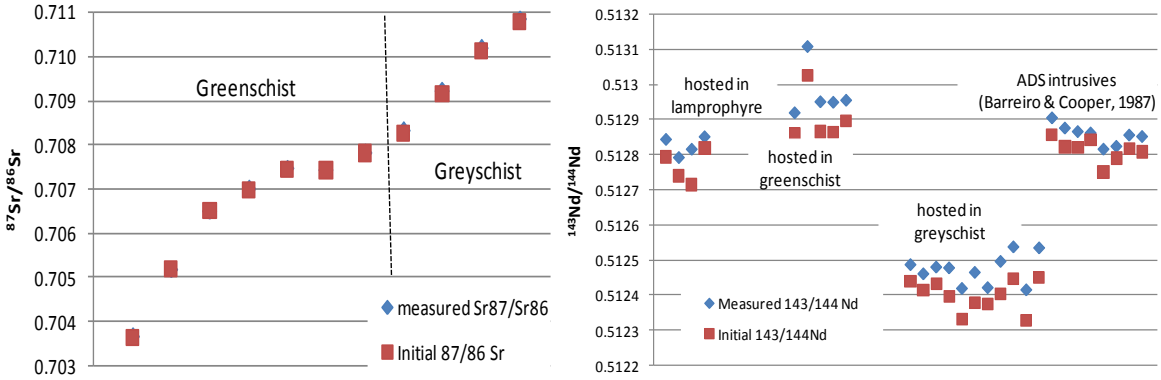

Fig. 6.2.1) Comparison of measured Sr and Nd isotopic ratios and values corrected for age-dependent increase of ^{87}Sr and ^{143}Nd content. X-axis just for display. Standard deviation of analyses smaller than symbols.

6.2.2- Isotope ratios of unaltered rock and metamorphic calcite

Samples of hydrothermally unaltered greyschist analysed for the Nd and Sr isotopic ratios are from the Bullendale and Shotover Valley and from Mt. Alta diatreme. Greenschist samples were collected at Bullendale, Red Rock and the Treble Cone/ Black Peak area.

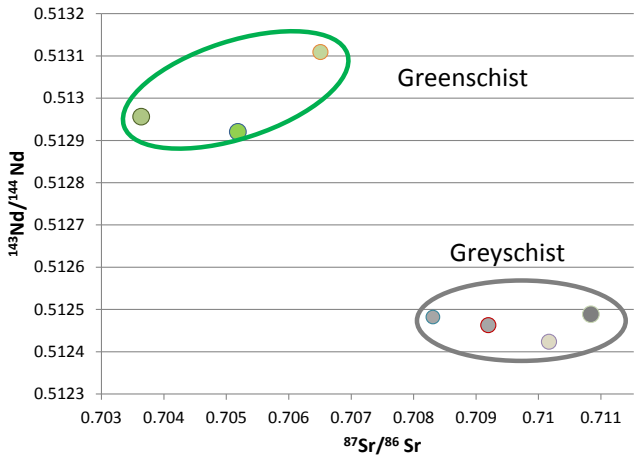

Fig. 6.2.2) Sr and Nd isotope ratios of unaltered grey- and greenschist. Errors smaller than symbols used.

A clear distinction between green- and greyschist can be made based on their Sr isotopic ratios. In greyschist samples, Sr isotopic ratios are 0.7095 +/-0.0020, whereas those of in greenschist are lower (0.705 +/- 0.002) (Fig. 6.2.2). Similar to the strontium isotopic system, values of the Nd isotopic ratios can be divided into two groups which are also lithology dependent. Greenschist specimens have $^{143}Nd/^{144}Nd$ values between 0.5129 and 0.5131. Those of greyschist range from 0.5124 to 0.5125 (Fig. 6.2.2). For both isotope systems, the values are independent of the location the rock was taken. Of some unaltered green- and greyschist samples, calcite has been analysed for its Sr isotopic composition by solution-ICPMS. This calcite has always a slightly lower Sr ratio than the rock it is hosted by (Fig. 6.2.3).

Sample	$^{87}Sr/^{86}Sr$	2*σ	Substance
'BUL2C'	0.709198	0.000028	Whole rock
Bul2Ccc	0.708340	0.000013	Calcite
BD180.6-2WR	0.710170	0.000013	Whole rock
BD180.6-1cc	0.709417	0.000016	Calcite
TP7Dp	0.706017	0.000014	Calcite
TP7D'	0.706509	0.000039	Whole rock

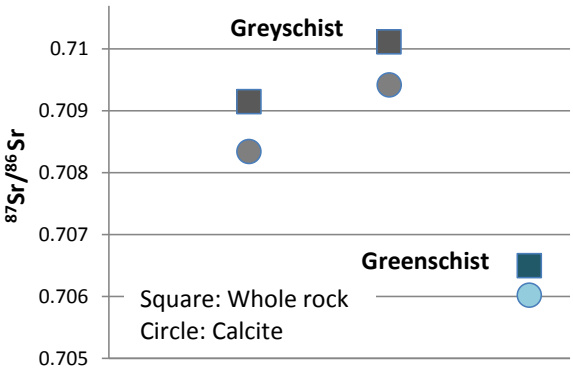

Fig. 6.2.3) Sr isotope ratios of metamorphic calcite and its host rock. All values obtained from solution. To obtain the calcite values in BUL2C and BD180.6 the whole rock powder was treated with conc. HCl and the Sr in that solution was then analysed. For TP7D the calcite was manually separated and then dissolved in conc. HCl. The calcite always has a lower $^{87}Sr/^{86}Sr$ ratio than the whole rock it is hosted by. X-axis just for display.

6.2.3- Variation of $^{87}Sr/^{86}Sr$ across alteration halos

In some of the previously described greenschist alteration halos (chapter 3), in addition to unaltered greenschist, their most altered counterparts have been analysed for their Sr isotopic composition. These are samples from the Treble Cone (TP7D/A) and part of the Bullendale (BUL4Cc/Ca) transects (Fig. 3.2.14&7). In the TP7 set, in addition to the wall rock, the carbonate in the leucocratic layer has been analysed by LA-ICP-MS. In the BUL4C sample set, isotopic ratios of the veins in the centre of the alteration halo have been determined, also using LA-ICP-MS. The altered rocks have higher $^{87}Sr/^{86}Sr$ ratios than the corresponding unaltered greenschist (Fig. 6.2.4). The veins in the centre of the alteration halo of BUL4C have slightly lower Sr isotopic ratios compared to the adjacent altered rock and values scatter over a relatively wide range (Fig. 6.2.4). In the TP7 set the $^{87}Sr/^{86}Sr$ ratios of the carbonate from the leucocratic layers is similar to the whole rock (Fig. 6.2.4).

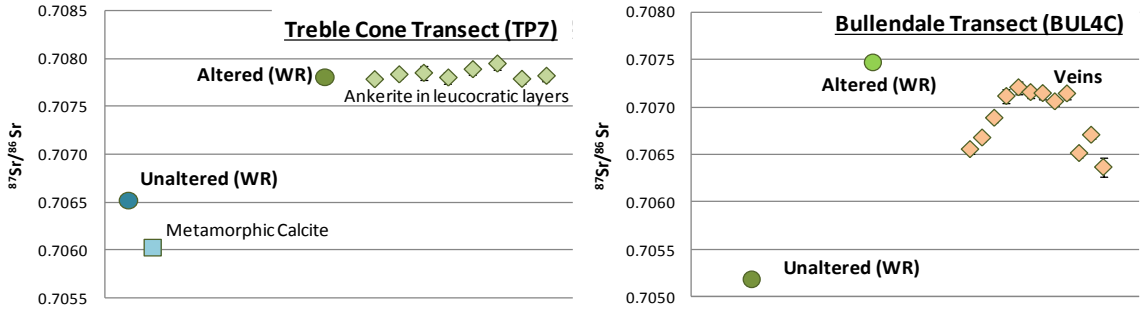

Fig. 6.2.4) Sr isotope ratios of unaltered, altered greenschist, ankeritic veins and carbonate in leucocratic layers. X-axis just for display. Circles=whole rock (WR) by solution. Squares: Picked separate by solution. Diamond: in-situ.

6.2.4- Discussion

For both radiogenic isotope systems, the measured values of the whole rocks (Fig. 6.2.2) lie in the range of values for similar rocks from the Otago and Alpine Schist and mafic rocks reported in the literature (Horton et al., 2003; Adams & Graham, 1997, Frost & Coombs, 1989; Bierlein & Craw et al., 2009). The isotopic ratio of the metamorphic calcite in greenschist is similar to metamorphic calcite veins hosted in greenschist analysed by Cooper et al. (2016).

The overall lower values of $^{87}Sr/^{86}Sr$ in greenschist compared to greyschist correlate with the lower content of muscovite in greenschist. Muscovite is the major Rb-bearing mineral in the rocks (see chapter 4.3), and hence over time will obtain a high $^{87}Sr/^{86}Sr$ due to the decay of ^{87}Rb. As muscovite is more common in greyschist than in greenschist, $^{87}Sr/^{86}Sr$ ratios in greyschist is expected to be higher than in greenschist, which is accentuated by the fact that greenschist contains more of the Rb-poor but Sr-rich epidote. The evaluation that epidote should have a low isotopic ratio is supported by Cooper et al. (2016), who measured the values of $^{87}Sr/^{86}Sr$ of epidote in greenschist in the Alpine schist; the $^{87}Sr/^{86}Sr$ values range between 0.704-0.705. Variations of Sr isotopic ratios between the greenschist sets (TP7 and BUL4C; Fig. 6.2.4) can be attributed to different muscovite content in these two samples; the greenschist of the TP7 set have a higher muscovite content and following a higher $^{87}Sr/^{86}Sr$ ratio, compared to the muscovite-poorer greenschist of BUL4C. This principle can also be employed to explain the difference between the Sr isotopic ratios of the whole rock and the calcite it hosts (Fig. 6.2.3). Carbonate contains essentially no Rb, hence retains it low $^{87}Sr/^{86}Sr$ ratio from the time of its crystallisation. The isotopic ratios of the whole rock, on the other hand, represent a mixed value of the

less and more Rb rich and hence radiogenic minerals and the Sr isotopic ratio of the whole rock increases over time and is large compared to the carbonate within it.

The higher Sr isotopic ratio and content (see chapter 4) in the altered compared to the unaltered rock and their similarity to the vein material in the case of the BUL4C samples (Fig. 6.2.3), corresponds well with the replacement mechanism taking place in the rocks, "dissolution-precipitation". During the time the components are in solution, they mix with the elements dissolved in the fluid. The newly precipitating mineral reflects this mixing. The similarity of veins and adjacent rock in the BUL 4C sample (Fig. 6.2.4), indicates that the infiltrating fluid did not only add Sr to the rock and mixed with it, but also that the fluid penetrating the rock and the fluid forming the veins approached isotopic equilibrium. The distinct increase in $^{87}Sr/^{86}Sr$ (Fig. 6.2.4) shows that much more fluid- transported Sr needs to enter the rock than is present in it today; ergo the system is fluid-buffered and some of the rock-originated Sr, together with the remaining fluid-derived Sr, leaves the rock. The higher $^{87}Sr/^{86}Sr$ ratios in the veins and altered rock -compared to the unaltered rock- suggest that some of the Sr is derived from the greyschist, in addition to greenschist derived Sr (see below for further discussion).

The $^{87}Sr/^{86}Sr$ values of the veins in the BU4C set are slightly lower than the corresponding altered host rock. This difference could be related to the change of $^{87}Sr/^{86}Sr$ value over time, as the whole rock contains ^{87}Rb, while the carbonate does not. This hypothesis can "easily" be checked. For this, it is assumed that carbonate and altered wall rock had the same Sr isotopic ratio at the time of alteration and a similar calculation as for the age correction for the whole rock (see above) is carried out. The calculated age for which the whole rock and carbonate have the same Sr isotopic ratio, would be the age of formation. For the BUL4C sample, this is the case when the age is about 700 Ma, which is unrealistic. Hence, the difference lower isotopic ratio of hydrothermal carbonate vs. its host rock must have been caused by different processes, such as mixing of Sr from different sources. Concerning the relatively low and variable $^{87}Sr/^{86}Sr$ values of veins in BUL4C (Fig. 6.2.4), this can be attributed to a change of the isotopic composition of the fluid during the time of the alteration. Cause for this would be that the Sr source or the proportion of source minerals for the fluid changed, i.e. more and less Sr from muscovite. The similarity of the carbonate in the leucocratic layers and the whole rock in TP7A shows that throughout the whole rock Sr redistribution and mixing was complete in the sample. This is interesting insofar that the carbonate in the leucocratic layers is zoned (see chapter 3) which shows that elements, such as Mg and Fe, did not reach chemical equilibrium. This also extends earlier conclusions that Sr is more mobile compared to Mg and Fe on a cm to meter scale to that Sr is also more mobile than Mg and Fe on a mm scale.

6.3) Radiogenic isotope ratios of hydrothermal, metamorphic and magmatic carbonate

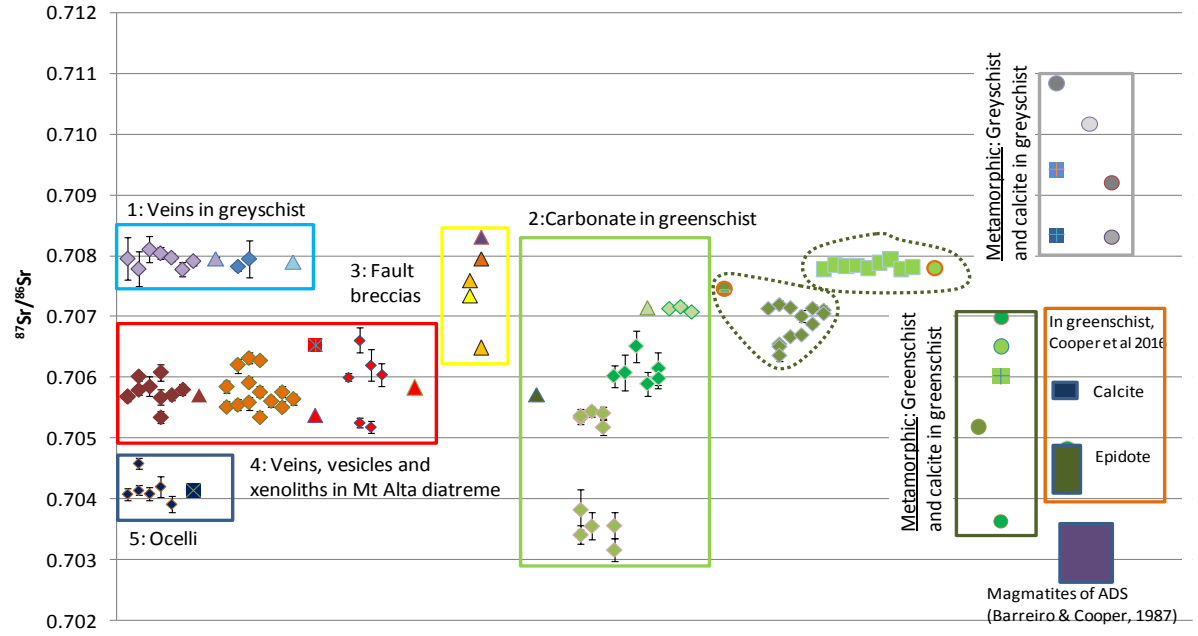

Fig. 6.3.1) Overview of all Sr isotopic ratios measured of carbonate and whole rock analyses in different settings, including those discussed earlier. Diamond shapes: in-situ. Other shapes: from solution; circles: whole rock; squares: carbonate separates from wall rock; triangles: mineral separates from veins. The same colour of symbols corresponds to the same sample as for some samples Sr isotope ratios were obtained in-situ but also by solution. In each case analyses are plotted next to each other. Dashed lines encircle carbonate shown in Fig. 6.2.4. Bottom right hand corner: data from other studies for comparison. X-axis just for display.

6.3.1- Strontium

Strontium ratios of hydrothermal and magmatic carbonate scatter over a wide range, from 0.703 to 0.708. According to host lithology and setting, five groups of hydrothermal and magmatic carbonate have been distinguished. These are carbonate hosted in 1) greyschist; 2) greenschist; 3) silicified and clastic breccias and adjacent veins, 4) in the diatreme at Mt Alta and 5) ocelli in lamprophyre (Fig. 6.3.1).

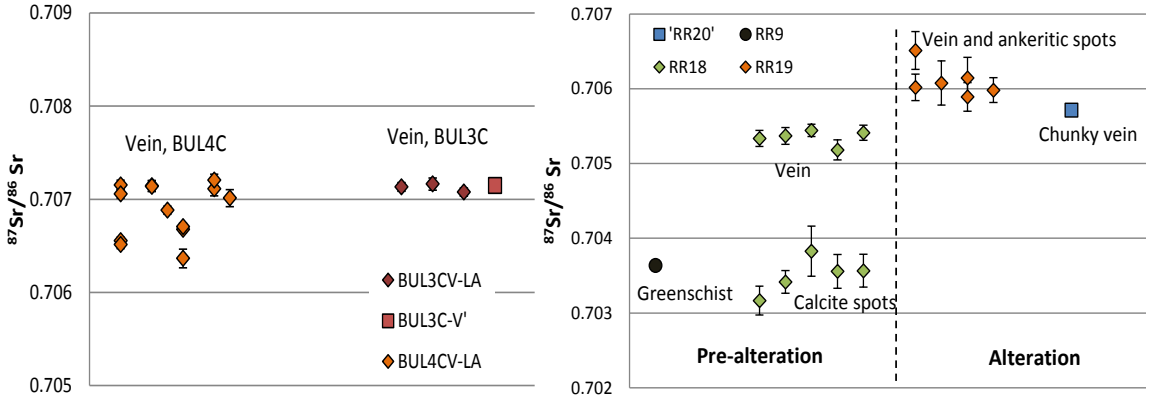

Fig. 6.3.2) Left) Sr Isotope ratios of veins in greenschist from Bullendale. **Right)** Isotopic composition of carbonate and unaltered, magnetite-bearing greenschist at Red Rock. Note the different scale of the y-axes. X-axis just for display. Diamond: in-situ measurements; square: from solution.

The highest $^{87}Sr/^{86}Sr$ ratios are measured in carbonate veins in greyschist, where ratios lie around 0.7080 +/-0.0005 (Fig. 6.3.1; light blue box). Carbonate veins in the greenschist at Bullendale have lower ratios (ca. 0.7050 - 0.7075), mostly at around 0.7073. Within sample BUL4C, the isotopic values vary considerably, as mentioned above (Fig. 6.3.2). In RR 18, $^{87}Sr/^{86}Sr$ values of calcite in veins (Fig. 3.2.23A&B), which formed prior to the ankeritic alteration, lie between 0.7050 and 0.7055. In veins of RR19, ratios are higher (ca. 0.7060), while the sparry veins with chalcopyrite (RR20) have intermediate $^{87}Sr/^{86}Sr$ ratios (0.7057). In RR18, $^{87}Sr/^{86}Sr$ values of the calcitic spots (Fig. 3.2.23A&B) lie between 0.703 and 0.704. These values are in the range of magnetite-bearing greenschist from Red Rock. (Note that the greenschist with the calcitic spots also contains abundant magnetite.) In RR19, the ankerite replacing the calcite in these types of spots has similar $^{87}Sr/^{86}Sr$ ratios as the ankeritic veins in these samples.

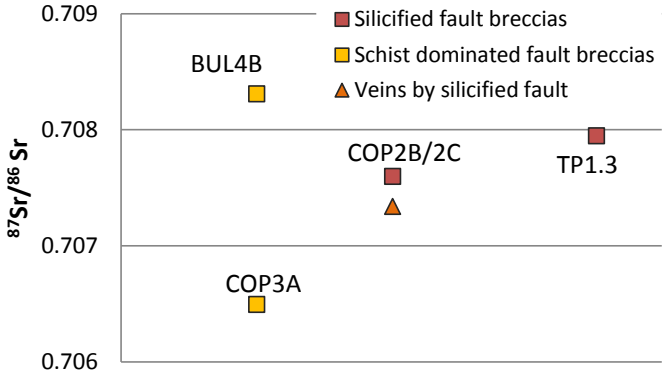

Fig. 6.3.3) Sr isotope ratios of calcite in schist-dominated fault breccias (yellow) and in and by silicified fault breccias (red). All values determined from solution. Note: At least the fault of COP2B/C is auriferous

Carbonate from silicified breccias and adjacent veins from Copper Creek and Treble Cone have $^{87}Sr/^{86}Sr$ ratios intermediate of greenschist- and greyschist- hosted veins (between 0.707-0.708) (Fig. 6.3.1&3). Carbonate in schist-dominated fault breccias from Bullendale and Copper Creek have been analysed (Fig. 2.3.6; BUL4A & COP3A). The carbonate in the Bullendale example has Sr isotopic ratios similar to greyschist-hosted veins (around 0.7084), while the calcite of COP3A has a relatively low Sr value (0.7065) (Fig. 6.3.3). Sr isotopic ratios of carbonate in veins at Mt Alta lie between 0.705 and 0.7067, which overlaps with the group of greenschist-hosted veins. In the sample of little altered lamprophyre (AD2A; Fig. 2.4.14 & 5.2.8), most Sr isotopic ratios lie at around 0.7057. The Sr isotopic ratios of carbonate in ALT2C butter over a wide range; carbonate at the vein rim (murky), replaced phenocrysts and xenolith (type B, C &D; naming the same as in chapter 5; Fig. 5.2.9&10) in the lamprophyre have $^{87}Sr/^{86}Sr$ ratios of roughly 0.706-0.7067, while the clear carbonate in the vein centre (type A) has a considerably lower $^{87}Sr/^{86}Sr$ ratios (ca 0.7052) (Fig. 6.3.4). In the texturally similar sample AD2B, values also scatter over a wide range, but no clear distinction between the carbonate in the different settings can be made. However, on average the clear carbonate in the vein centre (type X) has lower isotopic ratios compared to the murky one (Type Y). The clear carbonate component embedded in lamprophyre in AD2B (Type Z; Fig. 5.2.10)) has isotopic ratios very similar to the optically and chemically similar clear carbonate vein in ALT2C (type A in Fig. 5.2.9; Fig. 6.3.4). The vein in the diatreme hosted greyschist block (ALT1.2) has similar values as the other carbonate at Mt Alta (Fig. 6.3.4). The fifth group, which comprises ocelli in lamprophyre, has $^{87}Sr/^{86}Sr$ ratios of 0.704 to 0.7046 (Fig. 6.3.1; dark blue box).

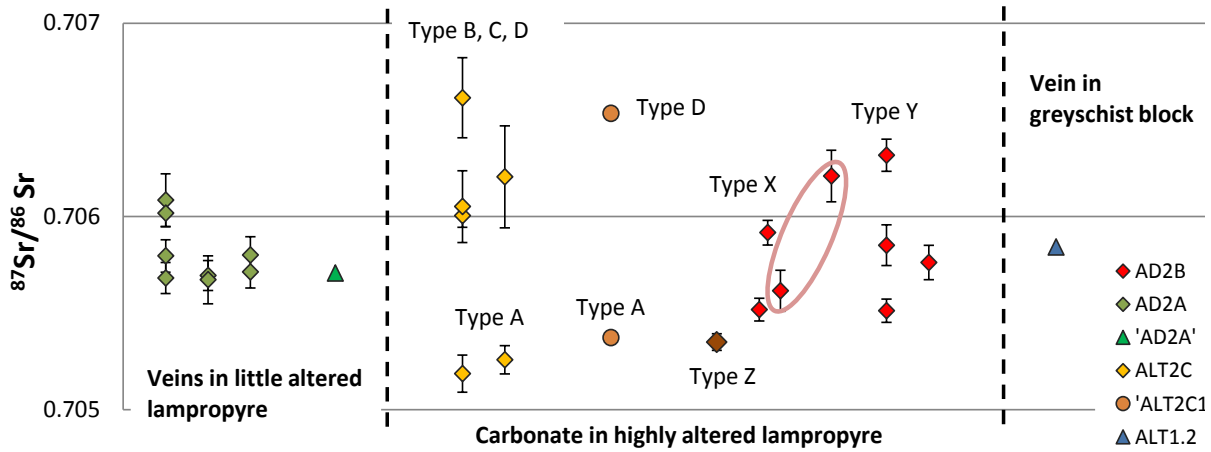

Fig. 6.3.4) Sr isotope ratios of carbonate in the diatreme at Mt Alta. Red circle encircles two parts of 1 analyses where the laser crossed the border between the two optically different carbonate types. Circles and triangle from solution (errors smaller than symbols used); diamonds: in-situ measurements.

6.3.2- Neodymium

Nd isotopic ratios were determined of some carbonate samples in addition to Sr isotopic ratios (Fig. 6.3.5). The values of $^{143}Nd/^{144}Nd$ lie between 0.51240 and 0.51310. The highest values (around 0.5129-0.5131) belong to veins, which are hosted by greenschist. Values between 0.51278 and 0.51286 occur in ocelli and veins embedded in lamprophyre. Veins which are in the diatreme setting but hosted by greyschist (ALT1.2) have a much lower $^{143}Nd/^{144}Nd$ value (0.51253). This value is in the range of carbonate in veins and breccias which are also hosted in greyschist but outside the diatreme ($^{143}Nd/^{144}Nd$ =0.5124-0.51255; Fig. 6.3.5)

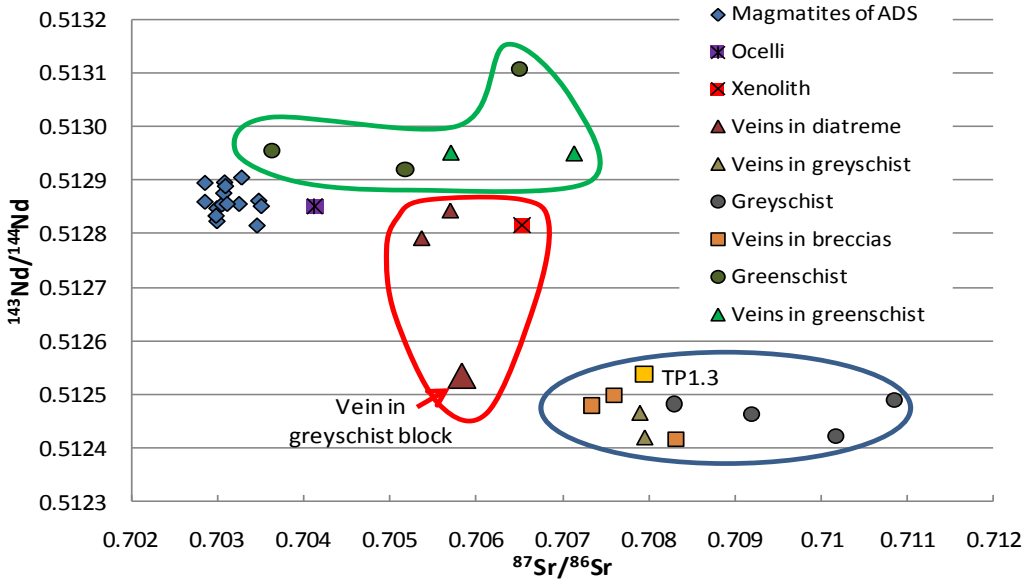

Fig. 6.3.5) $^{143}Nd/^{144}Nd$ vs. $^{87}Sr/^{86}Sr$ ratios of hydrothermal carbonates (squares& triangles). For comparison, isotopic ratios of the different host lithologies are also plotted (circles and diamonds). Errors smaller than symbols used.

Comparing the Sr and Nd isotopic values of the carbonate with the lithology they are hosted by, a close similarity of values is found, especially for the Nd isotopes (Fig. 6.3.5). Regarding Sr, carbonate hosted in greyschist has slightly lower ratios, while $^{87}Sr/^{86}Sr$ ratios of carbonate in greenschist are similar or

higher than greenschist (Fig. 6.3.1&5).. Sr isotopic values of ocelli are about 0.0005 higher than unaltered magmatitic rocks of the Alpine Dike Swarm. Veins and other carbonate in Alta Diatreme have similar, though slightly lower Nd isotopic ratios than the unaltered magmatitic rocks of the ADS. Overall, it can be said that ratios of $^{144}Nd/^{143}Nd$ are wall rock dependent, while Sr isotopic ratios are wall rock and setting dependent.

6.3.3- Discussion

The lower $^{87}Sr/^{86}Sr$ ratios of hydrothermal carbonate hosted in greyschist compared to their host rock at Bullendale (Fig. 6.3.1) can be explained several ways. For one, it may be that the veins got all their Sr from the immediate wall rock but are older than suggested. Using the same calculations as earlier (section 6.2.2.3), this age would have been over 500 Ma, and hence not a possibility. Another possibility is that the vein precipitating fluid got its Sr load from different lithologies or different minerals. Regarding mixing of Sr from different rock type, this can be tested by calculating of how much of the Sr would be derived from greenschist and greyschist to make up the isotopic composition of vein carbonate. The equations used are:

$$x \bullet c \bullet {}^{87/86}Sr_{(GnS)} + y \bullet k \bullet {}^{87/86}Sr_{(GrS)} = {}^{87/86}Sr_{(Vein)} \quad ; \quad x+y=1 \quad ;$$

$$c = \frac{Sr\ conc.in\ GnS}{Sr\ conc.in\ GnS+GrS} \quad ; \quad k = \frac{Sr\ conc.in\ GrS}{Sr\ conc.in\ GnS+GrS}$$

Table 6.3.1) Model calculation of how much GnS and GrS need to contribute their Sr to produce the isotopic composition of a GrS-hosted vein.

Sample	87/86 Sr	Sr(ppm)
GnS (BUL4Cc)	0.70519	411
GrS (BUL2C)	0.70920	243
vein (BUL2B)	0.70791	2800

Proportion of GnS (%)	32.1
Prop. of GnS considering different Sr content (%)	19.0

For the example calculation, the isotopic composition and Sr content of unaltered greyschist (BUL2C), unaltered greenschist (BUL4Cc) and greyschist-hosted vein (BUL2B) are taken. According to these calculations, the rock package would have to contain about 19% greenschist to give the vein its isotopic composition (Table 6.3.1). This ratio is in contrast with the geology in this area, where greyschist makes up over 90% of the present rock mass. Hence, in the case of carbonate veins in greyschist at Bullendale, mixing of fluids purely from greenschist and greyschist is most likely not the sole reason for isotopic composition of the carbonate veins. Instead it is suggested that the isotopic ratios in the veins reflect that not all of the rocks' minerals contribute equally to the element load in the fluid. Epidote, which is a major bearer of Sr and with low Sr isotopic ratio (see above, Cooper et al., 2016), has a low tolerance for CO_2 in the fluid and is broken down completely, while muscovite is often only replaced at grain boundaries at the same CO_2 content (chapter 3.2). Overall, most of the alteration-sensitive Ca-bearing metamorphic phases (actinolite, epidote, titanite) have little Rb (this study), and hence they should have lower Sr isotopic ratios than the whole rock. Hence, the carbonate-precipitating fluid in the greyschist hosted vein will retrieve most of its Sr from these Ca-Sr rich minerals and only some from the Rb richer phases, giving the fluid an intermediate Sr isotopic ratio. That only certain minerals contribute to a fluid's load has also been suggested in other studies (i.e. Aquilina et al., 1997; Horton et al., 2003).

In contrast to greyschist-hosted carbonate, veins hosted in greenschist at Bullendale have Sr isotopic ratios larger than their unaltered host rock (Fig. 6.2.4-3.2). To achieve this some of the incoming fluid needed to come from a more radiogenic source. In the Bullendale Greenschist this radiogenic source is greyschist. As greyschist is much more abundant than greenschist and also forms

thicker layers, most of the Sr in the fluid will be derived from the greyschist. This is supported by the $^{87}Sr/^{86}Sr$ ratios of the greenschist-hosted veins as they are more similar to the greyschist-hosted veins than they are to the greenschist isotopic composition (Fig.6.3.1).

Mixing from different sources can also explain the large variation of $^{87}Sr/^{86}Sr$ ratios in carbonate at Mt Alta (Fig. 6.3.4) where values of the carbonate are intermediate between the isotopic compositions lamprophyre and greyschist (Fig. 6.3.1). Although values in these carbonate are similar to those of carbonate in greenschist, it is unlikely that Sr from greenschist has any impact on the isotopic composition of the veins as the "next" greenschist is over 100 m to east of the sample location (Fig. 2.1.5) and because there are other Sr-rich lithologies (greyschist & lamprophyre) closer by. A good sample show casing the mixing is ALT2C. The higher $^{87}Sr/^{86}Sr$ values of the vein rim (0.706-0.7067) (Type B&C in chapter 5) suggest that the Sr was derived predominantly from greyschist compared to the central part of the veins (type A in chapter 5) where the isotopic ratio is lower (0.7052), indicating a stronger influence from magmatic Sr. The less radiogenic Sr of the type A supports the conclusion drawn earlier (chapter 5) that the convex REE pattern of this carbonate type suggests a direct link to the magmatic fluid system. Interestingly, the more juvenile fluid formed the carbonate in the vein centre, suggesting not only that there were several pulses of fluid precipitating the carbonate, but also that the components in the fluid had different sources.

The chemistry of the carbonate and their host rock, give information about the scale of their relative mobility. Hydrothermal carbonate in ALT1.2, which is a sample of veins in a greyschist block in the diatreme, the $^{87}Sr/^{86}Sr$ ratio is much lower than in other greyschist hosted veins but is in the range of carbonate hosted by lamprophyre in the diatremes (Fig. 6.3.1&5). This suggests that Sr from greyschist and lamprophyre are mixed and that Sr can be transported in the fluid for several meters at a minimum. Regarding the Nd isotopes, the close similarity between wall rock and carbonate (Fig. 6.3.5), indicates that the bulk of the Nd is derived from the immediate surroundings and does not get transported as far as Sr. Supporting this is that the carbonate in veins in the greyschist block in the diatreme breccia (ALT 1.2) has a Nd isotopic ratio very similar to greyschist (Fig. 6.3.5). However, the Nd isotopic ratios of these veins are slightly higher than most other greyschist-hosted veins, which could indicate that some of the Nd was derived from the magmatic rocks. Similar to the example of ALT1.2, veins in lamprophyres are at the "lower end" of the Nd spectrum of the magmatitic rocks (Fig. 6.3.5) potentially due to a small amount of Nd being derived from greyschist. Another indication that Nd may be mobile to some extent can be found at outcrop TP1, which is near the boundary of a green- and greyschist (Fig. 2.1.3). Here, the breccia-hosted carbonate (TP1.3) has $^{144}Nd/^{143}Nd$ values at the higher end of most other greyschist-hosted carbonate (Fig. 6.3.5). The conclusion that some of the carbonate's Nd was dissolved in the fluids would correspond with the conclusions drawn in chapter 5 that the different REE patterns of the carbonate veins require fractionating processes to take place whilst in the fluid, hence require some mobility in the fluid. Nevertheless, most of the Nd in the carbonate is derived from the immediate wall rock.

6.4) Stable Isotopes - carbon and oxygen

In this section of the chapter, I will present and discuss the stable isotope composition of the carbonate in the different geological settings studied in this thesis. These data were collected to gain information about the source of the fluid(s) precipitating the carbonate in the different locations. This question about the fluid source is of interest especially in respect to the fluid that was present in the gold-bearing structures in the Shotover and if this fluid could have had any connection to the magmatic fluid system.

6.4.1- Calcite in unaltered metamorphic rock

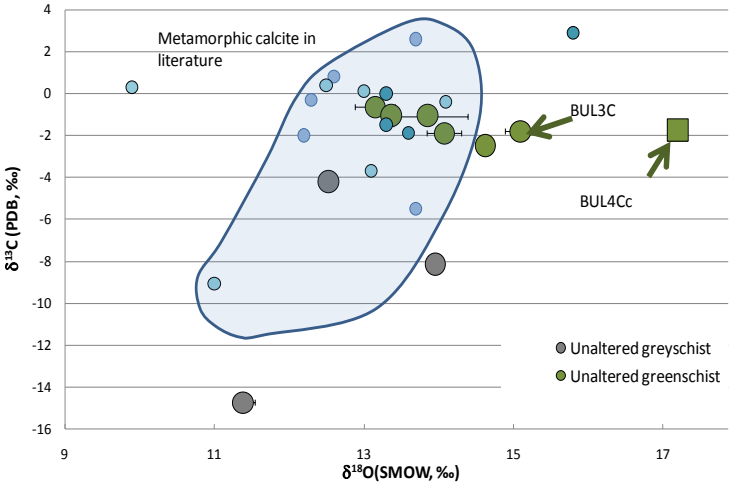

Fig. 6.4.1) Metamorphic calcite analysed in this study compared to most of the metamorphic calcite analysed in previous studies (blue shade, blue markers; data from Blattner & Copper, 1974; Devereux, 1968; White, 1998).

Metamorphic calcite from three greyschist and five greenschist samples were analysed for their stable isotope compositions, using whole rock powders (Fig. 6.4.1). Additionally, the isotopic composition of the thick, boudinaged, metamorphic calcite veins at outcrop TP5 (Fig. 2.2.2 A-C) was also determined (Fig. 6.4.1). The samples of greyschist-hosted calcite have a wide range of values, especially regarding carbon (-15 to 3). $\delta^{13}C$ values are more confined for greenschist-hosted calcite, and they are slightly larger with respect to oxygen isotopic ratios (Fig. 6.4.1). The highest $\delta^{18}O$ values has carbonate from the Bullendale greenschist, especially BUL4C (Fig. 6.4.1). Most values plot in or close to the field defined by metamorphic calcite determined in previous studies (Craw et al., 2009; White, 1998; blue circles in Fig. 6.4.1). The reason why BUL4Cc and less so BUL3C, do not plot in this field, can be attributed to the fact that these samples show beginning of growth of hydrothermal carbonate (See chapter 3.2). Hence, not all carbonate in these samples is metamorphism- but also alteration-related. This alteration-related calcite is more common in BUL4C compared to BUL3C, which is reflected in the particularly high $\delta^{18}O$ values in BUL4Cc.

6.4.2- Isotope ratio variations across alteration halos

Of the samples sets that were studied in chapter 3 and 4, the values of $\delta^{18}O$ and $\delta^{13}C$ of the carbonate in the unaltered rock, the altered counterparts and where available of the central veins were also determined (Fig. 6.4.2). Figure 6.4.2 shows that across the alteration halos, the rock gradually approaches the isotopic composition of the altering feature in the centre of the alteration halos (e.g. veins, fault breccias). An exception to this are the Murdoch Creek (BUL2) and Treble Cone Transect (TP7), where this change in isotopic ratios is not as gradual (Fig. 6.4.2).

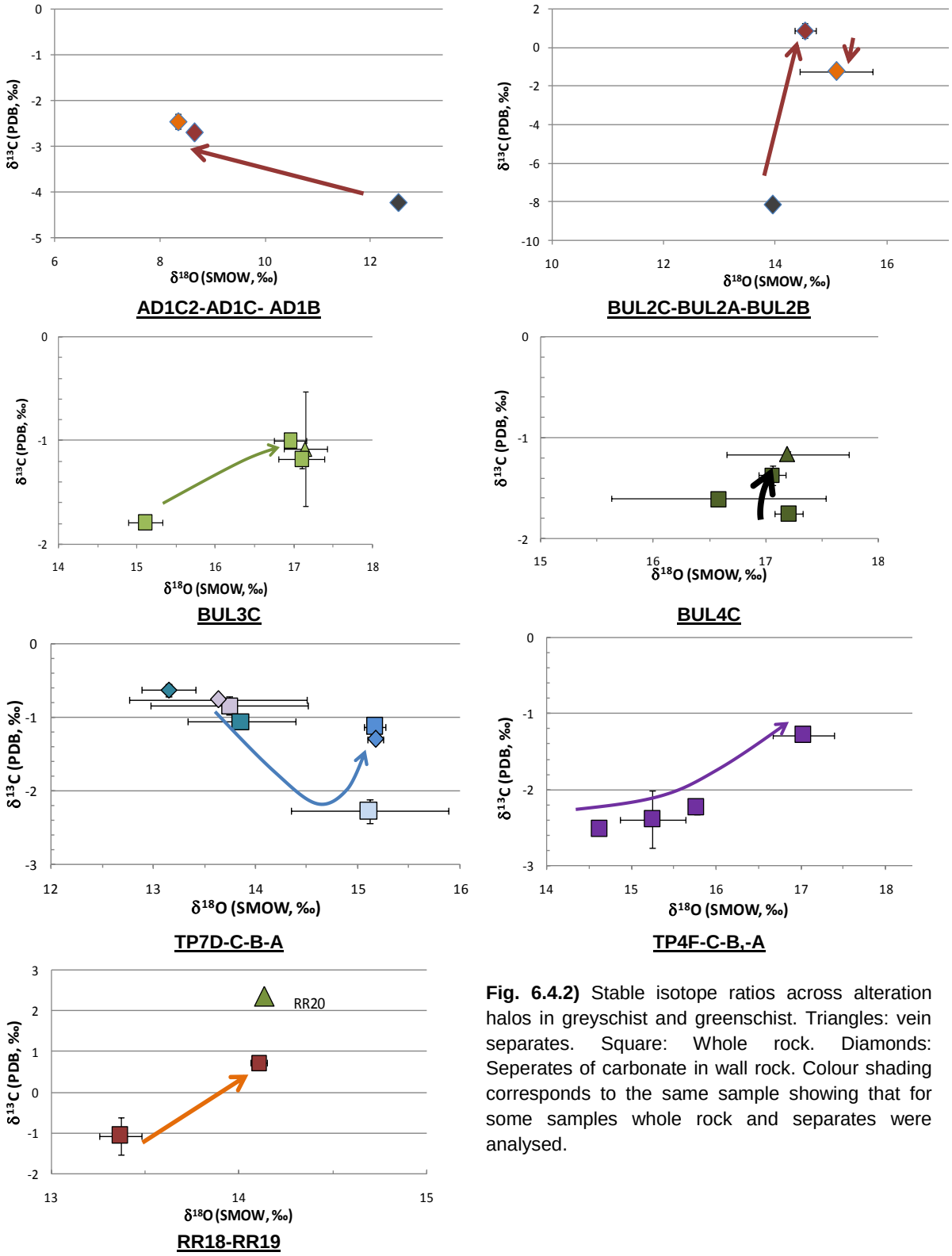

Fig. 6.4.2) Stable isotope ratios across alteration halos in greyschist and greenschist. Triangles: vein separates. Square: Whole rock. Diamonds: Seperates of carbonate in wall rock. Colour shading corresponds to the same sample showing that for some samples whole rock and separates were analysed.

In all but the Mt Alta Transect, the altered rock is has larger $\delta^{18}O$ values compared to the unaltered rock of the transect (Fig. 6.4.2). Greenschist-hosted alteration halos at Treble Cone and Bullendale approach $\delta^{13}C$ values of -1 to -1.2 ‰ in the centre of the halos and veins (Fig. 6.4.2). The same is true for the set of BUL2 (Murdoch Creek Transect) for the unaltered greyschist and central vein but the most altered rock of this set has a $\delta^{13}C$ value of about +1‰ (Fig. 6.4.2). In the Mt Alta setting, the carbon isotope ratio of the carbonate in the alteration-causing breccia lies at around -2.6‰. At

Red Rock, the ankeritic spots in RR19 have $\delta^{13}C$ values of about + 0.8 compared to -1‰ in the calcitic spots in the unaltered sample of RR18. $\delta^{18}O$ values are about 0.6 ‰ higher in RR19 compared to RR18 (Fig. 6.4.2).

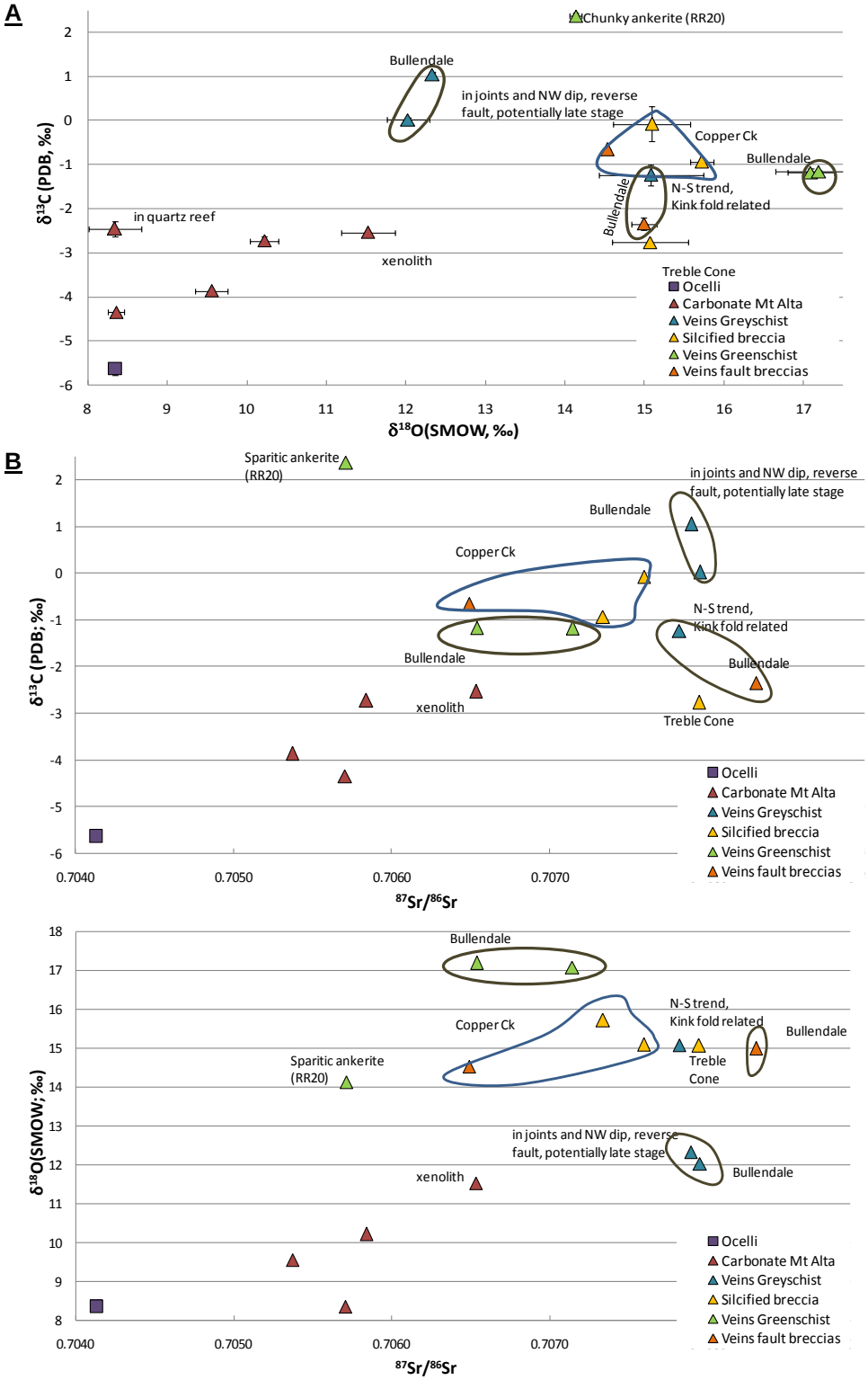

Fig. 6.4.3) A: Stable isotopic composition of carbonate in veins, breccias and ocelli. **B:** Stable isotopic ratios (oxygen and carbon) vs. Sr isotopic ratios of the hydrothermal carbonate present.

6.4.3- Stable and radiogenic isotopic ratios of void-filling carbonate

Stable isotope ratios of void-filling, mostly hydrothermal carbonate (calcite and ankerite) in veins, breccias and ocelli associated with Cenozoic structures were determined. Values scatter over a wide range, from about 6 up to 18 ‰ regarding $\delta^{18}O$ and -6 up to 2.5 ‰ for $\delta^{13}C$ (Fig. 6.4.3).

Of the carbonate analysed, ankerite from Mt Alta and calcitic ocelli have the lowest $\delta^{18}O$ ratios (between 7 and 12) while carbonate from the Shotover has the highest. The lowest $\delta^{13}C$ values are found in ocelli (c. 5.5‰), while the highest are in the chunky ankerite at Red Rock (RR20) (Fig. 6.4.3A). Outside the diatremes, carbonate hosted in veins in greyschist is on average about 1-2 ‰ lighter than ankeritic veins in greenschist. Carbonate in breccias has similar carbon isotopic ratios to the greenschist-hosted veins, but is about 1‰ lighter regarding $\delta^{18}O$ values (Fig. 6.4.3A). Veins from joints and faults outcrop B3 (BUL3A and BUL3A) have relatively low oxygen values but high carbon isotope values (c. 12.2 and 0-1 respectively). Ocelli have the lowest Sr, O and C isotopic values, while carbonate from Bullendale has the highest. A linear correlation of $\delta^{13}C$ and $^{87}Sr/^{86}$ Sr is recognised for carbonate at Mt Alta, and less so for carbonate at Bullendale and Treble Cone (Fig. 6.4.4B). A similar correlation is present regarding oxygen and Sr for the carbonate at Mt Alta, but such a relation cannot be recognised for the carbonate outside the diatreme.

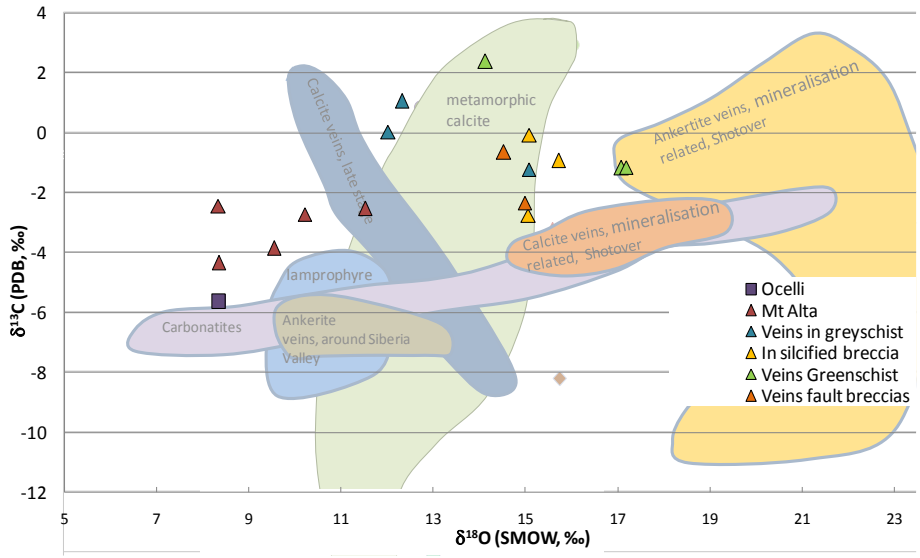

Fig. 6.4.4) Stable isotope ratios of hydrothermal carbonate analysed in this study compared to stable isotope ratios of carbonate of a similar age and hosted in relevant structures (veins, fault, gold mineralisation, carbonatites, lamprophyre. Data from White, 1984; Blattner & Cooper,1974; Craw et al., 2009.

Comparing the data collected in this study with data reported in the literature, it shows that stable isotope ratios of ocelli plot within the field of calcitic carbonatites and close to lamprophyres (White, 1984; Blattner & Cooper,1974) (Fig. 6.4.4) while the ankeritic veins at Mt Alta diatreme plot "above" the field defined by lamprophyres and carbonatites (Fig. 6.4.4). Carbonate of fault breccias and kink fold-related veins at Bullendale, Copper Creek and Treble Cone plot in a field overlapping slightly with fields defined by carbonate found in gold mineralisation-related veins (Craw et al., 2009).

6.4.4- Discussion

Assessing the isotopic composition of the hydrothermal carbonate not hosted in the diatreme (Fig. 6.4.2&3), a few samples have distinctly different isotopic composition from the (other) void-filling hydrothermal carbonate. This is carbonate from structures at B3 (blue triangles in Fig. 6.4.4), the chunky ankerite veins at Red Rock (RR20; green triangle with a positive $\delta^{13}C$ value in Fig. 6.4.4) and the

ankeritic spots in RR19 (Fig. 6.4.2). Concerning the carbonate in the structures at B3 it has already shown in chapter 2.3 that the structural age of those features is unclear. As the stable isotopic ratios of these samples are very different from any of the carbonate in this area (Fig. 6.4.3), it is suggested that the carbonate in these structures are not of the same generation as the kink folds and partly gold-bearing faults. The composition of the carbonate of B3 are relatively similar to late stage carbonate veins reported by Craw et al., 2009 (Fig. 6.4.5), suggesting they may also be late stage. Concerning the carbonate at Red Rock the dissimilarity of the carbonate's isotopic composition, the common occurrence of chalcopyrite, different texture of veins (thick chunky/ sparry veins as RR20) and the spatial separation from the other studied structures by the Moonlight fault, suggest that the fluid source and plumbing system was separate from that in the other study areas.

The change of isotopic composition of carbonate across the alteration halos (Fig. 6.4.2) can either be attributed to kinetic effects or to equilibrium fractionation of the minerals involved. In case of a kinetically controlled isotopic variation, the light isotopes travel further outward in the alteration halo compared to heavy isotopes (Hoefs, 2008). Therefore, the $\delta^{13}C$ and $\delta^{18}O$ values should become smaller towards the outer edge of the alteration halo and the change of isotope values in the altered to unaltered rock should be abrupt. In some cases the decrease of $\delta^{13}C$ and $\delta^{18}O$ value is recognised but not in others (AD1C/C2, TP7A-D), showing that kinetic fractionation was not the controlling factor for the stable isotopic ratios across the alteration halos here. This is in agreement with the relatively high temperatures (>120°C) and high fluid/rock ratio, both supporting near complete attainment of isotopic equilibrium. Consequently, the trend across the alteration halo is most likely attributed to the mixing of hydrothermal and metamorphic carbon and oxygen and the different fractionation properties of calcite and ankerite (i.e. Bierlein et al., 2004, Fein et al., 1994).

Concerning the ankeritic marble from Niger Diatreme, the stable isotopic ratios of this are $\delta^{13}C$ = 2.49 +/- 0.21; $\delta^{18}O$=14.2 +/- 0.11 (see appendix L) are in the range of metamorphic marbles reported by Blattner & Cooper, 1974. Together with the low REE concentrations of this rock (Fig. 5.2.16) and textures, the isotopic data strongly supports the interpretation of chapter 2.4 that this rock is a metamorphic, albeit partly hydrothermally altered, marble.

6.5) Isotopic composition of the fluid

In this section chapter I will discuss the potential sources of the carbon and oxygen in the carbonates analysed. For this, I will first constrain the temperature, as isotope fractionation between substances is strongly temperature dependent.

6.5.1- Physical conditions of crystallisation - temperature

To constrain the temperature of alteration and veining, several approaches can be taken; estimation of the temperature of the wall rock based on depth of formation and geothermal gradient, and/ or the temperature of the vein formation, which can be based on fluid inclusions, the isotopic and/ or chemical composition of the vein precipitates.

6.5.1.1: Temperature of unaltered wall rock

Assuming an average geothermal gradient of 30°C/km and using the depths estimated in chapter 2.5, the temperature of the rock in the Shotover settings would have been between 60 and 120°C, 30-120°C at Treble Cone and Red Rock. At Red Rock, the temperature would have been also around 60-120°C. At Mt Alta temperatures should have been less than 30°C and at Niger Diatreme could have been up to 90°C. However, for the diatreme-hosted rocks, this may have been higher due to heat conduction from the nearby diatreme and intrusives. Overall, it is reminded that the greenschist facies

schist in the area is hence only meta-stable and only kinetic effects (i.e. activation energy) hinder it from transforming into lower grade rock.

6.5.1.2: Temperature of vein precipitation

In the past several methods have been proposed for the determination of crystallisation temperatures of fluid. Two of these are based on the chemical and isotopic composition of vein precipitates. These two were attempted for this study. However, results yielded are inconsistent and unrealistic due to the systems not fully attaining chemical equilibrium. The exact procedures and constraints are given in appendix M. Another way to determine crystallisation temperatures is based on the homogenisation temperatures of fluid inclusions in vein precipitates and which gives minimum crystallisation temperatures. The examination of fluid inclusions was not part of this study, but fluid inclusions in hydrothermal quartz have been analysed in parts of the Shotover Valley (Craw, 1989 & 1991) and Mt Alta (Clough 1988). In the Shotover area, fluid inclusions in hydrothermal quartz have homogenisation temperature of 140-190°C and freezing temperatures between 0 and -1.6 °C, indicating a low salinity fluid (Craw, 1989 and 1991). These homogenisation temperature values require a correction regarding the pressure they formed at. Using the study by Brown & Lamb (1989) and assuming pure water with a density between 0.8 to 1 g/cm^3 this results in an "increase" of homogenisation temperature by about 18°C per km. Hence, at a depth between 2 and 4 km this would mean a fluid temperature would have been at least 175 - 260°C.

At Mt Alta, a wide range of temperature of hydrothermal fluids is attested for by fluid inclusions in quartz reported by Clough (1988), who identified two fluid types. In the quartz in the reefs, homogenisation temperatures are around 155-185°C and have freezing temperatures of -1.3 to -2.2°C. The fluid also contained some CO_2. Late stage, prismatic quartz has considerably higher homogenisation temperatures (350 - 380°C) and freezing temperatures of -0.1 to -0.5°C (Clough, 1988). Due to the shallow depth of formation, no pressure correction like in the Shotover example is necessary. Overall, the large differences in homogenisation temperatures indicate a big variation of fluid temperatures of precipitation, which could in turn be a result of repeatedly intruding dikes heating the water in the surrounding rock. The different freezing temperatures indicate different chemistry of the water at least regarding salinity or CO_2.

6.5.2- Isotopic composition of the fluid precipitating the carbonate

To be able to interpret the stable isotope data fully and to assess what possible fluid sources are, the temperature dependent fractionation of isotopes in the different components in the system need to be considered These components are H_2O, CO_2 (g), CO_2 (aq), dissolved carbonate species, Mg-(Fe)-dolomite and calcite. Regarding the oxygen isotope system, the fractionation of mineral relative to H_2O and dissolved CO_2 need to be considered. However, the fractionation values given between carbonate and H_2O in the literature (i.e. Golyshev et al., 1981) "automatically" contain part of the fractionation between dissolved CO_2 (from the carbonate) and water. Additionally, CO_2 only makes up a relatively small part of the carbonate-precipitating fluid and it is expected that the fluid-carbonate oxygen isotope fractionations is largely controlled by interaction of the water and the carbonate.

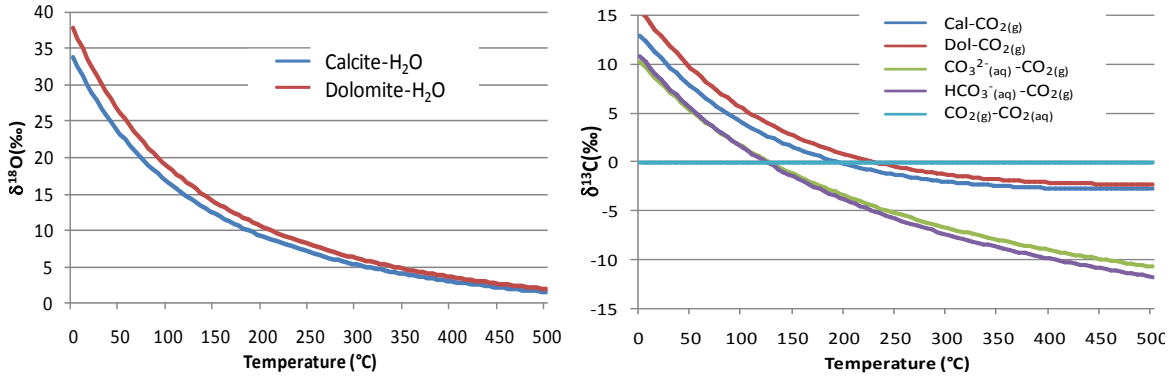

Fig. 6.5.1) Curves for oxygen and carbon isotope fractionation between different substances. For references see text.

With respect to the carbon isotope system, fractionation between CO_2 (aq) and the carbonate need to be considered. As in all studies concerned with isotope fractionation only fractionation between gaseous CO_2 and carbonate is reported in the literature, it is also necessary to identify the difference between gaseous and dissolved CO_2. The study of Ohmoto & Rye (1979) shows that there is essentially no difference in carbon isotopic composition of gaseous and dissolved CO_2 at temperatures above c. 80°C. Due to this, this fractionation is ignored in the cases discussed here. Another aspect to keep in mind is the pH-dependent speciation of carbonate in the fluid. Towards higher temperatures the transition point of CO_2 (aq) - HCO_2^- and HCO_3^- - CO_3^{2-} in a fluid shifts towards a higher pH (see Fig. 8 in Phillips & Powell, 2010). Accordingly, the dominant carbon-species in the fluid at the deposit will be CO_2, while it can be bicarbonate or CO_2 in a low temperature fluid. Hence, fractionation between bicarbonate (aq) and CO_2(g) and carbonate(aq) and CO_2 (g) need to be considered.

For many systems, several studies investigated fractionation of the involved substances. The fractionation models used here have been selected in respect to the calibration temperatures and it was attempted to select data from the same publication or authors. For the oxygen fractionation between calcite and water the study by Golyshev et al. (1981) and for dolomite and water that of Matthews & Katz (1977) are used respectively. For the fractionation of CO_2(g) and CO_2 (aq) for temperatures below 80°C data by Vogel et al., 1970 should be used, while above 80°C it would be the study by Ohmoto & Rye, 1979. For the fractionation bicarbonate (aq) and CO_2(g) and carbonate(aq) and CO_2 (g), models of Mook et al. (1974) and Ohmoto & Rye (1979) were used. All chosen fractionation models are summarised in Fig. 6.5.1.

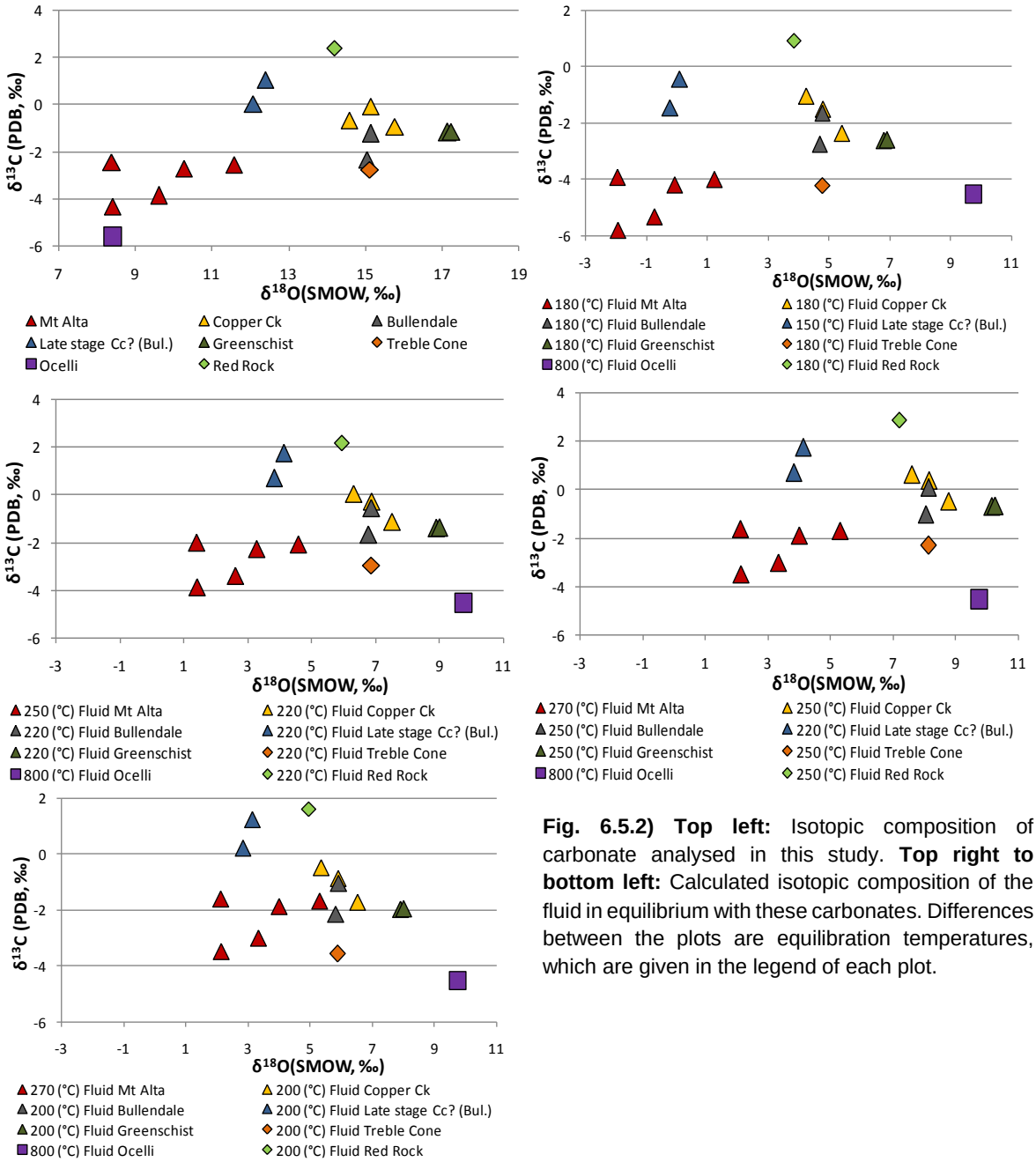

Fig. 6.5.2) Top left: Isotopic composition of carbonate analysed in this study. **Top right to bottom left:** Calculated isotopic composition of the fluid in equilibrium with these carbonates. Differences between the plots are equilibration temperatures, which are given in the legend of each plot.

Using above fractionation data, the fluid composition from which the carbonate precipitated was calculated. For the carbonate hosted in veins and breccias, I used several values for the precipitation temperature, due to the uncertainties regarding the temperature estimates. Regarding ocelli crystallisation temperatures, similar rocks from Hungary crystallised at high temperatures of about 1000°C (Nedli & Toth, 2003). However, calcite would burn at these temperatures (Horton, pers. comm) and a crystallisation temperature below/ around 800°C is more realistic. The results of the calculation are displayed in Fig. 6.5.2. In most calculations, the relative positioning of the carbonate and their corresponding fluids remain largely the same in a $\delta^{18}O$ vs. $\delta^{13}C$ diagram (Fig. 6.4.3 & Fig. 6.5.2). At the same time, the relative linear alignment of carbonate on the $^{87}Sr/^{86}Sr$ vs. $\delta^{13}C$ and $^{87}Sr/^{86}Sr$ vs. $\delta^{18}O$ isotope plot (Fig. 6.4.3&4) also remains. An exception to this are the ocelli where the fluid plots relatively to the far right in the $\delta^{13}C$ vs. $\delta^{18}O$ plot and for calculations where fluids at Mt Alta Diatreme were relatively hot compared to the fluids outside the diatremes (Fig. 6.5.2).

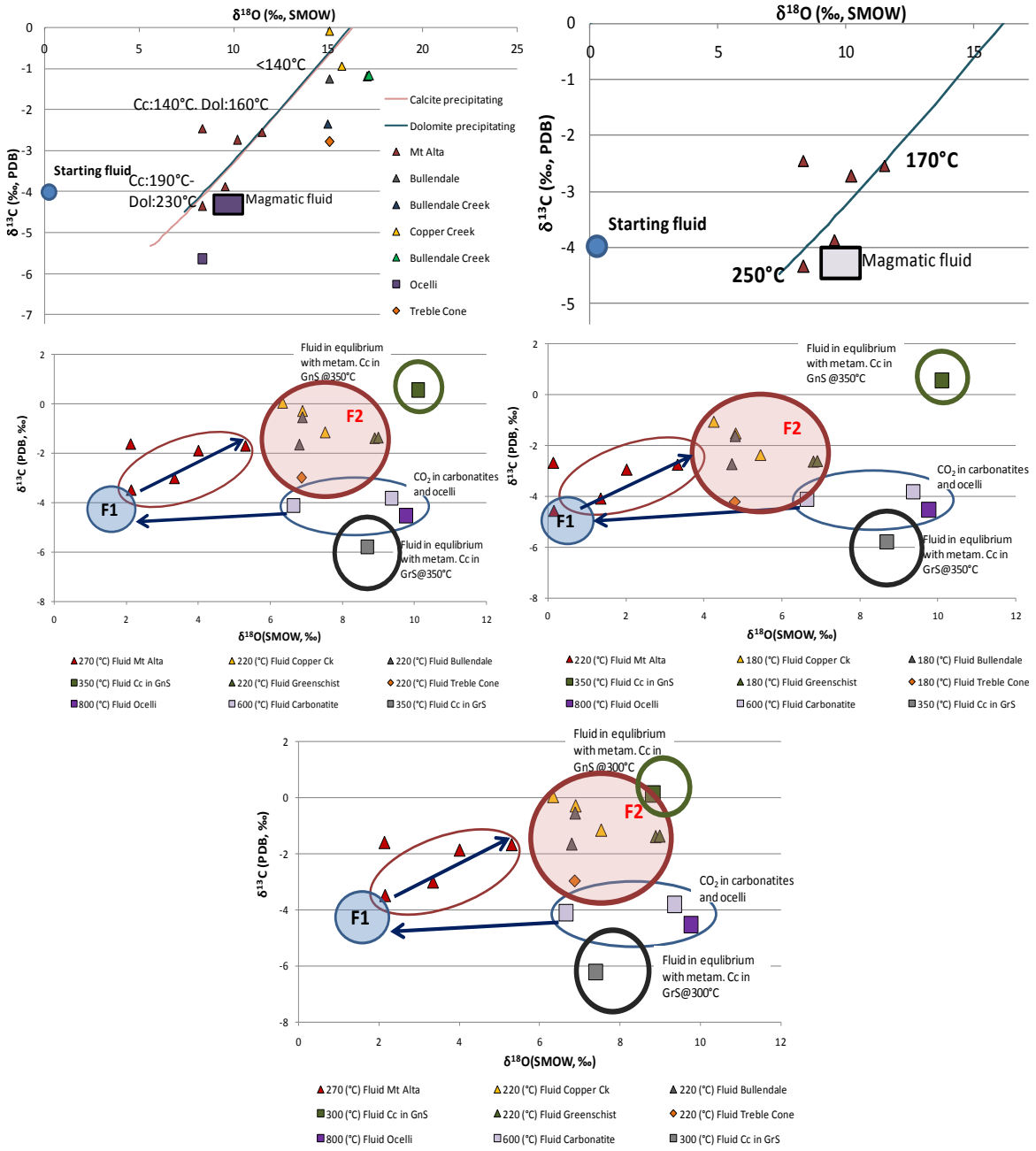

Fig. 6.6.1) Top left: Model calculation in which carbonate in veins and breccia is precipitated from one fluid composition at different temperatures. Due to the varying fractionation behaviour, calcite and dolomite of the same isotopic composition would have different precipitation temperatures as is indicated by the numbers above whole $\delta^{13}C$ values. Top right: Excerpt of the graph on the left. Here only carbonate from Mt Alta is plotted and the line depicts precipitation trend of dolomite from the starting fluid. Temperatures give the bracket at which the ankerite at Mt Alta would have precipitated. Bottom three graphs: Calculated compositions of fluids in equilibrium with the vein- and breccia-hosted carbonate at different temperatures. Temperatures are numbers in legends of plots. Two fluid end members can be defined. F1 =Fluid type 1; F2=Fluid type 2. For comparison fluids in equilibrium calcite in greenschist and carbonatite and ocelli are also plotted. The temperature estimates for the carbonatite crystallisation are based on Cooper & Paterson (2008).

6.6) Sources of carbon and oxygen in the fluid

To explain the arrangement of the fluid compositions shown in Fig. 6.5.4, two main mechanisms can play a role; Case 1: there was one fluid composition from which the different carbonates precipitated under different temperatures. Case 2: there were two different fluids from which the carbonates

precipitated. (Note: For this the analyses of carbonates from Red Rock and the calcitic veins at Bullendale which plot in the late stage calcite field in Fig. 6.4.4 are omitted from these considerations. The reasoning for this are that those carbonate are very different from the other carbonate, which is likely due to a different fluid system.)

Case 1: For the calculations the composition of the fluid would have a $\delta^{18}O$ of about 2 ‰ and $\delta^{13}C$ around -3‰ (Fig. 6.6.1).The carbonate precipitating would take place at around 250°C in the Mt Alta Diatreme hosted carbonate and at less than 150°C around Bullendale and Copper Creek in the Shotover. Just looking at the carbonate precipitated at Mt Alta, the linear trend in the carbonate can be attributed to precipitation temperatures between 250 and 170°C given ankerite/ dolomite precipitates. At the same time there is a linear increase in Sr isotope ratios from 0.7055 - 0.7067 under consideration of information from Fig. 6.4.3. (Note: There are no Sr isotope data for carbonate from the quartz reef)

Case 2: Two fluids are suggested. "Type 1" fluid produced carbonate which has low $\delta^{18}O$ (~-2-2‰), $\delta^{13}C$ (~-4‰) and $^{87}Sr/^{86}Sr$ (~0.704) values, and which is only found closely associated with the diatremes. "Type 2" fluid precipitated carbonate with higher $\delta^{18}O$ (~ 15‰), $\delta^{13}C$ (~0‰) and $^{87}Sr/^{86}Sr$ (~ 0.708) values and which was present outside the diatreme setting (Fig. 6.6.1). As shown in Fig. 6.6.1, the composition of these fluids is temperature dependent.

Under consideration of Fig. 6.6.1 both cases can be applicable but in different settings. At Mt Alta the linear relationship for the carbonate can either be the result of mixing of the two suggested fluids. However, the carbonate can just as well have precipitated from chemically the same fluid (Fluid type 1) at different temperatures. If the latter is the case however it needs to be addressed why simultaneously with an increase in $\delta^{18}O$ and $\delta^{13}C$ also $^{87}Sr/^{86}Sr$ increase. Here it may be that the hot fluid with originally low isotope values ($\delta^{18}O$ and $\delta^{13}C$ also $^{87}Sr/^{86}Sr$) interacts with the schistous wall rock of the diatreme. During this the fluid will not only cool down but also dissolve components from the metamorphic rock. One of these components is Sr which has relatively high Sr isotope ratios (>0.708), hence the cooling fluid would reach a higher Sr isotope ratio. As the schist only contains little calcite, the influence on the stable isotope composition of the fluid would be minimal. Concerning the carbonate from the Shotover and Treble Cone area, precipitation from the chemically the same fluid as at Mt Alta (fluid type 1) seems unlikely, as in that case most of the carbonate analysed would have precipitated at temperatures below 200°C and those in the Copper Creek Fault at less than 140°C, which is below the temperatures inferred for these kinds of faults (Craw, 1989; see above). Additionally, the carbonates in the Shotover and Treble Cone plot quite far from the calculated trend (Fig. 6.6.1), even when considering uncertainties concerning fractionation behaviours during precipitation. Hence, it is likely that the carbonates in areas outside the ADS precipitated from a fluid distinctly different from that at Mt Alta. This fluid would correspond to fluid type 2.

Summarising, the data suggest that two distinct fluid types played a role in the formation of the carbonates, one within the constraints of the ADS and one outside the ADS. When assessing the sources of the fluids, the interaction of the fluid with the wall rock of the fluid conduit, the abundance of the respective isotopes in wall rock and fluid, uncertainties regarding temperature estimates and an overlap of values from the different potential end member fluids need to be considered (Hoefs, 2008; Yardley et al. 1993; Menzies et al., 2014; Dipple & Ferry, 1992). This makes a clear determination of the source often impossible only based on the isotopic and it is essential that regional geology and structures are given strong consideration.

6.6.1- Source of fluid type 1

Fluid type 1 has $\delta^{18}O$ values between -2 and 2 and $\delta^{13}C$ values of around -5 to -4 (Fig. 6.6.1). Based on the geographic occurrence and the low Sr isotopic ratio in carbonate forming from this fluid (ca. 0.705, Fig. 6.4.3), it is proposed that fluid type 1 has major contribution from the magmatic system. Comparing the calculated fluid forming the carbonate in the ocelli and carbonatites and that forming the carbonate in the veins at Mt Alta, it shows that the carbon isotopic values would have been similar in both settings (Fig. 6.6.1). Additionally, the calculated $\delta^{13}C$ values of the vein-forming fluid lie in the range of mantle-sourced carbon (-5 to-8‰ (Graham, 2002); ~ -5 ‰ (Deines, 2002); around -3.5 to -5 ‰ (Griesshaber et al., 1992) but the $\delta^{18}O$ values are too low for pure magmatic fluid. The low oxygen values can be attained either by (1) precipitation of a mineral phase with high $\delta^{18}O$ values or (2) mixing with meteoric (or sea) water, which generally has oxygen isotopic ratios smaller than 0 SMOW (=standard mean ocean water. Also Craig, 1961). Concerning the precipitation of a mineral that is particularly high in $\delta^{18}O$, none of the sampled carbonate and quartz in this area have $\delta^{18}O$ values greater than 15. Minerals with high $\delta^{18}O$ may exist at depth, but this cannot be tested and seems unlikely. Mixing of a magmatic fluid with meteoric water, on the other hand, is very likely as the diatreme breccia is a zone of high permeability and being a structure that formed within a few km of the surface. Hence, it is reasonable that meteoric waters can percolate through the entire diatreme. As meteoric water is rich in oxygen (H_2O) but poor in carbon (Cox et al., 2014) relative to the magmatic fluid (as evident by the existence of ocelli and carbonatites) mixing of these two fluids would result in a decrease of the $\delta^{18}O$ values but not (considerably) those of $\delta^{13}C$. Hence fluid type one (Fig. 6.6.1) is most likely a mixed fluid with magmatic C and magmatic and meteoric O.

6.6.2- Sources of components in fluid type 2

Fluid type 2 has $\delta^{18}O$ and $\delta^{13}C$ values of around +4 to +9‰ and -3 to +1‰, respectively, and several sources are possible: magmatic, metamorphic, sedimentary and/ or meteoric. Especially the carbon sources for fluid type 2 are erratic, as there is no very close spatial relationship to any major carbon-bearing source (e.g., limestone, marble, or the Alpine Dike Swarm). However, using the isotopic composition (stable and radiogenic) of the carbonate and by carefully assessing the geological and tectonic setting, constraints can be made regarding the origin of volatiles in fluid type 2.

6.2.2.1: Possibility 1: Fluid from dehydration during metamorphism

It has been suggested that generation of metamorphic fluids in the Southern Alps happens during retrograde metamorphism due to the rapid, near isothermal exhumation of the Haast Schist along the Alpine Fault (Koons et al, 1998; Vry et al., 2010) and that these fluids can then form hydrothermal deposits (i.e. Menzies et al, 2014; Horton et al., 2003; Templeton et al, 1998). However, the fast exhumation only began less than 10 Ma ago (5-8 Ma, Little et al., 2005; Batt et al., 2004) and although some exhumation took place in the Oligocene-Miocene (Batt et al., 2004), there is no suggestion that this was rapid enough to cause the near-isothermal devolatilisation described by Vry et al. (2010) and Koons et al., (1998).

Another way to generate fluid due to dehydration of rock is during prograde metamorphism and which has been shown to have taken place in the Otago Schist (Turnbull et al., 2001; Norris & Henley, 1974; Cox, 1993, Breeding & Ague, 2002). However, metamorphism of the Otago Schist in the study area took place in the Early Cretaceous (Gray & Foster, 2004) which was long before the hydrothermal deposits in the Shotover and surrounding areas formed (Mid-Cenozoic; Craw et al., 2006). Although it has been suggested by some authors (Norris & Henley, 1976; Goldfarb et al 1991) that fluids may be trapped for millions of years or that they form only after peak pressure conditions

in the orogen due to the slow heat conduction of rocks (England & Thomson, 1984; Spear, 1993; Pitcairn et al., 2006) it is highly unlikely that fluid resided at depth for such a long time, especially as several tectonic events after peak-metamorphism took place. These are, for example, late-stage orogenic intracrustal shear zone (i.e. Hyde Macraes Shear zone in East Otago and Invincible in NW Otago (Hay & Craw, 1993; Craw et al., 2009; Pitcairn et al., 2006)), which were followed by exhumation and formation of decompression-related joint systems (Weinberger et al., 2010) and crustal extension and of graben and half-gräben formation (Laird & Bradshaw, 2004). Overall, there was "ample opportunity" for the metamorphically-formed fluid to escape the rock pile before the tectonic movements in the Cenozoic commenced.

6.6.2.2: Possibility 2: Fractionated magmatic fluid

As opposed to carbon from the metamorphic rock, the carbon in the fluid could also come from the magmatic system as this has been proven to contain abundant CO_2 (see above). Additionally, it has been shown that C and O in ankeritic veins can be derived from the carbonatite system (White, 1998). Veins from near the Siberia Fault, which is within the constraints of the ADS but north of the study areas here (Fig. 1.3), have very similar isotopic composition to the unfractionated carbonatites (Fig. 6.4.4). In the cases examined here, the carbonate have higher $\delta^{13}C$ values and also the average of calculated $\delta^{13}C$ values of fluid type 2 do not support a primary magmatic CO_2 source for fluid type 2 (Fig. 6.6.1). However, this does not exclude fractionated magmatic CO_2 caused by continuous crystallisation of carbonate minerals during cooling (Rayleigh fractionation). The magnitude of this fractionation can be calculated assuming a closed system in which carbonate (here calcite) precipitates from a finite reservoir of CO_2-bearing fluid. The magnitude of the change in the remaining fluid and precipitating carbonate is dependent on starting temperature, size of reservoir and precipitation rate (Fig. 6.6.2). I performed this calculation only for the carbon isotope system, as carbon is a better tracer for the CO_2 source than oxygen due to carbon's smaller abundance in the wall rock of the analysed veins. $\delta^{18}O$ values in the carbonate will be more likely a mixed value of wall rock and fluid-derived oxygen.

The calculations show that the higher the starting temperature is, the smaller the change in the remaining, especially for small precipitation rates (Fig. 6.6.2). In most cases, the calculated fluid does not reach "high enough" $\delta^{13}C$ values to be similar to the values of fluid type 2 (Fig. 6.6.1&2). In the cases that the fluid's composition is close to that proposed for fluid type 2, already a significant amount of carbon must have been extracted from the reservoir (Fig. 6.6.1). Hence, a carbonate body of about 10 times the volume of the carbonate at the surface should exist at depth under the here studied carbonate outcrops. It is questionable, if such a big carbonate body could exist at depth without any signs of magmatism at the same time (e.g. dikes), especially as carbonatites and CO_2 are only a relatively minor parts of the ADS (Cooper, 1986).

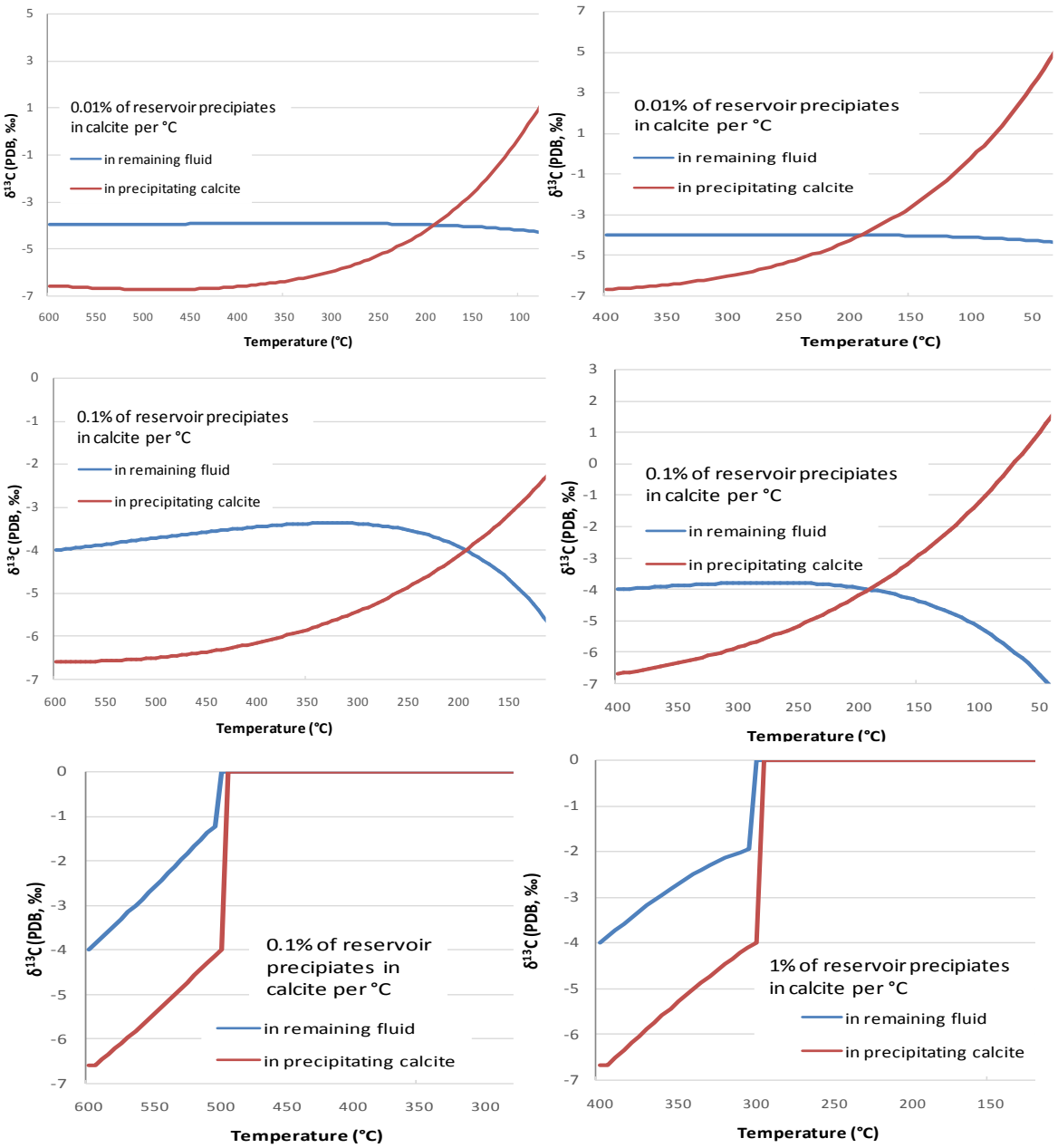

Fig. 6.6.2) Several model calculations of the evolution of the isotopic composition of the fluid and precipitating calcite during cooling. Note for the lower two plates: The rapid increase and zero values are when the carbon in the fluid has been consumed by precipitating calcite. Fractionation data used for calculation from Ohmoto & Rye (1979).

Another aspect that does not support a magmatic source for the carbon is the linear trend stable isotope ratios of carbonatites in the ADS (Fig. 6.6.3). This trend has been interpreted to be result of Rayleigh fractionation (Cooper & Paterson, 2008) and this fractionation has been calculated and the results are shown in Fig. 6.6.3. (As a control fractionation data from several studies were used.) These calculations show that the remnant fluid does not change its carbon isotope ratio values considerably. Assuming that throughout the studied region the initial carbonatitic fluid had the same starting composition and crystallisation rate, these calculations support that fluid type 2 is not fractionated magmatic fluid. For a detailed description and discussion of this fractionation model and the boundary conditions please refer to appendix N.

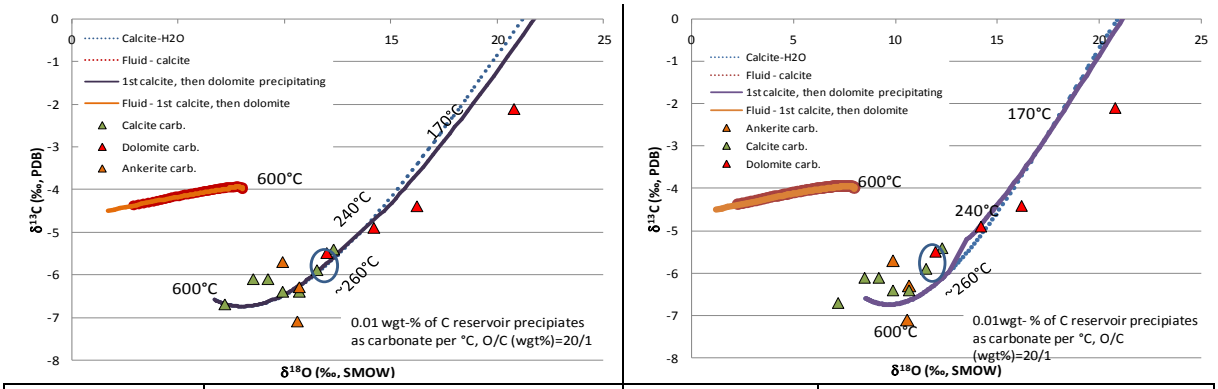

Calcite (oxygen)	Golyshev et al. (1981) Theoretical	Calcite (oxygen)	Golyshev et al. (1981) Experimental
Dolomite (oxygen)	Golyshev et al. (1981) Theoretical	Dolomite (oxygen)	Matthews & Katz (1977) Experimental
Calcite (carbon)	Ohmoto & Rye (1979)	Calcite (carbon)	Ohmoto & Rye (1979)
Dolomite (carbon)	Ohmoto & Rye (1979)	Dolomite (carbon)	Ohmoto & Rye (1979)

Fig. 6.6.3) Models of Rayleigh fractionation in the carbonatite system, using the same starting and precipitation conditions as in Fig. 6.6.2. Carbonatite compositions are from Paterson (1993) and Blattner & Cooper (1974). The circled markers are calcite and dolomite from the same sample. To evaluate the dependency of the calculated carbonate composition on fraction data used, I used two different data sets for oxygen fractionation. See appendix N for details.

Another way to test if part of the fluid of fluid type 2 has magmatic origin would be analyse the He isotopic ratios ($^3He/^4He$) in addition to carbon isotope values, However, studies on He-3/He-4 in crustal fluids in other parts of the world have shown that mantle-derived He and C are only found at major faults, such as the Hunsrück Fault and the Alpine Fault (i.e Bräuer et al., 2003; Griesshaber et al. 1992; Menzies et al., 2016). In comparison, the faults whose precipitates have been studied here are far smaller in scale and regional importance. If the relationship identified by afore mentioned scientist can be transferred to the system here it would support that the carbon in the carbonate veins in the Shotover area does not come from a magmatic source. Again, to test this He isotope ratios would need to be measures

6.6.2.3: Possibility3: Deeply circulating meteoric fluid

The hydrothermal deposits studied here precipitated in extensional structures which formed at the time of the inception of the Alpine Fault in an overall compressional tectonic regime which also caused the first uplift of the area of today's Southern Alps and adjacent areas (Batt et al., 2004). These tectonics were preceded by overall extensional tectonics; in the Late Eocene fault-bound basin formed in what is today Otago (Kamp, 1986) and these basins were bounded by topographic highs, horsts and accommodated deposition of sediments (i.e. Bob's Cove Beds.; Turnbull et al., 1975; Kamp, 1986). It has been shown in today active fault-bound graben and basin systems (i.e. the Upper Rhine Graben, Blue Nile River Basin) that meteoric water can circulate through the underlying rock pile simply driven by the topographical differences or hydraulic head (i.e. Bjørlykke, 1993; Kebede et al., 2005; Person & Garven, 1989). These waters can reach many kilometres depth, depending on permeability and fluid circulation system and can form fluid cells at depth (Garven, 1995; Nesbitt et al., 1989; Pribnow & Schellschmidt, 2000; Upton et al., 1995; Yardley et al., 1993). Fluid flow is often focused within the sediments as they are generally relatively permeable due to their high primary porosity. Here this would have been the sediments of Bob's Cove Beds (Kamp et al., 2015). It has, however, also been

shown that the water percolates through crystalline basement, provided secondary permeability features exist (Aquilina et al., 1997, Pauwels et al. 1993). Regarding the Otago Schist, joints are common occurrences and which provide pathways for fluid to flow (Jenkin et al., 1994; Weinberger et al., 2010). Based on this, it is hence reasonable to suggest that in a pre-Alpine Fault age, fluid circulation through the Otago Schist took place in the study area. At the time of change in the tectonic regime and with the initiation of the Alpine Fault, old faults reactivated or changed their sense (i.e. Moonlight Fault) and new faults formed (i.e. the Au-mineralised faults). These faults provided pathways for deep seated fluid and allowing upwelling of the hot fluids that would have largely gotten there during the times of extensional tectonics. As some relief formed associated with the inception of the Alpine Fault, it may be that at this time meteoric fluid also penetrating into the rock pile, potentially aiding the circulation of deep seated fluids. The latter would be analogous to today's Southern Alps (i.e. Menzies et al, 2014, Cox et al., 2014).

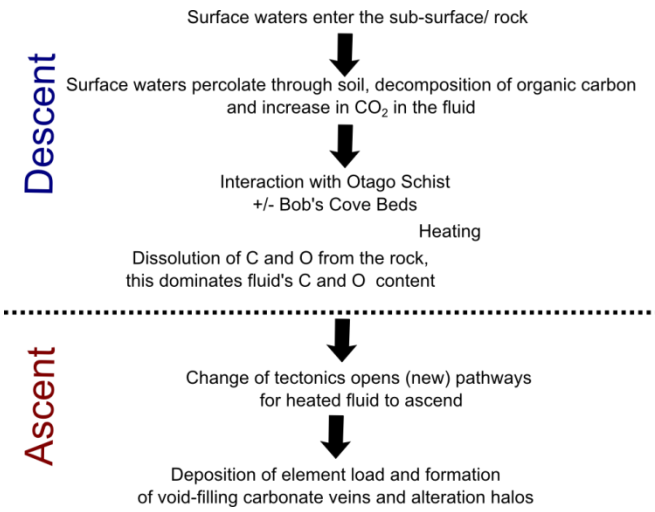

Fig. 6.6.4) Model of the evolution of fluid type 2 if it is meteoric in origin.

Primary meteoric and other surface waters in equilibrium with the atmosphere are relatively CO_2-poor (i.e. Cox et al., 2014), which makes it an unlikely primary carbon source for the CO_2 in the fluids forming the carbonate. However, during the descend this water will interact with the surrounding rock/ soil picking up and exchanging elements in an attempt to attain chemical equilibrium (i.e. Dipple & Ferry, 1992, Jamtveit & Hammer, 2012; Yardley et al., 1993). As a result of the interaction of the meteoric water with the soil, decomposition of organic carbon in the soil layer takes place and the CO_2 content in the water increases 7-10 fold (Horton, pers. comm). This hypothesis is backed by the study by Atkinson (1977) who showed that with increasing depth there is as increase in CO_2 content in groundwater which will also partly be the result of increased CO_2 solubility with increasing pressure. Another rocktype the water percolates through is the limestone of the Bob's Cove Fm, which will also provide C to the fluid. However, as the bulk of the fluid is mostly percolating through Otago Schist, the descending fluid will interact most extensively with these metamorphic rocks. A strong indicator that this exchange took place here are the oxygen isotopic ratios of the calculated fluid of fluid type 2 (Fig. 6.6.1). These values are much higher than would be expected for surface waters but on the other hand are similar to metamorphic waters (Fig. 6.6.1, Hoefs, 2008). Such interaction of descending surface waters and the Otago Schist have also been described in other studies (Barnes et al., 1979; Cox et al., 2014; Horton et al., 2003; Jenkin et al., 1994; Menzies et al., 2014; Reyes et al., 2010). Additionally, the calculated isotopic fluid composition is only slightly lower to very similar to 300-350°C hot fluid in equilibrium with greenschist-hosted calcite (Fig. 6.6.1). The choice of the temperature of this rock-interacting fluid (300-350°C) is based on the widely accepted model that fluids descend to depth, heat up, dissolve components from the rock, ascend, cool and precipitate the studied mineral deposits.

Although the calculated fluid type 2 is quite similar to the fluid in equilibrium with greenschist-hosted calcite, the scatter of $\delta^{13}C$ over 2‰ and generally lower $\delta^{13}C$ of fluid type 2 suggest that greenschist is not the only source of the fluid's carbon. Some of this scatter can be attributed to the

fact that metamorphic calcite in greenschist does not have uniform isotopic composition either (Fig. 6.4.1). Nonetheless, based on the average low $\delta^{13}C$ values still suggest that there were several sources for the C and that mixing took place. Marbles occur in association with greenschist but the calcite in these rock types has a $\delta^{13}C$ of around 0‰ (Hoefs, 2008) which also results in fluid with relatively high $\delta^{13}C$ values, similar to that in equilibrium with greenschist. Carbonate from Bob's Cove sediments also has $\delta^{13}C$ values of around 0‰ (appendix L) and relatively cold surface waters will have low $\delta^{13}C$ values (~ -9 ‰ at 25°C). A source with relatively low $\delta^{13}C$ ratios is quartz-feldspathic greyschist. This rock contains graphite and calcite. CO_2 in equilibrium with graphite, which has $\delta^{13}C$ around -19.5 ‰ (Billia, 2013), should have $\delta^{13}C$ values around -6 to -8 ‰ (using Ohmoto & Rye (1979) at T between 200 and 350°C). Fluid in equilibrium with calcite would have a $\delta^{13}C$ of around - 6‰ (Fig. 6.6.1), keeping in mind that just like in greenschist, isotopic compositions of calcite in greyschist scatter over several ‰ (Fig. 6.4.1). Although greyschist contains only little metamorphic calcite, its dominance over the other mentioned lithologies and proximity to the deposits make it a viable source for the carbon in the fluid. The reason why the isotopic signature of the fluid seems to be dominated by greenschist-derived carbon although greyschist is more common can be attributed to greenschist having far more calcite than greyschist. Greenschist can contain up to 30% calcite (see chapter 3) and has also in the other studies been found to be calcite-rich than greyschist (Craw, 1981; Pitcairn, 2004). When water percolates through the rock it will hence proportionally take up more carbon from greenschist. Additionally, the study areas are in the Aspiring Lithological Unit, which contains relatively large volumes of greenschist and also marble compared to the rest of the Haast Schist, accentuating this effect. The simplified model for the evolution of fluid type 2 is shown in Fig. 6.6.4. Alternatively, carbon from the magmatic system could also contribute to the fluid.

Overall, there is good evidence that the oxygen in the fluid is derived from the Otago Schist, although the original fluid was most likely meteoric fluid. There is still ambiguity on the carbon source though and just with my data this problem is not resolvable. However, the data from Craw et al. (2009) (Fig. 6.4.4) may aid. The carbonate that formed from fluid type 2 is similar isochemically and also concerning its structural setting to carbonate in the auriferous faults in the Shotover (Fig. 6.4.4). Their mineralisation-related ankerite in Craw et al., however, plots in a much wider array than the data here, especially carbon. Their carbonate and my carbonate outside the Shotover formed at the same time in the same system hence likely the same fluid type. As those carbonates partly have $\delta^{13}C$ values <4‰. These carbonates cannot be the precipitates of a magmatic fluid, assuming similar precipitation temperatures throughout (180-250°C). However, instead they could be precipitates of fluids where the carbonate was derived from greyschist-originated graphite or calcite.

Summarising, fluid type 2 and hence the gold precipitating fluid is most likely rock-exchanged meteoric water, which has also been suggested by Craw et al. (2009). Overall, the interpretation that orogenic gold deposits form due to deeply circulating meteoric fluid has been employed for similar deposits in other parts of the world (i.e. Yardley et al., 1993; Nesbit et al., 1986; Nesbitt& Muehlenbachs 1989) and it shows that deposits of precious metals or rare minerals do not necessarily require an exotic fluid (Dipple & Ferry, 1992b). This also concurs with the results of Mortensen et al. (2010) according to which the Pb was derived from the Otago Schist and analogous to it also Au. It may seem farfetched that water should percolate many km through the Otago Schist, however, Cox et al. (2014) showed that the chemistry of spring waters change in response to earthquakes happening many hundred km away, illustrating that the fluid systems in New Zealand's Southern Alps can be extensive and complex, despite being a rock pile with a low primary porosity.

6.6.3-Summary of potential sources for volatiles in the fluids

In above sections (6.6.1&2), it has been shown that most of the analysed carbonate are precipitates of two fluid types (Fig. 6.6.1). The data point to fluid type 1 being a mixture of magmatic and meteoric fluid. Concerning fluid type 2 (Fig. 6.6.1) it is concluded that this fluid was most likely originally meteoric water that penetrated the Otago Schist. This fluid circulation would have been enabled by the secondary porosity of the rock and would have been driven by topography. During the flow of the fluid through the rock pile, the fluid interacts with rock to attain chemical and isotopic equilibrium. During this fluid-rock interaction, the originally largely CO_2-poor fluid would have not only leached metals, i.e. Sr and Ca, but also C and O from the metamorphic rock. This hypothesis does not exclude that some of the fluid's C and O may have been derived from the magmatic system of the ADS. However, nothing points unambiously towards this esepcially when considering the stable isotope data from Craw et al. (2009).Overall, the likelihood that magmatic fluid played a role outside the confines of the ADS is very small.

6.7) Fe isotopic composition of whole rocks and selected metamorphic and hydrothermal minerals

In recent years, the use of the Fe isotope system has increasingly been a tool in various fields of the geosciences, such as cosmo-geochemistry, hydrothermal alteration and volcanics (i.e. Dideriksen et al., 2006; Hezel et al., 2010; Johnson et al., 2010; Rouxel et al., 2003). Fe isotope ratios can be used not only for sourcing of the Fe but also give information about the reaction history of the Fe as iron occurs in several oxidation states which gives rise to isotope fractionation during redox reactions (Hoef, 2008). In this study, I measured the iron isotopic composition of a selection of samples in order to give some insights into the behaviour of Fe isotopes in carbonate-dominated hydrothermal system.

Table 6.7.1) Samples analysed for Fe isotopic composition

Sample	Separate or whole rock	Description
BUL4CV	Separate	Vein in GnS
BUL4Ca	Whole rock	Altered GnS
BUL4Cb	Whole rock	Altered GnS
BUL4Cc	Whole rock	Unaltered GnS
TP7A2	Whole rock	Altered GnS
TP7A	Whole rock	Altered GnS
TP7A-Ank	Separate	Ankerite in altered GnS
TP7D	Whole rock	Unaltered GnS
TP7D-chl	Separate	Chlorite in unaltered GnS
TP7D-epi	Separate	Epidote in unaltered GnS
TP4A	Whole rock	Altered GnS
TP4F	Whole rock	Unaltered GnS
TP4C	Whole rock	Little altered GnS

6.7.1- Methods

Samples analysed are a subset of those described in chapter 3-6. Samples were whole rock samples, and separates of epidote, chlorite and ankerite (Table 6.7.1). For the BUL samples ankerite of a vein from the alteration halo was separated. From the TP7A a separate of unoxydised ankerite was picked. The grains were bigger than 0.2 mm and are most likely from the leucocratic layers, which are believed to have formed from the replacement of metamorphic calcite. From TP 7D epidote and chlorite were picked.

The Fe isotope measurements were carried out at Bonn University using a NEPTUNE ICP-MS. Overall they were 13 samples and 1 blank. The silicate-bearing samples (whole rock, epidote and chlorite) were dissolved in a 2:1 concentrated HF/ concentrated HNO_3 solution. These solutions were then evaporated and taken up in 6N HCl. The carbonates and second batch of whole rock sample TP7A were only treated with conc. HCl in order to dissolve only the carbonate fraction. This was then

also evaporated. The Fe separation was done by chromatography following the procedure of Dauphas et al. (2004). The Fe-bearing solution was then measured at the Rheinische Friedrich-Wilhelm Universität zu Bonn, Germany using a NEPTUNE MC-ICP-MS. Each sample solution was analysed three times. Results are normalised against the standard reference material IRMM-14 (elemental iron).

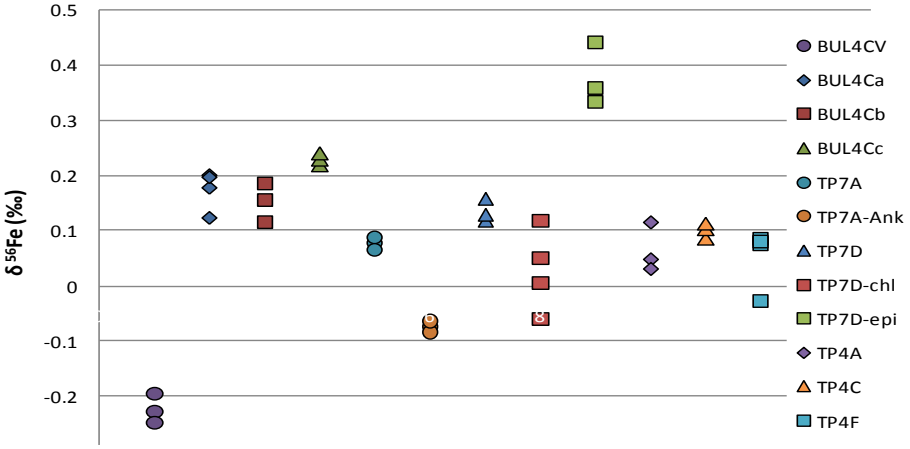

Fig. 6.7.1) Results of Fe isotope ratio measurements in the different samples. Each sample was analysed three times. Analytical error bars are smaller than the errors calculated from the different analyses, and which are shown in the next figure. X-axis just for display.

6.7.2- Results

All ankerite analysed have δ^{56}Fe values consistently below 0‰; ankerite in veins in BUL4C has δ^{56}Fe value of around -0.2 ‰, while the ankerite of the leucocratic layer of TP7A has a value of c. -0.07‰ (Fig. 6.7.2 A&B). In the rock adjacent to the vein in BUL4C, the δ^{56}Fe increase slightly away from the vein and this increase is coupled with an increasing Fe content of the rock (Fig. 6.7.2A). A positive correlation of Fe content and δ^{56}Fe can also be seen for the sample set of TP4 (all whole rock analyses) (Fig. 6.7.2C). In the TP7 set, the altered rock is also isotopically slightly lighter than unaltered rock of this set but there is no correlation between Fe content and δ^{56}Fe values (Fig. 6.7.2B). Epidote has higher δ^{56}Fe values than chlorite (Fig. 6.7.2B) and the whole rock of TP7D.

6.7.3- Discussion

The data presented above, point to several processes controlling the iron isotopic composition of the analysed substances. The minerals with divalent iron in their crystal structure (ankerite & chlorite) have lower δ^{56}Fe values than minerals with trivalent Fe (epidote). That minerals with trivalent Fe are on average enriched in ^{56}Fe compared to those with divalent Fe is a common phenomenon (i.e. Beard et al., 2003; Markl et al., 2006; pers. com. N. Teutsch, 2016). The relatively high δ^{56}Fe of the ankerite from TP7A (Fig. 6.7. 2B) compared to the ankerite in the veins of BUL4C (Fig. O. 2A) likely reflects that this carbonate has not reached chemical equilibrium with altering fluid, as shown in chapter 3.2.

Within each alteration halo, the bulk δ^{56}Fe value seems to get smaller towards the centre of alteration (i.e. towards to the altering feature and primary fluid conduit) which corresponds with the increase of hydrothermal, Fe-bearing carbonate which is theoretically isotopically lighter than metamorphic minerals with trivalent Fe (see above). However, this decrease is only very subtle and within the error (Fig. 6.7.2); results are therefore inconclusive. Nevertheless, the fact that the ankeritic vein in BUL4C has a much lower δ^{56}Fe value than in the surrounding rock (Fig. 6.7.2A) indicates that

the remaining fluid needs to be relative to the rock enriched in Fe with high δ^{56}Fe, as it has been shown earlier that the veins received their bulk Fe from the wall rock.

Summarizing, the presented data show systematic trends across the alteration halos and certain properties of the different minerals. In most cases, crystallographic effects and red-ox state of the Fe seem to strongly control these trends, but other processes may also play a role. However, the analysis and discussions presented here are only reconnoitring and in future projects it would be worth to have a closer look at the Fe isotopic characteristics in hydrothermal alteration halos and minerals associated with it, as Fe isotopes would be a tool to assess iron mobility and reaction processes.. As mentioned above some analyses have large errors and in addition to obtaining a more complete data set, it is also necessary to improve the measurement set up and obtain more precise analyses.

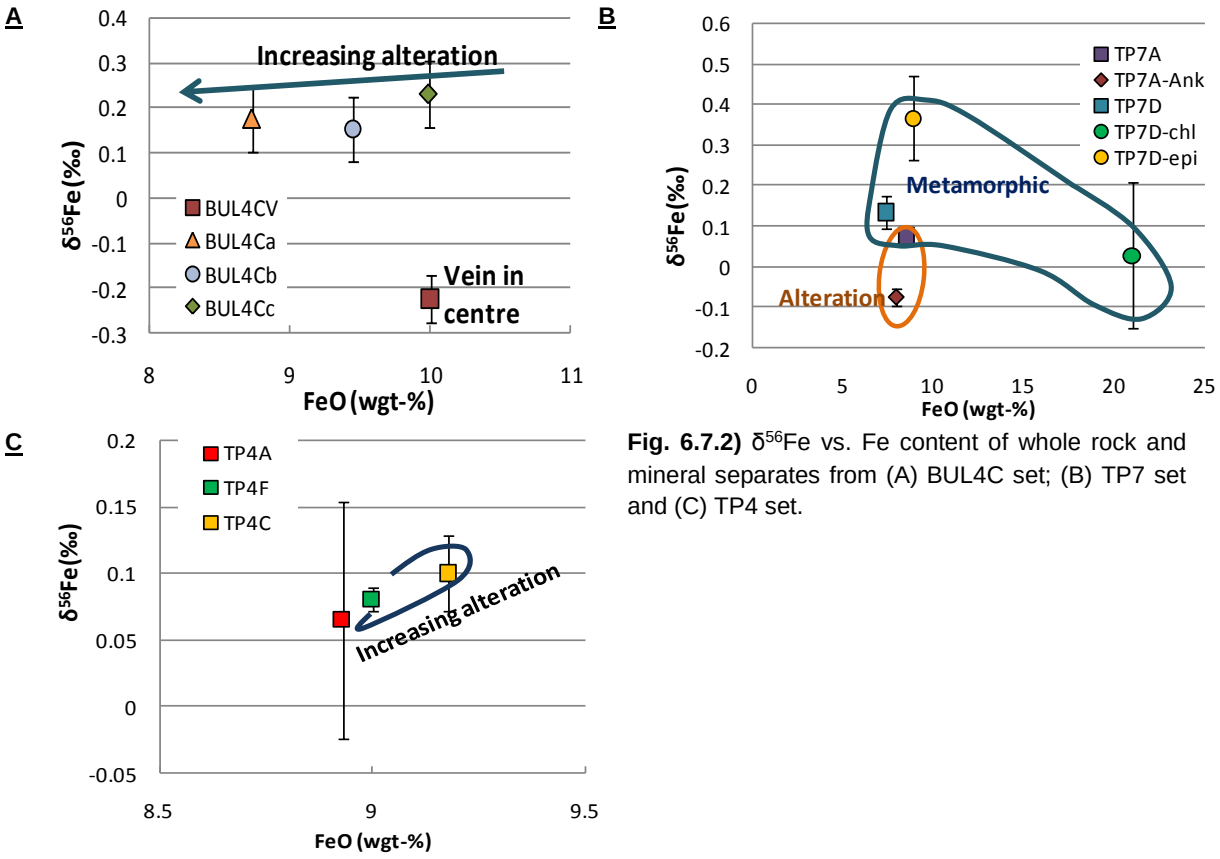

Fig. 6.7.2) δ^{56}Fe vs. Fe content of whole rock and mineral separates from (A) BUL4C set; (B) TP7 set and (C) TP4 set.

6.7) Conclusions

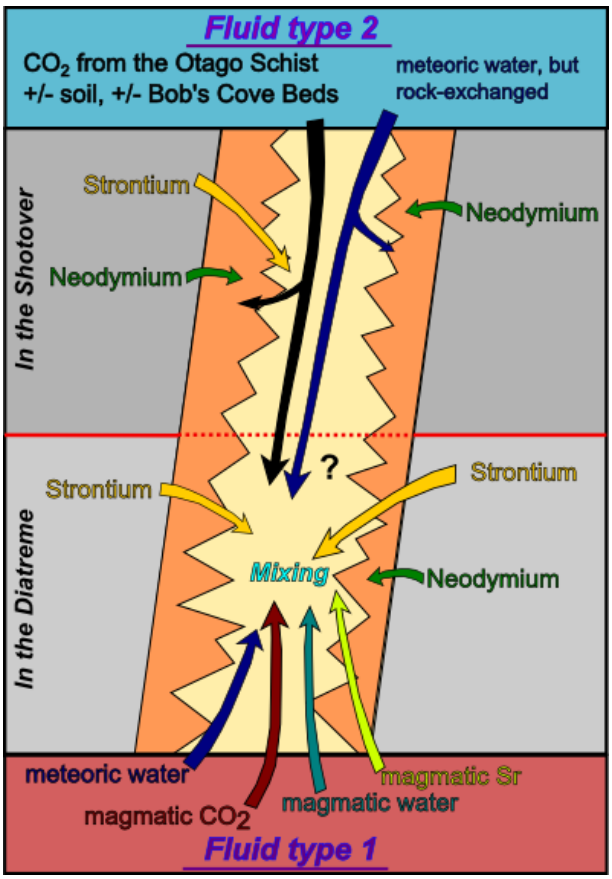

Fig. 6.8.1) Model of the evolution of fluid type 1 and fluid type 2. In veins outside the diatreme, the carbonate components are derived from fluid type 2 and the metamorphic rock (GnS and GrS) in that area. In the diatreme, carbonate compositions are controlled by fluid type 1 and potentially mixing of fluid type 1 and 2. Sr and Nd are derived from rocks inside the diatreme (Lamp & GrS) and Sr is (probably) also derived from the GrS surrounding the diatreme.

The data, descriptions and calculations presented in this chapter, show that the different elements in void-filling carbonate can be transported over different distances (Fig. 6.8.1). Nd isotopes suggest that the LREE are largely derived from the immediate wall rock of the hydrothermal precipitate, while mixed Sr isotopic ratios show that Sr can be transported over several metres at least. Sr isotopic ratios of veins also suggest that only certain minerals contribute their Sr to the fluid, which concurs with observations made in earlier chapters that only certain minerals break down in response to infiltrating fluid.

Concerning the "carrier fluid" of these metals, two different types have been proposed. Fluid type 1 derives its volatiles from magmatic and meteoric sources, while fluid type 2 is most likely ultimately meteoric in origin but interacted with the rock whilst circulating through the Otago Schist, causing its chemical and isotopic composition to approach equilibrium with the host rock. During this process C and O were leached from the rock and taken up by the fluid. A change in tectonics caused opening of fluid pathways, resulting in fluid type 2 to rise and form the hydrothermal carbonate (+/- gold) deposits. Overall, there is no convincing evidence that magmatic Sr, C and O were components in the fluids producing the hydrothermal minerals outside the ADS, including the gold deposits. Mixing of fluid type 1 and 2 may have taken place at Mt Alta Diatreme (Fig. 6.6.1). However, to test this hypothesis it is first necessary to determine the crystallisation temperatures of the carbonate samples.

CHAPTER 7) A SYNTHESIS

In this study, hydrothermal, carbonate-rich deposits in western Otago were investigated. Some of these are auriferous, while others are linked to alkaline magmatism. The hydrothermal activity took place in the Oligocene-Miocene, contemporaneously with the initiation of the Alpine Fault (Craw et al., 2006; Cooper et al., 1987). The hydrothermal deposits are manifestations of the interaction of CO_2-bearing fluids and rock; fluids infiltrated the fluid conduit's wall rock, causing the formation of hydrothermal alteration halos, and precipitate carbonate and other hydrothermal minerals in veins, faults and other voids. Throughout this study, a few key questions were investigated:

Where did the elements come from? How far have the different elements been transported? What could the controls for the mobility have been?

Under this very broad topic, several aspects were addressed: The texture of replacement reactions; chemical changes of the whole rock during hydrothermal alteration; mineral chemistry of alteration-related minerals in the alteration halos and veins; enrichment and depletion of the different elements in the hydrothermal deposits; source and transport distances of components in the fluid.

Establishing this information allowed to not only obtain/ confirm insight into orogenic gold deposits, such as establishing source regions for fluids or co-occurrence of arsenic and gold, but also gave information on what the controls for mobility and immobility of other elements, like the REE, could be.

7.1) Mineral reactions

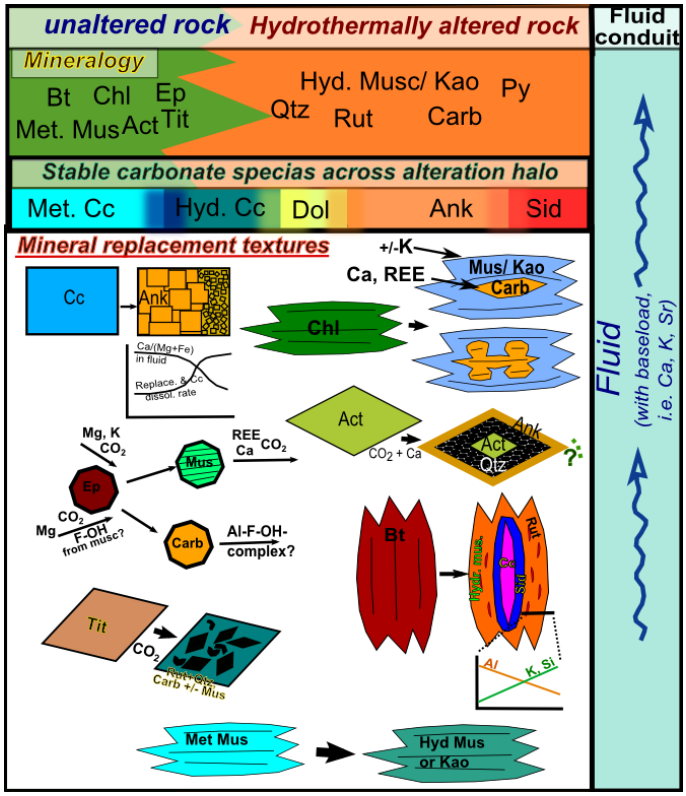

Fig. 7.1) Schematic model of mineralogical changes happening green- and greyschist due to fluid flowing along a fluid conduit and infiltrating the rock.

During the hydrothermal alteration of green- and greyschist, the same metamorphic minerals are unstable or stable at the influx of hydrothermal fluid. Stable minerals are apatite, zircon, monazite, albite, quartz. Unstable minerals are biotite, chlorite, epidote, muscovite and titanite. These minerals are replaced by hydrothermal muscovite/ kaolinite, quartz, rutile, carbonate and pyrite (Fig. 7.1). Mineral replacement takes place by dissolution-precipitation and is initially pseudomorph.

The stable carbonate species in the rock depends on the relative location within the alteration halo hence CO_2/Ca ratio in the fluid. With increasing CO_2/Ca the succession is hydrothermal calcite-dolomite-ankerite-siderite, with

adjacent carbonate zones overlapping (e.g. Fig.3.2.21&22; Fig.7.1).

7.1.1- Specific mineral reactions

In cases where calcite in leucocratic layers is replaced by ankeritic carbonate, the replacing carbonate is generally grainy at the rim and chemically zoned but optically continuous in the centre of the old grain (Fig. 3.2.17&18). The different textures are likely the response to locally differing replacement rates which are limited by diffusion rate of components in the fluid through the already replaced carbonate (Fig. 7.1; Jonas et al., 2015).

Epidote is replaced either by muscovite in rocks without metamorphic muscovite or carbonate when the metamorphic rock contained metamorphic muscovite. This suggests the Al from the epidote may have been mobilised in F-OH complexes (Schott & Tagirov, 2001).

Throughout all samples, titanite has been replaced by rutile crystallites and symplectites, together with quartz, carbonate (primarily as calcite) and sometimes other minerals such as muscovite.

Chlorite was replaced by kaolinite/ muscovite and carbonate (commonly ankerite) +/- quartz (Fig. 7.1). The ankerite either forms lenses in the chlorite, pushing old cleavage plains apart or it grows with a cauliflower-like texture across the cleavage plains (e.g. Fig. 3.2.11 & 18). The difference in phyllosilicate is a response to the K^+/H^+ ratio in the fluid at the replacement site (Tosdal et al., 2009). As the systems studied here are neither fully rock- nor fully fluid-buffered, this ratio strongly depends on the rock type which is being altered. If the rock has a high K content (e.g. greyschist), the K^+/H^+ ratio of the fluid entering the rock will increase due to the chemical exchange during fluid-rock interaction.

Replacement products of actinolite are ankerite and quartz which are arranged in rims around the remaining actinolite (Fig. 3.2.10; Fig. 7.1). The rim texture suggests that quartz was less soluble than the carbonate on a local scale, which would coincide with an elevated CO_2 content in the fluid; carbonate is more soluble hence mobile in CO_2-bearing fluid than quartz (Manning et al., 2013; Walther & Orville, 1983).

In the replacement of biotite, Ti in biotite forms rutile exsolution. The hydrothermal muscovite replacing most of the biotite becomes more Al rich and Si poor towards the contact to carbonate (Fig. 3.2.6; Fig. 7.1), probably marking the site where the fluid entered the mineral. The succession siderite-calcite (Fig. 3.2.6; Fig. 7.1) indicates a relatively abrupt change (decrease) in the CO_2/Ca ratio of the fluid, as otherwise ankerite would have formed.

Although in none of the studied alteration halos gold was found, the same mineral reactions are commonly found associated with orogenic gold deposits, including the ones at Bullendale and Copper Creek (Craw et al., 2006&2009; MacKenzie et al., 2007; this study). A major difference between gold-bearing and gold-barren cases in this area appears to be that in the gold-associated alteration halos arsenopyrite forms as well as pyrite. Some of the pyrite has been corroded at the rims and has been overgrown by arsenopyrite. Another difference can be found in the phyllosilicate mineralogy in the alteration halo. In altered greenschist near the gold-bearing Copper Creek Fault kaolinite rather than hydrothermal muscovite occurs, and which is interpreted to be the product of the breakdown of chlorite (Fig. 7.2; MacKenzie et al., 2007, own observations). The reason for this is most likely that the gold-precipitating fluid had a lower K^+/H^+ ratio than the gold-barren fluid.

In contrast to the altered greenschist, in altered greyschist metamorphic muscovite throughout has been partially replaced by hydrothermal muscovite, although in the gold-bearing halos kaolinite can have formed, too. The reason for this mineralogy difference is that the fluid in the greyschist was influenced by the K-rich composition of the greyschist. Hence locally, i.e. within the

greyschist the K^+/H^+ ratio would have been high enough to form hydrothermal muscovite, even if kaolinite formed at the same event in the greenschist.

Summarizing, there is evidence of S in all alteration halos but only in the gold-bearing cases is there evidence for amounts of arsenic in the fluid large enough to form arsenopyrite. Additionally, the fluid in the gold-bearing sites had probably a lower K^+/H^+ ratio, as indicated by the difference in phyllosilicate species (Fig. 7.2).

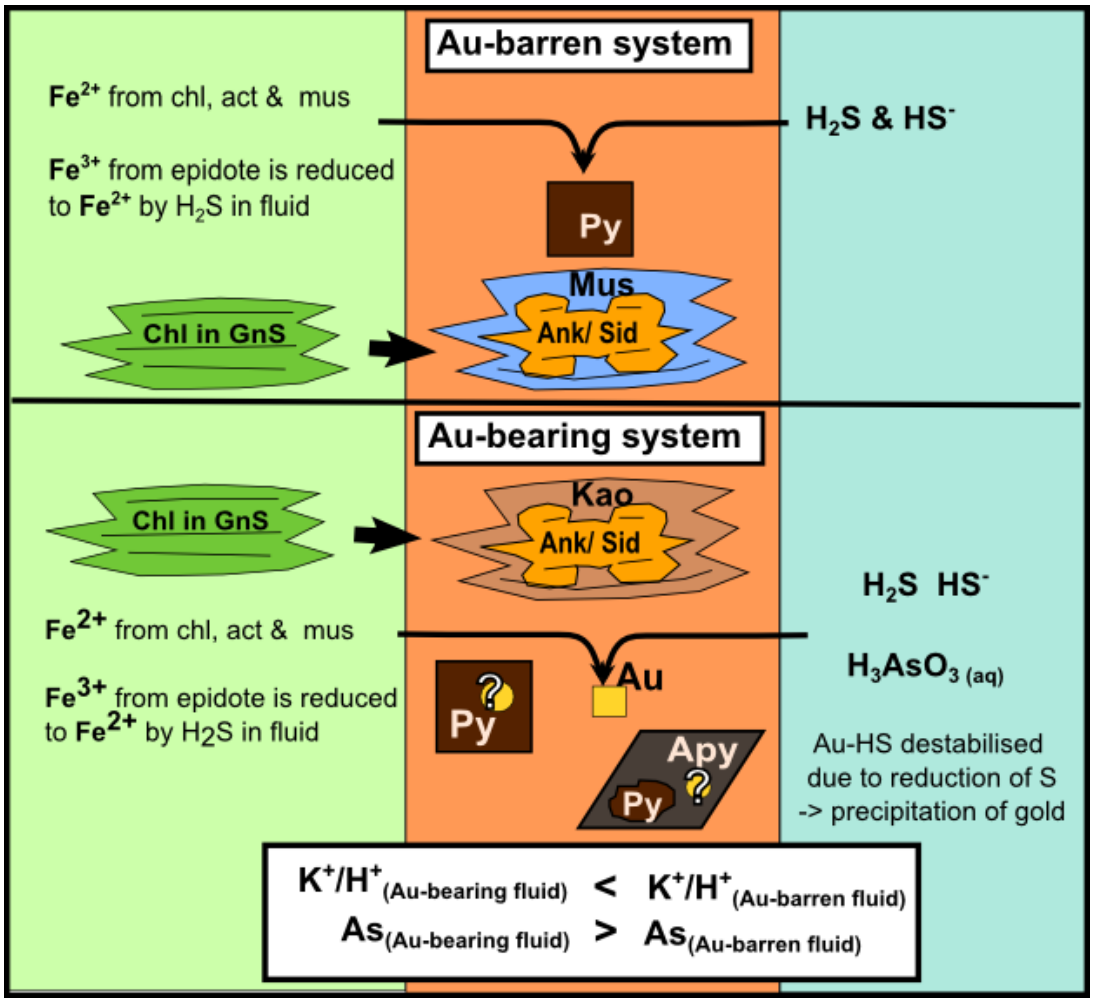

Fig. 7.2) Schematic model of the key differences in the altered gold-barren greenschist from Bullendale and gold-associated greenschist at Copper Creek. Concerning gold enclosed in sulphides, the literature is not clear in which of the two gold is contained.

7.2) Element mobility in the alteration halo and the fluid conduit

The influx of fluid into the rock not only causes mineral breakdown but also mobilisation of various elements on micrometre- to metre scale. Overall, chemical changes are smaller and less consistent in greyschist than in greenschist, as before the fluid entered the alteration site, it passed predominantly through greyschist. Resultant it is closer to equilibrium with the greyschist wall rock.

Of all elements examined the LILE show the relative biggest changes and are often enriched, especially in originally mica-poor greenschist (2 to 20 times enrichment; Fig. 4.2.8). By isotopic means (Fig. 6.2.4; Fig. 6.3.4) it could further be shown that Sr can be transported at least for several metres in the fluid and that Sr from different sources can mix. As greyschist is the most common lithology in the area, most of the studied hydrothermal features retrieved their Sr from greyschist, as can be deduced from the ratios of the LILE (Fig. 4.2.13) in addition to Sr isotopic ratios. In addition to mixing

of Sr from different sources it is further proposed that the Sr transported by the fluid is predominantly derived from minerals with little Rb, such as epidote as opposed to Sr from muscovite. This hypothesis is based on the relative low $^{87}Sr/^{86}Sr$ ratios of veins in greyschist compared to their host rock (section 6.3) and which is supported by the observation that epidote is much more sensitive to the influx of CO_2-bearing fluid than muscovite (chapter 3). In only very close proximity (<1.5 cm) of the fluid conduits, the altered rock is enriched in W (around 20-35 times; Fig. 4.2.9) which suggests that W can only be transported in the fluid. This may be the result of higher temperatures in the fluid compared to the wall rock. Fe, Mg and Ca were typically leached from the rock (Fig. 4.2.6) and these elements were (partly) incorporated in the veins (section 5.4.4.2). The Fe released in the rock is not only incorporated by ankerite but also by pyrite.

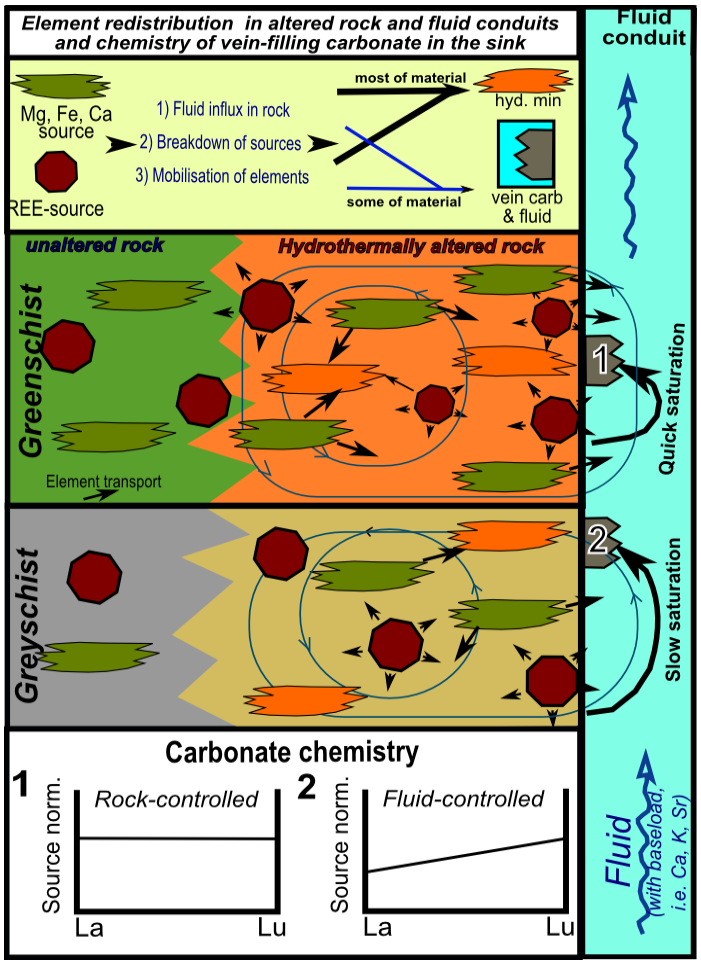

Fig. 7.3) Schematic model describing the element redistribution in the wall rock and chemistry of the carbonate in the veins.

It has been shown that the mobility of elements is often dependent on the metamorphic and the alteration-related mineralogy in the wall rock. As stated above, small scale (<mm) mobility of Al is encountered in rocks with metamorphic mica, and it was proposed that Al is mobilised in F-OH complexes. Another example of a similar relationship can be found for the REE. There is no sign of large scale (>cm) mobilisation of REE within the alteration halo but they can display mobility on mm-scale. This mobility of REE seems to be controlled by the minerals forming (section 4.3.9.2). Consequently, a reason why the bulk of the REE is not leached from the rock is that the carbonate forming in the hydrothermally altered rock can accommodate REE, inhibiting them from be extracted from the rock and forming deposits elsewhere. This is also in agreement with studies on REE mobility, such as those by Hopf (1993) or Köhler et al. (2005). Nonetheless, it is suggested that in a thin zone (>few mm) right next to the fluid conduit the REE need to be leached from the rock and brought into the fluid; this conclusion is based on the REE patterns and ratios of Nd isotopes in the vein-filling carbonate, which show a close relationship between wall rock and vein (section 5.4.4) and that the bulk of the Nd in vein-filling carbonate was transported only for a short distance (cm to a few m max; Section 6.3.2).

7.2.1- Chemistry of void-filling carbonate

The chemical composition of the void-filling carbonate is a complex interplay of fluid- and rock-controlled processes. Based on the chemical composition of the altered wall rock, it is concluded that only a small portion of the wall rocks chemical content is brought into solution and incorporated by

the vein minerals (Fig. 7.3). (The precipitation of the void carbonate is probably the result of decreasing pressure and/or increase in pH.)

In the case of veins are hosted in greenschist, only small volumes of rock need to be leached to provide the major elements necessary to form the vein carbonate. Hence, REE leached from the wall rock by the fluid are also precipitated soon after dissolution and the REE pattern reflects largely the REE available from the source and the carbonate's REE composition is largely rock-controlled (Section 5.4.2 and 5.4.4; Fig. 7.3).

In case of veins hosted in greyschist, relatively large volumes of rock need to be leached to enrich the major elements of the vein carbonate sufficiently in the fluid. At the same time REE are also dissolved in the fluid. Due to the relatively long residence time of the major components in the fluid, REE are also in solution for longer, having time to approach equilibrium regarding their complex stability and hence the REE pattern reflects fluid-controlled processes (Section 5.4.2 and 5.4.4; Fig. 7.3).

7.3) Source of the volatile components in the fluids

One of the main objectives for this thesis was to investigate if there was any connection between the orogenic gold in the Shotover area and the alkaline magmatism and associated hydrothermal system of the Alpine Dike Swarm. For the gold in the Shotover case it has been shown by Mortensen et al. (2010) that the gold was likely derived from the Otago Schist. A non-magmatic source is also in agreement with gold-deposits of this kind in other parts of the world (e.g. Taylor et al., 1994; Ashley et al., 1994). Concerning the volatile components in the hydrothermal fluids, a common source could have been responsible for the formation of all the hydrothermal deposits studied here. However, based on the regional geological/ tectonic setting and stable and radiogenic isotopic composition of the hydrothermal carbonates in the different settings, two main fluid types have been proposed to have been present in the area at the time. These fluid types are:

Fluid type 1: mixed magmatic and meteoric fluid.
Fluid type 2: rock-exchanged meteoric water.

The only place where isotopic composition of hydrothermal carbonate gives evidence of involvement of fluid type 1 is in the diatreme (and within the confines of the ADS, White, 1998) (Fig. 7.4) hence within the constraints of the ADS. In contrast to the relatively localised occurrence of fluid type 1, fluid type 2 was present throughout the Otago Schist at least south of the ADS, as is suggested by the similar isotopic composition of the carbonates in that area (Fig. 6.4.3). Based on the carbon isotope ratios, much of the carbon has probably been derived from greenschist (section 6.6.2.3). There is some suggestion that at the diatreme fluid type 1 and 2 mixed in various proportions, which is evident not only by the stable isotopic composition of the carbonate, but also $^{87}Sr/^{86}Sr$ ratios (Fig. 6.6.1).

Circulation of the originally meteoric water of fluid type 2 through the Otago Schist is interpreted to have been driven by gravitational forces enabling the fluid to reach many km depth (section 6.6.2.3). The topography necessary to drive the circulation formed as a result of extension just prior to the initiation of the Alpine Fault (Carter, 1988; Kamp, 1986) and potentially also during the initiation of the Alpine Fault and the uplift associated with it (Section 1.3; Fig. 7.4). During the flow through the Otago Schist, the fluid interacted with the conduits' wall rock, exchanging elements and heating up. Due to the change in tectonic movement manifested by the Alpine Fault and reverse

movements of the previously extensional Moonlight Fault, deep seated fluid cells were tapped and hot, rock- exchanged type 2 fluids rose towards the surface (Fig. 7.4), transporting amongst others gold. These fluids then formed the here studied hydrothermal deposits and the orogenic gold deposits in the Shotover area.

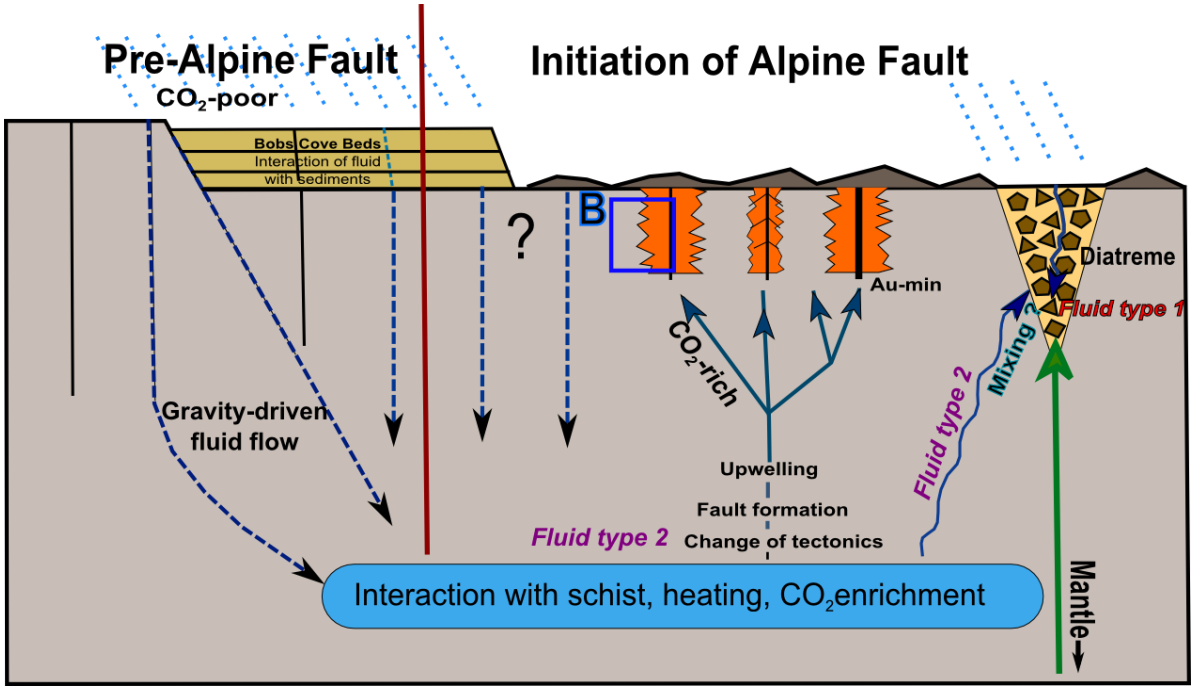

Fig. 7.4) Schematic model of the fluids involved in the formation of the hydrothermal and Shotover-gold deposits studied. Discussions see text. Box B is representation of Fig. 7.1 and 7.2.

7.4) Remaining questions and future work

- Much of the interpretation of the stable isotope data in chapter 6 depends on the crystallisation temperatures. In confining the temperatures better than was achievable here, it would be possible to draw also more confined conclusions. It would also help to find out if mixing of fluid type 1 and 2 took place at Mt Alta Diatreme.
- Why did not more gold deposits form in the area, for example at Treble Cone? Is this related to the different greyschist types found in the area, the precipitation temperature or because the gold deposits formed from a different fluid cell than the other carbonate.
- Just before the Kaikoura orogeny began, areas in Southern New Zealand accommodated extensional tectonics (e.g. Carter, 1988; Kamp, 1986), which should cause the development of a high geothermal gradient. Considering that fluids are heated and subsequently dissolve components is a high geothermal gradient an important factor for gold mineralisation in Shotover-type gold deposits?
- All aspects studied here are the result of the interaction between fluid and rock. To substantialize the interpretations drawn here further, studies focusing more on the fluid chemistry are needed, such as carrying out thermodynamic modelling or doing detailed fluid inclusion analyses.
- Seeing that the hydrothermal deposits at Red Rock are very different compared to the other deposits (abundant Cu mineralisation, different isotopic composition of the carbonate) poses the question what the cause for this is, such as temperature, age or fluid and metal source.
- Analysing minerals and rocks for major and trace element contents in other hydrothermal deposits around the world can show if the processes observed/ inferred here are applicable elsewhere. Such knowledge would not only help in understanding economically important

elements (e.g. in what settings are REE mobilised) but also how certain components are trapped, such as the bonding of CO_2 in carbonate. Unfortunately, due to the time and scope limitations of this thesis, I could not investigate how and if the information gathered here could complement research on the topic of the sequestration of anthropogenic CO_2.

REFERENCES

Adams, C. J., & Cooper, A. F. (1996). K-Ar age of a lamprophyre dike swarm near Lake Wanaka, west Otago, South Island, New Zealand. *New Zealand Journal of Geology and Geophysics*, *39*(1), 17-23.

Adams, C. J., & Graham, I. J. (1997). Age of metamorphism of Otago Schist in eastern Otago and determination of protoliths from initial strontium isotope characteristics. *New Zealand Journal of Geology and Geophysics*, *40*(3), 275-286.

Ague, J. J. (1994). Mass transfer during Barrovian metamorphism of pelites, south-central Connecticut; I, Evidence for changes in composition and volume. *American Journal of Science*, *294*(8), 989-1057.

Al-Aasm, I. S., Taylor, B. E., & South, B. (1990). Stable isotope analysis of multiple carbonate samples using selective acid extraction. *Chemical Geology: Isotope Geoscience Section*, *80*(2), 119-125.

Anovitz, L. M., & Essene, E. J. (1987). Phase equilibria in the system CaCO3-MgCO3-FeCO3. *Journal of Petrology*, *28*(2), 389-415.

Aquilina, L., Pauwels, H., Genter, A., & Fouillac, C. (1997). Water-rock interaction processes in the Triassic sandstone and the granitic basement of the Rhine Graben: Geochemical investigation of a geothermal reservoir. *Geochimica et cosmochimica acta*, *61*(20), 4281-4295.

Ashley, P. M., Cook, N. D. J., Hill, R. L., & Kent, A. J. R. (1994). Shoshonitic lamprophyre dykes and their relation to mesothermal Au-Sb veins at Hillgrove, New South Wales, Australia. *Lithos*, *32*(3), 249-272.

Atkinson, T. C. (1977). Carbon dioxide in the atmosphere of the unsaturated zone: an important control of groundwater hardness in limestones. *Journal of Hydrology*, *35*(1), 111-123.

Barnes, I., Downes, C. J., & Hulston, J. R. (1978). Warm springs, South Island, New Zealand, and their potentials to yield laumontite. *American journal of science*, *278*(10), 1412-1427.

Barreiro, B. A., & Cooper, A. F. (1987). A Sr, Nd, and Pb isotope study of alkaline lamprophyres and related rocks from Westland and Otago, South Island, New Zealand. *Geological Society of America Special Papers*, *215*, 115-126.

Barry, J.M. (1966). Structural analysis in the Middle Shotover Valley, north-west Otago. Unpublished MSc. Thesis. University of Otago, New Zealand.

Batt, G. E., Baldwin, S. L., Cottam, M. A., Fitzgerald, P. G., Brandon, M. T., & Spell, T. L. (2004). Cenozoic plate boundary evolution in the South Island of New Zealand: New thermochronological constraints. *Tectonics*, *23*(4).

Bau, M. (1991). Rare-earth element mobility during hydrothermal and metamorphic fluid-rock interaction and the significance of the oxidation state of europium. *Chemical Geology*, *93*(3), 219-230.

Bau, M., & Alexander, B. (2006). Preservation of primary REE patterns without Ce anomaly during dolomitization of Mid-Paleoproterozoic limestone and the potential re-establishment of marine anoxia immediately after the “Great Oxidation Event”. *South African Journal of Geology*, *109*(1-2), 81-86.

Bau, M., & Möller, P. (1992). Rare earth element fractionation in metamorphogenic hydrothermal calcite, magnesite and siderite. *Mineralogy and Petrology*, *45*(3-4), 231-246.

Bea, F. (1996). Residence of REE, Y, Th and U in granites and crustal protoliths; implications for the chemistry of crustal melts. *Journal of petrology*, *37*(3), 521-552.

Bea, F., Pereira, M. D., & Stroh, A. (1994). Mineral/leucosome trace-element partitioning in a peraluminous migmatite (a laser ablation-ICP-MS study). *Chemical Geology*, *117*(1), 291-312.

Beard, B. L., Johnson, C. M., Skulan, J. L., Nealson, K. H., Cox, L., & Sun, H. (2003). Application of Fe isotopes to tracing the geochemical and biological cycling of Fe. *Chemical Geology*, *195*(1), 87-117.

Belousova, E. A., Griffin, W. L., O'Reilly, S. Y., & Fisher, N. I. (2002). Apatite as an indicator mineral for mineral exploration: trace-element compositions and their relationship to host rock type. *Journal of Geochemical Exploration*, *76*(1), 45-69.

Bénézeth, P., Dandurand, J. L., & Harrichoury, J. C. (2009). Solubility product of siderite (FeCO 3) as a function of temperature (25–250 C). *Chemical Geology*, *265*(1), 3-12.

Benson, S. M., & Cole, D. R. (2008). CO2 sequestration in deep sedimentary formations. *Elements*, *4*(5), 325-331.

Bessinger, B., & Apps, J. A. (2003). The hydrothermal chemistry of gold, arsenic, antimony, mercury and silver. *Lawrence Berkeley National Laboratory*.

Bierlein, F. P., & Craw, D. (2009). Petrogenetic character and provenance of metabasalts in the aspiring and Torlesse Terranes, South Island, New Zealand: Implications for the gold endowment of the Otago Schist?. *Chemical Geology*, *260*(3), 301-315.

Bierlein, F. P., Arne, D. C., & Cartwright, I. (2004). Stable isotope (C, O, S) systematics in alteration haloes associatedwith orogenic gold mineralization in the Victorian gold province, SE Australia. *Geochemistry: Exploration, Environment, Analysis*, *4*(3), 191-211.

Bierlein, F. P., Arne, D. C., McKnight, S., Lu, J., Reeves, S., Besanko, J., ... & Cooke, D. (2000). Wall-rock petrology and geochemistry in alteration halos associated with mesothermal gold mineralization, central Victoria, Australia. *Economic Geology*, *95*(2), 283-311.

Bierlein, F. P., Waldron, H. M., & Arne, D. C. (1999). Behaviour of rare earth and high field strength elements during hydrothermal alteration of meta-turbidites associated with mesothermal gold mineralization in central Victoria, Australia. *Journal of Geochemical Exploration*, *67*(1), 109-125.

Billia, M. (2013) The effects of fluids on the deformational behaviour of the mid-crustal coupling zone: Insights from the Alpine Fault, NZ. (PhD)

Bishop, D. G. (1972). Progressive metamorphism from prehnite-pumpellyite to greenschist facies in the Dansey Pass area, Otago, New Zealand. *Geological Society of America Bulletin*, *83*(11), 3177-3198.

Bjørlykke, K. (1993). Fluid flow in sedimentary basins. *Sedimentary Geology*, *86*(1), 137-158.

Blattner, P., & Cooper, A. F. (1974). Carbon and oxygen isotopic composition of carbonatite dikes and metamorphic country rock of the Haast Schist terrain, New Zealand. *Contributions to mineralogy and petrology*, *44*(1), 17-27.

Blundy, J., & Wood, B. (1994). Prediction of crystal-melt partition coefficients from elastic moduli. *Nature*, *372*(6505), 452-454.

Bradshaw, J. D. (1989). Cretaceous geotectonic patterns in the New Zealand region. *Tectonics*, *8*(4), 803-820.

Bräuer, K., Kämpf, H., Strauch, G., & Weise, S. M. (2003). Isotopic evidence (3He/4He, of fluid-triggered intraplate seismicity. *Journal of Geophysical Research: Solid Earth*, *108*(B2).

Breeding, C. M., & Ague, J. J. (2002). Slab-derived fluids and quartz-vein formation in an accretionary prism, Otago Schist, New Zealand. *Geology*, *30*(6), 499-502.

Brookins, D. G. (1989). Aqueous geochemistry of rare earth elements. *Reviews in Mineralogy and Geochemistry*, *21*(1), 201-225.

Brown, E. H. (1977). The crossite content of Ca-amphibole as a guide to pressure of metamorphism. *Journal of Petrology*, *18*(1), 53-72.

Brown, P. E., & Lamb, W. M. (1989). P-V-T properties of fluids in the system H 2 O±CO 2±NaCl: New graphical presentations and implications for fluid inclusion studies. *Geochimica et Cosmochimica Acta*, *53*(6), 1209-1221.

Browne, P. R. L. (1978). Hydrothermal alteration in active geothermal fields. *Annual Review of Earth and Planetary Sciences*, *6*, 229-250.

Carmichael, D. M. (1969). On the mechanism of prograde metamorphic reactions in quartz-bearing pelitic rocks. *Contributions to Mineralogy and Petrology*, *20*(3), 244-267.

Carter, R. M. (1988). Post-breakup stratigraphy of the KaikouraSynthem (Cretaceous-Cenozoic), continental margin, southeastern New Zealand. *New Zealand journal of geology and geophysics*, *31*(4), 405-429.

Cetiner, Z. S., Wood, S. A., & Gammons, C. H. (2005). The aqueous geochemistry of the rare earth elements. Part XIV. The solubility of rare earth element phosphates from 23 to 150 C. *Chemical Geology*, *217*(1), 147-169.

Chacko, T., & Deines, P. (2008). Theoretical calculation of oxygen isotope fractionation factors in carbonate systems. *Geochimica et Cosmochimica Acta*, *72*(15), 3642-3660.

Christie, A. B., & Brathwaite, R. L. (2003). Hydrothermal alteration in metasedimentary rock-hosted orogenic gold deposits, Reefton goldfield, South Island, New Zealand. *Mineralium deposita*, *38*(1), 87-107.

Clayton, R. N., O'Neil, J. R., & Mayeda, T. K. (1972). Oxygen isotope exchange between quartz and water. *Journal of Geophysical Research*, *77*(17), 3057-3067.

Clough, M.C. (1988). The Minaret EL 33378 - Report on the field work carried out during December 1987. Ministry of Economic Development New Zealand Unpublishe Mineral Report.

Cooper, A. F. (1970)

Cooper, A. F. (1979). Petrology of ocellar lamprophyres from western Otago, New Zealand. *Journal of petrology*, *20*(1), 139-163.

Cooper, A. F. (1986). A carbonatitic lamprophyre dike swarm from the Southern Alps, Otago and Westland. *Late Cenozoic volcanism in New Zealand. Royal Society of New Zealand bulletin*, *23*, 313-336.

Cooper, A. F. (1996). Nb-rich baotite in carbonatites and fenites at Haast River, New Zealand. *Mineralogical magazine*, *60*(3), 473-482.

Cooper, A. F., & Paterson, L. A. (2008). Carbonatites from a lamprophyric dyke-swarm, South Westland, New Zealand. *The Canadian Mineralogist*, *46*(4), 753-777.

Cooper, A. F., & Reay, A. (1983). Lithology, field relationships, and structure of the Pounamu Ultramafics from the Whitcombe and Hokitika Rivers, Westland, New Zealand. *New Zealand journal of geology and geophysics*, *26*(4), 359-379.

Cooper, A. F., Barreiro, B. A., Kimbrough, D. L., & Mattinson, J. M. (1987). Lamprophyre dike intrusion and the age of the Alpine fault, New Zealand. *Geology*, *15*(10), 941-944.

Cooper, A. F., Collins, A. K., Palin, J. M., & Spratt, J. (2015). Mineralogical evolution and REE mobility during crystallisation of ancylite-bearing ferrocarbonatite, Haast River, New Zealand. *Lithos*, *216*, 324-337.

Cooper, A. F., Palin, J. M., & Collins, A. K. (2016). Fenitization of metabasic rocks by ferrocarbonatites at Haast River, New Zealand. *Lithos*, *244*, 109-121.

Cooper, A. F., Paterson, L. A., & Reid, D. L. (1995). Lithium in carbonatites-consequence of an enriched mantle source?. *Mineralogical Magazine*, *59*(3), 401-408.

Cox, S. C., Menzies, C. D., Sutherland, R., Denys, P. H., Chamberlain, C., & Teagle, D. A. H. (2015). Changes in hot spring temperature and hydrogeology of the Alpine Fault hanging wall, New Zealand, induced by distal South Island earthquakes. *Geofluids*, *15*(1-2), 216-239.

Cox, S.C. (1985) Niger Peak Geology. Unpublished BSc. Hons. Thesis. University of Otago, New Zealand.

Cox, S.C. (1993). Veins, fluid, fractals, scale and schist: In ainvestigation of fluid rock interaction during deformation of the Torlesse terrane, NZ. Unpublished PhD thesis. University of Otago. Dunedin

Craw, D. (1981). Lithology, structure and metamorphism in the Mt. Aspiring area, West Otago and a study of the biotite in Otago. *Unpublished PhD thesis. University of Otago, Dunedin*.

Craw, D. (1984). Lithologic variations in Otago Schist, Mt Aspiring area, northwest Otago, New Zealand. *New Zealand journal of geology and geophysics*, *27*(2), 151-166.

Craw, D. (1985). Structure of schist in the Mt Aspiring region, northwestern Otago, New Zealand. *New Zealand journal of geology and geophysics*, *28*(1), 55-75.

Craw, D. (1989). Shallow-level, late-stage gold mineralisation in Sawyers Creek, Shotover valley, northwest Otago, New Zealand. *New Zealand journal of geology and geophysics*, *32*(3), 385-393.

Craw, D. (1995). Reinterpretation of the erosion profile across the southern portion of the Southern Alps, Mt Aspiring area, Otago, New Zealand. *New Zealand journal of geology and geophysics*, *38*(4), 501-507.

Craw, D. (2002). Geochemistry of late metamorphic hydrothermal alteration and graphitisation of host rock, Macraes gold mine, Otago Schist, New Zealand. *Chemical Geology*, *191*(4), 257-275.

Craw, D., Begbie, M., & MacKenzie, D. (2006). Structural controls on Tertiary orogenic gold mineralization during initiation of a mountain belt, New Zealand. *Mineralium Deposita*, *41*(7), 645-659.

Craw, D., Reay, A., & Johnstone, R. D. (1991). Hydrothermal alteration geochemistry of Nugget gold vein system, Shotover valley, northwest Otago, New Zealand. *New Zealand journal of geology and geophysics*, *34*(4), 419-427.

Craw, D., Upton, P., & MacKenzie, D. J. (2009). Hydrothermal alteration styles in ancient and modern orogenic gold deposits, New Zealand. *New Zealand Journal of Geology and Geophysics*, *52*(1), 11-26.

Dahl, O. (1969). Irregular distribution of iron and magnesium among coexisting biotite and garnet. *Lithos*, *2*(2), 311-322.

Dauphas, N., Janney, P. E., Mendybaev, R. A., Wadhwa, M., Richter, F. M., Davis, A. M., ... & Foley, C. N. (2004). Chromatographic separation and multicollection-ICPMS analysis of iron. Investigating mass-dependent and-independent isotope effects. *Analytical Chemistry*, *76*(19), 5855-5863.

Davies, J. F., Whitehead, R. E., Huang, J., & Nawaratne, S. (1990). A comparison of progressive hydrothermal carbonate alteration in Archean metabasalts and metaperidotites. *Mineralium Deposita*, *25*(1), 65-72.

De Caritat, P., Hutcheon, I., & Walshe, J. L. (1993). Chlorite Geothermometry: A Review. *Clays and clay minerals*, *41*(2), 219-239.

Deer, W. A., Howie, R. A., & Zussman, J. (1986). Epidote group. *Deer WA, Howie RA, Zussman J Disilicates and ring silicates. Second edition. London, Longman Scientific and Technical*, 2-179.

Deer, W. A., Howie, R. A., & Zussman, J. (Eds.). (2009). Rock Forming Minerals: Layered Silicates Excluding Micas and Clay Minerals, Volume 3B. Geological Society of London.

Deines, P. (2002). The carbon isotope geochemistry of mantle xenoliths. *Earth-Science Reviews*, *58*(3), 247-278.

Demény, A., Harangi, S., Fórizs, I., & Nagy, G. (1997). Primary and secondary features of analcimes formed in carbonate-zeolite ocelli of alkaline basalts (Mecsek Mts., Hungary): textures, chemical and oxygen isotope compositions. *Geochemical Journal*, *31*(1), 37-47.

Devereux, I. (1968). OXYGEN ISOTOPE RATIOS OF MINERALS FROM REGIONALLY METAMORPHOSED SCHISTS OF OTAGO NEW ZEALAND. *New Zealand Journal of Science*, *11*(3), 526.

Dideriksen, K., Baker, J. A., & Stipp, S. L. S. (2006). Iron isotopes in natural carbonate minerals determined by MC-ICP-MS with a 58 Fe–54 Fe double spike. *Geochimica et Cosmochimica Acta*, *70*(1), 118-132.

Dilles, J. H., & Einaudi, M. T. (1992). Wall-rock alteration and hydrothermal flow paths about the Ann-Mason porphyry copper deposit, Nevada; a 6-km vertical reconstruction. *Economic Geology*, *87*(8), 1963-2001

Dipple, G. M., & Ferry, J. M. (1992). Fluid flow and stable isotopic alteration in rocks at elevated temperatures with applications to metamorphism. *Geochimica et Cosmochimica Acta*, *56*(9), 3539-3550.

Dipple, G. M., & Ferry, J. M. (1992)b. Metasomatism and fluid flow in ductile fault zones. *Contributions to Mineralogy and Petrology*, *112*(2-3), 149-164.

Douce, A. E. P. (1993). Titanium substitution in biotite: an empirical model with applications to thermometry, O 2 and H 2 O barometries, and consequences for biotite stability. *Chemical Geology*, *108*(1), 133-162.

Ebert, W. L., Bates, J. K., & Bourcier, W. L. (1991). The hydration of borosilicate waste glass in liquid water and steam at 200 C. *Waste Management*, *11*(4), 205-221.

Essene, E. J. (1983). Solid solutions and solvi among metamorphic carbonates with applications to geologic thermobarometry. *Reviews in Mineralogy and Geochemistry*, *11*(1), 77-96.

Evans, K. A., Phillips, G. N., & Powell, R. (2006). Rock-buffering of auriferous fluids in altered rocks associated with the Golden Mile-style mineralization, Kalgoorlie gold field, Western Australia. *Economic Geology*, *101*(4), 805-817.

Fein, J. B., & Walther, J. V. (1987). Calcite solubility in supercritical CO2瑕 H2O fluids. *Geochimica et Cosmochimica Acta*, *51*(6), 1665-1673.

Fein, J. B., Graham, C. M., Holness, M. B., Fallick, A. E., & Skelton, A. D. L. (1994). Controls on the mechanisms of fluid infiltration and front advection during regional metamorphism: a stable

isotope and textural study of retrograde Dalradian rocks of the SW Scottish Highlands. *Journal of Metamorphic Geology*, *12*(3), 249-260.
Ferry, J. M. (2000). Patterns of mineral occurrence in metamorphic rocks. *American Mineralogist*, *85*(11-12), 1573-1588.
Ferry, J. T., & Spear, F. S. (1978). Experimental calibration of the partitioning of Fe and Mg between biotite and garnet. *Contributions to mineralogy and petrology*, *66*(2), 113-117.
Fleet, M. E., Deer, W. A., Howie, R. A., & Zussman, J. (Eds.). (2003). Rock-Forming Minerals: Micas. Geological Society of London.
Floyd, P. A., & Winchester, J. A. (1978). Identification and discrimination of altered and metamorphosed volcanic rocks using immobile elements. *Chemical Geology*, *21*(3), 291-306.
Foerster, H. J. (1998). The chemical composition of REE-Y-Th-U-rich accessory minerals in peraluminous granites of the Erzgebirge-Fichtelgebirge region, Germany, Part I: The monazite-(Ce)-brabantite solid solution series. *American Mineralogist*, *83*(3-4), 259-272.
Fournier, R. O., & Potter, R. W. (1982). An equation correlating the solubility of quartz in water from 25 to 900 C at pressures up to 10,000 bars. *Geochimica et Cosmochimica Acta*, *46*(10), 1969-1973.
Friedman, I. & O'Neil, J.R. (1977). Chapter KK. Compilation of Stable Isotope Fractionation Factors of Geochemical Interest. In: Data of Geochemistry sixth edition. Technical Editor: Michael Fleischer. Geological Survey Professional Paper. 440-KK.
Frisch, W., Dunkl, I., & Kuhlemann, J. (2000). Post-collisional orogen-parallel large-scale extension in the Eastern Alps. *Tectonophysics*, *327*(3), 239-265.
Frost, C. D., & Coombs, D. S. (1989). Nd isotope character of New Zealand sediments; implications for terrane concepts and crustal evolution. *American journal of science*, *289*(6), 744-770.
Gamble, M.N. (1984). Mt Alta, Triple Peak Geology. Unoublished BSc. Hons. Thesis. University of Otago, New Zealand.
Garven, G. (1995). Continental-scale groundwater flow and geologic processes. *Annual Review of Earth and Planetary Sciences*, *23*, 89-118.
Gemmell, J. B. (2007). Hydrothermal alteration associated with the Gosowong epithermal Au-Ag deposit, Halmahera, Indonesia: Mineralogy, geochemistry, and exploration implications. *Economic Geology*, *102*(5), 893-922.
Genkin, A. D., Bortnikov, N. S., Cabri, L. J., Wagner, F. E., Stanley, C. J., Safonov, Y. G., ... & Gamyanin, G. N. (1998). A multidisciplinary study of invisible gold in arsenopyrite from four mesothermal gold deposits in Siberia, Russian Federation. *Economic Geology*, *93*(4), 463-487.
Gifkins, C. C., Herrmann, W., & Large, R. R. (2005). Altered volcanic rocks: A guide to description and interpretation.
Golyshev, S. I., Padalko, N. L., & Pechenkin, S. A. (1981). Fractionation of stable isotopes of carbon and oxygen in carbonate systems. *Geokhimiya*, (10), 1427-1441.
Golyshev, S. I., Padalko, N. L., & Pechenkin, S. A. (1981). Fractionation of stable isotopes of carbon and oxygen in carbonate systems. *Geokhimiya*, (10), 1427-1441.
Graham, D. W. (2002). Noble gas isotope geochemistry of mid-ocean ridge and ocean island basalts: Characterization of mantle source reservoirs. *Reviews in mineralogy and geochemistry*, *47*(1), 247-317.
Grant, J. A. (1986). The isocon diagram; a simple solution to Gresens' equation for metasomatic alteration. *Economic Geology*, *81*(8), 1976-1982.
Gray, D. R., & Foster, D. A. (2004). 40 Ar/39 Ar thermochronologic constraints on deformation, metamorphism and cooling/exhumation of a Mesozoic accretionary wedge, Otago Schist, New Zealand. *Tectonophysics*, *385*(1), 181-210.
Gresens, R. L. (1967). Composition-volume relationships of metasomatism. *Chemical geology*, *2*, 47-65.
Griesshaber, E., O'nions, R. K., & Oxburgh, E. R. (1992). Helium and carbon isotope systematics in crustal fluids from the Eifel, the Rhine Graben and Black Forest, FRG. *Chemical Geology*, *99*(4), 213-235.

Guidotti, C. V., Cheney, J. T., & Guggenheim, S. (1977). Distribution of titanium between coexisting muscovite and biotite in pelitic schists from northwestern Maine. *American Mineralogist*, *62*(5-6), 438-448.

Guidry, M. W., & Mackenzie, F. T. (2003). Experimental study of igneous and sedimentary apatite dissolution: control of pH, distance from equilibrium, and temperature on dissolution rates. *Geochimica et Cosmochimica Acta*, *67*(16), 2949-2963.

Haas, J. R., Shock, E. L., & Sassani, D. C. (1995). Rare earth elements in hydrothermal systems: estimates of standard partial molal thermodynamic properties of aqueous complexes of the rare earth elements at high pressures and temperatures. *Geochimica et Cosmochimica Acta*, *59*(21), 4329-4350.

Harouiya, N., Chaïrat, C., Köhler, S. J., Gout, R., & Oelkers, E. H. (2007). The dissolution kinetics and apparent solubility of natural apatite in closed reactors at temperatures from 5 to 50 C and pH from 1 to 6. *Chemical Geology*, *244*(3), 554-568.

Hay, R., & Craw, D. (1993). Syn-metamorphic gold mineralisation, Invincible Vein, NW Otago Schist, New Zealand. *Mineralium deposita*, *28*(2), 90-98.

Helz, G. R., & Holland, H. D. (1965). The solubility and geologic occurrence of strontianite. *Geochimica et Cosmochimica Acta*, *29*(12), 1303-1315.

Hemley, J. J., Cygan, G. L., Fein, J. B., Robinson, G. R., & d'Angelo, W. M. (1992). Hydrothermal ore-forming processes in the light of studies in rock-buffered systems; I, Iron-copper-zinc-lead sulfide solubility relations. *Economic Geology*, *87*(1), 1-22.

Henderson, P. (Ed.). (2013). *Rare earth element geochemistry* (Vol. 2). Elsevier.

Henley, R. W., & Norris, R. J. (1974). The Central Otago metavolcanics—remnant of a spreading axis?(Abs.). In *Geological Society of Nz Conference, Wellington*.

Hezel, D. C., Needham, A. W., Armytage, R., Georg, B., Abel, R. L., Kurahashi, E., ... & Russell, S. S. (2010). A nebula setting as the origin for bulk chondrule Fe isotope variations in CV chondrites. *Earth and Planetary Science Letters*, *296*(3), 423-433.

Ho, S. E., Groves, D. I., & Phillips, G. N. (1990). Fluid inclusions in quartz veins associated with Archaean gold mineralization: clues to ore fluids and ore depositional conditions and significance to exploration. In: Stable Isotopes and Significance to Exploration, *University of Western Australia Publication*, *23*, 35-50.

Hoefs, J. (2008). *Stable isotope geochemistry*. Springer Science & Business Media.

Hoernle, K., White, J. V., van den Bogaard, P., Hauff, F., Coombs, D. S., Werner, R., ... & Cooper, A. F. (2006). Cenozoic intraplate volcanism on New Zealand: Upwelling induced by lithospheric removal. *Earth and Planetary Science Letters*, *248*(1), 350-367.

Hoffbauer, R., Hoernes, S., & Fiorentini, E. (1994). Oxygen isotope thermometry based on a refined increment method and its application to granulite-grade rocks from Sri Lanka. *Precambrian Research*, *66*(1-4), 199-220.

Hopf, S. (1993). Behaviour of rare earth elements in geothermal systems of New Zealand. *Journal of Geochemical Exploration*, *47*(1-3), 333-357.

Horie, K., Hidaka, H., & Gauthier-Lafaye, F. (2008). Elemental distribution in apatite, titanite and zircon during hydrothermal alteration: Durability of immobilization mineral phases for actinides. *Physics and Chemistry of the Earth, Parts A/B/C*, *33*(14), 962-968.

Horton, T. W., Blum, J. D., Craw, D., Koons, P. O., & Chamberlain, C. P. (2003). Oxygen, carbon, and strontium isotopic constraints on timing and sources of crustal fluids in an active orogen: South Island, New Zealand. *New Zealand Journal of Geology and Geophysics*, *46*(3), 457-471.

Hoskin, P. W. O., & Black, L. P. (2000). Metamorphic zircon formation by solid-state recrystallization of protolith igneous zircon. *Journal of metamorphic Geology*, *18*(4), 423-439.

Howell, D. G. (1980). Mesozoic accretion of exotic terranes along the New Zealand segment of Gondwanaland. *Geology*, *8*(10), 487-491.

Hutton, C. O. (1943). Limburgite from Nevis Bluff, Kawarau Gorge, Central Otago. Royal Society of New Zealand.

Hutton, C. O., & Turner, F. J. (1936). Metamorphic zones in northwest Otago. In *Transactions of the Royal Society of New Zealand* (Vol. 65, No. 4, pp. 405-406).

Ionov, D. A., Griffin, W. L., & O'Reilly, S. Y. (1997). Volatile-bearing minerals and lithophile trace elements in the upper mantle. *Chemical Geology*, *141*(3), 153-184.

Jagoutz, E., Palme, H., Baddenhausen, H., Blum, K., Cendales, M., Dreibus, G., ... & Lorenz, V. (1979). The abundances of major, minor and trace elements in the earth's mantle as derived from primitive ultramafic nodules. In *Lunar and Planetary Science Conference Proceedings* (Vol. 10, pp. 2031-2050).

Jamtveit, B., & Yardley, B. (Eds.). (2012). *Fluid flow and transport in rocks: mechanisms and effects*. Springer Science & Business Media.

Janots, E., Engi, M., Berger, A., Allaz, J., Schwarz, J. O., & Spandler, C. (2008). Prograde metamorphic sequence of REE minerals in pelitic rocks of the Central Alps: implications for allanite–monazite–xenotime phase relations from 250 to 610 C. *Journal of Metamorphic Geology*, *26*(5), 509-526.

Janots, E., Negro, F., Brunet, F., Goffé, B., Engi, M., & Bouybaouene, M. L. (2006). Evolution of the REE mineralogy in HP–LT metapelites of the Sebtide complex, Rif, Morocco: monazite stability and geochronology. *Lithos*, *87*(3), 214-234.

Jenkin, G. R. T., Craw, D., & Fallick, A. E. (1994). Stable isotopic and fluid inclusion evidence for meteoric fluid penetration into an active mountain belt; Alpine Schist, New Zealand. *Journal of metamorphic geology*, *12*(4), 429-444.

Jiang, S. Y., Wang, R. C., Xu, X. S., & Zhao, K. D. (2005). Mobility of high field strength elements (HFSE) in magmatic-, metamorphic-, and submarine-hydrothermal systems. *Physics and Chemistry of the Earth, Parts A/B/C*, *30*(17), 1020-1029.

Johnson, C. M., Bell, K., Beard, B. L., & Shultis, A. I. (2010). Iron isotope compositions of carbonatites record melt generation, crystallization, and late-stage volatile-transport processes. *Mineralogy and petrology*, *98*(1-4), 91-110.

Jonas, L., Müller, T., Dohmen, R., Baumgartner, L., & Putlitz, B. (2015). Transport-controlled hydrothermal replacement of calcite by Mg-carbonates. *Geology*, *43*(9), 779-782.

Kamp, P. J. (1986). The mid-Cenozoic Challenger Rift System of western New Zealand and its implications for the age of Alpine fault inception. *Geological Society of America Bulletin*, *97*(3), 255-281.

Kamp, P. J., Vincent, K. A., & Tayler, M. J. (2015). Cenozoic sedimentary and volcanic rocks of New Zealand: A reference volume of lithology, age and paleoenvironments with maps (PMAPs) and database.

Kaven, J. O., Hickman, S. H., McGarr, A. F., & Ellsworth, W. L. (2015). Surface Monitoring of Microseismicity at the Decatur, Illinois, CO2 Sequestration Demonstration Site. *Seismological Research Letters*.

Kawachi, Y. (1974). Geology and petrochemistry of weakly metamorphosed rocks in the upper Wakatipu district, southern New Zealand. *New Zealand journal of geology and geophysics*, *17*(1), 169-208.

Kebede, S., Travi, Y., Alemayehu, T., & Ayenew, T. (2005). Groundwater recharge, circulation and geochemical evolution in the source region of the Blue Nile River, Ethiopia. *Applied Geochemistry*, *20*(9), 1658-1676.

Kerrich, R., & Wyman, D. A. (1994). The mesothermal gold-lamprophyre association: significance for an accretionary geodynamic setting, supercontinent cycles, and metallogenic processes. *Mineralogy and Petrology*, *51*(2-4), 147-172

Kerrick, D. M. (1988). Al2SiO5-bearing segregations in the Lepontine Alps, Switzerland: Aluminum mobility in metapelites. *Geology*, *16*(7), 636-640.

Knauss, K. G., & Wolery, T. J. (1988). The dissolution kinetics of quartz as a function of pH and time at 70 C. *Geochimica et Cosmochimica Acta*, *52*(1), 43-53.

Knauss, K. G., & Wolery, T. J. (1988). The dissolution kinetics of quartz as a function of pH and time at 70 C. *Geochimica et Cosmochimica Acta*, *52*(1), 43-53.

Köhler, S. J., Harouiya, N., Chaïrat, C., & Oelkers, E. H. (2005). Experimental studies of REE fractionation during water–mineral interactions: REE release rates during apatite dissolution from pH 2.8 to 9.2. *Chemical Geology*, *222*(3), 168-182.
Köhler, S. J., Harouiya, N., Chaïrat, C., & Oelkers, E. H. (2005). Experimental studies of REE fractionation during water–mineral interactions: REE release rates during apatite dissolution from pH 2.8 to 9.2. *Chemical Geology*, *222*(3), 168-182.
Kontak, D. J., & Jackson, S. J. (1999). Documentation of variable trace-and rare-earth-element abundances in carbonates from auriferous quartz veins in Meguma lode gold deposits. Nova Scotia. *Canadian mineralogist*, *37*, 469-488.

Koons, P. O., & Craw, D. (1991). Gold mineralization as a consequence of continental collision: an example from the Southern Alps, New Zealand. *Earth and planetary science letters*, *103*(1-4), 1-9.

Koons, P. O., Craw, D., Cox, S. C., Upton, P., Templeton, A. S., & Chamberlain, C. P. (1998). Fluid flow during active oblique convergence: a Southern Alps model from mechanical and geochemical observations. *Geology*, *26*(2), 159-162.

Koons, P. O., Norris, R. J., Craw, D., & Cooper, A. F. (2003). Influence of exhumation on the structural evolution of transpressional plate boundaries: An example from the Southern Alps, New Zealand. *Geology*, *31*(1), 3-6.

Korzhinskiy, M. A. (1987). The solubility of corundum in an HCl fluid and forms taken by Al. *Geochemistry International*, *24*, 105-109.

Kuyunko, N. S., Malinin, S. D., & Khodakovskiy, I. L. (1983). An experimental study of aluminum ion hydrolysis at 150, 200, and 250 C. *Geochem. Intl.*, *20*(2), 76-86.

Laird, M. G., & Bradshaw, J. D. (2004). The break-up of a long-term relationship: the Cretaceous separation of New Zealand from Gondwana. *Gondwana Research*, *7*(1), 273-286.
Laird, M. G., & Bradshaw, J. D. (2004). The break-up of a long-term relationship: the Cretaceous separation of New Zealand from Gondwana. *Gondwana Research*, *7*(1), 273-286.
Lamarche, G., Collot, J. Y., Wood, R. A., Sosson, M., Sutherland, R., & Delteil, J. (1997). The Oligocene-Miocene Pacific-Australia plate boundary, south of New Zealand: Evolution from oceanic spreading to strike-slip faulting. *Earth and Planetary Science Letters*, *148*(1), 129-139.

Lamb, S. H., & Bibby, H. M. (1989). The last 25 Ma of rotational deformation in part of the New Zealand plate-boundary zone. *Journal of structural geology*, *11*(4), 473-492.

Landis, C. A., Campbell, H. J., Aslund, T., Cawood, P. A., Douglas, A., Kimbrough, D. L., ... & Willsman, A. (1999). Permian-Jurassic strata at Productus Creek, Southland, New Zealand: implications for terrane dynamics of the eastern Gondwanaland margin. *New Zealand journal of geology and geophysics*, *42*(2), 255-278.

Landtwing, M. R., Pettke, T., Halter, W. E., Heinrich, C. A., Redmond, P. B., Einaudi, M. T., & Kunze, K. (2005). Copper deposition during quartz dissolution by cooling magmatic–hydrothermal fluids: the Bingham porphyry. *Earth and Planetary Science Letters*, *235*(1), 229-243.

Large, R. R., & McGoldrick, P. J. (1998). Lithogeochemical halos and geochemical vectors to stratiform sediment hosted Zn–Pb–Ag deposits, 1. Lady Loretta Deposit, Queensland. *Journal of Geochemical Exploration*, *63*(1), 37-56.

Large, R. R., McPhie, J., Gemmell, J. B., Herrmann, W., & Davidson, G. J. (2001). The spectrum of ore deposit types, volcanic environments, alteration halos, and related exploration vectors in submarine volcanic successions: some examples from Australia. *Economic Geology*, *96*(5), 913-938.

Large, R., Thomas, H., Craw, D., Henne, A., & Henderson, S. (2012). Diagenetic pyrite as a source for metals in orogenic gold deposits, Otago Schist, New Zealand. *New Zealand Journal of Geology and Geophysics*, *55*(2), 137-149.

Lee, D. E., Lee, W. G., & Mortimer, N. (2001). Where and why have all the flowers gone? Depletion and turnover in the New Zealand Cenozoic angiosperm flora in relation to palaeogeography and climate. *Australian Journal of Botany*, *49*(3), 341-356.

LeMasurier, W. E., & Landis, C. A. (1996). Mantle-plume activity recorded by low-relief erosion surfaces in West Antarctica and New Zealand. *Geological Society of America Bulletin*, *108*(11), 1450-1466.

Li, X., Kwak, T. A. P., & Brown, R. W. (1998). Wallrock alteration in the Bendigo gold ore field, Victoria, Australia: uses in exploration. *Ore Geology Reviews*, *13*(1), 381-406.

Little, T. A., & Jones, A. (1998). Seven million years of strike-slip and related off-fault deformation, northeastern Marlborough fault system, South Island, New Zealand. *Tectonics*, *17*(2), 285-302.

Little, T. A., Cox, S. Vry, J. K., & Batt, G. (2005). Variations in exhumation level and uplift-rate along the oblique-slip Alpine fault, central Southern Alps, New Zealand. Geological Society of America Bulletin. 117(5-6), 707-723.

Liu, W., & McPhail, D. C. (2005). Thermodynamic properties of copper chloride complexes and copper transport in magmatic-hydrothermal solutions. *Chemical Geology*, *221*(1), 21-39.

Lorenz, V. (1986). On the growth of maars and diatremes and its relevance to the formation of tuff rings. *Bulletin of Volcanology*, *48*(5), 265-274.

Lumpkin, G. R., & Geisler-Wierwille, T. (2012). Minerals and natural analogues. *Rudy JM Konings (Editor-in-Chief), Comprehensive Nuclear Materials*, *5*, 563-600.

Luo, Y.Y.-R., Byrne, R.H., 2004. Carbonate complexation of yttriumand the rare earth elements innatural waters. Geochim. Cosmochim. Acta 68, 691–699. http://dx.doi.org/10.1016/S0016

MacKenzie, D. J., Craw, D., & Begbie, M. (2007). Mineralogy, geochemistry, and structural controls of a disseminated gold-bearing alteration halo around the schist-hosted Bullendale orogenic gold deposit, New Zealand. *Journal of Geochemical Exploration*, *93*(3), 160-176.

MacKinnon, T. C. (1983). Origin of the Torlesse terrane and coeval rocks, South Island, New Zealand. *Geological Society of America Bulletin*, *94*(8), 967-985.

Manning, C. E., Shock, E. L., & Sverjensky, D. (2013). The chemistry of carbon in aqueous fluids at crustal and uppermantle conditions: experimental and theoretical constraints. *Rev Mineral Geochem*, *75*, 109-148.

Markl, G., Von Blanckenburg, F., & Wagner, T. (2006). Iron isotope fractionation during hydrothermal ore deposition and alteration. *Geochimica et Cosmochimica Acta*, *70*(12), 3011-3030.

Martin, A. P., Cooper, A. F., & Price, R. C. (2013). Petrogenesis of Cenozoic, alkalic volcanic lineages at Mount Morning, West Antarctica and their entrained lithospheric mantle xenoliths: Lithospheric versus asthenospheric mantle sources. *Geochimica et Cosmochimica Acta*, *122*, 127-152.

Martin, L. H., Schmidt, M. W., Mattsson, H. B., & Guenther, D. (2013). Element partitioning between immiscible carbonatite and silicate melts for dry and H2O-bearing systems at 1–3 GPa. *Journal of Petrology*, egt048.

Matthews, A., & Katz, A. (1977). Oxygen isotope fractionation during the dolomitization of calcium carbonate. *Geochimica et Cosmochimica Acta*, *41*(10), 1431-1438.

McCuaig, T. C., & Kerrich, R. (1998). P—T—t—deformation—fluid characteristics of lode gold deposits: evidence from alteration systematics. *Ore Geology Reviews*, *12*(6), 381-453.

McNeil, A. M., & Kerrich, R. (1986). Archean lamprophyre dykes and gold mineralization, Matheson, Ontario: the conjunction of LILE-enriched mafic magmas, deep crustal structures, and Au concentration. *Canadian Journal of Earth Sciences*, *23*(3), 324-343.

Menzies, C. D., Teagle, D. A., Craw, D., Cox, S. C., Boyce, A. J., Barrie, C. D., & Roberts, S. (2014). Incursion of meteoric waters into the ductile regime in an active orogen. *Earth and Planetary Science Letters*, *399*, 1-13.

Menzies, C. D., Teagle, D. A., Niedermann, S., Cox, S. C., Craw, D., Zimmer, M., ... & Erzinger, J. (2016). The fluid budget of a continental plate boundary fault: Quantification from the Alpine Fault, New Zealand. *Earth and Planetary Science Letters*, *445*, 125-135.

Michard, A. (1989). Rare earth element systematics in hydrothermal fluids. *Geochimica et Cosmochimica Acta*, *53*(3), 745-750.

Michard, A., & Albarede, F. (1986). The REE content of some hydrothermal fluids. *Chemical Geology*, *55*(1-2), 51-60.

Migdisov, A. A., & Williams-Jones, A. E. (2007). An experimental study of the solubility and speciation of neodymium (III) fluoride in F-bearing aqueous solutions. *Geochimica et Cosmochimica Acta*, *71*(12), 3056-3069.

Migdisov, A. A., Williams-Jones, A. E., & Wagner, T. (2009). An experimental study of the solubility and speciation of the Rare Earth Elements (III) in fluoride-and chloride-bearing aqueous solutions at temperatures up to 300 C. *Geochimica et Cosmochimica Acta*, *73*(23), 7087-7109.

Migdisov, A., Williams-Jones, A. E., Brugger, J., & Caporuscio, F. A. (2016). Hydrothermal transport, deposition, and fractionation of the REE: Experimental data and thermodynamic calculations. *Chemical Geology*.

Möller, P., Lüders, V., Schröder, J., & Luck, J. (1991). Element partitioning in calcite as a function of solution flow rate: a study on vein calcites from the Harz Mountains. *Mineralium Deposita*, *26*(3), 175-179.

Mook, W. G., Bommerson, J. C., & Staverman, W. H. (1974). Carbon isotope fractionation between dissolved bicarbonate and gaseous carbon dioxide. *Earth and Planetary Science Letters*, *22*(2), 169-176.

Morey, A. A., Tomkins, A. G., Bierlein, F. P., Weinberg, R. F., & Davidson, G. J. (2008). Bimodal distribution of gold in pyrite and arsenopyrite: examples from the Archean Boorara and Bardoc shear systems, Yilgarn Craton, Western Australia. *Economic Geology*, *103*(3), 599-614.

Morey, G. W., Fournier, R. O., & Rowe, J. J. (1962). The solubility of quartz in water in the temperature interval from 25 to 300 C. *Geochimica et Cosmochimica Acta*, *26*(10), 1029-1043.

Mortensen, J. K., Craw, D., MacKenzie, D. J., Gabites, J. E., & Ullrich, T. (2010). Age and origin of orogenic gold mineralization in the Otago Schist Belt, South Island, New Zealand: Constraints from lead isotope and 40Ar/39Ar dating studies. *Economic Geology*, *105*(4), 777-793.

Mortimer, N. (2000). Metamorphic discontinuities in orogenic belts: example of the garnet–biotite–albite zone in the Otago Schist, New Zealand. *International journal of earth sciences*, *89*(2), 295-306.

Mortimer, N. (2004). New Zealand's geological foundations. *Gondwana Research*, *7*(1), 261-272.

Mortimer, N., & Roser, B. P. (1992). Geochemical evidence for the position of the Caples–Torlesse boundary in the Otago Schist, New Zealand. *Journal of the Geological Society*, *149*(6), 967-977.

Mumin, A.H., Fleet, M.E:, Chryssoulis, S.l. (1994) Gold mineralization in As-rich mesothermal gold ores of the Bogosu-Prestea mining district of the Ashanti Gold Belt, Ghana: remobilization of ?invisible? gold. Mineralium deposita , Vol.29(6), p.445-460.

Nedli, Z., & Tóth, T. M. (2003). Petrography and mineral chemistry of rhönite in ocelli of alkali basalt from Villány Mts, SW Hungary. *Acta Mineralogica-Petrographica*, *44*, 51-56.

Nesbitt, B. E., & Muehlenbachs, K. (1989). Geology, geochemistry, and genesis of mesothermal lode gold deposits of the Canadian Cordillera: Evidence for ore formation from evolved meteoric water. *Econ Geol Mon*, *6*, 553-563.

Nesbitt, B. E., Muehlenbachs, K., & Murowchick, J. B. (1989). Genetic implications of stable isotope characteristics of mesothermal Au deposits and related Sb and Hg deposits in the Canadian Cordillera. *Economic Geology*, *84*(6), 1489-1506.

Nesbitt, B. E., Murowchick, J. B., & Muehlenbachs, K. (1986). Dual origins of lode gold deposits in the Canadian Cordillera. *Geology*, *14*(6), 506-509.

Norris, R. J., & Bishop, D. G. (1990). Deformed conglomerates and textural zones in the Otago schists, South Island, New Zealand. *Tectonophysics*, *174*(3-4), 331-349.

Norris, R. J., & Cooper, A. F. (2001). Late Quaternary slip rates and slip partitioning on the Alpine Fault, New Zealand. *Journal of Structural Geology*, *23*(2), 507-520.

Norris, R. J., Carter, R. M., & Turnbull, I. M. (1978). Cainozoic sedimentation in basins adjacent to a major continental transform boundary in southern New Zealand. *Journal of the Geological Society*, *135*(2), 191-205.

Oelkers, E. H., & Poitrasson, F. (2002). An experimental study of the dissolution stoichiometry and rates of a natural monazite as a function of temperature from 50 to 230 C and pH from 1.5 to 10. *Chemical Geology*, *191*(1), 73-87.

Oelkers, E. H., Gislason, S. R., & Matter, J. (2008). Mineral carbonation of CO2. *Elements*, *4*(5), 333-337.

Ohmoto, H.; and Rye, R.O. (1979) Isotopes of sulfur and carbon; In H.L. Barnes (Ed.) Geochemistry of hydrothermal ore deposits, 509-561

Ohta, A., & Kawabe, I. (2000). Rare earth element partitioning between Fe oxyhydroxide precipitates and aqueous NaCl solutions doped with NaHCO3: Determinations of rare earth element complexation constants with carbonate ions. *Geochemical Journal*, *34*(6), 439-454.

O'Neil, J.R., Clayton, R.N. and Mayeda, T.K. (1969). Oxygen isotope fractionation in divalent metal carbonates; J. Chem. Phys. 51(12), 5547-5558

Ordóñez-Calderón, J. C., Polat, A., Fryer, B. J., Gagnon, J. E., Raith, J. G., & Appel, P. W. U. (2008). Evidence for HFSE and REE mobility during calc-silicate metasomatism, Mesoarchean (~ 3075Ma) Ivisaartoq greenstone belt, southern West Greenland. *Precambrian Research*, *161*(3), 317-340.

Pan, Y. U. A. N. M. I. N. G., & Fleet, M. E. (1996). Rare earth element mobility during prograde granulite facies metamorphism: significance of fluorine. *Contributions to Mineralogy and Petrology*, *123*(3), 251-262.

Pan, Y., Fleet, M. E., & MacRae, N. D. (1993). Late alteration in titanite (CaTiSiO5): redistribution and remobilization of rare earth elements and implications for U/Pb and Th/Pb geochronology and nuclear waste disposal. *Geochimica et Cosmochimica Acta*, *57*(2), 355-367.

Pauwels, H., Fouillac, C., & Fouillac, A. M. (1993). Chemistry and isotopes of deep geothermal saline fluids in the Upper Rhine Graben: Origin of compounds and water-rock interactions. *Geochimica et Cosmochimica Acta*, *57*(12), 2737-2749.

Pearce, M. A., Timms, N. E., Hough, R. M., & Cleverley, J. S. (2013). Reaction mechanism for the replacement of calcite by dolomite and siderite: implications for geochemistry, microstructure and porosity evolution during hydrothermal mineralisation. *Contributions to Mineralogy and Petrology*, *166*(4), 995-1009.

Perdikouri, C., Piazolo, S., Kasioptas, A., Schmidt, B. C., & Putnis, A. (2013). Hydrothermal replacement of Aragonite by Calcite: interplay between replacement, fracturing and growth. *European Journal of Mineralogy*, *25*(2), 123-136.

Person, M. and Garven, G. (1989). Hydrologic Constraints on the Thermal Evolution of the Rhine Graben, in Hydrogeological Regimes and Their Subsurface Thermal Effects (eds A. E. Beck, G. Garven and L. Stegena), American Geophysical Union, Washington, D. C.. Vol 47

Phillips, G. N. (1986). Geology and alteration in the Golden Mile, Kalgoorlie. *Economic Geology*, *81*(4), 779-808.

Phillips, G. N. (1986). Geology and alteration in the Golden Mile, Kalgoorlie. *Economic Geology*, *81*(4), 779-808.

Phillips, G. N., & Evans, K. A. (2004). Role of CO2 in the formation of gold deposits. *Nature*, *429*(6994), 860-863.

Phillips, G. N., & Powell, R. (2010). Formation of gold deposits: a metamorphic devolatilization model. *Journal of Metamorphic Geology*, *28*(6), 689-718.

Pin, C., Joannon, S., Bosq, C., Le Fèvre, B., & Gauthier, P. J. (2003). Precise determination of Rb, Sr, Ba, and Pb in geological materials by isotope dilution and ICP-quadrupole mass spectrometry following selective separation of the analytes. *Journal of analytical atomic spectrometry*, *18*(2), 135-141.

Pitcairn, I. K., Teagle, D. A., Craw, D., Olivo, G. R., Kerrich, R., & Brewer, T. S. (2006). Sources of metals and fluids in orogenic gold deposits: insights from the Otago and Alpine Schists, New Zealand. *Economic Geology*, *101*(8), 1525-1546.

Pitcairn, I.K.. (2004). Sources of fluids and metals in orogenic gold deposits:The Otago schists, New Zealand: Unpublished Ph.D. thesis, Southampton, U.K., University of Southampton, 362 p.

Poitrasson, F., Oelkers, E., Schott, J., & Montel, J. M. (2004). Experimental determination of synthetic NdPO 4 monazite end-member solubility in water from 21 C to 300 C: Implications for rare earth element mobility in crustal fluids. *Geochimica et Cosmochimica Acta*, *68*(10), 2207-2221.

Pokrovski, G. S., Kara, S., & Roux, J. (2002). Stability and solubility of arsenopyrite, FeAsS, in crustal fluids. *Geochimica et Cosmochimica Acta*, *66*(13), 2361-2378.
Prewitt, C. T., Sueno, S., & Papike, J. J. (1976). The crystal structures of high albite and monalbite at high temperatures. *American Mineralogist*, *61*(11-12), 1213-1225.
Pribnow, D., & Schellschmidt, R. (2000). Thermal tracking of upper crustal fluid flow in the Rhine Graben. *Geophysical Research Letters*, *27*(13), 1957-1960.
Putnis, A. (2002). Mineral replacement reactions: from macroscopic observations to microscopic mechanisms. *Mineralogical Magazine*, *66*(5), 689-708.
Putnis, A. (2009). Mineral replacement reactions. *Reviews in mineralogy and geochemistry*, *70*(1), 87-124.
Putnis, C. V., & Mezger, K. (2004). A mechanism of mineral replacement: isotope tracing in the model system KCl-KBr-H 2 O. *Geochimica et Cosmochimica Acta*, *68*(13), 2839-2848.
Ragnarsdóttir, K. V., & Walther, J. V. (1985). Experimental determination of corundum solubilities in pure water between 400–700 C and 1–3 kbar. *Geochimica et Cosmochimica Acta*, *49*(10), 2109-2115.
Ramos, F. C., & Rosenberg, P. E. (2012). Age and origin of quartz-carbonate veins associated with the Coeur d'Alene mining district, Idaho and western Montana: insights from isotopes and rare-earth elements. *Economic Geology*, *107*(6), 1321-1339.
Ratschbacher, L., Merle, O., Davy, P. & Cobbold, P. (1991) Lateral extrusion in the Eastern Alps, Part 1: Boundary conditions and experiments scaled for gravity. Tectonics. 10.2. 245-256.
Ratschbacher, L., Merle, O., Davy, P. & Cobbold, P. (1991). Lateral extrusion in the Eastern Alps, Part 1: boundary conditions and experiments scaled for gravity. Tectonics. 10(2). 245-256.
Raufaste, C., Jamtveit, B., John, T., Meakin, P., & Dysthe, D. K. (2011, May). The mechanism of porosity formation during solvent-mediated phase transformations. In *Proceedings of the Royal Society of London A: Mathematical, Physical and Engineering Sciences* (Vol. 467, No. 2129, pp. 1408-1426). The Royal Society.
Reyes, A. G., Christenson, B. W., & Faure, K. (2010). Sources of solutes and heat in low-enthalpy mineral waters and their relation to tectonic setting, New Zealand. *Journal of Volcanology and Geothermal Research*, *192*(3), 117-141.
Richardson, S.M. & Richardson, J.W. (1982). Crystal structure of a pink muscovite from Archer's Post, Kenya: implications for reverse pleochroism in dioctahedral micas. *American Mineralogist. 67.* 69-75.
Rimstidt, J. D., Balog, A., & Webb, J. (1998). Distribution of trace elements between carbonate minerals and aqueous solutions. *Geochimica et Cosmochimica Acta*, *62*(11), 1851-1863.
Rimstidt, J.D. (1997) Chapter 10-Gangue Mineral Transport and deposition. Ed. Barnes, H.L. (1997) Geochemistry of hydrothermal ore deposits. 3rd edition, John Wiley &Sons inc. 972. Pages. 487-515
Rock, N. M., & Groves, D. I. (1988). Can lamprophyres resolve the genetic controversy over mesothermal gold deposits?. *Geology*, *16*(6), 538-541.
Rolland, Y., Cox, S., Boullier, A. M., Pennacchioni, G., & Mancktelow, N. (2003). Rare earth and trace element mobility in mid-crustal shear zones: insights from the Mont Blanc Massif (Western Alps). *Earth and Planetary Science Letters*, *214*(1), 203-219.
Rosenbaum, J., & Sheppard, S. M. F. (1986). An isotopic study of siderites, dolomites and ankerites at high temperatures. *Geochimica et Cosmochimica Acta*, *50*(6), 1147-1150.
Rosenberg, P. E., & Holland, H. D. (1964). Calcite-dolomite-magnesite stability relations in solutions at elevated temperatures. *Science*, *145*(3633), 700-701.
Roser, B. P., & Cooper, A. F. (1990). Geochemistry and terrane affiliation of Haast Schist from the western Southern Alps, New Zealand. *New Zealand journal of geology and geophysics*, *33*(1), 1-10.
Ross, P. S., & White, J. D. (2006). Debris jets in continental phreatomagmatic volcanoes: a field study of their subterranean deposits in the Coombs Hills vent complex, Antarctica. *Journal of Volcanology and Geothermal Research*, *149*(1), 62-84.

Ross, P. S., White, J. D., Zimanowski, B., & Büttner, R. (2008). Multiphase flow above explosion sites in debris-filled volcanic vents: insights from analogue experiments. *Journal of Volcanology and Geothermal Research*, *178*(1), 104-112.

Rouxel, O., Dobbek, N., Ludden, J., & Fouquet, Y. (2003). Iron isotope fractionation during oceanic crust alteration. *Chemical Geology*, *202*(1), 155-182.

Rupert Sutherland (1999) Cenozoic bending of New Zealand basementterranes and Alpine Fault displacement: A brief review, New Zealand Journal of Geology andGeophysics, 42:2, 295-301,

Saldi, G. D., Daval, D., Guo, H., Guyot, F., Bernard, S., Le Guillou, C., ... & Knauss, K. G. (2015). Mineralogical evolution of Fe–Si-rich layers at the olivine-water interface during carbonation reactions. *American Mineralogist*, *100*(11-12), 2655-2669.

Schwartz, G. M. (1958). Alteration of biotite under mesothermal conditions. *Economic Geology*, *53*(2), 164-177.

Segnit, E. R., Holland, H. D., & Biscardi, C. J. (1962). The solubility of calcite in aqueous solutions—I The solubility of calcite in water between 75° and 200° at CO 2 pressures up to 60 atm. *Geochimica et Cosmochimica Acta*, *26*(12), 1301-1331.

Seward, T. M., Williams-Jones, A. E., & Migdisov, A. A. (2014). 13.2 The Chemistry of Metal Transport and Deposition by Ore-Forming Hydrothermal Fluids.

Seyfried, W. E., & Ding, K. (1993). The effect of redox on the relative solubilities of copper and iron in Cl-bearing aqueous fluids at elevated temperatures and pressures: an experimental study with application to subseafloor hydrothermal systems. *Geochimica et Cosmochimica Acta*, *57*(9), 1905-1917.

Shannon, R. T. (1976). Revised effective ionic radii and systematic studies of interatomic distances in halides and chalcogenides. *Acta Crystallographica Section A: Crystal Physics, Diffraction, Theoretical and General Crystallography*, *32*(5), 751-767.

Sharp, Z. D., & Kirschner, D. L. (1994). Quartz-calcite oxygen isotope thermometry: A calibration based on natural isotopic variations. *Geochimica et Cosmochimica Acta*, *58*(20), 4491-4501.

Shiro, Y., & Sakai, H. (1972). Calculation of the reduced partition function ratios of α-, β-quartzs and calcite. *Bulletin of the Chemical Society of Japan*, *45*(8), 2355-2359.

Siever, R. (1962). Silica solubility, 0-200 C., and the diagenesis of siliceous sediments. *The Journal of Geology*, 127-150.

Skublov, S., & Drugova, G. (2003). Patterns of trace-element distribution in calcic amphiboles as a function of metamorphic grade. *The Canadian Mineralogist*, *41*(2), 383-392.

Smith, D. (1977). The origin and interpretation of spinel-pyroxene clusters in peridotite. *The Journal of Geology*, 476-482.

Smith, M. P., Gleeson, S. A., & Yardley, B. W. D. (2013). Hydrothermal fluid evolution and metal transport in the Kiruna District, Sweden: contrasting metal behaviour in aqueous and aqueous–carbonic brines. *Geochimica et cosmochimicaacta*, *102*, 89-112.

Somasundaran, P., Amankonah, J. O., & Ananthapadmabhan, K. P. (1985). Mineral—solution equilibria in sparingly soluble mineral systems. *Colloids and Surfaces*, *15*, 309-333.

Spandler, C., Hermann, J., Arculus, R., & Mavrogenes, J. (2003). Redistribution of trace elements during prograde metamorphism from lawsonite blueschist to eclogite facies; implications for deep subduction-zone processes. *Contributions to Mineralogy and Petrology*, *146*(2), 205-222.

Spear, F.S. (1993) Metamorphic processes: Michigan, Bookcrafters, Mineralogical Society of America Monograph Series 1, 799 p

Stipp, M., StuÈnitz, H., Heilbronner, R., & Schmid, S. M. (2002). The eastern Tonale fault zone: a 'natural laboratory'for crystal plastic deformation of quartz over a temperature range from 250 to 700 C. *Journal of Structural Geology*, *24*(12), 1861-1884.

Stosch, H. G. (2002). Geochemie der Seltenen Erden: Skript zur Vorlesung am Mineralogisch-Petrographischen Institut der Universität zu Köln, 1988–1993, Skript mit Ergänzungen von 1998 und Sommer 2000.

Sun, W., Nešić, S., & Woollam, R. C. (2009). The effect of temperature and ionic strength on iron carbonate (FeCO 3) solubility limit. *Corrosion Science*, *51*(6), 1273-1276.

Sutherland, R. (1995) The Australia-Pacific boundary and Cenozoic plate motions in the SW Pacific: Some constraints from Geosat data. TECTONICS, VOL. 14, 4, PAGES 819-831.
Tagirov, B. & Schott, J. (2001) Aluminium speciation in crustal fluids revisted. Geochim. Cosmo. Acta. 65,21. 3965-3992.
Tapponnier, P., Peltzer, G., Le Dain, A.Y., Armijo, R. & Cobbold, P. (1982) Propagating extrusion tectonics in Asia: New insights from simple experiments with pasticine. Geology. 10. 611-616.
Taylor, H. P., & Epstein, S. (1962). Relationship Between O18/O16 Ratios in Coexisting Minerals of Igneous and Metamorphic Rocks Part 1: Principles and Experimental Results. *Geological Society of America Bulletin*, *73*(4), 461-480.
Taylor, W. R., Rock, N. M., Groves, D. I., Perring, C. S., & Golding, S. D. (1994). Geochemistry of Archean shoshonitic lamprophyres from the Yilgarn Block, Western Australia: Au abundance and association with gold mineralization. *Applied geochemistry*, *9*(2), 197-222.
Templeton, A. S., Chamberlain, C. P., Koons, P. O., & Craw, D. (1998). Stable isotopic evidence for mixing between metamorphic fluids and surface-derived waters during recent uplift of the Southern Alps, New Zealand. *Earth and Planetary Science Letters*, *154*(1), 73-92.
Terada, Y., Nakai, I., & Kawashima, T. (1993). Instrumental Achievements Crystal Structure of Bastnaesite (Ce, La, Nd, Sm, Gd) CO 3 F. *Analytical sciences*, *9*(4), 561-562.
Terakado, Y., & Masuda, A. (1988). The coprecipitation of rare-earth elements with calcite and aragonite. *Chemical Geology*, *69*(1), 103-110.
Tippett, J. M., & Kamp, P. J. (1993). The role of faulting in rock uplift in the Southern Alps, New Zealand. *New Zealand journal of geology and geophysics*, *36*(4), 497-504.
Tosdal, R. M., Dilles, J. H., & Cooke, D. R. (2009). From source to sinks in auriferous magmatic-hydrothermal porphyry and epithermal deposits. *Elements*, *5*(5), 289-295.
Townsend, P. D., & Rowlands, A. P. (2000). Information encoded in cathodoluminescence emission spectra. In *Cathodoluminescence in Geosciences* (pp. 41-57). Springer Berlin Heidelberg.
Turnbull, I. M. (2000). Geology of the Wakatipu Area. Institute of Geological & Nuclear Sciences 1: 250,000 Geological Map 18. *Institute of Geological & Nuclear Sciences Limited. Lower Hutt, New Zealand*, *1*.
Turnbull, I. M., Barry, J. M., Carter, R. M., & Norris, R. J. (1975). The Bobs Cove beds and their relationship to the Moonlight Fault Zone. *Journal of the Royal Society of New Zealand*, *5*(4), 355-394.
Turnbull, I. M., Mortimer, N., & Craw, D. (2001). Textural zones in the Haast Schist—a reappraisal. *New Zealand Journal of Geology and Geophysics*, *44*(1), 171-183.
Upton, P., Koons, P. O., & Chamberlain, C. P. (1995). Penetration of deformation-driven meteoric water into ductile rocks: isotopic and model observations from the Southern Alps, New Zealand. *New Zealand Journal of Geology and Geophysics*, *38*(4), 535-543.
Valentine, G. A., & White, J. D. (2012). Revised conceptual model for maar-diatremes: Subsurface processes, energetics, and eruptive products. *Geology*, *40*(12), 1111-1114.
Valsami-Jones, E., Ragnarsdottir, K. V., Putnis, A. A. A., Bosbach, D., Kemp, A. J., & Cressey, G. (1998). The dissolution of apatite in the presence of aqueous metal cations at pH 2–7. *Chemical Geology*, *151*(1), 215-233.
Veksler, I. V., Dorfman, A. M., Dulski, P., Kamenetsky, V. S., Danyushevsky, L. V., Jeffries, T., & Dingwell, D. B. (2012). Partitioning of elements between silicate melt and immiscible fluoride, chloride, carbonate, phosphate and sulfate melts, with implications to the origin of natrocarbonatite. *Geochimica et Cosmochimica Acta*, *79*, 20-40.
Vogel, J. C., Grootes, P. M., & Mook, W. G. (1970). Isotopic fractionation between gaseous and dissolved carbon dioxide. *Zeitschrift für Physik*, *230*(3), 225-238.
Vry, J., Powell, R., Golden, K. M., & Petersen, K. (2010). The role of exhumation in metamorphic dehydration and fluid production. *Nature Geoscience*, *3*(1), 31-35.
Walker, F. D. L., Lee, M. R., & Parsons, I. (1995). Micropores and micropermeable texture in alkali feldspars: geochemical and geophysical implications. *Mineralogical Magazine*, *59*(3), 505-534.

Wallace, R. C. (1975). Mineralogy and petrology of xenoliths in a diatreme from South Westland, New Zealand. *Contributions to mineralogy and petrology*, *49*(3), 191-199.
Walther JV, Orville P (1983). The extraction-quench technique for determination of the thermodynamic properties of solute complexes: application to quartz solubility in fluid mixtures. American Mineralogist, 68, 731–41.
Wang, Y., & Xu, H. (2001). Prediction of trace metal partitioning between minerals and aqueous solutions: a linear free energy correlation approach. *Geochimica et Cosmochimica Acta*, *65*(10), 1529-1543.
Wang, Y., & Xu, H. (2001). Prediction of trace metal partitioning between minerals and aqueous solutions: a linear free energy correlation approach. *Geochimica et Cosmochimica Acta*, *65*(10), 1529-1543.
Wang, Y., Wang, Y., & Merino, E. (1995). Dynamic weathering model: Constraints required by coupled dissolution and pseudomorphic replacement. *Geochimica et Cosmochimica Acta*, *59*(8), 1559-1570.
Watson, E. B., Chemiak, D. J., Hanchar, J. M., Harrison, T. M., & Wark, D. A. (1997). The incorporation of Pb into zircon. *Chemical Geology*, *141*(1), 19-31.
Wedepohl, K. H. (1995). The composition of the continental crust. *Geochimica et cosmochimica Acta*, *59*(7), 1217-1232.
Weinberger, R., Eyal, Y., & Mortimer, N. (2010). Formation of systematic joints in metamorphic rocks due to release of residual elastic strain energy, Otago Schist, New Zealand. *Journal of Structural Geology*, *32*(3), 288-305.
Weis, D., Kieffer, B., Maerschalk, C., Barling, J., de Jong, J., Williams, G. A., ... & Goolaerts, A. (2006). High-precision isotopic characterization of USGS reference materials by TIMS and MC-ICP-MS. *Geochemistry, Geophysics, Geosystems*, *7*(8).
White, J. D., & Ross, P. S. (2011). Maar-diatreme volcanoes: a review. *Journal of Volcanology and Geothermal Research*, *201*(1), 1-29.
White, R. W., Powell, R., & Phillips, G. N. (2003). A mineral equilibria study of the hydrothermal alteration in mafic greenschist facies rocks at Kalgoorlie, Western Australia. *Journal of Metamorphic Geology*, *21*(5), 455-468.
White, S. R. (2002). The Siberia Fault Zone, northwest Otago, and kinematics of mid-Cenozoic plate boundary deformation in southern New Zealand. *New Zealand Journal of Geology and Geophysics*, *45*(2), 271-287.
White, S.R. (1998). The mid-Cenozoic Siberia Fault Zone (SFZ), northwest Otago, New Zealand, and study of greenschist facies metamorphism in Haast Schist. PhD Thesis. University of Otago, New Zealand.
Wigley, T. M. L. (1973). The incongruent solution of dolomite. *Geochimica et Cosmochimica Acta*, *37*(5), 1397-1402.
Will, T. M., Powell, R., Holland, T., & Guiraud, M. (1990). Calculated greenschist facies mineral equilibria in the system CaO− FeO− MgO− Al2O3− SiO2− CO2− H2O. *Contributions to Mineralogy and Petrology*, *104*(3), 353-368.
Willey, J. D. (1974). The effect of pressure on the solubility of amorphous silica in seawater at 0 C. *Marine Chemistry*, *2*(4), 239-250.
Winter, J. D. (2001). An introduction to igneous and metamorphic petrology.
Wood, S. A. (2006). Rare earth element systematics of acidic geothermal waters from the Taupo Volcanic Zone, New Zealand. *Journal of Geochemical Exploration*, *89*(1), 424-427.
Yardley, B. W. D. Banks, D. A. Bottrell S. H. & Diamond, L.W.(1993) Post-metamorphic gold-quartz veins from N.W. Italy: the composition and origin of the ore fluid Mineralogical Magazine, September 1993, VoL 57, pp. 407-422
Yardley, B. W., & Lloyd, G. E. (1995). Why metasomatic fronts are really metasomatic sides. *Geology*, *23*(1), 53-56.
Zhang, Y., & Xu, Z. (1995). Atomic radii of noble gas elements in condensed phases. *American Mineralogist*, *80*(7-8), 670-675.

Zheng, Y. F. (1993). Calculation of oxygen isotope fractionation in anhydrous silicate minerals. *Geochimica et Cosmochimica Acta*, *57*, 1079-1079.

Zheng, Y.F. (1994) Oxygen isotope fractionation in metal monoxides; Mineral. Mag. 58A, 1000-1001

Zhong, S., & Mucci, A. (1995). Partitioning of rare earth elements (REEs) between calcite and seawater solutions at 25 C and 1 atm, and high dissolved REE concentrations. *Geochimica et Cosmochimica Acta*, *59*(3), 443-453.